MICROALGAE BIOLOGY AND BIOTECHNOLOGY

EDITED BY: Matteo Ballottari, EonSeon Jin, Dimitris Petroutsos and Lutz Wobbe
PUBLISHED IN: Frontiers in Plant Science

frontiers Research Topics

frontiers

ISSN 1664-8714
ISBN 978-2-88966-527-3
DOI 10.3389/978-2-88966-527-3

About Frontiers

Frontiers is more than just an open-access publisher of scholarly articles: it is a pioneering approach to the world of academia, radically improving the way scholarly research is managed. The grand vision of Frontiers is a world where all people have an equal opportunity to seek, share and generate knowledge. Frontiers provides immediate and permanent online open access to all its publications, but this alone is not enough to realize our grand goals.

Frontiers Journal Series

The Frontiers Journal Series is a multi-tier and interdisciplinary set of open-access, online journals, promising a paradigm shift from the current review, selection and dissemination processes in academic publishing. All Frontiers journals are driven by researchers for researchers; therefore, they constitute a service to the scholarly community. At the same time, the Frontiers Journal Series operates on a revolutionary invention, the tiered publishing system, initially addressing specific communities of scholars, and gradually climbing up to broader public understanding, thus serving the interests of the lay society, too.

Dedication to Quality

Each Frontiers article is a landmark of the highest quality, thanks to genuinely collaborative interactions between authors and review editors, who include some of the world's best academicians. Research must be certified by peers before entering a stream of knowledge that may eventually reach the public - and shape society; therefore, Frontiers only applies the most rigorous and unbiased reviews.
Frontiers revolutionizes research publishing by freely delivering the most outstanding research, evaluated with no bias from both the academic and social point of view. By applying the most advanced information technologies, Frontiers is catapulting scholarly publishing into a new generation.

What are Frontiers Research Topics?

Frontiers Research Topics are very popular trademarks of the Frontiers Journals Series: they are collections of at least ten articles, all centered on a particular subject. With their unique mix of varied contributions from Original Research to Review Articles, Frontiers Research Topics unify the most influential researchers, the latest key findings and historical advances in a hot research area! Find out more on how to host your own Frontiers Research Topic or contribute to one as an author by contacting the Frontiers Editorial Office: frontiersin.org/about/contact

MICROALGAE BIOLOGY AND BIOTECHNOLOGY

Topic Editors:
Matteo Ballottari, University of Verona, Italy
EonSeon Jin, Hanyang University, South Korea
Dimitris Petroutsos, UMR5168 Laboratoire de Physiologie Cellulaire Vegetale (LPCV), France
Lutz Wobbe, Bielefeld University, Germany

Citation: Ballottari, M., Jin, E., Petroutsos, D., Wobbe, L., eds. (2021). Microalgae Biology and Biotechnology. Lausanne: Frontiers Media SA.
doi: 10.3389/978-2-88966-527-3

Table of Contents

frontiers in Plant Science

EDITORIAL
published: 18 January 2021
doi: 10.3389/fpls.2020.628267

Editorial: Microalgae Biology and Biotechnology

Dimitris Petroutsos[1], *Lutz Wobbe*[2], *EonSeon Jin*[3] *and Matteo Ballottari*[4]*

[1] Univ. Grenoble Alpes, CNRS, CEA, INRAe, IRIG-LPCV, Grenoble, France, [2] Center for Biotechnology (CeBiTec), Faculty of Biology, Bielefeld University, Bielefeld, Germany, [3] Department of Life Science, Hanyang University, Seoul, South Korea, [4] Department of Biotechnology, University of Verona, Verona, Italy

Keywords: microalgae, cyanobacteria, genetic engineering, terpenoids, triacylglycerols, CRISPR-Cas9

Editorial on the Research Topic

Microalgae Biology and Biotechnology

The interest for industrial exploitation of microalgae dates back to the end of the last century. The combination of the light energy-capturing ability of photosynthesis with the high yields of controlled microbial cultivation make microalgae potentially valuable organisms for economical, industrial-scale production processes in areas including nutrition, aquaculture, pharmaceuticals, and biofuels. Moreover, microalgae allow to produce biomass even in not arable land, exploiting the light energy available marginal areas. Several national and international research programs were deeply involved in the investigation of microalgae biodiversity and their characterization. More recently, strong efforts were reported by the scientific community for the development of biotechnological tools and omics data required to domesticate and improve microalgae strains for their applicative use. Several microalgal species were indeed included among the possible "novel food" sources for human consumption and some strains are nowadays considered for high-value metabolites to be used in the cosmetic sector, for fish/animal feed, for the production of bioplastics, drugs, or other commodities. Microalgae also have a high potential for environmental applications, being used as biostimulants, fertilizers and/or biopesticides in agriculture, reducing the negative environmental impact of fertilizers and pesticides. Finally, the potential use of microalgae biomass for biofuels has been considered, even if more research efforts are still required to achieve sustainability of this application.

This Research Topic highlights recent advances in the comprehension of microalgae biology, which is necessary to design strategies for their biotechnological application. Despite the great biodiversity of microalgae, most of the research described is focused on a few tens' species. The work by Wang et al. proved an example of light-driven changes of phytoplankton population in an eutrophic highland lake in China. Significant positive relationships were observed between taxonomic diversity and functional diversity of phytoplankton, which were positively correlated with light conditions. Bioprospecting of natural species is an important task for the microalgae research communities in order to find new species and new metabolic features to expand the potential of microalgae for their biotechnological application. Kareya et al. investigated the molecular mechanisms of the CO_2-driven carbon partitioning in the marine oleaginous microalgae *Microchloropsis gaditana* NIES 2587. The results obtained identified the key metabolites and the key metabolic pathways affected by high/low availability of CO_2: this information could then be used to re-direct the carbon flow to improve the metabolic efficiency of target metabolic products.

OPEN ACCESS

Edited by:
Paulo Arruda,
Campinas State University, Brazil

Reviewed by:
Jean-Philippe Steyer,
Institut National de Recherche pour l'agriculture, l'alimentation et l'environnement (INRAE), France

***Correspondence:**
Matteo Ballottari
matteo.ballottari@univr.it

Specialty section:
This article was submitted to Plant Biotechnology, a section of the journal Frontiers in Plant Science

Received: *11 November 2020*
Accepted: *22 December 2020*
Published: *18 January 2021*

Citation:
Petroutsos D, Wobbe L, Jin E and Ballottari M (2021) Editorial: Microalgae Biology and Biotechnology. Front. Plant Sci. 11:628267. doi: 10.3389/fpls.2020.628267

The influence of the environmental conditions on the cell functions was also investigated in detail by Kuo et al., where the role of nitric oxide in the regulation of autophagy in *Chlamydomonas reinhardtii* was investigated. Autophagy and cell death are important events occurring in stress conditions that significantly influence biomass and metabolite productivity of microalgal cultures: the work herein reported demonstrates that nitric oxide mediated autophagy under lethal high light intensity. Resistance to high light and photooxidative stress is mainly related to antioxidants accumulation. In the work herein reported by Kim et al., the resistance to ROS was improved in the cyanobacterium *Synechococcus elongatus* PCC 7942 by overexpression of the enzyme Dehydroascorbate reductase (DHAR) which catalyzes the glutathione-dependent reduction of oxidized ascorbate. Carotenoids are other antioxidants strongly involved in the mitigation of oxidative stress. Carotenoids are produced in microalgal cells by the terpenoid biosynthetic pathway. Feng et al. report the crystal structure at 2.7Å of the cyanobacterial Geranylgeranyl Pyrophosphate Synthase (CrtE), one of the key enzymes involved in the formation of the terpene precursors, identifying also some specific residues involved in the catalytic activity.

Genetic engineering of microalgal strains requires specific and advanced tools, which are still lacking in many cases. Among the most critical tools for a successful modification of microalgal genomes are efficient and reliable selection markers, to be used for screening of transformed/mutated/edited colonies. In the study conducted by de Carpentier et al., a novel marker for *Chlamydomonas reinhardtii* is developed based on the resistance to the antibiotic blasticidin S, using the *Bacillus cereus* blasticidin S deaminase (BSR) gene. The identification of new selectable markers for the modification of microalgal genomes is important considering the endogenous resistance to specific antibiotics observed in several species, and the possibility to combine different constructs in a single strain, requiring multiple selection markers. Synthetic biology application requires, indeed, insertion of usually multiple genes in microalgae. As described in Shahar et al., the expression of heterologous genes in *C. reinhardtii* is strongly dependent on the copy number of the gene of interest. The possibility to generate site-specific mutants and gene overexpression in *C. reinhardtii* is here described by Kim et al., where an advanced method based on CRISPR-CAS9 mediated non-homologous end joining (NHEJ) is reported. The method reported is based on recombinant ribonucleoprotein CAS9 assembled *in vitro* and electroporated in *C. reinhardtii* cells potentially allow to generate mutants in any non-lethal gene. Moreover, it can be used to express a heterologous gene of interest avoiding position-effects. Besides important milestones being reached for the genetic engineering of several microalgal strains, in many cases transformation protocols still need to be set-up and optimized. In the case of the cyanobacterium *Synechocystis* multiple genome copies are present per cell, with the consequence that segregating mutations across all genome copies can be time-consuming: Pope et al. are here presenting a novel transformation protocol in the case of *Synechocystis* sp. PCC 6803 involving phosphate depletion which strongly reduce the time required to obtain fully segregated mutants.

Finally, this Research Topic reports some recent biotechnological application of specific microalgae strains for the production of target metabolites. The work by Hammel et al. describes a successful approach to improve biomass productivity in *C. reinhardtii* by overexpression of one of the Calvin-Benson cycle enzyme, the sedoheptulose-1,7-bisphosphatase (SBP1) which catalyzes a rate- limiting step of this carbon fixation cycle. Overexpression of SBP1 increases biomass yield and photosynthetic efficiency, thus representing a promising genetic engineering strategy for other microalgal species. Improvement of carbon fixation reactions requires also an efficient carbon storage capacity in order to be effective. In the work herein reported by Li et al. a strong increase in starch and biomass content was achieved in *C. reinhardtii* by overexpression of the regulatory gene Gcn5-Related N-Acetyltransferase, paving the way for future application of this regulatory system to boost starch accumulation. One of the other main macromolecules found in microalgal cells with storage function is lipids. The interest for lipids produced in microalgae is extremely high due to their potential use as biofuels or food feedstocks. In the work published by Muñoz et al. three enzymes involved in the Kennedy pathway, namely glycerol-3-phosphate acyltransferase (GPAT), lysophosphatidic acid acyltransferase (LPAT), and diacylglycerol acyltransferase (DGAT), which catalyze key steps in the formation of triacylglycerol, were overexpressed in *Neochloris oleoabundans*. The Kennedy pathway is the key metabolic process, required for the accumulation of triacylglyceroles (TAGs) in microalgal cells. The phenotype of single GPAT, LPAT, or DGAT overexpressor was characterized by an increased cellular TAG content without having a significant impact on the growth rate of the strains. Finally, in this Research Topic, genetic engineering approaches targeting cyanobacteria are reported showing the feasibility of D-lactate production by editing the photosynthetic alternative electron transport flows in a strain expressing a variant of the *C. reinhardtii* D-lactate dehydrogenase and an *E.coli* lactate permease (Selão et al.). Cyanobacteria are also here reported by Betterle et al., as an efficient platform for the production of biopharmaceutical and biotherapeutic proteins, demonstrating the possibility to produce interferon alpha-2 (IFN) protein up to 12% of total cellular protein in soluble form. IFN is a member of the Type I interferon cytokine family, well-known for its antiviral and anti-proliferative functions: the results achieved by Betterle et al. pave the way for sustainable production of biopharmaceutical proteins, including those with antiviral properties, by microalgae cultivation. Another class of important biomolecules.

In conclusion, this Research Topic covers representative aspects of the ongoing research on microalgae biology and biotechnology; these aspects span from the investigation of the molecular mechanisms of key cell functions to the development of advanced tools for genetic engineering, which collectively may allow to produce high-value products as food supplements, biopharmaceutical and biotherapeutic proteins or potentially biofuels.

AUTHOR CONTRIBUTIONS

MB draft the editorial text. DP, LW, and EJ revised and approved the final version of the editorial text. All authors contributed to the article and approved the submitted version.

FUNDING

This research was supported by the Korea CCS R&D Center (NRF-2014M1A8A1049273) funded by the Korean government (Ministry of Science and ICT) to EJ, the ERC Starting Grant SOLENALGAE (679814) to MB, HFSP (RGP0046/2018), GRAL LabEX GRAL (ANR-10-LABX-49-01), and ANR MetaboLIGHT (18-CE20-0006-01) to DP.

Conflict of Interest: The authors declare that the research was conducted in the absence of any commercial or financial relationships that could be construed as a potential conflict of interest.

frontiers in Plant Science

ORIGINAL RESEARCH
published: 29 November 2019
doi: 10.3389/fpls.2019.01573

Effect of Single and Combined Expression of *Lysophosphatidic Acid Acyltransferase, Glycerol-3-Phosphate Acyltransferase*, and *Diacylglycerol Acyltransferase* on Lipid Accumulation and Composition in *Neochloris oleoabundans*

Camilo F. Muñoz[1], Ruud A. Weusthuis[1], Sarah D'Adamo[1] and René H. Wijffels[1,2]*

[1] *Bioprocess Engineering, Wageningen University and Research, Wageningen, Netherlands,* [2] *Biosciences and Aquaculture, Nord University, Bodø, Norway*

OPEN ACCESS

Edited by:
EonSeon Jin, Hanyang University, South Korea

Reviewed by:
Enrique Martinez Force, Spanish National Research (CSIC) Spain
Jianhua Fan, East China University of Science and Technology, China

***Correspondence:**
Camilo F. Muñoz
camilo.munozsegovia@wur.nl

Specialty section:
This article was submitted to Plant Biotechnology, a section of the journal Frontiers in Plant Science

Received: *17 June 2019*
Accepted: *11 November 2019*
Published: *29 November 2019*

Citation:
Muñoz CF, Weusthuis RA, D'Adamo S and Wijffels RH (2019) Effect of Single and Combined Expression of Lysophosphatidic Acid Acyltransferase, Glycerol-3-Phosphate Acyltransferase, and Diacylglycerol Acyltransferase on Lipid Accumulation and Composition in Neochloris oleoabundans. Front. Plant Sci. 10:1573. doi: 10.3389/fpls.2019.01573

Microalgal lipids are promising feedstocks for food and biofuels. Since lipid production by microalgae is not yet economically feasible, genetic engineering is becoming a promising strategy to achieve higher lipid accumulation and productivities. Enzymes involved in the Kennedy pathway such as glycerol-3-phosphate acyltransferase (GPAT), lysophosphatidic acid acyltransferase (LPAT), and diacylglycerol acyltransferase (DGAT) catalyze key steps in the formation of triacylglycerol, which is the main constituent of lipids in *N. oleoabundans*. The overexpression of these enzymes in the targeted strain has a great potential to further increase their triacylglycerol content. We overexpressed single and multiple encoding genes for *LPAT*, *GPAT*, and *DGAT* from *Acutodesmus obliquus* in *N. oleoabundans*. Strains overexpressing single genes produced up to 52% and 45% g · gDW^{-1}, which corresponds to 1.3- and 1.4-fold increase in total fatty acids and triacylglycerols, respectively. The orchestrated expression of the three genes resulted in 49% and 39% g · gDW^{-1}, which is 1.2-folds increase in total fatty acids and triacylglycerols. Single expression of *LPAT*, *GPAT,* and *DGAT* genes resulted in higher lipid productivities during starvation without a significant effect on growth and photosynthetic activity during replete conditions. On the other hand, the simultaneous expression of *LPAT*, *GPAT,* and *DGAT* genes resulted in 52% lower growth rate, 14% lower photosynthetic activity and 4-folds increase in cell diameter. Moreover, the multigene expressing line showed a decrease in carbohydrates and protein content and an increase in pigments during nitrogen starved condition. The single and multiple expression of heterologous genes *LPAT*, *GPAT,* and *DGAT* showed to significantly enhanced the lipid accumulation in *N. oleoabundans*. Single gene expression resulted in higher lipid production and productivities without having a significant impact in the physiological status of the strains. This approach shows the potential for the generation of microalgal strains with higher economical potential for the production of lipids.

Keywords: biodiesel, triacylglycerol, *Neochloris oleoabundans*, green microalgae, glycerol-3-phosphate acyltransferase, lysophosphatidic acid acyltransferase, diacylglycerol acyltransferase

INTRODUCTION

The continuous growth of the world population is increasing the global demand for food and fuel. Current oil production derives mainly from oleaginous crops and non-renewable fossil reserves, whose utilization causes a negative environmental impact (Alptekin et al., 2014; Moody et al., 2014; Majidian et al., 2018). It has been shown that the use of biodiesel over fossil fuels decreases greenhouse gas emissions and crop cultivation for fuel production creates a direct competition with food and feed production (Gharabaghi et al., 2015; Hanaki and Portugal-Pereira, 2018). Additionally, agricultural crop cultivation for oil production requires large amounts of arable lands and fresh-water. In the last few decades, microalgae have attracted attention for their potential to become a sustainable renewable feedstock for food and fuel production (Griffiths and Harrison, 2009; Medipally et al., 2015). Microalgae are aquatic photosynthetic microorganisms, thus capable to use sunlight and water to fix CO_2 into biomass. Unlike higher plants, they do not need arable land and have significantly higher biomass yields and productivities (Brennan and Owende, 2010; Remmers et al., 2018). Moreover, some microalgal species can accumulate large amounts of triacylglycerol (TAG) as storage compounds, which can be converted into biodiesel by transesterification (Breuer et al., 2012; Benvenuti et al., 2017; Faried et al., 2017).

Oleaginous microalgae strains such as *Neochloris oleoabundans* can produce TAG up to 44% of their dry weight (Breuer et al., 2012). Since high production costs are currently involved in the process, yields, and productivities have to be improved in order to allow for full commercial scale production (Ruiz et al., 2016; Benvenuti et al., 2017). Several strategies have been proposed for their great potential to reduce the elevated costs. Efficient cultivation systems and optimization of processes and growth conditions could reduce operational costs. Additionally, costs can be reduced by selection of microalgal strains with enhanced productivities or the use of genetically improved strains which can be achieved by laboratory evolution, random mutagenesis and direct genetic manipulation (Radakovits et al., 2010; Remmers et al., 2018). Recent advances in genetic engineering and the development of new genetic tools have allowed the genetic modification of microalgae, increasing our understanding in the fatty acid biosynthesis pathways (Radakovits et al., 2010; Vazquez-Villegas et al., 2018). Several studies have shown that genes encoding key enzymes in the Kennedy pathway are potential candidates for genetic engineering to enhance TAG productivities (Banerjee et al., 2016; Ng et al., 2017). The Kennedy pathway is responsible for the synthesis of triacylglycerols in the endoplasmic reticulum (**Figure 1**). TAG synthesis starts with the acylation of glycerol-3-phosphate (G3P) by glycerol 3-phosphate acyltransferase (GPAT) to form lyso-phosphatidic acid, which is further converted into phosphatidic acid (PA) by lysophophatidic acid acyltransferase (LPAT), phosphatidic acid phosphatase (PAP), and dephosphorylates PA producing diacylglycerol (DAG). Lastly, diacylglycerol acyltransferase (DGAT) catalyzes the formation of triacylglycerols using DAG and acyl-CoA as substrates (Yu et al., 2011). The Kennedy pathway intermediates PA and DAG are also intermediate precursors for membrane lipids such as anionic phosphoglycerides (e.g. phosphatidyl serine), glycosylglycerides (e.g. galactosylglycerides), and zwitterionic phosphoglycerides (e.g. phosphatidyl choline, phosphatidylethanolamines) (Li-Beisson et al., 2019).

Previous studies have shown that the overexpression of genes encoding these enzymes resulted in increased lipid content. The overexpression of *GPAT* in *Phaeodactylum tricornutum* increased the neutral lipid content up to 42.6% of total lipids per dry weight, which corresponds to 2-folds increase in fatty acid content compared to wild type strain (Niu et al., 2016). Overexpression of *LPAT* in *Chlamydomonas reinhardtii* led to 20% increase of oil content (Yamaoka et al., 2016) and an increase of 2.3-fold (up to 13%) in TAG levels was observed when *DGAT* was overexpressed in *P. tricornutum* (Zulu et al., 2017).

In this study, we successfully expressed genes involved in the lipid biosynthesis pathway from *Acutodesmus obliquus* into *Neochloris oleoabundans*. Since *Acutodesmus obliquus* has been previously reported to accumulate up to 45% of total lipids per dry weight, we have cloned the encoding genes GPAT, LPAT and DGAT from *A. obliquus* (Breuer et al., 2013). In order to enhance lipid production in *N. oleoabundans,* we performed the single and combined gene expression of the three genes. In addition, we further investigated and characterized growth, lipid composition, and cellular biochemical composition of all transformant lines obtained.

MATERIALS AND METHODS

Microalga Strain and Culture Conditions

Neochloris oleoabundans UTEX 1185 was obtained from the University of Texas Culture Collection of Algae (UTEX). *N. oleoabundans* strain was grown in Freshwater (FW) medium as described by Breuer et al. (2012). Prior to experiments, cultures were maintained in shake flasks at 25°C on light:dark cycles of 16:8 h under a light intensity of 40 μmol m^{-2} s^{-1} on a rotary shaker (125 rpm). During nitrogen starvation experiments, *N. oleoabundans* was grown in 500 ml Erlenmeyer flasks. Cultures were placed in a shaker incubator operating at 25°C with light intensities of 150 μmol m^{-2} s^{-1} (light:dark cycles of 16:8), enriched with 5% CO_2, and continuous agitation of 150 rpm.

Escherichia coli NEB-Alpha5 (New England Biolabs) was grown at 37°C in Luria-Bertani (LB) broth or agar supplemented with 100 mg · L^{-1} of ampicillin as needed.

Plasmid Construction

The plasmids pUC-AcobLPAT, pUC-AcobGPAT, and pUC-AcobDGAT were constructed for the single expression of *LPAT*, *GPAT,* and *DGAT*. In order to overexpress all three genes simultaneously we constructed the expression vector pUC-AcobDGL. The plasmid pUC19 was obtained from Addgene and used as a backbone in all the constructs. pUC19 was digested with HindIII and NdeI restriction enzymes (Thermo Scientific) in order to linearize and remove the

Abbreviations: TAG, triacylglycerol; TFA, Total fatty acids; LPAT, Lysophosphatidic acid acyltransferase; GPAT, Glycerol -3-phophate acyltransferase; DGAT, Diacylglycerol acyltransferase; ER, Endoplasmic reticulum; GFP, Green fluorescent protein; PCR, Polymerase chain reaction; FW, Fresh water; DW, Dry weight; WT, Wild type.

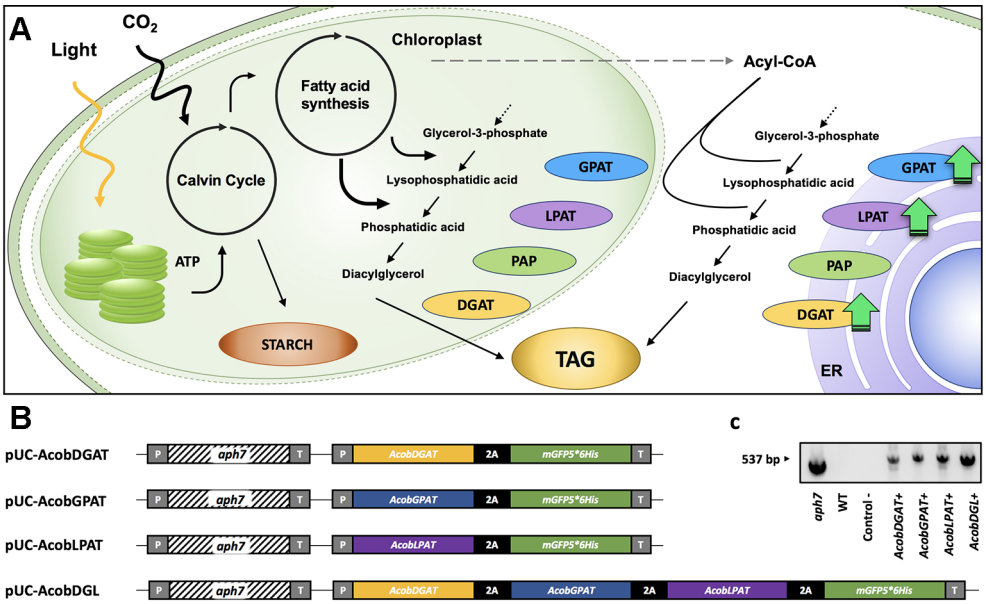

FIGURE 1 | TAG biosynthesis pathway **(A)**. glycerol 3-phosphate acyltransferase (GPAT), lysophosphatidic acid acyltransferase (LPAT), phosphatidic acid phosphatase (PAP), diacylglycerol acyltransferase (DGAT). Schematic representation of expression plasmids pUC-AcobDGAT, pUC-AcobGPAT, pUC-AcobLPAT, and pUC-AcobDGL **(B)**. PCR amplification of *aph7* gene from wild type (WT) and transformant lines **(C)**. CaMV35S promoter (P), hygromycin B resistance gene *aph7*, 3′ untranslated region CaMV (T), and 2A self-cleaving peptide of foot-and-mouth disease virus (FMDV).

multiple cloning site of the vector. The cassettes CaMV35Sp-Aph7-Ter and CaMV35Sp-2A-GFP-Ter were synthetized and assembled into the linearized pUC19. Both cassettes contain the cauliflower mosaic virus (CaMV) 35S promoter and terminator. Moreover, the cassette CaMV35Sp-2A-GFP-Ter contains a NedI restriction site between the promoter and the 2A self-cleaving sequence for insertion of genes of interest. The plasmid assembly was performed using HiFi DNA Assembly Master Mix (NEB) according to the manufacturer's instructions and transformed into NEB-Alpha5 *E. coli* competent cells (New Englands Biolabs). The construct containing both cassettes (pUC19-aph7-2A-GFP) was digested by NdeI restriction enzyme. Synthetized *LPAT*, *GPAT,* and *DGAT* containing overlap regions with pUC19-aph7-2A-GFP were inserted *via* HiFi assembly to generate pUC-AcobLPAT, pUC-AcobGPAT, and pUC-AcobDGAT. In order to generate the plasmid pUC-AcobDGL, we synthetized the sequences DGAT-2A, GPAT-2A, and LPAT. All synthesized sequences contained overlap regions and stop codons of each gene were replaced by 2A self-cleaving peptide of foot-and-mouth disease virus (FMDV). The three genes were assembled into linearized pUC19-aph7-2A-GFP by Hifi assembly and transformed into NEB-Alpha5 *E. coli* competent cells (New Englands Biolabs). The sequences encoding for LPAT, GPAT, and DGAT were obtained from the draft genome of *Acutodesmus obliquus* (Carreres et al., 2017) by sequence analysis (NCBI database) using Basic Local Alignment Search Tool (BLAST). All the sequences were identified as putative and no specific intracellular localization was predicted when using the prediction tool PredAlgo (Tardif et al., 2012).

Transformation of *N. oleoabundans* by Electroporation

N. oleoabundans cells were harvested and washed in electroporation buffer as described by Muñoz et al. (2018). The transformation mixture containing 2 μg · ml^{-1} of linearized plasmid and 25 μg · ml^{-1} of boiled salmon sperm DNA (D1626, Sigma) were incubated on ice for 15 min. The electroporation was performed in 2-mm electroporation cuvettes by applying 6 kV · cm^{-1}. Electroporated cells were recovered in the dark, transferred into 10 ml of FW medium and incubated overnight on dark at 25°C on a rotary shaker (125 rpm). After recovery, cells were harvested, re-suspended in 200 μl of FW medium and plated onto FW agar plates containing 50 μg · ml^{-1} of hygromycin B. Plates were incubated at 25°C, under light intensities of 60 μmol · m^{-2} s^{-1} (light:dark cycle cycles of 16:8) and supplemented with 2.5% CO_2.

Selection and Screening of Transformant Lines

Selection of transformant lines was performed on FW agar plates containing 50 μg · ml^{-1} of hygromycin B. Antibiotic resistant colonies obtained on plate were transferred to new plates containing 75 μg · ml^{-1} of hygromycin B. Identification of positive transformants was performed by PCR amplification of the hygromycin resistance gene (*aph7*) with primers used by Munoz et al. (2018). DNA extraction and colony PCR were performed by using Phire Plant Direct PCR Master Mix (ThermoFisher Scientific). Colonies obtained on selective plates were transferred to 20 μl of dilution buffer (provided in the kit), mixture was vortexed for 30 s and 0.5 μl was used as DNA

template in the PCR reaction. Phire hot start II DNA polymerase was used for the PCR amplification of *aph7* gene following the manufacturer's instructions. Positive transformants were inoculated in liquid FW medium containing 75 μg · ml^{-1} of hygromycin B and grown in 48 microwell plates. Fast growing transformants were identified by optical density measurements at 750 nm. Moreover, we visualized transformants by fluorescence microscopy and selected transformants with high green fluorescence signals for subsequent analysis. Detection of green fluorescent protein was performed with the fluorescence microscope EVOS FL Auto Cell Imaging System incorporating a GFP excitation/emission cube (EVOS FL, ThermoFisher Scientific).

Growth, Cell Diameter, Cell Number, and Dry Weight Determination

The optical density was monitored at a wavelength of 750 nm using a UV-VIS spectrophotometer (Hach Lange DR6000). Cell concentration and cell size were measured in triplicate with the Beckman Coulter Multisizer III (Beckman Coulter Inc., USA) using a 50 μm aperture tube. Microscopic analysis was performed with the microscope EVOS FL Auto Cell Imaging System (EVOS FL, ThermoFisher Scientific). All samples were diluted 200 times in Isotone® II diluent solution before measurements. Dry weight concentration was determined by filtrating 10 ml of culture broth on a pre-dried and pre-weight 55 mm Whatman glass fibre filter paper (GF/F; Whatman International Ltd, Maidstone, UK). The filter was washed with filtered demineralized water and subsequently dried overnight at 100 °C before weighing. The dry weight of the samples was calculated from the difference in weight between the dry filters with and without biomass.

Measurement of Photosynthetic Activity

Quantum yield (Fv/Fm) was measured by chlorophyll a fluorescence at 455 nm using a fluorometer AquaPen-C AP-C100 (Photon Systems Instrument, Czech Republic). Samples were diluted to an OD_{750} of 0.5 and adapted to dark for 15 min at room temperature before measurement (Janssen et al., 2018).

Determination of Lipid Content and Fatty Acid Composition

Total fatty acid content and lipid composition were determined as described by Breuer et al. (2013). Lipids were extracted from 10 mg of freeze dried biomass. Cells were mixed with chloroform:methanol (1:1.25, v:v) containing tripentadecanoin (T4257, Sigma Aldrich) and 1,2–dipentadecanoyl–sn–glycero–3–phospho–(1'–rac-glycerol) (sodium salt) (840434, Avanti Polar Lipids Inc.) as internal standard for TAG and polar lipid fraction, respectively. Biomass was disrupted using a beat beater, chloroform:methanol was subsequently evaporated and the extract was dissolved in hexane:diethylether (7:1 v/v). Neutral or apolar lipids containing triacylglycerols were separated from polar lipids using a Sep-Pak Vac silica cartridge (6cc, 1g, Waters). Apolar lipids were extracted by loading 10 ml hexane:diethylether (7:1 v/v) and polar lipids by loading 10 ml of methanol:acetone:hexane (2:2:1 v/v/v). Both lipid extracts were quantified using a gas chromatography (GC-FID) as described by Breuer et al. (2013). The total apolar and polar lipid content was calculated as a sum of the individual fatty acids of these fractions.

Carbohydrates Determination

The total carbohydrate content was determined according to DuBois et al. (1956) and Herbert et al. (1971). Phenol-sulphuric acid was added to 10 mg of freeze dried microalgae and absorbance was measured at 483 nm. Glucose monohydrate was used as a standard.

Protein Determination

The total protein content was determined using a colorimetric assay (Bio-Rad DC protein assay) according to manufacturer's instructions. Total protein content was analysed in 10 mg of freeze dried biomass and bovine serum albumin (BSA) was used as a standard.

Pigment Determination

Pigment composition was determined as described by Lichtenthaler (1987). The experiment was performed in triplicate and absorbance was measured at 470, 652, and 665 nm. Chlorophyll a, chlorophyll b, total chlorophyll, and total carotenoids were calculated using Arnon's equations.

Calculations

The average and maximum volumetric biomass productivities were calculated as described by Breuer et al. (2012). The growth rate was calculated using the equation $\mu = \ln(X_2/X_1)/(t_2 - t_1)$, where μ is the specific growth rate, X_1 and X_2 are the biomass (dry weight) at time 1 (t_1) and time 2 (t_2), respectively.

Statistical Analysis

All the experiments in this study were performed in biological triplicates. The data were represented as mean ± standard deviation (SD). Statistical analysis were performed using the student's *t* test and a P value < 0.05 was considered statistically significant.

RESULTS

Experimental Design, Plasmid Construction and Selection of Transformants

In order to increase triacylglycerol content in *N. oleoabundans*, we constructed four expression vectors. The plasmids pUC-AcobDGAT, pUC-AcobGPAT, and pUC-AcobLPAT were constructed for the single expression of the genes encoding DGAT, GPAT, and LPAT, respectively. The plasmid pUC-AcobDGL was constructed in order to assess the simultaneous expression of the three genes (**Figure 1**). The expression of selectable marker (*Streptomyces hygroscopicus* aminoglycoside phosphotransferase gene *aph7*, inferring resistance to hygromycin), reporter gene (encoding green fluorescence protein, mGFP5), and genes of interest were regulated under the CaMV35S promoter

and terminator. Moreover, a 2A self-cleaving peptide of foot-and-mouth disease virus (FMDV) was used for polycistronic expression of the gene(s) of interest and mGFP5, in both the single and multiple gene expression vectors. In general, viral-derived 2A peptides are used for enabling a single transcript to translate discrete protein products of multiple transgenes in eukaryotes and are widely used to tie resistance markers to the production of target proteins. Having a fluorescent protein (mGFP5) at the end of the 2A polycistronic construct confers the capability to directly select for positive transformant lines. The selection for positive GFP fluorescence shows clear evidence of concomitantly expression of all the upstream genes (Daniels et al., 2014; Wang et al., 2015; Liu et al., 2017; Poliner et al., 2018). Around 200 hygromycin B resistant colonies were obtained on plates containing FW agar medium and 50 μg · ml^{-1} hygromycin B. Only 15% of the transformant lines survived when transferred to a higher antibiotic concentration, which were confirmed to contain the hygromycin B resistance gene *aph7* (**Figure 1C**). We then identified the fast-growing transformants with high green fluorescence signals on liquid medium by measuring OD_{750} and using a fluorescence microscope, respectively, and we selected them for subsequent analysis. The selected positive transformants expressing the single genes *DGAT*, *GPAT,* and *LPAT* from *A. obliquus* were named AcobDGAT+, AcobGPAT+, and AcobLPAT+, respectively. The name AcobDGL+ was assigned to the *N. oleoabundans* cell lines expressing the three genes simultaneously.

Growth Analysis and Characterization of Engineered Strains

In order to characterize and determine the effect of gene overexpression in the selected transformant lines, we analyzed growth, morphology, and photosynthetic efficiency (**Figure 2**). Biological replicates were cultivated in flasks under standard growth conditions and then transferred to nitrogen-depleted medium. During replete and deplete conditions all transformant lines showed lower cell numbers per volume compared to the wild type strain (**Figure 2B**). Although the cell numbers were lower, AcobGPAT+ and AcobLPAT+ showed similar optical densities and dry weights compared to the wild type during nitrogen replete and deplete conditions (**Figures 2A–C**). On the other hand, the strains AcobDGAT+ and AcobDGL+ showed significantly lower values of optical density, cell number, and dry weight (end-point *P* value < 0.05).

To determine the effect of gene overexpression on photosynthetic performance, we monitored the chlorophyll

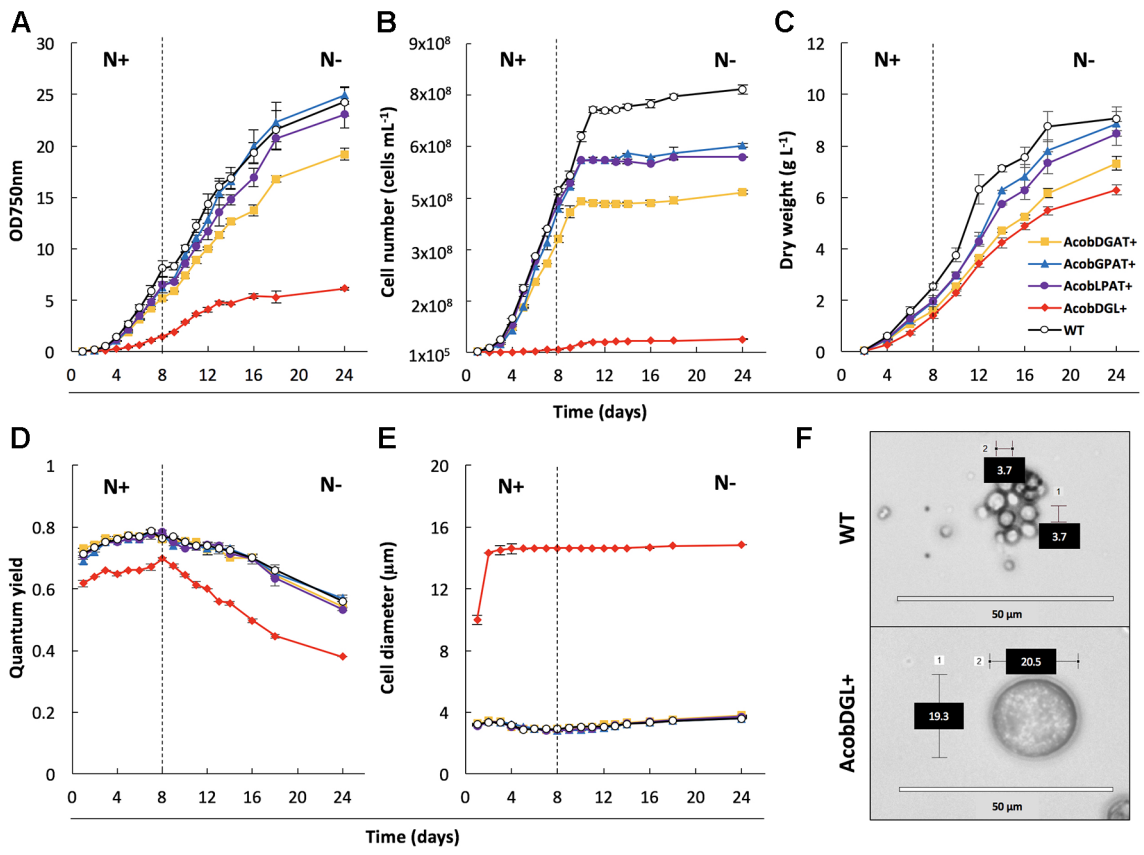

FIGURE 2 | Analysis of cell growth and photosynthetic efficiency. Measurements of optical density at 750 nm **(A)**, cell number **(B)**, dry weight **(C)**, quantum yield **(D)** and cell diameter **(E)** in wild type (WT) strain and transformant lines. Microscopic image of wild type strain and *N. oleoabundans* expressing *DGAT*, *GPAT,* and *LPAT* simultaneously **(F)**. Dashed lines indicate the moment at which nitrogen starvation started. The data represent the average of n = 3 replicate experiments. Standard deviation bars are shown.

fluorescence Fv/Fm of transformant lines and compared them with the *N. oleoabundans* wild type line. Compared to the control, no significant differences were observed in photosynthetic efficiency in the lines overexpressing single genes (end-point P value < 0.05). Wild type, AcobDGAT+, AcobGPAT+, and AcobLPAT+ showed an increase in quantum yield from 0.7 to 0.8 when grown in replete conditions, which decreased in deplete conditions to a minimum value of 0.6 at the end point of measurement. However, the three-gene overexpressing line AcobDGL+ showed a significantly lower quantum yield value (end-point P value <0.05), reaching the lowest values of 0.6 during replete conditions and 0.4 during nitrogen deplete conditions (**Figure 2D**). We further investigated the cell diameter of all transformant and wild type lines by microscopic analysis. Control and transformant lines overexpressing single genes showed no differences in cell size and during replete and deplete conditions they had cell diameters between 3.7 and 4.0 μm. On the contrary, AcobDGL+ was considerably larger (**Figure 2E**), showing an average size around 14 μm in cell diameter, with some cells reaching 20 μm in diameter (**Figure 2F**).

Biochemical Composition of Engineered Strains

Carbohydrates, proteins, and pigments were analyzed in transformant and wild type control lines during cultivation in standard and nitrogen-starved conditions.

As shown in **Figure 3A**, no substantial differences were observed in carbohydrate content between the wild type and transformant lines during replete conditions. During deplete conditions, AcobDGL+ showed the lowest carbohydrate content of 0.24 g · gDW^{-1} at day 24, while no differences were observed in the lines expressing single genes and control.

In the wild type control line, a maximum of 0.35 g · gDW^{-1} and a minimum of 0.20 g · gDW^{-1} of protein content was reached during replete and deplete conditions, respectively (**Figure 3B**). Interestingly, the total protein content was higher in all transformant lines during nitrogen replete conditions and lower during starvation, compared to wild type. Furthermore, we analyzed chlorophyll a, chlorophyll b, and carotenoid content at day 24 during nitrogen deplete conditions. As shown in **Figure 3C**, AcobDGAT+ showed similar chlorophyll and carotenoid content (total pigment content of 4.5 mg · gDW^{-1}) compared to wild type. AcobGPAT+ and AcobLPAT+ resulted in lower pigment content, being AcobLPAT+ the lowest with 2 mg · gDW^{-1}. Interestingly, AcobDGL+ showed higher values in chlorophyll and carotenoid content reaching 7.5 mg · gDW^{-1} of total pigment content compared to the control.

Effect of Gene Expression on Fatty Acid Synthesis

The total fatty acid (TFA) and triacylglycerol (TAG) contents were analyzed throughout nitrogen replete and deplete conditions. As shown in **Figure 4A**, the total fatty acid content during nitrogen replete conditions was similar among transformant and wild type control lines. Only AcobDGL+ showed an increase in TAG content, having 0.9% g · gDW^{-1} of TAG compared to 0.1% g · gDW^{-1} present in AcobDGAT+, AcobGPAT+, AcobLPAT+, and wild type. The maximum TFA and TAG content was achieved at day 24 during nitrogen deplete conditions for all the transformant lines and wild type. In these conditions, the expression of the single genes encoding DGAT, GPAT, and LPAT showed the highest TFA and TAG content at around 52% and 45% g · gDW^{-1}, respectively. The simultaneous overexpression of the three genes in AcobDGL+ showed lower TFA and TAG (49% and 39% g · gDW^{-1} respectively) compared to the single gene expression, but higher compared to the wild type control line. We also analyzed the total fatty acids composition of the polar and apolar (TAG) fraction (**Figure 4B**). Although the total polar lipid content of the transformant lines during replete and deplete conditions was similar to wild type, it showed differences in composition. In

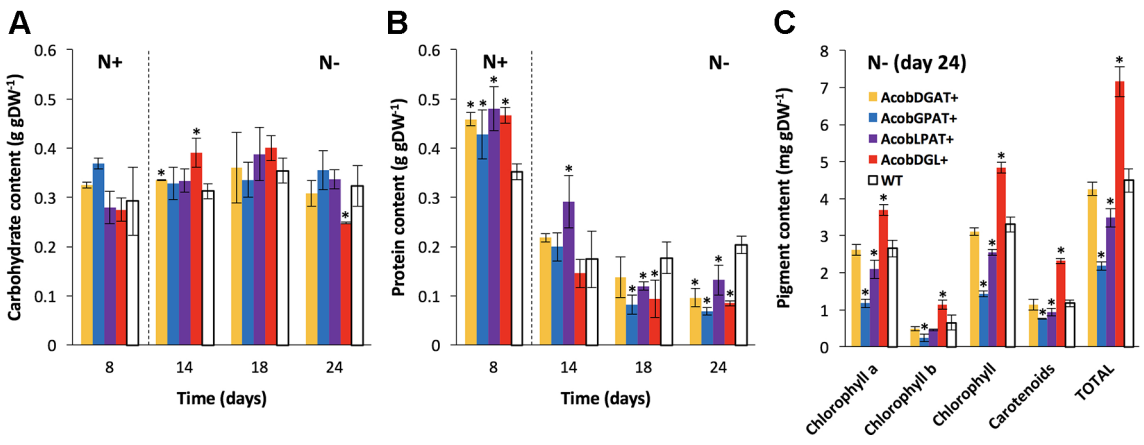

FIGURE 3 | Biochemical composition in *N. oleoabundans* wild type strain and transformant lines. Carbohydrate **(A)**, protein **(B)**, and pigment **(C)** content in wild type (WT) and transformant lines. Dashed lines indicate the moment at which nitrogen starvation started. Pigment content as determined for all strains at day 24 under nitrogen starvation. Chlorophyll represents the sum of chlorophyll a and chlorophyll b. Total pigments correspond to the sum of total chlorophyll and carotenoids. The data represent the average of n = 3 replicate experiments. Standard deviation bars are shown. Significant difference between wild type strain and transformant lines is indicated at $P < 0.05$ (*).

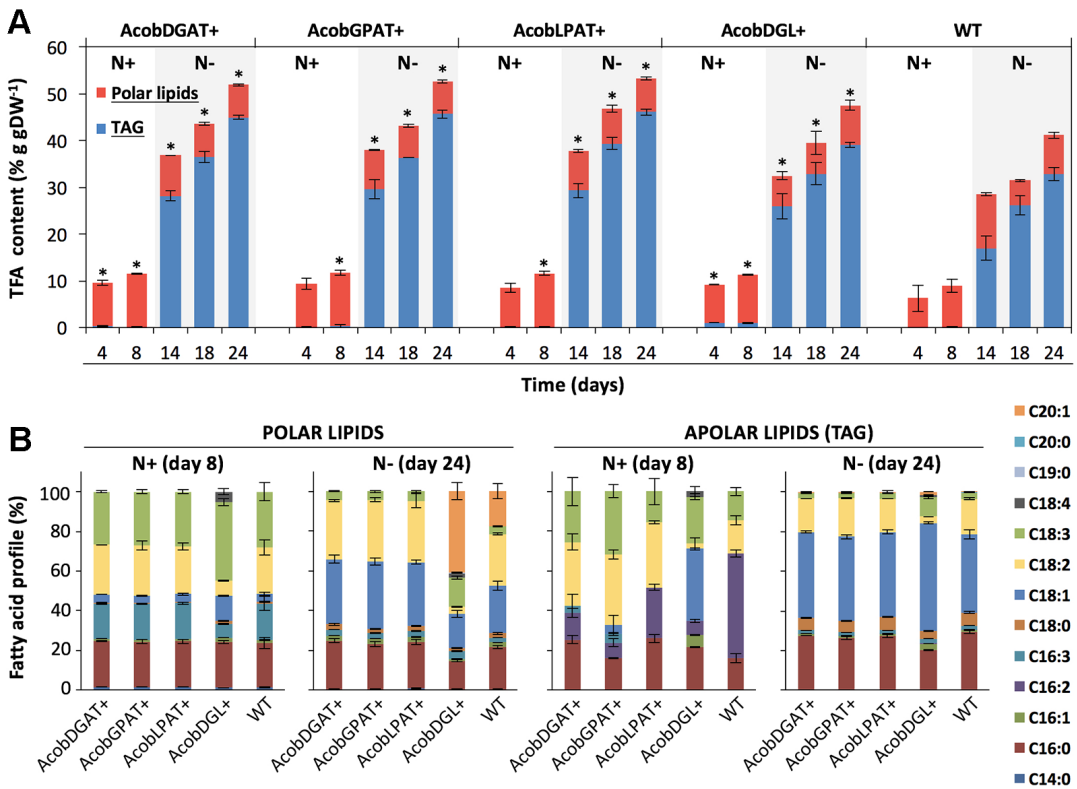

FIGURE 4 | Total fatty acid (TFA), triacylglycerols (TAG), and fatty acid composition in *N. oleoabundans* wild type strain and transformant lines. Total fatty acids: TAG and polar lipids **(A)**. Polar and apolar lipid (TAG) composition at days 8 and 24 during nitrogen replete (N+) and depleted (N-) nitrogen conditions, respectively **(B)**. The data represent the average of n = 3 replicate experiments. Standard deviation bars are shown. Significant difference between wild type strain and transformant lines is indicated at $P < 0.05$ (*).

particular, during nitrogen replete conditions, we observed an increase in C18:3 and decrease in C16:3 and C18:2 fatty acids in the polar lipid fraction for AcobDGL+, and no significant difference for the single gene expressing lines compared to wild type. During nitrogen deplete conditions, interestingly, no C20:1 was produced in AcobDGAT+, AcobGPAT+, and AcobLPAT+, while they showed an increase of C18:1 compared to wild type. Differently, AcobDGL+ showed 2.4 and 3.9-fold increase in C20:1 and C18:3 fatty acids content, respectively, with a reduced C16:0, C18:1, and C18:2 content, compared to wild type.

Similarly, also the apolar (TAG) fraction presented differences in composition. During replete conditions, AcobDGL+ showed an increase in C18:1 and the presence of C18:4 and C16:1. For the strains expressing single genes we observed a substantial decrease in C16:2 and increase in C18:2 in the apolar (TAG) fraction. Moreover, AcobDGAT+, AcobGPAT+, and AcobDGL+ showed the presence of 16:3, and AcobDGAT+, AcobLPAT+, and AcobDGL+ had higher C16:0 content compared to wild type. Under deplete conditions, the apolar lipid composition of the transformant lines expressing single genes showed a similar distribution compared to wild type, while AcobDGL+ showed an increase in C18:3, C18:1, and C20:1 fatty acids and a decrease in C16:0 and C18:2 fatty acids.

Impact of Single and Multi-Gene Expression on Biomass and Fatty Acid Productivities

In order to determine performance of all the tested lines, we calculated the volumetric biomass, total fatty acid, and triacylglycerol productivities. As shown in **Table 1**, during nitrogen replete conditions, *N. oleoabundans* wild type showed high volumetric biomass productivity (413 mg · L^{-1} d^{-1}) and growth rate (1.23 d^{-1}). The most affected in both volumetric biomass productivity (231 mg · L^{-1} d^{-1}) and growth rate (0.59 d^{-1}) was the three-gene expressing line AcobDGL+. Under nitrogen-depleted conditions, AcobDGAT+, AcobGPAT+, AcobLPAT+, and wild type reached higher volumetric biomass productivities compared to AcobDGL+. The highest volumetric TFA and TAG productivities were obtained during nitrogen-depleted conditions for all the lines. However, remarkably, AcobGPAT+ and AcobDGL+ showed higher volumetric TAG productivity in replete conditions, which were 1- and 4.5-fold higher than wild type, respectively. Under deplete conditions, all the lines expressing single genes showed high TFA and TAG productivities compared to AcobDGL+ and wild type, with AcobLPAT+ reaching the highest values (248.0 and 235 mg· L^{-1} d^{-1}, respectively).

TABLE 1 | Growth rate and average volumetric productivities of biomass, total fatty acids (TFA), and triacylglycerols (TAG) for nitrogen replete (N+) and nitrogen deplete (N-) conditions.

Strains	Volumetric biomass productivity ($mg \cdot L^{-1} d^{-1}$)	Volumetric TFA productivity ($mg \cdot L^{-1} d^{-1}$)	Volumetric TAG productivity ($mg \cdot L^{-1} d^{-1}$)	Growth rate (d^{-1})
WT N+	413.1 ± 50	46.7 ± 8	0.6 ± 0.1	1.23 ± 0.01
WT N-	386.5 ± 35	172.6 ± 4	192.4 ± 21	–
AcobDGAT+ N+	254.1 ± 12	34.9 ± 6	0.4 ± 0.1	1.01 ± 0.01
AcobDGAT+ N-	383.1 ± 26	212.9 ± 31	202.5 ± 38	–
AcobGPAT+ N+	321.7 ± 25	46.1 ± 8	1.3 ± 0.2	1.04 ± 0.01
AcobGPAT+ N-	422.2 ± 44	230.2 ± 20	224.2 ± 32	–
AcobLPAT+ N+	324.4 ± 36	46.4 ± 8	0.5 ± 0.1	1.05 ± 0.01
AcobLPAT+ N-	426.5 ± 40	248.0 ± 26	235.3 ± 42	–
AcobDGL+ N+	231.8 ± 23	33.5 ± 6	2.7 ± 0.5	0.59 ± 0.01
AcobDGL+ N-	307.9 ± 33	167.0 ± 42	142.5 ± 47	–

The data represent the average of n = 3 replicate experiments.

DISCUSSION

The oleaginous microalga *Neochloris oleoabundans* has been previously shown to be an industrially relevant strain for biofuel production due to its ability to produce large amounts of lipids, mainly in the form of TAGs, during stress conditions (i.e. nitrogen deprivation) (Li et al., 2008; de Jaeger et al., 2018). With the recent advances in biotechnology, tools and techniques for the genetic modification of microalgae are expanding quickly and they could be used for the generation of improved strains with enhanced lipid productivities. It has been demonstrated that overexpression of genes involved in the Kennedy pathway in microalgae species such as *Chlamydomonas reinhardtii*, *Phaeodactylum tricornutum,* and *Nannochloropsis oceanica* can lead to higher lipids content. Overexpression of the endogenous LPAT encoding gene in *C. reinhardtii* resulted in an increase of 20% in total fatty acids (Yamaoka et al., 2016). Similarly, the overexpression of endogenous GPAT encoding gene in *P. tricornutum* led to an enhanced neutral lipid content (2-fold higher than wild type) and specifically, to a significant increase in unsaturated fatty acid profile (Niu et al., 2016). Moreover, the DGAT enzyme, responsible for the last step in TAG biosynthesis, has been regarded as a promising target for improving TAG content in multiple studies. Deng et al. (2012), previously showed that overexpression of the endogenous DGAT encoding gene in *C. reinhardtii* can result in an increase of total fatty acids by 48% and 43% of its dry weight when grown under nitrogen replete and deplete conditions, respectively.

In our study, we report the expression of LPAT, GPAT, and DGAT encoding genes from the microalga *Acutodesmus obliquus* in *N. oleoabundans*. Our results demonstrate that the single expression of LPAT, GPAT, and DGAT encoding genes lead to higher lipid accumulation per dry weight during deplete conditions compared to wild type, mainly due to a ~1.3-fold increase in their TAG content. The lipid composition of the apolar fraction remains unchanged compared to wild type, being oleic acid (C18:1), palmitic acid (C16:0), and linoleic acid (C18:2) as the main constituents. Although single gene expression did not lead to higher lipid content during nitrogen replete conditions, we observed a different fatty acid distribution in the apolar fraction. In particular, hexadecadienoic acid (C16:2) decreased and linoleic acid (C18:2) increased substantially compared to wild type. The single expression of *LPAT*, *GPAT,* and *DGAT* genes showed no changes in polar lipid distribution during nitrogen replete conditions. However, during nitrogen depleted conditions all the three transformant lines seem to favor the production of oleic acid (C18:1) at the expenses of eicosenoic acid (C20:1), which diminished, compared to wild type.

In our attempt to increase the lipid content in *N. oleoabundans* even further, we overexpressed the three LPAT, GPAT, and DGAT encoding genes simultaneously. Unexpectedly, in this case we saw an increase in the total fatty acids content of a factor of 1.2-folds compared to wild type, which was lower compared to what we have observed for the single expressing lines. Also in this case, the major increase was observed in the TAG fraction (**Figure 4A**). In particular, the apolar fraction (TAG) of the multiple gene expressing line contained an increase in C18:1 and C18:3 fatty acids, and a reduction in C18:0, C16:0 and C18:2, compared to the single expressing lines and wild type apolar lipid distribution. This suggests that the orchestrated expression of these enzymes shifts the lipid composition towards long unsaturated fatty acid chains. Oleic acid (C18:1) is the major fatty acid produced by *N. oleoabudans* and *A. obliquus*. Moreover, in *A. obliquus* fatty acid profile linolenic acid (C18:3) has higher relative abundance compared to C18:2 (Breuer et al., 2013). Taken together, these findings may suggest a preference of *A. obliquus* enzymes for both C18:1 and C18:3 fatty acids to be integrated in the triacylglycerols of *N. oleoabundans*. It also suggests that these enzymes are interfering with other lipid metabolic pathway, such as fatty acid elongation and desaturation. Furthermore, also during nitrogen replete conditions the apolar fraction showed an increase in oleic and linolenic fatty acids. Interestingly, the simultaneous gene expression led to substantial changes in the fatty acid profile of the polar fraction. Since the main component of cellular membranes are polar lipids, we hypothesize that the alteration in the lipid distribution might also be correlated to the significant increase in cell size of the multiple gene expressing line. The Kennedy pathway enzymes share precursor like PA and DAG with the enzymes for the biosynthethic pathway of the membrane lipids, such as phosphoglycerides and glycosylglycerides. Further investigations could be focused in understanding which lipid species and how the intermediate

precursor pools are affected by the enhanced expression of a heterologous Kennedy pathway, which could elucidate the lipid metabolism in microalgae.

In order to determine whether overexpression of *LPAT*, *GPAT,* and *DGAT* genes had an effect on biomass and fatty acid productivities we calculated the volumetric productivities of all transformants. The highest volumetric TFA and TAG productivities were obtained during nitrogen-starved conditions by single gene expressing lines. Moreover, the expression of single genes led to the highest TFA and TAG productivities, compared to the multiple gene expression and wild type. Previous studies reported that the heterologous expression of *DGAT* in *Scenedesmus obliquus* and *Phaeodactylum tricornutum* increased lipid content and lipid productivities (Chen et al., 2016; Zulu et al., 2017). The dual overexpression of the endogenous *LPAT* and *GPAT* in *P. tricornutum* and the multiple expression of the heterologous *LPAT*, *GPAT*, *PAP,* and *DGAT* in *Chlorella minutissima* showed an enhanced lipid content and productivities as well (Hsieh et al., 2012; Wang et al., 2018). Previous studies have reported no effect on growth when overexpressing genes involved in the Kennedy pathway. In our study, the highest volumetric biomass productivity and highest growth rate were achieved by *N. oleoabundans* wild type during nitrogen replete conditions. During nitrogen deplete conditions the specific growth rate was similar among the single overexpressing lines and wild type, while the transformant line expressing the three genes simultaneously was the most affected, with a growth rate reduced by half, compared to the replete conditions. Conversely, Wang et al. (2018) recently reported that the dual expression of *GPAT* and *LPAT* in *P. tricornutum* enhanced growth rate during the mid-log phase, however this was not observed in our transformant line (**Figure 2B**).

In previous reports, it has been shown that the overexpression of these single enzymes did not affect the photosynthetic efficiency of the transformant lines. Thus, it has been hypothesized that the increased availability of fatty acid precursors for TAG synthesis, such as PA, induced by the overexpression of these enzymes, may also serve as precursors for the synthesis of plastidic membranes, resulting in elevated photosynthetic efficiencies (Niu et al., 2013; Niu et al., 2016; Balamurugan et al., 2017). In our study, we did not observe a significant change in photosynthetic efficiencies in the lines overexpressing single genes, compared to wild type. On the other hand, the multiple gene expression showed a significantly reduced photosynthetic activity, indicating that the introduction of these three genes results in an increased metabolic load that has a direct impact on the physiological status of the cells. In this regard, the reduced quantum yield and size enlargement in this transformant line may also be related to a stress component, which could be correlated to the alteration of both polar and apolar lipid compositions, interestingly different compared to wild type and the single gene expressing lines.

We further investigated the biochemical composition of all transformant lines in order to determine the effect of gene expression on the synthesis of cellular components. Our results showed that only when the three genes were overexpressed the carbohydrate content was reduced at the end of the experiment. Moreover, all the transformant lines showed a reduced protein content during nitrogen depleted conditions. Similarly, Balamurugan et al. (2017) and Wang et al. (2018) reported that overexpression of *GPAT* or dual expression of *GPAT* and *LPAT* in *P. tricornutum*, respectively, led to lower protein and carbohydrate content in starved conditions. These results suggest that carbohydrate and protein metabolism are redirected towards lipid production, and in particular, the orchestrated expression of the three genes has a stronger impact in redirecting the carbon flux from carbohydrates to lipids. On the other hand, during nitrogen replete experiments, we observed higher protein content compared to the wild type strain as a result of the high expression of *LPAT*, *GPAT,* and *DGAT* genes, which is in accordance with previous studies (Dinamarca et al., 2017). Other cellular components such as chlorophylls and carotenoids were also affected by the gene expression. AcobGPAT+ and AcobLPAT+ showed a reduced chlorophyll a, chlorophyll b and carotenoid content, suggesting that the carbon flux might have been redirected towards lipid production. Contrarily, the transformant line expressing the three genes simultaneously showed higher chlorophyll and carotenoid content, compared to wild type and the single gene expressing lines. Since the multi-gene expressing line showed a detrimental effect in the photosynthetic efficiency, lower protein and carbohydrate content, we hypothesize that the higher pigment content in the cells may be induced to prevent photoinhibition and oxidative stress.

CONCLUSIONS

In this study, we report the effect of the heterologous overexpression of *LPAT*, *GPAT,* and *DGAT* genes in *N. oleoabundans*. Single and multiple gene expression resulted in an enhanced lipid production for all the transformant lines. We demonstrated that higher neutral lipid content and lipid productivities were achieved when single genes were expressed during nitrogen depleted conditions. Moreover, the single gene expression did not affect growth, biomass productivities and photosynthetic activities significantly. Interestingly, the simultaneous expression of *LPAT*, *GPAT,* and *DGAT* had a negative effect on growth and photosynthetic activity, which resulted in 4-fold bigger cells, lower biomass, and lipid productivities. However, during replete conditions, we observed the highest TAG productivity, which was 4.5-fold higher than wild type. This result indicates that the orchestrated expression of the three genes can induce TAG production during nitrogen replete conditions. However, in order to maximize lipid productivities even further, optimal cultivation conditions and homologous and dual-gene expression need to be investigated in future work. Moreover, future investigations on the alteration of lipid species and precursor pools by the heterologous expression of the Kennedy pathway can help to further elucidate the lipid metabolism in microalgae. Overall, our results provide insights regarding the Kennedy pathway related lipid production and composition, and the improvement of TAG production in microalgae. This approach could lead to the generation of microalgal strains with economical potential for the successful biofuel production.

DATA AVAILABILITY STATEMENT

All datasets generated for this study are included in the article/supplementary material.

AUTHOR CONTRIBUTIONS

CM designed the experiment. CM performed the experiments, analyzed, interpreted the data, and wrote the manuscript. SD'A, RAW, and RHW supervised the project. All authors contributed to the work, discussed the results, read, and approved the final version of this manuscript.

FUNDING

This research project was funded by the National Commission of Scientific and Technologic Research of Chile (CONICYT).

REFERENCES

Alptekin, E., Canakci, M., and Sanli, H. (2014). Biodiesel production from vegetable oil and waste animal fats in a pilot plant. *Waste Manage.* 34, 2146–2154. doi: 10.1016/j.wasman.2014.07.019

Balamurugan, S., Wang, X., Wang, H. L., An, C. J., Li, H., Li, D. W., et al. (2017). Occurrence of plastidial triacylglycerol synthesis and the potential regulatory role of AGPAT in the model diatom *Phaeodactylum tricornutum*. *Biotechnol. Biofuels* 10, 97. doi: 10.1186/s13068-017-0786-0

Banerjee, C., Dubey, K. K., and Shukla, P. (2016). Metabolic engineering of microalgal based biofuel production: prospects and challenges. *Front. Microbiol.* 7, 432. doi: 10.3389/fmicb.2016.00432

Benvenuti, G., Ruiz, J., Lamers, P. P., Bosma, R., Wijffels, R. H., and Barbosa, M. J. (2017). Towards microalgal triglycerides in the commodity markets. *Biotechnol. Biofuels* 10, 188. doi: 10.1186/s13068-017-0873-2

Brennan, L., and Owende, P. (2010). Biofuels from microalgae—A review of technologies for production, processing, and extractions of biofuels and co-products. *Renew Sust. Energ Rev.* 14, 557–577. doi: 10.1016/j.rser.2009.10.009

Breuer, G., Lamers, P. P., Martens, D. E., Draaisma, R. B., and Wijffels, R. H. (2012). The impact of nitrogen starvation on the dynamics of triacylglycerol accumulation in nine microalgae strains. *Bioresour. Technol.* 124, 217–226. 80, 50628. doi: 10.1016/j.biortech.2012.08.003

Breuer, G., Evers, W. A., de Vree, J. H., Kleinegris, D. M., Martens, D. E., Wijffels, R. H., et al. (2013). Analysis of fatty acid content and composition in microalgae. *J. Vis Exp.* 80, 50628 doi: 10.3791/50628

Carreres, B. M., de Jaeger, L., Springer, J., Barbosa, M. J., Breuer, G., van den End, E. J., et al. (2017). Draft genome sequence of the oleaginous green alga *Tetradesmus obliquus* UTEX 393. *Genome Announc.* 5, e01449–e01416. doi: 10.1128/genomeA.01449-16

Chen, C. Y., Kao, A. L., Tsai, Z. C., Chow, T. J., Chang, H. Y., Zhao, X. Q., et al. (2016). Expression of type 2 diacylglycerol acyltransferase gene DGTT1 from *Chlamydomonas reinhardtii* enhances lipid production in *Scenedesmus obliquus*. *Biotechnol. J.* 11, 336–344. doi: 10.1002/biot.201500272

Daniels, R. W., Rossano, A. J., Macleod, G. T., and Ganetzky, B. (2014). Expression of multiple transgenes from a single construct using viral 2A peptides in *Drosophila*. *PloS One* 9, e100637. doi: 10.1371/journal.pone.0100637

de Jaeger, L., Carreres, B. M., Springer, J., Schaap, P. J., Eggink, G., Martins Dos Santos, V. A. P., et al. (2018). *Neochloris oleoabundans* is worth its salt: Transcriptomic analysis under salt and nitrogen stress. *PloS One* 13, e0194834. doi: 10.1371/journal.pone.0194834

Deng, X. D., Gu, B., Li, Y. J., Hu, X. W., Guo, J. C., and Fei, X. W. (2012). The roles of acyl-CoA: Diacylglycerol acyltransferase 2 genes in the biosynthesis of triacylglycerols by the green algae *Chlamydomonas reinhardtii*. *Mol. Plant* 5, 945–947. doi: 10.1093/mp/sss040

Dinamarca, J., Levitan, O., Kumaraswamy, G. K., Lun, D. S., and Falkowski, P. G. (2017). Overexpression of a diacylglycerol acyltransferase gene in *Phaeodactylum tricornutum* directs carbon towards lipid biosynthesis. *J. Phycol.* 53, 405–414. doi: 10.1111/jpy.12513

DuBois, M., Gilles, K. A., Hamilton, J. K., Rebers, P. A., and Smith, F. (1956). Colorimetric method for determination of sugars and related substances. *Anal. Chem.* 28, 350–356. doi: 10.1021/ac60111a017

Faried, M., Samer, M., Abdelsalam, E., Yousef, R. S., Attia, Y. A., and Ali, A. S. (2017). Biodiesel production from microalgae: Processes, technologies and recent advancements. *Renew Sust. Energ Rev.* 79, 893–913. doi: 10.1016/j.rser.2017.05.199

Gharabaghi, M., Amrei, H. D., Zenooz, A. M., Guzullo, J. S., and Ashtiani, F. Z. (2015). Biofuels: bioethanol, biodiesel, biogas, biohydrogen from plants and microalgae. CO_2 sequestration, biofuels and depollution. Environmental Chemistry for a Sustainable World. (Springer, Cham). 5, 233–274. doi: 10.1007/978-3-319-11906-9_6

Griffiths, M. J., and Harrison, S. T. L. (2009). Lipid productivity as a key characteristic for choosing algal species for biodiesel production. *J. Appl. Phycol.* 21, 493–507. doi: 10.1007/s10811-008-9392-7

Hanaki, K., and Portugal-Pereira, J. (2018). The effect of biofuel production on greenhouse gas emission reductions. *Biofuels Sustain.* Science for Sustainable Societies. Springer, Tokyo. 53–71. doi: 10.1007/978-4-431-54895-9_6

Herbert, D., Phipps, P. J., and Strange, R. E. (1971). Chemical analysis of microbial cells. *Methods Microbiol.* 5B, 209–344. doi: 10.1016/S0580-9517(08)70641-X

Hsieh, H. J., Su, C. H., and Chien, L. J. (2012). Accumulation of lipid production in *Chlorella minutissima* by triacylglycerol biosynthesis-related genes cloned from *Saccharomyces cerevisiae* and *Yarrowia lipolytica*. *J. Microbiol.* 50, 526–534. doi: 10.1007/s12275-012-2041-5

Janssen, J. H., Driessen, J. L. S. P., Lamers, P. P., Wijffels, R. H., and Barbosa, M. J. (2018). Effect of initial biomass-specific photon supply rate on fatty acid accumulation in nitrogen depleted *Nannochloropsis gaditana* under simulated outdoor light conditions. *Algal Res.* 35, 595–601. doi: 10.1016/j.algal.2018.10.002

Li, Y., Horsman, M., Wang, B., Wu, N., and Lan, C. Q. (2008). Effects of nitrogen sources on cell growth and lipid accumulation of green alga *Neochloris oleoabundans*. *Appl. Microbiol. Biotechnol.* 81, 629–636. doi: 10.1007/s00253-008-1681-1

Li-Beisson, Y., Thelen, J. J., Fedosejevs, E., and Harwood, J. L. (2019). The lipid biochemistry algae. *Proq. Lipid Res.* 74, 31–68. doi: 10.1016/j.plipres.2019.01.003

Lichtenthaler, H. K. (1987). Chlorophylls and carotenoids: pigments of photosynthetic biomembranes. *Methods Enzymol.* 148, 350–382. doi: 10.1016/0076-6879(87)48036-1

Liu, Z., Chen, O., Wall, J. B. J., Zheng, M., Zhou, Y., Wang, L., et al. (2017). Systematic comparison of 2A peptides for cloning multi-genes in a polycistronic vector. *Sci. Rep.* 7, 2193. doi: 10.1038/s41598-017-02460-2

Majidian, P., Tabatabaei, M., Zeinolabedini, M., Naghshbandi, M. P., and Chisti, Y. (2018). Metabolic engineering of microorganisms for biofuel production. *Renew Sust. Energ Rev.* 82, 3863–3885. doi: 10.1016/j.rser.2017.10.085

Medipally, S. R., Yusoff, F. M., Banerjee, S., and Shariff, M. (2015). Microalgae as sustainable renewable energy feedstock for biofuel production. *BioMed. Res. Int.* 2015, 13. doi: 10.1155/2015/519513

Moody, J. W., McGinty, C. M., and Quinn, J. C. (2014). Global evaluation of biofuel potential from microalgae. *Proc. Natl. Acad. Sci.* 11, 8691– 8696. doi: 10.1073/pnas.1321652111

Muñoz, C. F., de Jaeger, L., Sturme, M. H. J., Lip, K. Y. F., Olijslager, J. W. J., Springer, J., et al. (2018). Improved DNA/protein delivery in microalgae – A simple and reliable method for the prediction of optimal electroporation settings. *Algal Res.* 33, 448–455. doi: 10.1016/j.algal.2018.06.021

Ng, I. S., Tan, S. I., Kao, P. H., Chang, Y. K., and Chang, J. S. (2017). Recent developments on genetic engineering of microalgae for biofuels and bio-based chemicals. *Biotechnol. J.* 12, 1700015. doi: 10.1002/biot.201600644

Niu, Y. F., Zhang, M. H., Li, D. W., Yang, W. D., Liu, J. S., Bai, W. B., et al. (2013). Improvement of neutral lipid and polyunsaturated fatty acid biosynthesis by overexpressing a type 2 diacylglycerol acyltransferase in marine diatom *Phaeodactylum tricornutum*. *Mar. Drugs* 11, 4558–4569. doi: 10.3390/md11114558

Niu, Y. F., Wang, X., Hu, D. X., Balamurugan, S., Li, D. W., Yang, W. D., et al. (2016). Molecular characterization of a glycerol-3-phosphate acyltransferase reveals key features essential for triacylglycerols production in *Phaeodactylum tricornutum*. *Biotechnol. Biofuels* 9, 60. doi: 10.1186/s13068-016-0478-1

Poliner, E., Pulman, J. A., Zienkiewicz, K., Childs, K., Benning, C., and Farré, E. M. (2018). A toolkit for *Nannochloropsis oceanica* CCMP1779 enables gene stacking and genetic engineering of the eicosapentaenoic acid pathway for enhanced long-chain polyunsaturated fatty acid production. *Plant Biotechnol. J.* 16, 298–309. doi: 10.1111/pbi.12772

Radakovits, R., Jinkerson, R. E., Darzins, A., and Posewitz, M. C. (2010). Genetic engineering of algae for enhanced biofuel production. *Eukaryot Cell.* 9, 486–501. doi: 10.1128/EC.00364-09

Remmers, I. M., Wijffels, R. H., Barbosa, H. J., and Lamers, P. P. (2018). Can we approach theoretical lipid yields in microalgae? *Trends In Biotechnol.* 36, 265–276. doi: 10.1016/j.tibtech.2017.10.020

Ruiz, J., Olivieri, G., de Vree, J., Bosma, R., Willems, P., Reith, J. H., et al. (2016). Towards industrial products from microalgae. *Energ. Environ. Sci.* 9, 3036–3043. doi: 10.1039/C6EE01493C

Tardif, M., Atteia, A., Specht, M., Cogne, G., Rolland, N., Brugière, S., et al. (2012). PredAlgo: a new subcellular localization prediction tool dedicated to green algae. *Mol. Biol. Evol.* 29, 3625–3639. doi: 10.1093/molbev/mss178

Vazquez-Villegas, P., Torres-Acosta, M. A., Garcia-Echauri, S. A., Aguilar-Yanez, J. M., Rito-Palomares, M., and Ruiz-Ruiz, F. (2018). Genetic manipulation of microalgae for the production of bioproducts. *Front. Biosci. (Elite Ed).* 10, 254–275. doi: 10.2741/e821

Wang, Y., Wang, F., Wang, R., Zhao, P., and Xia, Q. (2015). 2A self-cleaving peptide-based multi-gene expression system in the silkworm *Bombyx mori*. *Sci. Rep.* 5, 16273. doi: 10.1038/srep16273

Wang, X., Dong, H. P., Wei, W., Balamurugan, S., Yang, W. D., Liu, J. S., et al. (2018). Dual expression of plastidial GPAT1 and LPAT1 regulates triacylglycerol production and the fatty acid profile in *Phaeodactylum tricornutum*. *Biotechnol. Biofuels* 11, 318. doi: 10.1186/s13068-018-1317-3

Yamaoka, Y., Achard, D., Jang, S., Legéret, B., Kamisuki, S., Ko, D., et al. (2016). Identification of a *Chlamydomonas* plastidial 2-lysophosphatidic acid acyltransferase and its use to engineer microalgae with increased oil content. *Plant Biotechnol. J.* 14, 2158–2167. doi: 10.1111/pbi.12572

Yu, W. L., Ansari, W., Schoepp, N. G., Hannon, M. J., Mayfield, S. P., and Burkart, M. D. (2011). Modifications of the metabolic pathways of lipid and triacylglycerol production in microalgae. *Microb Cell Fact.* 10, 91. doi: 10.1186/1475-2859-10-91

Zulu, N. N., Popko, J., Zienkiewicz, K., Tarazona, P., Herrfurth, C., and Feussner, I. (2017). Heterologous co-expression of a yeast diacylglycerol acyltransferase (ScDGAT1) and a plant oleosin (AtOLEO3) as an efficient tool for enhancing triacylglycerol accumulation in the marine diatom *Phaeodactylum tricornutum*. *Biotechnol. Biofuels* 10, 187. doi: 10.1186/s13068-017-0874

Conflict of Interest: The authors declare that the research was conducted in the absence of any commercial or financial relationships that could be construed as a potential conflict of interest.

frontiers in Plant Science

ORIGINAL RESEARCH
published: 31 January 2020
doi: 10.3389/fpls.2019.01700

Enhanced Production of D-Lactate in Cyanobacteria by Re-Routing Photosynthetic Cyclic and Pseudo-Cyclic Electron Flow

*Tiago Toscano Selão[1], Jasmin Jebarani[1], Nurul Aina Ismail[2], Birgitta Norling[1] and Peter Julian Nixon[1,2]**

[1] School of Biological Sciences, Nanyang Technological University, Singapore, Singapore, [2] Department of Life Sciences, Imperial College London, London, United Kingdom

Cyanobacteria are promising chassis strains for the photosynthetic production of platform and specialty chemicals from carbon dioxide. Their efficient light harvesting and metabolic flexibility abilities have allowed a wide range of biomolecules, such as the bioplastic polylactate precursor D-lactate, to be produced, though usually at relatively low yields. In order to increase photosynthetic electron flow towards the production of D-lactate, we have generated several strains of the marine cyanobacterium *Synechococcus* sp. PCC 7002 (Syn7002) with deletions in genes involved in cyclic or pseudo-cyclic electron flow around photosystem I. Using a variant of the *Chlamydomonas reinhardtii* D-lactate dehydrogenase (LDH^{SRT}, engineered to efficiently utilize NADPH *in vivo*), we have shown that deletion of either of the two flavodiiron *flv* homologs (involved in pseudo-cyclic electron transport) or the Syn7002 *pgr5* homolog (proposed to be a vital part of the cyclic electron transport pathway) is able to increase D-lactate production in Syn7002 strains expressing LDH^{SRT} and the *Escherichia coli* LldP (lactate permease), especially at low temperature (25°C) and 0.04% (v/v) CO_2, though at elevated temperatures (38°C) and/or high (1%) CO_2 concentrations, the effect was less obvious. The Δ*pgr5* background seemed to be particularly beneficial at 25°C and 0.04% (v/v) CO_2, with a nearly 7-fold increase in D-lactate accumulation in comparison to the wild-type background (≈1000 vs ≈150 mg/L) and decreased side effects in comparison to the *flv* deletion strains. Overall, our results show that manipulation of photosynthetic electron flow is a viable strategy to increase production of platform chemicals in cyanobacteria under ambient conditions.

Keywords: cyanobacteria, cyclic electron flow, Mehler-like reaction, metabolic engineering, D-lactate

OPEN ACCESS

Edited by:
Dimitris Petroutsos, UMR5168 Laboratoire de Physiologie Cellularie Vegetale (LPCV), France

Reviewed by:
Gilles Peltier, CEA Cadarache, France
Jianping Yu, National Renewable Energy Laboratory (DOE), United States

***Correspondence:**
Peter Julian Nixon
p.nixon@imperial.ac.uk

Specialty section:
This article was submitted to Plant Biotechnology, a section of the journal Frontiers in Plant Science

Received: *15 September 2019*
Accepted: *03 December 2019*
Published: *31 January 2020*

Citation:
Selão TT, Jebarani J, Ismail NA, Norling B and Nixon PJ (2020) Enhanced Production of D-Lactate in Cyanobacteria by Re-Routing Photosynthetic Cyclic and Pseudo-Cyclic Electron Flow. Front. Plant Sci. 10:1700. doi: 10.3389/fpls.2019.01700

INTRODUCTION

There is currently great interest in exploring the use of photoautotrophs such as the prokaryotic cyanobacteria to produce industrially important molecules including biofuels, specialty chemicals and pharmaceutical/nutritional products (Woo, 2017). Cyanobacteria use sunlight to drive the biosynthesis of organic molecules from water and carbon dioxide during the process of oxygenic

photosynthesis. Compared to commonly used platforms, such as the yeast *Saccharomyces cerevisiae* and the bacterium *Escherichia coli*, cyanobacteria do not require an organic carbon feedstock and use solar energy for growth, important advantages for the development of a low-cost, carbon-neutral production system.

Rapid progress is being made to develop the necessary genetic tools to manipulate cyanobacteria, especially the model cyanobacteria *Synechococcus* sp. PCC 7002 and *Synechocystis* sp. PCC 6803 [reviewed in Sun et al. (2018)], and a wide range of metabolic engineering experiments have been performed to alter central carbon metabolism to improve the yields of diverse target molecules [reviewed in (Xiong et al., 2017)].

However, less work has been directed at engineering the light reactions of oxygenic photosynthesis, e.g. to enhance the availability of reductive power to drive biosynthetic processes within the cyanobacterial cell. NADPH is produced by ferredoxin:$NADP^+$ reductase (FNR) using reduced ferredoxin generated by photosystem I (PSI) (Lea-Smith et al., 2016). Besides being used for CO_2 fixation in the Calvin-Benson-Bassham cycle, reduced ferredoxin also drives a variety of other reductive processes including nitrogen and sulphur assimilation (Hanke and Mulo, 2013), the reduction of plastoquinone during cyclic electron flow around PSI to generate ATP (Shikanai and Yamamoto, 2017), and the conversion of oxygen to water by flavodiiron (Flv) proteins in a Mehler-like reaction (Helman et al., 2003; Allahverdiyeva et al., 2013). It has been estimated that 15-30% of the electrons coming from the oxidation of water might ultimately be used by Flv to reduce oxygen back to water in so-called pseudocyclic electron flow (Helman et al., 2003).

Cyclic electron flow around PSI in cyanobacteria is currently thought to occur *via* two main routes: the NDH (NADH dehydrogenase-like) pathway, involving a PSI/NDH-1 supercomplex (Gao et al., 2016; Schuller et al., 2019), and the poorly characterized antimycin-sensitive Pgr5 pathway (Yeremenko et al., 2005). In plant chloroplasts, PGR5 is thought to function as a complex with PGRL1 (DalCorso et al., 2008), whereas in cyanobacteria, PGRL1 homologues are absent (Labs et al., 2016). Although NDH and PGR5 play physiologically important roles in cyclic electron flow, it is still unclear whether their roles are direct or indirect (Nandha et al., 2007; Nawrocki et al., 2019). One dramatic feature of the *pgr5* mutant of *Arabidopsis* is an inability to downregulate photosynthetic electron flow, which leads to aberrant over-reduction of the acceptor side of PSI and enhanced photodamage to PSI (Munekage et al., 2002) especially under fluctuating light (Suorsa et al., 2012). In contrast, the *pgr5* null mutant of *Synechocystis* sp. PCC 6803 (hereafter Syn6803) shows more robust growth under these conditions (Allahverdiyeva et al., 2013).

Here we have tested whether loss of Flv and Pgr5 functions in cyanobacteria, which are predicted to lead to an enhanced reduction state of the ferredoxin and NADPH electron acceptors downstream of PSI, can be exploited to enhance the biosynthesis of molecules dependent on reducing power (**Figure 1**). To do this, we have established a strain of the cyanobacterium *Synechococcus* sp PCC 7002 (henceforth Syn7002) that produces D-lactate *via* the NADPH-mediated reduction of pyruvate and examined D-lactate production in mutants lacking either one or both of the two Flv subunits found in Syn7002 (annotated as Flv1 and Flv3) as well as Pgr5. Our results indicate that manipulation of both these alternative electron transport pathways does indeed improve D-lactate production when cyanobacteria are grown at a lower temperature (25°C) than that optimal for growth and in air-levels of CO_2. Our work demonstrates that re-routing photosynthetic electron flow is a useful target for metabolic engineering in cyanobacteria.

MATERIALS AND METHODS

Strains, Media, and Growth Conditions

Syn7002 was routinely grown in A+ medium (Stevens et al., 1973) with D7 micronutrients (Arnon et al., 1974), as previously described (Selão et al., 2019). For growth in ambient CO_2 conditions, cultures were incubated in an FH-1200 growth chamber (HiPoint, Taiwan) and cell growth under 1% CO_2-enriched air was performed in a 740-FHC LED growth chamber (HiPoint, Taiwan), at a constant light intensity of 250 μmol photons·m^{-2}·s^{-1}. Strain growth and testing was routinely done in 15 ml cultures grown in upright tissue culture flasks (Corning, part #3056), inoculated at a starting OD_{730} of 0.05, measured in a 1 cm-light path Cary 300Bio (Varian) spectrophotometer using AD7 as blank. For large-scale growth monitoring, OD_{730} was measured in 150 μL of cultures (diluted as needed to $OD_{730} < 0.5$ with regular AD7) in 96-well plates using a Hidex Sense plate reader (Hidex) and converting to the equivalent OD_{730} by the Cary spectrophotometer, using an in-house derived 70-point calibration curve (R^2 = 0.9818). Each individual replicate was measured in duplicate. Whole cell spectra were recorded in 96-well plates, using the Hidex Sense plate reader, as described above.

Escherichia coli Stellar supercompetent cells, utilized for all cloning steps, were routinely grown in Luria-Bertani (LB) medium, supplemented with appropriate antibiotics as indicated.

Cloning and Cyanobacterial Transformation

All plasmids (see **Table 1**) were constructed using the pEASY-Uni Seamless Cloning and Assembly Kit (TransGen Biotech, China), according to manufacturer's instructions (unless otherwise specified) and transformed into supercompetent *Escherichia coli* Stellar supercompetent cells (TaKaRa). For a list of primers employed, please consult **Table S1**. Syn7002 transformation was performed as previously described (Selão et al., 2019), with strains selected in AD7-agar [AD7 supplemented with 1.2% (w/v) agar and 1 g/L sodium thiosulfate prior to autoclaving] using antibiotics (50 μg·ml^{-1} spectinomycin, 10 μg·ml^{-1} chloramphenicol, or 50 μg·ml^{-1} erythromycin or combinations thereof) and/or 100 μM acrylate, for constructs targeting the *acsA* locus (Begemann et al., 2013). Full genomic segregation was tested by colony

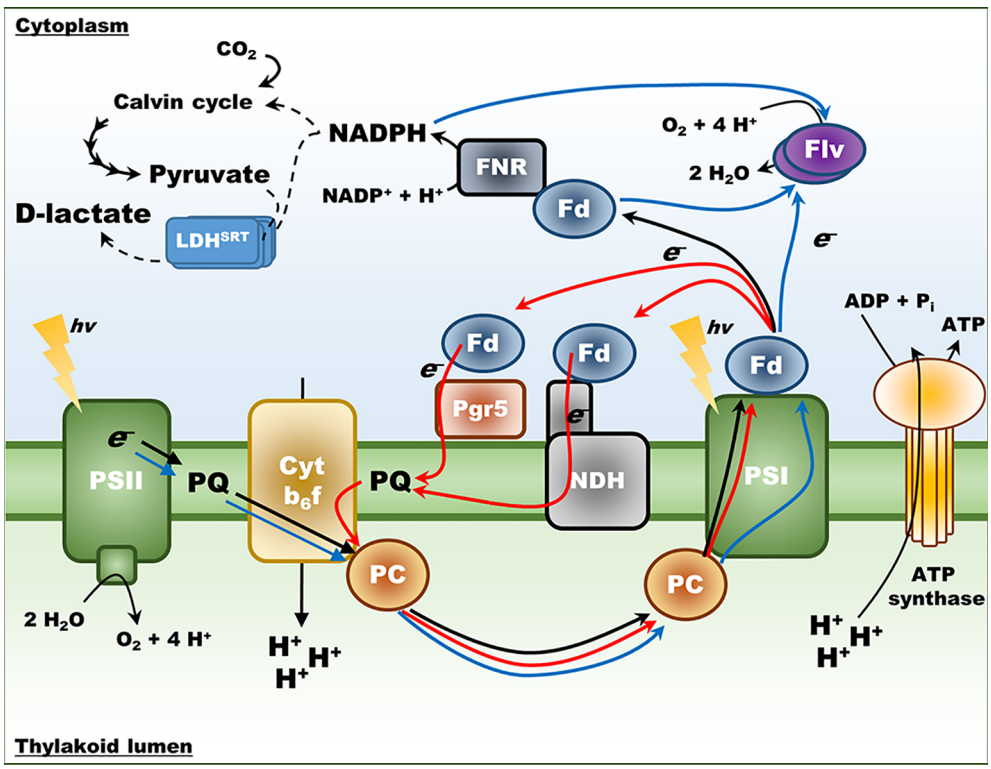

FIGURE 1 | Schematic representation of photosynthetic electron transport in cyanobacteria. Black arrows – Linear Electron Flow (LEF) from water to $NADP^+$. Red arrows – Cyclic Electron Flow (CEF), both the pathway involving Pgr5 and the pathway involving NDH. Blue arrows – pseudo-Cyclic Electron Flow (pCET), mediated by the Flv proteins. The D-lactate dehydrogenase variant (LDH^{SRT}) is included for reference, converting pyruvate derived from the Calvin cycle into D-lactate and utilizing NADPH as an electron source. PSI, photosystem I; PSII, photosystem II, Fd, ferredoxin; FNR, ferredoxin:$NADP^+$ oxidoreductase; PC, plastocyanin; Cyt b_6f, cytochrome b_6f.

TABLE 1 | List of plasmids used or generated in this study.

Plasmid name	Origin	Features
pUC19	Stratagene	*E. coli* cloning vector
pGEM-T	Promega	*E. coli* cloning vector
pAcsA-cLac143-YFP	(Markley et al., 2015)	cLac143 promoter for IPTG inducible expression in *Synechococcus* sp. PCC 7002
pET28b-crLDHwt	(Burgess et al., 2016)	pET28b vector for IPTG inducible expression of the *C. reinhardtii* LDH in *E. coli*
pSJ044	This work	pUC19 – *acsA*::$P_{cLac143}$-LDH^{WT}
pSJ045	This work	pUC19 – *acsA*::$P_{cLac143}$-LDH^{WT}+*lldp*
pSJ041	This work	pUC19 – *acsA*::$P_{cLac143}$-LDH^{SRT}
pSJ042	This work	pUC19 – *acsA*::$P_{cLac143}$-LDH^{SRT}+*lldp*
pSJ046	This work	pUC19 – *acsA*::$P_{cLac143}$-LDH^{ARSRR}
pSJ047	This work	pUC19 – *acsA*::$P_{cLac143}$-LDH^{ARSRR}+*lldp*
pSJ026	This work	pGEM-T – Syn7002 *flv1* gene with 500 bp up and downstream homology regions
pSJ028	This work	pGEM-T – Syn7002 *flv3* gene with 500 bp up and downstream homology regions
pSJ023	This work	pUC19 – Syn7002 *pgr5* gene with 500 bp up and downstream homology regions
pSJ058	This work	pGEM-T – Syn7002 *flv1*::*CmR*
pSJ038	This work	pGEM-T – Syn7002 *flv3*::*SpR*
pSJ074	This work	pUC19 – Syn7002 *pgr5*::*EryR*

PCR using specific primers (see **Table S1**). All plasmid sequences were confirmed by Sanger sequencing.

For D-lactate producing strains, the chloroplast-targeted D-lactate dehydrogenase (LDH) encoded by *Chlamydomonas reinhardtii* (without its cognate transit peptide) was amplified using Q5 polymerase (NEB) from the pET28b-crLDHwt vector (Burgess et al., 2016) and cloned into the pAcsA-cLac143-YFP vector (Markley et al., 2015), substituting the *yfp* gene in its entirety and generating pSJ044. The *lldp* gene (encoding lactate permease) was amplified from *E. coli* Stellar cells and introduced downstream from the *ldh* gene, with the strong AGGAGA RBS (Markley et al., 2015) sequence 8 bp upstream of its start codon, generating pSJ045. To generate a crLDH variant able to utilize NADPH, the sequence of the *C. reinhardtii* LDH was aligned with the sequence of the *Lactobacillus delbrueckii* 11842 LDH (see **Figure S1**) and the nucleotide binding motif (D181 to N185 in the *L. delbrueckii* enzyme) was targeted for site-directed mutagenesis, using previously described variants (Li et al., 2015; Meng et al., 2016) as a guide. The equivalent amino acids in the *C. reinhardtii* LDHwt sequence ($D^{208}I^{209}K^{210}P^{211}N^{212}$, see **Figure S1**) were mutated to either $S^{208}R^{209}T^{210}$ or ARSRR using Restriction-Free

cloning (Van Den Ent and Löwe, 2006; Bond and Naus, 2012) in both pSJ044 and pSJ045, resulting in pSJ041 and pSJ042 or pSJ046 and pSJ047, respectively (see **Table 1**).

For KO of the *flv1* (*A1743*), *flv3* (*A1321*) and *pgr5* (*A1477*) genes, DNA sequences from 500 bp up- to 500 bp downstream of the corresponding genes were amplified from Syn7002 genomic DNA and inserted into either pGEM-T Easy (in the case of *flv1* and *flv3*) or an XbaI-digested pUC19 fragment (in the case of *pgr5*), resulting in plasmids pSJ026, pSJ028 and pSJ023, respectively. These plasmids were reverse PCR amplified using the primers stated in **Table S1** and a chloramphenicol-resistance cassette (from pSK9, a kind gift from Annegret Wilde, University of Freiburg), a spectinomycin-resistance cassette (from pBAD42) or an erythromycin-resistance cassette (from pE194, Elhai and Wolk, 1988) were amplified with 15 bp overhangs. These were then assembled into the corresponding linearized plasmid backbones, generating pSJ058, pSJ038, and pSJ074, respectively. These plasmids were then used to transform Syn7002 WT, as described above, alone or in combination, generating the corresponding KO strains. Once full segregation was confirmed (see **Figure S2**), KO strains were transformed with pSJ042, generating D-lactate producing strains (see **Table 2**).

D-Lactate Concentration Measurements

All D-lactate producing cultures were induced 24 hours after inoculation with the addition of 0.5 mM isopropyl-β-D-thiogalactoside (IPTG, GoldBio) from a sterile 1M stock solution. D-lactate production in cyanobacterial cultures was measured in the culture supernatants, following a centrifugation step (20,000 g, 5 min, room temperature) to remove cells and incubation of the cleared supernatant at 98°C, 5 min, to inactivate remaining enzymatic activity. Cleared and heat-treated supernatants were frozen at -20°C until further use. D-lactate concentrations were measured in duplicate using the D-lactate (Rapid) assay kit (K-DATE, Megazyme) in 96-well plates, following the manufacturer's instructions.

TABLE 2 | List of all strains used or generated in this study.

Strain	Genotype
WT	*Synechococcus* sp. PCC 7002 wild-type
cSJ003	Δ*acs*A::$P_{cLac143}$ *ldh*^{WT}
cSJ004	Δ*acs*A::$P_{cLac143}$ *ldh*^{WT} - *lldP*
cSJ005	Δ*acs*A::$P_{cLac143}$ *ldh*^{ARSRR}
cSJ006	Δ*acs*A::$P_{cLac143}$ *ldh*^{ARSRR} - *lldP*
cSJ007	Δ*acs*A::$P_{cLac143}$ *ldh*^{SRT}
cSJ008	Δ*acs*A::$P_{cLac143}$ *ldh*^{SRT} - *lldP*
cSJ030	Δ*flv1*::CmR
cSJ019	Δ*flv3*::SpR
cSJ111	Δ*pgr5*::EryR
cSJ031	Δ*flv1*::CmR Δ*flv3*::SpR
cSJ072	Δ*pgr5*::EryR Δ*flv1*::CmR
cSJ076	Δ*pgr5*::EryR Δ*flv3*::SpR
cSJ042	Δ*flv1*::CmR Δ*acs*A::$P_{cLac143}$ *ldh*^{SRT} - *lldP*
cSJ048	Δ*flv3*::SpR Δ*acs*A::$P_{cLac143}$ *ldh*^{SRT} - *lldP*
cSJ038	Δ*pgr5*::EryR Δ*acs*A::$P_{cLac143}$ *ldh*^{SRT} - *lldP*
cSJ052	Δ*flv1*::CmR Δ*flv3*::SpR Δ*acs*A::$P_{cLac143}$ *ldh*^{SRT} - *lldP*
cSJ075	Δ*flv1*::CmR Δ*pgr5*::EryR Δ*acs*A::$P_{cLac143}$ *ldh*^{SRT} - *lldP*
cSJ079	Δ*flv3*::SpR Δ*pgr5*::EryR Δ*acs*A::$P_{cLac143}$ *ldh*^{SRT} - *lldP*

Western Blotting Analysis

Cultures at the indicated time points were centrifuged (5000 g, 15 min, room temperature), washed once with 1 mM Tris buffer (pH 7.5), and resuspended in the same buffer, supplemented with Protease Inhibitor Tablets, EDTA-free (Pierce). Whole cell lysates were obtained as previously described (Selão et al., 2016), with the exception that cells were lysed using glass beads (Sartorius, 0.17–0.18 mm diameter) and a bead beater (SpeedMill Plus, AnalyticJena). Protein content in cleared whole cell lysates was estimated using the Peterson method (Peterson, 1977) and 15 μg total protein were separated in 12.5% SDS-PAGE precast gels (GE Healthcare). Proteins were transferred to PVDF membranes, probed with specific antibodies raised in rabbit against Flv3 (a kind gift from Toshiharu Shikanai, Kyoto University; see Yamamoto et al., 2016), secondary goat anti-rabbit HRP-conjugated antibodies, and developed as described (Selão et al., 2016).

RESULTS

Construction of D-Lactate Producing Strain of PCC 7002

To test the impact of re-routing photosynthetic electron flow on biosynthesis, we generated a strain of the cyanobacterium Syn7002 that produces D-lactate, which can be easily assayed and is an important chemical feedstock in its own right (Eiteman and Ramalingam, 2015). We introduced into Syn7002 a DNA sequence encoding the recently characterized NAD^+-specific D-LDH (D-nLDH; EC 1.1.1.28) from the green alga *Chlamydomonas reinhardtii* (Burgess et al., 2016) and generated two derivatives (LDH^{SRT} and LDH^{ARSRR}) that were re-engineered on the basis of previous work to change the co-enzyme specificity of the enzyme to allow the use of NADPH (Li et al., 2015; Meng et al., 2016). All stains were constructed so that transcription of the D-LDH genes was under the control of the $cLac_{143}$ promoter (thus inducible by IPTG) and included downstream the *E. coli lldP* gene encoding a lactate permease, previously shown to improve D-lactate export in cyanobacteria (Li et al., 2015) (**Figure 2**). Analysis of D-lactate production under photoautotrophic conditions (0.04% or 1% CO_2 (v/v) and 38°C) revealed that the highest titer (≈1 g/L, 4 days post-induction, at 38°C and 1% (v/v) CO_2) occurred with the LDH^{SRT} strain co-expressing LldP (cSJ008, **Figure 2**), which was therefore used as the test or control strain for all subsequent experiments. All other strains produced less than 20 mg/L.

Effect of Single Knock-Outs of the *flv1*, *flv3,* and *pgr5* Genes in Different Conditions

In Syn6803, there are 4 Flv proteins (Flv1-4), which form two distinct heterodimeric complexes (Flv1/3 and Flv2/4) with roles in oxygen reduction downstream of PSI (Zhang et al., 2012; Allahverdiyeva et al., 2013; Shimakawa et al., 2015; Santana-Sanchez et al., 2019). In addition, it remains possible that under certain conditions, all four Flv proteins might form homodimers

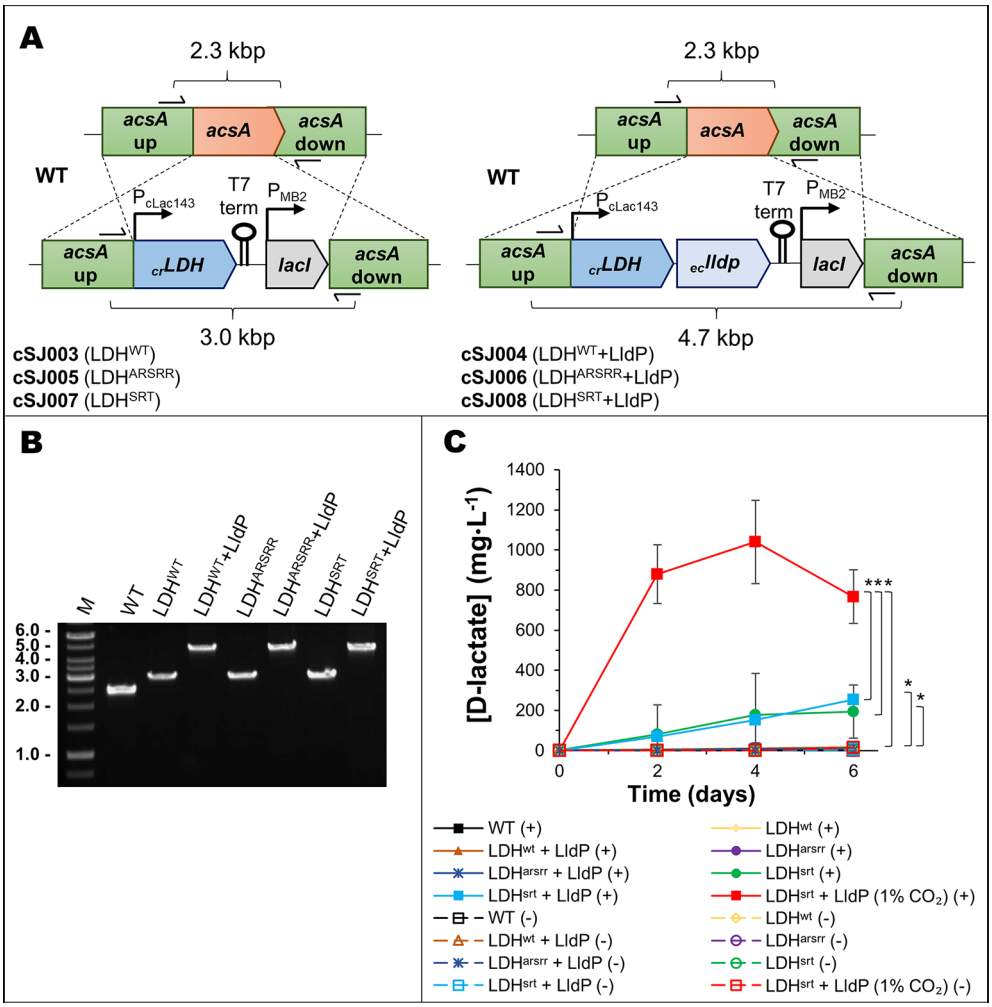

FIGURE 2 | Cloning and production test of a mutated D-lactate dehydrogenase in Syn7002. **(A)** Schematic of the *acsA* gene locus modification in strains cSJ003/cSJ005/cSJ007 (*left*, with *ldh* gene only) and strains cSJ004/cSJ006/cSJ008 (*right*, with *ldh* and *lldp* genes in operon). Different components not to scale. **(B)** 1% agarose gel of colony PCR of the strains indicated, using primers shown in A). **(C)** D-lactate production test of the strains indicated, at 38°C, in either ambient air or 1% CO_2, and a light intensity of 250 µmol photons·m^{-2}·s^{-1}. Error bars indicate a 95% confidence interval based on the standard error of the mean for triplicate cultures. Asterisks denote statistically relevant differences between indicated strains.

of unknown function (Hackenberg et al., 2009; Mustila et al., 2016; Santana-Sanchez et al., 2019). Only two Flv proteins, annotated as Flv1 and Flv3, based on similarities to the Flv subunits in Syn6803, are found in Syn7002. However, detailed studies on the role of Flv1 and Flv3 in Syn7002 are lacking, with only a double *flv1/flv3* KO mutant so far studied in detail (Shimakawa et al., 2016). In order to ascertain the baseline effect of the different mutations, growth of the strains with single gene deletions in either *flv1* (cSJ030), *flv3* (cSJ019), or *pgr5* (cSJ111) was monitored under different growth conditions (**Figure 3A**). Knock-out (KO) of either of the *flv* genes in Syn7002 resulted in only a mild growth defect at 25°C and at ambient CO_2 concentrations (final cell density between 73% and 80% of WT cultures under the same conditions). However, either increased temperature or higher CO_2 concentration (even at 25°C) allowed the cells to grow at near WT rates (**Figure 3A**) and accumulate similar cell densities. An immunoblot analysis (**Figure 3B**) using a specific antibody for Flv3 showed that Flv3 still accumulated upon deletion of the *flv1* gene, supporting the possibility that Flv3 is capable of functioning independently of Flv1 in Syn7002. The Δ*pgr5* strain, on the other hand, showed no obvious growth defect in all conditions tested (**Figure 3A**). Attempts to inactivate the NDH pathway by deleting *ndhF1* proved to be impractical as the resulting strain grew extremely poorly under the growth conditions used (data not shown).

Expression of the LDH^{SRT}-LldP operon in the single KO strains had very different effects depending on growth conditions. At 38°C and high CO_2 conditions [1% (v/v)], all strains were able to produce D-lactate efficiently (**Figure 4**), with

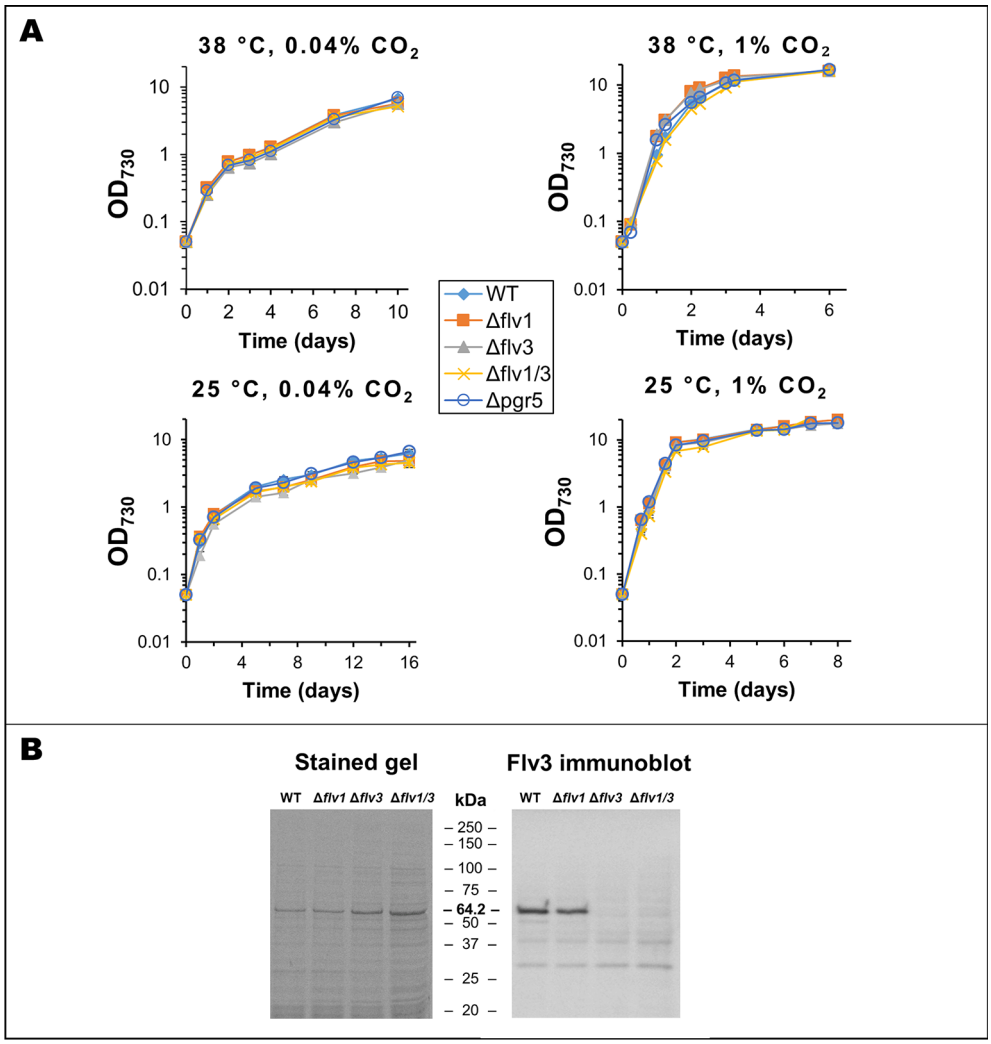

FIGURE 3 | Analysis of *flv* and *pgr5* knock-out strains. **(A)** Growth curves for WT, *Δflv1*, *Δflv3*, *Δflv1/Δflv3*, and *Δpgr5* strains in different conditions. Data is an average of 3 biological replicates, measured in technical duplicates. In all cases, the total light intensity was 250 µmol photons·m-2·s-1. **(B)** Analysis of Flv3 expression in different strains. *Left panel*: Coomassie stained SDS-PAGE gel of whole cell lysates from WT and different flv deletion strains. *Right panel*: Immunoblot using same samples, developed using a specific anti-Flv3 antibody (a kind gift from Toshiharu Shikanai). All lanes loaded with 15 µg total protein. Numbers on the left of each image represent the migration of respective molecular weight markers.

the producing strain in the *flv1* KO background (cSJ042) excreting D-lactate at slightly greater levels than that of the WT control strain (cSJ008), although the difference was not statistically significant. In contrast, deletion of *pgr5* (cSJ038) negatively affected D-lactate production under this growth regime. At 25°C and high CO_2, however, this effect was reversed, with strain cSJ038 (lacking *pgr5*) producing significantly more D-lactate than the WT control strain. Strain cSJ048 (lacking *flv3*) also produced significantly more D-lactate than strain cSJ042 (lacking *flv1)* (**Figure 4**), again suggesting that the two *flv* paralogs are not equivalent in Syn7002. Curiously, the growth of strains cSJ038 and cSJ048 was more severely affected than that of strains cSJ008 and cSJ042 (**Figure S3**).

Under air CO_2 concentrations, all single KO strains displayed slightly higher D-lactate production titers at 38°C than the control strain, cSJ008, reaching ≈350-370 mg/L vs ≈280 mg/L, respectively (**Figure 4**); though, again, deletion of *flv3* or *pgr5* affected growth rates more severely than deletion of *flv1* (**Figures S3** and **S4**). At 25°C and ambient CO_2, the effect of the different mutations was more obvious, with the strains producing approximately 4 to 6.5-fold more D-lactate than the WT control strain (cSJ008) (≈580 to ≈1000 mg/L compared to ≈150mg/L, **Figure 4**). Strain cSJ038 (lacking *pgr5*) gave the highest titer and was able to produce ≈1 g/L of D-lactate at the endpoint of the experiment (**Figure 4**). Under these growth conditions, the *flv* KO cultures were severely affected, having

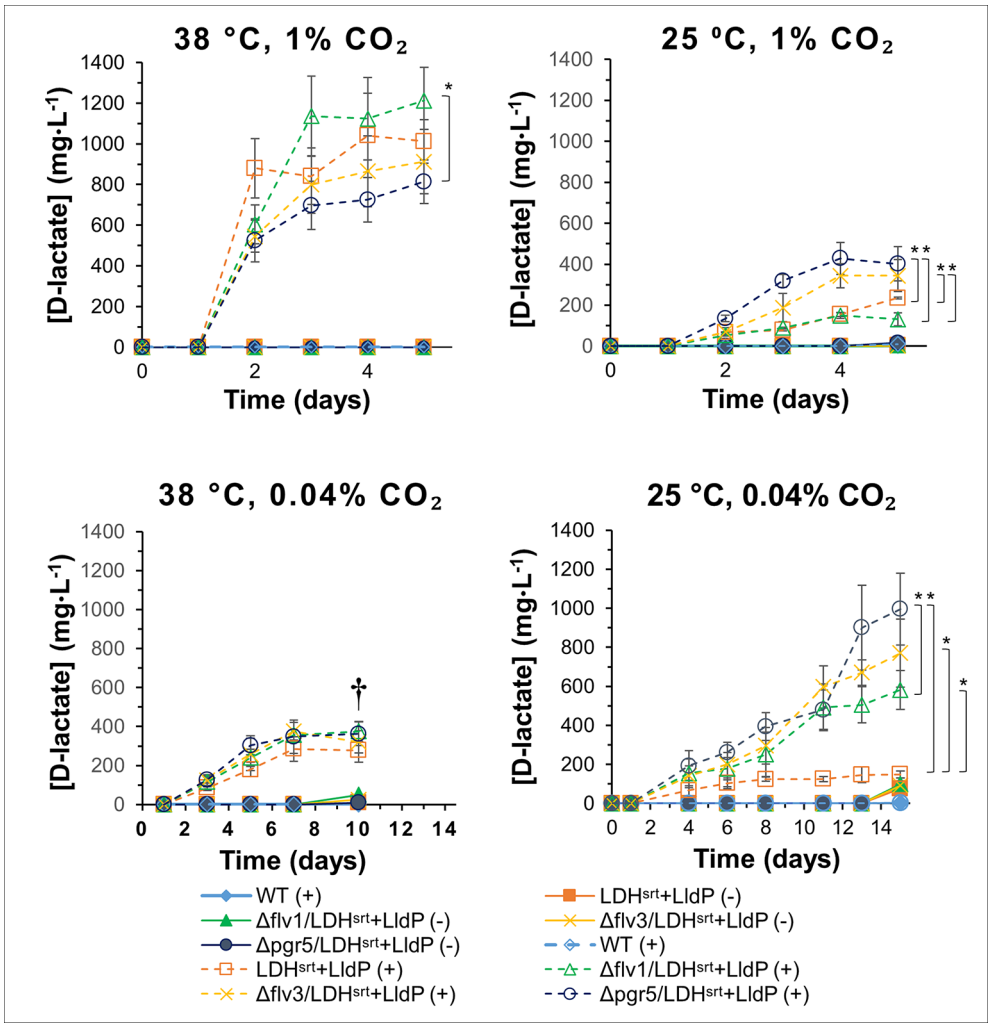

FIGURE 4 | D-lactate production in several electron transport single mutants under different growth conditions. D-lactate concentrations in culture supernatants were measured at the time points indicated, in the absence (-) or presence (+) of 0.5 mM IPTG. Error bars indicate a 95% confidence interval based on the standard error of the mean for triplicate cultures. Asterisks denote statistically relevant differences between indicated strains. † - Culture death.

lower chlorophyll content than both cSJ008 and cSJ038 at 5 days post-induction (**Figures S5A, B**), though cell density was on par with the remaining strains (**Figure S3**).

Effect of Double Knock-Outs of the *flv1*, *flv3*, and *pgr5* Genes in Different Conditions

Given that the *flv1* and *flv3* single KO mutants behaved differently, we set out to compare D-lactate production in double *flv1*/*flv3* KO strains as well as in *flv* KO combinations with Δ*pgr5*, in different growth conditions. At 38°C and 1% (v/v) CO_2, the effect of different double KO combinations was minimal, with a very marginal decrease in production titers in the Δ*flv3*/Δ*pgr5* (cSJ079) strain (**Figure 5**); whereas at 25°C and 1% (v/v) CO_2, all KO combinations had a clear positive effect on D-lactate production, resulting in increased productivity per cell density (**Figure S7**), though at the cost of stunted growth and decreased strain fitness (**Figure S6**). Under ambient CO_2 conditions, the effect on D-lactate production of the different background mutations was highly dependent on temperature. While at 38°C, combinations of *flv1* or *flv3* KO with *pgr5* KO increased D-lactate production, the double *flv1*/*flv3* KO had a slightly negative impact, both in terms of titer (**Figure 5**) as well as in per cell density productivity (**Figure S7**). As mentioned, under these conditions, single *flv* gene deletions (in cSJ042 and cSJ048, **Figure 4**) did not decrease D-lactate production, which again supports the idea that Flv1 and Flv3 may be able to act independently to some extent.

At lower temperature, all strains behaved similarly, with a strong enhancement of D-lactate production titers (**Figure 5**)

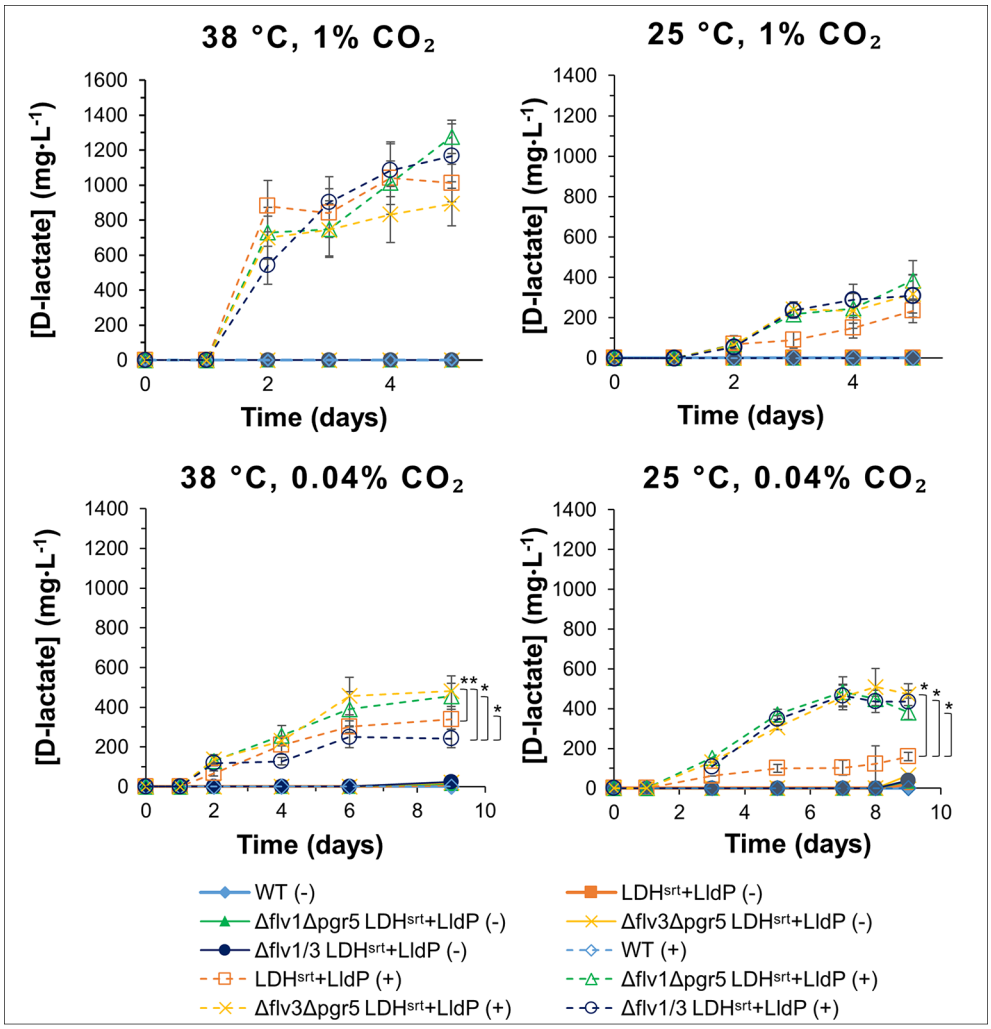

FIGURE 5 | D-lactate production in several electron transport double mutants under different growth conditions. D-lactate concentrations in culture supernatants were measured at the time points indicated, in the absence (-) or presence (+) of 0.5 mM IPTG. Error bars indicate a 95% confidence interval based on the standard error of the mean for triplicate cultures. Asterisks denote statistically relevant differences between indicated strains.

and per cell density productivities (**Figure S7**), even though growth was affected in all double KO strains (**Figure S6**). It should be noted that the double KO backgrounds did not allow as high production titers at low temperature and ambient CO_2 concentrations as the single KO strains (**Figure 4**), with double KO strains having a stunted growth in comparison to single KO strains (**Figure S6**). In that respect, the enhancement of D-lactate production granted by the single *pgr5* KO at 25°C and ambient CO_2 seems to be negated in the double KO strains when any of the *flv* genes was also deleted, though, interestingly, chlorophyll content of the D-lactate producing double KO strains was not as severely affected in comparison to strain cSJ008 as that of single KO strains (**Figure S5** and **S8**), though this may also be related to the overall lower production titers attained by the double KO strains.

pH Control Improves D-Lactate Productivities

Given that D-lactate production at g/L concentrations severely decreases the pH of the medium to an average pH of between 5-6 four days post-induction (data not shown), thus inhibiting culture growth, different strategies were devised to test whether pH control would result in increased production. As shown in **Figure S9**, addition of extra buffer (50 mM HEPES, pH 8.0) allowed an increase in production titers of roughly 30% after 3 days. However, cultures suffered a significant decline after the third day, with D-lactate concentrations also dropping. On the other hand, adjusting pH to ≈8.2 by adding a strong inorganic base (NaOH) whenever culture pH dropped below 7 had a better effect, with production after 3 days reaching ≈1.45 g/L, a titer almost double that of the previously reported maximum

for D-lactate producing strains of Syn7002 grown under similar conditions (Gordon et al., 2016). It is likely that using a continuous pH–monitoring online system would help to further improve production.

DISCUSSION

Our work has demonstrated that the manipulation of alternative electron transfer pathways associated with photosynthetic electron flow is a valid strategy for increasing photosynthetic production of biomolecules from the pyruvate node without utilizing a CO_2-enriched air supply.

Our results support the hypothesis, based on previous work in Syn6803 (Helman et al., 2003) and Syn7002 (Shimakawa et al., 2016), that loss of the Flv1 and Flv3 subunits in Syn7002 leading to over-reduction of the acceptor side of PSI in the light, thereby likely increasing the ratio of [NADPH]/[$NADP^+$] in the cell, improves the rate of reduction of pyruvate to D-lactate by an $NADP^+$-dependent LDH. Previous work has shown that *flv* transcript levels increase in Syn7002 in response to low CO_2 concentrations but not in response to a transient high light treatment (Ludwig and Bryant, 2012a). These observations correlate well with the observed increase in D-lactate production in Δ*flv* strains at low temperature and ambient CO_2 concentrations — conditions that promote elevated levels of NADPH due to slowed CO_2 fixation and reduced consumption of NADPH and ATP in the Calvin-Benson cycle. Furthermore, transcript levels for both *flv* genes were shown to increase in Syn7002 in response to low temperature, signaling that these genes may be important in the response to low temperature stress (Ludwig and Bryant, 2012b) and that their deletion under these conditions may therefore lead to a more severe response than at standard (higher temperature) conditions. Recent work also suggests that deletion of *flv* genes has pleiotropic effects in Syn6803 (Mustila et al., 2016), which might contribute to the growth defects we see in the various single and double *flv* mutants.

Previous studies on the two Flv subunits in Syn7002 has been limited to the analysis of a double KO mutant (Shimakawa et al., 2016). Our results suggest that disruption of either of the two *flv* homologues can disrupt the redox balance in the cell by (perhaps partially) disrupting alternative electron flow and PSI oxidation, especially at lower temperatures and CO_2 concentrations. However, at least in some conditions (such as at lower temperature and high CO_2), Flv1 and Flv3 are not functionally equivalent, with Flv3 playing a more important physiological role, in line with previous studies in Syn6803 (Hackenberg et al., 2009; Mustila et al., 2016). The heterodimeric complex of Flv1/3 was previously shown to have an important role in the rapid response of Syn6803 to fluctuating light (Allahverdiyeva et al., 2013), with the Flv2/4 heterodimer contributing mostly to a steady-state response induced by low carbon availability (Shimakawa et al., 2015; Santana-Sanchez et al., 2019). It is therefore possible that growing *flv* mutants under fluctuating light might further enhance D-lactate production through transient perturbations in the ratio of [NADPH]/[$NADP^+$]. Even though the transcriptome of *flv* mutant strains of Syn6803 has been thoroughly characterized in previous studies (Mustila et al., 2016), so far there has been no attempt to study changes to the global metabolome in response to these mutations. Given that Flv proteins are currently considered to be part of an electron overflow pathway to oxygen, our results could be explained by an increase in the intracellular [NADPH]/[$NADP^+$] ratio. However, in view of the pleiotropic effects of these mutations observed in previous studies (Mustila et al., 2016), a complete metabolome study will be necessary in order to more fully understand the full impact of *flv* and *pgr5* deletions in different cyanobacteria.

Disruption of the *pgr5* gene had a surprisingly strong effect on D-lactate production at lower temperatures and CO_2 concentrations. While little is known about the function of this protein in cyanobacteria, our results suggest that it has an important role in alternative electron flow and redox balance in the cell under limiting CO_2 and/or lower temperature. Strikingly, a D-lactate producing strain with a *pgr5* deletion, while only able to accumulate to lower cell densities, had higher per cell density productivity (**Figure S4**) and almost no loss of chlorophyll content in comparison to induced cSJ008 (**Figure S5**). Previously, an *A. thaliana pgr5*-null mutant was shown to have a significant growth defect at high light intensities (>150 μmol photons·m^{-2}·s^{-1}) when grown in ambient CO_2 conditions, a defect that could be partially suppressed when the strain was grown under CO_2-enriched air (Munekage et al., 2008). This was argued to be due to a shortfall in ATP synthesis that hindered effective carbon fixation in low CO_2 conditions combined with enhanced photoinhibition of PSI owing to an over-reduced acceptor side. Though further studies will be required to accurately pinpoint the mechanism of action of *pgr5* in Syn7002, deletion of *pgr5* may be a valid strategy to enhance production of molecules from the pyruvate node at ambient temperature (thus obviating the extra energy expenditure to keep cultures at the relatively high temperature of 38°C) and CO_2 concentrations. While the strains developed here do require longer timespans to reach similar titers to WT background strains grown at elevated temperature and CO_2 concentrations, our work demonstrates that high titers are achievable under "standard" conditions, with further developments now focusing on decreasing the production time so as to increase economic viability of the process.

As recently discussed by Erdrich and co-workers (Erdrich et al., 2014), there is a discrepancy between the required ATP/NADPH ratio for biomass production (1.51), the ratio derived from photosynthetic linear electron flow (1.28) and that required for, e.g., efficient ethanol production (1.17). Therefore, in order to efficiently redirect carbon flux from biomass to product formation, mutations decreasing the ATP/NADPH ratio (by either increasing NADPH concentration and/or increasing ATP turnover rate) can have beneficial effects on production. One of the suggested modifications to achieve this goal is the disruption of the

pseudocyclic electron flow catalyzed by the Flv proteins, a suggestion that is supported by the findings in this work. Overall, our study validates the concept that re-routing cyclic and pseudocyclic electron flow in cyanobacteria is a viable strategy to improve direct bioconversion of CO_2 to relevant products (such as D-lactate) in a sustainable, eco-friendly manner.

DATA AVAILABILITY STATEMENT

All datasets generated for this study are included in the article/ **Supplementary Material**.

AUTHOR CONTRIBUTIONS

TS, BN and PN devised the experiments. TS, NI and JJ performed the experiments. TS, JJ, BN and PN analyzed the data. TS and PN wrote the manuscript.

FUNDING

This work was supported by NTU grants M4080306 to BN and M4081714 to PN.

ACKNOWLEDGMENTS

The authors would like to thank Prof. Bertil Andersson for his support and encouragement and his fundamental role in establishing the CyanoSynBio@NTU laboratory.

SUPPLEMENTARY MATERIAL

The Supplementary Material for this article can be found online at: https://www.frontiersin.org/articles/10.3389/fpls.2019.01700/full#supplementary-material

REFERENCES

Allahverdiyeva, Y., Mustila, H., Ermakova, M., Bersanini, L., Richaud, P., Ajlani, G., et al. (2013). Flavodiiron proteins Flv1 and Flv3 enable cyanobacterial growth and photosynthesis under fluctuating light. *Proc. Natl. Acad. Sci. U. S. A.* 110, 4111–4116. doi: 10.1073/pnas.1221194110

Arnon, D. I., McSwain, B. D., Tsujimoto, H. Y., and Wada, K. (1974). Photochemical activity and components of membrane preparations from blue-green algae. I. Coexistence of two photosystems in relation to chlorophyll a and removal of phycocyanin. *BBA - Bioenerg.* 357, 231–245. doi: 10.1016/0005-2728(74)90063-2

Begemann, M. B., Zess, E. K., Walters, E. M., Schmitt, E. F., Markley, A. L., and Pfleger, B. F. (2013). An organic acid based counter selection system for cyanobacteria. *PloS One* 8, e76594. doi: 10.1371/journal.pone.0076594

Bond, S. R., and Naus, C. C. (2012). RF-Cloning.org: an online tool for the design of restriction-free cloning projects. *Nucleic Acids Res.* 40, W209–W213. doi: 10.1093/nar/gks396

Burgess, S. J., Taha, H., Yeoman, J. A., Iamshanova, O., Chan, K. X., Boehm, M., et al. (2016). Identification of the elusive pyruvate reductase of *Chlamydomonas reinhardtii* chloroplasts. *Plant Cell Physiol.* 57, 82–94. doi: 10.1093/pcp/pcv167

DalCorso, G., Pesaresi, P., Masiero, S., Aseeva, E., Schünemann, D., Finazzi, G., et al. (2008). A complex containing PGRL1 and PGR5 is involved in the switch between linear and cyclic electron flow in Arabidopsis. *Cell* 47, 230–242. doi: 10.1016/j.cell.2007.12.028

Eiteman, M. A., and Ramalingam, S. (2015). Microbial production of lactic acid. *Biotechnol. Lett.* 37, 955–972. doi: 10.1007/s10529-015-1769-5

Elhai, J., and Wolk, C. P. (1988). A versatile class of positive-selection vectors based on the nonviability of palindrome-containing plasmids that allows cloning into long polylinkers. *Gene* 68, 119–138. doi: 10.1016/0378-1119(88)90605-1

Erdrich, P., Knoop, H., Steuer, R., and Klamt, S. (2014). Cyanobacterial biofuels: New insights and strain design strategies revealed by computational modeling. *Microb. Cell Fact.* 13, 128. doi: 10.1186/s12934-014-0128-x

Gao, F., Zhao, J., Chen, L., Battchikova, N., Ran, Z., Aro, E.-M., et al. (2016). The NDH-1L-PSI supercomplex is important for efficient cyclic electron transport in cyanobacteria. *Plant Physiol.* 172, 1451–1464. doi: 10.1104/pp.16.00585

Gordon, G. C., Korosh, T. C., Cameron, J. C., Markley, A. L., Begemann, M. B., and Pfleger, B. F. (2016). CRISPR interference as a titratable, trans-acting regulatory tool for metabolic engineering in the cyanobacterium *Synechococcus* sp. strain PCC 7002. *Metab. Eng.* 38, 170–179. doi: 10.1016/j.ymben.2016.07.007

Hackenberg, C., Engelhardt, A., Matthijs, H. C. P., Wittink, F., Bauwe, H., Kaplan, A., et al. (2009). Photorespiratory 2-phosphoglycolate metabolism and photoreduction of O_2 cooperate in high-light acclimation of *Synechocystis* sp. strain PCC 6803. *Planta* 230, 625–637. doi: 10.1007/s00425-009-0972-9

Hanke, G., and Mulo, P. (2013). Plant type ferredoxins and ferredoxin-dependent metabolism. *Plant Cell Environ.* 36, 1071–1084. doi: 10.1111/pce.12046

Helman, Y., Tchernov, D., Reinhold, L., Shibata, M., Ogawa, T., Schwarz, R., et al. (2003). Genes encoding A-type flavoproteins are essential for photoreduction of O_2 in cyanobacteria. *Curr. Biol.* 13, 230–235. doi: 10.1016/S0960-9822(03)00046-0

Labs, M., Rühle, T., and Leister, D. (2016). The antimycin A-sensitive pathway of cyclic electron flow: from 1963 to 2015. *Photosynth. Res.* 129, 231–238. doi: 10.1007/s11120-016-0217-2

Lea-Smith, D. J., Bombelli, P., Vasudevan, R., and Howe, C. J. (2016). Photosynthetic, respiratory and extracellular electron transport pathways in cyanobacteria. *Biochim. Biophys. Acta - Bioenerg.* 1875, 247–255. doi: 10.1016/j.bbabio.2015.10.007

Li, C., Tao, F., Ni, J., Wang, Y., Yao, F., and Xu, P. (2015). Enhancing the light-driven production of d-lactate by engineering cyanobacterium using a combinational strategy. *Sci. Rep.* 5, 9777. doi: 10.1038/srep09777

Ludwig, M., and Bryant, D. A. (2012a). Acclimation of the global transcriptome of the cyanobacterium *Synechococcus* sp. strain PCC 7002 to nutrient limitations and different nitrogen sources. *Front. Microbiol.* 3, 145. doi: 10.3389/fmicb.2012.00145

Ludwig, M., and Bryant, D. A. (2012b). Synechococcus sp. strain PCC 7002 transcriptome: Acclimation to temperature, salinity, oxidative stress, and mixotrophic growth conditions. *Front. Microbiol.* 3, 354. doi: 10.3389/fmicb.2012.00354

Markley, A. L., Begemann, M. B., Clarke, R. E., Gordon, G. C., and Pfleger, B. F. (2015). Synthetic biology toolbox for controlling gene expression in the cyanobacterium *Synechococcus* sp. strain PCC 7002. *ACS Synth. Biol.* 4, 595–603. doi: 10.1021/sb500260k

Meng, H., Liu, P., Sun, H., Cai, Z., Zhou, J., Lin, J., et al. (2016). Engineering a d-lactate dehydrogenase that can super-efficiently utilize NADPH and NADH as cofactors. *Sci. Rep.* 6, 24887. doi: 10.1038/srep24887

Munekage, Y., Hojo, M., Meurer, J., Endo, T., Tasaka, M., and Shikanai, T. (2002). PGR5 is involved in cyclic electron flow around photosystem I and is essential for photoprotection in *Arabidopsis*. *Cell* 110, 361–371. doi: 10.1016/S0092-8674(02)00867-X

Munekage, Y. N., Genty, B., and Peltier, G. (2008). Effect of PGR5 impairment on photosynthesis and growth in *Arabidopsis thaliana*. *Plant Cell Physiol.* 49, 1688–1698. doi: 10.1093/pcp/pcn140

Mustila, H., Paananen, P., Battchikova, N., Santana-Sánchez, A., Muth-Pawlak, D., Hagemann, M., et al. (2016). The flavodiiron protein Flv3 functions as a homo-oligomer during stress acclimation and is distinct from the Flv1/Flv3 hetero-

oligomer specific to the O_2 photoreduction pathway. *Plant Cell Physiol.* 57, 1468–1483. doi: 10.1093/pcp/pcw047

Nandha, B., Finazzi, G., Joliot, P., Hald, S., and Johnson, G. N. (2007). The role of PGR5 in the redox poising of photosynthetic electron transport. *Biochim. Biophys. Acta - Bioenerg.* 1767, 1252–1259. doi: 10.1016/j.bbabio.2007.07.007

Nawrocki, W. J., Bailleul, B., Cardol, P., Rappaport, F., Wollman, F. A., and Joliot, P. (2019). Maximal cyclic electron flow rate is independent of PGRL1 in *Chlamydomonas*. *Biochim. Biophys. Acta - Bioenerg.* 1860, 425–432. doi: 10.1016/j.bbabio.2019.01.004

Peterson, G. L. (1977). A simplification of the protein assay method of Lowry et al. which is more generally applicable. *Anal. Biochem.* 83, 346–356. doi: 10.1016/0003-2697(77)90043-4

Santana-Sanchez, A. I., Solymosi, D., Mustila, H., Bersanini, L., Aro, E.-M., and Allahverdiyeva, Y. (2019). Flv1-4 proteins function in versatile combinations in O_2 photoreduction in cyanobacteria. *Elife* 8, e45766. doi: 10.7554/eLife.45766

Schuller, J. M., Birrell, J. A., Tanaka, H., Konuma, T., Wulfhorst, H., Cox, N., et al. (2019). Structural adaptations of photosynthetic complex I enable ferredoxin-dependent electron transfer. *Science*, 257–260. doi: 10.1126/science.aau3613

Selão, T. T., Zhang, L., Knoppová, J., Komenda, J., and Norling, B. (2016). Photosystem II assembly steps take place in the thylakoid membrane of the cyanobacterium *Synechocystis* sp. PCC 6803. *Plant Cell Physiol.* 57, 95–104. doi: 10.1093/pcp/pcv178

Selão, T. T., Włodarczyk, A., Nixon, P. J., and Norling, B. (2019). Growth and selection of the cyanobacterium *Synechococcus* sp. PCC 7002 using alternative nitrogen and phosphorus sources. *Metab. Eng.* 54, 255–263. doi: 10.1016/j.ymben.2019.04.013

Shikanai, T., and Yamamoto, H. (2017). Contribution of cyclic and pseudo-cyclic electron transport to the formation of proton motive force in chloroplasts. *Mol. Plant* 10, 20–29. doi: 10.1016/j.molp.2016.08.004

Shimakawa, G., Shaku, K., Nishi, A., Hayashi, R., Yamamoto, H., Sakamoto, K., et al. (2015). FLAVODIIRON2 and FLAVODIIRON4 proteins mediate an oxygen-dependent alternative electron flow in *Synechocystis* sp. PCC 6803 under CO_2-limited conditions. *Plant Physiol.* 167, 472–480 doi: 10.1104/pp.114.249987

Shimakawa, G., Shaku, K., and Miyake, C. (2016). Oxidation of P700 in photosystem I is essential for the growth of cyanobacteria. *Plant Physiol.* 172, 1443–1450. doi: 10.1104/pp.16.01227

Stevens, S. E., Patterson, C. O. P., and Myers, J. (1973). The production of hydrogen peroxide by blue-green algae: a survey. *J. Phycol.* 9, 427–430. doi: 10.1111/j.1529-8817.1973.tb04116.x

Sun, T., Li, S., Song, X., Diao, J., Chen, L., and Zhang, W. (2018). Toolboxes for cyanobacteria: recent advances and future direction. *Biotechnol. Adv.* 36, 1293–1307. doi: 10.1016/j.biotechadv.2018.04.007

Suorsa, M., Järvi, S., Grieco, M., Nurmi, M., Pietrzykowska, M., Rantala, M., et al. (2012). PROTON GRADIENT REGULATION5 is essential for proper acclimation of *Arabidopsis* photosystem I to naturally and artificially fluctuating light conditions. *Plant Cell* 24, 2934–2948. doi: 10.1105/tpc.112.097162

Van Den Ent, F., and Löwe, J. (2006). RF cloning: a restriction-free method for inserting target genes into plasmids. *J. Biochem. Biophys. Methods* 67, 67–74. doi: 10.1016/j.jbbm.2005.12.008

Woo, H. M. (2017). Solar-to-chemical and solar-to-fuel production from CO_2 by metabolically engineered microorganisms. *Curr. Opin. Biotechnol.* 45, 1–7. doi: 10.1016/j.copbio.2016.11.017

Xiong, W., Cano, M., Wang, B., Douchi, D., and Yu, J. (2017). The plasticity of cyanobacterial carbon metabolism. *Curr. Opin. Chem. Biol.* 41, 12–19. doi: 10.1016/j.cbpa.2017.09.004

Yamamoto, H., Takahashi, S., Badger, M. R., and Shikanai, T. (2016). Artificial remodelling of alternative electron flow by flavodiiron proteins in *Arabidopsis*. *Nat. Plants* 2, 16012. doi: 10.1038/NPLANTS.2016.12

Yeremenko, N., Jeanjean, R., Prommeenate, P., Krasikov, V., Nixon, P. J., Vermaas, W. F. J., et al. (2005). Open reading frame ssr2016 is required for antimycin A-sensitive photosystem I-driven cyclic electron flow in the cyanobacterium *Synechocystis* sp. PCC 6803. *Plant Cell Physiol.* 46, 1433–1436. doi: 10.1093/pcp/pci147

Zhang, P., Eisenhut, M., Brandt, A. M., Carmel, D., Silén, H. M., Vass, I., et al. (2012). Operon *flv4-flv2* provides cyanobacterial photosystem II with flexibility of electron transfer. *Plant Cell* 24, 1952–1971. doi: 10.1105/tpc.111.094417

Conflict of Interest: The authors declare that the research was conducted in the absence of any commercial or financial relationships that could be construed as a potential conflict of interest.

frontiers in Plant Science

ORIGINAL RESEARCH
published: 14 February 2020
doi: 10.3389/fpls.2019.01784

The Integration of Multiple Nuclear-Encoded Transgenes in the Green Alga *Chlamydomonas reinhardtii* Results in Higher Transcription Levels

Noam Shahar[1], *Shira Landman*[1], *Iddo Weiner*[1,2], *Tamar Elman*[1], *Eyal Dafni*[1], *Yael Feldman*[1], *Tamir Tuller*[2,3] *and Iftach Yacoby*[1]*

[1] The George S. Wise Faculty of Life Sciences, School of Plant Sciences and Food Security, Tel Aviv University, Tel Aviv, Israel, [2] Department of Biomedical Engineering, The Iby and Aladar Fleischman Faculty of Engineering, Tel Aviv University, Tel Aviv, Israel, [3] The Sagol School of Neuroscience, Tel Aviv University, Tel Aviv, Israel

OPEN ACCESS

Edited by:
Dimitris Petroutsos,
UMR5168 Laboratoire de Physiologie Cellulaire Vegetale (LPCV), France

Reviewed by:
Ales Kovarik,
Academy of Sciences of the Czech Republic (ASCR), Czechia
Pierre Crozet,
Sorbonne Universités, France
Lutz Wobbe,
Bielefeld University, Germany

***Correspondence:**
Iftach Yacoby
iftachy@tauex.tau.ac.il

Specialty section:
This article was submitted to Plant Biotechnology, a section of the journal Frontiers in Plant Science

Received: 26 August 2019
Accepted: 20 December 2019
Published: 14 February 2020

Citation:
Shahar N, Landman S, Weiner I, Elman T, Dafni E, Feldman Y, Tuller T and Yacoby I (2020) The Integration of Multiple Nuclear-Encoded Transgenes in the Green Alga Chlamydomonas reinhardtii Results in Higher Transcription Levels. Front. Plant Sci. 10:1784. doi: 10.3389/fpls.2019.01784

The integration of genes into the nuclear genome of *Chlamydomonas reinhardtii* is mediated by Non-Homologous-End-Joining, thus resulting in unpredicted insertion locations. This phenomenon defines 'the position-effect', which is used to explain the variation of expression levels between different clones transformed with the same DNA fragment. Likewise, nuclear transgenes often undergo epigenetic silencing that reduces their expression; hence, nuclear transformations require high-throughput screening methods to isolate clones that express the foreign gene at a desirable level. Here, we show that the number of integration sites of heterologous genes results in higher mRNA levels. By transforming both a synthetic ferredoxin-hydrogenase fusion enzyme and a Gaussia-Luciferase reporter protein, we were able to obtain 33 positive clones that exhibit a wide range of synthetic expression. We then performed a droplet-digital polymerase-chain-reaction for these lines to measure their transgene DNA copy-number and mRNA levels. Surprisingly, most clones contain two integration sites of the synthetic gene (45.5%), whilst 33.3% contain one, 18.1% include three and 3.1% encompass four. Remarkably, we observed a positive correlation between the raw DNA copy-number values to the mRNA levels, suggesting a general effect of which transcription of transgenes is partially modulated by their number of copies in the genome. However, our data indicate that only clones harboring at least three copies of the target amplicon show a significant increment in mRNA levels of the reporter transgene. Lastly, we measured protein activity for each of the reporter genes to elucidate the effect of copy-number variation on heterologous expression.

Keywords: copy-number variation, *Chlamydomonas reinhardtii*, Microalgae, the position-effect, droplet-digital PCR

INTRODUCTION

Two main approaches are routinely used for transforming the green alga *Chlamydomonas reinhardtii*; the first includes integration into the chloroplast genome whilst the second includes integration into the nucleus. As opposed to its plastomic counterpart, nuclear transformation of *C. reinhardtii* is practically easier to perform and does not require selective cycles to obtain transgene homoplasmicity (Yamano et al., 2013). However, the integration of synthetic genes into the nuclear genome predominantly occurs randomly *via* Non-Homologues-End-Joining (NHEJ), leading to a large population of transformed cells with varied expression levels (Yamano et al., 2013; Weiner et al., 2018). Such phenomenon requires high-throughput screening methods for isolation of clones expressing the recombinant protein of interest at a desirable level, a non-trivial task that varies between target transgenes.

Such heterogeneity of nucleus-transformed clones is mainly explained by the "position effect", a common phenomenon in which the expression of foreign genes is modulated by the genomic properties of their integration sites (León and Fernández, 2007; Zhang et al., 2014). It was previously shown that in order to average out position effects, one should collect at least 240 transformed colonies of *C. reinhardtii* (Lodha et al., 2008). Moreover, it was shown that the integration of plasmids occasionally results in deletions of genomic sequences, genomic rearrangements, and insertion of short DNA sequences (derived from fragmented DNA of lysed cells that are co-transformed along with the cassette) (Zhang et al., 2014; Jinkerson and Jonikas, 2015). Furthermore, gene silencing is an additional factor that plays a role in hindering heterologous expression in microalgae; it was shown to occur both at the transcriptional and post-transcriptional levels (Wu-scharf and Cerutti, 2000; Shaver et al., 2010), and is most likely part of an "immune system" protecting the cell against viral infections and transposable elements. Overall, the process of obtaining nuclear-transformed clones with a reasonably high expression of synthetic genes in *C. reinhardtii* is challenging.

In attempts to overcome these limitations, recent studies have developed different genetic approaches; for example, by performing an Ultraviolet (UV) mutagenesis on transformed clones with low transgene expression levels, two clones that further displayed a significant increase in the accumulation of the foreign gene were isolated (UVM-4 and UVM-11) (Neupert et al., 2009). Additional transformations into these clones resulted in a relatively high and uniform expression of heterologous genes (Barahimipour et al., 2015; Barahimipour et al., 2016). It was demonstrated that this unique phenotype of UVM-4 and UVM-11 is due to a gain-of-function mutation in the chromatin modification gene H4Ac, which most likely plays a key-role in repressing the chromatin state at the time of exogenous DNA integration (Barahimipour et al., 2016). Another approach used is the development of a detection system for measuring the frequency of homologues recombination (HR) events to successfully select clones with a desired integration site (Nour-Eldin et al., 2018). In yet another path, sequence optimization techniques were applied on target genes to mimic endogenous features of ORFs (e.g., the particularly high GC-content of the *Chlamydomonas* nuclear genome and the introduction of native introns into transgenes), and by that reducing the number of false clones (i.e., resistant to the selective pressure, but do not express the target transgene) and increase overall heterologous expression (Baier et al., 2018; Weiner et al., 2018). Furthermore, the development of the CRISPR/Cas9 genetic system in *C. reinhardtii* could potentially reduce the position-effect by "directing" the inserted transgene into a specific locus (Shin et al., 2016; Greiner et al., 2017).

Another important genetic feature that is known to create population diversity is the Copy-Number Variation (CNV); it is defined as a DNA segment found at variable copy quantities in a homogenic population of cells. CNV is linked to dozens of diseases (Redon et al., 2006; Malhotra and Sebat, 2012), but also serves as an important means to create and conserve population heterogenicity (Redon et al., 2006). In the context of synthetic biology, and especially in plants — where transgenes are mostly integrated randomly into the nuclear genome — it was shown that heterologous genes can be inserted more than once into different genomic locations, or as tandem repeats at a single locus to play either a positive or negative role on their expression (Stockhaus et al., 1987; Hobbs et al., 1990; De Block, 1993; Hobbs et al., 1993; Jorgensen et al., 1996; Que et al., 1997; Ku et al., 1999; Schubert et al., 2004; Wang et al., 2015; Zhang et al., 2015); while integration into distant loci mainly results in a synergistic effect (i.e., the expression is increased proportionally to its cognate DNA copy-number), repeat arrangements often induce transgene-silencing. However, a comprehensive study by Schubert et al., which was carried on 132 transgenic lines of *Arabidopsis thaliana* using three different reporters, emphasized the positive effect of copy-number on expression levels regardless to the genomic position and/or arrangement (repeats or inverted repeats) (Schubert et al., 2004). Generally, copy-number analysis in transgenic plants is carried out to select for lines that harbor a single copy of the integrated gene, as these typically segregate in a Mendelian fashion and are less prone to exhibit gene-silencing (Wang et al., 2015). Hence, such synthetic-CNV (sCNV) can be a major element that increases variation of nuclear transgenic lines in *C. reinhardtii* as well. For example, it was previously suggested that strategies that intentionally tend to increase transgenes copy-number may improve synthetic expression in *C. reinhardtii* (Lauersen et al., 2016). Another study indirectly approved the positive effect of transgenes copy-number by transforming *C. reinhardtii* with several different plasmids that contained the same synthetic gene, fused onto different fluorescence proteins (Wichmann et al., 2018). However, a large-scale analysis of sCNV has not yet been studied in *C. reinhardtii* or in any other microalga.

Today, several methods are used for copy-number analysis: (i) the traditional southern-blot, (ii) Quantitative PCR (qPCR), and (iii) droplet-digital PCR (ddPCR) (Southern, 1975; Schloss, 1990; Hindson et al., 2011; Wang et al., 2015; Zhang et al., 2015; Stefano et al., 2016; Collier et al., 2017). While southern-blot is a powerful tool (e.g., it provides additional information regarding the genomic organization and the integrity of the integrated

cassette), it is arduous to use for a large number of samples, as it involves many laborious and time consuming steps, and was shown to yield unpredictable results when high number of DNA copies are examined (Collier et al., 2017). The recently developed ddPCR method was shown to detect the copy-number of genes as accurately as southern-blot analysis (Hindson et al., 2011; Pinheiro et al., 2012; Collier et al., 2017), and can be performed on a multiple number of samples simultaneously. Moreover, ddPCR has been optimized for CNV analysis in crop-plants (Demeke et al., 2014; Collier et al., 2017); for these reasons, we used ddPCR analysis to examine sCNV in *C. reinhardtii*.

In this work we studied the correlation between the number of DNA integration events, mRNA levels and expression levels in engineered strains of *C. reinhardtii*. For that purpose, we transformed both a synthetic ferredoxin-hydrogenase fusion enzyme (fd-hyd) (Eilenberg et al., 2016; Weiner et al., 2018) and a Gaussia-Luciferase reporter protein (gLuc) (Shao and Bock, 2008) into the nuclear genome of *C. reinhardtii*. We obtained 33 clones that exhibit a wide range of synthetic expression levels, and subsequently performed for each ddPCR to measure transgene DNA copy-number and mRNA levels. Finally, we measured protein activity for each of these clones to elucidate the impact of sCNV on heterologous expression.

MATERIALS AND METHODS

Algal Cultures, Growth Conditions and Chlorophyll Determination

The algal cultures of the wild-type clone CC-124 and the $hyda_{1,2}$ double-mutant (Meuser et al., 2012) were grown in Tris-Acetate-Phosphate (TAP) medium at 25°C under continuous cool daylight and cool white fluorescent lights (90 μmol m-2 s-1) stirring in 100 ml Erlenmeyers capped with silicone sponge enclosures. Experiments were performed when the cultures reached the density of $3x10^6$ cells/ml (as determined by Celeromics cell counter) that corresponds to chlorophyll concentrations of ~9 μg Chl/ml.

C. reinhardtii Nuclear Transformation

DNA sequences were synthesized and cloned (using a recombination-based technique - CloneEZ™), into the pSL18::aph7 (Fischer and Rochaix, 2001) or pChlamy_1 (GeneArt™) plasmids, under the control of the endogenous *PSAD* or *HSP70A/RBCS2* promoters for fd-hyd and gLuc, respectively. 2 μg of linearized fd-hyd and gLuc plasmids were transformed by electroporation into $1.5*10^7$ cells of $hyda_{1,2}$ double-mutant knockout strain and the wild-type strain CC-124, respectively, following the GeneArt *Chlamydomonas* Engineering Kit protocol (Life Technologies). Initial screening was carried out on Hygromycin (10 μg/ml).

Rhodobacter capsulatus High Throughput Screen

Prepared precisely as described in (Wecker et al., 2011). Algal strains, overlaid with engineered H_2-sensing *R. capsulatus*, were scanned using the Fuji FLA-5100 fluorescence imager. A 473 nm laser was used for excitation whereas 510 nm or 665 nm filters were used for quantifying GFP fluorescence and chlorophyll density, respectively.

Luciferase *In Vivo* Assay

The protocol for Luciferase *in vivo* screening was adopted from (Mayfield and Schultz, 2004; Shao et al., 2007; Shao and Bock, 2008; Rasala et al., 2011) with the following modifications: the algal colonies were incubated for 10 minutes in dark, and then 10 μl of 0.01 mM Coelenterazine were dropped onto each colony. Finally, the plate was scanned for bioluminescence using the MicroChemi 6.0 camera.

Nucleic Acids Extraction

One hundred milligrams of the cell pellet were taken for total RNA extraction using a RNeasy Plant Mini Kit (Qiagen 74903, http://www.qiagen.com/). One microgram of purified RNA from each sample was used for synthesis of complementary DNA (cDNA) using Applied Bio-System High-Capacity cDNA Reverse-Transcription Kit (with random primers). Thirty milligrams of the cell pellet were taken for total DNA extraction using an OMEGA E.Z.N.A SP Plant DNA kit. DNA and RNA concentrations were quantified by a Thermo Scientific™ NanoDrop™ 2000 Spectrophotometer.

Droplet Digital PCR

The ddPCR reaction mixture was prepared from a QX200™ ddPCR™ EvaGreen Supermix, 250 nM primers, 5 ng of cDNA/1 ng of DNA template (the cDNA quantity was based on the initial amount of RNA concentration used for the reverse-complementation) and DDW to a total volume of 22 μl. Each reaction mixture was loaded into a DG8™ Cartridge (Bio-Rad), and a volume of 70 μl of QX200™ Droplet Generation Oil was loaded into the oil-well of each channel. The DG8™ Cartridge was then placed into the QX200™ Droplet Generator. Next, 40 μl of the created droplets were transferred to a ddPCR™ 96-Well Plate. The plate was heat-sealed with a foil seal and further undergone PCR using C1000 Touch™ Thermal Cycler. Subsequently, the 96-well PCR plate was placed onto the QX200™ Droplet Reader. Further analysis of the data was performed using QuantaSoft™, where the absolute concentration of each target (fd-hyd or gLuc) was normalized to the absolute quantification of the reference gene *CBLP*. The primers used were:

- fd-hyd (5'- TCGCCATGCTGGAGAAGTC -3', 5'- AGCTGGACACGTAGGGGAT -3');
- gLuc (5'- CCCAAGTGGACCTGTGTGTG -3', 5'- CACTTCTTCAGCAGGTCGCTA -3');
- *CBLP* (5'- AAAGCCACGGACAGCACATC-3', 5'- GATGGCCAGTTCTGCCTGAC-3').

fd-hyd Induction

Anaerobic induction was carried out as follows: liquid cell cultures (40 ml) at mid log phase ($3x10^6$ cells/ml) were

concentrated by centrifugation (2,800 g for 7 min) and re-suspended in 4 ml of TAP HEPES buffer (50 mM HEPES, pH 7.8). The concentrated cells were transferred into septum stopper sealed 14 ml glass serum vials (Wheaton), covered by aluminum foil and purged for 30 min with Argon at room temperature. Thereafter, the concentrated cultures were incubated in dark, at room temperature, under 60 rpm agitation for additional 90 minutes.

Hydrogenase Activity Assay by Methyl-Viologen

Carried out precisely as described in (Eilenberg et al., 2016). Following two hours of dark anaerobiosis, cells were transferred into a buffer containing reduced methyl viologen and Triton-X for lysing the cells. A 500 µl sample was drawn from the headspace and the H_2 concentration was determined by gas chromatography. The amount of enzyme was calculated based on the constant fd-hyd specific activity (Yacoby et al., 2011).

Statistical Analysis

Pearson Correlation

Pearson correlation coefficients (rho) and p-values were calculated using python's "scipy.stats.pearsonr" function.

Two-Way ANOVA

To determine whether the effect of both the reporter type (fd-hyd or gLuc) and the DNA copy-number on the mRNA levels is significant, a two-way ANOVA test was carried out using SPSS.

Tukey's Range Test

To determine which of the copy-number group mRNA levels means are statistically different from each other, a Tukey's range test was performed using SPSS.

RESULTS

All data are summarized in **Table S1**.

Construction and Isolation of an Array of Clones With Varied Expression Levels

To obtain clones with a wide-range of synthetic expression levels, we took advantage of the random integration predominately occurring in the nuclear genome and performed two transformations, distinguished by the promoter, 5'UTR, reporter gene, 3'UTR and the presence of an intron (see supplemented 'DataSheet 1_v1' for GenBank files of full annotated plasmid sequences); (i) the $_p$ PSAD:fd-hyd cassette contains an optimized Hydrogenase (HYDA1) enzyme fused to an N-terminal Ferredoxin gene under the control of the native Photosystem I reaction center subunit II (PSAD) regulatory sequences. It was transformed into a mutant strain of *C. reinhardtii* which shows a negligible production of gaseous hydrogen (*the* $hyda_1$ and $hyda_2$ double-mutant strain) in order to screen for colonies that restored their ability to produce hydrogen. (ii) the $_p$ HSP70A/RBCS2:gLuc plasmid, which is comprised of an optimized Gaussia-Luicferase gene under the control of the native Heat-Shock Protein 70A promoter fused to the promoter of the Rubisco Small subunit 2 (RBCS2), and contains the first intron of the RBCS2 gene. It was transformed into the wild-type CC-124 strain (**Figure 1A**, *Algal Cultures, Growth Conditions and Chlorophyll Determination* and *C. reinhardtii Nuclear Transformation*, the ratio of plasmid to cells used is $\frac{1\ ng}{10{,}000\ cells}$). For each construct, we obtained 100 colonies for further analysis. To screen for hydrogen-producing colonies, we used an engineered *Rhodobacter capsulatus* that expresses GFP in the presence of gaseous hydrogen (Wecker et al., 2011; Wecker and Ghirardi, 2014) (**Figure 1B**, *Rhodobacter capsulatus High Throughput Screen*). To screen for gLuc positive colonies, we used a Luciferase *in vivo* assay, as described in (Shao and Bock, 2008) (**Figure 1C**, *Luciferase In Vivo Assay*). A total of 33 positive clones (17 fd-hyd and 16 gLuc, ~16% out of the initial collected pool) were collected for further analysis.

DNA Copy-Number and mRNA Level Quantifications

To quantify the number of transgenes integration events that occurred in each of the fd-hyd and the gLuc expressing clones, we extracted total DNA and performed digestion using the restriction enzyme *ScaI*, in order to exclude the possibility that tandem target duplications or targets found in the same chromosome would be encapsulated by the same droplet (*Nucleic Acids Extraction,* the cut site was located outside the amplicons). Next, we used the digested DNA template of each clone for two independent ddPCR reactions using the EvaGreen Supermix; the first reaction amplified an amplicon within the target reporter gene (fd-hyd or gLuc) and the second reaction amplified an amplicon within a reference gene, known to harbor a single copy in the *C. reinhardtii* genome (*CBLP)* (Schloss, 1990). The number of target molecules per µl ('concentration', retrieved by QuantaSoft™), obtained for each target gene was divided by the concentration obtained for the reference gene (**Figure 2A**); this ratio provided a non-integer number, which was further rounded to obtain the target's DNA copy-number (*Droplet Digital PCR*). Importantly, we did not detect major differences in the sCNV distribution between the fd-hyd and the gLuc expressing clones (**Figure 2B**), thus excluding the possibility that the sequence composition of the coding-sequence or the regulatory elements affects the integration efficiency in our conditions. Interestingly, we observed that the most frequent number of integration events is two (45.5%), whereas one integration site was found in 33.3% of all clones (**Figure 2C**). Additionally, 18.1% and 3.1% of clones contained three and four target copies, respectively (**Figure 2C**).

To quantify the mRNA levels for the fd-hyd clones we anaerobically incubated the cultures (in order to induce the fd-hyd expression for the later Hydrogenase activity assay, which was sampled from the same cultures), extracted total RNA and used a similar ddPCR analysis (without template restriction), normalized by the same reference house-keeping gene *CBLP* (Schloss, 1990) (*Nucleic Acids Extraction, Droplet Digital PCR, fd-hyd Induction*, **Figure 3A**). The same procedure was carried out on the gLuc clones, without anaerobic incubation (**Figure 3B**). Although our

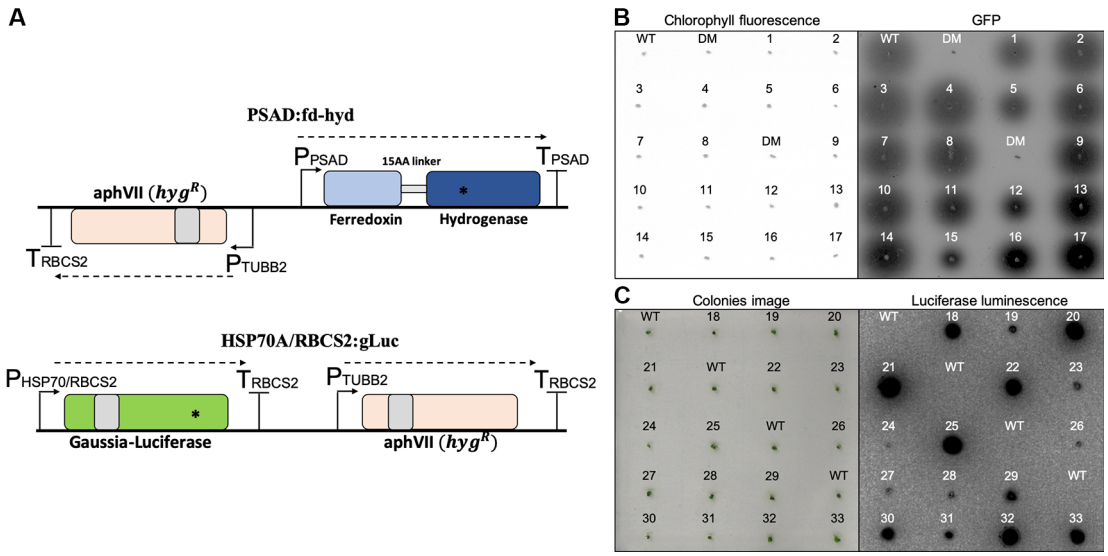

FIGURE 1 | Construction and selection of positive transformants expressing the reporter genes. **(A)** Plasmid maps of the fd-hyd (upper) and the gLuc (bottom) reporter genes. The fd-hyd transgene was cloned into a modified pSL18 vector (the *paro*^{R} was replaced by the *hyg*^{R}) under the control of the PSAD regulatory sequences. The gLuc transgene was cloned into pChlamy_1 plasmid (*hyg*^{R}) under the control of the HSP70A/RBCS2 promoters and the RBCS2 terminator. Gray boxes represent the first intron of the RBCS2 within the coding-sequences. Asterisks (*) represent the ddPCR amplicon loci of fd-hyd (51bp) and gLuc (85 bp). The cut site of *ScaI* is found outside the amplicon area (not shown). **(B)** *Rhodobacter* assay for selected hydrogen producing colonies. fd-hyd colonies were overlaid with engineered H_2-sensing *R. capsulatus* and were scanned using a 473 nm laser for excitation whereas 510 nm or 665 nm filters were used for quantifying GFP fluorescence (right) and chlorophyll density (left), respectively. **(C)** *in-vivo* Luciferase assay for the gLuc selected colonies; gLuc colonies were incubated for 10 min in dark, and then 10 µl of 0.01 mM Coelenterazine were dropped onto each colony. The left panels refer to either the detection of the colonies chlorophyll **(A)** or the photographs of colonies prior to luminescence imaging **(B)**. The right panels refer to GFP fluorescence emitted by *R. capsulatus* (A) or luminescence emitted by gLuc **(B)**. WT = CC-124 wild-type strain (which naturally produces hydrogen), DM = hyda$_{1,2}$ double-mutant strain (does not produce hydrogen). The numbers refer to clone indices.

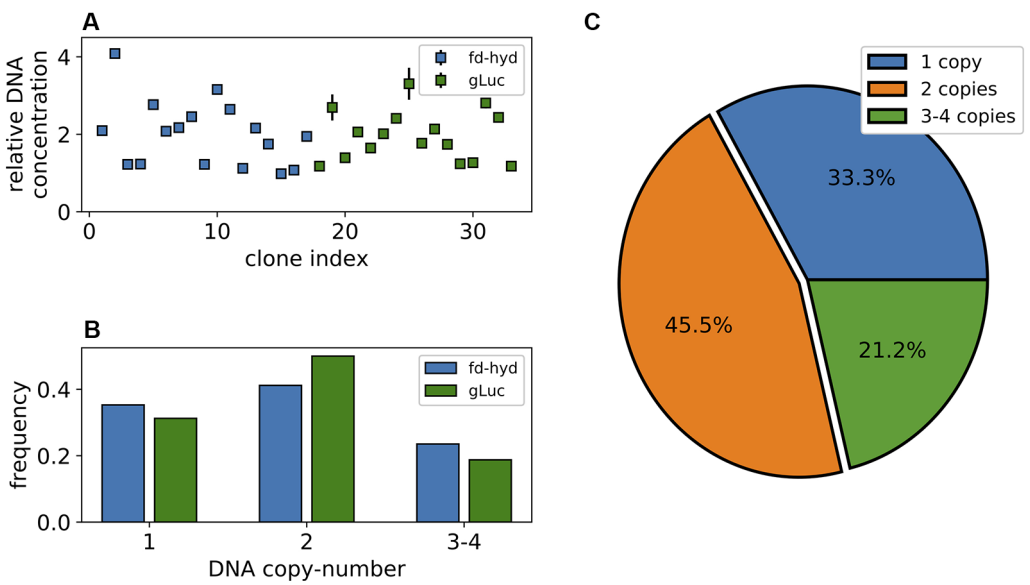

FIGURE 2 | Synthetic copy-number variation of the fd-hyd and the gLuc transgenic clones. **(A)** Transgenes DNA copy-number in 33 nucleus-transformed clones. Copy-number values are calculated as the ratio of the target's concentration to the reference gene (*CBLP*) concentration. The error bars represent the maximum and minimum values of Poisson distribution for the 95% confidence interval, as given by the QuantaSoft™ software. **(B)** The ratio of clones found in each copy-number group separated by the reporter gene. **(C)** Distribution of transgenes' copy-number in all clones.

results show that the gLuc transcript levels are generally lower than the fd-hyd mRNA abundance, we observed a significant correlation between the raw DNA copy-number values (the non-integer numbers received by the ratio of target-to-reference concentration) to the mRNA levels in each reporter separately (**Figures 3C, D** and *Pearson Correlation*; Pearson's rhos are 0.56, p = 0.02 and 0.55, p = 0.027 for the fd-hyd and the gLuc clones, respectively), indicating the positive effect of a transgene copy-number on its transcription level. Moreover, by grouping the mRNA levels to their cognate copy-number values (and by that reducing the variation created by the position effect), we observed a significant difference in transcription between the copy-number groups both in the fd-hyd and the gLuc clones (*Two-Way ANOVA*; 2-way ANOVA p = 0.002). Subsequently, we detected a significant separation between two-copies to ≥ three-copies groups, whereas the difference between one-copy to two-copies did not yield a significant difference (**Figure 3E** and *Tukey's Range Test*; Tukey's range test p = 0.03 and p = 0.93, respectively).

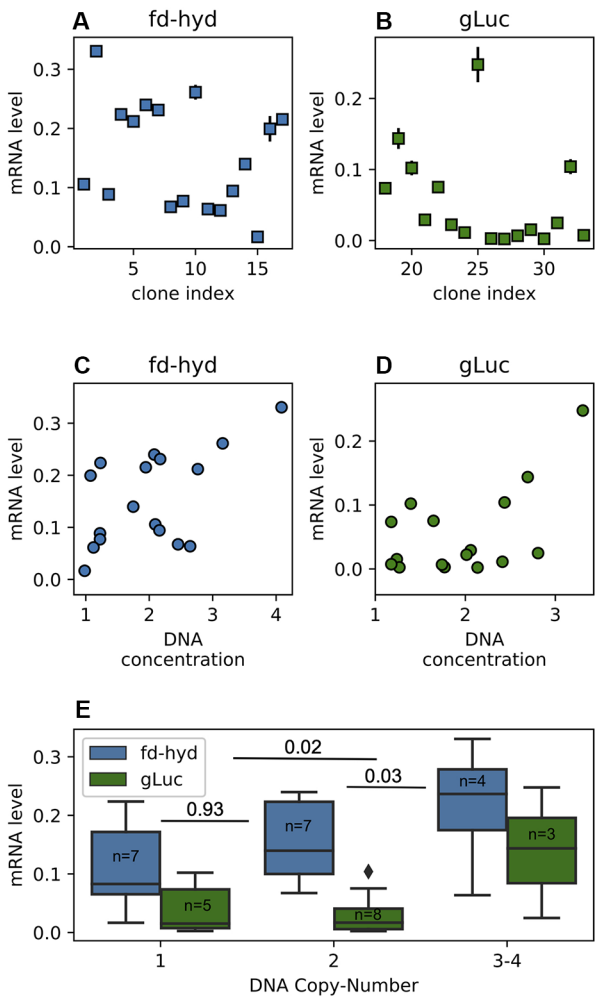

FIGURE 3 | Transgenes mRNA abundance in the fd-hyd and the gLuc clones. **(A, B)** Transgenes relative mRNA abundance in the fd-hyd and the gLuc clones, respectively. The mRNA levels are calculated as the ratio of the target's concentration to the reference gene (*CBLP*) concentration. The error bars represent the maximum and minimum values of Poisson distribution for the 95% confidence interval, as given by the QuantaSoft™ software. **(C, D)** The effect of the relative raw DNA concentration (non-integer values) on transcription levels in the fd-hyd and the gLuc clones, respectively. Pearson correlation coeffcients are 0.56, p = 0.02 and 0.55, p = 0.027 for the fd-hyd and the gLuc clones, respectively. **(E)** The effect of the DNA copy-number on transcription levels. P-values were calculated using two-way ANOVA post-hoc test, and are shown between each copy-number group. The line within each box represents the median. The number of samples for each group is indicated within each box. The copy-number group "3-4" also contains one clone that harbors a copy-number of four (fd-hyd clone #2).

Quantification of Protein Activity

To measure the fd-hyd active protein abundance we used the MV quantification assay (*Hydrogenase Activity Assay by Methyl-Viologen*) on three biological repeats (**Table S1**). To measure the gLuc reporter activity, we plated the colonies onto three independent plates while shuffling positions (**Figure S1, Table S1**) and performed a Luciferase *in-vivo* assay (Mayfield and Schultz, 2004; Rasala et al., 2011). To calculate the relative protein activity we used the image analysis software CFQuant (https://www.energylabtau.com/cfquant) (Dafni et al., 2019), and obtained the values of "Area" (i.e., sum of pixels) divided by the colony size. In order to reduce the variation between plates even further, these values were divided to the highest value within the same plate; this also allowed us to retrieve a normalized quantity which can further be averaged and compared between plates. We observed a strong positive correlation between the mRNA and protein activity in both constructs (**Figures 4A, B**, Pearson rhos are 0.55, p = 0.023 and 0.69, p = 0.003 for the fd-hyd and the gLuc clones, respectively). Finally, the direct correlation of the raw DNA values to protein activity levels is significant in the fd-hyd clones, whereas in the gLuc clones this effect is weak (**Figure S2**, Pearson rhos are 0.61, p = 0.009, and 0.11, p = 0.67 for the fd-hyd and the gLuc clones, respectively).

DISCUSSION

In this work, we suggest that in addition to already known factors (e.g., position-effects, epigenetic-silencing, location in 3D genomic organization, chromatin state, local DNA folding, interruption of native genes), the number of integration sites for a synthetic gene transformed into the nucleus of *C. reinhardtii* is yet another important feature that affects its transcription level and may contribute to the expression-heterogeneity between transgenic clones. By accurately measuring the number of integration sites of two different reporter genes in 33 nucleus-transformed clones, we revealed that the transformed transgene is usually integrated within one to two loci (~79%), whereas in most cases it is inserted two times (**Figure 2C**, based on the plasmid-to-cells ratio of 1:10,000). We observed that the two constructs used in this study show roughly the same distribution of DNA copy-number in the genome, even though they vary in the type of gene, sequence composition, presence of introns and the regulatory elements (**Figure 2B**). Importantly, because fragmented plasmids (that may carry the resistance gene solely) may potentially

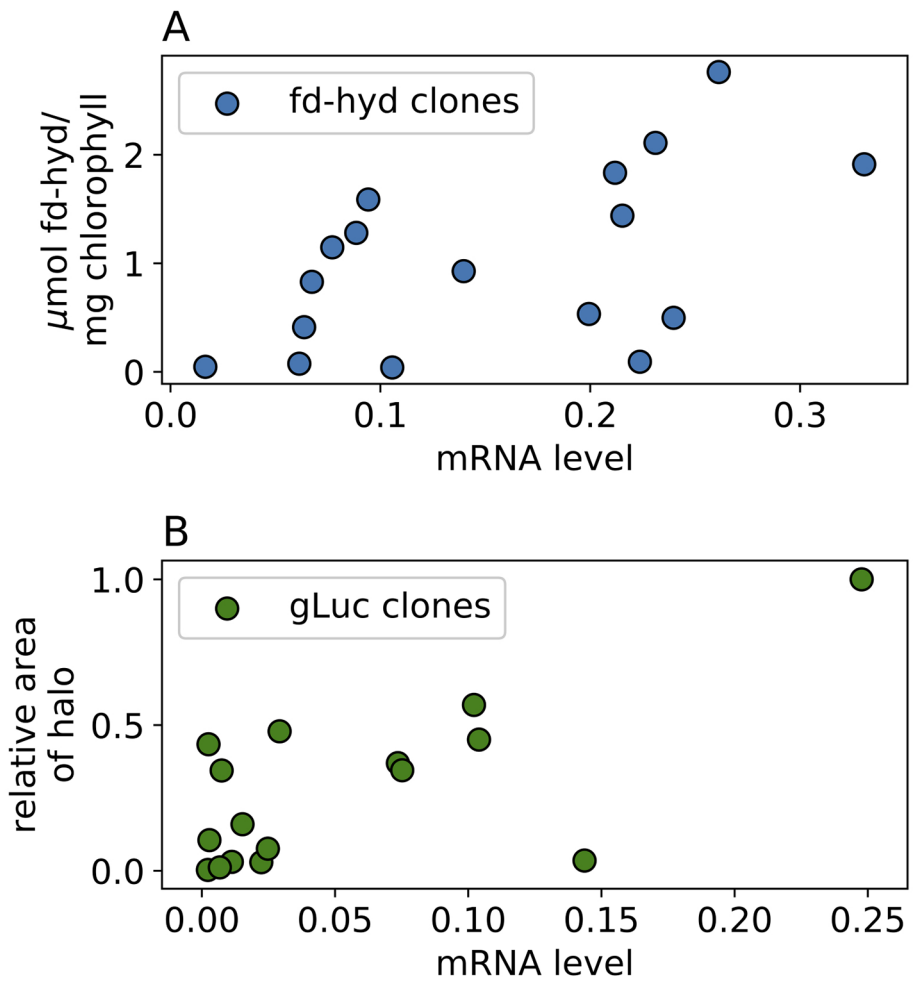

FIGURE 4 | The effect of mRNA levels on protein abundance in the fd-hyd and the gLuc clones. **(A)** the fd-hyd protein activity was measured using MV. The values are $\frac{\mu mol\ fd-hyd}{mg\ chlorophyll}$ X 10^6 **(B)** gLuc protein values were calculated using CFQuant's "Area" value normalized to the colony size (Dafni et al., 2019). Pearson rhos are 0.55, p = 0.023 and 0.69, p = 0.003 for the fd-hyd and the gLuc clones, respectively. All values show mean of three biological repeats.

integrate the genome at the time of transformation, we chose to assess the copy-number based on amplicons that are found within the reporter transgene sequences themselves.

To understand the effect of transgene copy-number on transcript levels, we measured the mRNA abundance in the transgenic clones. We were able to show that transgene DNA copy-number positively correlates with its conjugated mRNA levels, with the major effect of three and four copies (**Figures 3C–E**). However, it is critical to note that some clones with multiple integration sites exhibit low transcription levels, and vice-versa (i.e., some clones with a single copy-number show relatively high mRNA levels, **Figures 3C, D**); these exceptions may be explained by other factors (in which their degree varies between transgenes) that can potentially affect transcription; for example (i) the "position-effect", (ii) gene-silencing, (iii) integration of fragmented plasmids, and/or (iv) antagonistic effects of multiple insertion sites. Importantly, these "outliers" seem to be more frequent in the gLuc clones, a fact that together with their global reduction in mRNA levels (**Figures 3A, B**) emphasizes the notion that the nature of the sequence (e.g., regulatory elements, presence of introns, CDS properties) does affect transcription features. In order to reduce the effect (or "noise") of the above-mentioned factors we presented the data as averages of level of expression, separated by the copy-number groups (**Figure 3E**). Based on our experimental conditions, three integration events had the highest impact on transcription. According to this, one can estimate that multiple DNA copies of the transgene do not synergistically affect transcription (as a major part of transgene copies would not be expressed at all); alternatively, it can be hypothesized that the higher the transgene's copy-number is, the chances of at least one cassette to integrate into a highly expressed DNA region are increased. With that, it is tempting to use sCNV analysis in order to screen for highly expressing clones in *C. reinhardtii* (when no efficient

screening method exists) by searching for clones that harbor at least three copies of the integrated transgene.

Finally, we measured the recombinant protein abundance (as a function of protein activity) in our library (**Figures 4A, B**); the results align with earlier evidences, where the correlation between mRNA to protein levels in the nuclear genome of *C. reinhardtii* is high (Baier et al., 2018; Weiner et al., 2018). Yet, several lines show notable exceptions from this rule (e.g., clones with high mRNA levels show low/negligible levels of protein); these results may be explained by either post-transcriptional mechanisms of gene-silencing, and/or deletions or mutations at the synthetic gene regulatory elements (which may reduce translation efficiency), or at the CDS region (which may produce non-mature mRNAs, or yield a non-functional protein). Lastly, the direct effect of DNA copy-number on protein levels in the fd-hyd clones is significantly sound (**Figure S2A**); however, the same analysis yielded poor results on the gLuc clones (**Figure S2B**). As mentioned above, as the mRNA levels of the gLuc lines are less affected by their cognate DNA copy-number, let alone the protein levels - which are subject to more regulations (e.g., post-transcriptional and post-translational modifications).

DATA AVAILABILITY STATEMENT

All datasets generated for this study are included in the article/ **Supplementary Material**.

AUTHOR CONTRIBUTIONS

NS and IY designed the research. NS, SL, IW, TE, and YF performed the experimental procedures. NS, IW, and ED performed the computational procedures. NS, IW, TT and IY wrote the paper.

FUNDING

The single source of this research is Israel Science foundation grant number 1646/16.

ACKNOWLEDGMENTS

We would like to thank Professor Matthew Posewitz for the $hyda_{1,2}$ dodble knockout mutant, Professors Matt Wecker and Maria Ghirardi for the H_2-sensing *R. capsulatus*, and Dr. Hila Kobo for ddPCR consultation.

SUPPLEMENTARY MATERIAL

The Supplementary Material for this article can be found online at: https://www.frontiersin.org/articles/10.3389/fpls.2019.01784/full#supplementary-material

REFERENCES

Baier, T., Wichmann, J., Kruse, O., and Lauersen, K. J. (2018). Intron-containing algal transgenes mediate efficient recombinant gene expression in the green microalga *Chlamydomonas reinhardtii*. *Nucleic Acids Res.* 46, 6909–6919. doi: 10.1093/nar/gky532

Barahimipour, R., Strenkert, D., Neupert, J., Schroda, M., Merchant, S. S., and Bock, R. (2015). Dissecting the contributions of GC content and codon usage to gene expression in the model alga *Chlamydomonas reinhardtii*. *Plant J.* 84, 704–717. doi: 10.1111/tpj.13033

Barahimipour, R., Neupert, J., and Bock, R. (2016). Efficient expression of nuclear transgenes in the green alga Chlamydomonas: synthesis of an HIV antigen and development of a new selectable marker. *Plant Mol. Biol.* 90, 403–418. doi: 10.1007/s11103-015-0425-8

Collier, R., Dasgupta, K., Xing, Y.-P., Hernandez, B. T., Shao, M., Rohozinski, D., et al. (2017). Accurate measurement of transgene copy number in crop plants using droplet digital PCR. *Plant J.* 90, 1014–1025. doi: 10.1111/tpj.13517

Dafni, E., Weiner, I., Shahar, N., Tuller, T., and Yacoby, I. (2019). Image-processing software for high-throughput quantification of colony luminescence. *mSphere* 4, e00676–18. doi: 10.1128/msphere.00676-18

De Block, M. (1993). The cell biology of plant transformation: current state, problems, prospects and the implications for the plant breeding. *Euphytica*. 71, 1–4. doi: 10.1007/BF00023461

Demeke, T., Gräfenhan, T., Holigroski, M., Fernando, U., Bamforth, J., and Lee, S. J. (2014). Assessment of droplet digital PCR for absolute quantification of genetically engineered OXY235 canola and DP305423 soybean samples. *Food Control.* 46, 470–474. doi: 10.1016/j.foodcont.2014.06.018

Eilenberg, H., Weiner, I., Ben-Zvi, O., Pundak, C., Marmari, A., Liran, O., et al. (2016). The dual effect of a ferredoxin-hydrogenase fusion protein in vivo: Successful divergence of the photosynthetic electron flux towards hydrogen production and elevated oxygen tolerance. *Biotechnol. Biofuels* 9, 182. doi: 10.1186/s13068-016-0601-3

Fischer, N., and Rochaix, J. D. (2001). The flanking regions of PsaD drive efficient gene expression in the nucleus of the green alga *Chlamydomonas reinhardtii*. *Mol. Genet. Genomics* 265, 888–894. doi: 10.1007/s004380100485

Greiner, A., Kelterborn, S., Evers, H., Kreimer, G., Sizova, I., and Hegemann, P. (2017). Targeting of photoreceptor genes in *Chlamydomonas reinhardtii via* zinc-finger nucleases and CRISPR/Cas9. *Plant Cell.* 29, 2498–2518. doi: 10.1105/tpc.17.00659

Hindson, B. J., Ness, K. D., Masquelier, D. A., Belgrader, P., Heredia, N. J., Makarewicz, A. J., et al. (2011). High-throughput droplet digital PCR system for absolute quantitation of DNA copy number. *Anal. Chem.* 83, 8604–8610. doi: 10.1021/ac202028g

Hobbs, S. L. A., Kpodar, P., and DeLong, C. M. O. (1990). The effect of T-DNA copy number, position and methylation on reporter gene expression in tobacco transformants. *Plant Mol. Biol.* 15, 851–864. doi: 10.1007/BF00039425

Hobbs, S. L., Warkentin, T. D., and DeLong, C. M. (1993). Transgene copy number can be positively or negatively associated with transgene expression. *Plant Mol. Biol.* 21, 17–26. doi: 10.1007/BF00039614

Jinkerson, R. E., and Jonikas, M. C. (2015). Molecular techniques to interrogate and edit the Chlamydomonas nuclear genome. *Plant J.* 82, 393–412. doi: 10.1111/tpj.12801

Jorgensen, R. A., Cluster, P. D., English, J., Que, Q., and Napoli, C. A. (1996). Chalcone synthase cosuppression phenotypes in petunia flowers: Comparison of sense vs. antisense constructs and single-copy vs. complex T-DNA sequences. *Plant Mol. Biol.* 31, 957–973. doi: 10.1007/BF00040715

Ku, M. S. B., Agarie, S., Nomura, M., Fukayama, H., Tsuchida, H., Ono, K., et al. (1999). High-level expression of maize phosphoenolpyruvate carboxylase in transgenie rice plants. *Nat. Biotechnol.* 17, 76. doi: 10.1038/5256

Lauersen, K. J., Baier, T., Wichmann, J., Wördenweber, R., Mussgnug, J. H., Hübner, W., et al. (2016). Efficient phototrophic production of a high-value sesquiterpenoid from the eukaryotic microalga *Chlamydomonas reinhardtii*. *Metab. Eng.* 38, 331–343. doi: 10.1016/j.ymben.2016.07.013

León, R., and Fernández, E. (2007). Nuclear transformation of eukaryotic microalgae: historical overview, achievements and problems. *Adv. Exp. Med. Biol.* 616, 1–11. doi: 10.1007/978-0-387-75532-8_1

Lodha, M., Schulz-Raffelt, M., and Schroda, M. (2008). A new assay for promoter analysis in Chlamydomonas reveals roles for heat shock elements and the TATA box in HSP70A promoter-mediated activation of transgene expression. *Eukaryot. Cell.* 7, 172–176. doi: 10.1128/EC.00055-07

Malhotra, D., and Sebat, J. (2012). CNVs: Harbingers of a rare variant revolution in psychiatric genetics. *Cell.* 148, 1223–1241. doi: 10.1016/j.cell.2012.02.039

Mayfield, S. P., and Schultz, J. (2004). Development of a luciferase reporter gene, luxCt, for *Chlamydomonas reinhardtii* chloroplast. *Plant J.* 37, 449–458. doi: 10.1046/j.1365-313X.2003.01965.x

Meuser, J. E., D'Adamo, S., Jinkerson, R. E., Mus, F., Yang, W., Ghirardi, M. L., et al. (2012). Genetic disruption of both *Chlamydomonas reinhardtii* [FeFe]-hydrogenases: insight into the role of HYDA2 in H2 production. *Biochem. Biophys. Res. Commun.* 417, 704–709. doi: 10.1016/j.bbrc.2011.12.002

Neupert, J., Karcher, D., and Bock, R. (2009). Generation of Chlamydomonas strains that efficiently express nuclear transgenes. *Plant J.* 57, 1140–1150. doi: 10.1111/j.1365-313X.2008.03746.x

Nour-Eldin, H. H., Specht, E. A., Ostrand, J., Hoang, K. T. D., Karunanithi, P. S., and Mayfield, S. P. (2018). High-throughput system for quantifying and characterizing homologous recombination in *Chlamydomonas reinhardtii*. *Algal Res.* 31, 167–172. doi: 10.1016/j.algal.2018.02.005

Pinheiro, L. B., Coleman, V. A., Hindson, C. M., Herrmann, J., Hindson, B. J., Bhat, S., et al. (2012). Evaluation of a droplet digital polymerase chain reaction format for DNA copy number quantification. *Anal. Chem.* 84, 1003–1011. doi: 10.1021/ac202578x

Que, Q., Wang, H. Y., English, J. J., and Jorgensen, R. A. (1997). The frequency and degree of cosuppression by sense chalcone synthase transgenes are dependent on transgene promoter strength and are reduced by premature nonsense codons in the transgene coding sequence *Plant Cell.* 9, 1357–1368. doi: 10.1105/tpc.9.8.1357

Rasala, B. A., Muto, M., Sullivan, J., and Mayfield, S. P. (2011). Improved heterologous protein expression in the chloroplast of *Chlamydomonas reinhardtii* through promoter and 5' untranslated region optimization. *Plant Biotechnol. J.* 9, 674–683. doi: 10.1111/j.1467-7652.2011.00620.x

Redon, R., Ishikawa, S., Fitch, K. R., Feuk, L., Perry, G. H., Andrews, T. D., et al. (2006). Global variation in copy number in the human genome. *Nature.* 444, 444–454. doi: 10.1038/nature05329

Schloss, J. A. (1990). A Chlamydomonas gene encodes a G protein β subunit-like polypeptide. *MGG Mol. Gen. Genet.* 221, 443–452. doi: 10.1007/BF00259410

Schubert, D., Lechtenberg, B., Forsbach, A., Gils, M., Bahadur, S., and Schmidt, R. (2004). Silencing in Arabidopsis T-DNA transformants: the predominant role of a gene-specific RNA sensing mechanism versus position effects. *Plant Cell.* 16, 2561–2572. doi: 10.1105/tpc.104.024547

Shao, N., and Bock, R. (2008). A codon-optimized luciferase from Gaussia princeps facilitates the in vivo monitoring of gene expression in the model alga *Chlamydomonas reinhardtii*. *Curr. Genet.* 53, 381–388. doi: 10.1007/s00294-008-0189-7

Shao, N., Krieger-Liszkay, A., Schroda, M., and Beck, C. F. (2007). A reporter system for the individual detection of hydrogen peroxide and singlet oxygen: its use for the assay of reactive oxygen species produced in vivo. *Plant J.* 50, 475–487. doi: 10.1111/j.1365-313X.2007.03065.x

Shaver, S., Armando Casas-Mollano, J., Cerny, R. L., Cerutti, H. D., and Armando, J. (2010). Origin of the polycomb repressive complex 2 and gene silencing by an E(z) homolog in the unicellular alga Chlamydomonas. *Epigenetics* 54, 301–312. doi: 10.4161/epi.5.4.11608

Shin, S. E., Lim, J. M., Koh, H. G., Kim, E. K., Kang, N. K., Jeon, S., et al. (2016). CRISPR/Cas9-induced knockout and knock-in mutations in *Chlamydomonas reinhardtii*. *Sci. Rep.* 6, 27810. doi: 10.1038/srep27810

Southern, E. M. (1975). Detection of specific sequences among DNA fragments separated by gel electrophoresis. *J. Mol. Biol.* 98, 503–517. doi: 10.1016/S0022-2836(75)80083-0

Stefano, B., Patrizia, B., Cerboneschi, M., and Massimo, G. (2016). Inverse PCR and Quantitative PCR as Alternative Methods to Southern Blotting Analysis to Assess Transgene Copy Number and Characterize the Integration Site in Transgenic Woody Plants. *Biochem. Genet.* 54, 291–305. doi: 10.1007/s10528-016-9719-z

Stockhaus, J., Eckes, P., Blau, A., Schell, J., and Willmitzer, L. (1987). Organ-specific and dosage-dependent expression of a leaf/stem specific gene from potato after tagging and transfer into potato and tobacco plants. *Nucleic Acids Res.* 15, 3479–3491. doi: 10.1093/nar/15.8.3479

Wang, Y., Xiong, G., Hu, J., Jiang, L., Yu, H., Xu, J., et al. (2015). Copy number variation at the GL7 locus contributes to grain size diversity in rice. *Nat. Genet.* 47, 944–948. doi: 10.1038/ng.3346

Wecker, M. S. A., and Ghirardi, M. L. (2014). High-throughput biosensor discriminates between different algal H2-photoproducing strains. *Biotechnol. Bioeng.* 111, 1332–1340. doi: 10.1002/bit.25206

Wecker, M. S. A., Meuser, J. E., Posewitz, M. C., and Ghirardi, M. L. (2011). Design of a new biosensor for algal H2production based on the H2-sensing system of Rhodobacter capsulatus. *Int. J. Hydrogen Energy* 36, 11229–11237. doi: 10.1016/j.ijhydene.2011.05.121

Weiner, I., Atar, S., Schweitzer, S., Eilenberg, H., Feldman, Y., Avitan, M., et al. (2018). Enhancing heterologous expression in *Chlamydomonas reinhardtii* by transcript sequence optimization. *Plant J.* 94, 22–31. doi: 10.1111/tpj.13836

Wichmann, J., Baier, T., Wentnagel, E., Lauersen, K. J., and Kruse, O. (2018). Tailored carbon partitioning for phototrophic production of (E)-α-bisabolene from the green microalga *Chlamydomonas reinhardtii*. *Metab. Eng.* 45, 211–222. doi: 10.1016/j.ymben.2017.12.010

Wu-scharf, D., and Cerutti, H. D. (2000). Transgene and transposon silencing in *Chlamydomonas reinhardtii* by a DEAH-Box RNA helicase transgene and transposon silencing in Chlamydomonas reinhardtii by a DEAH-Box RNA Helicase. *Science* (80-.), 1159–1162. doi: 10.1126/science.290.5494.1159

Yacoby, I., Pochekailov, S., Toporik, H., Ghirardi, M. L., King, P. W., and Zhang, S. (2011). Photosynthetic electron partitioning between [FeFe]-hydrogenase and ferredoxin:NADP+-oxidoreductase (FNR) enzymes *in vitro*. *Proc. Natl. Acad. Sci.* 108, 9396–9401. doi: 10.1073/pnas.1103659108

Yamano, T., Iguchi, H., and Fukuzawa, H. (2013). Rapid transformation of *Chlamydomonas reinhardtii* without cell-wall removal. *J. Biosci. Bioeng.* 115, 691–694. doi: 10.1016/j.jbiosc.2012.12.020

Zhang, R., Patena, W., Armbruster, U., Gang, S. S., Blum, S. R., and Jonikas, M. C. (2014). High-throughput genotyping of green algal mutants reveals random distribution of mutagenic insertion sites and endonucleolytic cleavage of transforming DNA. *Plant Cell.* 26, 1398–1409. doi: 10.1105/tpc.114.124099

Zhang, Y., Liu, Y., Zhang, J., Wang, G., Wang, J., and Liu, Y. (2015). Assessment of transgene copy number and zygosity of transgenic maize overexpressing Cry1Ie gene with SYBRï¿½ Green qRT-PCR. *Vitr. Cell. Dev. Biol. - Plant* 51, 125–134. doi: 10.1007/s11627-014-9658-5

Conflict of Interest: The authors declare that the research was conducted in the absence of any commercial or financial relationships that could be construed as a potential conflict of interest.

frontiers in Plant Science

ORIGINAL RESEARCH
published: 03 March 2020
doi: 10.3389/fpls.2020.00237

Cyanobacterial Production of Biopharmaceutical and Biotherapeutic Proteins

*Nico Betterle, Diego Hidalgo Martinez and Anastasios Melis**

Department of Plant and Microbial Biology, University of California, Berkeley, Berkeley, CA, United States

Efforts to express human therapeutic proteins in photosynthetic organisms have been described in the literature. Regarding microalgae, most of the research entailed a heterologous transformation of the chloroplast, but transformant cells failed to accumulate the desired recombinant proteins in high quantity. The present work provides methods and DNA construct formulations for over-expressing in photosynthetic cyanobacteria, at the protein level, human-origin bio-pharmaceutical and bio-therapeutic proteins. Proof-of-concept evidence is provided for the design and reduction to practice of "*fusion constructs as protein overexpression vectors*" for the generation of the bio-therapeutic protein interferon alpha-2 (IFN). IFN is a member of the Type I interferon cytokine family, well-known for its antiviral and anti-proliferative functions. Fusion construct formulations enabled accumulation of IFN up to 12% of total cellular protein in soluble form. In addition, the work reports on the isolation and purification of the fusion IFN protein and preliminary verification of its antiviral activity. Combining the expression and purification protocols developed here, it is possible to produce fairly large quantities of interferon in these photosynthetic microorganisms, generated from sunlight, CO_2, and H_2O.

Keywords: fusion protein, interferon, therapeutic protein, transgene expression, *Synechocystis*

OPEN ACCESS

Edited by:
Lutz Wobbe,
Bielefeld University, Germany

Reviewed by:
Rima Menassa,
London Research and Development Centre, Agriculture and Agri-Food Canada, Canada
Karen Ann McDonald,
University of California, Davis, United States

****Correspondence:***
Anastasios Melis
melis@berkeley.edu

Specialty section:
This article was submitted to Plant Biotechnology, a section of the journal Frontiers in Plant Science

Received: *24 October 2019*
Accepted: *14 February 2020*
Published: *03 March 2020*

Citation:
Betterle N, Hidalgo Martinez D and Melis A (2020) Cyanobacterial Production of Biopharmaceutical and Biotherapeutic Proteins. Front. Plant Sci. 11:237. doi: 10.3389/fpls.2020.00237

INTRODUCTION

Efforts to express human therapeutic proteins in photosynthetic microorganisms abound in the literature. In their preponderance, these entail heterologous transformation of microalgal chloroplasts as a synthetic biology platform for the production of biopharmaceutical and therapeutic proteins (Dyo and Purton, 2018, and references therein). The vast majority of such efforts have employed transformation of the chloroplast in the model green microalga *Chlamydomonas reinhardtii* via double homologous recombination of exogenous constructs encoding heterologous proteins (Demain and Vaishna, 2009; Surzycki et al., 2009; Tran et al., 2009; Coragliotti et al., 2011; Gregory et al., 2013; Jones and Mayfield, 2013; Rasala and Mayfield, 2015; Baier et al., 2018). A common feature of these efforts is the low yield of the transgenic

Abbreviations: *cpc*, operon encoding the phycobilisome peripheral phycocyanin antenna; CpcA, α-subunit of phycocyanin; CpcB, β-subunit of phycocyanin; cpcB*IFN, construct containing the cpcB, Xa, and IFN sequences; cpcB*His*IFN, construct containing the cpcB, His-tag, Xa, and IFN sequences in this order; dcw, dry cell weight; IFN, interferon alpha-2; NptI, kanamycin resistance protein; Xa, factor Xa protease cleavage site.

proteins, rarely exceeding 1% of the total *Chlamydomonas reinhardtii* protein (Dyo and Purton, 2018). In general, there is a need to develop methods that will systematically and reliably over-express eukaryotic, including human therapeutic, proteins in photosynthetic microorganisms. The problem is exacerbated because of the frequent assumption in the field that a strong promoter will automatically cause gene overexpression when, in practice, SDS-PAGE fails to show presence of the transgenic protein and only sensitive Western blot analysis can offer evidence of low-levels of expression. A qualitative rule-of-thumb for overexpression in this respect is ability to detect the transgenic protein in SDS-PAGE analysis of total protein extracts.

Bacterial proteins can be heterologously over-expressed in cyanobacteria, reportedly up to 20% of total soluble protein, by using the strong *cpc* operon and possibly other endogenous or exogenous promoters (Kirst et al., 2014; Zhou et al., 2014; Formighieri and Melis, 2016; Vijay et al., 2019). Examples are afforded by Zhou et al. (2014), who described the function of a modified (partial) endogenous cyanobacterial promoter (*Pcpc560*), derived from the native cyanobacterial *cpc* operon promoter. They examined the efficacy of this promoter to express (i) the *trans*-enoyl-CoA reductase (Ter) protein from *Treponema denticola*, a Gram-negative and obligate anaerobic bacterium, and (ii) the D-lactate dehydrogenase (DldhE) protein from *Escherichia coli*. Both of these bacterial-origin genes and proteins were readily overexpressed in cyanobacteria under the control of the *Pcpc*. Kirst et al. (2014) showed that *Synechocystis* readily overexpressed, at the protein level and under the native *Pcpc*, the *nptI* gene from *E. coli*, encoding the neomycin phosphotransferase, a kanamycin resistance conferring protein. Similarly, Xiong et al. (2015) showed overexpression of the *Pseudomonas syringae efe* gene, encoding an ethylene forming enzyme, in *Synechocystis* sp. PCC 6803. Of interest, in this respect, is the demonstration of enhanced EFE protein accumulation upon transformation of *Synechocystis* with multiple copies of the *P. syringae efe* gene (Xiong et al., 2015). Likewise, Chaves and co-workers provided evidence that cyanobacteria will over-express, at the protein level, the *cmR* gene from *E. coli*, encoding a chloramphenicol resistance protein (Chaves et al., 2016), and the isopentenyl diphosphate isomerase (*fni*) gene from *Streptococcus pneumoniae,* either under the native *Pcpc* (Chaves et al., 2016) or heterologous *Ptrc* promoter (Chaves and Melis, 2018), strengthening the notion of relatively unhindered over-expression of heterologous bacterial genes in cyanobacteria. Evidence of over-expression in these cases was the visual detection and direct quantification of the transgenic proteins from the Coomassie-stained SDS-PAGE-resolved total cellular protein, offering a measure on the substantial presence of the recombinant protein.

However, recent experience has also shown that heterologous expression of eukaryotic plant and yeast genes occurs at low protein levels, regardless of the promoter used and mRNA levels achieved in the cyanobacterial cytosol (Formighieri and Melis, 2016). For example, plant terpene synthases could not be expressed well in cyanobacteria under the control of different strong endogenous and heterologous promoters (Formighieri and Melis, 2014; Englund et al., 2018). Heterologous expression in cyanobacteria of the isoprene synthase (Lindberg et al., 2010; Bentley and Melis, 2012), β-phellandrene synthase (Bentley et al., 2013), geranyl diphosphate (GPP) synthase from a higher plant origin (Bentley et al., 2014; Formighieri and Melis, 2017; Betterle and Melis, 2018), and the alcohol dehydrogenase (*ADH1*) gene from yeast (Chen and Melis, 2013), all showed low levels of recombinant protein expression, even under the control of strong endogenous (e.g., *psbA2, rbcL, cpc*) or strong heterologous promoters (e.g., *Ptrc*), and even after following a careful codon-use optimization of the target transgene (Lindberg et al., 2010; Bentley and Melis, 2012; Ungerer et al., 2012; Bentley et al., 2013; Chen and Melis, 2013; Formighieri and Melis, 2014; Englund et al., 2018). Similarly, only low levels of expression were reported for a chimeric complex of plant enzymes, including the ethylene synthase *efe* gene from *Solanum lycopersicum* (tomato) (Jindou et al., 2014; Xue and He, 2014), limonene synthase from *Mentha spicata* (spearmint) (Davies et al., 2014) and *Picea sitchensis* (Sitka spruce) (Halfmann et al., 2014b), the sesquiterpene farnesene and bisabolene synthases from *Picea abies* (Norway spruce) (Halfmann et al., 2014a) and *Abies grandis* (grand fir) (Davies et al., 2014). In these and other studies, transgenic protein levels were not evident on an SDS-PAGE Coomassie stain of protein extracts and, frequently, shown by sensitive Western blot analysis only, which was evidence for an admittedly low-level expression of plant-origin transgenes.

In separate work, Desplancq et al. (2005) showed that transgenic *Anabaena* sp. PCC 7120, a filamentous cyanobacterium, was able to express the *E. coli*, e.g., bacterial origin, maltose-binding protein (MBP), yielding up to 250 mg MBP per L culture. In further work, Desplancq et al. (2008) showed that *Anabaena* was also able to express 100 mg per L of gyrase B (GyrB), a 23 kD *E. coli* protein. This is consistent with the notion that cyanobacteria easily express other "bacterial" origin proteins. Animal-origin eukaryotic transgenes, however, are difficult to express in cyanobacteria. Desplancq et al. (2008) showed that the eukaryotic (human) oncogene E6 protein, when expressed in cyanobacteria, is toxic to the cells. Since efforts to express the oncogene E6 by itself failed due to toxicity of the product, Desplancq et al. (2008) undertook to express it as a fusion-protein with the highly-expressed maltose-binding protein as the leader sequence in an MBP*E6 fusion. This effort resulted in a meager yield of 1 mg protein per L after 5 days of *nir* induction, i.e., 0.4% of the amount measured with MBP as the solo recombinant protein. They suggested that the MBP*E6 fusion protein has an inhibitory effect on its own expression and further that this oncoprotein is toxic to *Anabaena* cells, evidenced from the about 50% inhibition in cell growth observed in the MBP*E6 expressing transformants.

Interferons (IFNs) are a group of signaling proteins made and released by host cells in response to the presence of viruses. Interferons are named for their ability to "interfere" with viral infections of eukaryotic cells. Typically, a cell infected by a virus would release interferons causing adjacent cells to increase their anti-viral defenses. IFNs belong to the large class of proteins known as cytokines, used for communication between cells to trigger the protective defenses of the immune system that help eradicate pathogens (Parkin and Cohen, 2001). IFNs

also activate immune cells, and increase host defenses by up-regulating antigen presentation. Interferon alpha-2 (IFN) is a member of the Type I interferon cytokine family, known for its antiviral and anti-proliferative functions. Recombinant *E. coli* (bacterial) expression of IFN resulted in the substantial formation of inclusion bodies, and required numerous purification and renaturing/refolding steps (Clark, 2001) that decreased the protein yield. Bis et al. (2014) described an expression and purification scheme for IFN using the pET-SUMO bacterial expression system and a single purification step. Using the SUMO protein, as the fusion tag, increased the soluble protein expression and minimized the amount of inclusion bodies in *E. coli*. Following protein expression, the SUMO tag was cleaved with the Ulp1 protease leaving no additional amino acids on the fusion terminus (Bis et al., 2014). The purified protein had antiviral and anti-proliferative activities comparable to the WHO International Standard, NIBSC 95/650, and the IFN standard available from PBL Assay Science.

There is a need to develop recombinant DNA technologies for the generation of low-cost biopharmaceutical proteins, without relying on animal systems, and without causing depletion of natural resources, emission of greenhouse gases, or other environmental degradation. In this respect, a direct photosynthetic production of such compounds is promising. Recent work from this lab contributed with the design of oligonucleotide fusion constructs as protein overexpression vectors that could be used in cyanobacteria for the over-expression of recalcitrant plant, animal, and human genes. It was successfully applied in the over-expression of transgenic terpene synthases from a variety of plants in these photosynthetic microorganisms. The barrier to expressing eukaryotic plant proteins in cyanobacteria at high levels was thus overcome by the fusion-constructs technology (Formighieri and Melis, 2015, 2016; Chaves et al., 2017; Betterle and Melis, 2018, 2019). In this approach, highly-expressed endogenous cyanobacteria genes, such as the *cpcB* gene, encoding the β-subunit of phycocyanin, or highly-expressed heterologous genes, such as the *nptI* gene, encoding the kanamycin resistance protein, have successfully served as leader sequences in the fusion formulation, resulting in the accumulation of eukaryotic proteins up to ∼20% of the total cyanobacterial protein (Formighieri and Melis, 2015, 2016). This fusion construct technology was successfully applied in this work to enable accumulation in *Synechocystis* of the human interferon, serving as a proof of principle in the cyanobacterial synthesis and accumulation of biopharmaceutical proteins.

MATERIALS AND METHODS

Synechocystis Strains, Recombinant Constructs, and Culture Conditions

The cyanobacterium *Synechocystis* sp. PCC 6803 (*Synechocystis*) was used as the experimental strain in this work and referred to as the wild type (WT). A gene sequence encoding the human interferon α-2 protein (hereafter referred to as IFN)[1], without the corresponding N-terminal signal peptide, was codon optimized for protein expression in *Synechocystis* using an open software system[2]. DNA constructs for *Synechocystis* transformation were synthesized by Biomatik USA (Wilmington, DE, United States). Sequences of the DNA constructs are shown in the **Supplementary Material**.

Synechocystis transformations were carried out according to established protocols (Williams, 1988; Lindberg et al., 2010; Eaton-Rye, 2011). Wild type and transformants were maintained on BG11 media supplemented with 1% agar, 10 mM TES-NaOH (pH 8.2) and 0.3% sodium thiosulfate. Liquid cultures of BG11 were buffered with 25 mM sodium bicarbonate, pH 8.2, and 25 mM dipotassium hydrogen phosphate, pH 9, and incubated in the light upon slow continuous bubbling with air at 26°C. Transgenic DNA copy homoplasmy in the cells was achieved upon transformant incubation on agar in the presence of increasing concentrations of chloramphenicol (3–25 μg/mL). Growth of the cells was promoted by using a balanced combination of white LED bulbs supplemented with incandescent light to yield a final Photosynthetically Active Radiation (PAR) intensity of ∼100 μmol photons m^{-2} s^{-1}.

Genomic DNA PCR Analysis of *Synechocystis* Transformants

Genomic DNA templates were prepared, as previously described (Formighieri and Melis, 2014). A 20 μL culture aliquot was provided with an equal volume of 100% ethanol followed by brief vortexing. A 200 μL aliquot of a 10% (w/v) Chelex®100 Resin (BioRad) suspension in water was added to the sample prior to mixing and heating at 98°C for 10 min to lyse the cells. Following centrifugation at 16,000 *g* for 10 min to pellet cell debris, 5 μL of the supernatant was used as a genomic DNA template in a 25 μL PCR reaction mixture. Q5® DNA polymerase (New England Biolabs) was used to perform the genomic DNA PCR analyses. A list of primers used is given in the **Supplementary Table S1**. Transgenic DNA copy homoplasmy in *Synechocystis* was tested using suitable primers listed in the **Supplementary Material**. The genomic DNA location of these primers is indicated in **Figure 1** for the appropriate DNA constructs.

Protein Analysis

Cells in the mid exponential growth phase (OD_{730} ∼1) were harvested by centrifugation at 4,000 *g* for 10 min. The pellet was resuspended in a solution buffered with 25 mM Tris-HCl, pH 8.2, also containing a cOmplete™ mini protease inhibitor cocktail (Roche; one 50 mg tablet was added per 50 mL suspension). Cells were broken by passing the suspension through a French press cell at 1,500 psi. A slow speed centrifugation (350 *g* for 3 min) was applied to remove unbroken cells. For protein electrophoretic analysis, sample extracts were solubilized upon incubation for 1 h at room temperature in the presence of 125 mM Tris-HCl, pH 6.8, 3.5% SDS, 10% glycerol, 2M urea, and 5% β-mercaptoethanol. SDS-PAGE was performed using Mini-PROTEAN TGX precast gels (BIORAD). Densitometric quantification of target proteins, as a percentage of the total cellular protein, was performed

[1]https://www.uniprot.org/uniprot/P01563

[2]https://www.idtdna.com/CodonOpt

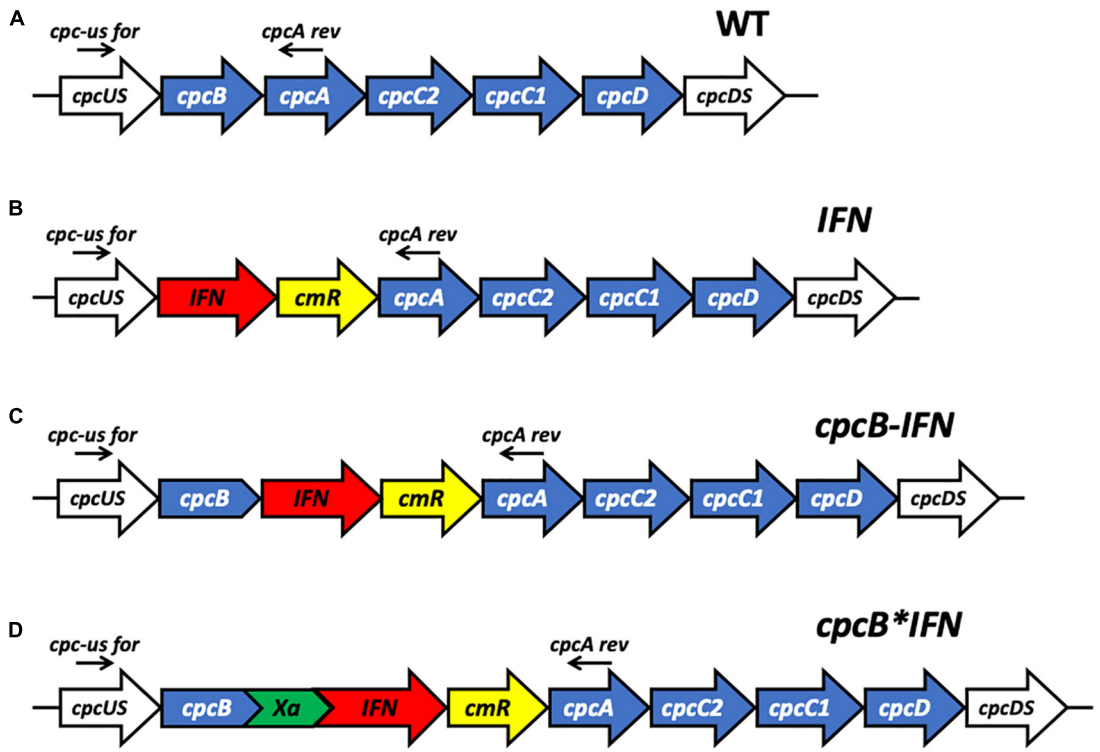

FIGURE 1 | Schematic overview of DNA constructs designed for the transformation of the *Synechocystis* PCC 6803 (*Synechocystis*) genome. **(A)** The native *cpc* operon, as it occurs in wild type S*ynechocystis*. This DNA sequence and associated strain are referred to as the wild type (WT). **(B)** Insertion in the *cpc* operon of the codon-optimized human interferon (*IFN*) gene followed by the chloramphenicol (*cmR)* resistance cassette in an operon configuration, replacing the phycocyanin-encoding β-subunit *cpcB* gene of *Synechocystis*. This DNA construct is referred to as *IFN*. **(C)** Insertion in the *cpc* operon of the codon-optimized *IFN* gene immediately downstream of the phycocyanin-encoding β-subunit *cpcB* gene of *Synechocystis,* followed by the *cmR* resistance cassette, in an operon configuration. This DNA construct is referred to as *cpcB-IFN*. **(D)** Insertion in the *cpc* operon of the codon-optimized *IFN* gene as a fusion construct with the phycocyanin-encoding β-subunit *cpcB* gene, with the latter in the leader sequence position. The fusion construct *cpcB*IFN* was followed by the *cmR* resistance cassette in an operon configuration. *cpcB* and *IFN* genes were linked by the DNA sequence encoding the Factor Xa cleavage site. The latter comprises the Ile-Glu/Asp-Gly-Arg amino acid sequence. This DNA construct is referred to as the *cpcB*IFN*.

using the BIORAD (Hercules, CA, United States) Image Lab software. A subsequent Western blot analysis entailed transfer of the SDS-resolved proteins to a 0.2 μm pore size PVDF membrane (Life Technologies, Carlsbad, CA, United States). Protein transfer to PVDF was followed by protein probing with rabbit-raised CpcA specific polyclonal antibodies (Abbiotec, San Diego, CA, United States), as previously described (Formighieri and Melis, 2015), or IFN-specific polyclonal antibodies (Abcam, Cambridge, MA, United States).

Recombinant Protein Purification

Total cellular extracts (concentration 100 μg dcw mL^{-1}) from wild-type and transformant strains of *Synechocystis* were gently solubilized upon incubation with 1% Triton X-100 at 0°C for 20 min. Solubilization of the extracts was conducted in an ice-water bath, upon gentle shaking. Following this solubilization treatment, samples were centrifuged at 10,000 *g* for 10 min to remove cell debris and insoluble material. His-Select resin (Sigma, St. Louis, MO, United States) was employed as a solid phase for protein binding and purification through cobalt affinity chromatography. Manufacturer's instructions were followed for both batch-type and column-based binding and purification. The washing solution was buffered with 20 mM Hepes, pH 7.5, and contained 150 mM NaCl and 10 mM imidazole to help remove non-target proteins. The elution solution was buffered with 20 mM Hepes, pH 7.5, and contained 150 mM NaCl and 250 mM imidazole to elute target protein from the resin.

Zn-Staining

SDS-PAGE was incubated in 5 mM zinc sulfate for 30 min (Li et al., 2016). To detect covalent chromophore-binding polypeptides, zinc induced fluorescence was monitored by Chemidoc imaging system (BIORAD), employing UV light as a light source. Loading of total protein extracts was the same as for the Coomassie-stained SDS-PAGE.

Interferon Activity

Viruses replicate by co-opting normal host cell functions, turning cells into viral factories. Interferon protects cells by binding to extracellular receptors activating a cascade of signals that shuts down both *de novo* protein and DNA synthesis, depriving the invader the means to replicate. This puts the cells into a semi

dormant state, preventing the production of new virus. This is most evident in the life cycle of lytic viruses, which normally burst or lyse target cells, but fail to do so when cells are in an interferon-induced antiviral state. Accordingly, one can assess interferon activity by visually comparing the number of intact/lysed cells for a particular concentration of interferon added (Rubinstein et al., 1981; Budd et al., 1984; Crisafulli et al., 2008).

A cytopathic effect (CPE) protection assay was employed to assess the capacity of cyanobacteria-derived interferon to lower viral infectivity. Human U20S osteosarcoma cells were seeded onto 24 well plates at a concentration of 5×10^5 cells per well and incubated overnight at 37°C and 5% CO_2. When confluent, cells were incubated with serial dilutions ranging from 1×10^{-3} to 1×10^{-7} μg/mL of either commercial interferon (IFN alpha 2 Cat. #11100-1 PBL Assay Science, Piscataway, NJ, United States), cyanobacteria-derived recombinant interferon Cpcb*His*IFN, or control diluent for 24 h prior to addition of vesicular stomatitis virus (VSV) (1×10^7) (pfu/mL), diluted to a final concentration of 200 plaques per well and incubated for 120 min at 37°C. Plaques were stabilized by adding premixed 2% methyl cellulose in 2x Dulbecco's modified Eagle's medium (DMEM) overlaid onto each well and incubated at 37°C overnight. At 24 h post-infection incubation with VSV, media were removed, cell monolayers were rinsed in PBS and stained using crystal violet (4% formaldehyde, glycerol and 0.5% crystal violet) for 1 h. Crystal violet stain was then removed, stained plates were washed in water and plaques subsequently counted.

RESULTS

*cpcB*IFN* Fusion Constructs

Case study of this experimental work is the heterologous expression of the mature human interferon α-2 protein[3], hereafter referred to as IFN, in the model cyanobacteria *Synechocystis* sp. PCC 6803 (*Synechocystis*). To validate the fusion constructs approach, three different DNA constructs were designed for the transformation of wild type (WT) *Synechocystis* through double homologous DNA recombination in the *cpc* operon locus (**Figure 1A**). Construct *IFN* (**Figure 1B**) was codon optimized for expression in *Synechocystis,* and designed to replace the *cpcB* gene in the *cpc* operon. In this case, *IFN* was followed by the chloramphenicol resistance cassette (*cmR*) in an operon configuration. Construct *cpcB-IFN* (**Figure 1C**) was designed to insert both the *IFN* and the *cmR* genes after the *cpcB* gene in an operon configuration. Finally, construct *cpcB*IFN* (**Figure 1D**) was conceived to replace the *cpcB* gene in the *cpc* operon with the fusion construct *cpcB*IFN,* followed by the *cmR* gene in an operon configuration. It is noteworthy that the Factor Xa cleavage-encoding sequence was inserted between the *cpcB* and *IFN* genes in the construct of **Figure 1D**. Factor Xa cleavage site was chosen because Factor Xa protease activity would free the N-terminus of the target protein, thus allowing recovery of the natural product (Kavoosi et al., 2007). The precise nucleotide sequence and spacers of these constructs is given in the **Supplementary Material** of this work. The above-described genetic manipulations caused a disruption in the physiological expression of the *cpc* operon and prevented the assembly of the phycocyanin peripheral antenna in the cyanobacteria. It is known that the *cpcB* gene and, in fact, the entire *cpc* operon can be deleted from the cyanobacterial genome, resulting in a smaller phycobilisome light-harvesting antenna size and requiring a higher light intensity for the saturation of photosynthesis but entailing no adverse cell or photosynthesis fitness effects (Ajlani and Vernotte, 1998; Page et al., 2012; Liberton et al., 2013; Kirst et al., 2014; Formighieri and Melis, 2015; Chaves et al., 2016).

Attainment of transgenic DNA copy homoplasmy in the three transformant strains was tested through genomic DNA PCR analysis. Primers *cpc-us for* and *cpcA rev* were designed on the flanking regions of the transgenic DNA insertion sites (**Figure 1**). PCR amplification using WT genomic DNA as a template generated a product of 1,289 bp (**Figure 2**). PCR amplification using DNA from the transformant IFN, CpcB-IFN, and CpcB*IFN strains generated the expected product sizes of 2,094, 2,723, and 2,619 bp, respectively. Attainment of DNA copy homoplasmy was evidenced by the absence of WT PCR products in the PCR amplification reactions of the IFN transformants.

Upon attainment of transgenic DNA copy homoplasmy, WT and transformant strains were grown photo-autotrophically in liquid BG-11 cultures. The visual phenotype was noticeably different between the WT and transformant strains, as shown in **Figure 3**. The WT cells had a blue–green coloration, consistent with the presence of blue phycocyanin and green chlorophyll pigments in their functional light-harvesting antennae. All transformant strains showed a yellow-green pigmentation, suggesting lack of phycocyanin, which is responsible for the blue pigmentation of the cells. This is consistent with previous results in the literature (Ajlani and Vernotte, 1998; Page et al., 2012; Kwon et al., 2013; Liberton et al., 2013; Kirst et al., 2014; Formighieri and Melis, 2015; Chaves and Melis, 2018) and underscores the absence of assembled phycocyanin rods in the transformants.

Protein analysis of total cell extracts from WT and transformant *Synechocystis* was implemented through SDS-PAGE followed by Coomassie blue staining and Western blot analysis (**Figure 4**). Two replicate samples of WT protein extracts showed the presence of CpcB β-subunit and CpcA α-subunit of phycocyanin as the dominant protein bands, migrating to ∼19 and ∼17 kD, respectively. Another dominant band in the SDS-PAGE profile was the large subunit of Rubisco (RbcL), migrating to about ∼56 kD (**Figure 4A**). The latter was used as a normalization factor in protein quantification and as a loading control of the gels.

CpcB and CpcA subunits were not evident in the protein extracts of the transformants because of inability of these transformants to assemble the phycobilisome-peripheral phycocyanin rods. The *IFN* and *cpcB-IFN* transformants failed to show accumulation of recombinant IFN protein in the expected ∼19 kD region, both in the SDS-PAGE and the associated Western blot (**Figure 4B**, IFN and CpcB-IFN), suggesting either

[3]https://www.uniprot.org/uniprot/P01563

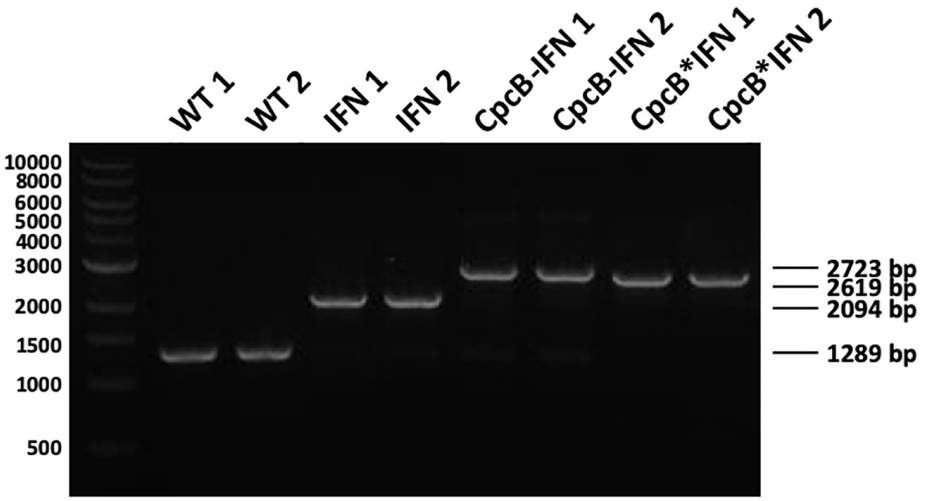

FIGURE 2 | Genomic DNA PCR analysis testing for transgenic DNA copy homoplasmy in *Synechocystis* transformants. Wild type and transformant strains were probed in genomic DNA PCR reactions for product generation and transgenic DNA segregation. Primers <*cpc-us for*> and <*cpcA rev*> showed substantially different and unique products in the wild type and the different transformants comprising the constructs of **Figure 1**. Wild type PCR products had a 1,289 bp size, whereas the IFN, cpcB-IFN, and the cpcB*IFN transformants generated 2,094, 2,723, and 2,619 bp size products, respectively. Absence of wild type products from the latter was evidence of DNA copy homoplasmy for the transformants. (The cpcB-IFN construct generated a product size slightly larger than that of the cpcB*IFN because it contained the *Synechocystis* native cpcB-cpcA intergenic DNA sequence. Please see gene nucleotide sequences in the **Supplementary Material**).

very-low levels or absence of the recombinant IFN protein from these samples. There results show that the powerful *cpc* promoter was not sufficient to support a measurable IFN (∼19 kD) protein expression/accumulation in *Synechocystis*. On the contrary, protein extracts from the *cpcB*IFN* fusion transformants showed a clear presence of an abundant protein with electrophoretic mobility to ∼36 kD. This band was attributed to accumulation of the CpcB*IFN fusion protein (**Figure 4A**, CpcB*IFN). Identification of the ∼36 kD protein was tested by Western blot analysis with specific polyclonal antibodies raised against the human IFN protein (**Figure 4B**, CpcB*IFN). A strong cross-reaction between the polyclonal antibodies and a protein band migrating to ∼36 kD suggested that this band is the recombinant CpcB*IFN protein. Moreover, cross-reactions were also detected with protein bands at a higher MW, suggesting the formation/presence of complexes (∼108 kD) containing the CpcB*IFN fusion protein. The higher MW band (∼250 kD) likely originates from aggregation of proteins containing the fusion CpcB*IFN construct, evidenced by their cross reaction with specific anti-IFN antibodies.

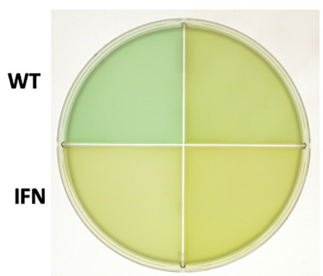

FIGURE 3 | Coloration of cells from photoautotrophically-grown liquid cultures showing a blue–green wild type (WT) phenotype, and greenish phenotype for the IFN, CpcB-IFN, and CpcB*IFN-containing transformants. The latter did not assemble phycocyanin rods, hence the absence of the distinct blue cyanobacterial coloration from the cells.

To evaluate the effect of DNA codon-use optimization on the IFN protein expression level, we designed CpcB*IFN fusion DNA constructs using the *Synechocystis* codon optimized IFN as well as the native unoptimized human DNA sequence, termed IFN' (IFN prime), for comparative expression measurements in *Synechocystis*. The latter construct harbored the same elements of the CpcB*IFN fusion, with the exception of the *IFN* gene that was replaced by the human native *IFN*' sequence (no codon-use optimization). Wild type (WT), *cpcB*IFN*', and *cpcB*IFN* transformant strains were grown in parallel, total cell proteins were extracted and subjected to SDS-PAGE analysis. Upon Coomassie staining of the SDS-PAGE (**Figure 5**), the WT protein extract showed as main subunits the 56 kD RbcL, 19 kD CpcB, and 17 kD CpcA. The latter two subunits were missing from the extract of the transformant cells, shown in three independent replicates per transformant in **Figure 5**. Densitometric analysis of Coomassie stained SDS-PAGE (**Figure 5**) showed the presence of RbcL to ∼12.5% of total cellular protein. Fusion constructs accumulated to ∼10.2% in the *cpcB*IFN*' and ∼11.8% in *cpcB*IFN* codon-optimized transformant strains. Validation of the Coomassie stained SDS-PAGE protein assignments was obtained through Western blot analysis with specific polyclonal antibodies (not shown). Since protein comprises in cyanobacteria about 50% of the biomass dry cell weight (dcw), it follows that cpcB*IFN':Biomass = 5.1% (w:dcw) and cpcB*IFN:Biomass = 5.9% (w:dcw).

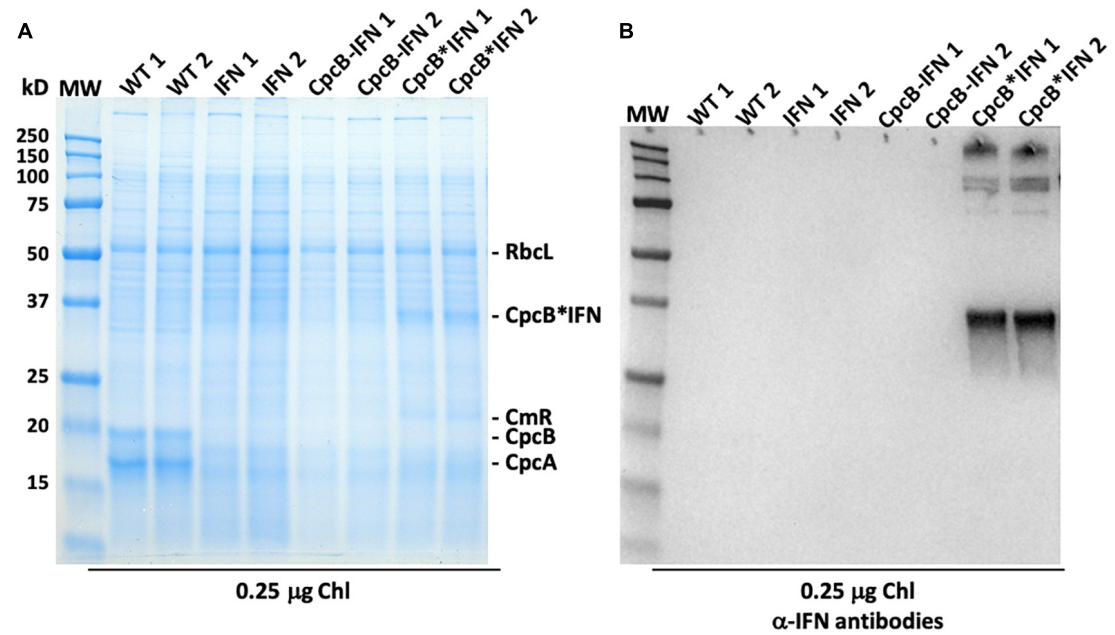

FIGURE 4 | Protein expression analysis of *Synechocystis* wild type and transformants. **(A)** Total cellular protein extracts were resolved by SDS-PAGE and visualized by Coomassie-stain. Two independent replicates of total protein extracts from wild type (WT), and IFN, CpcB-IFN, and CpcB*IFN transformant cells were loaded onto the SDS-PAGE. Individual native and heterologous proteins of interest are indicated to the right of the gel. Sample loading corresponds to 0.25 µg of chlorophyll. Note the clear presence of a heterologous protein migrating to ∼36 kD in the CpcB*IFN fusion extracts. **(B)** Total protein extracts of **(A)** were subjected to Western-blot analysis with loading of the lanes as per Figure **(A)**. Specific polyclonal antibodies against the human IFN protein were used to probe target proteins. Sample loading corresponds to 0.25 µg of chlorophyll. Note the specific antibody cross-reaction with proteins migrating to ∼36 and ∼108 kD in the cpcB*IFN fusion and the absence of a cross reaction with any protein from the IFN and cpcB-IFN transformant cells. The latter do not seem to make/accumulate IFN.

The above results showed that IFN successfully accumulated in *Synechocystis* only when expressed in a fusion construct configuration with the native highly-expressed CpcB subunit of phycocyanin, regardless of whether the *IFN* gene was codon-optimized or not. Aiming to isolate the recombinant fusion protein, we designed a new DNA construct referred to as the *cpcB*His*IFN*, based on the previous CpcB*IFN construct (**Figure 6**). A DNA fragment encoding the domain of six histidines and the Factor Xa cleavage-site was inserted between the *cpcB* and the *IFN* genes in the fusion construct. Addition of the His-tag between the CpcB and Factor Xa was designed to enable a recovery of the recombinant protein through column purification, whereas the cleavage Xa site would function in the excision of the CpcB*His moiety of the construct, thereby releasing the native form of the target IFN protein (Kavoosi et al., 2007). Protein analysis was then conducted on the homoplasmic transformant lines. Coomassie staining of the SDS-PAGE profile (**Figure 6**) showed the abundant RbcL, CpcB and CpcA subunits in the wild type extracts (**Figure 6**, WT). The *cpcB*IFN* transformants lacked the CpcB and CpcA proteins but accumulated the CpcB*IFN as a ∼36 kD protein (**Figure 6**, CpcB*IFN). The *cpcB*His*IFN* transformants also lacked the CpcB and CpcA proteins and accumulated an abundant protein band with a slightly higher apparent molecular mass than that of the CpcB*IFN (**Figure 6**, CpcB*His*IFN). This band was attributed to the CpcB*His*IFN protein. The fact that CpcB*His*IFN protein band showed a similar abundance as that of the CpcB*IFN construct suggested that the His-tag addition to the fusion construct did not adversely affect the expression level of this recombinant protein.

Batch-Based Purification of the CpcB*His*IFN Recombinant Protein

We initially applied a "batch" purification procedure to the recombinant CpcB*His*IFN protein using a His-Select resin (Sigma) and by following the manufacturer's instructions. The procedure was conducted in Eppendorf tubes, thereby minimizing the amount of resin and cell extract used. Total cell extracts from WT, *cpcB*IFN*, and *cpcB*His*IFN* fusion construct transgenic cells were employed in a side-by-side comparative resin treatment and purification analysis. Prior to incubation with the resin, cellular extracts were incubated on ice for 20 min in the presence of 1% Triton X-100 to disperse cellular aggregates that appeared to interfere with the precipitation of the resin upon centrifugation. Un-solubilized cell debris were pelleted and discarded following a brief centrifugation. The supernatant, containing the cellular protein extracts, was incubated with the resin for 5 min, followed by centrifugation to pellet the resin and any His-tagged proteins bound to it.

Lane 1 in **Figure 7** shows the cell extracts (upper panel) and the resin (lower panel) of the wild type, *cpcB*IFN*, and *cpcB*His*IFN* fusion construct transgenic cells prior to

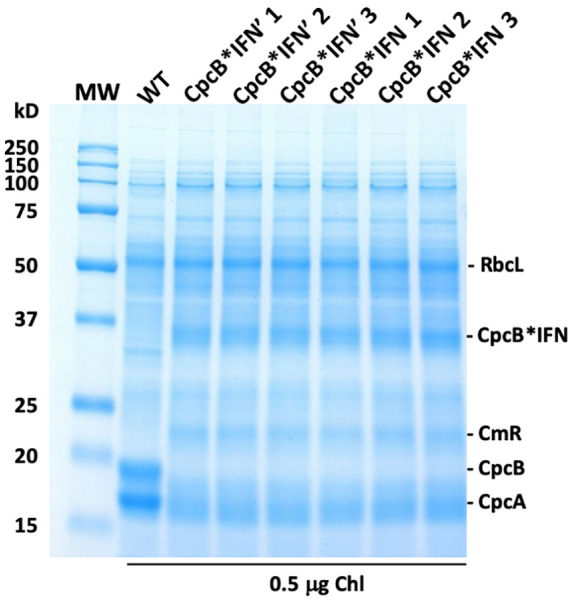

FIGURE 5 | Protein expression analysis of *Synechocystis* wild type (WT) and transformants harboring the *cpcB*IFN* fusion construct. Total cellular protein extracts were resolved by SDS-PAGE and visualized by Coomassie-stain. Two different versions of the IFN gene were used: the human native IFN' and the *Synechocystis* codon-optimized IFN gene. Note the presence of heterologous proteins migrating to ∼36 kD (CpcB*IFN) and ∼23 kD (CmR) in the transformants but not in the wild type. Also note the presence of the ∼19 kD CpcB β-subunit and the ∼17 kD CpcA α-subunit of phycocyanin in the wild type but not in the transformants. Sample loading corresponds to 0.5 µg of chlorophyll. Quantification of the CpcB*IFN protein accumulation relative to that of the Rubisco large subunit (RbcL) is given in the results of **Table 1**.

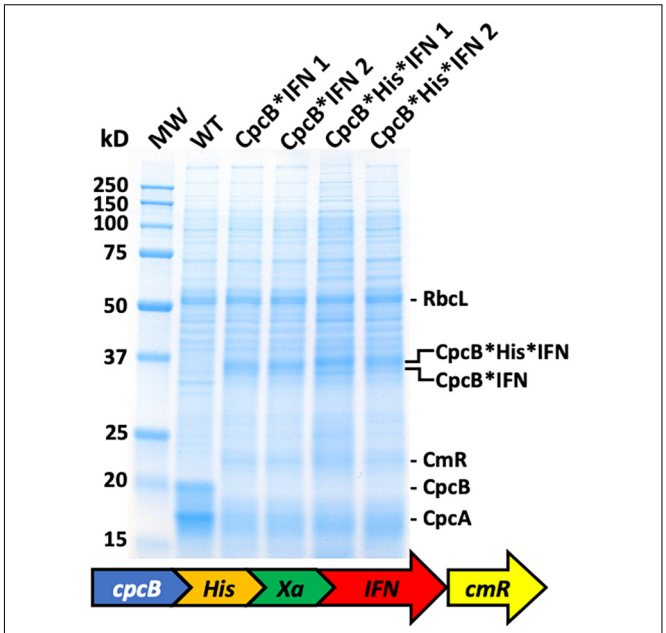

FIGURE 6 | Protein expression analysis of *Synechocystis* wild type (WT) and transformants harboring the *cpcB*His*IFN* fusion construct. Total cellular protein extracts were resolved by SDS-PAGE and visualized by Coomassie-stain. Two different versions of the fusion construct were used comprising the *CpcB*IFN* fusion and the more extensive *cpcB*His*IFN* fusion configuration, followed by the *cmR* resistance cassette. Equivalent amount of the CpcB*IFN and the CpcB*His*IFN fusion proteins were expressed in *Synechocystis*. Individual native and heterologous proteins of interest are indicated to the right of the gel. Sample loading corresponds to 0.25 µg of chlorophyll.

mixing cell extracts with the resin. Note the natural pink coloration of the resin.

Lane 2 in **Figure 7** shows the cell extracts (upper panel) and the resin pellet (lower panel) of the wild type, *cpcB*IFN*, and *cpcB*His*IFN* cell lines upon mixing cell extracts with the resin, incubating for 5-min, and following a subsequent centrifugation to pellet the resin. Note the blue coloration of the resin pellet and the green coloration of the supernatant. The blue coloration of the cpcB*fusion constructs, including the *cpcB*IFN* and *cpcB*His*IFN,* is attributed to the covalent binding of blue-colored phycobilin pigments to the CpcB protein (discussed in more detail in the results below).

Lanes 3–5 in **Figure 7** show the remaining cell extracts (upper panels) and the resin pellet (lower panels) of the wild type, *cpcB*IFN*, and *cpcB*His*IFN* cell lines following a consecutive repeated wash of the resin with a buffer containing 10 mM imidazole to remove non-target proteins. Note the clear supernatant and the pink coloration of the resin after the third wash (lane 5) for the wild type and *cpcB*IFN* transformants, suggesting absence of His-tagged proteins. Also note the blue coloration of the resin in the *cpcB*His*IFN* sample, which was retained in this pellet (lanes 3–5) in spite of the repeated 10 mM imidazole wash, suggesting the presence and binding to the resin of blue-colored His-tagged proteins.

Lanes 6–8 in **Figure 7** show the subsequent extracts (upper panel) and the resin pellet (lower panel) of the wild type, *cpcB*IFN*, and *cpcB*His*IFN* cell lines following a wash of the resin three times with a buffer containing 250 mM of imidazole, designed to dissociate His-tagged proteins from the resin. Note the bluish supernatant in lanes 6 and 7 of the *cpcB*His*IFN* cell lines only and the loss of the blue color from the corresponding resin pellet, suggesting a specific removal of His-tagged proteins from the resin under these conditions.

Fractions eluted from the resin upon application of 250 mM imidazole were analyzed by SDS-PAGE (**Figure 8**). Elution fractions from both WT and the *cpcB*IFN* transgenic extracts showed no protein bands in the Coomassie stained gels (**Figure 8**, left and middle panels), whereas eluent 1 (E1) from the *cpcB*His*IFN* extracts clearly showed the presence of protein bands, with the most abundant migrating to ∼36 kD, attributed to the CpcB*His*IFN fusion protein. Secondary bands migrating to ∼17, ∼27, and ∼108 kD were also noted (**Figure 8**, right panel). The ∼17 kD protein was attributed to the CpcA α-subunit of phycocyanin. The ∼27 kD protein could be the CpcG1 subunit of the phycobilisome, a phycocyanin rod-core linker polypeptide (Kondo et al., 2005), and the ∼108 kD band is tentatively attributed to a CpcB*His*IFN trimer, as it was shown to contain the CpcB*His*IFN fusion protein (see **Figure 4B**, also below).

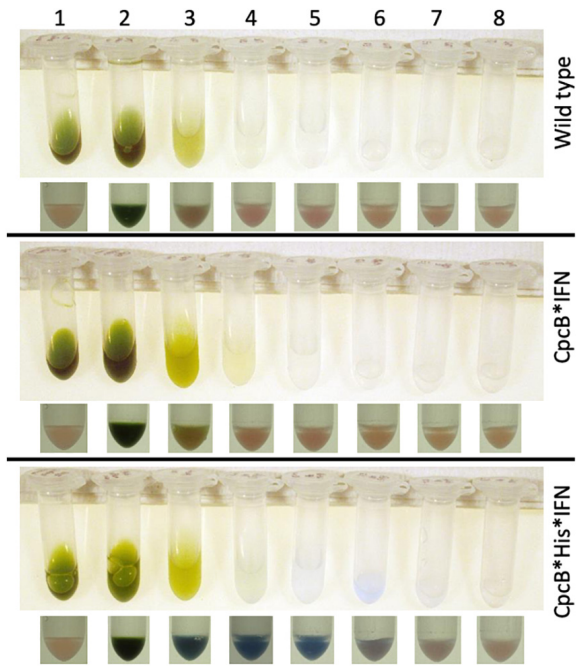

FIGURE 7 | Batch-scale purification of the recombinant CpcB*His*IFN protein through cobalt affinity chromatography. Protein purification was conducted employing a small amount of resin as solid phase. The latter was mixed and incubated with the cell extracts. The resin was pelleted and washed repeatedly with buffers containing imidazole at different concentrations. Lane 1 shows the cell extracts (upper panel) and the resin pellet (lower panel) of the wild type, CpcB*IFN, and CpcB*His*IFN fusion construct cells prior to incubation with the resin. Note the natural pink coloration of the latter. Lane 2 shows the cell extracts (upper panel) and the resin pellet (lower panel) of the wild type, CpcB*IFN, and CpcB*His*IFN fusion construct cells following a 5-min incubation with the resin in the presence of 10 mM imidazole. Note the blue coloration of the resin and the green coloration of the supernatant. Lanes 3–5 show the remaining cell extracts (upper panel) and the resin pellet (lower panel) of the wild type, CpcB*IFN, and CpcB*His*IFN fusion construct cells following a consecutive wash of the resin three times with a buffer containing 10 mM of imidazole. Note the resulting clear supernatant and the pink coloration of the resin after the third wash (lane 5) for the wild type and CpcB*IFN, suggesting absence of His-tagged proteins. Also note the blue coloration of the resin in the CpcB*His*IFN sample, which was retained in this pellet (lanes 3–5) in spite of the repeated wash, suggesting the presence of resin-bound blue-colored His-tagged proteins. Lanes 6–8 show the subsequent extracts (upper panel) and the resin pellet (lower panel) of the wild type, CpcB*IFN, and CpcB*His*IFN fusion construct cells following a wash three times with a buffer containing 250 mM of imidazole, designed to dissociate His-tagged proteins from the resin. Note the bluish supernatant in lanes 6 and 7 and the corresponding loss of the blue color from the resin pellet, suggesting the specific removal of His-tagged proteins from the resin.

These results suggest that CpcA and CpcG1 assemble with the CpcB*His*IFN, potentially as a CpcB*His*IFN-CpcA-CpcG1 complex, in a manner analogous to the α-β phycocyanin heterodimer assembly in the wild type, with the CpcG1 serving as a linker polypeptide, so that the complex binds to the column and elutes together from the resin upon application of 250 mM imidazole.

The nature of the pigmentation of proteins from elution fraction 1 of the cell extracts was investigated through spectrophotometric analysis (**Figure 9A**). The spectra of elution fraction 1, referred to as E1, from the WT and CpcB*IFN extracts did not show any absorbance features, consistent with absence of coloration in lanes 6–8 (**Figure 7**) of these samples. Eluent 1 from the CpcB*His*IFN sample showed a distinct absorbance band with a peak at ∼625 nm and a secondary broad band peaking in the UV-A region of the spectrum. This closely resembled the absorbance spectrum of phycocyanin from *Synechocystis* (Kirst et al., 2014), suggesting the presence of bilin pigment covalently-bound to protein(s) from the CpcB*His*IFN cell extracts. To further investigate this observation, absorbance spectra of total protein extracts from WT and *cpcB*His*IFN* transformant cells were also measured. These were compared with the absorbance spectrum of cells lacking phycocyanin due to a Δcpc operon deletion (Kirst et al., 2014). The spectrum of WT cells showed typical absorbance bands of chlorophyll at 680 nm and phycocyanin at 625 nm (**Figure 9B**, black line). The extract from the Δcpc transformants showed the specific Chl absorbance peak at 680 nm, whereas the phycocyanin absorbance peak at around 625 nm was missing (**Figure 9B**, red line). The absorbance spectrum from the *cpcB*His*IFN* transformant cells showed a substantially lower absorbance at about 625 nm due to depletion of phycocyanin, but this decrease was not as extensive as that observed with the Δcpc cells (**Figure 9B**, blue line). The difference, and apparent low-level absorbance of the *cpcB*His*IFN* cells at 625 nm, suggests that the CpcB protein, albeit in a fusion construct configuration with the IFN, and/or the CpcA protein that apparently accompanies this recombinant protein, manage to covalently bind at least some of the phycobilin pigment that is naturally associated with it, and which is manifested in the blue coloration of the E1 eluent.

Column-Based Purification of the CpcB*His*IFN Recombinant Proteins

Based on the initial encouraging results obtained with the "batch" purification approach, we proceeded to conduct a "column-based" purification of the His-tagged proteins (**Figure 10**). This experimental work was conducted as an alternative method in an attempt to elute a greater amount of the CpcB*His*IFN protein. Total protein extract from the *cpcB*His*IFN* transformant cells, mixed with 5 mM imidazole, was loaded onto the resin. Four subsequent washing steps were conducted with 10 mM imidazole to remove non-target proteins from the resin. After these washing steps, elution of the target protein with 250 mM imidazole was undertaken. The pigmentation pattern of the resulting fractions was in accordance with the results obtained with the "batch-based" purification (please see below).

Lane 1 in **Figure 10**, upper panel, shows the *cpcB*His*IFN* cell extracts that were incubated in the presence of 5 mM imidazole prior to loading on the resin. Lane 1 in **Figure 10**, lower panel, shows the SDS-PAGE protein profile of these extracts, indicating presence of all expected *Synechocystis* proteins.

Lane 2 in **Figure 10**, upper panel, shows the *cpcB*His*IFN* cell extracts upon loading and elution from the column but

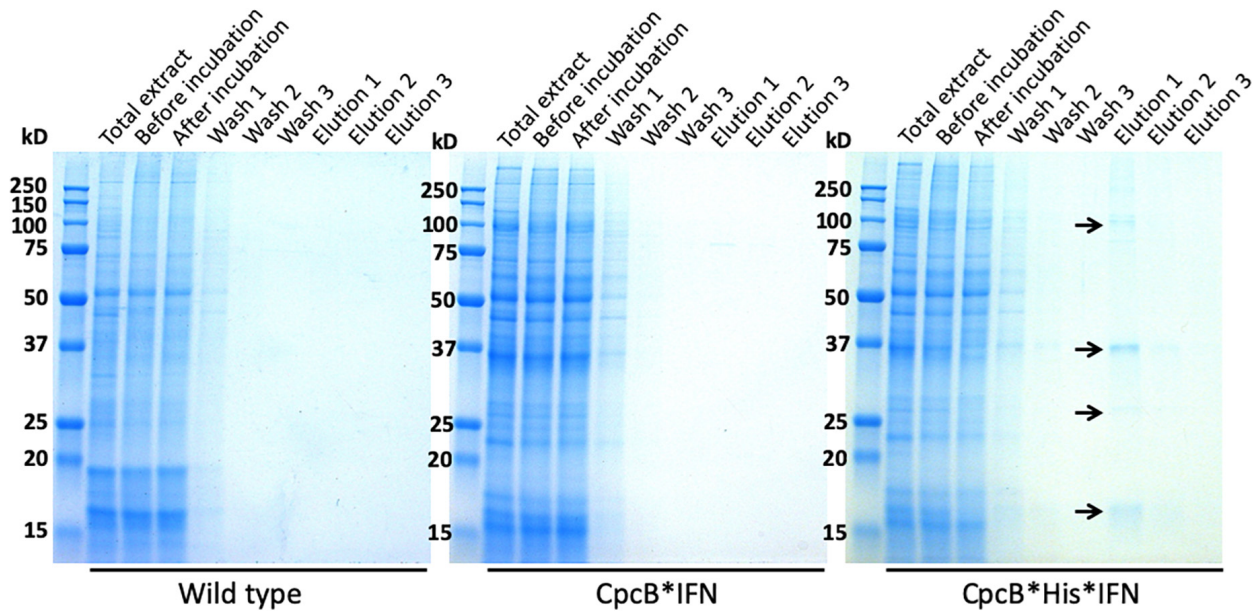

FIGURE 8 | Coomassie-stained SDS-PAGE gel analysis of fractions eluted with different imidazole concentrations. Fractions were obtained upon affinity chromatography purification as shown in **Figure 7**. Samples were loaded on a per volume basis. Note the ∼108, ∼38, and ∼17 kD proteins eluted from the CpcB*His*IFN extract (marked with arrows). Total cell extract loading corresponds to 0.25 μg of Chl.

prior to washing with additional imidazole. Lane 2 in **Figure 10**, lower panel, shows the SDS-PAGE protein profile of these extracts, obtained upon removal of the resin from the mix, again indicating presence of all expected *Synechocystis* proteins.

Lanes 3–6 in **Figure 10** (upper panel) show the *cpcB*His*IFN* cell extracts that were eluted from the resin upon four consecutive washes with 10 mM imidazole and (**Figure 10**, lower panel) the SDS-PAGE protein profile of these extracts, showing removal of the majority of cellular proteins in the first wash (**Figure 10**, lane 3) and the virtual absence of cell proteins in three additional (lane 4 to lane 6) wash steps with 10 mM imidazole.

Lanes 7–9 in **Figure 10** (upper panel) show the further removal of bound His-tagged proteins from the *cpcB*His*IFN* cell extracts. These eluted from the resin upon three consecutive washes with 250 mM imidazole. **Figure 10** (lower panel) is the SDS-PAGE protein profile of these extracts, showing substantial enrichment in mainly four proteins with apparent molecular weights of ∼108, 36, 27, and 17 kD. The majority of these proteins were eluted upon the first application of the 250 mM imidazole (**Figure 10**, lane 7), as subsequent elution treatments (**Figure 10**, lanes 8 and 9) produced much lower levels of protein eluent. Western blot analysis with specific anti-IFN antibodies showed strong cross reactions with the 36 and 108 kD protein bands only (**Figure 11**). The ∼17 kD protein was attributed to the CpcA α-subunit of phycocyanin, as it cross-reacted with CpcA-specific antibodies (not shown, but see also below), whereas the 27 kD protein was attributed to the CpcG1 linker polypeptide (Kondo et al., 2005) that helped to bind the CpcA α-subunit to the CpcB*His*IFN fusion complex, thereby explaining the simultaneous elution of all three proteins from the resin.

Blue Coloration of the Target Proteins

The blue coloration of the target proteins (**Figures 7**, **10**) and the absorbance spectral evidence of **Figure 9A**, suggested the presence of bilin in association with the recombinant CpcB*His*IFN protein. This finding was surprising as *CpcB*fusion* constructs are known to abolish the assembly of the phycocyanin peripheral rods of the phycobilisome (Formighieri and Melis, 2015, 2016; Chaves et al., 2017; Betterle and Melis, 2018, 2019), leading to the assumption of a CpcB inability to bind bilin. This assumption may not be entirely correct. To further test the spectrophotometric suggestion of bilin presence (**Figure 9A**), SDS-PAGE analysis of protein extracts from wild type, the *cpcB*His*IFN* transformant, and the resin column-based 1st eluent proteins of the latter (**Figure 12A**) were subjected to "zinc-staining" (please see section "Materials and Methods"). Zinc-staining is designed to specifically label the open tetrapyrroles that are covalently bound to *Synechocystis* proteins. **Figure 12B** shows the result of the Zn-staining of proteins in a duplicate gel, as the one shown in **Figure 12A**. In the WT, Zn-staining occurred for proteins migrating to ∼19 and ∼17 kD, attributed to the native CpcB and CpcA phycocyanin subunits. Zn-staining of the total CpcB*His*IFN transformant cell extract occurred for protein bands migrating to ∼36 and ∼17 kD, attributed to the CpcB*His*IFN and the CpcA proteins, respectively. Zn-staining of the first resin eluent (E1) fraction occurred for protein bands migrating to ∼108, ∼36 and ∼17 kD, putatively attributed to a CpcB*His*IFN trimer, the CpcB*His*IFN monomer and the CpcA proteins, respectively. These results corroborate the evidence based on spectrophotometry and

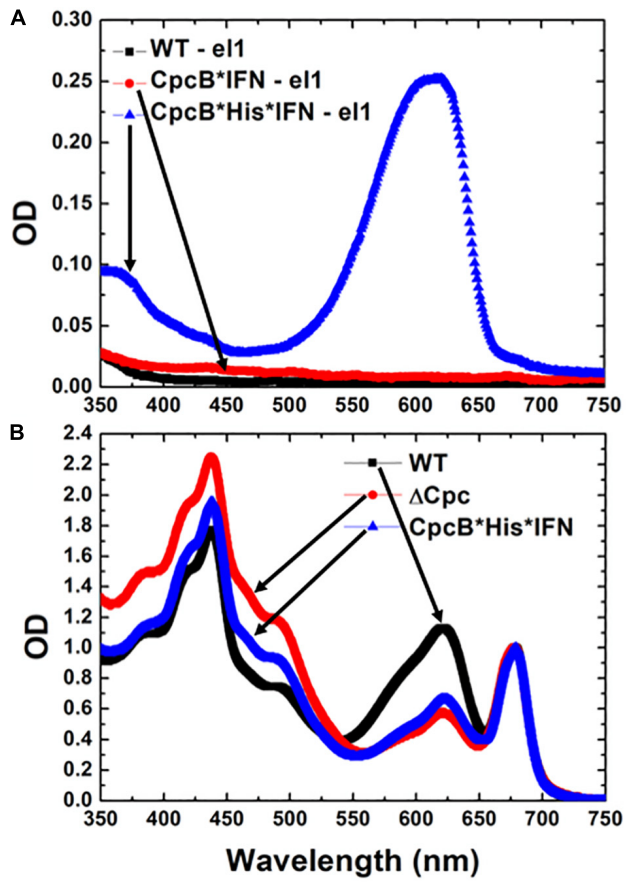

FIGURE 9 | Absorbance spectra of purified *Synechocystis* complexes. **(A)** Absorbance spectra of eluent E1 fractions from wild type, CpcB*IFN, and CpcB*His*IFN samples, as shown in **Figure 8**. **(B)** Absorbance spectra of cellular protein extracts from wild type, Δcpc deletion mutant (Kirst et al., 2014) and CpcB*His*IFN transformant cells.

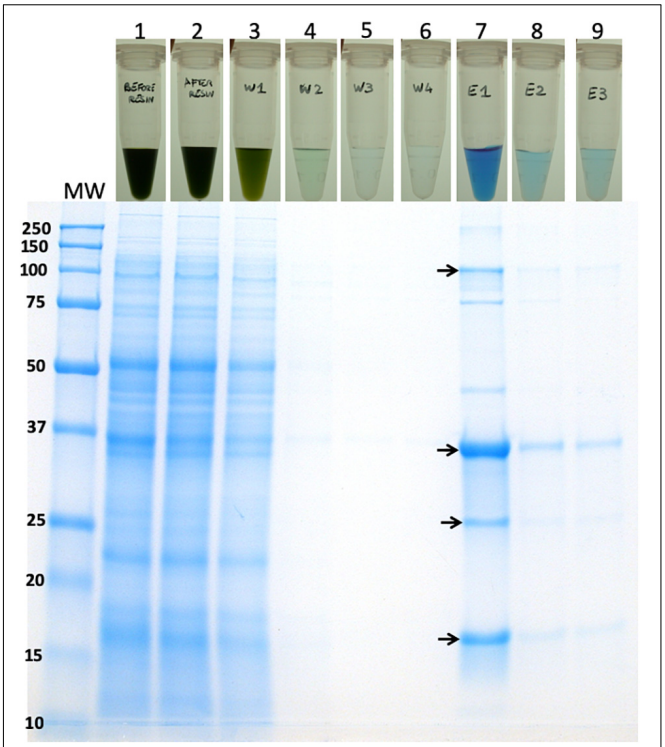

FIGURE 10 | Column-based purification of the CpcB*His*IFN fusion protein through cobalt affinity chromatography. Lane 1, upper panel, shows the CpcB*His*IFN cell extracts in the presence of 5 mM imidazole prior to resin application. Lane 1, lower panel, shows the SDS-PAGE protein profile of these extracts, indicating presence of all *Synechocystis* proteins. Lane 2, upper panel, shows the CpcB*His*IFN cell extracts after incubation with the resin but prior to washing with additional imidazole applications. Lane 2, lower panel, shows the SDS-PAGE protein profile of these extracts, obtained upon a prior removal of the resin from the mix, indicating presence of all *Synechocystis* proteins. Lanes 3–6, upper panel, show the CpcB*His*IFN cell extracts that passed through the resin upon four consecutive washes with 5 mM imidazole and, lower panel, the SDS-PAGE protein profile of these extracts, showing a steep depletion (from lane 3 to lane 6) of total protein. Lanes 7–9, upper panel, show the further removal of resin-bound proteins from the CpcB*His*IFN cell extracts that eluted upon three consecutive washes with 250 mM imidazole and, lower panel, the SDS-PAGE protein profile of these extracts, showing substantial enrichment in mainly four proteins with apparent molecular weights of 108, 36, 27, and 17 kD. The majority of these proteins were eluted with the first application of the 250 mM imidazole solution.

Western blot analysis, clearly showing the presence of bilin in association with the CpcB*His*IFN fusion and residual CpcA proteins.

*nptI*IFN* Fusion Constructs

To further explore the premise of fusion constructs in the expression and accumulation of biopharmaceutical proteins, a new fusion construct was designed for the transformation of wild type (WT) *Synechocystis,* based on the *nptI* gene serving as the leader sequence in a *nptI*IFN* configuration and through homologous DNA recombination in the *cpc* operon (**Figure 13A**). In such construct, the NptI protein served as the antibiotic selection marker, in addition to being the leader protein sequence in the fusion construct (Betterle and Melis, 2018, 2019). SDS-PAGE analysis of *Synechocystis* protein extracts was conducted (**Figure 13B**), and *cpcB*His*IFN* transformant showed the expected accumulation of a protein band migrating to about 36 kD (**Figure 13B**, cpcB*His*IFN). Conversely, two different lines of a transformant expressing the *nptI*His*IFN* construct in the *cpc* operon locus showed the presence of a 46 kD protein attributed to this fusion. Positive identification of these assignments was offered by the Western blot analysis of duplicate gels as the one shown in **Figure 13C**, further confirming the relative abundance of the fusion constructs expressed in the different *Synechocystis* genomic configurations.

Relative Antiviral Activity of the Natural IFN and CpcB*His*IFN Fusion Protein

A preliminary effort was undertaken to assess the activity of the cyanobacterial recombinant CpcB*His*IFN protein, as compared with that of commercially-available native

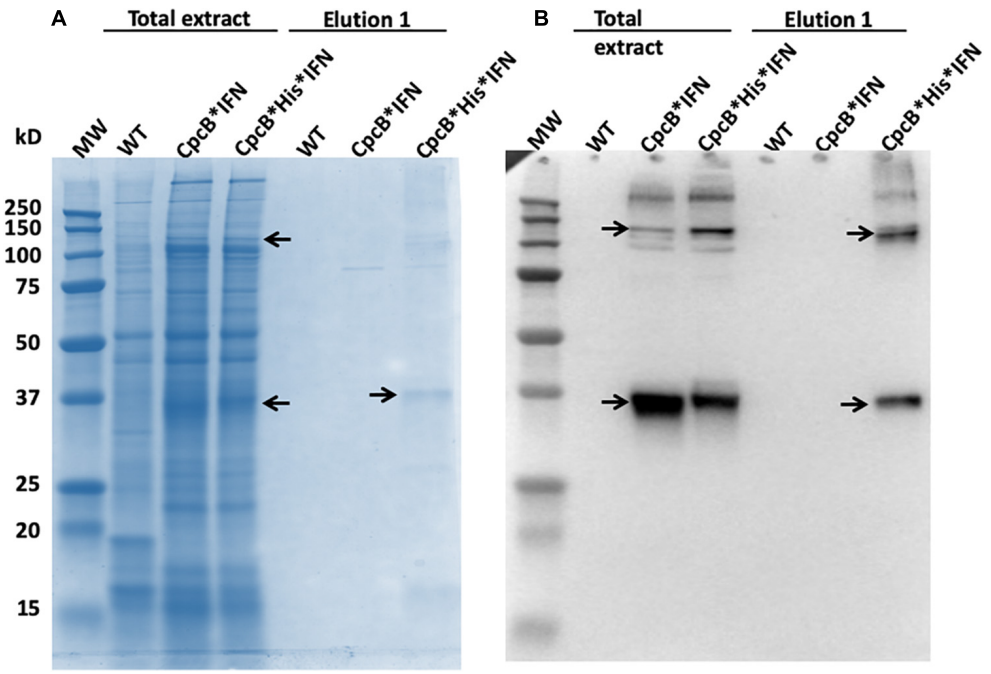

FIGURE 11 | (A) SDS-PAGE and Coomassie-staining analysis of *Synechocystis* wild type, CpcB*IFN, and CpcB*His*IFN total cell extract, and of proteins eluted from the resin column upon application of 250 mM imidazole. **(B)** Western blot analysis with specific IFN polyclonal antibodies of the proteins resolved in **(A)**. Note the heterologous ∼36 kD CpcB*His*IFN and the ∼108 kD putative CpcB*His*IFN trimer (marked by arrowheads).

interferon (please see section "Materials and Methods"). The results showed that 50 pg/mL of native IFN prevented 50% of cells from becoming infected by the VSV. Conversely, 500 pg/mL of fusion*IFN were needed to prevent 50% of cells from becoming infected by the VSV virus. Part of the difference in sensitivity is probably due to the CpcB leader sequence in the CpcB*His*IFN protein, which may have slowed down the activity of IFN. A consideration in this respect is that the fusion CpcB*His*IFN protein contains about equal molar parts of CpcB*His*Xa (19.4 kD) and IFN (19.2 kD), meaning that the above-mentioned specific activity was underestimated in the case of the fusion protein by a factor of about 2.

DISCUSSION

Molecular farming, defined as the use of vascular plants for the generation of specialty and commodity products, has been developed and applied, based on the advantage of the process because of minimal requirements of sunlight, carbon dioxide (CO_2), water, and fertilizer nutrient minerals for growth, simultaneously affording the generation of bio-products and CO_2 capture and mitigation (Daniell et al., 2001a,b; Ruf et al., 2001; Tregoning et al., 2003; Daniell, 2006; Oey et al., 2009; Matsuo and Atsumi, 2019). Drawbacks of the plant-based system, however, include the slow plant growth and productivity, the low product yields, a lack of guaranteed transgene containment, and the risk of contamination of the human food chain, if edible plant species are used as the host (Wilson and Roberts, 2012). Moreover, transgenic crops used for the production of heterologous proteins would be exposed to agrochemicals and pesticides in the field, while variable culture conditions and the impact of bacterial and fungal infections can lead to fluctuations in yield and product quality (Hellwig et al., 2004; Hidalgo et al., 2017). These plant-based limitations can be alleviated by the cultivation of transgenic cyanobacteria in fully-enclosed photobioreactors, affording better containment, much faster growth, and higher yields.

Recent work from this lab investigated aspects of eukaryotic plant gene transcription, mRNA accumulation, and protein synthesis and stability in cyanobacteria, as these affect the accumulation of heterologous recombinant proteins (Formighieri and Melis, 2016). This is an important issue for the field of synthetic biology as transgenes, and especially eukaryotic transgenes of plant and animal origin, typically are not well-expressed in cyanobacteria (Desplancq et al., 2005, 2008; Formighieri and Melis, 2014, 2015; Jindou et al., 2014). In such efforts, the choice of a strong promoter, such as *cpc*, was necessary but not sufficient to enable high levels of terpene synthase expression in cyanobacteria. Results pointed to the importance of efficient translation for protein accumulation (Formighieri and Melis, 2016). This also appeared to be the case in the present study, pertaining to cyanobacterial expression of interferon.

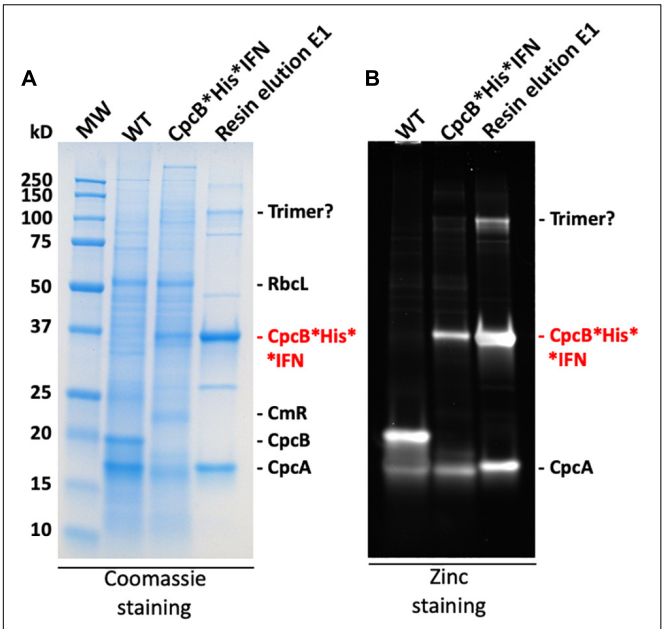

FIGURE 12 | (A) SDS-PAGE and Coomassie-stain analysis of *Synechocystis* wild type, CpcB*His*IFN, and resin-eluted proteins. **(B)** SDS-PAGE and Zinc-stain analysis of *Synechocystis* wild type, CpcB*His*IFN, and resin-eluted proteins. Zn-staining is designed to highlight the presence of bilin tetrapyrrole pigments. Individual native and heterologous proteins of interest are indicated to the right of the gels.

The promoter of the *cpc* operon controls expression of the abundant phycocyanin subunits and their associated linker polypeptides of the cyanobacterial phycobilisome light-harvesting antenna (**Figure 1A**). This endogenous strong promoter was employed in an effort to drive heterologous expression of the codon-optimized IFN gene. However, of the three IFN construct configurations (**Figures 1B–D**), only the fusion construct cpcB*IFN produced substantial amounts of the transgenic IFN protein (**Figure 1D**). Earlier real time RT-qPCR analysis revealed that such transgene constructs resulted in about equal rates of transcription and showed comparable steady-state levels of eukaryotic transgene mRNA (Formighieri and Melis, 2016). Hence, the rate of transcription does not appear to be the determinant of recombinant protein abundance in this case.

Protein synthesis was later investigated by analyzing the polyribosomes distribution profile associated with the various transcripts (Formighieri and Melis, 2016). A high density of polyribosomes in prokaryotes, such as cyanobacteria, was attributed to a ribosome pileup, when a slower ribosome migration rate on the mRNA causes multiple ribosomes to associate with the same mRNA molecule (Qin and Fredrick, 2013). This was observed to be the case for the **Figures 1B,C**-type constructs resulting in low transgenic protein accumulation. Conversely, a low density of polyribosomes is attributed to efficient ribosome migration on the mRNA, resulting in efficient translation and high levels of protein accumulation (Qin and Fredrick, 2013). This was observed to be the case for the **Figure 1D**-type constructs of high transgenic protein accumulation (Formighieri and Melis, 2016).

The significance of codon use optimization for enhancing heterologous protein expression in *Synechocystis* was acknowledged (Lindberg et al., 2010; Vijay et al., 2019). It is noteworthy in this study that codon optimization of the IFN gene (see Materials and Methods) allowed a slight enhancement of the fusion protein expression. Indeed, CpcB*IFN', with IFN' prime as the native human gene, accounted for 10.2% ± 0.2 (**Figure 5** and **Table 1**), whereas the CpcB*IFN, with IFN as the *Synechocystis* codon optimized gene accounted for 11.8 ± 0.1% of the total cellular protein. This result corroborated the premise that the main determinant for IFN expression in *Synechocystis* is the protein translation rate, enhanced through the protein fusion technology (Formighieri and Melis, 2016). It may be concluded that promoter strength and codon use optimization may be necessary but not by themselves sufficient to ensure high yield expression.

It is of interest that elution of the CpcB*His*IFN protein from the corresponding cell lysates showed a bluish coloration, which could serve as a marker for downstream protein processing and purification on an industrial scale. The bluish coloration was shown to be due to the binding of phycocyanobilin to both the CpcB protein in the CpcB*His*IFN recombinant protein and to the small amounts of the phycocyanin α-subunit present. Both of these apparently carry the tetrapyrrole chromophore, as evidenced by the typical phycocyanin absorbance spectra of these extracts (**Figure 9A**) and by the specific Zn-staining of these proteins (**Figure 12**). However, it must be noted that, unlike the *in vivo* situation, when about equal amounts of CpcB and CpcA are present (**Figure 5**, WT), there appears to be no stoichiometry of CpcB*His*IFN and CpcA in the transformants (**Figure 5**, IFN).

Small amounts of CpcA and of the CpcG1 linker may play a role in stabilizing the CpcB*His*IFN recombinant protein. This contention is supported by the column and resin chromatography, which co-isolated the CpcB*His*IFN fusion along with smaller amounts of the CpcA and CpcG1 linker proteins (**Figures 7**, **10**). This was likely due to the strong protein interactions occurring among phycocyanin subunits (Kondo et al., 2005; Arteni et al., 2009). Such interactions were apparently maintained through the process of cell protein extraction, and through the following mild Triton solubilization and affinity chromatography (see section "Materials and Methods"). Further efforts need be undertaken to chemically/physically disrupt the interactions among the CpcB*His*IFN, CpcA and CpcG1 phycocyanin subunits so as to isolate the CpcB*His*IFN fusion protein in pure form, while maintaining its functionality and bluish coloration.

A question in this work is the possible requirement of IFN glycosylation for function under *in vivo* conditions. According to Adolf et al. (1991), IFN α2 contains a single glycosylation site but recombinant IFNα2 proteins produced

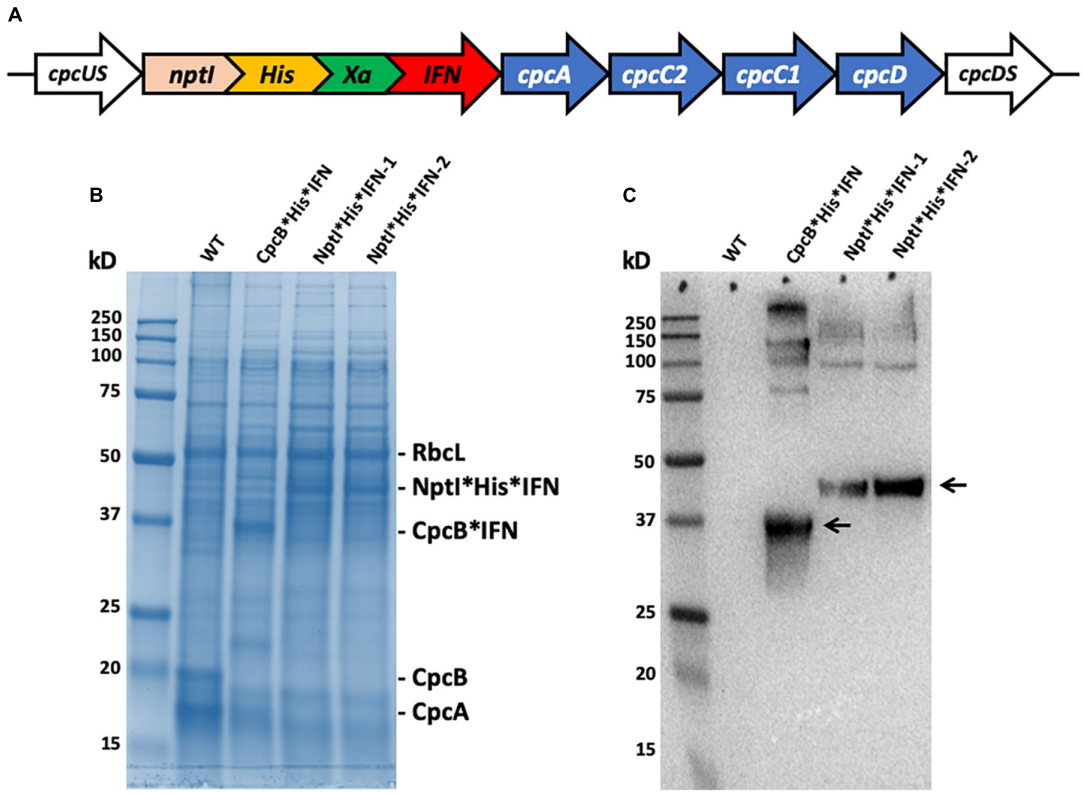

FIGURE 13 | (A) Map of the *nptI*IFN* fusion construct in the *cpc* operon locus. Note the presence of the His-tag and the Xa protease cleavage site in-between the two genes in the fusion. **(B)** SDS-PAGE and Coomassie staining of the protein extracts from wild type (WT), the *cpcB*His*IFN*, and two independent lines of the *nptI*His*IFN* transformants. **(C)** Western blot analysis of a duplicate gel as the one shown in **(B)**. Specific anti-IFN polyclonal antibodies were used in this analysis. Note the specific antibody cross reactions with protein bands migrating to ∼36 kD (CpcB*His*IFN) and ∼46 kD (NptI*His*IFN). Also note the antibody cross reactions with protein bands of higher molecular mass.

TABLE 1 | Quantification of the RbcL and CpcB*IFN fusion proteins as percent of the total *Synechocystis* proteins loaded onto the SDS-PAGE lanes of **Figure 5**.

Protein measured	CpcB* IFN' 1	CpcB* IFN' 2	CpcB* IFN' 3	CpcB* IFN 1	CpcB* IFN 2	CpcB* IFN 3
RbcL	12.1	12.4	13.2	11.9	12.9	12.6
CpcB*IFN	10.4	9.9	10.2	11.8	11.9	11.7

*RbcL levels were measured to account for ∼12.5 ± 0.5%, CpcB*IFN' accounted for 10.2 ± 0.2%, whereas the CpcB*IFN accounted for 11.8 ± 0.1% of the total cellular proteins.*

in bacteria and cyanobacteria are not glycosylated, as these microorganisms lack the necessary mammalian glycosylation genes and enzymes. However, the glycosylated version of IFN, purified from human leukocytes, shows similar biological activity to the unglycosylated IFN protein (Ghasriani et al., 2013). Furthermore, most of the human IFN-α species are devoid of detectable glycosylation sites (Pestka, 2007), making them suitable for production as biopharmaceuticals at scale in cyanobacteria.

Lastly, of import is the fact that heterologous IFN can also be overexpressed in cyanobacteria with the kanamycin resistance NptI protein in a NptI*His*IFN fusion construct, with the NptI serving as the leader sequence in this configuration (**Figure 13**). The latter may afford an alternative approach to the purification of the recombinant NptI*His*IFN than that described with the CpcB*His*IFN fusion construct. An advantage in this case would emanate from the fact that NptI, unlike CpcB, would not form a complex with the CpcA and CpcG1 proteins that express along with the CpcB*His*IFN fusion construct (**Figures 8**, **10**). This would simplify the isolation and purification of the recombinant protein. Future experimental work needs to be conducted with the NptI*IFN fusion construct, aiming to investigate alternatives in IFN biosynthesis, improved accumulation of the recombinant protein(s), and downstream processing and isolation of the native IFN from such a *Synechocystis* production process.

DATA AVAILABILITY STATEMENT

All datasets generated and analyzed in this work are included in the article/**Supplementary Material**. Included are GenBank accession and protein reference numbers of the genes employed, comprising IFN-α2 (*H. sapiens*), cpcB (*Synechocystis* sp. PCC 6803), cpcA (*Synechocystis* sp. PCC 6803), nptI (*E. coli*), and

cmR (*E. coli*) (**Supplementary Table S2**). Moreover, the codon-optimized nucleotide sequences, as expressed in *Synechocystis* for the purposes of this work, and the nucleotide sequences of the full constructs that were synthesized and employed are also shown in the **Supplementary Material**, pages 3–8.

AUTHOR CONTRIBUTIONS

All authors listed have made a substantial, direct and intellectual contribution to the work, and approved it for publication.

ACKNOWLEDGMENTS

The authors wish to thank Dr. Andrew C. S. Saphire for useful discussions.

SUPPLEMENTARY MATERIAL

The Supplementary Material for this article can be found online at: https://www.frontiersin.org/articles/10.3389/fpls.2020.00237/full#supplementary-material

REFERENCES

Adolf, G. R., Kalsner, I., Ahorn, H., Maurer-Fogy, I., and Cantell, K. (1991). Natural human interferon-alpha 2 is O-glycosylated. *Biochem. J.* 276(Pt 2), 511–518. doi: 10.1042/bj2760511

Ajlani, G., and Vernotte, C. (1998). Construction and characterization of a phycobiliprotein-less mutant of *Synechocystis* sp. PCC 6803. *Plant Mol. Biol.* 37, 577–580.

Arteni, A. A., Ajlani, G., and Boekema, E. J. (2009). Structural organisation of phycobilisomes from *Synechocystis* sp. strain PCC6803 and their interaction with the membrane. *Biochim. Biophys. Acta* 1787, 272–279. doi: 10.1016/j.bbabio.2009.01.009

Baier, T., Kros, D., Feiner, R. C., Lauersen, K. J., Müller, K. M., and Kruse, O. (2018). Engineered fusion proteins for efficient protein secretion and purification of a human growth factor from the green microalga *Chlamydomonas reinhardtii*. *ACS Synth. Biol.* 7, 2547–2557. doi: 10.1021/acssynbio.8b00226

Bentley, F. K., García-Cerdán, J. G., Chen, H.-C., and Melis, A. (2013). Paradigm of monoterpene (β- phellandrene) hydrocarbons production via photosynthesis in cyanobacteria. *Bioenergy Res.* 6, 917–929. doi: 10.1007/s12155-013-9325-4

Bentley, F. K., and Melis, A. (2012). Diffusion-based process for carbon dioxide uptake and isoprene emission in gaseous/aqueous two-phase photobioreactors by photosynthetic microorganisms. *Biotechnol. Bioeng.* 109, 100–109. doi: 10.1002/bit.23298

Bentley, F. K., Zurbriggen, A., and Melis, A. (2014). Heterologous expression of the mevalonic acid pathway in cyanobacteria enhances endogenous carbon partitioning to isoprene. *Mol. Plant* 7, 71–86. doi: 10.1093/mp/sst134

Betterle, N., and Melis, A. (2018). Heterologous leader sequences in fusion constructs enhance expression of geranyl diphosphate synthase and yield of (-phellandrene production in cyanobacteria (*Synechocystis*). *ACS Synth. Biol.* 7, 912–921. doi: 10.1021/acssynbio.7b00431

Betterle, N., and Melis, A. (2019). Photosynthetic generation of heterologous terpenoids in cyanobacteria. *Biotechnol. Bioeng.* 116, 2041–2051. doi: 10.1002/bit.26988

Bis, R. L., Stauffer, T. M., Singh, S. M., Lavoie, T. B., Krishna, M. G., and Mallela, K. M. G. (2014). High yield soluble bacterial expression and streamlined purification of recombinant human interferon a-2a. *Protein Expr. Purif.* 99, 138–146. doi: 10.1016/j.pep.2014.04.010

Budd, G. T., Bukowski, R. M., Miketo, L., Yen-Lieberman, B., and Proffitt, M. R. (1984). Phase-I trial of Ultrapure^{TM} human leukocyte interferon in human malignancy. *Cancer Chemother. Pharmacol.* 12, 39–42.

Chaves, J. E., and Melis, A. (2018). Biotechnology of cyanobacterial isoprene production. *Appl. Microbiol. Biotechnol.* 102, 6451–6458. doi: 10.1007/s00253-018-9093-3

Chaves, J. E., Rueda Romero, P., Kirst, H., and Melis, A. (2016). Role of isopentenyl-diphosphate isomerase in heterologous cyanobacterial (*Synechocystis*) isoprene production. *Photosynth. Res.* 130, 517–527. doi: 10.1007/s11120-016-0293-3

Chaves, J. E., Rueda-Romero, P., Kirst, H., and Melis, A. (2017). Engineering isoprene synthase expression and activity in cyanobacteria. *ACS Synth. Biol.* 6, 2281–2292. doi: 10.1021/acssynbio.7b00214

Chen, H.-C., and Melis, A. (2013). Marker-free genetic engineering of the chloroplast in the green microalga *Chlamydomonas reinhardtii*. *Plant Biotechnol. J.* 11, 818–828. doi: 10.1111/pbi.12073

Clark, E. D. (2001). Protein refolding for industrial processes. *Curr. Opin. Biotechnol.* 12, 202–207. doi: 10.1016/s0958-1669(00)00200-7

Coragliotti, A. T., Beligni, M. V., Franklin, S. E., and Mayfield, S. P. (2011). Molecular factors affecting the accumulation of recombinant proteins in the *Chlamydomonas reinhardtii* chloroplast. *Mol. Biotechnol.* 48, 60–75. doi: 10.1007/s12033-010-9348-4

Crisafulli, S., Pandya, Y., Moolchan, K., and Lavoie, T. B. (2008). Interferon gamma: activity and ELISA detection comparisons. *Biotechniques* 45, 101–102. doi: 10.2144/000112943

Daniell, H. (2006). Production of biopharmaceuticals and vaccines in plants via the chloroplast genome. *Biotechnol. J.* 10, 1071–1079. doi: 10.1002/biot.200600145

Daniell, H., Lee, S. B., Panchal, T., and Wiebe, P. O. (2001a). Expression of the native cholera toxin B subunit gene and assembly as functional oligomers in transgenic tobacco chloroplasts. *J. Mol. Biol.* 311, 1001–1009. doi: 10.1006/jmbi.2001.4921

Daniell, H., Streatfield, S. J., and Wycoff, K. (2001b). Medical molecular farming: production of antibodies, biopharmaceuticals and edible vaccines in plants. *Trends Plant Sci.* 6, 219–226. doi: 10.1016/s1360-1385(01)01922-7

Davies, F. K., Work, V. H., Beliaev, A. S., and Posewitz, M. C. (2014). Engineering limonene and bisabolene production in wild type and a glycogen-deficient mutant of *Synechococcus* sp. PCC7002. *Front. Bioeng. Biotechnol.* 2:21. doi: 10.3389/fbioe.2014.00021

Demain, A. L., and Vaishna, P. (2009). Production of recombinant proteins by microbes and higher organisms. *Biotechnol. Adv.* 27, 297–306. doi: 10.1016/j.biotechadv.2009.01.008

Desplancq, D., Rinaldi, A.-S., Horzer, H., Ho, Y., Nierengarten, H., Atkinson, R. A., et al. (2005). Combining inducible protein overexpression with NMR-grade triple isotope labeling in the cyanobacterium *Anabaena* sp. PCC 7120. *Biotechniques* 39, 405–411. doi: 10.2144/05393rr02

Desplancq, D., Rinaldi, A.-S., Horzer, H., Ho, Y., Nierengarten, H., Atkinson, R. A., et al. (2008). Automated overexpression and isotopic labelling of biologically active oncoproteins in the cyanobacterium *Anabaena* sp. PCC 7120. *Biotechnol. Appl. Biochem.* 51, 53–61. doi: 10.1042/BA20070276

Dyo, Y. M., and Purton, S. (2018). The algal chloroplast as a synthetic biology platform for production of therapeutic proteins. *Microbiology* 164, 113–121. doi: 10.1099/mic.0.000599

Eaton-Rye, J. J. (2011). Construction of gene interruptions and gene deletions in the cyanobacterium *Synechocystis* sp. strain PCC 6803. *Methods Mol. Biol.* 684, 295–312. doi: 10.1007/978-1-60761-925-3_22

Englund, E., Shabestary, K., Hudson, E. P., and Lindberg, P. (2018). Systematic overexpression study to find target enzymes enhancing production of terpenes in *Synechocystis* PCC 6803, using isoprene as a model compound. *Metab. Eng.* 49, 164–177. doi: 10.1016/j.ymben.2018.07.004

Formighieri, C., and Melis, A. (2014). Regulation of β-phellandrene synthase gene expression, recombinant protein accumulation, and monoterpene hydrocarbons production in *Synechocystis* transformants. *Planta* 240, 309–324. doi: 10.1007/s00425-014-2080-8

Formighieri, C., and Melis, A. (2015). A phycocyanin(phellandrene synthase fusion enhances recombinant protein expression and β-phellandrene (monoterpene) hydrocarbons production in *Synechocystis* (cyanobacteria). *Metab. Eng.* 32, 116–124. doi: 10.1016/j.ymben.2015.09.010

Formighieri, C., and Melis, A. (2016). Sustainable heterologous production of terpene hydrocarbons in cyanobacteria. *Photosynth. Res.* 130, 123–135. doi: 10.1007/s11120-016-0233-2

Formighieri, C., and Melis, A. (2017). Heterologous synthesis of geranyllinalool, a diterpenol plant product, in the cyanobacterium *Synechocystis*. *Appl. Microbiol. Biotechnol.* 101, 2791–2800. doi: 10.1007/s00253-016-8081-8

Ghasriani, H., Belcourt, P. J., Sauvé, S., Hodgson, D. J., Brochu, D., Gilbert, M., et al. (2013). A single N-acetylgalactosamine residue at threonine 106 modifies the dynamics and structure of interferon α2a around the glycosylation site. *J. Biol. Chem.* 288, 247–254. doi: 10.1074/jbc.M112.413252

Gregory, J. A., Topol, A. B., Doerner, D. Z., and Mayfield, S. (2013). Alga-produced cholera toxin-Pfs25 fusion proteins as oral vaccines. *Appl. Environ. Microbiol.* 79, 3917–3925. doi: 10.1128/AEM.00714-13

Halfmann, C., Gu, L., Gibbons, W., and Ruanbao Zhou, R. (2014a). Genetically engineering cyanobacteria to convert CO2, water, and light into the long-chain hydrocarbon farnesene. *Appl. Microbiol. Biotechnol.* 98, 9869–9877. doi: 10.1007/s00253-014-6118-4

Halfmann, C., Gu, L., and Zhou, R. (2014b). Engineering cyanobacteria for the production of a cyclic hydrocarbon fuel from CO2 and H2O. *Green Chem.* 16, 3175–3185. doi: 10.1039/c3gc42591f

Hellwig, S., Drossard, J., Twyman, R. M., and Fischer, R. (2004). Plant cell cultures for the production of recombinant proteins. *Nat. Biotechnol.* 22, 1415–1422. doi: 10.1038/nbt1027

Hidalgo, D., Abdoli-Nasab, M., Jalali-Javaran, M., Bru-Martinez, R., Cusido, R. M., Corchete, P., et al. (2017). Biotechnological production of recombinant tissue plasminogen activator protein (reteplase) from transplastomic tobacco cell cultures. *Plant Physiol. Biochem.* 118, 130–137. doi: 10.1016/j.plaphy.2017.06.013

Jindou, S., Ito, Y., Mito, N., Uematsu, K., Hosoda, A., and Tamura, H. (2014). Engineered platform for bioethylene production by a cyanobacterium expressing a chimeric complex of plant enzymes. *ACS Synth. Biol.* 37, 487–496. doi: 10.1021/sb400197f

Jones, C. S., and Mayfield, S. P. (2013). Steps toward a globally available malaria vaccine: harnessing the potential of algae for future low cost vaccines. *Bioengineered* 4, 164–167. doi: 10.4161/bioe.22577

Kavoosi, M., Creagh, A. L., Kilburn, D. G., and Haynes, C. A. (2007). Strategy for selecting and characterizing linker peptides for CBM9-tagged fusion proteins expressed in *Escherichia coli*. *Biotechnol. Bioeng.* 98, 599–610. doi: 10.1002/bit.21396

Kirst, H., Formighieri, C., and Melis, A. (2014). Maximizing photosynthetic efficiency and culture productivity in cyanobacteria upon minimizing the phycobilisome light-harvesting antenna size. *Biochim. Biophys. Acta* 1837, 1653–1664. doi: 10.1016/j.bbabio.2014.07.009

Kondo, K., Geng, X., Katayama, M., and Ikeuchi, M. (2005). Distinct roles of CpcG1 and CpcG2 in phycobilisome assembly in the cyanobacterium *Synechocystis* sp. PCC 6803. *Photosynth. Res.* 84, 269–273. doi: 10.1007/s11120-004-7762-9

Kwon, J. H., Bernát, G., Wagner, H., Rögner, M., and Rexrotha, S. (2013). Reduced light-harvesting antenna: consequences on cyanobacterial metabolism and photosynthetic productivity. *Algal Res.* 2, 188–195. doi: 10.1016/j.algal.2013.04.008

Li, Y., Lin, Y., Garvey, C. J., Birch, D., Corkery, R. W., Loughlin, P. C., et al. (2016). Characterization of red-shifted phycobilisomes isolated from the chlorophyll *f*-containing cyanobacterium *Halomicronema hongdechloris*. *Biochim. Biophys. Acta* 1857, 107–114. doi: 10.1016/j.bbabio.2015.10.009

Liberton, M., Collins, A. M., Page, L. E., O'Dell, W. O., O'Neill, H., Urban, W. S., et al. (2013). Probing the consequences of antenna modification in cyanobacteria. *Photosynth. Res.* 118, 17–24. doi: 10.1007/s11120-013-9940-0

Lindberg, P., Park, S., and Melis, A. (2010). Engineering a platform for photosynthetic isoprene production in cyanobacteria, using *Synechocystis* as the model organism. *Metab. Eng.* 12, 70–79. doi: 10.1016/j.ymben.2009.10.001

Matsuo, K., and Atsumi, G. (2019). CRISPR/Cas9-mediated knockout of the RDR6 gene in *Nicotiana benthamiana* for efficient transient expression of recombinant proteins. *Planta* 250, 463–473. doi: 10.1007/s00425-019-03180-9

Oey, M., Lohse, M., Kreikemeyer, B., and Bock, R. (2009). Exhaustion of the chloroplast protein synthesis capacity by massive expression of a highly stable protein antibiotic. *Plant J.* 57, 436–445. doi: 10.1111/j.1365-313X.2008.03702.x

Page, L. E., Liberton, M., and Pakrasi, H. (2012). Reduction of photoautotrophic productivity in the cyanobacterium *Synechocystis* sp. strain PCC 6803 by phycobilisome antenna truncation. *Appl. Environ. Microbiol.* 78, 6349–6351. doi: 10.1128/AEM.00499-12

Parkin, J., and Cohen, B. (2001). An overview of the immune system. *Lancet* 357, 1777–1789. doi: 10.1016/S0140-6736(00)04904-7

Pestka, S. (2007). The interferons: 50 years after their discovery, there is much more to learn. *J. Biol. Chem.* 282, 20047–20051. doi: 10.1074/jbc.r700004200

Qin, D., and Fredrick, K. (2013). Analysis of polysomes from bacteria. *Methods Enzymol.* 530, 159–172. doi: 10.1016/B978-0-12-420037-1.00008-7

Rasala, B. A., and Mayfield, S. P. (2015). Photosynthetic biomanufacturing in green algae; production of recombinant proteins for industrial, nutritional, and medical uses. *Photosynth. Res.* 123, 227–239. doi: 10.1007/s11120-014-9994-7

Rubinstein, S., Familletti, P. C., and Pestka, S. (1981). Convenient assay for interferons. *J. Virol.* 7, 755–758. doi: 10.1128/jvi.37.2.755-758.1981

Ruf, S., Hermann, M., Berger, I. J., Carrer, H., and Bock, R. (2001). Stable genetic transformation of tomato plastids and expression of a foreign protein in fruit. *Nat. Biotechnol.* 19, 870–875. doi: 10.1038/nbt0901-870

Surzycki, R., Greenham, K., Kitayama, K., Dibal, F., Wagner, R., Rochaix, J.-D., et al. (2009). Factors effecting expression of vaccines in microalgae. *Biologicals* 37, 133–138. doi: 10.1016/j.biologicals.2009.02.005

Tran, M., Zhou, B., Pettersson, P. L., Gonzalez, M. J., and Mayfield, S. P. (2009). Synthesis and assembly of a full-length human monoclonal antibody in algal chloroplasts. *Biotechnol. Bioeng.* 104, 663–673. doi: 10.1002/bit.22446

Tregoning, J. S., Nixon, P., Kuroda, H., Svab, Z., Clare, S., Bowe, F., et al. (2003). Expression of tetanus toxin fragment C in tobacco chloroplasts. *Nucleic Acids Res.* 31, 1174–1179. doi: 10.1093/nar/gkg221

Ungerer, J., Tao, L., Davis, M., Ghirardi, M., Maness, P.-C., and Yu, J. (2012). Sustained photosynthetic conversion of CO2 to ethylene in recombinant cyanobacterium *Synechocystis* 6803. *Energy Environ. Sci.* 5, 8998–9006.

Vijay, D., Akhtar, M. K., and Hess, W. R. (2019). Genetic and metabolic advances in the engineering of cyanobacteria. *Curr. Opin. Biotechnol.* 59, 150–156. doi: 10.1016/j.copbio.2019.05.012

Williams, J. G. K. (1988). Construction of specific mutations in photosystem II photosynthetic reaction center by genetic engineering methods in *Synechocystis* 6803. *Methods Enzymol.* 167, 766–778. doi: 10.1016/0076-6879(88)67088-1

Wilson, S. A., and Roberts, S. C. (2012). Recent advances towards development and commercialization of plant cell culture processes for the synthesis of biomolecules. *Plant Biotechnol. J.* 10, 249–268. doi: 10.1111/j.1467-7652.2011.00664.x

Xiong, W., Morgan, J. A., Ungerer, J., Wang, B., Maness, P.-C., and Yu, J. (2015). The plasticity of cyanobacterial metabolism supports direct CO2 conversion to ethylene. *Nat. Plants* 1:15053.

Xue, Y., and He, Q. (2014). Cyanobacteria as cell factories to produce plant secondary metabolites. *Front. Bioeng. Biotechnol.* 3:57. doi: 10.3389/fbioe.2015.00057

Zhou, J., Zhang, H., Meng, H., Zhu, Y., Bao, G., Zhang, Y., et al. (2014). Discovery of a super-strong promoter enables efficient production of heterologous proteins in cyanobacteria. *Sci. Rep.* 4:4500. doi: 10.1038/srep04500

Conflict of Interest: The authors declare that the research was conducted in the absence of any commercial or financial relationships that could be construed as a potential conflict of interest.

frontiers in Plant Science

ORIGINAL RESEARCH
published: 03 March 2020
doi: 10.3389/fpls.2020.00231

Expression of Heterologous *OsDHAR* Gene Improves Glutathione (GSH)-Dependent Antioxidant System and Maintenance of Cellular Redox Status in *Synechococcus elongatus* PCC 7942

Young-Saeng Kim[1], Seong-Im Park[2,3], Jin-Ju Kim[2,3], Joseph S. Boyd[4], Joris Beld[5], Arnaud Taton[4], Kyoung-In Lee[6], Il-Sup Kim[7], James W. Golden[4]* and Ho-Sung Yoon[2,3,7]**

[1] Research Institute for Dok-do and Ulleung-do, Kyungpook National University, Daegu, South Korea, [2] School of Life Sciences, BK21 Plus KNU Creative BioResearch Group, Kyungpook National University, Daegu, South Korea, [3] Department of Biology, Kyungpook National University, Daegu, South Korea, [4] Division of Biological Sciences, University of California, San Diego, La Jolla, CA, United States, [5] Department of Microbiology and Immunology, College of Medicine, Drexel University, Philadelphia, PA, United States, [6] Biotechnology Industrialization Center, Dongshin University, Naju, South Korea, [7] Advanced Bio Resource Research Center, Kyungpook National University, Daegu, South Korea

An excess of reactive oxygen species (ROS) can cause severe oxidative damage to cellular components in photosynthetic cells. Antioxidant systems, such as the glutathione (GSH) pools, regulate redox status in cells to guard against such damage. Dehydroascorbate reductase (DHAR, EC 1.8.5.1) catalyzes the glutathione-dependent reduction of oxidized ascorbate (dehydroascorbate) and contains a redox active site and glutathione binding-site. The *DHAR* gene is important in biological and abiotic stress responses involving reduction of the oxidative damage caused by ROS. In this study, transgenic *Synechococcus elongatus* PCC 7942 (TA) was constructed by cloning the *Oryza sativa* L. *japonica DHAR* (*OsDHAR*) gene controlled by an isopropyl β-D-1-thiogalactopyranoside (IPTG)-inducible promoter (*Ptrc*) into the cyanobacterium to study the functional activities of *OsDHAR* under oxidative stress caused by hydrogen peroxide exposure. *OsDHAR* expression increased the growth of *S. elongatus* PCC 7942 under oxidative stress by reducing the levels of hydroperoxides and malondialdehyde (MDA) and mitigating the loss of chlorophyll. DHAR and glutathione *S*-transferase activity were higher than in the wild-type *S. elongatus* PCC 7942 (WT). Additionally, overexpression of *OsDHAR* in *S. elongatus* PCC 7942 greatly increased the glutathione (GSH)/glutathione disulfide (GSSG) ratio in the presence or absence of hydrogen peroxide. These results strongly suggest that *DHAR* attenuates deleterious oxidative effects via the glutathione (GSH)-dependent antioxidant system in cyanobacterial cells. The expression of heterologous *OsDHAR* in *S. elongatus* PCC 7942 protected cells from oxidative damage through a GSH-dependent antioxidant system via GSH-dependent reactions at the redox active site and GSH binding site residues during oxidative stress.

Keywords: antioxidants, antioxidant-related enzymes, cyanobacterium, dehydroascorbate reductase, oxidative stress

OPEN ACCESS

Edited by:
Dimitris Petroutsos, UMR 5168 Laboratoire de Physiologie Cellulaire Vegetale (LPCV), France

Reviewed by:
Corinne Cassier-Chauvat, UMR 9198 Institut de Biologie Intégrative de la Cellule (I2BC), France
Sang-Soo Kwak, Korea Research Institute of Bioscience and Biotechnology (KRIBB), South Korea
Muriel Gugger, Institut Pasteur, France

****Correspondence:***
Il-Sup Kim
92kis@hanmail.net
James W. Golden
jwgolden@ucsd.edu
Ho-Sung Yoon
hsy@knu.ac.kr

Specialty section:
This article was submitted to Plant Biotechnology, a section of the journal Frontiers in Plant Science

Received: *24 June 2019*
Accepted: *14 February 2020*
Published: *03 March 2020*

Citation:
Kim Y-S, Park S-I, Kim J-J, Boyd JS, Beld J, Taton A, Lee K-I, Kim I-S, Golden JW and Yoon H-S (2020) Expression of Heterologous OsDHAR Gene Improves Glutathione (GSH)-Dependent Antioxidant System and Maintenance of Cellular Redox Status in Synechococcus elongatus PCC 7942. Front. Plant Sci. 11:231. doi: 10.3389/fpls.2020.00231

INTRODUCTION

The maintenance of cellular redox balance requires a steady-state equilibrium between oxidants and antioxidants. Under oxidative stress, loss of detoxification and accumulation of excess reactive oxygen species (ROS) leads to cell death through disruptions to redox balance, subsequent signaling, and cell rescue systems (Boyer, 1982; Owens, 2001; Rouhier et al., 2008). In aerobic cells, ROS degradation occurs through the GSH pools, which is catalyzed by a series of antioxidative enzymes localized primarily in intracellular and extracellular areas with high ROS production (Potters et al., 2002). Dehydroascorbate reductases (DHARs) are important to the GSH-dependent reduction of dehydroascorbate (DHA) to ascorbate, and their activities are shown to affect redox homeostasis in higher plants (Shimaoka et al., 2000; Urano et al., 2000; Dixon et al., 2002; Dixon and Edwards, 2010). The presence of a *DHAR* gene has yet to be conclusively established in the cyanobacterium *Synechococcus elongatus* PCC 7942.

In previous studies, we initially predicted that the GSH-bound *Oryza sativa* L. *japonica* DHAR (OsDHAR) structure might contain a GSH binding site (Do et al., 2016). A subsequent study reported the pronounced similarity of GSH binding sites in the conserved residues of glutathione *S*-transferases (GSTs), such as thioredoxin-like sites found in different species (Abdul Kayum et al., 2018). These residues indicate that the DHARs are GST-like proteins with GSH-dependent thiol transferase activity, with a cysteine at the active site instead of serine or tyrosine (Dixon et al., 2002). In DHAR activity, the first cysteine residue in the GSH binding site reacts with the sulfur atom in the GSH mixed disulfide bridges and promotes thiol transfer (Dixon et al., 2002; Dixon and Edwards, 2010). Mutation of the first cysteine residue induces significant losses of catalytic efficiency and GSH binding affinity at GSH binding site residues during abiotic stresses (Tang and Yang, 2013; Do et al., 2016).

There is also growing evidence that overexpression of *DHAR* enhances tolerance to many abiotic stresses. Overexpression of wheat *DHAR* conferred protection from ozone in transgenic tobacco (Chen and Gallie, 2005), and reinforcement of tobacco with the human *DHAR* gene increased tolerance to low temperatures and salt stress (Kwon et al., 2003). Overexpression of rice *DHAR* increased salt tolerance in *Arabidopsis* (Ushimaru et al., 2006) and resistance to oxidative stress in *Escherichia coli* (Shin et al., 2008). Overexpression of *Arabidopsis* cytosolic *DHAR* enhanced tolerance to drought and ozone stress in tobacco plants (Eltayeb et al., 2006), and overexpression of homologous *OsDHAR* containing a redox active site and GSH binding site residues in transgenic rice improved environmental adaptation and rice productivity in paddy fields (Kim et al., 2013). Although the relationship between *DHAR* expression and stress tolerance in plants is supported by a great deal of evidence, there is little information concerning the effect of *DHAR* overexpression in cyanobacteria. Cyanobacteria are believed to be the ancestors of photosynthetic eukaryotes as a result of an ancient endosymbiosis (Blank, 2013). The unicellular *S. elongatus* PCC 7942 has been used extensively as a cyanobacterial model for biochemical, physiological, and genetic studies of important cellular processes, such as prokaryotic nitrate reductases, cell division, responses to nutrient depletion, iron deprivation, and environmental abiotic stresses, such as ambient temperature and light intensity (Koksharova et al., 2006).

This study was undertaken to characterize biochemical and physiological features of *OsDHAR*-mediated stress tolerance in transgenic *S. elongatus* PCC 7942 under ROS-induced oxidative stress conditions. We found that the expression of heterologous *OsDHAR* in *S. elongatus* PCC 7942 conferred resistance to oxidative stress by helping to maintain cellular redox homeostasis through a GSH-dependent antioxidant system via GSH-dependent reactions. The multifaceted approach we employed provides new insights into the mechanisms of gene family expansion and functional evolution.

MATERIALS AND METHODS

Amino Acid Sequence Alignment

BLAST software[1] was used to align OsDHAR with known DHAR sequences using the National Center for Biotechnology Information (NCBI) database. Amino acid sequences were as follows: *O. sativa* DHAR (OsDHAR; accession no. AAL71856.1), *S. elongatus* PCC 7942 GST (SeGST; accession no. WP_011243077.1), *Synechocystis* sp. PCC6803 GST (StGST; accession no. WP_010872521.1), *Gloeobacter violaceus* PCC 7421 GST (GvGST; accession no. WP_011143013.1), *Prochlorococcus marinus* MIT9313 GST (PcGST; accession no. WP_011124721.1), *Acaryochloris marina* MBIC11017 GST (AmGST; accession no. WP_012161393.1), and *Cyanothece* sp. ATCC 51142 GST (CtGST; accession no. WP_009546792.1). The GSTs from these cells are soluble monomeric enzymes that contain a GSH-binding redox active site and similarly functional conserved residues comprised of different amino acids in other active sites.

Construction of Recombinant Plasmid *OsDHAR*

The *DHAR* gene from *O. sativa* L. *japonica* (accession no. AY074786.1; *OsDHAR*) coding region was amplified from cDNA using PCR with ExTaq polymerase (Takara Bio Inc., Shiga, Japan). PCR reaction conditions were as follows: initial denaturation at 95°C for 3 min, followed by 30 cycles of 95°C for 30 s, 53°C for 30 s, and 72°C for 1 min, and a final extension for 5 min at 72°C. The *OsDHAR* gene was cloned by PCR using OsDHAR-F-*Swa*I and OsDHAR-R-*Swa*I as the sense and antisense primers, respectively (**Supplementary Table S2**). The insertion of heterologous *OsDHAR* in *S. elongatus* PCC 7942 was constructed using the pAM4957 (pCV0069) a conjugative plasmid vector for chromosomal integration into recombinant complementation constructs at neutral site II (NS2).

Competent *E. coli* DH5α cells that had been conjugated by the *pAM4957:OsDHAR* plasmid were selected using nourseothricin (cloNAT, 50 $\mu g\ mL^{-1}$). Clones were confirmed by sequencing, then used to conjugate *S. elongatus* PCC

[1] http://clustalw.ddbj.nig.ac.jp/

7942. The plasmids harboring the *OsDHAR* encoding gene were sequenced using neutral site II (NS2) primers (**Supplementary Tables S1, S2**) complementary to the NS2 region to confirm proper gene ligation and direction. Finally, the resulting plasmid was assembled using the GeneArt Seamless Cloning and Assembly Kit (Life Technologies, Carlsbad, CA, United States). Plasmids harboring the *OsDHAR* encoding gene were constructed by recombinant complementation, and chromosomal integration into *S. elongatus* PCC 7942 NS2 using published protocols (Golden et al., 1987). Integration of the *pAM4957:OsDHAR* transgene into genomic DNA of the *S. elongatus* PCC 7942 was verified by PCR using Ptrc-F and OsDHAR-R primers (**Supplementary Table S2**) and the PCR PreMix kit (Bioneer, Daejeon, South Korea) according to the manufacturer's instructions.

Stress Conditions

Cyanobacteria were cultured in BG11 medium at 30°C in continuous light (80–120 μE $m^{-2}s^{-1}$) on a rotary shaker (120 rpm) for 7 days in Erlenmeyer flask. Then, the TA, EV, and WT *S. elongatus* PCC 7942 were cultured in liquid BG11 medium containing 2 mM isopropyl β-D-1-thiogalactopyranoside (IPTG) at 5 days before 2.5 mM H_2O_2 treatment at 7 days with shaking. The TA, and EV *S. elongatus* PCC 7942 were maintained in BG11 liquid or solid media supplemented with the appropriate antibiotics.

Initial absorbances at 730 nm (A_{730}) were adjusted to 0.03. Aliquots of each sample were then measured to adjust them to 0.03 in BG11 medium after culturing for 18 days at 30°C with shaking in liquid microbial lab flasks (**Supplementary Figure S2A**). Responses to oxidative stress were evaluated by allowing cells to reach the exponential phase (A_{730} = 0.3–0.35) before exposing them to 2.5 mM H_2O_2 at 7 days with shaking, after which A_{730} values were monitored each day through the end of the experiment.

For the cell-spotting assay, the growth following the presence (10 days) or absence (7 days) of 2.5 mM H_2O_2 with 2 mM IPTG for 3 days were measured at the TA, EV, and WT *S. elongatus* PCC 7942 (A_{730} = 0.25) and were then serially diluted 10-fold with distilled water. The diluted samples were spotted on agar-solidified BG11 medium and incubated for 3 days at 30°C. They were then photographed or counted. All experiments were performed three or more times.

Semi-Quantitative RT-PCR

The cDNA was reverse transcribed from total RNA using the SuperScript III kit (Life Technologies). For semi-qRT-PCR, the OsDHAR-qRT-PCR-F and OsDHAR-qRT-PCR-R (**Supplementary Table S2**) primer sets were used to amplify *OsDHAR*. The reaction sequence consisted of one cycle at 95°C for 3 min followed by 26 cycles at 94°C for 30 s, 54°C for 30 s, and 72°C for 40 s, and then a final extension at 72°C for 5 min. The semi-qRT-PCR amplicons were resolved on a 1.0% agarose gel by electrophoresis in 0.5X Tris/borate/EDTA buffer. The *rpoA* gene primer sets were used as a housekeeping control and were also amplified (**Supplementary Table S2**).

Western Blot Analysis

Western blot analysis of the crude extracts was performed by obtaining the total protein from cyanobacteria (A_{730} = 0.3) with suspension in five volumes of cold extraction buffer containing 150 mM NaCl, 50 mM Tris-HCl (pH 7.3), 1 mM EDTA, 2% β-mercaptoethanol, 1 mM dithiothreitol, 1 mM phenylmethylsulfonyl fluoride (PMSF), and an equal of volume of phenol saturated with Tris-HCl (pH 7.3). Protein was then extracted from the cells as previously described (Kim et al., 2018).

Briefly, crude protein extracts were prepared using glass beads. Cells grown for 7 days were exposed to 2.5 mM H_2O_2 for 24 h to induce cellular oxidative stress, followed by vigorous vortexing 10 times for 1 min each at 3-min intervals on ice. The protein extracts were cleared by centrifugation at 12,000 rpm for 20 min at 4°C. Finally, protein concentrations were determined using a Pierce bicinchoninic acid protein assay kit (Thermo Scientific, Waltham, MA, United States) (Komatsu et al., 2009; Peng et al., 2011).

Protein extracts (20 μg) were separated on a 10% SDS-PAGE gel at 100 V and transferred to polyvinylidene fluoride membranes (Bio-Rad, Hercules, CA, United States). Membranes were then incubated in blocking buffer consisting of 5% non-fat skim milk and 0.02% sodium azide in Tris-buffered saline plus Tween [TBST, 10% Tween-20, 20 mM Tris-HCl (pH 7.6), and 150 mM NaCl] for 1.5 h at room temperature. Antibodies to *O. sativa* DHAR (OsDHAR) were produced in rabbits hyperimmunized using proteins purified from *E. coli* (Younginfrontier, Seoul, South Korea). The blots were washed three times for 30 min with TBST, after which they were incubated with conjugated anti-rabbit secondary antibody (Santa Cruz Biotechnology, Santa Cruz, CA, United States) diluted with blocking buffer (without 0.02% sodium azide) for 4 h at room temperature. After washing with TBST, binding of antibody to protein immobilized on the blots was visualized using the SuperSignal West Femto substrate kit (Pierce, Rockford, IL, United States) and imaged using a MultiImage II Light Cabinet (DE-500; Alpha Innotech Corporation, San Leandro, CA, United States).

Chlorophyll Content and Dry Weight Measurement

Chlorophyll content assays were conducted by harvesting the TA, EV, and WT *S. elongatus* PCC 7942 from a 100 mL culture at an A_{730} of 0.3 after a 2-day exposure to 2.5 mM H_2O_2 in liquid BG11 medium containing 2 mM IPTG. Chlorophyll content was analyzed by treating cultures (100 mL, A_{730} = 0.3) with 2.5 mM H_2O_2 for 2 days. The cultivated cells were harvested, and the cell pellets were suspended in 90% methanol. Chlorophyll was extracted as previously described (Kim et al., 2017, 2018) with some modifications. The chlorophyll content of the cells was measured by scanning them over 260 to 800 nm using an Infinite M200 Pro microplate reader (Tecan, Männedorf, Switzerland). All assays were performed in biologically least three independent experiments. The dry weights of cells at 9 days after 2-day exposure to H_2O_2 were determined gravimetrically as previously described (Gorain et al., 2013; Kim et al., 2017).

Other dry weight samples were measured at 14 days after growth in the presence or absence of 2.5 mM H_2O_2 for 7 days (**Supplementary Figure S2B**).

Redox State and Measurement of Thiobarbituric Acid Reactive Substances (TBARS) Value

The intracellular levels of H_2O_2 in cells exposed to H_2O_2 with IPTG (H_2O_2-IPTG) for 24 h were determined using the ferrous oxidation-xylenol orange (FOX) reagent (100 μM xylenol orange, 250 μM ammonium ferrous sulfate, 100 mM sorbitol, and 25 mM sulfuric acid) by ferrous ion oxidation in the presence of the ferric ion indicator xylenol orange (Kim et al., 2011, 2018).

Cellular ROS levels were measured *in vivo* by harvesting of the TA, EV, and WT *S. elongatus* PCC 7942 from 100 mL culture (A_{730} = 0.3) after exposure to 2.5 mM H_2O_2 -IPTG with 2 mM IPTG for 2 h; these were incubated for 20 min at 30°C with 10 μM DCFHDA (Invitrogen, Carlsbad, CA, United States) in the dark (Wang and Joseph, 1999; Kim et al., 2018). Cells were then collected and examined using a model LSM700 fluorospectrophotometer (Carl Zeiss, Jena, Germany) at an excitation wavelength of 488 nm and an emission wavelength of 535 nm. Images were also captured by laser scanning confocal microscopy at an excitation wavelength of 488 nm (Huang et al., 2012). Levels of lipid peroxidation were evaluated in cells exposed to H_2O_2-IPTG with 2 mM IPTG for 24 h. The extent of oxidative damage to the lipids was determined by measuring malondialdehyde (MDA) content; this was achieved adding 10% trichloroacetic acid containing 0.65% 2-thiobarbituric acid (TBA) and heating at 95°C for 25 min. Finally, the MDA concentration of the resulting supernatant was measured at 532 nm (based on 600 nm) and estimated using an absorbance coefficient of 1.56 × 105, as described by Jiang and Zhang (2001) and Kim et al. (2018).

Analyses of Antioxidants and Antioxidant-Related Enzymes Under ROS-Induced Oxidative Stress

We evaluated potential mechanisms by which the TA tolerates oxidative stress by measuring GSH/GSSG ratio as they related to total GSH content during a 24-h exposure to H_2O_2. The TA, EV, and WT *S. elongatus* PCC 7942 were harvested by centrifugation and then washed twice with cold phosphate-buffered saline (PBS). We then measured GST activity by adding the crude protein of samples exposed to the H_2O_2 stress for 24 h to a lysis buffer containing 50 mM sodium phosphate (pH 7.5), 3 mM $MgCl_2$, 1 mM EDTA, 1 mM PMSF, and protease inhibitor cocktails. Total GSH content was measured as previously described (Jiang and Zhang, 2001). GST enzyme activity was detected as previously described using 1-chloro-2,4- dinitrobenzene as substrate (Dixit et al., 2015).

qRT-PCR

An RNA extraction of 3 different samples exposed to 2.5 mM H_2O_2 for 24 h for biologically least three independent experiments. Samples were frozen with liquid nitrogen and ground using a mortar and pestle. Total RNA was extracted using TRIzol reagent (Takara, Japan) according to the manufacturer's instructions, and reverse transcription reactions were performed with 2 μg total RNA using the SuperScript III First-Strand Synthesis System. The qRT-PCR analysis was performed using the TB Green Premix Ex Taq II (Tli RNaseH Plus) Kit (Takara, Japan) and QuantStudio3 Real-Time PCR system (Applied Biosystems, Foster City, CA, United States). The 20 μL reactions contained 12.5 μL of TB Green Premix Ex Taq II (Tli RNaseH Plus), 0.4 μL of ROX Reference Dye II, 200 ng of cDNA template, 0.4 μL of each primer (10 μM), and 6.26 μL of PCR-grade water. All samples were analyzed in biological triplicates as follows: initial preheating at 95°C for 30 s, followed by 40 cycles of 95°C for 3 s and 55°C for 30 s. The *rpoA* gene primer sets were used as a positive control. Fold changes in mRNA were calculated relative to the calibrator. Expression levels of GSH-related genes in **Figure 6** is presented relative to that in TA strains (which expression level was considered to be 1 of WT strains; described as relative values.) under stress condition (**Supplementary Figure S3**). Normalization and relative quantification were conducted using the $2^{-\Delta\Delta Ct}$ method (Livak and Schmittgen, 2001). The primers used for qRT-PCR analysis are listed in the **Supplementary Table S2**.

Statistical Analyses

All biochemical results from the TA were calculated relative to those of the EV and WT under normal conditions, which were defined as 100%. Significant differences among results for the TA, EV, and WT were determined by ANOVA. Comparisons between individual data points were performed using Student's *t*-test, and a *P*-value of less than 0.05 was considered statistically significant. All experiments were carried out three or more times, and all results are expressed as mean ± SD.

RESULTS

Sequence Analysis of OsDHAR Protein Motifs

The amino acid sequence motifs of OsDHAR were compared with the sequences of known GSTs to clarify the molecular properties of OsDHAR. Pairwise alignment of the sequences of OsDHAR and the other GSTs were conducted using BLAST software. OsDHAR displayed 24, 26, 25, 26, 20, and 23% similarity to SeGST, StGST, GvGST, PcGST, AmGST, and CtGST, respectively (**Figure 1A**, see section "Materials and Methods" for details of the GSTs). All contained a conserved site that bound GSH residues (Cys20, Pro61, and Ser74) (**Figure 1A**, red background) and similar functionally conserved residues (Pro21, Lys34, Lys47, Val60, and Asp73) (**Figure 1A**, blue background) that are likely involved in redox active site function. Other strictly conserved residues were not clearly evident (**Figure 1A**, green boxes). We used these results to construct a phylogenetic tree containing the *S. elongatus* PCC 7942 GST (SeGST; accession no. WP_011243077) that was 24% homologous to OsDHAR (accession no. AAL71856.1) (**Figure 1B**).

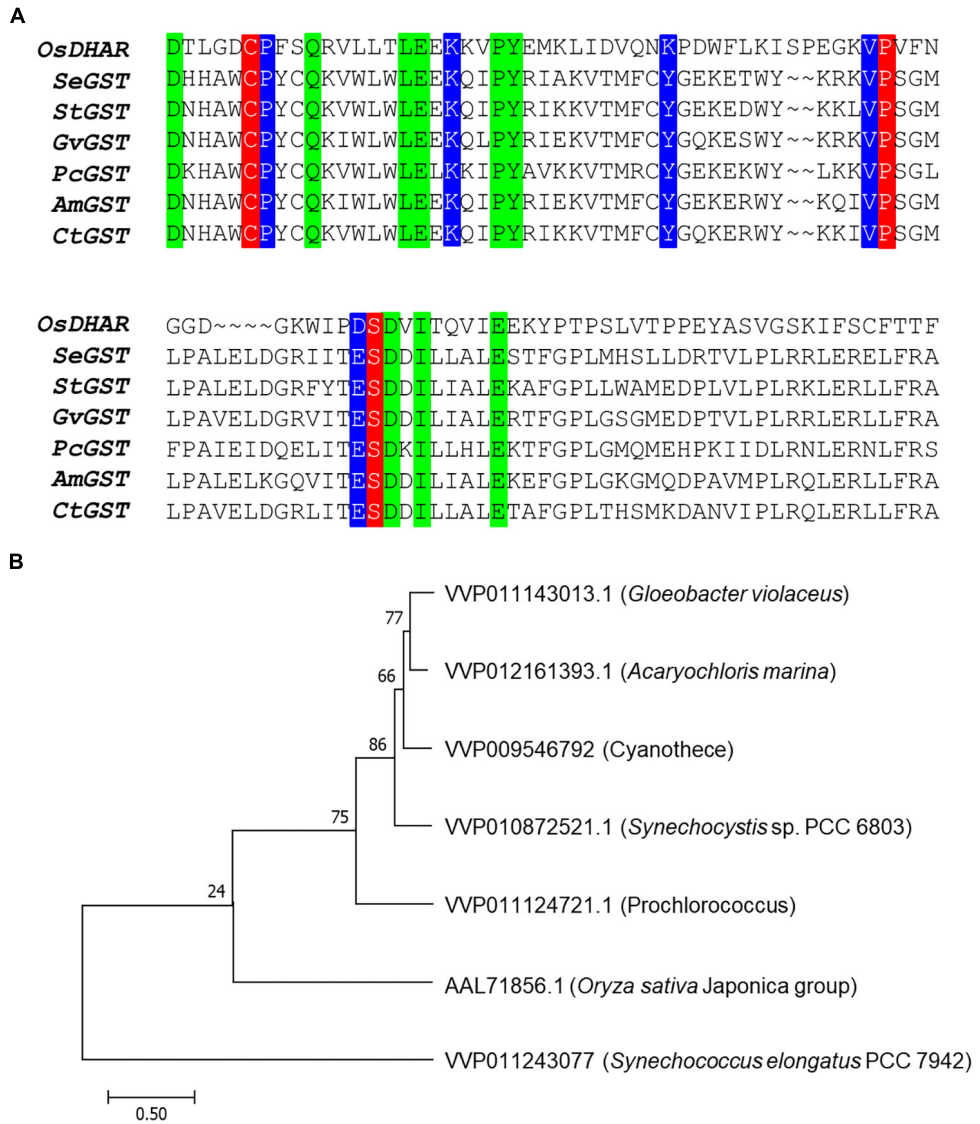

FIGURE 1 | Amino acid alignment of OsDHAR and six glutathione *S*-transferase (GSTs). **(A)** Alignment showing GSH binding site and GSTs with similarly functional conserved residues. Colored boxes indicate identical residues across sequences. All contain a conserved site with GSH binding residues (red background), GSTs having similar functional conserved residues (blue background), and strictly conserved residues (green boxes). **(B)** The phylogenetic trees show the evolutionary relationship between rice DHAR and the amino acids of cyanobacterium GSTs. OsDHAR, *Oryza sativa* DHAR; SeGST, *Synechococcus elongatus* PCC 7942 GST; StGST, *Synechocystis* sp. PCC6803 GST; GvGST, *Gloeobacter violaceus* PCC 7421 GST; PcGST, *Prochlorococcus marinus* MIT9313 GST; AmGST, *Acaryochloris marina* MBIC11017 GST; CtGST, *Cyanothece* sp. ATCC 51142 GST.

Cellular Response of the *OsDHAR*-Expressing in *S. elongatus* PCC 7942 Under H_2O_2 Stress Conditions

The expression of heterologous *OsDHAR* in *S. elongatus* PCC 7942 was constructed to evaluate the effect on tolerance to hydrogen peroxide (H_2O_2)-induced oxidative stress. *OsDHAR* was cloned into the pAM4957 (pCV0069) vector for NS2 chromosomal integration under the control of the IPTG-inducible promoter (*Ptrc*) (**Figure 2A**). Resistance to oxidative stress was evaluated in cyanobacterial *S. elongatus* PCC 7942 conjugated with the *pAM4957*:*OsDHAR* plasmid containing the *OsDHAR* gene or the pAM4957 vector alone plasmid containing the empty neutral site vector (EV) (**Supplementary Table S1**). Genotypes were confirmed by PCR using primers external to the *OsDHAR* gene (**Supplementary Table S2**) that produced the expected fragment size of 690 bp (**Figure 2B** and **Supplementary Table S1**).

We explored whether the *OsDHAR* gene was effectively expressed with a semi-quantitative RT-PCR analysis using primers internal to the *OsDHAR* gene (**Supplementary Table S2**). The *OsDHAR* gene was expressed in the TA, while no signal was detected in the empty vector (EV, pAM4957) or the wild-type

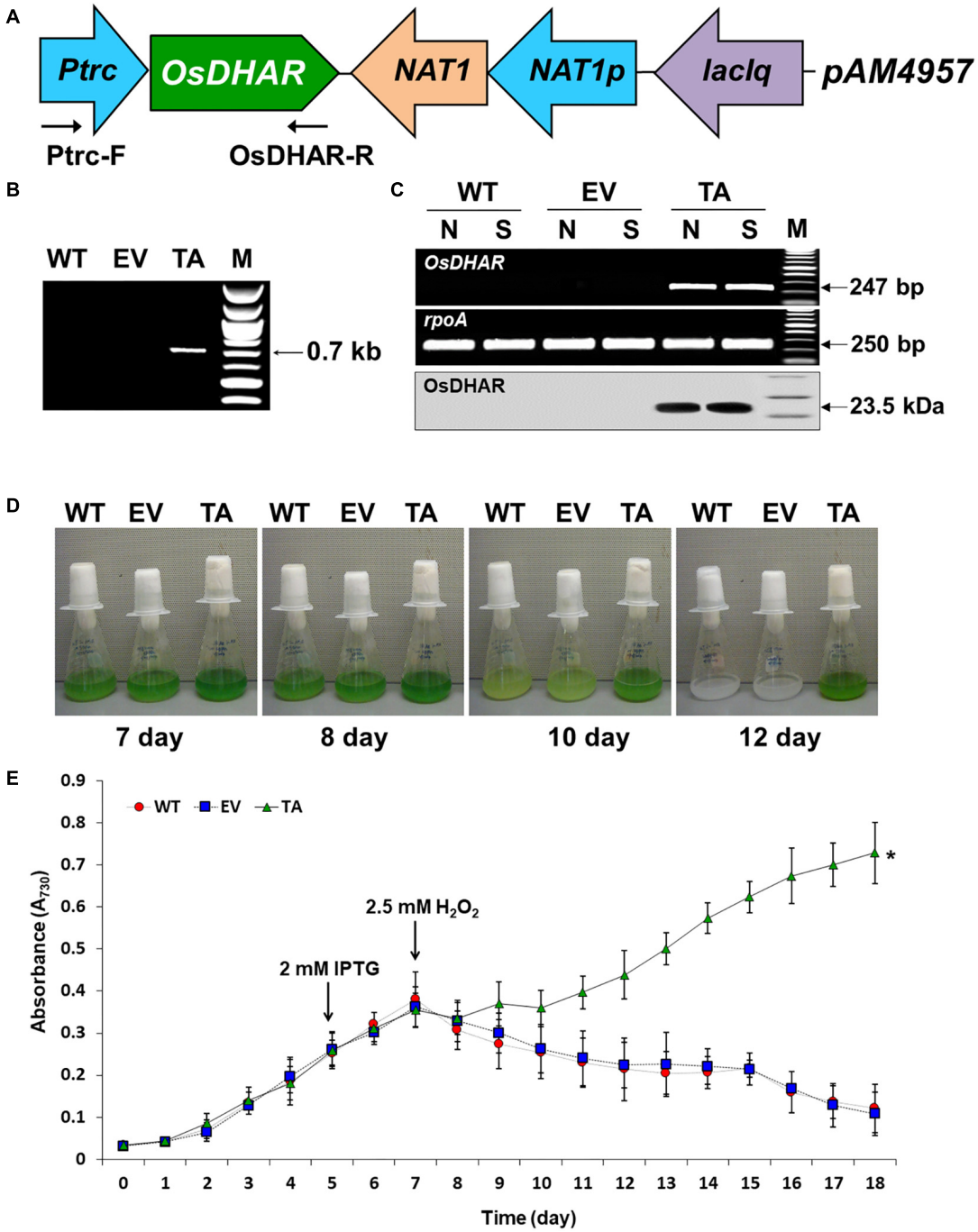

FIGURE 2 | Expression of the *OsDHAR* gene in the *S. elongatus* PCC 7942. **(A)** Schematic showing expression of *OsDHAR* in of *S. elongatus* PCC 7942. *Ptrc*, IPTG-inducible promoter; *OsDHAR*, dehydroascorbate reductase gene of *O. sativa*; NAT, antibiotic nourseothricin selection marker (cloNAT); and *LacIq*, lactose repressor promoter. Arrows indicate the direction of each gene. **(B,C)** PCR results verifying *OsDHAR* gene integration in the genome of the transgenic TA. **(B)** PCR of *OsDHAR* gene in transgenic TA to confirm genotype (690 bp). **(C)** Expression of the *OsDHAR* gene was confirmed by semi-quantitative RT-PCR (247 bp) and Western blot (23.5 kDa). N, normal conditions; S, stress conditions. The *rpoA* transcript was used as a control standard in the analysis (250 bp). **(D,E)** Growth profiles of the TA, EV, and WT *S. elongatus* PCC 7942. Growth levels of the different *S. elongatus* PCC 7942 were compared to determine whether the TA grew better under H_2O_2 stress conditions. After 7 days of growth under standard conditions, the TA, EV, and WT *S. elongatus* PCC 7942 were adjusted to an absorbance at 730 nm of 0.3 to 0.35 and then grown in BG11 medium containing 2.5 mM H_2O_2, then cultured for 18 days at 30°C with shaking in liquid microbial lab flasks. WT, WT *S. elongatus* PCC 7942; EV, empty vector *S. elongatus* PCC 7942; TA, TA *S. elongatus* PCC 7942. Error bars indicate ± SD of biologically least three independent experiments. Asterisks indicate significant differences between treatments as estimated by Student's *t*-test ($P < 0.05$).

(WT) *S. elongatus* PCC 7942 (**Figure 2C** and **Supplementary Table S1**). We also performed Western blot analyses to determine whether the *OsDHAR* gene was properly translated. The TA grown under H_2O_2 stress conditions presented with a single band in a Western blot analysis using the OsDHAR antibody. No signal was detected in the EV and WT under the same conditions (**Figure 2C**). These results indicated that the *OsDHAR* gene under the control of the *Ptrc* promoter was expressed in the TA during incubation in 2 mM IPTG at 30°C for 2 days before 2.5 mM H_2O_2 treatment.

Stress tolerance was measured based on growth kinetics, colony formation on plates, and chlorophyll content. The TA grew better than the EV and WT under H_2O_2 stress conditions (**Figure 2E**). The WT and control EV showed loss of pigment on days 7, 8, and 10 after exposure to H_2O_2 stress, and were completely bleached by day 12, whereas the TA showed loss of pigment on day 10 (**Figure 2D**).

Stress responses were also evaluated with a plate cell-spotting assay. Exponentially growing TA, EV, and WT (absorbance at 730 nm = 0.25) were exposed to 2.5 mM H_2O_2 with 2 mM IPTG for 3 days, and then serial dilutions were spotted on agar-solidified BG11 medium. Cell viability of the TA was better than that of the EV and WT following exposure to H_2O_2 stress. On the other hand, all individuals were similarly spotted under normal conditions (**Figure 3A**). Measurement of chlorophyll content after 2 days exposure to H_2O_2 revealed less loss of chlorophyll in the TA than in the EV and WT (**Figure 3B**). The total dry weight of the TA was twofold higher than that of the EA and WT under oxidative stress conditions (**Figure 3C**).

Redox states were determined based on cellular ROS levels assayed with the cytosolic oxidant-sensitive probe 2′,7′-dichlorodihydrofluorescein diacetate (DCFHDA), which measures the oxidative conversion of DCFHDA to the highly fluorescent compound dichlorofluorescein (DCF). All three the TA, EV, and WT *S. elongatus* PCC 7942 showed an increase in DCF fluorescence following exposure to 2.5 mM H_2O_2 with 2 mM IPTG for 2 h, but the fluorescence intensity of the probe was more pronounced in the control EV and WT than in the TA (**Figure 4A**). When the TA, EV, and WT were subjected to oxidative stress, the TA displayed ROS-mediated cellular damage with or without ROS generation and contained moderate green fluorescence in the intracellular space. In contrast, EV and WT showed much more intense green fluorescence (**Figure 4A**). DCFHDA fluorescence was quantified by individually mixing the TA, EV, and WT with 10 μM DCFHDA followed by incubation for 20 min in the dark. Fluorescence intensity was 1.5-fold higher in the EV and WT than in the TA in the presence of 2.5 mM H_2O_2 with 2 mM IPTG (**Figure 4D**). In a biochemical assay using the FOX reagent, cellular ROS levels in the TA were determined to be approximately 20% lower than those in the EV and WT in the presence of H_2O_2 (**Figure 4B**). The lower ROS production in the TA resulted in reduced accumulation of MDA due to lipid peroxidation compared to the EV and WT. MDA accumulations were 1.2-fold higher in the EV and WT than in the TA (**Figure 4C**).

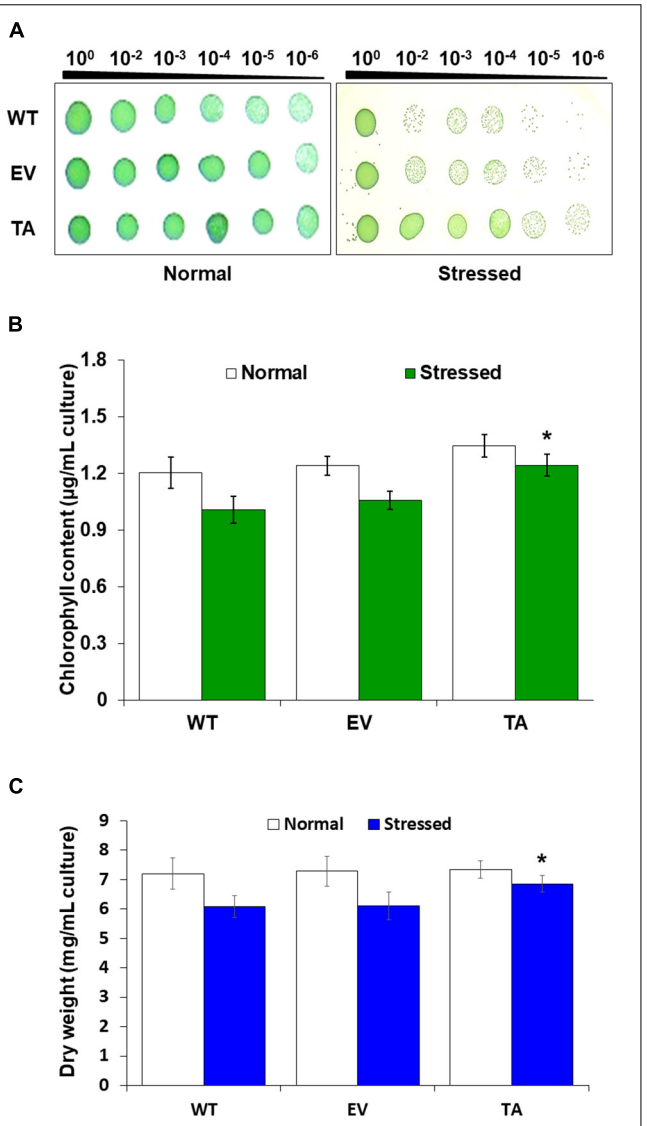

FIGURE 3 | Stress sensitivity in the *OsDHAR*-expressing transgenic TA. **(A)** Cell viability was evaluated based on number of colony-forming units and spotting assay. **(B)** Chlorophyll contents of grown for 2 days in the presence of 2.5 mM H_2O_2 (A_{730} = 0.3). **(C)** Dry weights measured at 7 and 9 days after growth in the presence or absence of 2.5 mM H_2O_2 for 2 days. Error bars indicate ± SD of biologically least three independent experiments. Asterisks indicate significant differences between treatments as estimated by Student's *t*-test ($P < 0.05$). WT, WT *S. elongatus* PCC 7942; EV, empty vector *S. elongatus* PCC 7942; TA, TA *S. elongatus* PCC 7942.

Effect of *OsDHAR* Expression on the GSH-Dependent Antioxidant System

We analyzed redox homeostasis in the *OsDHAR*-expressing transgenic by measuring the GSH pools to determine how *OsDHAR* expression affects total GSH content in cyanobacteria exposed to H_2O_2. In the TA, GSH redox status was expressed as the ratio of reduced GSH to oxidized GSSG (GSH/GSSG), was approximately 1.5-fold higher than those of the EV and WT (**Figure 5B**). The GSH/GSSG ratio in the TA were

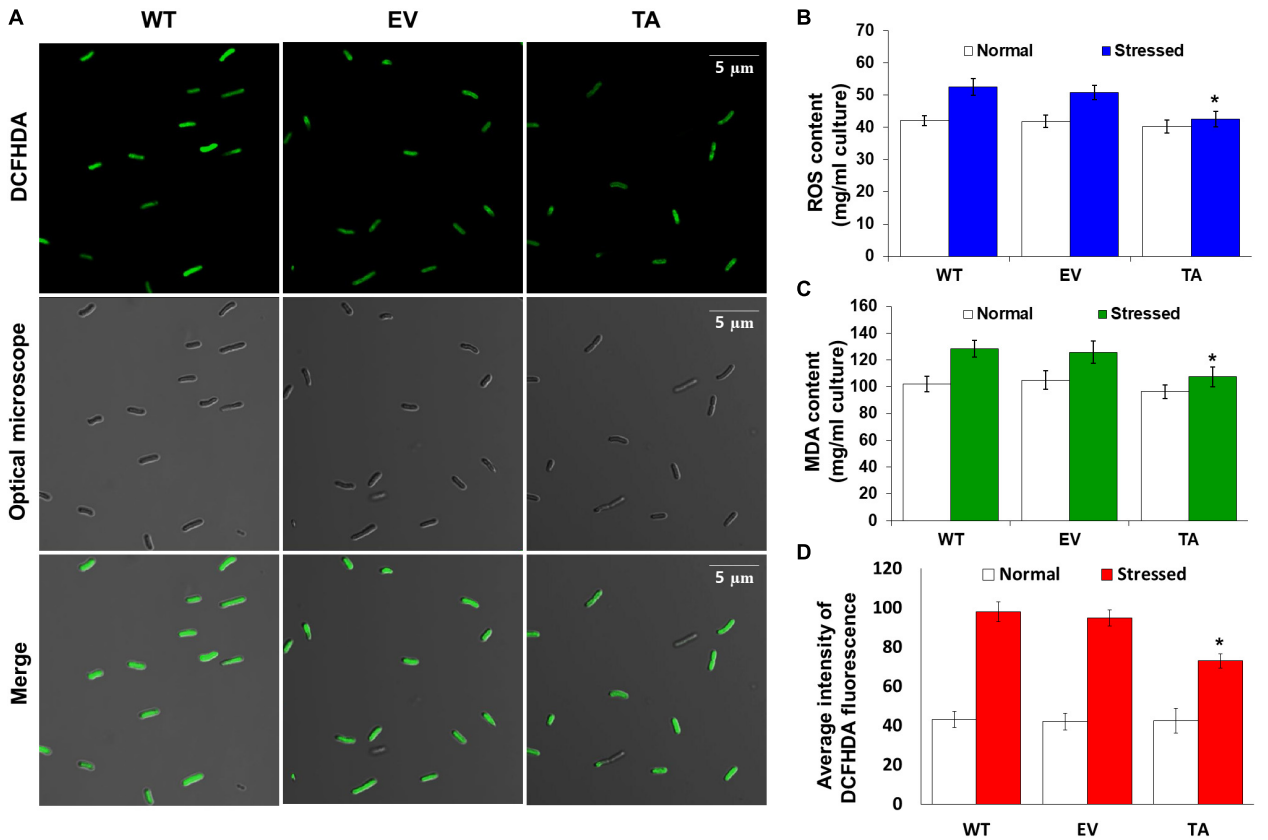

FIGURE 4 | Expression of the *OsDHAR* gene in *S. elongatus* PCC 7942 improves intracellular redox homeostasis. **(A)** Confocal microscopy images of cells stained with DCFHDA to measure levels of ROS after treatment with 2.5 mM H_2O_2 for 2 h. **(B)** Intracellular ROS levels were determined using intracellular H_2O_2 after treatment with 2.5 mM H_2O_2 for 24 h. **(C)** Levels of lipid peroxidation were determined by TBA assay using MDA after treatment to 2.5 mM H_2O_2-IPTG with 2 mM IPTG for 24 h. **(D)** DCFHDA fluorescence they also measured ROS production via a microplate reader after treatment with 2.5 mM H_2O_2 for 2 h. Error bars indicate ± SD of biologically least three independent experiments. Asterisks indicate significant differences between treatments as estimated by Student's *t*-test ($P < 0.05$).

higher under oxidative stress than under normal conditions. Similarly, the GSH/GSSG ratio in the EV and WT were also moderately increased under oxidative stress, although overall values were lower than those of the TA (**Figure 5B**). Conversely, oxidized GSSG content in the EV and WT increased tremendously over baseline values compared to the TA under oxidative stress and normal conditions (**Supplementary Figure S1**).

OsDHAR expression in the TA was also associated with increased GST activity under oxidative stress conditions (**Figure 5A**). These results indicate that enhanced resistance to the oxidative stress by maintaining of the cellular redox homeostasis during ROS-induced oxidative stress relates to the homology GST in cyanobacteria. For this reason, increased homeostasis correlated with total GSH content, and oxidized GSH and reduced GSH were observed in cyanobacteria harboring the *DHAR* gene. This result strongly suggests that the expression of DHAR (with its homology with GST) in *S. elongatus* PCC 7942 enhances tolerance of ROS-induced oxidative stress by maintaining cellular redox homeostasis using GSH alongside other antioxidant enzymes in cyanobacteria (**Figure 6** and **Supplementary Figure S3**). Thus, heterologous *OsDHAR* expression in the TA responded to oxidative stress by increasing the number of redox active sites, such as GSH binding sites, and GSTs with similar functionally conserved residues under these conditions (**Figures 1**, **5**). Altogether, our findings indicate that *OsDHAR* expression conferred tolerance to oxidative stress in *S. elongatus* PCC 7942 by interacting with GSH-dependent enzymes.

We explored this possibility further by conducting gene expression of the TA after exposure to H_2O_2-IPTG for 24 h. qRT-PCR identified GSH-dependent genes that were expressed in the TA after treatment with 2.5 mM H_2O_2-IPTG for 24 h in liquid BG11 medium containing 2 mM IPTG (**Supplementary Figure S3**). These genes included GST, thioredoxin reductase (TrxR), glutathione reductase (GR), catalase (CAT), glutathione peroxidase (GPX), 2-Cys peroxiredoxin (TRX), glutaredoxin (GRX), and peroxiredoxin (PRX) belonging to GSH-dependent reactions (**Figure 6** and **Supplementary Figure S3**). Our results indicate that heterologous *OsDHAR* expression in the TA can enhance

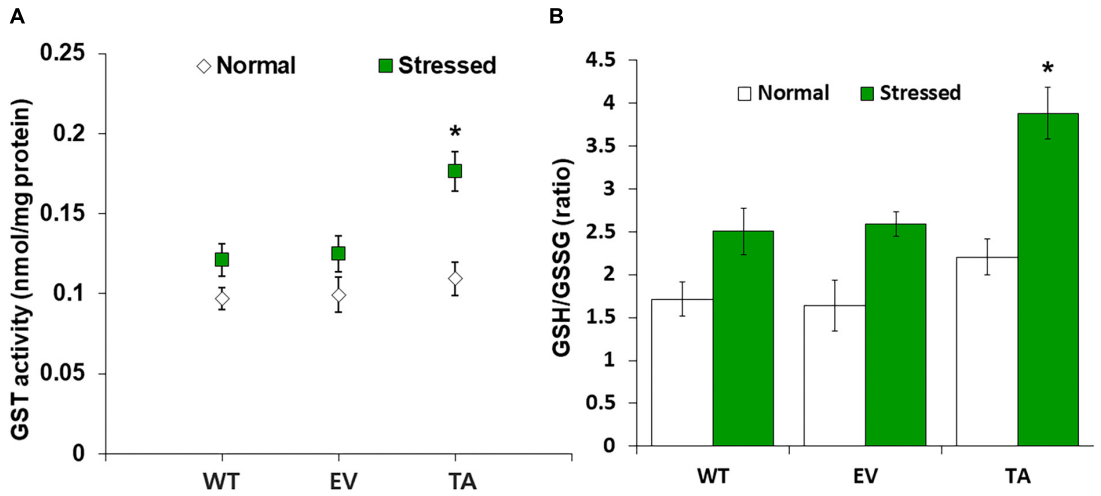

FIGURE 5 | Analysis of enzyme activity and antioxidant redox status in TA after H_2O_2 treatment. **(A)** Activity of GST under normal and stress conditions. **(B)** Intracellular GSH/GSSG redox ratios in WT, EV, and TA after exposure to 2.5 mM H_2O_2 for 24 h. White bars correspond to conditions before H_2O_2 treatment (normal conditions), and the GSH/GSSG redox ratios (green bars) correspond to conditions after H_2O_2 treatment (stress conditions). Data are shown as mean values ± SD of biologically least three independent experiments. Asterisks indicate significant differences between treatments as estimated by Student's *t*-test ($P < 0.05$). Measurements are an annotated in **Supplementary Figure S1**.

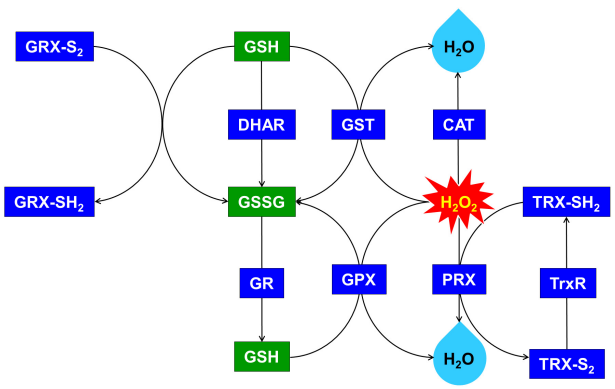

FIGURE 6 | Upregulated glutathione (GSH)-dependent antioxidant system and maintenance of cellular redox status through the overexpression of *OsDHAR* in *S. elongatus*. GRX, glutaredoxin; GST, glutathione *S*-transferase; GR, glutathione reductase; GPX, glutathione peroxidase; CAT, catalase; PRX, peroxiredoxin; TRX, thioredoxin; TrxR, thioredoxin reductase. qRT-PCR identified GSH-related genes that were annotated in **Supplementary Figure S3**.

tolerance through the maintenance of cellular redox homeostasis via the GSH-dependent antioxidant system during ROS-induced oxidative stress.

DISCUSSION

Heterologous OsDHAR and the other GSTs demonstrated pairwise alignment with a conserved site that bound to GSH residues and other similarly functional conserved residues (**Figure 1**). OsDHAR also contains interacting residues of the GSH binding site. This indicates that OsDHAR can supply a redox active site during ROS-induced oxidative stress (Pulido et al., 2010; Do et al., 2016; Kim et al., 2017). The similarity of the aforementioned conserved DHAR sequences indicated that the OsDHAR redox active site possesses strictly conserved residues, including a GSH binding site and similar functional conserved residues from cyanobacteria GSTs. This GSH-dependent antioxidant system can facilitate GSH-dependent reactions during ROS-induced oxidative stress (**Figure 6** and **Supplementary Figure S3**). As such, the redox active sites of OsDHAR participate in the maintenance of a stable cellular thiol/disulfide ratio, redox regulation, and refolding of oxidatively damaged proteins (Thomas et al., 1999; Hamnell-Pamment et al., 2005; Latifi et al., 2009; Anfelt et al., 2013; Kim et al., 2013; Abdul Kayum et al., 2018). In addition, we constructed a phylogenetic tree containing the *S. elongatus* PCC 7942 GST (SeGST; accession no. WP_011243077), which was 24% homologous to OsDHAR (accession no. AAL71856.1) (**Figure 1B**). The phylogenetic tree illustrated the evolutionary relationship between rice DHAR and cyanobacterial GST proteins.

We analyzed *OsDHAR*-mediated stress tolerance in transgenic *S. elongatus* PCC 7942 under H_2O_2 stress conditions because excess H_2O_2 is a major cause of oxidative stress in biological systems, and cyanobacteria are generally more sensitive to H_2O_2 than are other phototrophs (Drabkova et al., 2007; Banerjee et al., 2015). We investigated the mechanism by which *OsDHAR* gene overexpression increased H_2O_2 stress tolerance by examining the phenotypes and gene expression of the TA under H_2O_2 stress. There were no differences in phenotype among the TA, EV, and WT *S. elongatus* PCC 7942 grown under normal conditions (7 days; **Figure 2D**). Under H_2O_2 stress, however, most of the EV and WT had lost almost all their pigment

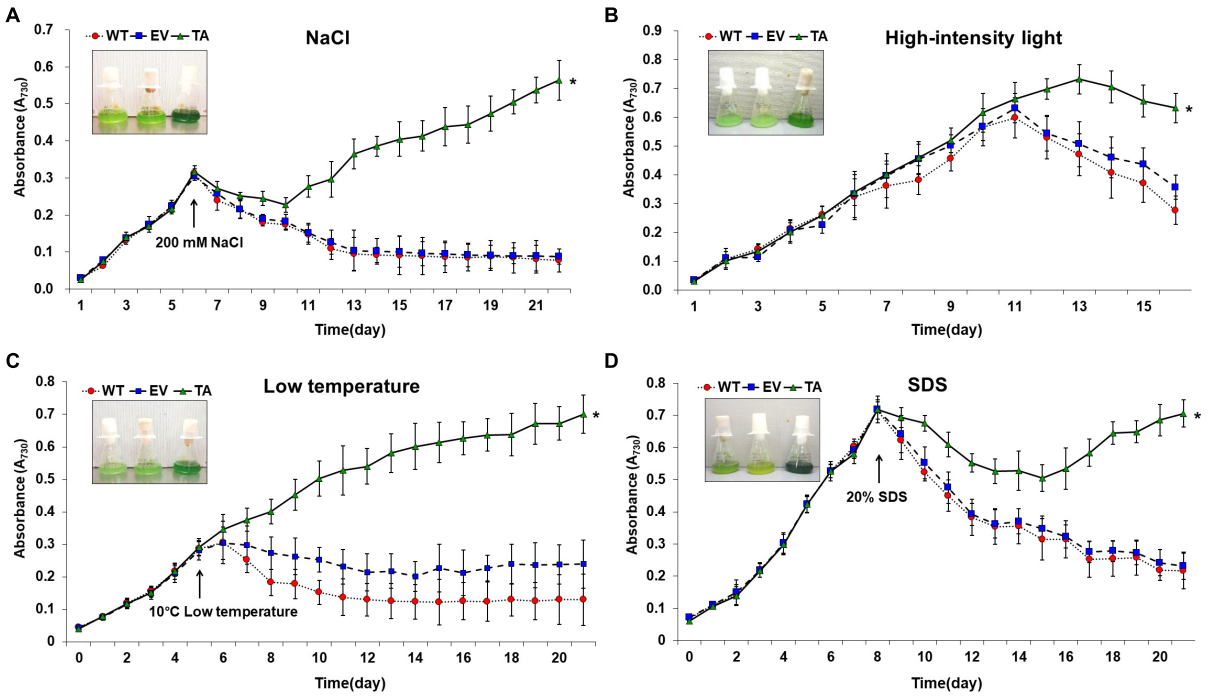

FIGURE 7 | Growth profiles of WT, EV, and TA in the presence of oxidative stressors, including **(A)** 200 mM NaCl after incubation for 6 days, **(B)** 250 μE high-intensity light during continuous incubation, **(C)** low temperature (10°C) after incubation for 5 days, and **(D)** 20% SDS after incubation for 8 days. Photographs were taken approximately 3 days after stress treatments at which point the sensitive phenotype appeared. Error bars indicate ± SD of biologically least three independent experiments. Asterisks indicate significant differences between treatments as estimated by Student's *t*-test ($P < 0.05$). WT, WT *S. elongatus* PCC 7942; EV, empty vector *S. elongatus* PCC 7942; TA, TA *S. elongatus* PCC 7942.

after 10 days, while the TA lost considerably less pigment over this same period. The TA also recovered quickly from H_2O_2 damage (12 days; **Figures 2D,E**) and overall TA survival rates were higher than those of the EV and WT. Results also demonstrated that the TA, EV, and WT possessed clear phenotypic differences that correlated with their ability (or inability) to recover from H_2O_2 damage. Specifically, the TA recuperated quickly after H_2O_2 treatment, whereas the EV and WT did not (**Figures 2D,E**).

Stress responses were also evaluated by plate cell-spotting assay following H_2O_2 stress. Cell viability of the TA was better than the EV and WT following exposure to 2.5 mM H_2O_2 for 3 days (**Figure 3A**). Measurement of chlorophyll content after a 2-day exposure to 2.5 mM H_2O_2 revealed a more loss of 18% less chlorophyll in the EV and WT compared to the TA (**Figure 3B**). Based on these results, the total dry weight of the TA was twofold higher than the EA and WT to H_2O_2 stress (**Figure 3C**).

The TA, EV, and WT were additionally exposed to oxidative stress due to high salt concentrations (200 mM NaCl), low temperature (10°C), excess light (250 μE high-intensity light), and sodium dodecyl sulfate (SDS, 20%) (**Figure 7**). When cells are exposed to high salinities or low temperatures, major processes of photosynthesis, protein synthesis, and energy and lipid metabolism are slowed or halted (Demiral and Turkan, 2006). In addition, the stress of excess light can induce damage to the reaction center of photosystem II and may lead to the perturbation or inhibition of photosynthetic electron transport in cells (Fryer et al., 2003; Kim et al., 2018). Previous studies have shown that multiple ion channel pores in cell participate to stress responses in cyanobacterial cells (Los and Murata, 2004; Kim et al., 2018). SDS and cold stress were a surfactant that damage lipid membranes, thereby disrupting cellular redox homeostasis and leading to apoptosis (Kwon et al., 2003; Tahara et al., 2012; Shin et al., 2013).

The TA displayed better growth than the control EV and WT in the presence of NaCl, high-intensity light, low temperature, and SDS (**Figure 7**). These results indicate that the expression of the *OsDHAR* gene in the TA conferred higher tolerance to oxidative stresses compared to that of the EV and WT. As already mentioned, DHAR participates in cellular detoxification, stress tolerance, and light signaling (Loyall et al., 2000; Thom et al., 2002; Benekos et al., 2010). Thus, DHAR as isozymes are critical to cellular detoxification of exogenous and endogenous harmful compounds. In aerobic cells, high DHAR activity enhances growth and development through increased chlorophyll fluorescence under oxidative stress, whereas it decreases chlorophyll in aging cells under the same conditions (Wang et al., 2010; Kim et al., 2013; Do et al., 2016). In cyanobacteria, H_2O_2-induced oxidative stress and the resulting excess ROS lead to cell death in

several types of cyanobacteria (Drabkova et al., 2007; Qian et al., 2010; Banerjee et al., 2015). We investigated the effects of oxidative stress produced by H_2O_2-generated ROS by analyzing ROS levels *in vitro* and *in vivo* in the TA, EV, and WT. Cellular ROS levels were assayed to evaluate cell rescue redox states with the cytosolic oxidant-sensitive probe 2′,7′-dichlorodihydrofluorescein diacetate (DCFHDA), which measures the oxidative conversion of DCFHDA to the highly fluorescent compound dichlorofluorescein (DCF). The TA displayed ROS-mediated cellular damage with and without the targeting signal, and contained weaker green fluorescence in the intracellular space than the EV and WT in the presence of 2.5 mM H_2O_2 (**Figure 4A**). DCFHDA fluorescence intensity was 1.5-fold higher in the EV and WT than the TA in the presence of 2.5 mM H_2O_2 (**Figure 4D**). Cellular ROS levels in the TA were found to be lower than those in the EV and WT through a biochemical assay using the FOX reagent in the presence of H_2O_2 (**Figure 4B**). Lower ROS production in the TA was associated with reduced accumulation of MDA due to lipid peroxidation compared to the EV and WT (**Figure 4C**). These results indicated that transgenic *OsDHAR* expression in the TA increased cell tolerance to oxidative stress by scavenging ROS and increasing chlorophyll content. These findings indicate that *OsDHAR* is key to oxidative tolerance through the maintenance of cellular redox homeostasis via a GSH-dependent antioxidant system.

Cells employ several mechanisms to combat toxic ROS generated by abiotic stresses like oxidants. The generated ROS can be scavenged by non-enzymatic antioxidants, such as GSH, or by enzymatic systems, such as the GSH pools involving DHAR (Noctor and Foyer, 1998; Kim et al., 2014). Different environmental stressors, including high salinity, low temperature, and drought, can activate *DHAR* expression, which goes on to regulate GSH pools (Urano et al., 2000; Jiang and Zhang, 2002; Kwon et al., 2003; Eltayeb et al., 2007; Gill and Tuteja, 2010). GSTs have been divided into eight classes: tau, phi, theta, zeta, lambda, EF1Bγ, DHAR, and tetrachlorohydroquinone dehalogenase (TCHQD) (Oakley, 2005; Lan et al., 2009; Dixon and Edwards, 2010; Jain et al., 2010; Liu et al., 2013).

Among these, DHAR and GST share considerable homology has been ubiquitously produced in eukaryotes and prokaryotes, such as plants, animals, fungi, and bacteria (Dixon et al., 2002; Liu et al., 2013; Rezaei et al., 2013; Ding et al., 2017). The homologous DHAR and GST have similar functions involving their redox active sites and GSH binding site residues (Dixon et al., 2002; Kim et al., 2013). Both DHAR and GST execute GSH-dependent thiol transferase activity to recycle antioxidants, including flavonoids, and quinones (Dixon et al., 2011). In this study, GST activity increased concomitantly with GSH via heterologous *OsDHAR* overexpression in cyanobacteria (**Figure 5** and **Supplementary Figure S1**). Cellular oxidative stress depends on maintaining a balance between ROS content and the antioxidant system (Tang et al., 2007; Kim et al., 2017, 2018). Increased production of antioxidants (GSH) and antioxidant enzymes (GST) can ameliorate excess ROS during oxidative stress. In this study, these phenomena were associated with TA resistance to oxidative stress (**Figures 2–7** and **Supplementary Figure S1**). We thereby conclude that the expression of heterologous *OsDHAR* in *S. elongatus* PCC 7942 enhanced tolerance to ROS-induced oxidative stress by maintaining cellular redox homeostasis through cooperation of the homologous GST in cyanobacterial cells.

Previous evidences have established a relationship between stress tolerance and the cellular redox homeostasis that is affected by *DHAR* overexpression in several cells (Horemans et al., 2000; Kwon et al., 2003; Ushimaru et al., 2006; Eltayeb et al., 2007; Qian et al., 2010; Wang et al., 2010). We confirmed that the TA was resistant to H_2O_2 stress and that this was related to an increased GSH/GSSG ratio (**Figure 5B**) and GST activity (**Figure 5A**). Our results indicated that heterologous *OsDHAR* expression in *S. elongatus* PCC 7942 confers tolerance to oxidative stress by interacting with GSH-dependent enzymes. Gene expression levels of the TA during exposure to H_2O_2 was also conducted to confirm this conclusion, and qRT-PCR identified GSH-related genes that were upregulated, including GST, TrxR, GR, CAT, GPX, TRX, GRX, and PRX, belonging to GSH-dependent reactions in the TA (**Figure 6** and **Supplementary Figure S3**). GSH-dependent antioxidation involving GST, GR, CAT, GPX, GRX, TrxR, PRX, and TRX are all involved in protecting cells from oxidative stress and minimizing subsequent cellular damage (Kingston-Smith and Foyer, 2000). In particular, the GSH-dependent enzymes are among the most potent protein-based protection mechanisms and occur in nearly all cells, from bacteria like *E. coli* to higher plants and animals (Meyer et al., 2012). We surmise that oxidative stress tolerance in the TA would be increased through improved maintenance of redox homeostasis compared to the WT and EV (**Figures 2–7** and **Supplementary Figure S3**).

Taken together, our findings indicate that the expression of *OsDHAR* in *S. elongatus* PCC 7942 maintained cellular redox homeostasis and protected cells from oxidative damage with the GSH-dependent antioxidant system via GSH-dependent reactions at the redox active site and GSH binding-site residues. However, genetic and molecular underpinnings of heterologous *OsDHAR* and homologous *SeGST* activity remain unclear. Cellular redox homeostasis and molecular processes involved in their response to various environmental conditions warrant further study.

We found that expression of the *OsDHAR* gene in the *S. elongatus* PCC 7942 increased tolerance to ROS-induced oxidative stress through the maintenance of cellular redox homeostasis with a GSH-dependent antioxidant system via GSH-dependent reactions. We anticipate that other antioxidant defense mechanisms might act synergistically to produce an effective defense response and protect cells during oxidative stress. The genetically modified cyanobacteria used in this study could help verify mutual functions between *O. sativa DHAR* and *S. elongatus* PCC 7942 *GST* genes. Further studies are needed to elucidate the mechanisms that underlie the increased oxidative stress tolerance observed in heterologous *OsDHAR*-expressing transgenic cyanobacterium.

DATA AVAILABILITY STATEMENT

The raw data supporting the conclusions of this article will be made available by the authors, without undue reservation, to any qualified researcher.

AUTHOR CONTRIBUTIONS

Y-SK, I-SK, AT, JG, and H-SY designed the experiments. S-IP, J-JK, and K-IL performed the experiments. The article was written by Y-SK, and edited by JSB and JB. All authors read and approved the final manuscript.

FUNDING

This work was funded by the Basic Science Research Program through the National Research Foundation of Korea (NRF) funded by the Ministry of Education (grant no. 2016R1A6A1A05011910) and (grant no. 2018R1D1A3B07049385), Korea. We are grateful for the financial support of the Next-Generation BioGreen 21 Program (grant nos. PJ01366701 and PJ013240), Korea and the US NIH-NIGMS (grant no. R01GM118815), United States (JG).

ACKNOWLEDGMENTS

We thank Susan S. Golden (the University of California, San Diego and Center for Chronobiology) for supplying *S. elongatus* PCC 7942. We also thank Spencer Diamond, Benjamin Rubin, Ryan K. Shultzaberger, You Chen, Amy T. Ma, Mizuho Ota, Susan E. Cohen, Mark L. Paddock, Yong-Ick Kim, David G. Welkie, Roger Tseng, and Cigdem Sancar for helpful discussions and assistance with the section "Materials and Methods."

SUPPLEMENTARY MATERIAL

The Supplementary Material for this article can be found online at: https://www.frontiersin.org/articles/10.3389/fpls.2020.00231/full#supplementary-material

REFERENCES

Abdul Kayum, M., Nath, U. K., Park, J. I, Biswas, M. K., Choi, E. K., Song, J. Y., et al. (2018). Genome-wide identification, characterization, and expression profiling of glutathione S-transferase (GST) family in pumpkin reveals likely role in cold-stress tolerance. *Genes (Basel)* 9:84. doi: 10.3390/genes9020084

Anfelt, J., Hallstrom, B., Nielsen, J., Uhlen, M., and Hudson, E. P. (2013). Using transcriptomics to improve butanol tolerance of *Synechocystis* sp. strain PCC 6803. *Appl. Environ. Microbiol.* 79, 7419–7427. doi: 10.1128/AEM.02694-13

Banerjee, M., Chakravarty, D., and Ballal, A. (2015). Redox-dependent chaperone/peroxidase function of 2-Cys-Prx from the cyanobacterium *Anabaena* PCC7120: role in oxidative stress tolerance. *BMC Plant Biol.* 15:60. doi: 10.1186/s12870-015-0444-2

Benekos, K., Kissoudis, C., Nianiou-Obeidat, I., Labrou, N., Madesis, P., Kalamaki, M., et al. (2010). Overexpression of a specific soybean *Gm*GSTU4 isoenzyme improves diphenyl ether and chloroacetanilide herbicide tolerance of transgenic tobacco plants. *J. Biotechnol.* 150, 195–201. doi: 10.1016/j.jbiotec.2010.07.011

Blank, C. E. (2013). Origin and early evolution of photosynthetic eukaryotes in freshwater environments: reinterpreting proterozoic paleobiology and biogeochemical processes in light of trait evolution. *J. Phycol.* 49, 1040–1055. doi: 10.1111/jpy.12111

Boyer, J. S. (1982). Plant productivity and environment. *Science* 218, 443–448. doi: 10.1126/science.218.4571.443

Chen, Z., and Gallie, D. R. (2005). Increasing tolerance to ozone by elevating foliar ascorbic acid confers greater protection against ozone than increasing avoidance. *Plant Physiol.* 138, 1673–1689. doi: 10.1104/pp.105.062000

Demiral, T., and Turkan, I. (2006). Exogenous glycinebetaine affects growth and proline accumulation and retards senescence in two rice cultivars under NaCl stress. *Environ. Exp. Bot.* 56, 72–79. doi: 10.1016/j.envexpbot.2005.01.005

Ding, N., Wang, A., Zhang, X., Wu, Y., Wang, R., Cui, H., et al. (2017). Identification and analysis of glutathione S-transferase gene family in sweet potato reveal divergent GST-mediated networks in aboveground and underground tissues in response to abiotic stresses. *BMC Plant Biol.* 17:225. doi: 10.1186/s12870-017-1179-z

Dixit, G., Singh, A. P., Kumar, A., Singh, P. K., Kumar, S., Dwivedi, S., et al. (2015). Sulfur mediated reduction of arsenic toxicity involves efficient thiol metabolism and the antioxidant defense system in rice. *J. Hazard. Mater.* 298, 241–251. doi: 10.1016/j.jhazmat.2015.06.008

Dixon, D. P., Davis, B. G., and Edwards, R. (2002). Functional divergence in the glutathione transferase superfamily in plants. Identification of two classes with putative functions in redox homeostasis in *Arabidopsis thaliana*. *J. Biol. Chem.* 277, 30859–30869. doi: 10.1074/jbc.m202919200

Dixon, D. P., and Edwards, R. (2010). Roles for stress-inducible lambda glutathione transferases in flavonoid metabolism in plants as identified by ligand fishing. *J. Biol. Chem.* 285, 36322–36329. doi: 10.1074/jbc.M110.164806

Dixon, D. P., Steel, P. G., and Edwards, R. (2011). Roles for glutathione transferases in antioxidant recycling. *Plant Signal. Behav.* 6, 1223–1227. doi: 10.4161/psb.6.8.16253

Do, H., Kim, I. S., Jeon, B. W., Lee, C. W., Park, A. K., Wi, A. R., et al. (2016). Structural understanding of the recycling of oxidized ascorbate by dehydroascorbate reductase (*OsDHAR*) from *Oryza sativa* L. *japonica*. *Sci. Rep.* 6:19498. doi: 10.1038/srep19498

Drabkova, M., Matthijs, H. C. P., Admiraal, W., and Marsalek, B. (2007). Selective effects of H2O2 on cyanobacterial photosynthesis. *Photosynthetica* 45, 363–369. doi: 10.1007/s11099-007-0062-9

Eltayeb, A. E., Kawano, N., Badawi, G. H., Kaminaka, H., Sanekata, T., Morishima, I., et al. (2006). Enhanced tolerance to ozone and drought stresses in transgenic tobacco overexpressing dehydroascorbate reductase in cytosol. *Physiol. Plantarum* 127, 57–65. doi: 10.1111/j.1399-3054.2006.00624.x

Eltayeb, A. E., Kawano, N., Badawi, G. H., Kaminaka, H., Sanekata, T., Shibahara, T., et al. (2007). Overexpression of monodehydroascorbate reductase in transgenic tobacco confers enhanced tolerance to ozone, salt and polyethylene glycol stresses. *Planta* 225, 1255–1264. doi: 10.1007/s00425-006-0417-7

Fryer, M. J., Ball, L., Oxborough, K., Karpinski, S., Mullineaux, P. M., and Baker, N. R. (2003). Control of ascorbate peroxidase 2 expression by hydrogen peroxide and leaf water status during excess light stress reveals a functional organisation of *Arabidopsis* leaves. *Plant J.* 33, 691–705. doi: 10.1046/j.1365-313x.2003.01656.x

Gill, S. S., and Tuteja, N. (2010). Reactive oxygen species and antioxidant machinery in abiotic stress tolerance in crop plants. *Plant Physiol. Biochem.* 48, 909–930. doi: 10.1016/j.plaphy.2010.08.016

Golden, S. S., Brusslan, J., and Haselkorn, R. (1987). Genetic engineering of the cyanobacterial chromosome. *Methods Enzymol.* 153, 215–231. doi: 10.1016/0076-6879(87)53055-5

Gorain, P. C., Bagchi, S. K., and Mallick, N. (2013). Effects of calcium, magnesium and sodium chloride in enhancing lipid accumulation in two green microalgae. *Environ. Technol.* 34, 1887–1894. doi: 10.1080/09593330.2013.812668

Hamnell-Pamment, Y., Lind, C., Palmberg, C., Bergman, T., and Cotgreave, I. A. (2005). Determination of site-specificity of S-glutathionylated cellular proteins. *Biochem. Biophys. Res. Commun.* 332, 362–369. doi: 10.1016/j.bbrc.2005.04.130

Horemans, N., Foyer, C. H., Potters, G., and Asard, H. (2000). Ascorbate function and associated transport systems in plants. *Plant Physiol. Biochem.* 38, 531–540. doi: 10.1016/s0981-9428(00)00782-8

Huang, T., Lin, J., Cao, J., Zhang, P., Bai, Y., Chen, G., et al. (2012). An exopolysaccharide from *Trichoderma pseudokoningii* and its apoptotic activity on human leukemia K562 cells. *Carbohydr. Polym.* 89, 701–708. doi: 10.1016/j.carbpol.2012.03.079

Jain, M., Ghanashyam, C., and Bhattacharjee, A. (2010). Comprehensive expression analysis suggests overlapping and specific roles of rice glutathione S-transferase genes during development and stress responses. *BMC Genomics* 11:73. doi: 10.1186/1471-2164-11-73

Jiang, M., and Zhang, J. (2001). Effect of abscisic acid on active oxygen species, antioxidative defence system and oxidative damage in leaves of maize seedlings. *Plant Cell Physiol.* 42, 1265–1273. doi: 10.1093/pcp/pce162

Jiang, M. Y., and Zhang, J. H. (2002). Water stress-induced abscisic acid accumulation triggers the increased generation of reactive oxygen species and up-regulates the activities of antioxidant enzymes in maize leaves. *J. Exp. Bot.* 53, 2401–2410. doi: 10.1093/jxb/erf090

Kim, I. S., Jin, I., and Yoon, H. S. (2011). Decarbonylated cyclophilin A Cpr1 protein protects *Saccharomyces cerevisiae* KNU5377Y when exposed to stress induced by menadione. *Cell Stress Chaperones* 16, 1–14. doi: 10.1007/s12192-010-0215-9

Kim, Y. S., Kim, I. S., Bae, M. J., Choe, Y. H., Kim, Y. H., Park, H. M., et al. (2013). Homologous expression of cytosolic dehydroascorbate reductase increases grain yield and biomass under paddy field conditions in transgenic rice (*Oryza sativa* L. *japonica*). *Planta* 237, 1613–1625. doi: 10.1007/s00425-013-1862-8

Kim, Y. S., Kim, I. S., Boyd, J. S., Taton, A., Golden, J. W., and Yoon, H. S. (2017). Enhanced biomass and oxidative stress tolerance of *Synechococcus elongatus* PCC 7942 overexpressing the *DHAR* gene from *Brassica juncea*. *Biotechnol. Lett.* 39, 1499–1507. doi: 10.1007/s10529-017-2382-6

Kim, Y. S., Kim, I. S., Shin, S. Y., Park, T. H., Park, H. M., Kim, Y. H., et al. (2014). Overexpression of dehydroascorbate reductase confers enhanced tolerance to salt stress in rice plants (*Oryza sativa* L. *japonica*). *J. Agron. Crop Sci.* 200, 444–456. doi: 10.1111/jac.12078

Kim, Y. S., Kim, J. J., Park, S. I., Diamond, S., Boyd, J. S., Taton, A., et al. (2018). Expression of *OsTPX* gene improves cellular redox homeostasis and photosynthesis efficiency in *Synechococcus elongatus* PCC 7942. *Front. Plant Sci.* 9:1848. doi: 10.3389/fpls.2018.01848

Kingston-Smith, A. H., and Foyer, C. H. (2000). Overexpression of Mn-superoxide dismutase in maize leaves leads to increased monodehydroascorbate reductase, dehydroascorbate reductase and glutathione reductase activities. *J. Exp. Bot.* 51, 1867–1877. doi: 10.1093/jexbot/51.352.1867

Koksharova, O. A., Klint, I., and Rasmussen, U. (2006). The first protein map of *Synechococcus* sp. strain PCC 7942. *Mikrobiologiia* 75, 765–774.

Komatsu, S., Yamamoto, R., Nanjo, Y., Mikami, Y., Yunokawa, H., and Sakata, K. (2009). A comprehensive analysis of the soybean genes and proteins expressed under flooding stress using transcriptome and proteome techniques. *J. Proteome Res.* 8, 4766–4778. doi: 10.1021/pr900460x

Kwon, S. Y., Choi, S. M., Ahn, Y. O., Lee, H. S., Lee, H. B., Park, Y. M., et al. (2003). Enhanced stress-tolerance of transgenic tobacco plants expressing a human dehydroascorbate reductase gene. *J. Plant Physiol.* 160, 347–353. doi: 10.1078/0176-1617-00926

Lan, T., Yang, Z. L., Yang, X., Liu, Y. J., Wang, X. R., and Zeng, Q. Y. (2009). Extensive functional diversification of the *Populus* glutathione S-transferase supergene family. *Plant Cell* 21, 3749–3766. doi: 10.1105/tpc.109.070219

Latifi, A., Ruiz, M., and Zhang, C. C. (2009). Oxidative stress in cyanobacteria. *FEMS Microbiol. Rev.* 33, 258–278. doi: 10.1111/j.1574-6976.2008.00134.x

Liu, Y. J., Han, X. M., Ren, L. L., Yang, H. L., and Zeng, Q. Y. (2013). Functional divergence of the glutathione S-transferase supergene family in *Physcomitrella patens* reveals complex patterns of large gene family evolution in land plants. *Plant Physiol.* 161, 773–786. doi: 10.1104/pp.112.205815

Livak, K. J., and Schmittgen, T. D. (2001). Analysis of relative gene expression data using real-time quantitative PCR and the 2-ΔΔCt method. *Methods* 25, 402–408. doi: 10.1006/meth.2001.1262

Los, D. A., and Murata, N. (2004). Membrane fluidity and its roles in the perception of environmental signals. *Biochim. Biophys. Acta* 1666, 142–157. doi: 10.1016/j.bbamem.2004.08.002

Loyall, L., Uchida, K., Braun, S., Furuya, M., and Frohnmeyer, H. (2000). Glutathione and a UV light-induced glutathione S-transferase are involved in signaling to chalcone synthase in cell cultures. *Plant Cell* 12, 1939–1950. doi: 10.1105/tpc.12.10.1939

Meyer, Y., Belin, C., Delorme-Hinoux, V., Reichheld, J. P., and Riondet, C. (2012). Thioredoxin and glutaredoxin systems in plants: molecular mechanisms, crosstalks, and functional significance. *Antioxid. Redox Signal.* 17, 1124–1160. doi: 10.1089/ars.2011.4327

Noctor, G., and Foyer, C. H. (1998). Ascorbate and glutathione: keeping active oxygen under control. *Annu. Rev. Plant Physiol. Plant Mol. Biol.* 49, 249–279. doi: 10.1146/annurev.arplant.49.1.249

Oakley, A. J. (2005). Glutathione transferases: new functions. *Curr. Opin. Struct. Biol.* 15, 716–723. doi: 10.1016/j.sbi.2005.10.005

Owens, S. (2001). Salt of the earth: genetic engineering may help to reclaim agricultural land lost due to salinisation. *EMBO Rep.* 2, 877–879. doi: 10.1093/embo-reports/kve219

Peng, L. F., Kapp, E. A., McLauchlan, D., and Jordan, T. W. (2011). Characterization of the asia oceania human proteome organisation membrane proteomics initiative standard using SDS-PAGE shotgun proteomics. *Proteomics* 11, 4376–4384. doi: 10.1002/pmic.201100169

Potters, G., De Gara, L., Asard, H., and Horemans, N. (2002). Ascorbate and glutathione: guardians of the cell cycle, partners in crime? *Plant Physiol. Biochem.* 40, 537–548. doi: 10.1016/s0981-9428(02)01414-6

Pulido, P., Spinola, M. C., Kirchsteiger, K., Guinea, M., Pascual, M. B., Sahrawy, M., et al. (2010). Functional analysis of the pathways for 2-Cys peroxiredoxin reduction in *Arabidopsis thaliana* chloroplasts. *J. Exp. Bot.* 61, 4043–4054. doi: 10.1093/jxb/erq218

Qian, H., Yu, S., Sun, Z., Xie, X., Liu, W., and Fu, Z. (2010). Effects of copper sulfate, hydrogen peroxide and N-phenyl-2-naphthylamine on oxidative stress and the expression of genes involved photosynthesis and microcystin disposition in *Microcystis aeruginosa*. *Aquat. Toxicol.* 99, 405–412. doi: 10.1016/j.aquatox.2010.05.018

Rezaei, M. K., Shobbar, Z. S., Shahbazi, M., Abedini, R., and Zare, S. (2013). Glutathione S-transferase (GST) family in barley: identification of members, enzyme activity, and gene expression pattern. *J. Plant Physiol.* 170, 1277–1284. doi: 10.1016/j.jplph.2013.04.005

Rouhier, N., Lemaire, S. D., and Jacquot, J. P. (2008). The role of glutathione in photosynthetic organisms: emerging functions for glutaredoxins and glutathionylation. *Annu .Rev. Plant Biol.* 59, 143–166. doi: 10.1146/annurev.arplant.59.032607.092811

Shimaoka, T., Yokota, A., and Miyake, C. (2000). Purification and characterization of chloroplast dehydroascorbate reductase from spinach leaves. *Plant Cell Physiol.* 41, 1110–1118. doi: 10.1093/pcp/pcd035

Shin, S. Y., Kim, I. S., Kim, Y. H., Park, H. M., Lee, J. Y., Kang, H. G., et al. (2008). Scavenging reactive oxygen species by rice dehydroascorbate reductase alleviates oxidative stresses in *Escherichia coli*. *Mol. Cells* 26, 616–620.

Shin, S. Y., Kim, M. H., Kim, Y. H., Park, H. M., and Yoon, H. S. (2013). Co-expression of monodehydroascorbate reductase and dehydroascorbate reductase from *Brassica rapa* effectively confers tolerance to freezing-induced oxidative stress. *Mol. Cells* 36, 304–315. doi: 10.1007/s10059-013-0071-4

Tahara, H., Uchiyama, J., Yoshihara, T., Matsumoto, K., and Ohta, H. (2012). Role of *Slr1045* in environmental stress tolerance and lipid transport in the cyanobacterium *Synechocystis* sp. PCC6803. *Biochim. Biophys. Acta* 1817, 1360–1366. doi: 10.1016/j.bbabio.2012.02.035

Tang, D., Shi, S., Li, D., Hu, C., and Liu, Y. (2007). Physiological and biochemical responses of *Scytonema javanicum* (cyanobacterium) to salt stress. *J. Arid Environ.* 71, 312–322.

Tang, Z. X., and Yang, H. L. (2013). Functional divergence and catalytic properties of dehydroascorbate reductase family proteins from *Populus tomentosa*. *Mol. Biol. Rep.* 40, 5105–5114. doi: 10.1007/s11033-013-2612-5

Thom, R., Cummins, I., Dixon, D. P., Edwards, R., Cole, D. J., and Lapthorn, A. J. (2002). Structure of a tau class glutathione S-transferase from wheat active in herbicide detoxification. *Biochemistry* 41, 7008–7020. doi: 10.1021/bi015964x

Thomas, D. J., Thomas, J. B., Prier, S. D., Nasso, N. E., and Herbert, S. K. (1999). Iron superoxide dismutase protects against chilling damage in the

cyanobacterium *Synechococcus* species PCC7942. *Plant Physiol.* 120, 275–282. doi: 10.1104/pp.120.1.275

Urano, J., Nakagawa, T., Maki, Y., Masumura, T., Tanaka, K., Murata, N., et al. (2000). Molecular cloning and characterization of a rice dehydroascorbate reductase. *FEBS Lett.* 466, 107–111. doi: 10.1016/s0014-5793(99)01768-8

Ushimaru, T., Nakagawa, T., Fujioka, Y., Daicho, K., Naito, M., Yamauchi, Y., et al. (2006). Transgenic *Arabidopsis* plants expressing the rice dehydroascorbate reductase gene are resistant to salt stress. *J. Plant Physiol.* 163, 1179–1184. doi: 10.1016/j.jplph.2005.10.002

Wang, H., and Joseph, J. A. (1999). Quantifying cellular oxidative stress by dichlorofluorescein assay using microplate reader. *Free Radic. Biol. Med.* 27, 612–616. doi: 10.1016/s0891-5849(99)00107-0

Wang, Z., Xiao, Y., Chen, W., Tang, K., and Zhang, L. (2010). Increased vitamin C content accompanied by an enhanced recycling pathway confers oxidative stress tolerance in *Arabidopsis*. *J. Integr. Plant Biol.* 52, 400–409. doi: 10.1111/j.1744-7909.2010.00921.x

Conflict of Interest: The authors declare that the research was conducted in the absence of any commercial or financial relationships that could be construed as a potential conflict of interest.

frontiers in Plant Science

ORIGINAL RESEARCH
published: 05 March 2020
doi: 10.3389/fpls.2020.00242

Blasticidin S Deaminase: A New Efficient Selectable Marker for *Chlamydomonas reinhardtii*

*Félix de Carpentier[1,2†], Jeanne Le Peillet[1†], Nicolas D. Boisset[1,2], Pierre Crozet[1], Stéphane D. Lemaire[1] and Antoine Danon[1]**

[1] Institut de Biologie Physico-Chimique, UMR 8226, CNRS, Sorbonne Université, Paris, France, [2] Université Paris-Saclay, Saint-Aubin, France

Chlamydomonas reinhardtii is a model unicellular organism for basic or biotechnological research, such as the production of high-value molecules or biofuels thanks to its photosynthetic ability. To enable rapid construction and optimization of multiple designs and strains, our team and collaborators have developed a versatile Chlamydomonas Modular Cloning toolkit comprising 119 biobricks. Having the ability to use a wide range of selectable markers is an important benefit for forward and reverse genetics in Chlamydomonas. We report here the development of a new selectable marker based on the resistance to the antibiotic blasticidin S, using the *Bacillus cereus* blasticidin S deaminase (*BSR*) gene. The optimal concentration of blasticidin S for effective selection was determined in both liquid and solid media and tested for multiple laboratory strains. In addition, we have shown that our new selectable marker does not interfere with other common antibiotic resistances: zeocin, hygromycin, kanamycin, paromomycin, and spectinomycin. The blasticidin resistance biobrick has been added to the Chlamydomonas Modular Cloning toolkit and is now available to the entire scientific community.

Keywords: blasticidin, *Chlamydomonas reinhardtii*, antibiotic resistance, selectable marker, synthetic biology, modular cloning, algal biotechnology

OPEN ACCESS

Edited by:
Dimitris Petroutsos, UMR 5168 Laboratoire de Physiologie Cellulaire Vegetale (LPCV), France

Reviewed by:
Xenie Johnson, Commissariat à l'Energie Atomique et aux Energies Alternatives (CEA), France
Véronique Larosa, University of Liège, Belgium
Ryutaro Tokutsu, National Institute for Basic Biology, Japan

***Correspondence:**
Antoine Danon
antoine.danon@ibpc.fr

† These authors have contributed equally to this work

Specialty section:
This article was submitted to Plant Biotechnology, a section of the journal Frontiers in Plant Science

Received: *13 November 2019*
Accepted: *17 February 2020*
Published: *05 March 2020*

Citation:
de Carpentier F, Le Peillet J, Boisset ND, Crozet P, Lemaire SD and Danon A (2020) Blasticidin S Deaminase: A New Efficient Selectable Marker for Chlamydomonas reinhardtii. Front. Plant Sci. 11:242. doi: 10.3389/fpls.2020.00242

INTRODUCTION

Chlamydomonas reinhardtii is a model microalga widely used for basic and biotechnological research such as photosynthesis, cilia/flagella, production of biofuels, or other molecules of interest (Georgianna and Mayfield, 2012; Barahimipour et al., 2016; Salomé and Merchant, 2019). In the last decades Chlamydomonas has been shown to be amenable to powerful genetic approaches including CRISPR-Cas9 gene editing (Jiang et al., 2014; Greiner et al., 2017; Kao and Ng, 2017). The creation of the Chlamydomonas Library Project (CLiP), which contains more than 62,000 mutants covering roughly 83% of Chlamydomonas genes (Li et al., 2019), has also greatly contributed to the development of Chlamydomonas reverse genetics. A wide range of molecular tools for engineering of the nuclear genome are also available in Chlamydomonas, most of which have been grouped in a Modular Cloning toolkit (Chlamy MoClo toolkit). This collection contains 119 biobricks (promoters, terminators, reporter genes, selectable markers, targeting peptides, antibiotic resistance genes, riboswitch, miRNA backbone, etc.), which can be easily assembled through Golden Gate cloning (Crozet et al., 2018). Most applications related to the manipulation

of nuclear gene expression require transformation of Chlamydomonas cells followed by selection of transformants on plates using a selectable marker, which is in most cases an antibiotic resistance gene enabling selection on a medium containing the appropriate antibiotic. In the case of multiple consecutive transformations several selectable markers are required. Therefore, it is essential for advanced genetic engineering to have as many selectable markers as possible. At the moment, six antibiotic resistances are commonly used in Chlamydomonas as selectable markers: zeocin (Stevens et al., 1996), hygromycin (Berthold et al., 2002), kanamycin (Barahimipour et al., 2016), paromomycin (Sizova et al., 2001), sulfadiazine (Tabatabaei et al., 2019), and spectinomycin (Meslet-Cladière and Vallon, 2011).

Blasticidin S (hereafter referred to as "blasticidin") is an antibiotic that inhibits cytosolic protein synthesis by blocking ribosomal translation termination (Svidritskiy et al., 2013). Blasticidin S deaminase (BSR) detoxifies blasticidin by catalyzing its deamination (Seto et al., 1966; Endo et al., 1987). The *BSR* gene has been successfully used as a selectable marker in mammals (Izumi et al., 1991), plants (Kamakura et al., 1990), yeasts (Kimura et al., 1994; Fukuda and Kizaki, 1999), and algae, including the diatom *Phaeodactylum tricornutum* (Buck et al., 2018) and the Chlamydomonas-related volvocine alga *Volvox carteri* (Ortega-Escalante et al., 2018).

We report here that blasticidin can be used as an antibiotic in Chlamydomonas, for all six laboratory strains tested. We show that BSR is functional in Chlamydomonas and can be used as a selectable marker, without conferring resistance to the other commonly used antibiotics. We also show that BSR can be used in combination with all other antibiotic resistance genes available in Chlamydomonas.

MATERIALS AND METHODS

Strains, Media, and Growth Conditions

If not otherwise specified, the reference strain used in the present study is CC-4533 (CMJ030), the CLiP library recipient strain used to generate the insertional mutants (Li et al., 2019). We also used other common laboratory strains CC-4051 (4A+) (Kim et al., 2005), CC-400 (cw15) (Roy Davies, 1972), CC-4425 (D66) (Schnell and Lefebvre, 1993), UVM4 (Neupert et al., 2009), and CC-124 (137c) (Pröschold et al., 2005). Chlamydomonas cells were grown on agar plates or liquid medium, using Tris-acetate-phosphate (TAP) medium (Gorman and Levine, 1965) at 25°C, under continuous light (40–60 μmol photon·m^{-2}·s^{-1}) and shaking (130 rpm). Growth analysis were performed in the Algem® labscale double photobioreactor systems (Algenuity, Stewartby, United Kingdom) under continuous light (200 μmol photons·m^{-2}·s^{-1}) and 120 rpm agitation in TAP or high salt medium (HSM) (Sueoka, 1960), with bubbling air. The absorbance at 740 nm was recorded every 10 min using the built-in sensor. The maximal growth rate was determined as the maximal slope of the growth curve (Δabs/Δtime). Linearity of the growth curve was estimated through linear regression every 200 min over a period of 13 h for TAP or 300 min over a period of 40 h for HSM condition. The slopes of these linear regressions were selected only for regressions displaying an $R^2 < 99.5\%$. Finally, the maximal slope was chosen as the maximal growth rate (**Supplementary Figure S2B**). Antibiotics used were blasticidin S (Sigma-Aldrich: SBR00022), zeocin (Invitrogen: R25005), hygromycin B (Sigma-Aldrich: H9773), kanamycin (Sigma-Aldrich: K1377), paromomycin (Sigma-Aldrich: P8692), or spectinomycin (Sigma-Aldrich: S4014). Chlamydomonas multi-well plates and Petri dishes were scanned using a Perfection V800 scanner (Epson).

Cell Death Quantification

Dead cells were detected using Evans blue (Sigma-Aldrich: E2129) at a final concentration of 0.2% w/v. Dead cells appear in blue whereas living cells that are impermeable to Evans blue remain green (Gaff and Okong'o-Ogola, 1971). Cells were observed with a microscope (Olympus BX43, Tokyo, Japan). For each sample multiple microscopic fields were analyzed and Evans blue-positive cells scored. For each value the percentage of dead cells was calculated on a minimum of 100 individuals.

Plasmid Construction

Protein and nucleic acid designs were performed *in silico* on Serial Cloner 2.6.1 software. *Bacillus cereus* BSR protein sequence (NCBI accession number: WP_076871832.1) was reverse translated using Chlamydomonas nuclear genome codon usage table[1]. The resulting *BSR* coding sequence was domesticated by removing *Bbs*I restriction sites, designed for the position B3–B5 of the common Plant MoClo syntax (Patron et al., 2015), synthetized (Twist Bioscience), and cloned by Golden Gate reaction with *Bsa*I-HFv2 (New England Biolabs) in pICH41308 (Weber et al., 2011) yielding plasmid pCM0-120, numbered according to the Chlamydomonas MoClo toolkit nomenclature (Crozet et al., 2018). Two other parts from the toolkit were used to build the *BSR* module (pCM1-029), the promoter $P_{A/R}$ coupled to the 5′UTR of RBCS2 (pCM0-020) and the 3′UTR of RBCS2 coupled to terminator T_{RBCS2} (pCM0-115) (Schroda et al., 2002; Crozet et al., 2018). The other antibiotic resistance genes were built using these same regulatory sequences and the coding sequence (CDS) from pCM0-077 (zeocin), pCM0-073 (hygromycin), pCM0-074 (paromomycin), pCM0-075 (kanamycin) and pCM0-076 (spectinomycin) generating the plasmids pCM1-030 (zeocin), pCM1-031 (hygromycin), pCM1-032 (kanamycin), pCM1-027 (paromomycin), and pCM1-033 (spectinomycin), respectively. All plasmid sequences are available in **Supplementary Files S1–S7**.

Chlamydomonas Transformation

Transformations were performed as previously described (Crozet et al., 2018). Briefly, Chlamydomonas cells were grown in TAP to early exponential phase (1–2 × 10^6 cells/mL), concentrated 100 times in TAP + 60 mM sucrose. After incubation of 250 μL of cells with DNA (55 fmol of purified resistance module excised with *Bbs*I-HF; New England Biolabs) at 4°C for 20 min, they were electroporated (2000 V/cm, 25 μF, no shunt resistance)

[1] www.kazusa.or.jp/codon/cgi-bin/showcodon.cgi?species=3055

and incubated for 16–20 h in 10 mL of TAP + 60 mM sucrose prior to be plated on TAP-agar complemented with appropriate antibiotic(s). Transformants were selected on TAP-agar medium containing blasticidin S (50 mg/L, unless otherwise specified), zeocin (15 mg/L), hygromycin B (20 mg/L), kanamycin (50 mg/L), paromomycin (20 mg/L), and/or spectinomycin (100 mg/L). Plates and transformants were analyzed after 5–7 days of growth in continuous light (50 μmol photon m^{-2} s^{-1}) at 25°C.

Insert Detection

Cells were pelleted (5 min, 2500 × *g*, room temperature) and lysed in 400 μL of extraction buffer (200 mM Tris-HCl pH 7.5; 200 mM NaCl; 25 mM EDTA; 0.5% SDS) for 10 min at 37°C under agitation (1400 rpm). After centrifugation (3 min, 17,000 × *g*, room temperature), the supernatant was harvested and the genomic DNA was precipitated with one volume of isopropanol for 10 min at room temperature, washed with 70% ethanol, dried and resuspended in water. PCR was performed using the Quick-Load® *Taq* 2× Master Mix (New England Biolabs) according to the manufacturer recommendations with the primers BSR.5 (5′-GCTGTACGAGGACAACAAGC-3′), TRBCS2.3 (5′-ACGGAGGATCGTTACAACC-3′), CBLP.5 (5′-GACGTCATCCACTGCCTGTG-3′), and CBLP.3 (5′-CGACGCATCCTCAACACACC-3′).

RESULTS

Chlamydomonas Is Sensitive to Blasticidin

To test the sensitivity of Chlamydomonas to blasticidin, the cells were grown in the presence of increasing blasticidin concentrations (25, 50, or 75 mg/L) in both solid and liquid cultures. Blasticidin was very effective to kill Chlamydomonas cells and the minimum efficient concentration was 50 mg/L in both conditions (**Figure 1A**). Many reference strains are used within the community and they present an important genetic diversity and substantial phenotypic differences (Gallaher et al., 2015). Compared to the reference strain of this study (CC-4533), some strain specific phenotypes, such as the absence of the cell wall, could alter blasticidin resistance. To assess whether this genetic diversity among common reference strains affects their sensitivity to blasticidin, CC-4051 (4A+), CC-400 (cw15), CC-4425 (D66+), UVM4, and CC-124 (137c) were cultivated on a solid medium supplemented or not with blasticidin (50 mg/L). In all cases, none of the strains survived in the presence of blasticidin, regardless of the initial number of cells tested (**Figure 1B**).

Blasticidin S Deaminase Can Be Used as a Selectable Marker in Chlamydomonas

To test whether the *BSR* module could be used as a selectable marker in Chlamydomonas, we engineered *B. cereus BSR* coding sequence to fit the optimal codon bias of Chlamydomonas nuclear genome. This has been already shown to improve transgene expression efficiency, including selection markers (Barahimipour et al., 2015, 2016). The engineered *BSR* coding sequence was then domesticated by removing *Bbs*I and *Bsa*I recognition motif and adding appropriate fusion sites of the Plant MoClo syntax (Patron et al., 2015). It was finally assembled with the parts $P_{A/R}$ (the hybrid promoter of *HSP70A* coupled to the 5′UTR of *RBCS2*) and T_{RBCS2} (coupling the 3′UTR and terminator of *RBCS2*) to form a functional module. $P_{A/R}$ is a chimeric constitutive promoter made up of *HSP70A* and *RBCS2* promoters that was proven to be very efficient in Chlamydomonas by significantly reducing gene silencing (Schroda et al., 2002). We also chose this promoter/terminator combination because it allows successful expression of the same *BSR* gene in Volvox (Ortega-Escalante et al., 2018). The resulting construct pCM1-029 (pCM stands for plasmid Chlamydomonas MoClo) is represented in **Figure 2A** using the MoClo nomenclature (Crozet et al., 2018). pCM0-120 and pCM1-029 plasmid sequences are available in **Supplementary Files S1, S2**, respectively. Cells transformed with pCM1-029 or an empty vector were incubated on plates containing blasticidin. Transformants appeared only when the cells were transformed with pCM1-029 (Blasticidin resistant cells are hereafter referred to as "Blast^R"), as shown in **Figure 2B**, indicating that *BSR* can be used as a selectable marker in Chlamydomonas. The insertion of the *BSR* module was confirmed by PCR in four independent Blast^R strains (**Supplementary Figure S1**).

To precisely evaluate the effect of blasticidin on the mortality of wild-type and Blast^R cells, we used Evans blue as a death marker (Gaff and Okong'o-Ogola, 1971). To avoid the heterogeneity that comes from the position of the transgene insertion locus, dozens of Blast^R colonies were collected from a Petri dish and then mixed in liquid culture (Blast^R culture). Wild-type and Blast^R cultures were grown in a 24-well plate with or without blasticidin, and the percentage of dead cells was evaluated several days after treatment. In the wild-type strain treated with blasticidin, the percentage of dead cells increased after 3 days and all the cells died after 5 days, while no significant levels of death was detected for Blast^R and untreated cells (**Figure 2C**). To assess a potential detrimental effect of BSR on Chlamydomonas, wild-type and Blast^R growth were quantified in a photobioreactor, in both mixotrophic (TAP) and autotrophic (HSM) conditions. No differences in the growth rate were observed suggesting that BSR does not affect growth or photosynthesis (**Supplementary Figure S2**).

Blasticidin Can Be Used in Combination With Other Antibiotics

To test the possible interactions of blasticidin with the other most commonly used selectable markers in Chlamydomonas, we first generated strains resistant to these antibiotics by transformation of wild-type cells with plasmids containing modules conferring resistance to zeocin (pCM1-030), hygromycin (pCM1-031), kanamycin (pCM1-032), paromomycin (pCM1-027), and spectinomycin (pCM1-033) under the control of the same regulatory sequences used for *BSR* in pCM1-029. Transformants were selected on plates containing the appropriate antibiotic

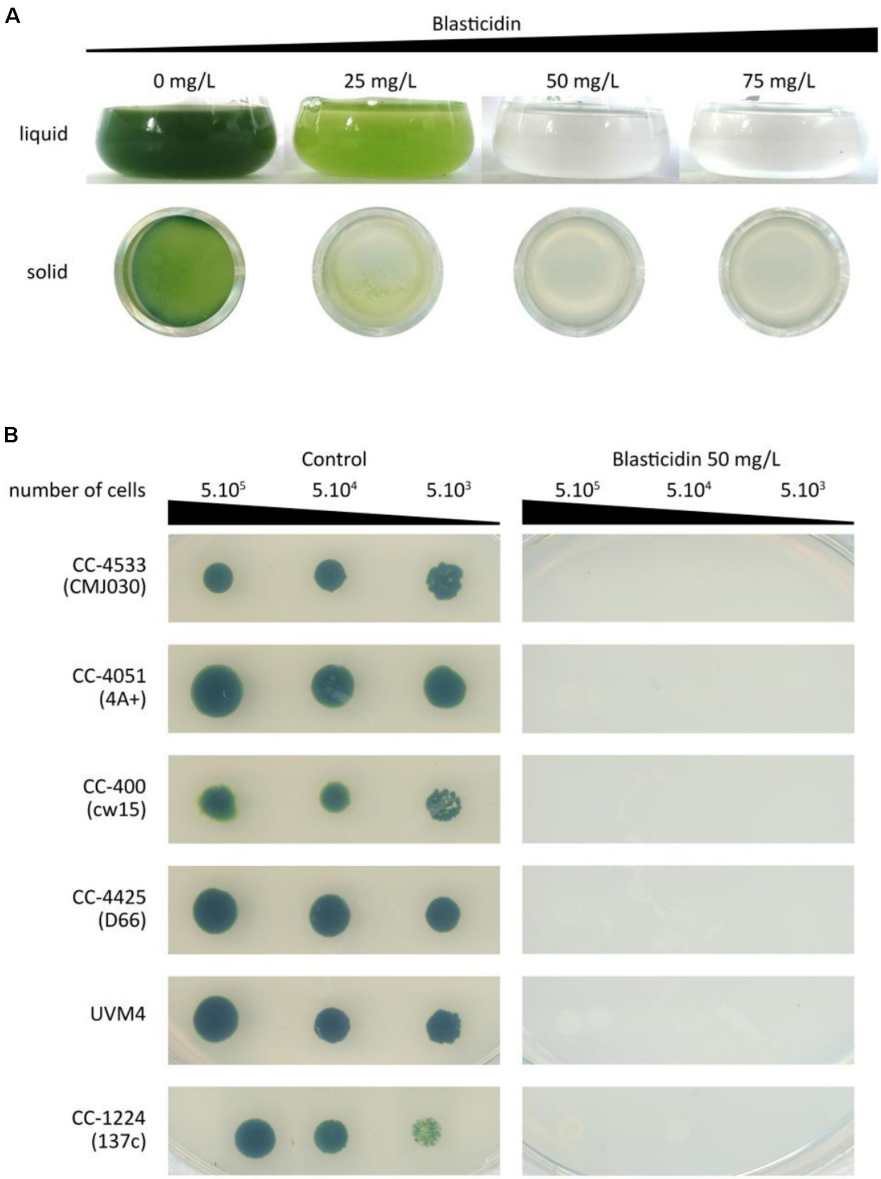

FIGURE 1 | Sensitivity of Chlamydomonas to blasticidin. **(A)** Chlamydomonas CC-4533 (CMJ030) was grown with increasing concentrations of blasticidin: 25, 50, or 75 mg/L, in both liquid and 24-well agar plates. For both liquid and solid media, cultures were photographed after 3 days of growth. **(B)** Spot tests were performed for six standard laboratory strains with or without blasticidin (50 mg/L). The results shown are representative of three biological replicates.

and pooled to take into account position effect, as for Blast^R culture. These cultures were called Zeo^R, Hygro^R, Kana^R, Paro^R, and Spec^R. The wild-type strain and the six antibiotic resistant cultures were cultivated in 96-well plates until exponential phase (5×10^6 cells/mL) prior to treatment with the different antibiotics. Five days after the addition of antibiotics, only the cells carrying the corresponding resistance gene survived the treatment, and importantly, only the Blast^R culture had survived upon blasticidin treatment (**Figure 3A**). It is to be noticed that Kana^R strains are also resistant to paromomycin (**Figure 3A**), as previously reported (Barahimipour et al., 2016).

If the resistance modules tested display no cross reactivity to one another, they can be combined to allow double selection. To use the *BSR* module and blasticidin in combination with another selectable marker, there must then be no interference between the different antibiotics and resistance modules. To verify possible interference, a single Blast^R strain was transformed with either pCM1-030 (zeocin resistance), pCM1-031 (hygromycin resistance), pCM1-032 (kanamycin resistance), pCM1-027 (paromomycin resistance), or pCM1-033 (spectinomycin resistance) (**Figure 3B**). Transformants were selected on plates containing both blasticidin and the appropriate antibiotic. For each combination tested, transformants resistant

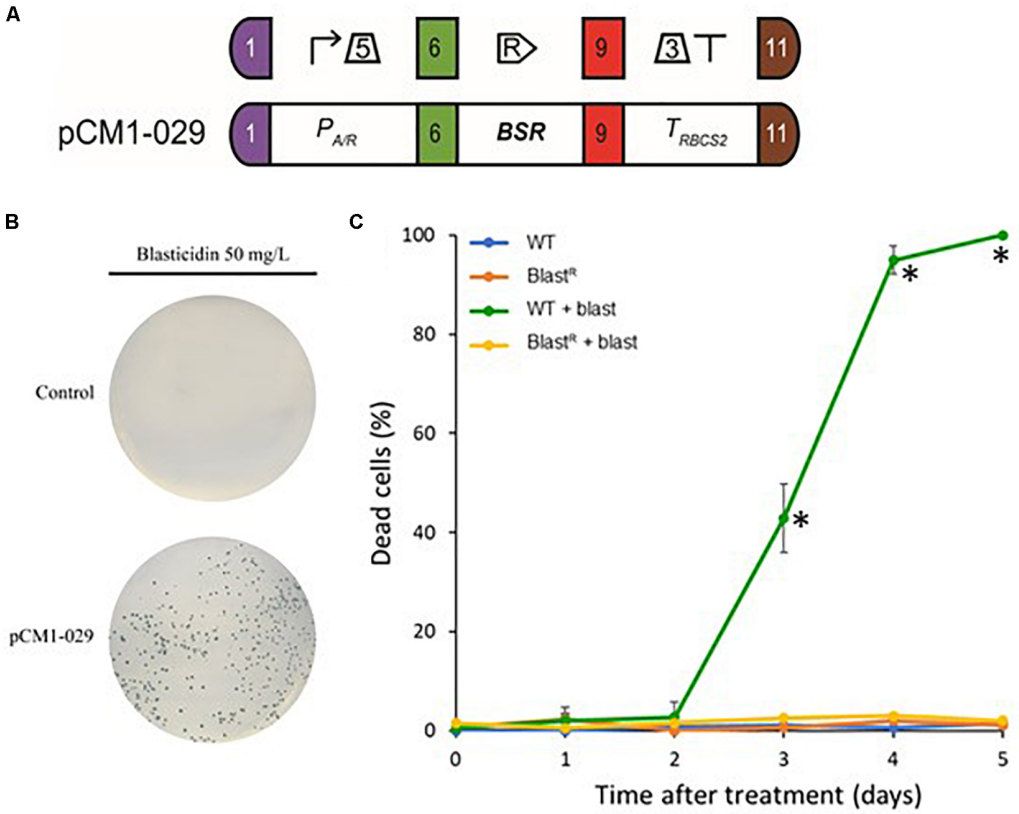

FIGURE 2 | Blasticidin S deaminase expression in Chlamydomonas. **(A)** The blasticidin resistance module pCM1-029 is built from a constitutive promoter ($P_{A/R}$ + 5′UTR of RBCS2), the BSR coding sequence and a terminator (3′UTR of RBCS2 + T_{RBCS2}) and was assembled using Golden Gate cloning. The numbers 1, 6, 9, and 11 stand for the standard fusion sites used for cloning (Crozet et al., 2018). SBOL2.0 visual syntax is shown above the module (Roehner et al., 2016). **(B)** CC-4533 cells were transformed with pCM1-029 or an empty vector (pICH47742) (Weber et al., 2011) and plated on TAP-agar supplemented with blasticidin (50 mg/L). Results are representative of three biological replicates. **(C)** The percentage of dead cells was evaluated using Evans blue in wild-type and Blast^R cultures with or without blasticidin, several days after treatment. Values represent the means and standard deviations of three independent experiments, symbol (*) shows the samples found to be significantly different doing an ANOVA analysis for each time points ($p < 0.001$).

to both antibiotics could be obtained (**Figure 3B**), indicating that no interference exists between the selectable markers tested.

DISCUSSION

Here we report the development of a new selectable marker for *C. reinhardtii*. Our data show that using blasticidin at a concentration of 50 mg/L ensures proper selection for all common laboratory strains of Chlamydomonas (**Figure 2C**). This concentration is slightly higher than the efficient concentration reported for *V. carteri* (Ortega-Escalante et al., 2018) or diatoms (Buck et al., 2018), but remains comparable with other antibiotics used in Chlamydomonas (Crozet et al., 2018).

We successfully engineered *BSR* coding sequence to adapt it to Chlamydomonas and no addition of intron was necessary for efficient expression, contrary to what was reported for *V. carteri* (Ortega-Escalante et al., 2018). Now that we have developed the blasticidin resistance module, seven antibiotic-based selectable markers are available for Chlamydomonas. This new tool can become important for advanced synthetic biology strategies requiring successive transformations of the same strain in combination with new engineering tools including the CLiP library (Li et al., 2019), the CRISPR/Cas technology (Jiang et al., 2014; Greiner et al., 2017; Kao and Ng, 2017) and the MoClo toolkit (Crozet et al., 2018). It is also important to increase the number of selectable markers available because the use of certain antibiotics should be taken with care. For instance zeocin is not always recommended since it can potentially cause DNA damages (Chankova et al., 2007; Čížková et al., 2019) and subsequent unwanted mutations. The kanamycin selectable marker *NPTII* is also conferring resistance to paromomycin (Barahimipour et al., 2015; **Figure 3A**) which makes it impossible to use in CLiP strains that are paromomycin resistant (Li et al., 2019). We show here that it is possible to use *BSR* and blasticidin in combination with all the other commonly used selectable markers in Chlamydomonas. *BSR* gene has been integrated as a new biobrick into the Chlamydomonas MoClo toolkit, and is now available to the entire community through the Chlamydomonas Resource Center[2].

[2]www.chlamycollection.org/

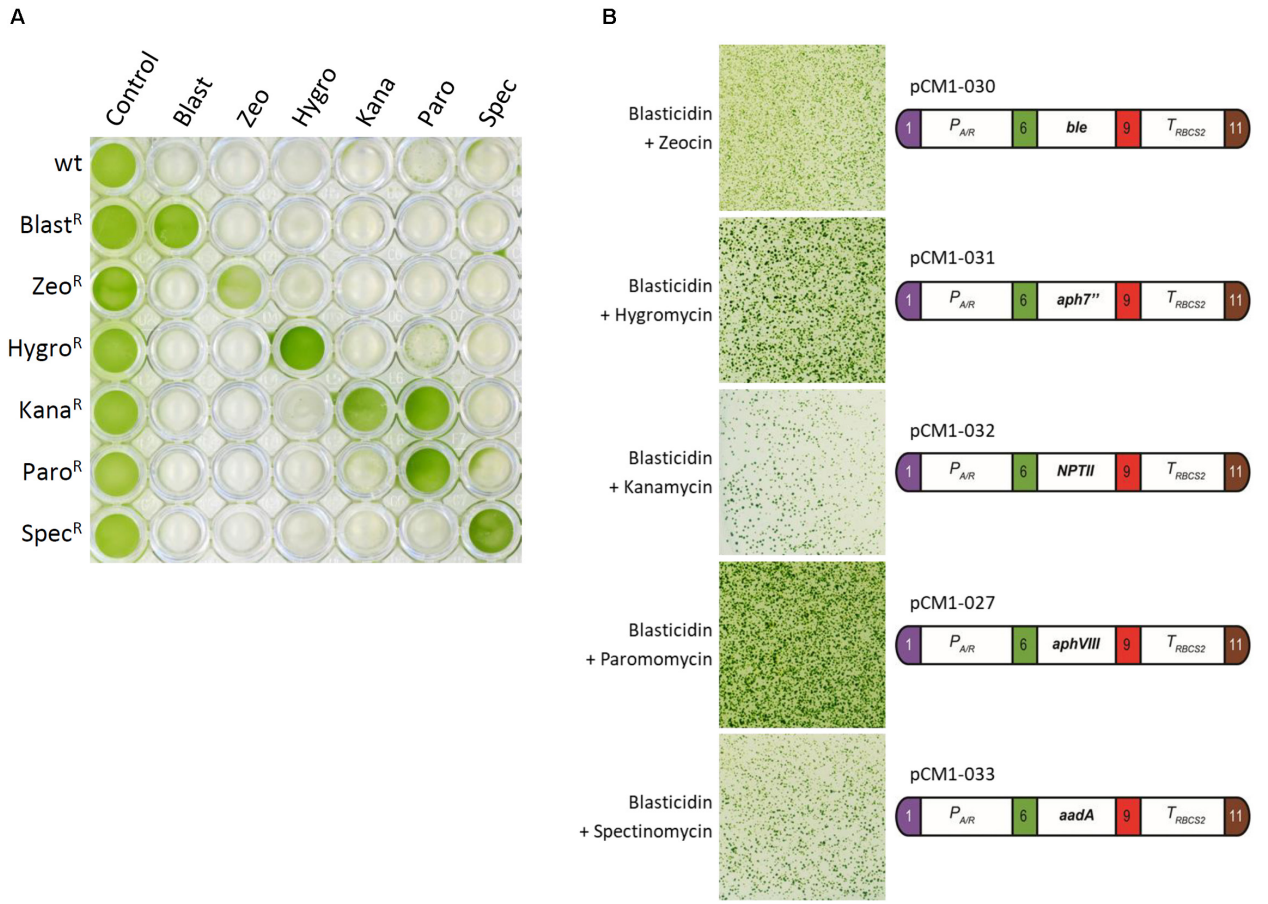

FIGURE 3 | Cross reactivity test. **(A)** Liquid cultures in exponential phase of wild-type strain and Zeo^R, Hygro^R, Kana^R, Paro^R, and Spec^R cultures were placed in a 96-well plate and treated with blasticidin (Blast, 50 mg/L), zeocin (Zeo, 15 mg/L), hygromycin B (Hygro, 20 mg/L), kanamycin (Kana, 50 mg/L), paromomycin (Paro, 20 mg/L), and spectinomycin (Spec, 100 mg/L) for 5 days. **(B)** A blasticidin resistant strain carrying pCM1-029 was independently transformed with the resistance modules to zeocin (pCM1-030), hygromycin (pCM1-031), kanamycin (pCM1-032), paromomycin (pCM1-027), and spectinomycin (pCM1-033). The numbers 1, 6, 9, and 11 stand for the standard fusion sites used for cloning (Crozet et al., 2018). Transformants were selected on plate containing both blasticidin and the appropriate antibiotic. The results showed are representative of three biological replicates. The full experiment with the different controls is available in **Supplementary Figure S3**.

DATA AVAILABILITY STATEMENT

All datasets generated for this study are included in the article/**Supplementary Material**.

AUTHOR CONTRIBUTIONS

FC, JL, PC, SL, and AD designed the study and analyzed the data. FC, JL, NB, PC, SL, and AD wrote the manuscript. FC, JL, NB, and AD performed the experiments.

FUNDING

This work was supported in part by the CNRS, Sorbonne Université, and Université Paris-Saclay, by Agence Nationale de la Recherche Grant 17-CE05-0001 CalvinDesign and by LABEX DYNAMO ANR-LABX-011.

ACKNOWLEDGMENTS

We thank Sandrine Bujaldon for providing the *Chlamydomonas reinhardtii* strains CC-4051, CC-400, and CC-124; Kevin Sarkissian for his help in the cloning; and Cyrielle Durand, Théo Le Moigne, Dr. Christophe Marchand, and Dr. Julien Henri for stimulating discussions and suggestions.

SUPPLEMENTARY MATERIAL

The Supplementary Material for this article can be found online at: https://www.frontiersin.org/articles/10.3389/fpls.2020.00242/full#supplementary-material

FIGURE S1 | Detection of the *BSR* module. pCM1-029 plasmid and the genomic DNA of the wild type (CC-4533) and four independent transformants Blast^R were used to amplify by PCR a fragment of the *BSR* resistance module. A product at the expected size (546 bp) was amplified only for pCM1-029 (positive control) and

the Blast^R transformants. Amplification of CBLP (Cre06.g278222) was used as a positive control for the experiment.

FIGURE S2 | Growth of wild-type (CC-4533) and Blast^R strains in a controlled photobioreactor. **(A)** Measurement of growth as detected by absorbance at 740 nm every 10 min, in TAP (mixotrophy) and HSM medium (autotrophy), light was set to 200 μmol photons·m^{-2}·s^{-1} with temperature and shaking set at 25°C and 120 rpm, respectively. **(B)** Quantification of the average growth rate of wild-type and Blast^R cells, corresponding to the growth curves shown in Graph **(A)**. Error bars represent the standard error to the mean of two biological replicates.

FIGURE S3 | Transformation of a blasticidin resistant strain with zeocin, hygromycin, kanamycin, paromomycin and spectinomycin resistance plasmids. A blasticidin resistant strain (Blast^R) carrying pCM1-029 was independently transformed with the resistance modules to zeocin (pCM1-030), hygromycin (pCM1-031), kanamycin (pCM1-032), paromomycin (pCM1-027), and spectinomycin (pCM1-033) or an empty vector (pICH50881). The numbers 1, 6, 9, and 11 stand for the standard fusion sites used for cloning (Crozet et al., 2018). Blast^R transformed cells were selected on plate containing both blasticidin and the appropriate antibiotic. CC-4533 was also transformed with the same five resistance modules or the empty vector and selected on the corresponding antibiotic with or without addition of blasticidin. The results showed are representative of three biological replicates.

FILE S1 | Annotated sequence of pCM0-120, the level 0 plasmid containing *BSR* coding sequence engineered for Chlamydomonas nuclear genome and designed for the position B3–B5 of the Chlamydomonas MoClo toolkit (Crozet et al., 2018).

FILE S2 | Annotated sequence of pCM1-029, the level 1 plasmid made up of the promoter AR ($P_{A/R}$ + 5′UTR of RBCS2), *BSR* coding sequence and the terminator of RBCS2 (3′UTR of RBCS2 + T_{RBCS2}) conferring blasticidin resistance in Chlamydomonas (Crozet et al., 2018).

FILE S3 | Annotated sequence of pCM1-027, the level 1 plasmid made up of the promoter AR ($P_{A/R}$ + 5′UTR of RBCS2), *aphVIII* coding sequence and the terminator of RBCS2 (3′UTR of RBCS2 + T_{RBCS2}) conferring paromomycin resistance in Chlamydomonas (Sizova et al., 2001; Crozet et al., 2018).

FILE S4 | Annotated sequence of pCM1-030, the level 1 plasmid made up of the promoter AR ($P_{A/R}$ + 5′UTR of RBCS2), *Ble* coding sequence and the terminator RBCS2 (3′UTR of RBCS2 + T_{RBCS2}) conferring zeocin resistance in Chlamydomonas (Stevens et al., 1996; Crozet et al., 2018).

FILE S5 | Annotated sequence of pCM1-031, the level 1 plasmid made up of the promoter AR ($P_{A/R}$ + 5′UTR of RBCS2), *aph7″* coding sequence and the terminator RBCS2 (3′UTR of RBCS2 + T_{RBCS2}) conferring hygromycin resistance in Chlamydomonas (Berthold et al., 2002; Crozet et al., 2018).

FILE S6 | Annotated sequence of pCM1-032, the level 1 plasmid made up of the promoter AR ($P_{A/R}$ + 5′UTR of RBCS2), *NPTII* coding sequence and the terminator RBCS2 (3′UTR of RBCS2 + T_{RBCS2}) conferring kanamycin resistance in Chlamydomonas (Barahimipour et al., 2016; Crozet et al., 2018).

FILE S7 | Annotated sequence of pCM1-029, the level 1 plasmid made up of the promoter AR ($P_{A/R}$ + 5′UTR of RBCS2), *aadA* coding sequence and the terminator RBCS2 (3′UTR of RBCS2 + T_{RBCS2}) conferring spectinomycin resistance in Chlamydomonas (Meslet-Cladière and Vallon, 2011; Crozet et al., 2018).

REFERENCES

Barahimipour, R., Neupert, J., and Bock, R. (2016). Efficient expression of nuclear transgenes in the green alga *Chlamydomonas*: synthesis of an HIV antigen and development of a new selectable marker. *Plant Mol. Biol.* 90, 403–418. doi: 10.1007/s11103-015-0425-8

Barahimipour, R., Strenkert, D., Neupert, J., Schroda, M., Merchant, S. S., and Bock, R. (2015). Dissecting the contributions of GC content and codon usage to gene expression in the model alga *Chlamydomonas reinhardtii*. *Plant J.* 84, 704–717. doi: 10.1111/tpj.13033

Berthold, P., Schmitt, R., and Mages, W. (2002). An engineered *Streptomyces hygroscopicus aph 7* Gene Mediates dominant resistance against hygromycin B in *Chlamydomonas reinhardtii*. *Protist* 153, 401–412. doi: 10.1078/14344610260450136

Buck, J. M., Río Bártulos, C., Gruber, A., and Kroth, P. G. (2018). Blasticidin-S deaminase, a new selection marker for genetic transformation of the diatom *Phaeodactylum tricornutum*. *PeerJ* 6:e5884. doi: 10.7717/peerj.5884

Chankova, S. G., Dimova, E., Dimitrova, M., and Bryant, P. E. (2007). Induction of DNA double-strand breaks by zeocin in *Chlamydomonas reinhardtii* and the role of increased DNA double-strand breaks rejoining in the formation of an adaptive response. *Radiat. Environ. Biophys.* 46, 409–416. doi: 10.1007/s00411-007-0123-2

Čížková, M., Slavková, M., Vítová, M., Zachleder, V., and Bišová, K. (2019). Response of the green alga *Chlamydomonas reinhardtii* to the DNA damaging agent zeocin. *Cells* 8:E735. doi: 10.3390/cells8070735

Crozet, P., Navarro, F. J., Willmund, F., Mehrshahi, P., Bakowski, K., Lauersen, K. J., et al. (2018). Birth of a photosynthetic chassis: a MoClo toolkit enabling synthetic biology in the microalga *Chlamydomonas reinhardtii*. *ACS Synth. Biol.* 7, 2074–2086. doi: 10.1021/acssynbio.8b00251

Endo, T., Furuta, K., Kaneko, A., Katsuki, T., Kobayashi, K., Azuma, A., et al. (1987). Inactivation of blasticidin S by *Bacillus cereus*. I. inactivation mechanism. *J. Antibiot.* 40, 1791–1793. doi: 10.7164/antibiotics.40.1791

Fukuda, H., and Kizaki, Y. (1999). A new transformation system of *Saccharomyces cerevisiae* with blasticidin S deaminase gene. *Biotechnol. Lett.* 21, 969–971. doi: 10.1023/A:1005613206138

Gaff, D. F., and Okong'o-Ogola, O. (1971). The Use of non-permeating pigments for testing the survival of cells. *J. Exp. Bot.* 22, 756–758. doi: 10.1093/jxb/22.3.756

Gallaher, S. D., Fitz-Gibbon, S. T., Glaesener, A. G., Pellegrini, M., and Merchant, S. S. (2015). Chlamydomonas genome resource for laboratory strains reveals a mosaic of sequence variation, identifies true strain histories, and enables strain-specific studies. *Plant Cell* 27, 2335–2352. doi: 10.1105/tpc.15.00508

Georgianna, D. R., and Mayfield, S. P. (2012). Exploiting diversity and synthetic biology for the production of algal biofuels. *Nature* 488, 329–335. doi: 10.1038/nature11479

Gorman, D. S., and Levine, R. P. (1965). Cytochrome f and plastocyanin: their sequence in the photosynthetic electron transport chain of *Chlamydomonas reinhardi*. *Proc. Natl. Acad. Sci. U.S.A.* 54, 1665–1669. doi: 10.1073/pnas.54.6.1665

Greiner, A., Kelterborn, S., Evers, H., Kreimer, G., Sizova, I., and Hegemann, P. (2017). Targeting of photoreceptor genes in *Chlamydomonas reinhardtii* via zinc-finger nucleases and CRISPR/Cas9. *Plant Cell* 29, 2498–2518. doi: 10.1105/tpc.17.00659

Izumi, M., Miyazawa, H., Kamakura, T., Yamaguchi, I., Endo, T., and Hanaoka, F. (1991). Blasticidin S-resistance gene (*bsr*): a novel selectable marker for mammalian cells. *Exp. Cell Res.* 197, 229–233. doi: 10.1016/0014-4827(91)90427-V

Jiang, W., Brueggeman, A. J., Horken, K. M., Plucinak, T. M., and Weeks, D. P. (2014). Successful transient expression of Cas9 and Single Guide RNA Genes in *Chlamydomonas reinhardtii*. *Eukaryot Cell* 13, 1465–1469. doi: 10.1128/EC.00213-14

Kamakura, T., Yoneyama, K., and Yamaguchi, I. (1990). Expression of the blasticidin S deaminase gene (*bsr*) in tobacco: fungicide tolerance and a new selective marker for transgenic plants. *Mol. Gen. Genet.* 223, 332–334. doi: 10.1007/bf00265072

Kao, P.-H., and Ng, I.-S. (2017). CRISPRi mediated phosphoenolpyruvate carboxylase regulation to enhance the production of lipid in *Chlamydomonas reinhardtii*. *Bioresour. Technol.* 245, 1527–1537. doi: 10.1016/j.biortech.2017.04.111

Kim, K.-S., Feild, E., King, N., Yaoi, T., Kustu, S., and Inwood, W. (2005). Spontaneous mutations in the ammonium transport gene AMT4 of *Chlamydomonas reinhardtii*. *Genetics* 170, 631–644. doi: 10.1534/genetics.105.041574

Kimura, M., Kamakura, T., Zhou Tao, Q., Kaneko, I., and Yamaguchi, I. (1994). Cloning of the blasticidin S deaminase gene (*BSD*) from *Aspergillus terreus* and its use as a selectable marker for *Schizosaccharomyces pombe*

and *Pyricularia oryzae*. *Mol. Gen. Genet.* 242, 121–129. doi: 10.1007/BF0039 1004

Li, X., Patena, W., Fauser, F., Jinkerson, R. E., Saroussi, S., Meyer, M. T., et al. (2019). A genome-wide algal mutant library and functional screen identifies genes required for eukaryotic photosynthesis. *Nat. Genet.* 51, 627–635. doi: 10.1038/s41588-019-0370-376

Meslet-Cladière, L., and Vallon, O. (2011). Novel shuttle markers for nuclear transformation of the green alga *Chlamydomonas reinhardtii*. *Eukaryotic Cell* 10, 1670–1678. doi: 10.1128/EC.05043-11

Neupert, J., Karcher, D., and Bock, R. (2009). Generation of *Chlamydomonas strains* that efficiently express nuclear transgenes. *Plant J.* 57, 1140–1150. doi: 10.1111/j.1365-313X.2008.03746.x

Ortega-Escalante, J. A., Kwok, O., and Miller, S. M. (2018). New Selectable Markers for *Volvox carteri* Transformation. *Protist* 170, 52–63. doi: 10.1016/j.protis. 2018.11.002

Patron, N. J., Orzaez, D., Marillonnet, S., Warzecha, H., Matthewman, C., Youles, M., et al. (2015). Standards for plant synthetic biology: a common syntax for exchange of DNA parts. *New Phytol.* 208, 13–19. doi: 10.1111/nph.13532

Pröschold, T., Harris, E. H., and Coleman, A. W. (2005). Portrait of a species: *Chlamydomonas reinhardtii*. *Genetics* 170, 1601–1610. doi: 10.1534/genetics. 105.044503

Roehner, N., Beal, J., Clancy, K., Bartley, B., Misirli, G., Grünberg, R., et al. (2016). Sharing structure and function in biological design with SBOL 2.0. *ACS Synth. Biol.* 5, 498–506. doi: 10.1021/acssynbio.5b00215

Roy Davies, D. (1972). Cell wall organisation in *Chlamydomonas reinhardi*. *Mol. Gen. Genet.* 115, 334–348. doi: 10.1007/BF00333172

Salomé, P. A., and Merchant, S. S. (2019). A series of fortunate events: introducing Chlamydomonas as a reference organism. *Plant Cell* 31, 1682–1707. doi: 10. 1105/tpc.18.00952

Schnell, R. A., and Lefebvre, P. A. (1993). Isolation of the *Chlamydomonas* regulatory gene NIT2 by transposon tagging. *Genetics* 134, 737–747.

Schroda, M., Beck, C. F., and Vallon, O. (2002). Sequence elements within an HSP70 promoter counteract transcriptional transgene silencing in *Chlamydomonas*. *Plant J.* 31, 445–455. doi: 10.1046/j.1365-313X.2002.01371.x

Seto, H., Ôtake, N., and Yonehara, H. (1966). Biological transformation of Blasticidin S by *Aspergillus fumigatus* sp. *Agric. Biol. Chem.* 30, 877–886. doi: 10.1080/00021369.1966.10858693

Sizova, I., Fuhrmann, M., and Hegemann, P. (2001). A *Streptomyces rimosus aphVIII* gene coding for a new type phosphotransferase provides stable antibiotic resistance to *Chlamydomonas reinhardtii*. *Gene* 277, 221–229. doi: 10.1016/s0378-1119(01)00616-3

Stevens, D. R., Purton, S., and Rochaix, J.-D. (1996). The bacterial phleomycin resistance gene *ble* as a dominant selectable marker in *Chlamydomonas*. *Mol. Gen. Genet.* 251, 23–30. doi: 10.1007/BF02174340

Sueoka, N. (1960). Mitotic replication of deoxyribonucleic acid in *Chlamydomonas Reinhardi*. *Proc. Natl. Acad. Sci. U.S.A.* 46, 83–91. doi: 10.1073/pnas.46.1.83

Svidritskiy, E., Ling, C., Ermolenko, D. N., and Korostelev, A. A. (2013). Blasticidin S inhibits translation by trapping deformed tRNA on the ribosome. *Proc. Natl. Acad. Sci. U.S.A.* 110, 12283–12288. doi: 10.1073/pnas.1304922110

Tabatabaei, I., Dal Bosco, C., Bednarska, M., Ruf, S., Meurer, J., and Bock, R. (2019). A highly efficient sulfadiazine selection system for the generation of transgenic plants and algae. *Plant Biotechnol. J.* 17, 638–649. doi: 10.1111/pbi. 13004

Weber, E., Engler, C., Gruetzner, R., Werner, S., and Marillonnet, S. (2011). A modular cloning system for standardized assembly of multigene constructs. *PLoS One* 6:e16765. doi: 10.1371/journal.pone.0016765

Conflict of Interest: The authors declare that the research was conducted in the absence of any commercial or financial relationships that could be construed as a potential conflict of interest.

frontiers in Plant Science

ORIGINAL RESEARCH
published: 05 March 2020
doi: 10.3389/fpls.2020.00179

Light, but Not Nutrients, Drives Seasonal Congruence of Taxonomic and Functional Diversity of Phytoplankton in a Eutrophic Highland Lake in China

Huan Wang[1], Dandan Zhao[1,2], Liang Chen[1,3], John P. Giesy[4,5], Weizhen Zhang[1,6], Changbo Yuan[1], Leyi Ni[1], Hong Shen[1] and Ping Xie[1,7]**

[1] Donghu Experimental Station of Lake Ecosystems, State Key Laboratory of Freshwater Ecology and Biotechnology, Institute of Hydrobiology, Chinese Academy of Sciences, Wuhan, China, [2] Guangzhou Chengyi Aquaculture Co., Ltd., Guangzhou, China, [3] State Key Laboratory of Eco-hydraulics in Northwest Arid Region, Faculty of Water Resources and Hydroelectric Engineering, Xi'an University of Technology, Xi'an, China, [4] Department of Veterinary Biomedical Sciences and Toxicology Centre, University of Saskatchewan, Saskatoon, SK, Canada, [5] Department of Environmental Science, Baylor University, Waco, TX, United States, [6] State Key Laboratory of Lake Science and Environment, Nanjing Institute of Geography and Limnology, Chinese Academy of Sciences, Nanjing, China, [7] State Key Laboratory of Plateau Ecology and Agriculture, Qinghai University, Xining, China

OPEN ACCESS

Edited by:
Dimitris Petroutsos,
UMR5168 Laboratoire de Physiologie Cellulaire Vegetale (LPCV), France

Reviewed by:
Péter Török,
University of Debrecen, Hungary
Denis Baurain,
University of Liège, Belgium

***Correspondence:**
Hong Shen
hongshen@ihb.ac.cn
Ping Xie
xieping@ihb.ac.cn

Specialty section:
This article was submitted to Plant Biotechnology, a section of the journal Frontiers in Plant Science

Received: 20 September 2019
Accepted: 06 February 2020
Published: 05 March 2020

Citation:
Wang H, Zhao D, Chen L, Giesy JP, Zhang W, Yuan C, Ni L, Shen H and Xie P (2020) Light, but Not Nutrients, Drives Seasonal Congruence of Taxonomic and Functional Diversity of Phytoplankton in a Eutrophic Highland Lake in China. Front. Plant Sci. 11:179. doi: 10.3389/fpls.2020.00179

Information on temporal dynamics of phytoplankton communities and their responses to environmental factors can provide insights into mechanisms driving succession of phytoplankton communities that is useful in programs to manage and or remediate undesirable assemblages. Populations of phytoplankton can be controlled by bottom-up factors such as nutrients and temperature or top-down such as predation by zooplankton. Traditionally, taxonomic diversity based on morphologies has been the measure used for analysis of responses to environmental factors. Recently, according to functional groupings, including functional groups (FG), morpho-FG (MFG), and morphology-based FG (MBFG), functional diversity has been used to represent functional aspects of phytoplankton communities. However, to what extent these taxonomic and functional groupings are congruent at seasonal time-scales and the main environmental factors, which drive succession, have remained less studied. Here, we analyzed absolute and relative proportions of a phytoplankton community during a 3-year period in Lake Erhai, a eutrophic highland lake in China. Alpha diversity and beta diversity, as measured by Shannon-Wiener and Bray-Curtis indices of taxonomic grouping and three functional groupings (FG, MFG, and MBFG) were applied to investigate environmental factors determining diversity. Significant, positive relationships were observed between taxonomic diversity and functional diversity that were strongly linked through seasons. In order to exclude the influence of dominant species' tolerance to extreme environments, the dominant species were excluded one by one, and the results showed that residual communities still exhibited similar patterns of succession. This synchronous temporal pattern was not principally driven by the dominant genera

(*Microcystis*, *Psephonema*, and *Mougeotia*). Instead, the entire phytoplankton community assemblages were important in the pattern. Most diversity indices of taxonomic and functional groupings were significantly correlated with solar irradiance, but not nutrient concentrations. Because the lake is eutrophic and there were already sufficient nutrients available, additional nutrients had little effect on seasonal taxonomic and functional diversity of phytoplankton in Lake Erhai.

Keywords: seasonal succession, environmental drivers, algal taxonomic and functional groupings, alpha and beta diversity, eutrophication

INTRODUCTION

Phytoplankton, including planktonic algae and cyanobacteria, are primary producers in aquatic ecosystems, which play key roles in providing food for and affecting other organisms, and in turn are regulated by interactions with other organisms (Hutchins and Boyd, 2016; Kohlbach et al., 2016). Due to their small sizes, short life cycles of individual taxa and rapidly changing community structures, successional changes in phytoplankton communities are useful, rapid, integrative indicators of ecosystem status and trends in aquatic systems (Camp et al., 2015; Zwart et al., 2015). Compositions of species in algal communities are widely used to quantify temporal fluctuations and succession of aquatic ecosystems (Rodrigues et al., 2015; Wu et al., 2017; Cupertino et al., 2019). Succession of phytoplankton is related to multiple environmental factors such as nutrient concentrations, temperature, and quantity and quality of light in aquatic systems (Malik and Saros, 2016; Paerl et al., 2016; Thomas et al., 2017). It has long been debated whether numbers and types of phytoplankton are controlled by bottom-up factors, such as absolute and relative concentrations of nutrients, including phosphorus (P) or nitrogen (N), or by top-down processes, such as predation by zooplankton and fishes (Vanni et al., 1990; Xie and Liu, 2001; Zhang et al., 2008). Understanding mechanisms of phytoplankton succession and investigating responses in species composition to environmental factors can improve predictive power for phytoplankton responses to environmental changes.

Phytoplankton have been classified by kingdom, phylum, class, order, family, genus and species based on morphological characteristics and or pigments (Hu and Wei, 2006; Reynolds, 2006). In aquatic ecology, algal taxonomic variation has been used for explaining community properties and environmental variation (Lehtinen et al., 2017; Rozema et al., 2017). However, various species of phytoplankton in the same taxonomic association might have different morphological or functional features and taxonomically different algae usually co-occur in the same habitats (Reynolds et al., 2002; Salmaso and Padisák, 2007; Padisák et al., 2009; Kruk et al., 2010). Different phytoplankton taxa living in similar habitats often have the same ecological functions considering functional, morphological, physiological and ecological traits (Reynolds et al., 2002; Salmaso and Padisák, 2007; Padisák et al., 2009; Kruk et al., 2010). Thus, classifications of phytoplankton into functional groupings have been proposed, because functional and ecological traits can reflect strong mechanisms of natural selection (Salmaso et al., 2015; Özkundakci et al., 2016; Fontana et al., 2018). These include functional groups (FG, **Table 1**) (Reynolds et al., 2002; Padisák et al., 2009), morpho-FG (MFG) (Salmaso and Padisák, 2007) and morphology-based FG (MBFG) (Kruk et al., 2010). FG represents the classical and the widest used system of classifying phytoplankton, based on habitat properties, environmental tolerance and trophic state. FG integrates a base of information and relies on expert judgment (Hu et al., 2013; Zhu et al., 2013). MFG is identified using *a priori* determined traits influencing functional processes and ecological characteristics (Naselli-Flores et al., 2007; Mihaljević et al., 2013; Deng et al., 2019). MBFG uses exclusively morphological/structural criteria in the definition of groups

TABLE 1 | Comparisons of taxonomic and three functional groupings, including functional groups (FG), morpho-FG (MFG), and morphology-based FG (MBFG).

Taxonomic and functional groupings	Number of groups	Main grouping criteria	Principle of subdivision	Applied Cases
Genus [based on (Hu and Wei, 2006)]	Not Applicable	Phylogenetic characteristics	Size, population/single cell, color, structure and other features that can be observed under a microscope	Winder et al., 2008; Wang et al., 2010; Yang et al., 2012; Wu et al., 2013
Functional groups (FG, based on Reynolds et al., 2002 and Padisák et al., 2009)	39	Habitat, tolerances and sensitivities	Nutrient levels, water depth, salt and fresh water, scour, stratification, pH, transparency, light intensity and grazing	Vinebrooke et al., 2004; Fonseca and Bicudo, 2008; Stanković et al., 2012; Zhu et al., 2013; Borics et al., 2016
Morpho-Functional Groups (MFG) [based on (Salmaso and Padisák, 2007)]	11 categories and 32 subcategories	Morphological and functional characteristics	size and form, mobility, potential mixotrophy, nutrient requirements, presence of gelatinous envelopes	Naselli-Flores et al., 2007; Mihaljević et al., 2013; Deng et al., 2019
Morphologically based functional groups (MBFG) [based on (Kruk et al., 2010)]	7	Morphological and structural characteristics	Size, flagella, siliceous structures, mucilage, aerotopes and surface/volume ratio	Petar et al., 2014; Beamud et al., 2015; Mihaljević et al., 2015; Bortolini et al., 2016; Kruk et al., 2017; Cupertino et al., 2019

and MBFG is an easier, but more effective classification that has only seven categories (Petar et al., 2014; Allende et al., 2019). Functional groupings with special traits can directly describe ecological processes, such as growth, sedimentation, grazing losses and nutrient acquisition (Weithoff, 2003). Functional groupings have been used as powerful and complementary approaches to describe dynamics of phytoplankton community assemblies and their ecological functions. Each of these methods has advantages and limitations.

Trait-based groupings have identified environmental factors that determine succession of phytoplankton communities in temperate (Weithoff et al., 2015), tropical (Costa et al., 2009; Rodrigues et al., 2018), subtropical (Becker et al., 2009) and Mediterranean (Becker et al., 2010) regions, such as the environmental resources, environmental change and predation (Reynolds, 1984; Salmaso and Padisák, 2007; Salmaso et al., 2015). Results of previous studies have shown that composition, biomass and diversity of phytoplankton is primarily determined by nutrients (Reynolds and Irish, 1997; Rangel et al., 2012). Results of other studies have shown that succession of phytoplankton communities is controlled by physical conditions such as light (Edwards et al., 2015), water temperature (Rasconi et al., 2017; Neukermans et al., 2018), mean depth (Pinckney et al., 2015), flushing rate (Cañavate et al., 2015) and their interactions (Hart et al., 2015; Edwards et al., 2016; Burson et al., 2018; Richardson et al., 2019). Competition for resources, predation, environmental change and rates of mutation and plasticity will affect succession of taxonomic and functional groupings, but whether there is seasonal congruence between functional and taxonomic groupings or not remains unclear in natural communities. If the answer is yes, then, how is this congruence driven by environmental factors?

Diversity indices, of algal taxonomic and functional groupings, such as Shannon-Wiener or Bray-Curtis, have been used to track succession of communities in response to environmental factors (Maloufi et al., 2016; Vallina et al., 2017). Diversity of phytoplankton communities based on taxonomy of algae can be used to describe patterns of succession and have been used to analyze the ecological status of assemblages of phytoplankton (Rodrigues et al., 2015; Wojciechowski et al., 2017). Functional diversity of algae is based mainly on similarities of morpho-functional traits between species and are directly related to environmental factors, therefore, functional diversity affects processes at all scales of community and ecosystem organization (Zwart et al., 2015; Vallina et al., 2017). Therefore, taxonomic plus functional classifications might be a useful combination to assess environmental factors influencing aquatic communities (Cupertino et al., 2019). It is critical to understand how various factors are coupled if ecosystems are to be managed and/or restored to provide particular ecological services for humans.

In this study, data from a 36-month study of phytoplankton in Lake Erhai, a eutrophic highland lake in China, was used to calculate diversity indices of taxonomic and three functional groupings, including FG, MFG, and MBFG. Three hypotheses were tested: (1) taxonomic and functional diversity are positively correlated and their diversity indices show the same synchronous seasonal patterns; (2) seasonal congruence is generally driven by one or a few dominant genera. In eutrophic systems, the genera *Microcystis, Psephonema*, *and Mougeotia*, which are adapted to conditions of greater concentrations of phosphorus, can determine the temporal pattern of functional and taxonomic groupings; and (3) seasonal congruence is caused by the fact that functional and taxonomic diversity respond in a similar way to environmental factors. To test for seasonal congruence and environmental drivers of phytoplankton taxonomic and functional groupings, in the present study, results of which are reported here, both alpha (α) and beta (β) diversities of genera grouping and three functional groupings (FG, MFG, and MBFG) of phytoplankton with monthly measurements were compared. In addition, to test if dominant genera were most important determinants of changes in composition of species, dominant genera, were sequentially removed and diversity indices were recalculated to determine if removing these genera would affect the seasonal patterns.

METHODS

Study Site and Sampling Method

The study was performed in Lake Erhai (25°36′-25°58′ N, 100° 05′-100°17′ E), the second largest, high-altitude freshwater lake on the Yunnan Plateau, China (**Figure 1**). Lake Erhai is located in the central zone of the Dali Bai Autonomous Prefecture in Yunnan Province. Lake Erhai has a total surface area of approximately 250 km^2, an elevation of 1,974 m and a volume of nearly 28.8×10^8 m^3. Mean and maximum depth are 10.5 and 20.5 m, respectively. Lake Erhai, is currently in the early stages of eutrophication (Lin et al., 2016; Wang et al., 2018), with concentration of total nitrogen (TN) of 0.7 mg/L (Zhu et al., 2018), total phosphorus (TP) of 0.03 mg/L (Zhu et al., 2018) and chlorophyll a (Chl a) of 13.33 μg/L during June 2013 to May 2015, with a peak value exceeding 30 μg/L (Wang et al., 2018), all of which exceed the threshold value of the eutrophication categories (TP > 0.03 mg/L, TN > 0.65 mg/L, and Chl *a* > 9 μg/L, Nürnberg, 1996). Samples were collected monthly, from 15 locations, between January 2012 and December 2014 (**Figure 1**). Composite, integrated samples were collected by combining samples of water from the upper (0.5 m below the water surface), middle (midway between the surface and the bottom), and lower (0.5 m above the sediment surface) portions of the water column at each site. Composite, integrated samples were used for analysis of nutrient concentration and phytoplankton.

Physical and Chemical Analysis

Water temperature (T) was measured at 0.5 m below the water surface at each sampling site using a YSI ProPlus multiparameter water quality meter (Yellow Springs, OH, USA). Water transparency (SD) was measured using a Secchi disk (20 cm diameter) *in situ*. Secchi depth is a visual measure of light

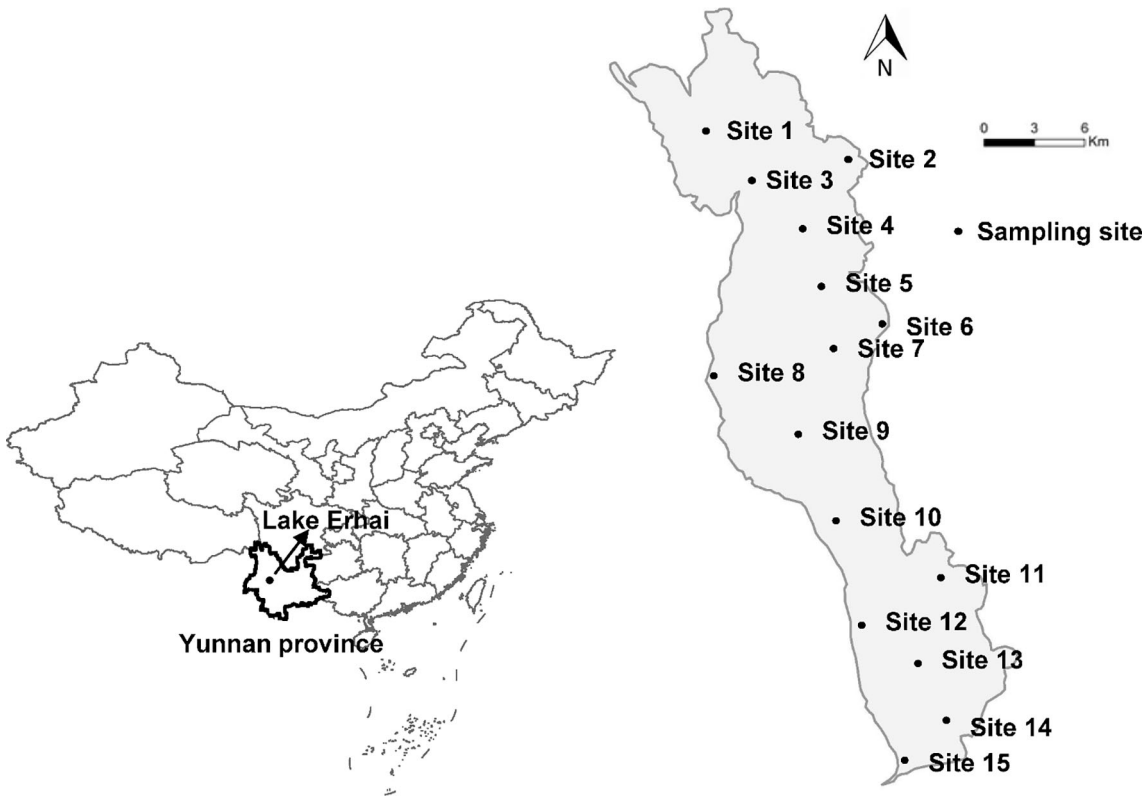

FIGURE 1 | Map of Lake Erhai and the location of the 15 sampling sites.

intensity, because light is absorbed by particles and soluble substances in the water, resulting in disappearance of view at a certain depth (Secchi, 1866; Preisendorfer, 1986). Concentrations of dissolved inorganic phosphorus (DIP) and ammonium (NH_4-N) in mixed samples were measured by use of standard preservation and analytical procedures established by Government Water Association (APHA-AWWA-WPCF, 1915).

Identification and Enumeration of Phytoplankton

One-liter samples were fixed with 10 ml Lugol's iodine solution and were concentrated to 50 ml with a siphon after sedimentation for 48 h in Utermhol chambers (Huang et al., 1999). After mixing, concentrated samples (0.1 ml) were observed with a phytoplankton-counting chamber (0.1 ml, Institute of Hydrobiology, Chinese Academy of Sciences, China) under 400× magnification using a light microscope (Olympus BX21, Tokyo, Japan). Cells of colonial or filamentous (e.g., *Microcystis*, *Psephonema*, *Mougeotia*, and *Oscillatoria*) algae were separated using an ultrasonic device (JY88-II, Scientiz, Ningbo, Zhejiang, China) before enumeration. Taxonomic identification of phytoplankton was performed according to Hu and Wei (Hu and Wei, 2006). Species were aggregated into kingdom, phylum, class, order, family, genus and species (if needed) levels.

Sorting of Functional Groupings

Three functional classification schemes, including FG, MFG, and MBFG, were performed. FG, based on genera or species, when possible, resulted in 39 groups (Reynolds et al., 2002), identified by use of alpha-numeric codes according to their similar morphology, environmental sensitivity and tolerance, based on Grime's (1979) seminal work on terrestrial vegetation, which were applied to phytoplankton. MFG was composed of 32 groups, based on motility, the potential capacity to obtain carbon and nutrients by mixotrophy, specific nutrient requirements, size and shape, and presence of gelatinous envelopes (Salmaso and Padisák, 2007). MBFG was composed of 7 groups based on eight morphological traits of phytoplankton, including flagella, mucilage, siliceous exoskeletal structures, aerotopes, gas vesicles, volume, surface/volume, and maximum linear dimension characterized by use of light microscopy (Kruk et al., 2010).

Statistical Analyses

Indices of α diversity, calculated by use of the Shannon-Wiener index (Shannon, 1948), and β diversity, calculated by use of the Bray-Curtis dissimilarity index (Bray and Curtis, 1957), were applied to characterize taxonomic groupings and three functional groupings, including FG, MFG, and MBFG. The

Shannon-Wiener index of each taxonomic and functional classification in each site for each month was calculated. The Bray-Curtis index was calculated to measure pairwise dissimilarity in species composition between sites within each month. Mean pairwise dissimilarity among sites for each month was used as a response variable, i.e. spatial β diversity within the lake. Both Shannon-Wiener and Bray-Curtis indices of each taxonomic and functional classification were calculated in the same way, with serial removal of the three most dominant genera, which were taxa accounting for more than 70% of total cell numbers. To investigate seasonality of environmental parameters and diversity indices, a locally weighted scatter smoothing function, using month as the predictor variable (Cleveland, 1981), was used to fit curves (span = 0.75) for these variables. To test if taxonomic and functional diversity indices were related, generalized linear mixed models [GLMMs (Bolker et al., 2009)] were used with pairs of mean diversity indices for each month from all sampling points as variables. To test how environmental factors affect taxonomic and functional diversity indices and drive the congruence effect, in the GLMMs, the mean values of each taxonomic and functional diversity index in the 15 sites for each month were used as response variables, and DIP, NH_4-N, T, and SD were used as predictors. To avoid pseudo-replication (pseudo-replication typically occurs when the number of observations or the number of data points is treated inappropriately as independent replicates) in the analysis of the correlation among diversity indices, a seasonal (month) effect was introduced as a random predictor variable (Hurlbert, 1984). All statistical analyses were conducted in R 3.1.0 (R Development Core Team, 2014).

RESULTS

Mean values of concentrations of nutrients, including NH_4-N and DIP, and physical parameters, including Secchi depth (SD) and water temperature (T), of the 15 sampling sites from January 2012 to December 2014 are shown (**Figure 2**). All parameters exhibited seasonal variations. Concentrations of NH_4-N were greatest during summer, while concentrations of DIP were greater during spring and autumn, SD was maximum in spring and T reached its maximum in August. Mean concentrations of NH_4-N, DIP, SD, and T were 0.039 mg/L, 0.006 mg/L, 2.22 m, and 18.12°C, respectively.

Patterns of succession of compositions of species in taxonomic and functional groupings of phytoplankton communities during the sampling period are shown (**Figure 3**). Cyanophyta, Chlorophyta and Bacillariophyta were the three dominant phyla. Cyanophyta was the dominant phylum from July to December (blooming period), whereas Bacillariophyta dominated from February to June. Populations of Chlorophyta peaked during summer and then decreased from summer to winter. Communities of cyanophyta were by the genera *Microcystis* and *Aphanizomenon,* and Chlorophyta was dominated by genera *Psephonema* and *Mougeotia* (**Figure 3A**-Genus). Thirty-two (32) FG groups were identified, with the primary three being M dominated by *Microcystis*, T dominated by *Psephonema*, and S1 dominated by *Oscillatoria* (**Figure 3A**-FG). A total of 23 MFG groups were identified with the primary three being X5b, dominated by *Microcystis*, X10a, dominated by *Psephonema*, and X5a, dominated by *Oscillatoria and Aphanizomenon* (**Figure 3A**-MFG). Seven (7) MBFG groups were identified, with the three primary being VII, dominated by *Microcystis*, IV, dominated by *Psephonema* and III, dominated by *Oscillatoria* (**Figure 3A**-MBFG).

For both α and β diversities, taxonomic (genus) and functional diversities of FG, MFG, and MBFG exhibited maxima during summer then decreased in autumn (**Figures 3B, C**). Significant positive correlations were also observed between taxonomic and functional groupings (**Figures 3D, E**). The coefficients of determination (R^2) between taxonomic and functional α diversities were ≥ 0.88 ($p < 0.05$) (**Figure 3D**) and the R^2 of β diversities were ≥ 0.95 ($p < 0.05$) (**Figure 3E**).

The dominant genera, which accounted for > 70% of total numbers of cells, were *Microcystis*, *Psephonema*, and *Mougeotia* (**Figure S1**). To check whether dominant genera affected seasonal patterns of diversity indices, these three dominant genera were removed serially. Successional patterns of taxonomic and functional groupings of the rest of the phytoplankton community are shown in **Figures S2A**, **S3A**, and **S4A** (supplementary information). The α (**Figures S2B**, **S3B**, and **S4B**) and β diversity (**Figures S2C**, **S3C**, and **S4C**) indices of the remaining phytoplankton community showed a

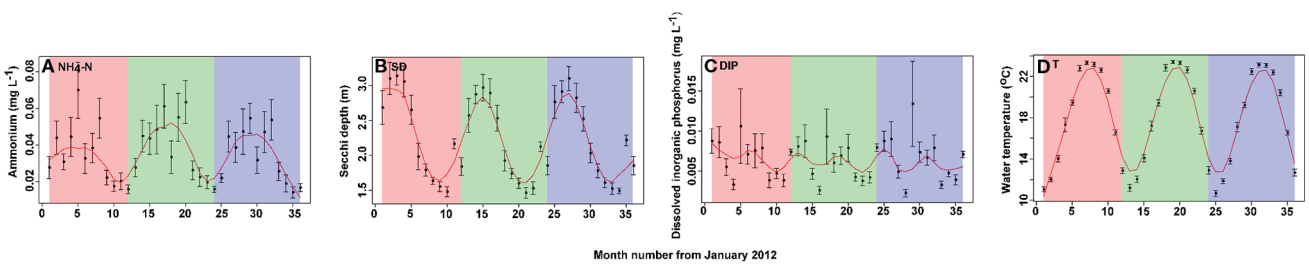

FIGURE 2 | Monthly time series of values of physical and chemical parameters in Lake Erhai from January 2012 to December 2014. **(A)** ammonium (NH_4-N), **(B)** Secchi depth (SD), **(C)** dissolved inorganic phosphorus (DIP), and **(D)** water temperature (T). Values are presented as the mean ± standard deviation (SD) among the 15 sites for each month. To detect the seasonality of environmental parameters, a locally weighted scatter smoothing function (Cleveland, 1981) was used to fit a smooth curve (span = 0.75) using month as the predictor variable.

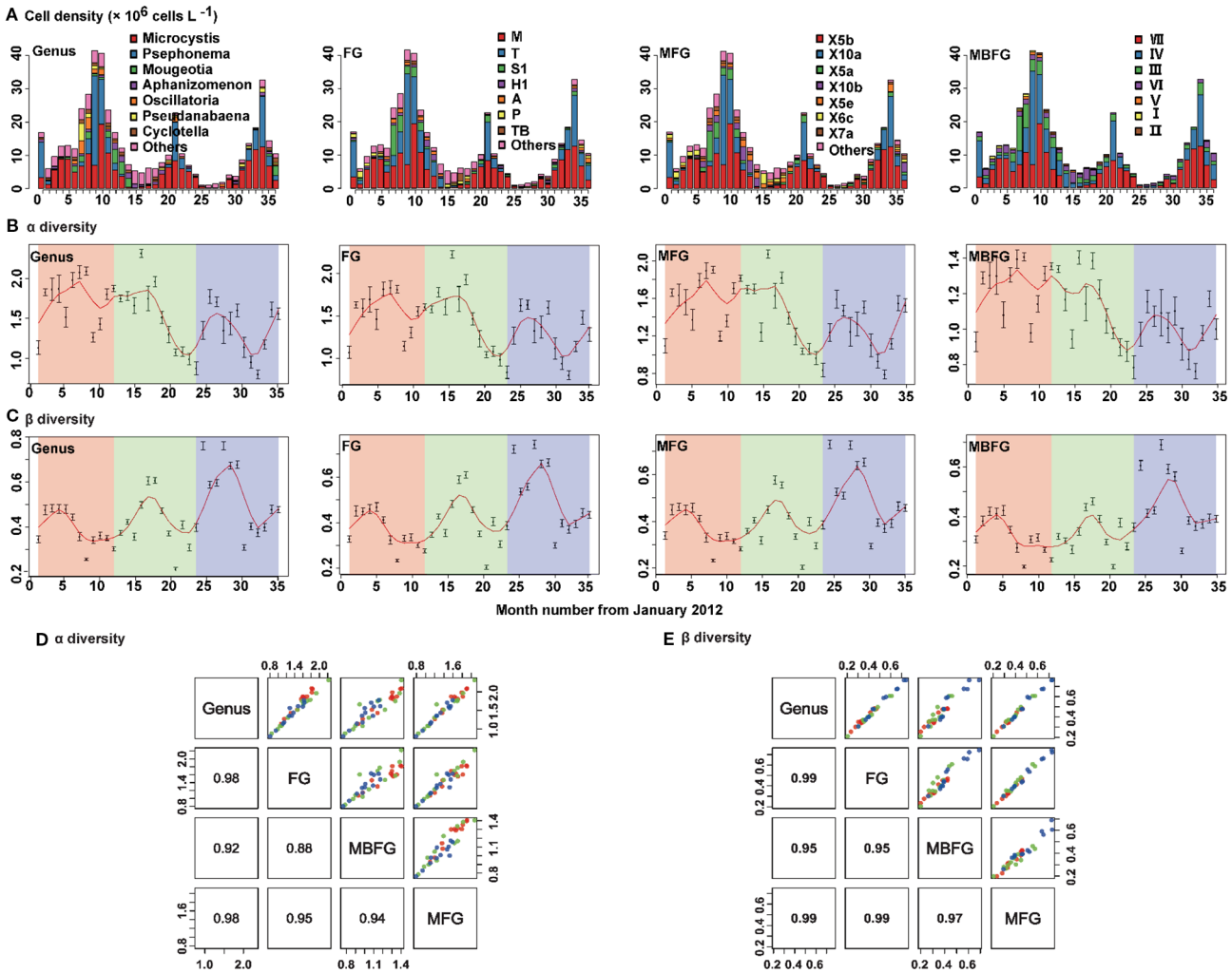

FIGURE 3 | Seasonal composition and successions of phytoplankton in Lake Erhai from January 2012 to December 2014 according to taxonomic and three functional groupings. **(A)** Cell density and composition, **(B)** alpha diversity (Shannon-Wiener diversity) indices, **(C)** beta diversity (Bray-Curtis dissimilarity) indices, **(D)** pair plot for linear fitting of alpha and **(E)** beta diversity. The order from left to right is genus, functional groups (FG), morpho-FG (MFG), and morphology-based FG (MBFG). The cell density values are presented as the mean of 15 sites for each month. Alpha and beta diversity values are presented as the mean ± standard deviation (SD) among the 15 sites for each month. To detect the seasonality of alpha and beta diversity indices, a locally weighted scatter smoothing function (Cleveland, 1981) was used to fit a smooth curve (span = 0.75) using month as the predictor variable. The numbers in the lower left columns in (d) and (e) are correlation coefficients (R^2) ($p < 0.05$).

similar seasonal pattern to those of the whole community, and significant correlations ($p < 0.001$) were found for genus, FG, MFG, and MBFG groupings (**Figure S5**).

Results of GLMMs showed that both α and β diversities of taxonomic and functional groupings responded similarly to environmental factors (**Table 2**). Except for α diversity of MFG and MBFG groupings, all the other diversity indices were significantly correlated with SD ($p < 0.05$) (**Table 2**). Meanwhile, β diversity of FG was significantly correlated with water temperature ($p < 0.05$) (**Table 2**). However, all diversities showed weaker correlations with concentrations of NH_4-N and DIP than with SD or water temperature.

DISCUSSION

In Lake Erhai, taxonomic and functional diversities were positively correlated and both alpha and beta indices showed the same synchronous seasonal pattern. The maximum species diversity was observed under multiple conditions of nutrient concentrations, where nutrients and light provided ample scope for coexistence of species (Török et al., 2016), therefore both functional and taxonomic diversity increased during spring, followed by a decrease in summer and then increasing in winter. Results of previous studies have shown that seasonal congruence occurs when selection acts predominantly on one trait so that

TABLE 2 | Generalized linear mixed models (GLMMs) results for environmental factors and diversity indices of taxonomic and three functional groupings, including functional groups (FG), morpho-FG (MFG), and morphology-based FG (MBFG).

	Group	(Intercept)	Ammonium	Phosphorus	Secchi depth	Water temperature	rvalue
Alpha diversity (Shannon-Wiener index)	Genus	0.851	0.65	0.652	**0.029**	0.226	0.244
	FG	0.668	0.723	0.7	**0.01**	0.115	0.322
	MFG	0.847	0.563	0.473	0.082	0.311	0.15
	MBFG	0.409	0.615	0.771	0.1	0.251	0.122
Beta diversity (Bray-Curtis index)	Genus	0.173	0.161	0.098	**0.002**	0.053	0.357
	FG	0.156	0.192	0.112	**0.003**	**0.047**	0.346
	MFG	0.183	0.121	0.073	**0.003**	0.051	0.334
	MBFG	0.246	0.143	0.131	**0.007**	0.053	0.255

The bolded numbers showed correlation coefficients (R2) with statistical significance ($p < 0.05$).

increase or decrease of species characterized by this trait will result in increase or decrease of both functional and taxonomic diversity (Weithoff et al., 2015). In this study, due to increases in light intensity, some groups, such as Bacillariophyta would be eliminated through competition because they could not adapt to strong light (Reynolds et al., 2002). However, other genera, such as *Microcystis* and *Psephonema* which are better adapted to the changed environment would outcompete (Reynolds et al., 2002). This seasonal congruence in phytoplankton species composition illustrate the changes in functional diversity in Lake Erhai and this algal succession is a distinguishable yearly cycle in many natural aquatic ecosystems (Lund, 1965; Reynolds, 2006). These results suggest that functional diversity may encompass the overall variability of taxonomic diversity. Interestingly, assemblage structure in simplified classifications (MBFG and MFG) was affected by the same environmental variation, further highlighting the similarity of taxonomic and functional groupings in this eutrophic highland lake.

During the entire study period, from 2012 to 2014, significant, positive correlations were observed between taxonomic and functional diversities. However, the seasonal congruence of taxonomic and functional diversities was not driven by the dominant genera, suggesting that the phytoplankton community consisted of species with similar adaptive strategies (Reynolds, 1984). Since coexisting species represented FG with different photosynthetic pigments, it was verified that niche differentiation in the light spectrum played a role. In eutrophic environments, adequate supply of nutrients promotes biomass growth (Agawin et al., 2000; Søndergaard et al., 2017), and the species interact through mutual shading, and the best light competitor (*Microcystis*) is expected to prevail, and results in blooms. Under the cover of *Microcystis*, conditions for growth of *Psephonema* and *Mougeotia* result in large numbers of those species. Light is considered especially important for *Microcystis* and FG M, X5b and VII (Reynolds et al., 2002; Salmaso and Padisák, 2007; Padisák et al., 2009; Kruk et al., 2010), which were most represented in Lake Erhai. Because the three dominant groups accounted for the majority of cell density (>70%), interferences of dominant species were excluded. However, the results were still significantly correlated, which suggested that responses of phytoplankton communities to the environment were not based on dominant effects of individual species.

Results of the study presented here revealed diversities of taxonomic and functional groupings responded in a similar way to light levels and there is no significant relationship between diversities and concentrations of nutrients. Results of previous studies showed that the seasonal pattern of diversity indices of both taxonomic and functional groupings is dependent on the environmental factors (Becker et al., 2010; Weithoff et al., 2015). The fundamental factors that determine algal seasonal diversity are the physico-chemical characteristics in the water column such as nutrient concentrations, water temperature and light (Smith, 1986; Reynolds, 1989; Jensen et al., 1994; Elliott, 2010). Understanding how environmental variations affect the biodiversity and succession of phytoplankton is a key challenge. Results of several studies have shown that composition and biomass of phytoplankton were shaped by nutrients in nutrient-poor environments (Alpine and Cloern, 1992; Watson et al., 1997). In oligotrophic environments, structures of algal communities are driven by strong competition for nutrients (Tsiola et al., 2016). Limitation by individual nutrients prevents accumulation of sufficient biomass of phytoplankton, so shading effects and competition for light are negligible. In addition, increasing nutrient loads caused changes in phytoplankton species composition by shifting the species interactions from competition for nutrients to competition for light (Burson et al., 2018). In this study, no significant correlation between nutrient concentrations and phytoplankton community structure were found over time in Erhai Lake. Instead, water transparency (SD) and water temperature were strongly related to seasonal succession of phytoplankton community, especially SD. Therefore, nutrient concentrations are not a constraint for phytoplankton in eutrophic Lake Erhai, with means of concentrations of 0.039 mg NH_4-N/L, 0.006 mg DIP/L, respectively (Wen and Ma, 2011). This result is consistent with the Liebig Law of the Minimum, which states that only one factor, such as a nutrient, can limit a biological process, such as primary productivity of phytoplankton (Liebig, 1840). For instance, in natural systems, concentrations of phosphorus (P) are often limiting (Krom et al., 1991). However, after cultural eutrophication during which P is added due to human activities, such as agriculture or urbanization, once the minimum is exceeded, P is no longer limiting to primary production. Relative proportions of nitrogen (N) and P needed to support

primary productivity is defined by the Redfield number, which is the ratio of N to P in cells (N/P ratio of 16) (Redfield, 1958). In North American lakes, succession of phytoplankton was determined not by predation by zooplankton or temperature or depletion of nutrients but rather sensitivities of species of phytoplankton to ultraviolet (UV) light (Gala and Giesy, 1991). Results of previous studies also showed that seasonal variation in phytoplankton community composition was affected by light (SD, water transparency and UV radiation) in eutrophic lakes (Sommaruga and Augustin, 2006; Wondie et al., 2007). In this study, light conditions, but not nutrients, is also the key driver of algal taxonomic and functional diversities in eutrophic Lake Erhai. Further studies might be required to explore how solar UV radiation and visible light affect the succession of phytoplankton in different lakes, especially in highland lakes with high intensities of light.

Since the MBFG approach is easier and less resource intensive than genus level and other functional classifications, it is suitable for routine biomonitoring, long-term studies, or to process large amounts of samples when comparing systems. Nonetheless, the genus-level taxonomic approach, FG and MFG provided the detailed information and multiple insights on assemblage dynamics of phytoplankton in this study, and using multiple classifications at the same time can provide the most detailed variation for further analysis.

CONCLUSIONS

In Lake Erhai, a eutrophic highland lake in China, significant positive relationships were observed between taxonomic diversity and functional diversity of phytoplankton, with a strong synchronous seasonal pattern of succession. Taxonomic and functional diversity can complement each other and provide a more comprehensive explanation of the driving effect of environmental changes on phytoplankton communities from biological and functional perspectives. Results of this study demonstrated that functional groupings can be used as simple avenues for studying temporal patterns of phytoplankton community assembly and the environmental drivers in eutrophic lake. Furthermore, the seasonal congruence was not driven by the dominated genera, *Microcystis*, *Psephonema*, and *Mougeotia*, which suggested that the algal community consisted of species with similar ecological strategies. Both functional diversity and taxonomic diversity were significantly, positively correlated with light conditions, but not concentrations of nutrients. Conclusively, light is the key driver of seasonal congruence of phytoplankton taxonomic and functional diversity in this eutrophic highland lake. Our results also showed that alternative functional groupings of phytoplankton can be reliable predictors of environment-biological relationships.

DATA AVAILABILITY STATEMENT

All datasets generated for this study are included in the article/ **Supplementary Material**.

AUTHOR CONTRIBUTIONS

PX and HS designed the study. HW and DZ conducted the experiments. HW led the data processing and manuscript writing. HS, LC and JG revised the manuscript. WZ and CY helped performance of data analysis. LN helped experimental process. All authors contributed to the final draft.

ACKNOWLEDGMENTS

We thank editor Dimitris Petroutsos and two anonymous reviewers for their constructive suggestions and professional editing. This work was jointly supported by the National Key Research and Development Program of China [grant number 2017YFA0605201], the National Natural Science Foundation of China [grant number 31700400], the Featured Institute Service Projects from Institute of Hydrobiology, Chinese Academy of Sciences [grant number Y85Z061601] and the State Key Laboratory of Freshwater Ecology and Biotechnology [grant number 2019FBZ03]. JG was supported by the "High Level Foreign Experts" program (#GDT20143200016) funded by the State Administration of Foreign Experts Affairs, the P.R. China to Nanjing University and the Einstein Professor Program of the Chinese Academy of Sciences. He was also supported by the Canada Research Chair program and a Distinguished Visiting Professorship in the Department of Environmental Sciences at Baylor University, Waco, Texas, USA. We thank Dr. Rong Zhu for her help during sample collection.

SUPPLEMENTARY MATERIAL

The Supplementary Material for this article can be found online at: https://www.frontiersin.org/articles/10.3389/fpls.2020.00179/full#supplementary-material

REFERENCES

Agawin, N. S., Duarte, C. M., and Agustí, S. (2000). Nutrient and temperature control of the contribution of picoplankton to phytoplankton biomass and production. *Limnol. Oceanogr.* 45 (3), 591–600. doi: 10.4319/lo.2000.45.3.0591

Allende, L., Fontanarrosa, M. S., Murno, A., and Sinistro, R. (2019). Phytoplankton functional group classifications as a tool for biomonitoring shallow lakes: a case study. *Knowl. Manage. Aquat. Ecosyst.* 420, 5. doi: 10.1051/kmae/2018044

Alpine, A. E., and Cloern, J. E. (1992). Trophic interactions and direct physical effects control phytoplankton biomass and production in an estuary. *Limnol. Oceanogr.* 37 (5), 946–955. doi: 10.4319/lo.1992.37.5.0946

American Public Health Association (APHA), American Water Works Association (AWWA) and Pollution Control Federation (WPCF) (1915).

Standard methods for the examination of water and wastewater (Washington, DC: American Public Health Association).

Beamud, S. G., León, J. G., Kruk, C., Pedrozo, F., and Diaz, M. (2015). Using trait-based approaches to study phytoplankton seasonal succession in a subtropical reservoir in arid central western Argentina. *Environ. Monit. Assess.* 187 (5), 271. doi: 10.1007/s10661-015-4519-1

Becker, V., Huszar, V. L. M., and Crossetti, L. O. (2009). Responses of phytoplankton functional groups to the mixing regime in a deep subtropical reservoir. *Hydrobiologia* 628 (1), 137–151. doi: 10.1007/s10750-009-9751-7

Becker, V., Caputo, L., Ordóñez, J., Marcé, R., Armengol, J., Crossetti, L. O., et al. (2010). Driving factors of the phytoplankton functional groups in a deep Mediterranean reservoir. *Water Res.* 44 (11), 3345–3354. doi: 10.1016/j.watres.2010.03.018

Bolker, B. M., Brooks, M. E., Clark, C. J., Geange, S. W., Poulsen, J. R., Stevens, M. H. H., et al. (2009). Generalized linear mixed models: a practical guide for ecology and evolution. *Trends In Ecol. Evol.* 24 (3), 127–135. doi: 10.1016/j.tree.2008.10.008

Borics, G., Tóthmérész, B., Várbíró, G., Grigorszky, I., Czébely, A., and Görgényi, J. (2016). Functional phytoplankton distribution in hypertrophic systems across water body size. *Hydrobiologia* 764 (1), 81–90. doi: 10.1007/s10750-015-2268-3

Bortolini, J. C., Moresco, G. A., de Paula, A. C. M., Jati, S., and Rodrigues, L. C. (2016). Functional approach based on morphology as a model of phytoplankton variability in a subtropical floodplain lake: a long-term study. *Hydrobiologia* 767 (1), 151–163. doi: 10.1007/s10750-015-2490-z

Bray, J. R., and Curtis, J. T. (1957). An ordination of the upland forest communities of southern Wisconsin. *Ecol. Monogr.* 27 (4), 325–349. doi: 10.2307/1942268

Burson, A., Stomp, M., Greenwell, E., Grosse, J., and Huisman, J. (2018). Competition for nutrients and light: testing advances in resource competition with a natural phytoplankton community. *Ecology* 99 (5), 1108–1118. doi: 10.1002/ecy.2187

Cañavate, J. P., Pérez-Gavilan, C., Mazuelos, N., and Manchado, M. (2015). Flushing-related changes of phytoplankton seasonal assemblages in marsh ponds of the warm temperate Guadalquivir river estuary (SW Spain). *Hydrobiologia* 744 (1), 15–33. doi: 10.1007/s10750-014-2051-x

Camp, J., Flo, E., Vila, M., Arin, L., Reñé, A., Sampedro, N., et al. (2015). "Pros and cons of biological quality element phytoplankton as a water-quality indicator in the NW Mediterranean Sea," in *Experiences from Ground, Coastal and Transitional Water Quality Monitoring* (Springer), 135–160. doi: 10.1007/698-2015-392

Cleveland, W. S. (1981). LOWESS: A program for smoothing scatterplots by robust locally weighted regression. *Am. Stat.* 35 (1), 54. doi: 10.2307/2683591

Costa, L., Huszar, V., and Ovalle, A. (2009). Phytoplankton functional groups in a tropical estuary: hydrological control and nutrient limitation. *Estuar. Coasts* 32 (3), 508–521. doi: 10.1007/s12237-009-9142-3

Cupertino, A., Gücker, B., Von Rückert, G., and Figueredo, C. C. (2019). Phytoplankton assemblage composition as an environmental indicator in routine lentic monitoring: Taxonomic versus functional groups. *Ecol. Indic.* 101, 522–532. doi: 10.1007/s12237-009-9142-3

Deng, J., Salmaso, N., Jeppesen, E., Qin, B., and Zhang, Y. (2019). The relative importance of weather and nutrients determining phytoplankton assemblages differs between seasons in large Lake Taihu, China. *Aquat. Sci.* 81 (3), 48. doi: 10.1007/s00027-019-0645-0

Edwards, K. F., Thomas, M. K., Klausmeier, C. A., and Litchman, E. (2015). Light and growth in marine phytoplankton: allometric, taxonomic, and environmental variation. *Limnol. Oceanogr.* 60 (2), 540–552. doi: 10.1002/lno.10033

Edwards, K. F., Thomas, M. K., Klausmeier, C. A., and Litchman, E. (2016). Phytoplankton growth and the interaction of light and temperature: A synthesis at the species and community level. *Limnol. Oceanogr.* 61 (4), 1232–1244. doi: 10.1002/lno.10282

Elliott, J. (2010). The seasonal sensitivity of cyanobacteria and other phytoplankton to changes in flushing rate and water temperature. *Global Change Biol.* 16 (2), 864–876. doi: 10.1111/j.1365-2486.2009.01998.x

Fonseca, B. M., and Bicudo, C. (2008). Phytoplankton seasonal variation in a shallow stratified eutrophic reservoir (Garças Pond, Brazil). *Hydrobiologia* 600 (1), 267–282. doi: 10.1007/s10750-007-9240-9

Fontana, S., Thomas, M. K., Moldoveanu, M., Spaak, P., and Pomati, F. (2018). Individual-level trait diversity predicts phytoplankton community properties better than species richness or evenness. *ISME J.* 12 (2), 356. doi: 10.1038/ismej.2017.160

Gala, W. R., and Giesy, J. P. (1991). Effects of ultraviolet radiation on the primary production of natural phytoplankton assemblages in Lake Michigan. *Ecotoxicol. Environ. Saf.* 22 (3), 345–361. doi: 10.1016/0147-6513(91)90084-3

Grime, J. P. (1979). Plant strategies and vegetation processes. (New York: John Wiley).

Hart, J., Phlips, E., Badylak, S., Dix, N., Petrinec, K., Mathews, A., et al. (2015). Phytoplankton biomass and composition in a well-flushed, sub-tropical estuary: The contrasting effects of hydrology, nutrient loads and allochthonous influences. *Mar. Environ. Res.* 112, 9–20. doi: 10.1016/j.marenvres.2015.08.010

Hu, H., and Wei, Y. (2006). *The Freshwater Algae of China-Systematics, Taxonomy and Ecology* (Science Press).

Hu, R., Han, B., and Naselli-Flores, L. (2013). Comparing biological classifications of freshwater phytoplankton: a case study from South China. *Hydrobiologia* 701 (1), 219–233. doi: 10.1007/s10750-012-1277-8

Huang, X., Chen, W., and Cai, Q. (1999). *Survey, observation and analysis of lake ecology*. Standard Methods for Observation and Analysis in Chinese Ecosystem Research Network, Series V.

Hurlbert, S. H. (1984). Pseudoreplication and the design of ecological field experiments. *Ecol. Monogr.* 54 (2), 187–211. doi: 10.2307/1942661

Hutchins, D. A., and Boyd, P. W. (2016). Marine phytoplankton and the changing ocean iron cycle. *Nat. Climate Change* 6, 1072. doi: 10.1038/nclimate3147

Jensen, J., Jeppesen, E., Olrik, K., and Kristensen, P. (1994). Impact of nutrients and physical factors on the shift from cyanobacterial to chlorophyte dominance in shallow Danish lakes. *Can. J. Fish. Aquat. Sci.* 51 (8), 1692–1699. doi: 10.1139/f94-170

Kohlbach, D., Graeve, M., A. Lange, B., David, C., Peeken, I., and Flores, H. (2016). The importance of ice algae-produced carbon in the central Arctic Ocean ecosystem: Food web relationships revealed by lipid and stable isotope analyses. *Limnol. Oceanogr.* 61 (6), 2027–2044. doi: 10.1002/lno.10351

Krom, M., Kress, N., Brenner, S., and Gordon, L. (1991). Phosphorus limitation of primary productivity in the eastern Mediterranean Sea. *Limnol. Oceanogr.* 36 (3), 424–432. doi: 10.2307/2837508

Kruk, C., Huszar, V. L., Peeters, E. T., Bonilla, S., Costa, L., LÜRLING, M., et al. (2010). A morphological classification capturing functional variation in phytoplankton. *Freshw. Biol.* 55 (3), 614–627. doi: 10.1111/j.1365-2427.2009.02298.x

Kruk, C., Segura, A. M., Costa, L. S., Lacerot, G., Kosten, S., Peeters, E. T., et al. (2017). Functional redundancy increases towards the tropics in lake phytoplankton. *J. Plankton Res.* 39 (3), 518–530. doi: 10.1093/plankt/fbw083

Lehtinen, S., Tamminen, T., Ptacnik, R., and Andersen, T. (2017). Phytoplankton species richness, evenness, and production in relation to nutrient availability and imbalance. *Limnol. Oceanogr.* 62 (4), 1393–1408. doi: 10.1002/lno.10506

Liebig, J. (1840). *Die organische Chemie in ihrer Anwendung auf Agricultur und Physiologie* (F. Vieweg und Sohn).

Lin, Q., Liu, E., Zhang, E., Li, K., and Shen, J. (2016). Spatial distribution, contamination and ecological risk assessment of heavy metals in surface sediments of Erhai Lake, a large eutrophic plateau lake in southwest China. *Catena* 145, 193–203. doi: 10.1016/j.catena.2016.06.003

Lund, J. W. G. (1965). The ecology of the freshwater phytoplankton. *Biol. Rev.* 40 (2), 231–290. doi: 10.1111/j.1469-185X.1965.tb00803.x

Malik, H. I., and Saros, J. E. (2016). Effects of temperature, light and nutrients on five Cyclotella sensu lato taxa assessed with *in situ* experiments in arctic lakes. *J. Plankton Res.* 38 (3), 431–442. doi: 10.1093/plankt/fbw002

Maloufi, S., Catherine, A., Mouillot, D., Louvard, C., Couté, A., Bernard, C., et al. (2016). Environmental heterogeneity among lakes promotes hyper β-diversity across phytoplankton communities. *Freshw. Biol.* 61 (5), 633–645. doi: 10.1111/fwb.12731

Mihaljević, M., Špoljarić, D., Stević, F., and Pfeiffer, T. Ž. (2013). Assessment of flood-induced changes of phytoplankton along a river–floodplain system using the morpho-functional approach. *Environ. Monit. Assess.* 185 (10), 8601–8619. doi: 10.1007/s10661-013-3198-z

Mihaljević, M., Stević, F., Špoljarić, D., and Pfeiffer, T. Ž. (2015). Spatial Pattern of Phytoplankton Based on the Morphology-Based Functional Approach along a River–Floodplain Gradient. *River Res. Appl.* 31 (2), 228–238. doi: 10.1002/rra.2739

Nürnberg, G. K. (1996). Trophic state of clear and colored, soft-and hardwater lakes with special consideration of nutrients, anoxia, phytoplankton and fish. *Lake Reserv. Manage.* 12 (4), 432–447. doi: 10.1080/07438149609354283

Naselli-Flores, L., Padisák, J., and Albay, M. (2007). Shape and size in phytoplankton ecology: do they matter? *Hydrobiologia* 578 (1), 157–161. doi: 10.1007/s10750-006-2815-z

Neukermans, G., Oziel, L., and Babin, M. (2018). Increased intrusion of warming Atlantic water leads to rapid expansion of temperate phytoplankton in the Arctic. *Global Change Biol.* 24 (6), 2545–2553. doi: 10.1111/gcb.14075

Özkundakci, D., Gsell, A. S., Hintze, T., Täuscher, H., and Adrian, R. (2016). Winter severity determines functional trait composition of phytoplankton in seasonally ice-covered lakes. *Global Change Biol.* 22 (1), 284–298. doi: 10.1111/gcb.13085

Padisák, J., Crossetti, L. O., and Naselli-Flores, L. (2009). Use and misuse in the application of the phytoplankton functional classification: a critical review with updates. *Hydrobiologia* 621 (1), 1–19. doi: 10.1007/s10750-008-9645-0

Paerl, H. W., Gardner, W. S., Havens, K. E., Joyner, A. R., McCarthy, M. J., Newell, S. E., et al. (2016). Mitigating cyanobacterial harmful algal blooms in aquatic ecosystems impacted by climate change and anthropogenic nutrients. *Harmful Algae* 54, 213–222. doi: 10.1016/j.hal.2015.09.009

Petar, Ž., Marija, G. U., Koraljka, K. B., Anđelka, P.-M., and Judit, P. (2014). Morpho-functional classifications of phytoplankton assemblages of two deep karstic lakes. *Hydrobiologia* 740 (1), 147–166. doi: 10.1007/s10750-014-1950-1

Pinckney, J. L., Benitez-Nelson, C. R., Thunell, R. C., Muller-Karger, F., Lorenzoni, L., Troccoli, L., et al. (2015). Phytoplankton community structure and depth distribution changes in the Cariaco Basin between 1996 and 2010. *Deep Sea Res. Part I: Oceanogr. Res. Papers* 101, 27–37. doi: 10.1016/j.dsr.2015.03.004

Preisendorfer, R. W. (1986). Secchi disk science: Visual optics of natural waters 1. *Limnol. Oceanogr.* 31 (5), 909–926. doi: 10.4319/lo.1986.31.5.0909

R Development Core Team. (2014). *R: A language and environment for statistical computing* (Vienna, Austria: R Foundation for Statistical Computing).

Rangel, L. M., Silva, L. H., Rosa, P., Roland, F., and Huszar, V. L. (2012). Phytoplankton biomass is mainly controlled by hydrology and phosphorus concentrations in tropical hydroelectric reservoirs. *Hydrobiologia* 693 (1), 13–28. doi: 10.1007/s10750-012-1083-3

Rasconi, S., Winter, K., and Kainz, M. J. (2017). Temperature increase and fluctuation induce phytoplankton biodiversity loss–Evidence from a multi-seasonal mesocosm experiment. *Ecol. Evol.* 7 (9), 2936–2946. doi: 10.1002/ece3.2889

Redfield, A. C. (1958). The biological control of chemical factors in the environment. *Am. Sci.* 46 (3), 230A–2221. doi: 10.1086/646891

Reynolds, C., and Irish, A. (1997). Modelling phytoplankton dynamics in lakes and reservoirs: the problem of in-situ growth rates. *Hydrobiologia* 349 (1-3), 5–17. doi: 10.1023/a:1003020823129

Reynolds, C. S., Huszar, V., Kruk, C., Naselli-Flores, L., and Melo, S. (2002). Towards a functional classification of the freshwater phytoplankton. *J. Plankton Res.* 24 (5), 417–428. doi: 10.1093/plankt/24.5.417

Reynolds, C. (1984). Phytoplankton periodicity: the interactions of form, function and environmental variability. *Freshw. Biol.* 14 (2), 111–142. doi: 10.1111/j.1365-2427.1984.tb00027.x

Reynolds, C. S. (1989). Physical determinants of phytoplankton succession. (Springer Plankton Ecol: Succession In Plankton Communities), 9–56. doi: 10.1007/978-3-642-74890-5_2

Reynolds, C. S. (2006). *The ecology of phytoplankton* (Cambridge University Press). doi: 10.1017/CBO9780511542145

Richardson, J., Feuchtmayr, H., Miller, C., Hunter, P., Maberly, S. C., and Carvalho, L. (2019). The response of cyanobacteria and phytoplankton abundance to warming, extreme rainfall events and nutrient enrichment. *Global Change Biol.* doi: 10.1111/gcb.14701

Rodrigues, L. C., Simões, N. R., Bovo-Scomparin, V. M., Jati, S., Santana, N. F., Roberto, M. C., et al. (2015). Phytoplankton alpha diversity as an indicator of environmental changes in a neotropical floodplain. *Ecol. Indic.* 48, 334–341. doi: 10.1016/j.ecolind.2014.08.009

Rodrigues, L. C., Pivato, B. M., Vieira, L. C. G., Bovo-Scomparin, V. M., Bortolini, J. C., Pineda, A., et al. (2018). Use of phytoplankton functional groups as a model of spatial and temporal patterns in reservoirs: a case study in a reservoir of central Brazil. *Hydrobiologia* 805 (1), 147–161. doi: 10.1007/s10750-017-3289-x

Rozema, P., Venables, H., Van De Poll, W., Clarke, A., Meredith, M., and Buma, A. (2017). Interannual variability in phytoplankton biomass and species composition in northern Marguerite Bay (West Antarctic Peninsula) is governed by both winter sea ice cover and summer stratification. *Limnol. Oceanogr.* 62 (1), 235–252. doi: 10.1002/lno.10391

Søndergaard, M., Lauridsen, T. L., Johansson, L. S., and Jeppesen, E. (2017). Nitrogen or phosphorus limitation in lakes and its impact on phytoplankton biomass and submerged macrophyte cover. *Hydrobiologia* 795 (1), 35–48. doi: 10.1007/s10750-017-3110-x

Salmaso, N., and Padisák, J. (2007). Morpho-functional groups and phytoplankton development in two deep lakes (Lake Garda, Italy and Lake Stechlin, Germany). *Hydrobiologia* 578 (1), 97–112. doi: 10.1007/s10750-006-0437-0

Salmaso, N., Naselli-Flores, L., and Padisak, J. (2015). Functional classifications and their application in phytoplankton ecology. *Freshw. Biol.* 60 (4), 603–619. doi: 10.1111/fwb.12520

Secchi, A. (1866). "Relazione della Esperienze Fatta a Bordo della Pontificia Pirocorvetta L'lmmacolata Conceziorze per Determinare La Transparenza de1 Mare (Reports on Experiments made on Board the Papal Steam Sloop L'lmmacolata Concezione to Determine the Transparency of the Sea)," in *From Cmdr. A. Cialdi, Sul moto ondoso de1 mare e su le correnti di esso specialment auquelle littorali, 2nd ed.* (Dep. of the Navy, Office of Chief of Naval Operations). ON1 Transl. A-655, Op-923 M4B., pp. 258e288 (in Italian).

Shannon, C. E. (1948). A mathematical theory of communication. *Bell Syst. Tech. J.* 27 (3), 379–423. doi: 10.1002/j.1538-7305.1948.tb00917.x

Smith, V. H. (1986). Light and nutrient effects on the relative biomass of blue-green algae in lake phytoplankton. *Can. J. Fish. Aquat. Sci.* 43 (1), 148–153. doi: 10.1139/f86-016

Sommaruga, R., and Augustin, G. (2006). Seasonality in UV transparency of an alpine lake is associated to changes in phytoplankton biomass. *Aquat. Sci.-Res. Across Boundaries* 68 (2), 129–141. doi: 10.1007/s00027-006-0836-3

Stanković, I., Vlahović, T., Gligora Udovič, M., Várbíró, G., and Borics, G. (2012). Phytoplankton functional and morpho-functional approach in large floodplain rivers. *Hydrobiologia* 698 (1), 217–231. doi: 10.1007/s10750-012-1148-3

Török, P., Krasznai, E., Bácsiné Béres, V., Bácsi, I., Borics, G., and Tóthmérész, B. (2016). Functional diversity supports the biomass-diversity humped-back relationship in phytoplankton assemblages. *Funct. Ecol.* 30 (9), 1593–1602. doi: 10.1111/1365-2435.12631

Thomas, M. K., Aranguren-Gassis, M., Kremer, C. T., Gould, M. R., Anderson, K., Klausmeier, C. A., et al. (2017). Temperature–nutrient interactions exacerbate sensitivity to warming in phytoplankton. *Global Change Biol.* 23 (8), 3269–3280. doi: 10.1111/gcb.13641

Tsiola, A., Pitta, P., Fodelianakis, S., Pete, R., Magiopoulos, I., Mara, P., et al. (2016). Nutrient limitation in surface waters of the oligotrophic Eastern Mediterranean Sea: an Enrichment Microcosm Experiment. *Microbial Ecol.* 71 (3), 575–588. doi: 10.1007/s00248-015-0713-5

Vallina, S. M., Cermeno, P., Dutkiewicz, S., Loreau, M., and Montoya, J. M. (2017). Phytoplankton functional diversity increases ecosystem productivity and stability. *Ecol. Modell.* 361, 184–196. doi: 10.1016/j.ecolmodel.2017.06.020

Vanni, M. J., Luecke, C., Kitchell, J. F., Allen, Y., Temte, J., and Magnuson, J. J. (1990). Effects on lower trophic levels of massive fish mortality. *Nature* 344 (6264), 333. doi: 10.1038/344333a0

Viktória, B., Török, P., Kókai, Z., Lukács, Á., Enikő, T., Tóthmérész, B., et al. (2017). Ecological background of diatom functional groups: Comparability of classification systems. *Ecol. Indic.* 82, 183–188. doi: 10.1016/j.ecolind.2017.07.007

Vinebrooke, D. R., Cottingham, L. K., Norberg, M. S. J., Dodson, I. S., Maberly, C. S., and Sommer, U. (2004). Impacts of multiple stressors on biodiversity and ecosystem functioning: The role of species co-tolerance. *Oikos* 104 (3), 451–457. doi: 10.1111/j.0030-1299.2004.13255.x

Wang, X., Qin, B., Gao, G., and Paerl, H. W. (2010). Nutrient enrichment and selective predation by zooplankton promote Microcystis (Cyanobacteria) bloom formation. *J. Plankton Res.* 32 (4), 457–470. doi: 10.1093/plankt/fbp143

Wang, H., Zhu, R., Zhang, J., Ni, L., Shen, H., and Xie, P. (2018). A Novel and Convenient Method for Early Warning of Algal Cell Density by Chlorophyll Fluorescence Parameters and Its Application in a Highland Lake. *Front. Plant Sci.* 9, 869. doi: 10.3389/fpls.2018.00869

Watson, S. B., McCauley, E., and Downing, J. A. (1997). Patterns in phytoplankton taxonomic composition across temperate lakes of differing nutrient status. *Limnol. Oceanogr.* 42 (3), 487–495. doi: 10.4319/lo.1997.42.3.0487

Weithoff, G., Rocha, M. R., and Gaedke, U. (2015). Comparing seasonal dynamics of functional and taxonomic diversity reveals the driving forces underlying

phytoplankton community structure. *Freshw. Biol.* 60 (4), 758–767. doi: 10.1111/fwb.12527

Weithoff, G. (2003). The concepts of 'plant functional types' and 'functional diversity' in lake phytoplankton – a new understanding of phytoplankton ecology? *Freshw. Biol.* 48 (9), 1669–1675. doi: 10.1046/j.1365-2427.2003.01116.x

Wen, H., and Ma, G. (2011). Study of Water Quality and Algae in Erhai Lake during 2008-2010 [J]. *Environ. Sci. Manage.* 11, 009. doi: 10.3969/j.issn.1673-1212.2011.11.010

Winder, M., Reuter, J. E., and Schladow, S. G. (2008). Lake warming favours small-sized planktonic diatom species. *Proc. R. Soc. B: Biol. Sci.* 276 (1656), 427–435. doi: 10.1098/rspb.2008.1200

Wojciechowski, J., Heino, J., Bini, L. M., and Padial, A. A. (2017). Temporal variation in phytoplankton beta diversity patterns and metacommunity structures across subtropical reservoirs. *Freshw. Biol.* 62 (4), 751–766. doi: 10.1111/fwb.12899

Wondie, A., Mengistu, S., Vijverberg, J., and Dejen, E. (2007). Seasonal variation in primary production of a large high altitude tropical lake (Lake Tana, Ethiopia): effects of nutrient availability and water transparency. *Aquat. Ecol.* 41 (2), 195–207. doi: 10.1007/s10452-007-9080-8

Wu, Z., Cai, Y., Liu, X., Xu, C. P., Chen, Y., and Zhang, L. (2013). Temporal and spatial variability of phytoplankton in Lake Poyang: the largest freshwater lake in China. *J. Great Lakes Res.* 39 (3), 476–483. doi: 10.1016/j.jglr.2013.06.008

Wu, N., Dong, X., Liu, Y., Wang, C., Baattrup-Pedersen, A., and Riis, T. (2017). Using river microalgae as indicators for freshwater biomonitoring: Review of published research and future directions. *Ecol. Indic.* 81, 124–131. doi: 10.1016/j.ecolind.2017.05.066

Xie, P., and Liu, J. (2001). Practical success of biomanipulation using filter-feeding fish to control cyanobacteria blooms: a synthesis of decades of research and application in a subtropical hypereutrophic lake. *Sci. World J.* 1, 337–356. doi: 10.1100/tsw.2001.67

Yang, J., Yu, X., Liu, L., Zhang, W., and Guo, P. (2012). Algae community and trophic state of subtropical reservoirs in southeast Fujian, China. *Environ. Sci. Pollut. Res.* 19 (5), 1432–1442. doi: 10.1007/s11356-011-0683-1

Zhang, X., Xie, P., and Huang, X. (2008). A review of nontraditional biomanipulation. *Sci. World J.* 8, 1184–1196. doi: 10.1100/tsw.2008.144

Zhu, K., Bi, Y., and Hu, Z. (2013). Responses of phytoplankton functional groups to the hydrologic regime in the Daning River, a tributary of Three Gorges Reservoir, China. *Sci. Total Environ.* 450, 169–177. doi: 10.1016/j.scitotenv.2013.01.101

Zhu, R., Wang, H., Chen, J., Shen, H., and Deng, X. (2018). Use the predictive models to explore the key factors affecting phytoplankton succession in Lake Erhai, China. *Environ. Sci. Pollut. Res.* 25 (2), 1283–1293. doi: 10.1007/s11356-017-0512-2

Zwart, J. A., Solomon, C. T., and Jones, S. E. (2015). Phytoplankton traits predict ecosystem function in a global set of lakes. *Ecology* 96 (8), 2257–2264. doi: 10.1890/14-2102.1

Conflict of Interest: The authors declare that the research was conducted in the absence of any commercial or financial relationships that could be construed as a potential conflict of interest.

frontiers in Plant Science

ORIGINAL RESEARCH
published: 20 March 2020
doi: 10.3389/fpls.2020.00306

Site-Specific Gene Knock-Out and On-Site Heterologous Gene Overexpression in *Chlamydomonas reinhardtii* via a CRISPR-Cas9-Mediated Knock-in Method

*Jongrae Kim†, Sangmuk Lee†, Kwangryul Baek and EonSeon Jin**

Department of Life Science, Research Institute for Natural Science, Hanyang University, Seoul, South Korea

Chlamydomonas reinhardtii is being transformed from a model organism to an industrial organism for the production of pigments, fatty acids, and pharmaceuticals. Genetic modification has been used to increase the economic value of *C. reinhardtii*. However, low gene-editing efficiency and position-effects hinder the genetic improvement of this microorganism. Recently, site-specific double-stranded DNA cleavage using CRISPR-Cas9 system has been applied to regulate a metabolic pathway in *C. reinhardtii*. In this study, we proved that site-specific gene expression can be induced by CRISPR-Cas9-mediated double-strand cleavage and non-homologous end joining (NHEJ) mechanism. The CRISPR-Cas9-mediated knock-in method was adopted to improve gene-editing efficiency and express the reporter gene on the intended site. Knock-in was performed using a combination of ribonucleoprotein (RNP) complex and DNA fragment (antibiotics resistance gene). Gene-editing efficiency was improved via optimization of a component of RNP complex. We found that when the gene *CrFTSY* was targeted, the efficiency of obtaining the desired mutant by the knock-in method combined with antibiotic resistance was nearly 37%; 2.5 times higher than the previous reports. Additionally, insertion of a long DNA fragment (3.2 and 6.4 kb) and site-specific gene expression were analyzed. We demonstrated the knock-out phenotype of *CrFTSY* and on-site inserted gene expression of luciferase and mVenus at the same time. This result showed that CRISPR-Cas9-mediated knock-in can be used to express the gene of interest avoiding position-effects in *C. reinhardtii*. This report could provide a new perspective to the use of gene-editing. Furthermore, the technical improvements in genetic modification may accelerate the commercialization of *C. reinhardtii*.

Keywords: *Chlamydomonas reinhardtii*, genetic modification, CRISPR-Cas9, knock-in, on-site gene overexpression

OPEN ACCESS

Edited by:
Goetz Hensel,
Leibniz Institute of Plant Genetics and Crop Plant Research (IPK), Germany

Reviewed by:
Fantao Kong,
Dalian University of Technology, China
Sang Jun Sim,
Korea University, South Korea
Zhangli Hu,
Shenzhen University, China

***Correspondence:**
EonSeon Jin
esjin@hanyang.ac.kr

† These authors have contributed equally to this work

Specialty section:
This article was submitted to Plant Biotechnology, a section of the journal Frontiers in Plant Science

Received: *04 November 2019*
Accepted: *03 March 2020*
Published: *20 March 2020*

Citation:
Kim J, Lee S, Baek K and Jin E (2020) Site-Specific Gene Knock-Out and On-Site Heterologous Gene Overexpression in Chlamydomonas reinhardtii via a CRISPR-Cas9-Mediated Knock-in Method. Front. Plant Sci. 11:306. doi: 10.3389/fpls.2020.00306

INTRODUCTION

Chlamydomonas reinhardtii is widely used as a model organism and considered to be a potential cell factory to produce value-added compounds (Khan et al., 2018; Salomé and Merchant, 2019). Production of compounds such as zeaxanthin, sesquiterpene, bio-hydrogen, and human epidermal growth factor, have been reported in *C. reinhardtii* (Torzillo and Seibert, 2013; Lauersen et al., 2016; Baek et al., 2018; Baier et al., 2018a). These reports have increased the attention on the commercial use of *C. reinhardtii*. Moreover, the availability of *C. reinhardtii* as a biotechnological platform has been maximized through easy genetic modification techniques (Scaife et al., 2015).

Genetic modifications have been used to enhance the production of value-added compounds and produce fine chemicals in *C. reinhardtii* (Fu et al., 2019; Salomé and Merchant, 2019). Although gene transformation in *C. reinhardtii* is well-developed and easy, gene overexpression in *C. reinhardtii* is considered to be a huge obstacle for the advancement of the industry (Doron et al., 2016). Strategies such as developing a strong promoter (Kumar et al., 2013; Scranton et al., 2016; López-Paz et al., 2017), increasing translation using introns (Baier et al., 2018b), increasing gene expression stability using self-cleaving peptides (Rasala et al., 2012; Plucinak et al., 2015), developing a new reporter system using ferredoxin fused hydrogenase for effective screening (Eilenberg et al., 2016), and sequence-based optimization of RNA transcription (Weiner et al., 2018) have been developed for enhancing gene overexpression. The gene expression system is gradually being optimized by improving the technique. Though gene expression is notably advanced in *C. reinhardtii*, random insertion of the transformed gene is still problematic (Weiner et al., 2018; Jia et al., 2019). The random insertion leads to different levels of protein expression of the same gene called position-effect and also causes unexpected mutations. Therefore, the present study aimed to improve the heterologous gene expression technique by avoiding position-effects and inserting genes effectively at the desired site.

For the specific gene knock-out, gene-editing techniques like zinc-finger nuclease (ZFN) and transcription activator-like effector nuclease (TALEN) are used to create specific double-stranded DNA cleavages (Gaj et al., 2013). However, these techniques have high off-target mutation tendency and low feasibility (Gupta and Musunuru, 2014). Using the clustered regularly interspaced short palindromic repeats-associated protein 9 (CRISPR-Cas9) in eukaryotes, researchers can edit (cleave and knock-out) specific locations on genome more easily (Jinek et al., 2012; Cho et al., 2013; Cong et al., 2013; Mali et al., 2013). CRISPR-Cas9 system requires three basic components: the nuclease CRISPR-associated protein 9 (Cas9) cleaving the *RuvC* site which is 3-nucleotide far from PAM, a CRISPR RNA (crRNA) containing a 20-base pair sequence complementary to the target DNA, and a trans-activating crRNA (tracrRNA). crRNA and tracrRNA can be physically linked to form single guide RNA (gRNA) (Jinek et al., 2012). In *C. reinhardtii*, the CRISPR-Cas9 was first applied via DNA vector system in 2014 and recently ribonucleoprotein (RNP) system has been developed (Jiang et al., 2014; Baek et al., 2016; Guzmán-Zapata et al., 2019). CRISPR-Cas9 system is the ideal tool for gene-editing; however, it requires efficient selective markers for reducing the time and labor. Presently, phenotypic changes such as visual changes are used to improve the selection efficiency, however, the method is less efficient, requires a lot of labor (Baek et al., 2016; Shin et al., 2016; Greiner et al., 2017; Jeong et al., 2017b), and is not suitable for most genes. Therefore, gene-editing methods using counter-selective markers such as adenine phosphoribosyl transferase (APT), nitrate reductase (NR), peptidylprolyl isomerase (FKB12), tryptophan synthase beta subunit (TSB), and orotidine 5′-phosphate decarboxylase (UMP) have been recently proposed (Shin et al., 2016; Wang et al., 2016; Jiang and Weeks, 2017; Serif et al., 2018; Guzmán-Zapata et al., 2019). Counter selection can be efficient; however, they are eventually dependent on specific phenotypes. To overcome this limitation, pre-selection using antibiotic resistance for enhancing the efficiency of gene-editing has been reported (Shin et al., 2016; Jiang and Weeks, 2017). However, the conditions have not been optimized and the gene-editing efficiency reported has not exceeded >15% till date (Greiner et al., 2017).

As mentioned above, advanced gene expression tools and gene-editing techniques have played a major role in increasing the commercial use of *C. reinhardtii*. However, the efficiency of these methods is low and the rate of unintended mutations is high. In this study, to develop the new technique of genetic modification in *C. reinhardtii*, we investigated the knock-in method to improve gene-editing efficiency while inducing gene expression at the desired location. Phenotypic studies indicated that the two desired characteristics were obtained simultaneously. We optimized the technique that increased gene-editing efficiency to >30% and successfully demonstrated site-specific gene expression by avoiding random mutations.

MATERIALS AND METHODS

Culture Condition

Chlamydomonas reinhardtii CC4349, CC124, and CC503 (purchased from *Chlamydomonas* Resource Center, University of Minnesota, United States) were maintained photoheterotrophically in Tris-Acetate-Phosphate (TAP) medium at 25°C with continuous light (80 μmol photons m^{-2} s^{-1}) on an orbital shaker (100 rpm). The cells were cultivated till the log phase in liquid TAP medium under the same conditions for all the experiments. For the selection and maintenance of transformant lines, solid TAP medium fortified with 30 μg/mL hygromycin-B (Thermo Fisher, MA, United States) for ΔCrFTSY-Ga and with 30 μg/mL hygromycin-B, 30 μg/mL paromomycin (Sigma-Aldrich, MO, United States) for ΔCrFTSY-mV, were used.

Knock-in Mutant Generation by CRISPR-Cas9

To optimize the gene-specific knock-out efficiency, RNP method was used and the optimal conditions were determined with slight

modification according to the method described previously (Baek et al., 2016). The target sequence of *CrFTSY* and the gRNA sequence, 5′-CGATCTTCAGAGCAGTGCGG-3′, that was the same as that of the previous study (Baek et al., 2016), were used to avoid the off-target effect. Cas9 protein was purchased from ToolGen Inc. (Seoul, South Korea) and gRNA was synthesized *in vitro* using GeneArt™ Precision gRNA Synthesis Kit (Thermo Fisher, MA, United States) following the manufacturer's protocol. The inserted DNA fragments, *aph7* gene (aminoglycoside phosphotransferase7, resistance against hygromycin B) (1.6 kb) (**Figure 1** left) and *aph7-GLuc* (Gaussia Luciferase) (3.2 kb) (**Figure 2A**) DNA cassettes, were amplified by polymerase chain reaction using amplifying primers (sense: 5′-CGGTTCCTGGCCTTTTGCTGG-3′ and antisense: 5′-CAAGTACCATCAACTGACGTTACATTCTG-3′). The inserted DNA fragment, *aph8* (aminoglycoside phosphotransferase8, resistance against paromomycin) – *mVenus* (yellow fluorescence protein) – *aph7* (6.4 kb) (**Figure 6A**) DNA cassette, was linearized by restriction enzyme (*Sca*I, *Spe*I). All the inserted DNA fragments were purified by agarose gel extraction.

To generate the target-specific knock-in mutant using RNP in *Chlamydomonas*, 2×10^7 cells were transformed with Cas9 protein premixed with gRNA (RNP complex). Lyophilized Cas9 protein was dissolved in gRNA solution prepared with nuclease-free water and the mixture was incubated for 10 min at room temperature (20–25°C) to make a complex. Cells mixed with the RNP complex were transferred into 4 mm cuvettes and transformed by Gene Pulser Xcell™ Electroporation Systems (Bio-Rad, CA, United States) set at 600 V, 50 μF, and 200 Ω. After transformation, the cells were incubated overnight (16–20 h) and spread on the selective medium. Colonies appeared within 2 weeks. The antibiotic resistance colonies were transferred to liquid medium for the sequence analysis. This pre-selected colony number is classified as "candidate" for the calculation of knock-in efficiency.

Identification of DNA Sequence of CrFTSY and Inserted DNA Sequence

The genomic DNA was prepared from the colonies grown on selective medium using the Chelex-100 method (Wan et al., 2011). Targeted region (around 200 bp from gRNA sequence) was amplified by PCR with specific primers (sense: 5′-GGTGTCCCCGCAATCACCAAC-3′, antisense: 5′-CACCCACACCCACCTTGAGCGAG-3′). The PCR product was purified by agarose gel electrophoresis and sequenced using Sanger sequencing by Macrogen Inc. (Seoul, South Korea).

Measurement of Chlorophyll Content

Wild-type and mutant cells were cultured in liquid TAP medium untill the mid-log phase. To make comparison of colorimetric analysis, the cultured cells were collected from the liquid media, and 2.5×10^6 cells were deposited on solid TAP medium. The cells were incubated for 24 h and the difference in color characteristics was compared. For measurement of the chlorophyll contents, 1×10^7 cells were suspended in 80% (v/v) acetone, and the absorbance was measured by spectrophotometer at wavelength of 663 and 647 nm. The formula used for calculating the content is given by Melis et al. (1987).

Measurement of Gaussia Luciferase Activity

Luciferase activity was measured by a previously reported protocol (Kim et al., 2018) with slight modifications to confirm *GLuc* expression. *GLuc* is secreted in the medium hence, its activity was measured using the complete cell culture (Ruecker et al., 2008) and it is more sensitive than using only the cells. The mutant cells were cultured till the absorbance at 750 nm reached 1.0 indicating mid-log phase. A small volume (200 μL) of culture was used for the luciferase assay using the *Renilla* Luciferase Assay Kit (Promega, WI, United States). The cells were suspended in 40 μL of lysis buffer and lysed by vigorous vortexing. The lysed cells were pelleted by centrifugation at 13,000 rpm for 5 min. Then, 80 μL supernatant was mixed with equal volume of substrate solution. The chemiluminescence was measured immediately after mixing the two solutions in a Glo Max™ 20/20 luminometer (Promega, WI, United States). The statistical difference was analyzed by Student's *t*-test (p-value < 0.05).

Fluorescence Microscopic Analysis

ΔCrFTSY-mV was cultivated in selective medium as mentioned above. Five microliters of cultured cells were dropped on a glass slide and covered with a coverslip. Fluorescence was detected by a fluorescence microscope (Eclipse Ni, Nikon, Tokyo, Japan). Fluorescence detection wavelengths were 540 ± 20 nm with YFP filter for mVenus and 630 ± 30 nm with Texas RED filter for auto-fluorescence of chlorophyll. The magnification was 400×.

Southern Blot Analysis

Southern blot was used to confirm single DNA insertion in mutants. Genomic DNA was extracted from cells in the log phase by the CTAB method (Porebski et al., 1997). The genomic DNA was isolated (20 μg) and digested by *Pvu*II or *Sma*I restriction enzymes. Digested genomic DNA was separated using 0.8% agarose gel and transferred to a nylon membrane by capillary transfer. Membrane attached DNA was developed through hybridization with an aph7 probe and amplified by PCR with specific primers (sense: 5′-ATGATTCCTACGCGAGCCTG-3′, antisense: 5′-ATCCGGCTCATCACCAGGTA-3′) using the Gene Images AlkPhos Direct Labeling and Detection System (Amersham, Little Chalfont, Bucks, United Kingdom). The process was carried out according to the manufacturer's protocol.

Western Blot Analysis

Cultivated cells (1×10^6) were boiled in SDS-PAGE loading buffer, electrophoresed on 15% SDS-polyacrylamide gels, and transferred to a PVDF membrane using Xcell II blot module

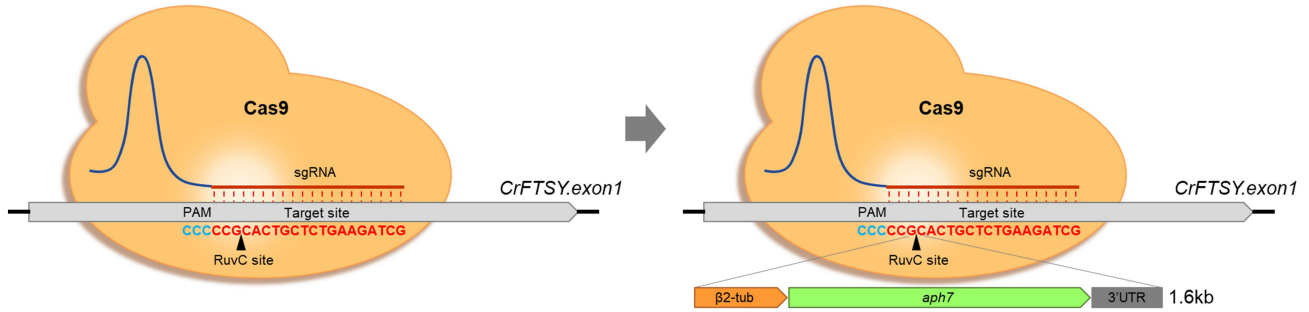

FIGURE 1 | Optimization of gene-editing condition based on CRISPR-Cas9-mediated knock-in strategy. Formal knock-out method by CRISPR-Cas9 **(Left)** and knock-in with donor DNA **(Right)**. The inserted DNA fragment consisted of β2-tubulin promoter, aph7 (hygromycin-B resistance), rbcs2 3′UTR.

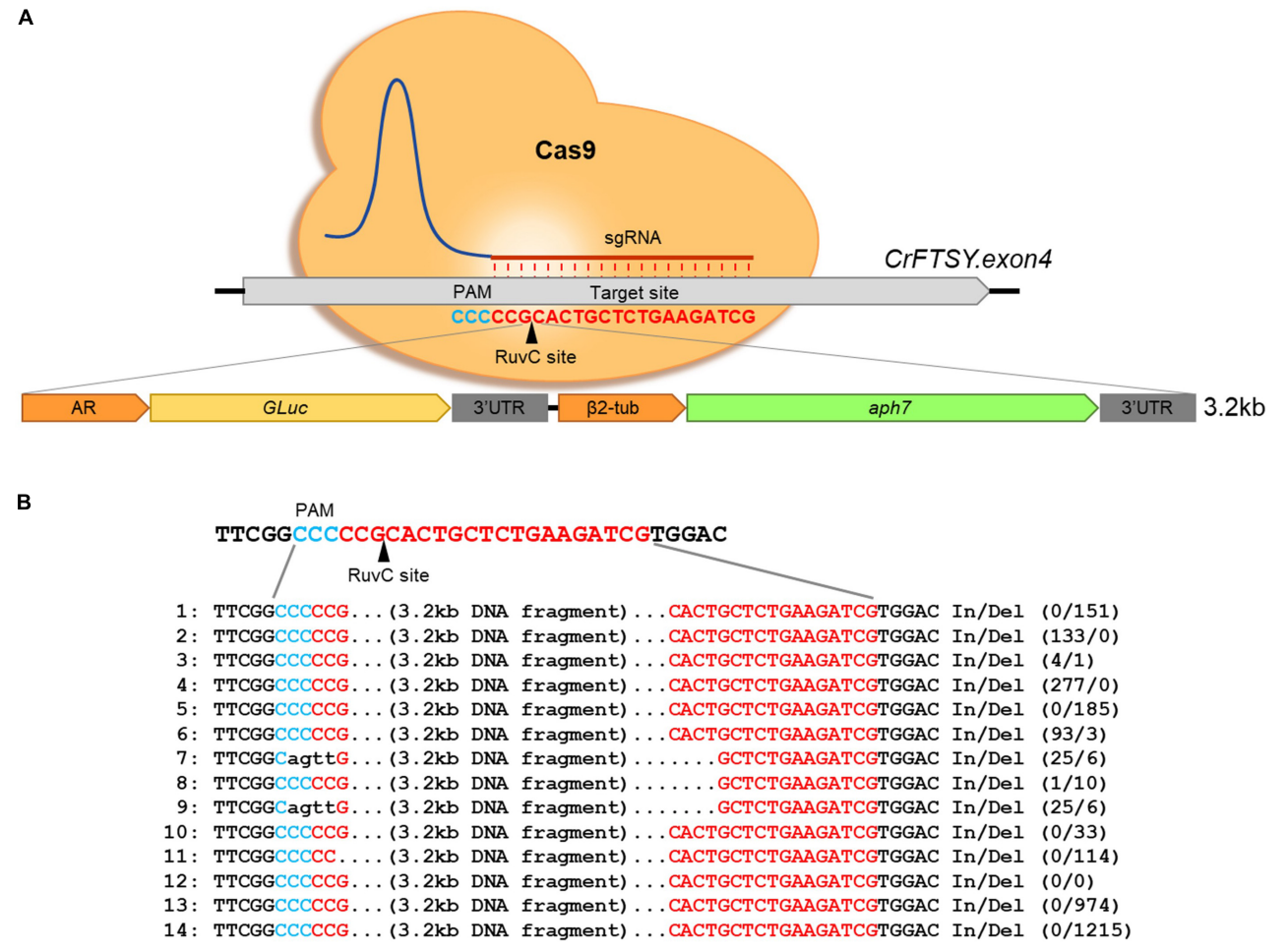

FIGURE 2 | Target-specific long length DNA insertion via CRISPR-Cas9-mediated knock-in method. **(A)** Schematic diagram of large DNA fragment insertion in *CrFTSY*. Target-specific DNA cleavage via CRISPR-Cas9 and insertion of the large gene of interest (3.2 kb, *GLuc-aph7* DNA cassette) simultaneously. **(B)** Sequence analysis done by the Sanger sequencing method to identify the inserted DNA fragment on Δ*CrFTSY*-Ga.

(Thermo Fisher, MA, United States). GLuc antibody (NEB, MA, United States) was used to detect GLuc protein. ATP-β antibody (Agrisera, Vännäs, Sweden) was used as a reference. HRP-conjugated goat anti-rabbit IgG (H + L) antibody (Life Technologies, CA, United States) was used as a secondary antibody. GLuc and ATP-β were visualized on an X-ray film by chemiluminescence using EPD Western Reagent (ELPIS-BIOTECH, Daejeon, South Korea).

RESULTS

Improvement of Gene-Editing Efficiency by CRISPR-Cas9-Mediated Knock-in

In this study, the selective marker system *aph7* DNA cassette was used to optimize the knock-in method in *C. reinhardtii*. This strategic knock-in method was induced by CRISPR-Cas9-mediated knock-out, and the selective marker gene was inserted into the cleaved site by NHEJ (**Figure 1**). The mutants were screened more effectively by the expression of the antibiotic selective marker in the inserted DNA fragment.

Although the knock-in method has been reported previously, the gene-editing efficiency was very low (under 15%). Therefore, in this study gene-editing efficiency was analyzed by using different concentrations of RNP complex required for transformation (**Table 1**). Every single experiment resulted in a different number of colonies but a similar percentage of positive colonies (**Supplementary Figure 1**). The gene-editing efficiency of *CrFTSY* (Δ*CrFTSY*) was observed to be maximum at 36.8%, when transformed with 100 μg Cas9 and 70 μg gRNA. Even on transformation with 10 μg Cas9 and 7 μg gRNA, Δ*CrFTSY* efficiency was >16.5%, which was higher than previously reported (Baek et al., 2016; Shin et al., 2016; Greiner et al., 2017). Thus, we optimized the concentration of RNP complex for maximum gene-editing efficiency. Additionally, we investigated the gene-editing efficiency depending on the presence or absence of a cell wall. The gene-editing efficiency in *C. reinhardtii* strains CC503 (no cell wall) and CC124 (with cell wall) were observed under the same method and it was found to be similar to that of *C. reinhardtii* CC4349 (**Supplementary Figure 2**). This result indicated that the knock-in method is universally applicable independent of the cell type.

Insertion of Long-Length DNA Fragment on Intended Site

In the gene expression using foreign DNA, transformed foreign DNA integrates in the nuclear genome of *C. reinhardtii*. This DNA integration in the genome predominantly leads to unexpected mutations and position-effects (Leon and Fernandez, 2007). Therefore, we investigated the possibility of on-site foreign gene expression through the knock-in method to reduce position effects. Firstly, a 3.2 kb long DNA fragment was transformed into the target site of by the knock-in method described above (**Figure 2A**). Large DNA insertion in the target site was confirmed by genomic PCR in 14 positives among 39 candidates (36% gene-editing efficiency) of ΔCrFTSY_Ga colonies in which *GLuc-aph7* DNA cassette was inserted into *CrFTSY* (**Supplementary Figure 3**). ΔCrFTSY-Ga DNA was sequenced and compared with the expected sequence after integration (**Figure 2B** and **Supplementary Data Sheet 2**). Targeted DNA sequences on *CrFTSY* were neatly cleaved by Cas9 in ΔCrFTSY-Ga mutants except mutants 7 and 9. Among the 14 positive mutants, clean insertion without any In/Del was detected only in mutant 12. As evident in this result, the inserted DNA sequence resulted in mutations during integration into the genome. Thus, it is important to identify the exact sequence of the insertion site. Although the problems related to the mutations of inserted DNA remain unsolved, however, this result showed that the insertion of DNA longer than 3 kb is possible at the desired site.

Expression of the Foreign Gene at the Desired Site by Knock-in

We also analyzed the expression of the foreign genes at the desired site. To confirm the normal expression of *GLuc* inserted at the target site, we confirmed the copy number of DNA insert in ΔCrFTSY-Ga mutants. Mutant 2 was excluded in the further analysis as it was mixed with non-mutant cells. Mutants 13 and 14 were also excluded as the promoter sequence of *GLuc* got deleted. Southern blot analysis was performed to determine the copy number of DNA insert. Genomic DNA was digested by restriction enzymes and hybridized with the specific probe. All ΔCrFTSY-Ga mutants had a single copy of the DNA insert (**Figure 3** and **Supplementary Figure 4**). This result suggests that luciferase activity observed in the next experiment was due to a single Gaussia luciferase gene inserted on *CrFTSY*.

Chlamydomonas reinhardtii with mutation in *CrFTSY* appeared to be pale green in color compared to the color of the wild type due to the reduction in chlorophyll content on a theoretical basis (Kirst et al., 2012). We observed that 11 ΔCrFTSY-Ga mutants obtained were pale green in color compared to that of the wild type on solid TAP medium (**Figure 4A**). Moreover, to validate this visual difference between WT and mutants, we measured the chlorophyll content of all the samples, including WT (**Figure 4B**). The levels of chlorophyll-a (4.80 ± 0.76 nmol mL^{-1}) and -b (1.34 ± 0.53 nmol mL^{-1}) in

TABLE 1 | Gene-editing efficiency obtained via the knock-in method.

	RNP complex							
Cas9 protein (μg)	200	10	1.6	200	100	50	20	10
gRNA (μg)	140	7.5	0.32	140	70	35	14	7
Donor DNA (μg)	0	1	0.3	1	1	1	1	1
	Gene-editing efficiency							
Positives (%)	0.56	1.4	14.8	35.2	36.8	33.8	27.4	16.5
References	Baek et al., 2016	Shin et al., 2016	Greiner et al., 2017	In this study				

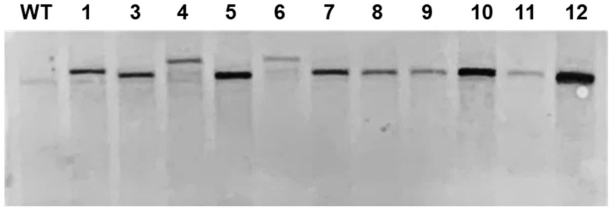

FIGURE 3 | Southern blot for validation of copy number of an inserted DNA fragment. Extracted genomic DNA was digested by *Sma*I and blotted on a nylon membrane. The *aph7* probe was used for detection of DNA integration.

A

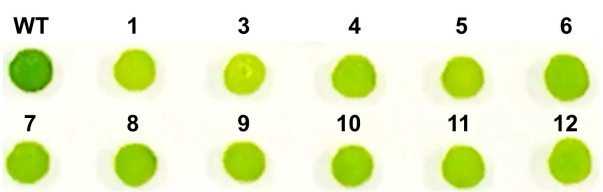

B

Chlorophylls (nmol/mL)	WT	1	3	4	5	6
Chl a	7.63±0.43	4.09±0.66	6.15±2.48	4.66±0.25	4.46±0.05	5.19±0.70
Chl b	3.53±0.83	0.97±0.40	2.13±1.07	1.23±0.34	1.20±0.42	1.54±0.45

7	8	9	10	11	12
4.84±0.49	4.77±0.82	4.67±0.70	4.28±0.59	4.82±0.54	4.83±0.54
1.28±0.43	1.32±0.53	1.20±0.48	1.13±0.50	1.31±0.51	1.40±0.71

FIGURE 4 | Phenotypic characteristics of *CrFTSY* knock-out. Wild-type and ΔCrFTSY-Ga mutants grew on TAP agar medium under 80 μmol photon m^{-2} s^{-1} light. **(A)** Pale green color was detected in ΔCrFTSY-Ga mutants compared to dark green color exhibited by wild type. **(B)** Amount (nmol mL^{-1}) of Chlorophyll-a and -b of ΔCrFTSY-Ga mutants (n = 3; the values shown are means ± SD).

ΔCrFTSY-Ga mutants were reduced to 63 and 38% of wild type chlorophyll-a and chlorophyll-b (7.63 ± 0.43 and 3.53 ± 0.83), respectively. Therefore, the chlorophyll a/b ratio was increased by 1.8 ± 0.2-fold in ΔCrFTSY-Ga mutants compared to that of wild type, as also shown in the previous report (Baek et al., 2016). The results clearly reflected the phenotypic differences when the *FTSY* was knocked out (**Figure 4**).

The foreign gene expression on the intended site was verified by confirming the protein expression of GLuc (**Supplementary Figure 5**) and measuring the luciferase activity (**Figure 5**). We used the cultured cells and medium together for the luciferase analysis as mentioned before. As shown in **Figure 5**, all Δ*CrFTSY*-Ga mutants successfully expressed *GLuc* while luciferase activity was negligible in the wild type. The results of this experiment demonstrated that a gene of interest can be expressed on the desired site without random insertional mutation. Mean difference between *GLuc* activity in 11 different mutants was 20%, which was significantly lower than the mean difference (75%) found in random integration mutants (Kim et al., 2018). This constant expression level in 11 mutants was possible due to the insertion of a single copy of DNA fragment at the intended site on the genome.

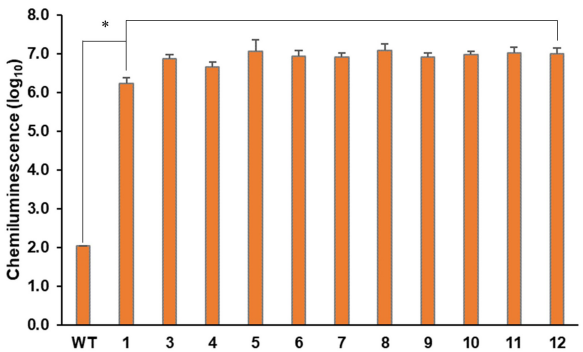

FIGURE 5 | Phenotypic characteristics of expression of the inserted DNA fragment. *Gaussia* luciferase assays from ΔCrFTSY-Ga mutants were performed in triplicate independently. The asterisk indicates the statistical difference determined by Student's t-test (n = 3; the values shown are means ± SD; $p < 0.05$).

Determination of the Maximum Size of DNA Fragment Inserted on Target by Knock-in

We tested the possibility of insertion of a DNA fragment larger than 3.2 kb through the knock-in method, which confirmed the insertion of a 6.4 kb long DNA fragment in the target site. For this additional experiment, we used the same methodology as described in the section "Expression of the Foreign Gene at the Desired Site by Knock-in." The DNA insertion in the target site was confirmed by genomic PCR. Four positives among 12 candidates (33% gene-editing efficiency) of ΔCrFTSY_mV in which *aph8-mVenus-aph7* DNA cassette was inserted into *CrFTSY* were obtained (**Supplementary Figure 6**). From the sequence analysis at the insertion site, we found long length In/Del mutations (**Figure 6A** and **Supplementary Data Sheet 2**). Two mutants (mutants 1 and 2) had 126 bp insertion and two different mutants (mutants 3 and 4) had around 700 bp deletion. As in the above result (**Figure 2**), In/Del occurred non-specifically in this experiment. Nevertheless, the knock-in method deleted the desired genes and reconfirmed that the introduction of DNA fragment for overexpression was effective. mVenus expression in the selected mutant was

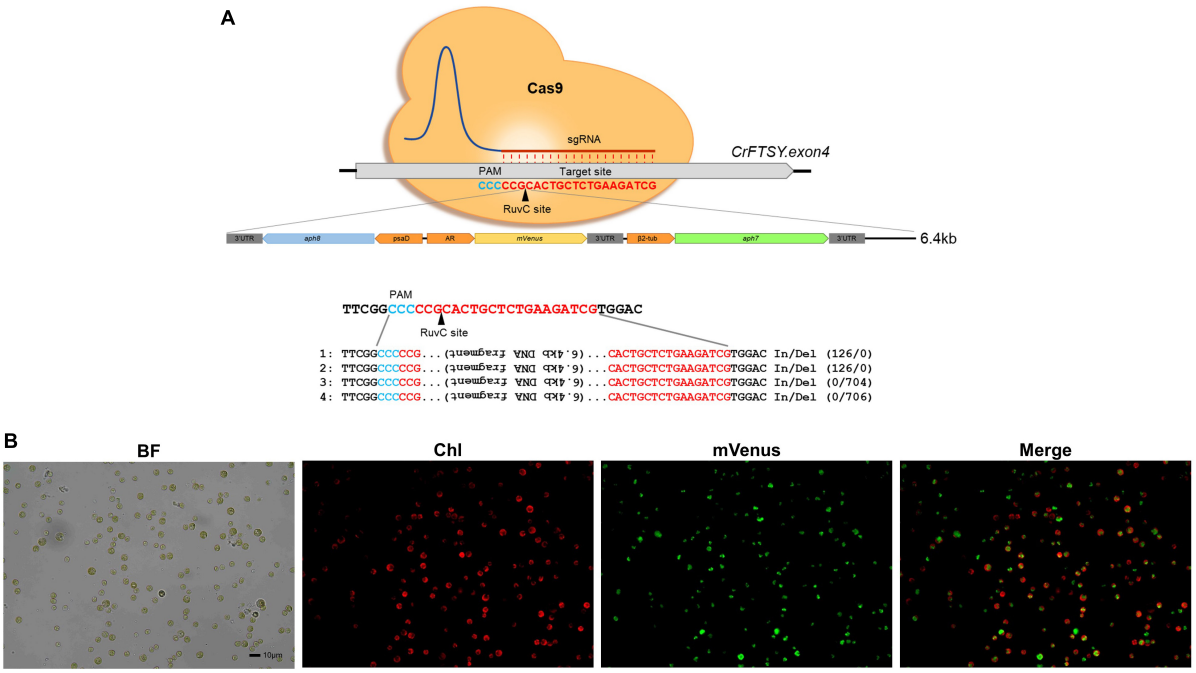

FIGURE 6 | Target specific 6.4 kb long DNA (*aph8–mVenus–aph7* DNA cassette) insertion via CRISPR-Cas9-mediated knock-in. **(A)** Sequence analysis of target site and inserted DNA fragment. **(B)** Visualization of mVenus expression in Δ*CrFTSY*_mV at insertion site by fluorescence microscopy (red, chlorophyll; green, *mVenus*). Scale bar indicates 10 μm.

visualized by fluorescence microscopy (**Figure 6B**). Hence, we confirmed that a DNA fragment of up to 6.4 kb long could be inserted at the desired location and overexpressed. From these results, we demonstrated that the CRISPR-Cas9-mediated knock-in method was an effective method that allowed the gene deletion and overexpression of foreign genes in a single experiment.

DISCUSSION

Increasing the commercial use of *C. reinhardtii* requires improvement of the strain by genetic modification for the production of high-value compounds. *C. reinhardtii* has been extensively studied for fundamental research and industrial use based on its genome sequence data and well-developed molecular tool kit (Scaife et al., 2015; Crozet et al., 2018; Salomé and Merchant, 2019). Moreover, the genetic modification techniques are highly developed and the engineering strategies of metabolic pathways are well established (Plucinak et al., 2015; Baier et al., 2018b; Fu et al., 2019; Kong et al., 2019).

Despite several refined concepts, the improvement of *C. reinhardtii* is still not sufficient and simple. Due to the non-specific disruption of genes generating the desired mutants has been difficult, hampering reverse-genetic studies (Fu et al., 2019; Park et al., 2019). The existing transformation methods of *C. reinhardtii* cannot target a specific gene, thus researchers cannot regulate precisely the desired genes (Leon and Fernandez, 2007; Jia et al., 2019; Kim et al., 2019). These problems can be overcome by the recently developed gene-editing techniques. Gene-editing techniques based on RNP using Cas9 proteins are being recognized as the most effective gene specific knock-out methods to date (Patel et al., 2019). Cas9-mediated gene knock-out has been reported for several genes and the use of donor DNA with RNP, called knock-in, has emerged recently. However, the gene-editing efficiency reported in previous studies was not satisfactory (Shin et al., 2016; Greiner et al., 2017; Jeong et al., 2017a).

Recently, some reports suggested that gene selection can be achieved with high yields (up to 30%) through counter selection without the use of antibiotic genes (Jiang and Weeks, 2017; Serif et al., 2018; Guzmán-Zapata et al., 2019). However, these methods are mostly functional for specific genes and cannot be applied universally.

In this study, we used the antibiotic gene (*aph7*) as donor DNA to ensure high selection efficiency for the optimization of the Cas9-mediated knock-in method. In contrast to the previously reported CRISPR-Cas9-mediated knock-out methods, the use of a selective marker in the knock-in method of our study enhanced the knock-out efficiency by inserting of an external DNA into the cleaved site (**Figure 1**). The method of using the antibiotic gene employed in this study has been proven to be generally applicable while effectively performing the gene-editing of other genes (*AGP* and *LCYE*) (unpublished data). Therefore, we suggest that the use of antibiotic genes as donor DNA is an efficient method when using the RNP-based gene-editing. In addition, through the optimization of RNP complex used in this study, the gene-editing efficiency was increased up to 37% (**Table 1** and

Supplementary Figure 1). These results indicate that the RNP complex of 100 μg:70 μg (Protein:gRNA) is optimal for the target specific gene editing in *C. reinhardtii*.

An additional benefit of establishing the knock-in method is that it avoids the position-effects of random mutations that occur during the transformation process. We strategically utilized this methodology to validate the expression of the gene of interest at the desired position (**Figures 2–5**). The successful expression of the report gene (*GLuc* and *mVenus*) and the fact that the single copy of DNA insert was integrated into genome showed that our strategy of avoiding position-effect and expressing the gene of interest at the target location successful (**Figures 3–6**). The success of our target-oriented gene insertion strategy could provide a new strategic perspective for future *C. reinhardtii* improvement studies.

In this paper, we reported an improved gene-editing technique. Despite several improvements in different techniques, researchers still face the problem of tedious processes for species improvement. Even though the target-oriented gene insertion based on knock-in method was performed, validation for the precise knock-in was still required. Besides, due to the lack of information on the sites effectively targeted by Cas9, the location of gene insertion is limiting, which unavoidably involves the deletion of one gene. Therefore, it is important to discover target locations with high gene-editing efficiency without affecting the biological function of the cell. As our results show in **Figures 2**, **6**, the inserted gene was integrated into genomic DNA by NHEJ, therefore it is necessary to develop a technique to prevent the mutation in sequences in the integration process.

DATA AVAILABILITY STATEMENT

The raw data supporting the conclusions of this article will be made available by the authors, without undue reservation, to any qualified researcher.

AUTHOR CONTRIBUTIONS

EJ and JK conceived and designed the experiments. KB confirmed the optimal condition of RNP. JK and SL performed the knock-in study and analyzed the gene expression. JK, SL, and EJ wrote the manuscript. All authors reviewed the manuscript.

FUNDING

This study was supported by the Korea Carbon Capture & Sequestration R&D Center (KCRC) (NRF-2014M1A8A1049273), and the Basic Core Technology Development Program for the Oceans and the Polar Regions (NRF-2015M1A5A1037053) of the National Research Foundation of Korea, Ministry of Science and ICT, Government of Korea.

SUPPLEMENTARY MATERIAL

The Supplementary Material for this article can be found online at: https://www.frontiersin.org/articles/10.3389/fpls.2020.00306/full#supplementary-material

REFERENCES

Baek, K., Kim, D. H., Jeong, J., Sim, S. J., Melis, A., Kim, J. S., et al. (2016). DNA-free two-gene knockout in *Chlamydomonas reinhardtii* via CRISPR-Cas9 ribonucleoproteins. *Sci. Rep.* 6:30620. doi: 10.1038/srep30620

Baek, K., Yu, J., Jeong, J., Sim, S. J., Bae, S., and Jin, E. (2018). Photoautotrophic production of macular pigment in a *Chlamydomonas reinhardtii* strain generated by using DNA−free CRISPR−Cas9 RNP−mediated mutagenesis. *Biotechnol. Bioeng.* 115, 719–728. doi: 10.1002/bit.26499

Baier, T., Kros, D., Feiner, R. C., Lauersen, K. J., MüLler, K. M., and Kruse, O. (2018a). Engineered fusion proteins for efficient protein secretion and purification of a human growth factor from the green microalga *Chlamydomonas reinhardtii*. *ACS Synth. Biol.* 7, 2547–2557. doi: 10.1021/acssynbio.8b00226

Baier, T., Wichmann, J., Kruse, O., and Lauersen, K. J. (2018b). Intron-containing algal transgenes mediate efficient recombinant gene expression in the green microalga *Chlamydomonas reinhardtii*. *Nucleic Acids Res.* 46, 6909–6919. doi: 10.1093/nar/gky532

Cho, S. W., Kim, S., Kim, J. M., and Kim, J.-S. (2013). Targeted genome engineering in human cells with the Cas9 RNA-guided endonuclease. *Nat. Biotechnol.* 31, 230–232. doi: 10.1038/nbt.2507

Cong, L., Ran, F. A., Cox, D., Lin, S., Barretto, R., Habib, N., et al. (2013). Multiplex genome engineering using CRISPR/Cas systems. *Science* 339, 819–823. doi: 10.1126/science.1231143

Crozet, P., Navarro, F. J., Willmund, F., Mehrshahi, P., Bakowski, K., Lauersen, K. J., et al. (2018). Birth of a photosynthetic chassis: a MoClo toolkit enabling synthetic biology in the microalga *Chlamydomonas reinhardtii*. *ACS Synth. Biol.* 7, 2074–2086. doi: 10.1021/acssynbio.8b00251

Doron, L., Segal, N. A., and Shapira, M. (2016). Transgene expression in microalgae—from tools to applications. *Front. Plant Sci.* 7:505. doi: 10.3389/fpls.2016.00505

Eilenberg, H., Weiner, I., Ben-Zvi, O., Pundak, C., Marmari, A., Liran, O., et al. (2016). The dual effect of a ferredoxin-hydrogenase fusion protein in vivo: successful divergence of the photosynthetic electron flux towards hydrogen production and elevated oxygen tolerance. *Biotechnol. Biof.* 9:182. doi: 10.1186/s13068-016-0601-3

Fu, W., Nelson, D. R., Mystikou, A., Daakour, S., and Salehi-Ashtiani, K. (2019). Advances in microalgal research and engineering development. *Curr. Opin. Biotechnol.* 59, 157–164. doi: 10.1016/j.copbio.2019.05.013

Gaj, T., Gersbach, C. A., and Barbas Iii, C. F. (2013). ZFN, TALEN, and CRISPR/Cas-based methods for genome engineering. *Trends Biotechnol.* 31, 397–405. doi: 10.1016/j.tibtech.2013.04.004

Greiner, A., Kelterborn, S., Evers, H., Kreimer, G., Sizova, I., and Hegemann, P. (2017). Targeting of photoreceptor genes in *Chlamydomonas reinhardtii* via zinc-finger nucleases and CRISPR/Cas9. *Plant Cell* 29, 2498–2518. doi: 10.1105/tpc.17.00659

Gupta, R. M., and Musunuru, K. (2014). Expanding the genetic editing tool kit: ZFNs, TALENs, and CRISPR-Cas9. *J. Clin. Invest.* 124, 4154–4161. doi: 10.1172/JCI72992

Guzmán-Zapata, D., Sandoval-Vargas, J. M., Macedo-Osorio, K. S., Salgado-Manjarrez, E., Castrejón-Flores, J. L., Oliver-Salvador, M. D. C., et al. (2019). Efficient editing of the nuclear APT reporter gene in *Chlamydomonas reinhardtii* via expression of a CRISPR-Cas9 module. *Int. J. Mol. Sci.* 20:1247. doi: 10.3390/ijms20051247

Jeong, J., Baek, K., Kirst, H., Melis, A., and Jin, E. (2017a). Loss of RP54 function leads to a truncated light-harvesting antenna size in *Chlamydomonas*

reinhardtii. *Biochim. Biophys. Acta Bioenerg.* 1858, 45–55. doi: 10.1016/j.bbabio.2016.10.007

Jeong, J., Baek, K., Yu, J., Kirst, H., Betterle, N., Shin, W., et al. (2017b). Deletion of the chloroplast LTD protein impedes LHCI import and PSI–LHCI assembly in *Chlamydomonas reinhardtii*. *J. Exp. Bot.* 69, 1147–1158. doi: 10.1093/jxb/erx457

Jia, B., Xie, X., Wu, M., Lin, Z., Yin, J., Huang, Y., et al. (2019). Understanding the functions of endogenous DOF transcript factor in *Chlamydomonas reinhardtii*. *Biotechnol. Biof.* 12:67. doi: 10.1186/s13068-019-1403-1

Jiang, W., Brueggeman, A. J., Horken, K. M., Plucinak, T. M., and Weeks, D. P. (2014). Successful transient expression of Cas9 and single guide RNA genes in *Chlamydomonas reinhardtii*. *Eukaryot. Cell* 13, 1465–1469. doi: 10.1128/EC.00213-14

Jiang, W. Z., and Weeks, D. P. (2017). A gene-within-a-gene Cas9/sgRNA hybrid construct enables gene editing and gene replacement strategies in *Chlamydomonas reinhardtii*. *Algal Res.* 26, 474–480. doi: 10.1016/j.algal.2017.04.001

Jinek, M., Chylinski, K., Fonfara, I., Hauer, M., Doudna, J. A., and Charpentier, E. (2012). A programmable dual-RNA–guided DNA endonuclease in adaptive bacterial immunity. *Science* 337, 816–821. doi: 10.1126/science.1225829

Khan, M. I., Shin, J. H., and Kim, J. D. (2018). The promising future of microalgae: current status, challenges, and optimization of a sustainable and renewable industry for biofuels, feed, and other products. *Microb. Cell Fact.* 17:36. doi: 10.1186/s12934-018-0879-x

Kim, J., Kwak, H. S., Sim, S. J., and Jin, E. (2019). Overexpression of malic enzyme isoform 2 in *Chlamydomonas reinhardtii* PTS42 increases lipid production. *Bioresour. Technol. Rep.* 7:100239. doi: 10.1016/j.biteb.2019.100239

Kim, J., Liu, L., Hu, Z., and Jin, E. (2018). Identification and functional analysis of the psaD promoter of *Chlorella vulgaris* using heterologous model strains. *Int. J. Mol. Sci.* 19:1969. doi: 10.3390/ijms19071969

Kirst, H., García-Cerdán, J. G., Zurbriggen, A., and Melis, A. (2012). Assembly of the light-harvesting chlorophyll antenna in the green alga *Chlamydomonas reinhardtii* requires expression of the TLA2-CpFTSY gene. *Plant Physiol.* 158, 930–945. doi: 10.1104/pp.111.189910

Kong, F., Yamaoka, Y., Ohama, T., Lee, Y., and Li-Beisson, Y. (2019). Molecular genetic tools and emerging synthetic biology strategies to increase cellular oil content in *Chlamydomonas reinhardtii*. *Plant Cell Physiol.* 60, 1184–1196. doi: 10.1093/pcp/pcz022

Kumar, A., Falcao, V. R., and Sayre, R. T. (2013). Evaluating nuclear transgene expression systems in *Chlamydomonas reinhardtii*. *Algal Res.* 2, 321–332. doi: 10.1016/j.algal.2013.09.002

Lauersen, K. J., Baier, T., Wichmann, J., Wördenweber, R., Mussgnug, J. H., Hübner, W., et al. (2016). Efficient phototrophic production of a high-value sesquiterpenoid from the eukaryotic microalga *Chlamydomonas reinhardtii*. *Metab. Eng.* 38, 331–343. doi: 10.1016/j.ymben.2016.07.013

Leon, R., and Fernandez, E. (2007). "Nuclear transformation of eukaryotic microalgae," in *Transgenic Microalgae as Green Cell Factories. Advances in Experimental Medicine and Biology*, Vol. 616, eds R. León, A. Galván, and E. Fernández (New York, NY: Springer), 1–11. doi: 10.1007/978-0-387-75532-8_1

López-Paz, C., Liu, D., Geng, S., and Umen, J. G. (2017). Identification of *Chlamydomonas reinhardtii* endogenous genic flanking sequences for improved transgene expression. *Plant J.* 92, 1232–1244. doi: 10.1111/tpj.13731

Mali, P., Yang, L., Esvelt, K. M., Aach, J., Guell, M., Dicarlo, J. E., et al. (2013). RNA-guided human genome engineering via Cas9. *Science* 339, 823–826. doi: 10.1126/science.1232033

Melis, A., Spangfort, M., and Andersson, B. (1987). Light−absorption and electron−transport balance between photosystem II and photosystem I in spinach chloroplasts. *Photochem. Photobiol.* 45, 129–136. doi: 10.1111/j.1751-1097.1987.tb08413.x

Park, S., Nguyen, T. H. T., and Jin, E. (2019). Improving lipid production by strain development in microalgae: strategies, challenges and perspectives. *Bioresour. Technol.* 262:121953. doi: 10.1016/j.biortech.2019.121953

Patel, V. K., Soni, N., Prasad, V., Sapre, A., Dasgupta, S., and Bhadra, B. (2019). CRISPR–Cas9 system for genome engineering of photosynthetic microalgae. *Mol. Biotechnol.* 61, 541–561. doi: 10.1007/s12033-019-00185-3

Plucinak, T. M., Horken, K. M., Jiang, W., Fostvedt, J., Nguyen, S. T., and Weeks, D. P. (2015). Improved and versatile viral 2 A platforms for dependable and inducible high−level expression of dicistronic nuclear genes in *Chlamydomonas reinhardtii*. *Plant J.* 82, 717–729. doi: 10.1111/tpj.12844

Porebski, S., Bailey, L. G., and Baum, B. R. (1997). Modification of a CTAB DNA extraction protocol for plants containing high polysaccharide and polyphenol components. *Plant Mol. Biol. Report.* 15, 8–15. doi: 10.1007/bf02772108

Rasala, B. A., Lee, P. A., Shen, Z., Briggs, S. P., Mendez, M., and Mayfield, S. P. (2012). Robust expression and secretion of Xylanase1 in *Chlamydomonas reinhardtii* by fusion to a selection gene and processing with the FMDV 2A peptide. *PLoS One* 7:e43349. doi: 10.1371/journal.pone.0043349

Ruecker, O., Zillner, K., Groebner-Ferreira, R., and Heitzer, M. (2008). Gaussia-luciferase as a sensitive reporter gene for monitoring promoter activity in the nucleus of the green alga *Chlamydomonas reinhardtii*. *Mol. Genet. Genom.* 280, 153–162. doi: 10.1007/s00438-008-0352-3

Salomé, P. A., and Merchant, S. S. (2019). A series of fortunate events: introducing *Chlamydomonas* as a reference organism. *Plant Cell* 31, 1682–1707. doi: 10.1105/tpc.18.00952

Scaife, M. A., Nguyen, G. T., Rico, J., Lambert, D., Helliwell, K. E., and Smith, A. G. (2015). Establishing *Chlamydomonas reinhardtii* as an industrial biotechnology host. *Plant J.* 82, 532–546. doi: 10.1111/tpj.12781

Scranton, M. A., Ostrand, J. T., Georgianna, D. R., Lofgren, S. M., Li, D., Ellis, R. C., et al. (2016). Synthetic promoters capable of driving robust nuclear gene expression in the green alga *Chlamydomonas reinhardtii*. *Algal Res.* 15, 135–142. doi: 10.1016/j.algal.2016.02.011

Serif, M., Dubois, G., Finoux, A.-L., Teste, M.-A., Jallet, D., and Daboussi, F. (2018). One-step generation of multiple gene knock-outs in the diatom *Phaeodactylum tricornutum* by DNA-free genome editing. *Nat. Commun.* 9:3924. doi: 10.1038/s41467-018-06378-9

Shin, S.-E., Lim, J.-M., Koh, H. G., Kim, E. K., Kang, N. K., Jeon, S., et al. (2016). CRISPR/Cas9-induced knockout and knock-in mutations in *Chlamydomonas reinhardtii*. *Sci. Rep.* 6:27810. doi: 10.1038/srep27810

Torzillo, G., and Seibert, M. (2013). "Hydrogen production by *Chlamydomonas reinhardtii*," in *Handbook of Microalgal Culture: Applied Phycology and Biotechnology*, 2nd Edn, eds A. Richmond and Q. Hu (Oxford: Blackwell Publishing Ltd.), 417–432.

Wan, M., Rosenberg, J. N., Faruq, J., Betenbaugh, M. J., and Xia, J. (2011). An improved colony PCR procedure for genetic screening of *Chlorella* and related microalgae. *Biotechnol. Lett.* 33, 1615–1619. doi: 10.1007/s10529-011-0596-6

Wang, Q., Lu, Y., Xin, Y., Wei, L., Huang, S., and Xu, J. (2016). Genome editing of model oleaginous microalgae *Nannochloropsis* spp. by CRISPR/Cas9. *Plant J.* 88, 1071–1081. doi: 10.1111/tpj.13307

Weiner, I., Atar, S., Schweitzer, S., Eilenberg, H., Feldman, Y., Avitan, M., et al. (2018). Enhancing heterologous expression in *Chlamydomonas reinhardtii* by transcript sequence optimization. *Plant J.* 94, 22–31. doi: 10.1111/tpj.13836

Conflict of Interest: The authors declare that the research was conducted in the absence of any commercial or financial relationships that could be construed as a potential conflict of interest.

frontiers in Plant Science

ORIGINAL RESEARCH
published: 15 April 2020
doi: 10.3389/fpls.2020.00372

An Improved Natural Transformation Protocol for the Cyanobacterium *Synechocystis* sp. PCC 6803

*Matthew A. Pope, Josh A. Hodge and Peter J. Nixon**

Sir Ernst Chain Building-Wolfson Laboratories, Department of Life Sciences, Imperial College London, London, United Kingdom

The naturally transformable cyanobacterium *Synechocystis* sp. PCC 6803 is a widely used chassis strain for the photosynthetic production of chemicals. However, *Synechocystis* possesses multiple genome copies per cell which means that segregating mutations across all genome copies can be time-consuming. Here we use flow cytometry in combination with DNA staining to investigate the effect of phosphate deprivation on the genome copy number of the glucose-tolerant GT-P sub-strain of *Synechocystis* 6803. Like the PCC 6803 wild type strain, the ploidy of GT-P cells grown in BG-11 medium is growth phase dependent with an average genome copy number of 6.05 ± 0.27 in early growth (OD_{740} = 0.1) decreasing to 2.49 ± 0.11 in late stationary phase (OD_{740} = 7). We show that a 10-fold reduction in the initial phosphate concentration of the BG-11 growth medium reduces the average genome copy number of GT-P cells from 4.51 ± 0.20 to 2.94 ± 0.13 and increases the proportion of monoploid cells from 0 to 6% after 7 days of growth. In addition, we also show that the DnaA protein, which unusually for bacteria is not required for DNA replication in *Synechocystis*, plays a role in restoring polyploidy upon subsequent phosphate supplementation. Based on these observations, we have developed an alternative natural transformation protocol involving phosphate depletion that decreases the time required to obtain fully segregated mutants.

Keywords: ploidy, natural transformation, flow cytometry, cyanobacteria, phosphate depletion

OPEN ACCESS

Edited by:
EonSeon Jin,
Hanyang University, South Korea

Reviewed by:
Rei Narikawa,
Shizuoka University, Japan
David John Lea-Smith,
University of East Anglia, United Kingdom

***Correspondence:**
Peter J. Nixon
p.nixon@imperial.ac.uk

Specialty section:
This article was submitted to Plant Biotechnology, a section of the journal Frontiers in Plant Science

Received: *28 October 2019*
Accepted: *16 March 2020*
Published: *15 April 2020*

Citation:
Pope MA, Hodge JA and Nixon PJ (2020) An Improved Natural Transformation Protocol for the Cyanobacterium Synechocystis sp. PCC 6803. Front. Plant Sci. 11:372. doi: 10.3389/fpls.2020.00372

INTRODUCTION

Cyanobacteria are photoautotrophic prokaryotes capable of converting light into chemical energy via oxygenic photosynthesis. This characteristic has spurred interest in using cyanobacteria as solar-powered microbial cell factories to produce a variety of carbon-based chemicals (Angermayr et al., 2015; Sengupta et al., 2018).

Synechocystis sp. PCC 6803 (hereafter *Synechocystis*) is widely used as a model cyanobacterium for fundamental and applied research because it is naturally transformable (Grigorieva and Shestakov, 1982; Kufryk et al., 2002), can grow heterotrophically on glucose (Anderson and McIntosh, 1991), and has a publicly available genome sequence (Ikeuchi, 1996; Morris et al., 2014; Tichý et al., 2016). Exogenous DNA molecules introduced into *Synechocystis* via natural transformation may replicate independently on a suitable plasmid (Mermet-Bouvier et al., 1993) or be incorporated into the genome via double homologous recombination (Grigorieva and Shestakov, 1982; Shestakov et al., 1985). As such *Synechocystis* is widely used in the field of

biotechnology with engineered strains producing a variety of industrially relevant chemical commodities (Xue and He, 2018; Katayama et al., 2018; Gale et al., 2019).

The genome of *Synechocystis* consists of a circular chromosome and seven plasmids (Kaneko et al., 2003). Like many other prokaryotes (Pecoraro et al., 2011; Soppa, 2011), *Synechocystis* is polyploid meaning it possess multiple genome copies per cell (Griese et al., 2011; Tichý et al., 2016; Zerulla et al., 2016). Initial reports on wild-type *Synechocystis* sp. PCC 6803 (Labarre et al., 1989) suggested 12 chromosome copies per cell but the presence of up to 142 copies during exponential growth was reported for a glucose-tolerant strain (Griese et al., 2011). These discrepancies might be a consequence of growth conditions, differences in sub-strains or the techniques used to measure genome copy number.

The molecular details underpinning the regulation of DNA replication and ploidy in cyanobacteria remain unclear although ploidy has been positively correlated with cell size and internal protein concentration (Zheng and O'Shea, 2017) and is influenced by phosphate availability (Zerulla et al., 2016). Unusually, DNA replication in *Synechocystis* is asynchronous and does not occur at a defined origin (Ohbayashi et al., 2015), and the DnaA protein, which is an essential DNA replication initiation factor in most bacteria (Messer, 2002; Katayama et al., 2010), is not crucial for replication (Richter et al., 1998; Ohbayashi et al., 2015).

One disadvantage of polyploidy is that it impedes the construction of mutants. Mutations introduced into the genome must present themselves in all genome copies before a mutant phenotype is revealed or maintained stably. Normally, antibiotic-resistance cassettes are used to select for positive transformants, which will initially possess both wild-type and mutated genomes. Re-streaking single colonies on antibiotic-containing medium is then used to segregate mutations across all genome copies. This segregation process typically takes several weeks and can be a bottleneck in the construction of mutant strains. Non-lethal genetic disruptions may be fully segregated after two rounds of selection, however, if essential loci are disrupted, fully segregated mutants may never be obtained. The time required to generate fully segregated mutants varies in each laboratory and is dependent the cyanobacterial background-strain and the type of mutation (Lea-Smith et al., 2016).

Here we have tested the feasibility of improving the segregation process in *Synechocystis* by identifying conditions in which the number of genome copies in the recipient cell is reduced. This was achieved by systematically examining the degree of ploidy as a function of phosphate availability in the medium and the growth phase. Cells were stained with the DNA specific fluorochrome, SYBR Green I, and flow cytometry was used to determine the DNA content of individual cells within a large population by comparing the fluorescence intensity from each cell to that of monoploid *E. coli* cells containing a known amount of DNA (4.6 Mbp), a method used previously by Majerník et al. (2005) for *Methanothermobacter thermautotrophicus* and Tichý et al. (2016) for *Synechocystis*.

Our approach confirms that the degree of ploidy is dependent on phosphate availability and furthermore identifies a physiological role for DnaA in determining the extent of ploidy and the rate with which polyploidy is restored following the addition of phosphate after phosphate deprivation. Based on our observations, we have developed a revised natural transformation protocol involving cells pre-grown in low-phosphate medium that reduces the time required to obtain fully segregated mutants.

MATERIALS AND METHODS

Bacterial Strains and Culture Conditions

The following strains were used: the glucose-tolerant GT-P sub-strain of *Synechocystis* sp. PCC 6803 (Tichý et al., 2016), *E. coli* K-12 MG1655 (Blattner et al., 1997), and *E. coli* 10-β (New England BioLabs). *E. coli* was grown in M9 minimal medium supplemented with glucose (**Supplementary Tables 1–5**).

Synechocystis GT-P was grown in either liquid BG-11 medium (Rippka et al., 1979) or on BG-11 agar plates (Stanier et al., 1979) at 31°C and pH 8.2 {buffered with 1 mM N-[Tris(hydroxymethyl)methyl]-2-aminoethanesulfonic acid (TES)} under continuous white fluorescent illumination of 40 μmol photons $m^{-2}s^{-1}$. Three different types of BG-11 medium, differing in the amount of added phosphate, were used: conventional BG-11 (referred to as "high-phosphate") containing 175 μM K_2HPO_4, "low phosphate" containing 17.5 μM K_2HPO_4 or "no-phosphate" with no added phosphate. The composition of high-phosphate, low-phosphate and no-phosphate BG-11 growth media can be found in **Supplementary Tables 6–17**. Antibiotics were present in the following concentrations: kanamycin (10–50 μg ml^{-1}), chloramphenicol (20 μg ml^{-1}), and ampicillin (100 μg ml^{-1}) (**Supplementary Table 18**).

Generation of *Synechocystis* GT-P Δ*dnaA* and Δ*psbD1/C* Mutants

To assemble the Δ*dnaA* gene-deletion construct, an InFusion Cloning Kit (Takara Biosciences) was used to generate a linear DNA molecule consisting of a chloramphenicol-resistance cassette (PCR amplified from pBAD33 vector) flanked by 500 bp of DNA upstream and downstream of the *dnaA_sll0848* open reading frame of *Synechocystis* GT-P. The primers used to amplify each DNA part were DnaA_H1_F (5′-TTTAGCCAATCGTCG AGGAC-3′) and DnaA_H1_R (5′-ACCCCTGGCGATCGGCGA TTATGAG-3′) for the upstream region; primers CamR_DnaA_F (5′-CATAATCGCCGATCGCCAGGGGT**TGATCGGCACGTA AGAGGTTCCAAC**-3′) and CamR_DnaA_R (5′-CACCAATAG AGTTTTCCTACTAAGT**GGCGTTTAAGGGCACCAATAACT GC**-3′) for the chloramphenicol-resistance cassette and primers DnaA_H2_F (5′-ACTTAGTAGGAAAACTCTATTGGTG-3′) and DnaA_H2_R (5′-ATTGTCCAAAGTCTCTGGGC-3′) for the downstream region, with sequences in bold depicting regions homologous to the chloramphenicol-resistance cassette.

The final linear DNA molecule was ligated into the pGEM-T vector (Promega A137A) to generate plasmid pDnaAKO_Cam^R which was used to transform *Synechocystis* GT-P via natural transformation.

The Δ*psbD1/C* gene deletion construct was kindly provided by Dr. Jianfeng Yu of Imperial College London.

Genotyping

Deletion of the *dnaA_sll0848* open reading frame was confirmed by single colony PCR (**Supplementary Figure 1**). A single colony was picked and resuspended in 50 μl of distilled deionized water (hereafter $_{dd}H_2O$) in a 200 μl PCR tube. The cell suspension was placed in 80°C water for 30 s then dipped into liquid nitrogen for 5 s. This process was repeated 10 times. The PCR tube was then centrifuged to pellet cell debris. 1 μl of the supernatant was used as template for the PCR genotyping reaction. MyTaq 2X MasterMix (BioLine) was used with primers DnaA_seq_F (5′-TCTCATAATCGCCGATCGCCA-3′) and DnaA_seq_R (5′-GAGATAACCACTCGCACTTGC-3′). A 10 μl reaction was prepared consisting of 1 μl supernatant, 0.2 μl forward primer (final concentration 10 μM), 0.2 μl reverse primer (final concentration 10 μM), 5 μl MyTaq 2X MasterMix, and 3.6 μl $_{dd}H_2O$. Reaction conditions were as follows: 2 min at 98°C then 30 cycles of 15 s at 98°C, 30 s at 60°C, and 30 s at 72°C followed by 5 min at 72°C.

Deletion of the *psbD1/C* cluster was confirmed by single colony PCR as described above using primers *psbD1/C*_Forward (5′-TAGACCCCTGGCGATCGGCGATTAT-3′) and *psbD1/C*_Reverse (5′-TTGCCAAAGTATTCTCCTGAT TTAAATGATATTGAGCA-3′).

Preparation of *E. coli* Reference Cells

A single colony was picked from a LB agar plate and used to inoculate 5 ml of M9 minimal medium. Cells were grown by shaking (100 rpm) at 21°C for 7 days. 100 μl of cell culture was used to inoculate another 5 ml of M9 minimal medium and grown at 21°C for a further 7 days. 20 μg ml^{-1} of chloramphenicol was then added to the cell culture to inhibit protein biosynthesis (Dinos et al., 2016) and cells were incubated for a further 60 min. 100 μl of the cell culture were then harvested by centrifugation and fixed in ice-cold 70% ethanol/H_2O and stored at −20°C.

Flow Cytometric Analysis of DNA Stained Cells

50 μl of cells were collected by centrifugation from a liquid culture ($OD_{740} \leq 1$ for *Synechocystis* GT-P and $OD_{600} \leq 1$ for *E. coli*), resuspended in ice-cold 70% (v/v) ethanol and stored in the dark at −20°C for up to 3 weeks. Subsequently, ethanol-fixed *Synechocystis* or *E. coli* cells were pelleted by centrifugation. The pellet was washed twice in TE Buffer (10 mM Tris, 1 mM EDTA, pH 8.0) and resuspended to a final concentration of 1×10^7 cells ml^{-1} (OD_{740} of 0.1). 1 μl of RNAse A (10 mg ml^{-1}) was added to the cells and incubated at 37°C for 1 h. SYBR Green I DNA stain (ThermoFisher Scientific S7585) was added at a 1:10,000 dilution in TE buffer and cells were covered in foil and incubated at room temperature for 30 min.

All analyses were conducted on a BD Biosciences LSR II cytometer. Three biological replicates of each strain were analyzed. 96-well flat bottom plates were used to load samples onto the cytometer with 200 μl of stained cells in each well. Control samples containing filter-sterilized TE buffer and unstained *Synechocystis* GT-P and *E. coli* cells were used to confirm that the population of incidents were desired cells. SYBR Green I stained cells were excited with 488 nm light and the emission spectra were captured in the 530/30 nm channel. Genome copies were allocated to DNA frequency peaks as described by Mori et al. (1996). All analysis of flow cytometric data was conducted on FlowJo™ software as described in **Supplementary Figures 2, 3**.

Natural Transformation of *Synechocystis* GT-P

Phosphate-Deprivation Protocol

10 ml of low-phosphate liquid BG-11 medium without glucose was inoculated with GT-P or Δ*dnaA Synechocystis* cells, obtained from low-phosphate BG-11 liquid cultures, to a starting OD_{740} of 0.03. Cells were grown under 40 μmol photons m^{-2} s^{-1} of fluorescent white light, shaking at 100 rpm at 31°C in air for 7 days. An appropriate volume of cells was collected by centrifugation in a 2 ml eppendorf tube, washed twice in no-phosphate BG-11 and resuspended in 1 ml of no-phosphate BG-11 to give a final OD_{740} of 1. Cells were collected again by centrifugation and 1 μg of Δ*psbD/C* plasmid DNA (**Supplementary Figure 4**) was added to the tube. No-phosphate BG-11 was added to a final volume of 50 μl. Cells were resuspended and left in low light (10–20 μmol photons m^{-2} s^{-1}) in 31°C for 6 h, with agitation every hour by flicking the tube.

After 6 h the 50 μl cell suspension was spread onto a 0.45 μm nitrocellulose filter membrane (Whatman) and placed onto a no-phosphate BG-11 agar plate containing 5 mM D-glucose. The plate was incubated at 31°C under 40 μmol photons m^{-2} s^{-1} of fluorescent white light for 24 h. After 24 h the filter membrane was transferred to a no-phosphate BG-11 agar plate containing 10 μg ml^{-1} of kanamycin and 5 mM D-glucose and left to incubate similarly for 7 days. The filter membrane was then transferred to a low-phosphate BG-11 agar plate containing 10 μg ml^{-1} of kanamycin and 5 mM D-glucose and left to incubate until single colonies appeared. Colonies were re-streaked once on low-phosphate BG-11 agar plates (25 μg ml^{-1} of kanamycin) with 5 mM glucose. We then screened single colonies by testing for photoautotrophic growth on high-phosphate BG-11 agar plates (25 μg ml^{-1} of kanamycin) without glucose. Cells were incubated at 31°C under 40 μmol photons m^{-2} s^{-1} of fluorescent white light for 7 days prior to PCR genotyping.

Conventional Protocol

The conventional protocol is described as above except each step was conducted with high-phosphate BG-11 and *Synechocystis* cells used for transformation were obtained from an exponentially growing culture (OD_{740} of 0.1–0.3).

Statistical Analyses

To test the effect of phosphate availability on genome copy number in GT-P and Δ*dnaA Synechocystis* cells, a linear mixed modeling approach was used (Breslow and Clayton, 1993; Pinheiro and Chao, 2006). The response variable was fit using the natural log of the fluorescence intensity (FI in arbitrary units) of the DNA stained cells. The fixed factors were *phosphate condition*

(three levels; high-, low-, and no-phosphate), *sampling time* (five levels: Day 2, 7, 21, 26, and 28) and cell type (two levels: Δ*dnaA* and GT-P). A three-way interaction model was fitted in order to estimate the mean fluorescence of the cell type in a phosphate condition at a particular sampling time of interest. The data set consisted of multiple observations of the same cell cultures (3 for Δ*dnaA* and 3 for GT-P), therefore *replicate* was fitted as a random intercept. Model assumptions were checked, and outliers screened. To examine the differences between conditions, least squares means were compared using pairwise *t*-tests with a Bonferroni correction to adjust for multiple testing. A *t*-value greater than 16.25 or lower than −16.25 was interpreted as a significant difference. All statistical analyses were conducted in the R environment (R Development Core Team, 2011).

RESULTS

Dependence of Genome Copy Number on Phosphate Availability

Previous work using quantitative PCR (qPCR) to determine genome copy number has described a correlation between environmental phosphate concentration and genome copy number in the original motile wild-type *Synechocystis* PCC 6803 strain: after 7 days of growth in BG-11 medium prepared with 0.13 mM phosphate, the average genome copy number remained unchanged (10 ± 1 to 10 ± 2) while growth in the absence of phosphate decreased the average genome copy number from 10 ± 1 to 4 ± 1 (Zerulla et al., 2016).

Given the potential problems of using qPCR to determine copy number, we opted to use flow cytometry to quantify the genome copy number of a glucose-tolerant sub-strain of *Synechocystis* (GT-P) (Tichý et al., 2016) with the added advantage that it would allow us to examine to what extent the concentration of environmental phosphate affected genome copy number on a single cell basis. *Synechocystis* cells were incubated with the fluorochrome SYBR Green I (Life Technologies), which binds stoichiometrically to dsDNA molecules (Zipper et al., 2004; Clarindo and Carvalho, 2011). Stained cells were excited at 497 nm and the intensity of fluorescence at 520 nm recorded. *E. coli* MG1655 cells grown in minimal medium with a doubling time of ≥16 h and then treated with chloramphenicol were used as the reference as monoploid cells enriched under these conditions contain a genome size of 4.6 Mbp (Skarstad et al., 1983) (**Supplementary Figures 2, 3**). Assuming 1:1 ratios of plasmids (total size 0.38 Mbp) to chromosome (3.57 Mbp), the *Synechocystis* GT-P monoploid genome is approximately 3.95 Mbp, or 86% the size of the *E. coli* genome, in excellent agreement with the observed ratio of average fluorescence intensities of 0.86:1 assigned to monoploid *Synechocystis* GT-P and *E. coli* cells, respectively (**Supplementary Table 22**).

For each time course experiment, *Synechocystis* cells were grown in liquid BG-11 medium containing 0, 17.5 or 175 μM of added K_2HPO_4 (termed no-phosphate, low-phosphate and high-phosphate, respectively). For *Synechocystis* GT-P, all three cultures exhibited equivalent growth rates over the first 4 days with a doubling time of approximately 24 h (**Figure 1A**). However, the final OD achieved by each culture was different, with cultures grown in the absence of added phosphate giving a final OD_{740} of 1.8 compared to OD_{740} of 6 and OD_{740} of 9 for low and high-phosphate BG-11, respectively (**Figure 1A**). The ability of *Synechocystis* to grow in the absence of added phosphate has been observed previously (Zerulla et al., 2016) and is probably due to their ability to use stored phosphate in the form of polyphosphate bodies as well as DNA (Morohoshi et al., 2002; Van De Meene et al., 2006). The addition of 175 μM K_2HPO_4 after 26 days led to renewed growth for both the low and no-phosphate cultures, but not for high-phosphate, suggesting that phosphate was limiting for these cultures (**Figure 1A**).

Linear mixed modeling (**Supplementary Table 19**) and least square means analyses (**Supplementary Tables 20–22**) were used to interpret the flow cytometry data and generate estimated average genome copy numbers within a 95% confidence interval. After 2 days of growth, cells exhibited an estimated average genome copy number of 6.05 ± 0.27 (median: 5), 6.51 ± 0.29 (median: 5), and 5.76 ± 0.25 (median: 5) when grown in high, low and no-phosphate BG-11, respectively, with a maximum value of 16 and minimum value of 2 (**Figures 2A–C**). After 7 days of growth, cells grown in high-phosphate BG-11 possessed on average 4.51 ± 0.2 (median: 4) genome copies with no cells exhibiting monoploidy (**Figure 2A**) whereas cells grown in low (**Figure 2B**) and no-phosphate BG-11 (**Figure 2C**) exhibited significantly fewer genome copies with average values of 2.94 ± 0.13 (median: 3) and 2.91 ± 0.13 (median: 3), respectively, with 6% of the population monoploid.

48 h after phosphate supplementation, high-phosphate cultures maintained an average genome copy number of 2.81 ± 0.12 (median: 3) (**Figure 3A**). However, low and no-phosphate cultures exhibited a significant increase in average genomes from 2.84 ± 0.13 (median: 3) to 5.7 ± 0.25 (median: 5) and 2.93 ± 0.13 (median: 3) to 6.13 ± 0.27 (median: 7), respectively, with each population displaying an almost even distribution of 2–12 copies (**Figures 3B,C**). These data suggest that DNA replication and cell division are rapidly induced upon addition of phosphate to the medium.

DnaA Plays a Role in Controlling Ploidy

Previous work has shown that the DnaA protein is not needed for DNA replication in *Synechocystis* and that a *dnaA* null mutant grows as well as WT in BG-11 medium (Richter et al., 1998; Katayama et al., 2010; Ohbayashi et al., 2015). However, the effects on growth and ploidy under phosphate limiting conditions have not been examined.

We found that an independently constructed *dnaA* null mutant made in the GT-P background (**Supplementary Figure 1**) did indeed grow as well as GT-P when grown in high and low-phosphate BG-11 but showed a slight difference when grown under no-phosphate, exhibiting stationary phase at an OD_{740} of 0.8 compared to an OD_{740} of 1.2 for GT-P (**Figures 1A,B**). The response of the Δ*dnaA* cells to the addition of 175 μM of K_2HPO_4 at 26 days was not significantly different to that of GT-P.

The average genome copy number of Δ*dnaA* cells was 5.34 ± 0.23 (median: 5) and 5.59 ± 0.25 (median: 5) per cell

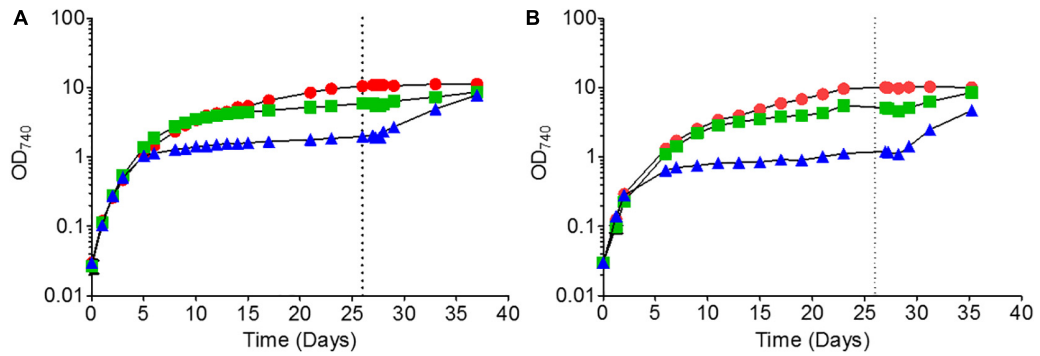

FIGURE 1 | Growth of **(A)** *Synechocystis* GT-P and **(B)** *Synechocystis* Δ*dnaA* in high, low and no-phosphate BG-11. The average OD_{740} of three biological replicates is shown. Error bars are smaller than the size of the symbols. The vertical dashed line at 624 h indicates the time point where a further 175 μM K_2HPO_4 was added to the cultures. Cells were grown under 40 μmol photons m^{-2} s^{-1} of white light at 100 rpm and 31°C.

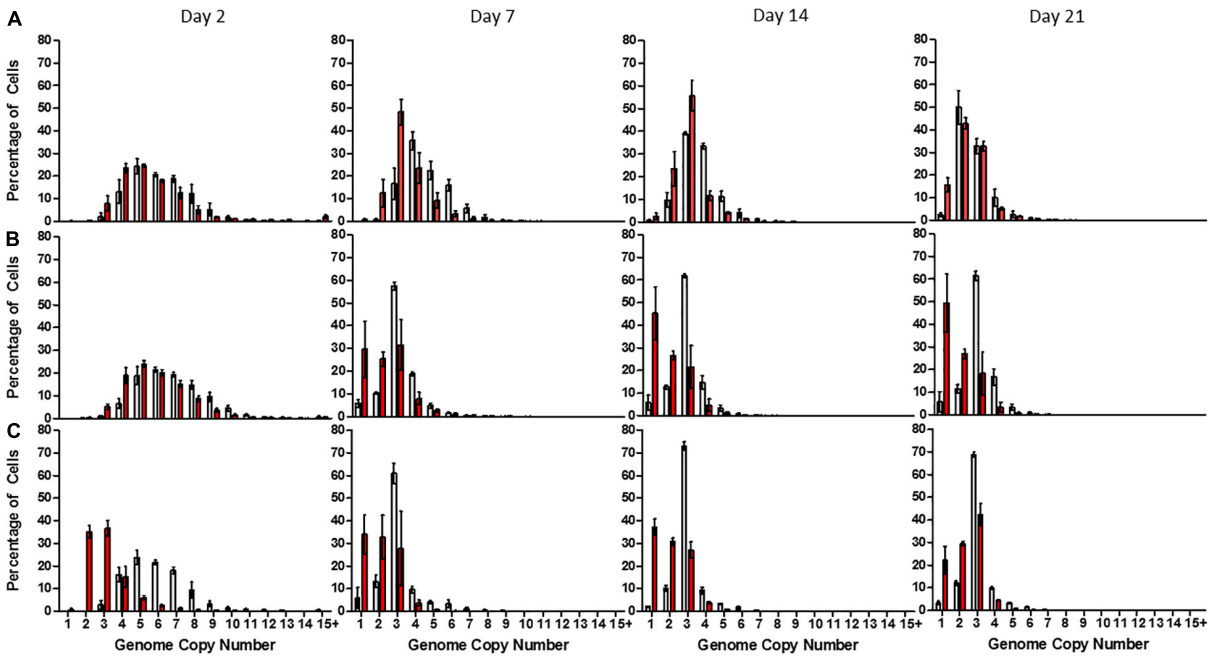

FIGURE 2 | Distribution of genome copy number in populations of *Synechocystis* GT-P (gray) and *Synechocystis* Δ*dnaA* (red) after 2, 7, 14, and 21 days growth in **(A)** high phosphate **(B)** low phosphate, and **(C)** no-phosphate BG-11. The average genome distribution of three biological replicates are shown with error bars. The *x*-axis portrays the genome copy number per cell and the *y*-axis the percentage of cells within a sample of 50,000 cells. Cells were grown under 40 μmol photons m^{-2} s^{-1} of white light, at 100 rpm and 31°C.

when measured 2 days after inoculation into high and low-phosphate BG-11, compared to 6.05 ± 0.27 (median: 5) (high-phosphate) and 6.51 ± 0.29 (median: 5) (low-phosphate) for GT-P (**Figures 2A,B**). However, Δ*dnaA* cells grown in no-phosphate BG-11 exhibited an average genome copy of 2.9 ± 0.13 (median: 3) as opposed to 5.76 ± 0.25 (median: 5) for GT-P (**Figure 2C**).

In addition, after 7 days, Δ*dnaA* cells grown in low-phosphate displayed an average genome copy of 2.17 ± 0.10 (median: 2) per cell, compared to 2.94 ± 0.13 (median: 2) for GT-P, and the proportion of monoploid cells increased from 6 to 30%, respectively (**Figures 2B,C**). The average genome copy of GT-P cells grown in high-phosphate BG-11 was 4.51 ± 0.20 (median: 4), compared to 3.35 ± 0.15 (median: 3) for Δ*dnaA* cells, after 7 days of growth (**Figure 2A**).

A dramatic and significant difference was observed between GT-P and the Δ*dnaA* cells grown in low-phosphate BG-11 upon supplementation with phosphate at day 26 (**Figures 3B,C**). After 48 h, GT-P cells grown in low and no-phosphate BG-11 possessed an average genome copy number of 5.70 ± 0.25 (median: 5) and 6.13 ± 0.27 (median: 7), respectively, with over 50% of cells possessing >5 copies. Δ*dnaA* cells grown in low-phosphate media had an average genome copy of 2.92 ± 0.13, and a median value of 3 displayed by 67% of the population, and no cell contained more than eight genome copies, despite

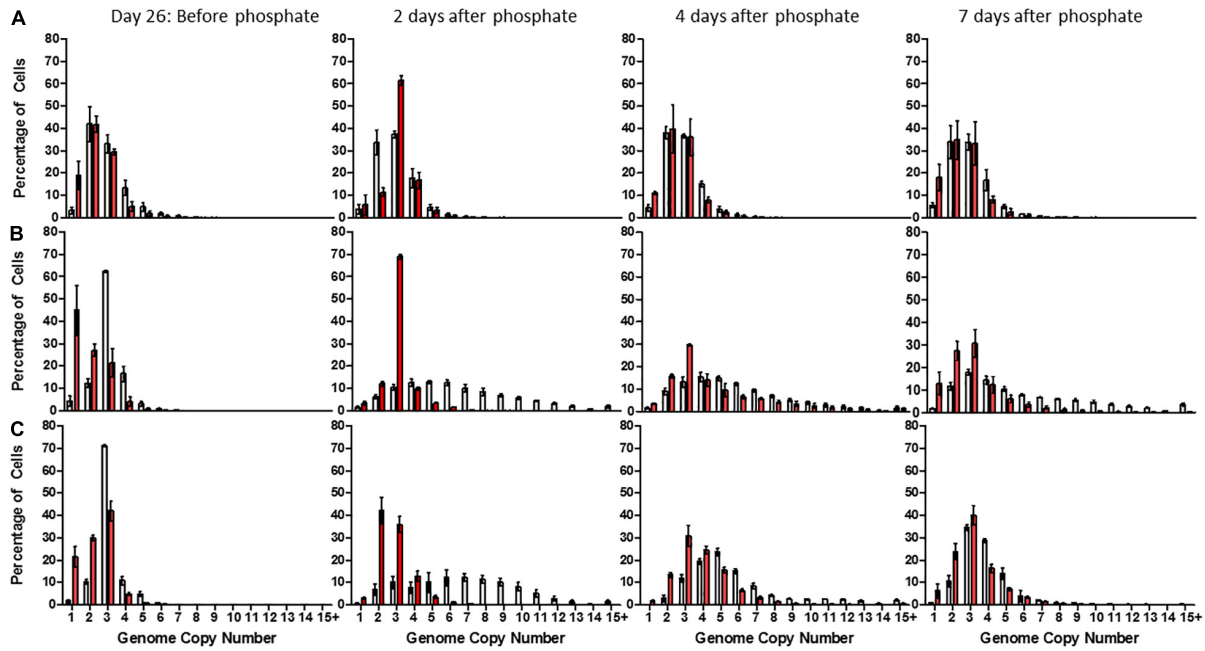

FIGURE 3 | Distribution of genome copy number in populations of *Synechocystis* GT-P (gray) and *Synechocystis* Δ*dnaA* (red) after 26 days growth in **(A)** high phosphate **(B)** low phosphate, and **(C)** no-phosphate BG-11 and 2, 4, and 7 days after phosphate supplementation. The average genome distribution of three biological replicates are shown with error bars. The *x*-axis portrays the genome copy number per cell and the *y*-axis the percentage of cells within a sample of 50,000 cells. Cells were grown under 40 μmol photons m^{-2} s^{-1} of white light, at 100 rpm and 31°C.

restoration of cell growth (**Figure 3**). Overall, DnaA seems to play a physiologically important role in re-establishing ploidy after phosphate starvation.

Phosphate-Deprivation Natural Transformation Protocol for *Synechocystis* GT-P

Given that phosphate depletion leads to a significant reduction in median genome copy number and an increase in the proportion of monoploid cells (**Figures 2B,C**), we reasoned that growing cells under phosphate limiting conditions may decrease the time required to obtain fully segregated mutants.

To test this, we devised a simple transformation experiment in which cells were transformed with a plasmid that replaces the *psbD1/C* locus with a kanamycin-resistance cassette (**Supplementary Figure 4**). *psbD (sll0848)* encodes the D2 subunit of photosystem II and *psbC (sll0851)* encodes the CP43 apopolypeptide. The resulting fully segregated knockout mutant is incapable of growing photoautotrophically (Carpenter et al., 1990; Yu and Vermaas, 1990) but can be propagated photoheterotrophically in medium supplemented with 5 mM glucose. This means that partially segregated transformants will grow on both BG-11 and BG-11 + glucose plates whereas fully segregated transformants will only grow on BG-11 + glucose plates.

GT-P cells (~1 × 10^9) pre-grown in low-phosphate BG-11 were transformed and, after 24 h recovery on non-selective no-phosphate BG-11 agar plates, were incubated on selective no-phosphate BG-11 plates for 7 days. The number of kanamycin-resistant colonies obtained at this stage was approximately 100-fold less than obtained with the conventional transformation protocol using high-phosphate BG-11 medium but still gave hundreds of colonies (**Supplementary Figure 5**). Colonies were picked and streaked once again onto low-phosphate selective medium (containing 25 μg ml^{-1} kanamycin) and incubated for 7 days until single colonies appeared. Growth of the subsequent individual colonies was screened on BG-11 plates devoid of glucose.

About 90% of the kanamycin-resistant colonies obtained using the conventional protocol maintained the ability to grow photoautotrophically suggesting they were still partially segregated, which was confirmed by colony-PCR genotyping, which showed that 9 out of 10 colonies grown on the BG-11 agar plate with 5 mM glucose possessed residual copies of the wild-type genome (**Figure 4A**). In contrast, using the phosphate deprivation protocol, none of the transformants was able to grow photoautotrophically after one round of selection and the *psbD1/C* operon could only be detected in one out of 10 transformants tested by PCR genotyping (**Figure 4B**).

Approximately two out of 10 kanamycin-resistant colonies obtained after transforming the Δ*dnaA* mutant using the conventional protocol had segregated after one round of selection (**Figure 5A**), consistent with the reduced ploidy in this strain compared to GT-P cells (**Figure 2**). As expected, all colonies were fully segregated when using the phosphate deprivation natural transformation protocol (**Figure 5B**).

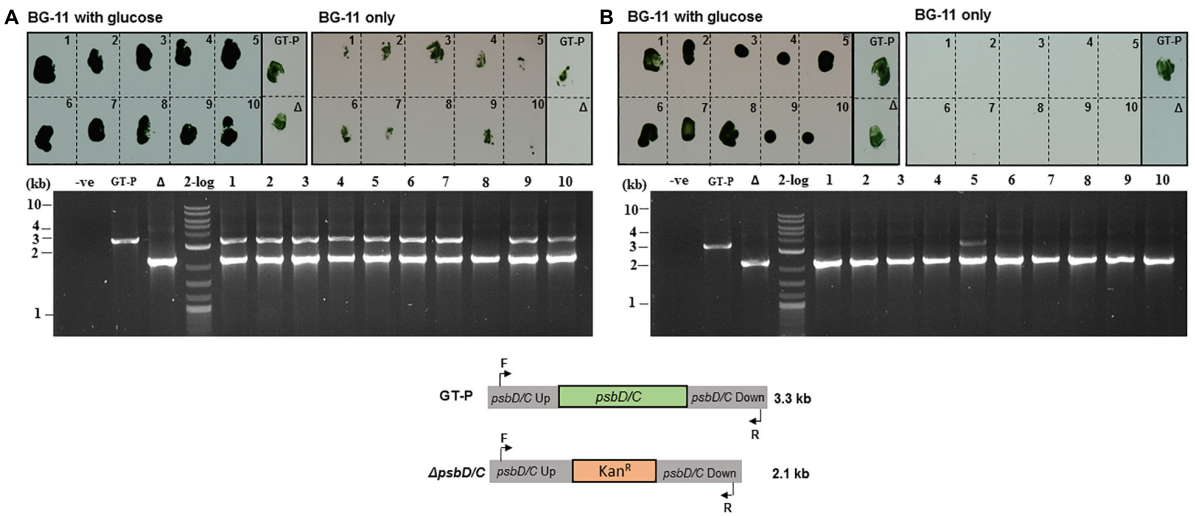

FIGURE 4 | *Synechocystis* GT-P transformed using the **(A)** conventional and **(B)** phosphate-deprivation transformation protocol using a Δ*psbD1/C* gene-deletion construct. Ten kanamycin-resistant colonies obtained with each protocol (see "Materials and Methods") were screened for growth on high-phosphate BG-11 plates with glucose or high-phosphate BG-11 only plates. PCR genotyping was used to test the segregation status of 10 colonies from **(A)** and **(B)**.

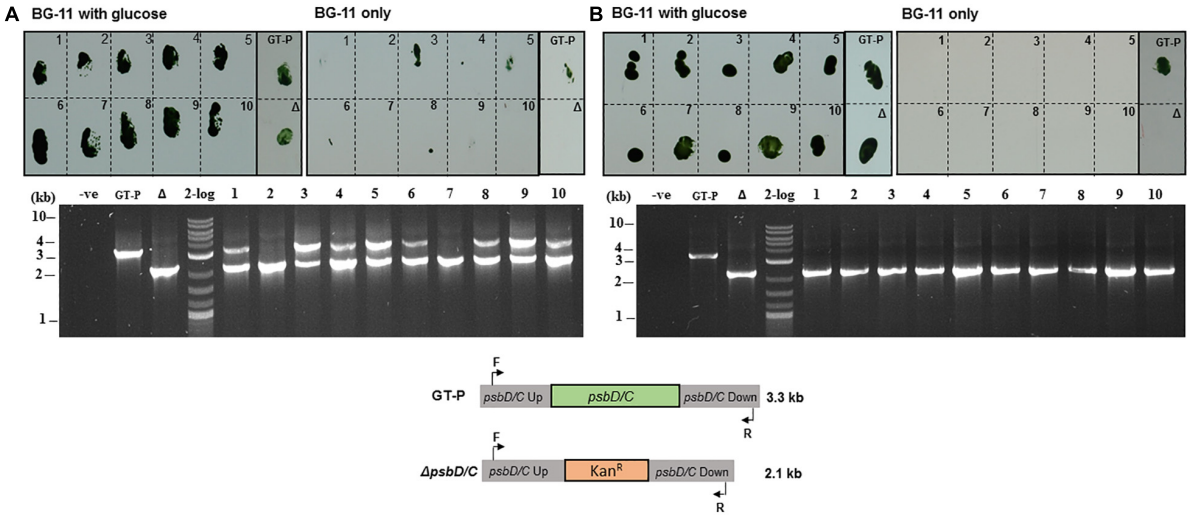

FIGURE 5 | *Synechocystis* Δ*dnaA* transformed using **(A)** conventional and **(B)** phosphate-deprivation transformation protocol using a Δ*psbD1/C* gene-deletion construct. Ten kanamycin-resistant colonies obtained with each protocol (see materials and methods) were screened for growth on high-phosphate BG-11 plates with glucose or high-phosphate BG-11 only plates. PCR genotyping was used to test the segregation status of 10 colonies from **(A)** and **(B)**.

DISCUSSION

Using flow cytometry coupled with DNA staining, we report for the first time the population distribution of genome copies in the glucose-tolerant GT-P strain of *Synechocystis* sp. PCC 6803 and a Δ*dnaA* mutant grown under phosphate replete and starvation conditions. *Synechocystis* GT-P possesses a single circular chromosome of 3.57 Mbp and seven endogenous plasmids yielding a total genome size of 3.96 Mbp, assuming each endogenous plasmid is present at an equivalent ratio to the chromosome. Under our experimental conditions, GT-P cells grown in conventional BG-11 medium displayed average genome copy numbers of 6.05 ± 0.27, 4.51 ± 0.20, and 2.49 ± 0.11 (median values: 5, 3, and 2) during exponential, linear and stationary phases, respectively (**Figure 2**). Tichý et al. (2016) have previously used a similar approach to determine an average of 9 ± 2 copies per cell in the GT-P strain, but they did not specify the growth phase nor examine the population distribution.

qPCR and UV-spectroscopic methods used previously to determine genome copy number in *Synechocystis* have yielded a range of average values from 12 copies per cell in the wild-type PCC 6803 strain (Labarre et al., 1989) to average values of 142 ± 5 during exponential growth, 47 ± 7 during linear growth, and 43 ± 3 in stationary phase in a glucose-tolerant strain

(Griese et al., 2011) and, in a later study, 15 ± 2, 7 ± 2, and 2 ± 1 in exponential, linear and stationary phases, respectively, for another glucose-tolerant strain (Kasuza sub-strain) (Zerulla et al., 2016). In the same study, the qPCR method was used to show that the average genome copy number of six different sub-strains of *Synechocystis* ranged from 30 to 2 genome copies per cell depending on sub-strain and growth phase (Zerulla et al., 2016).

The qPCR approach requires cell numbers to be determined prior to extraction of gDNA which is then quantified by qPCR methods, whereas the spectroscopic approach uses absorbance measurements of purified DNA at 260 nm to quantify DNA. Obviously, the accuracy of these approaches is dependent on reliable methods for both counting the number of cells within a population and for effective lysis of cells and downstream processing and quantification of DNA. A major disadvantage of these methods is that they do not provide information on the heterogeneity of genome copy number within the cell population.

We have demonstrated that a 10-fold reduction of phosphate in the BG-11 medium decreases the average genome copy number and increases the proportion of monoploid cells within a population. After 7 days in low-phosphate medium, *Synechocystis* GT-P possessed an average genome copy number of 2.94 ± 0.13 (median: 3) and 6% of the population (out of 50,000 analyzed) were monoploid compared to an average of 4.51 ± 0.2 (median: 4) and 0% monoploid cells when grown in high-phosphate BG-11 (**Figure 2**). A similar trend has previously been reported for the motile *Synechocystis* PCC 6803 strain which reduced its genome copy from 10 ± 2 (pre-culture) to 4 ± 2 (OD_{740} of 0.5) after 7 days of growth in the absence of phosphate (Zerulla et al., 2016).

Our work has also revealed a physiological role for the DnaA protein in regulating ploidy in *Synechocystis* GT-P. Our results indicate the Δ*dnaA* mutant can grow as well as GT-P in high-phosphate BG-11 but that growth is impaired in low and no-phosphate cultures (**Figure 1B**). Furthermore, when grown in low and no phosphate BG-11, the Δ*dnaA* mutant exhibited a greater proportion of monoploid cells (30% compared to 6% in GT-P) (**Figures 1B,C**). Compared to GT-P, the recovery of ploidy in Δ*dnaA* cells grown in low and no-phosphate BG-11 was also impaired after the addition of phosphate. Overall our results indicate a physiological role for DnaA in regulating DNA replication and controlling ploidy when grown under phosphate limitation.

We have exploited these observations to develop a new protocol for the efficient segregation of mutations in *Synechocystis* GT-P. Using the phosphate deprivation protocol, we have demonstrated that 90% of the analyzed transformants created in the GT-P background had fully segregated after two rounds of selection compared to 10% when using the conventional phosphate-replete protocol (**Figures 4**, **5**). We hypothesize that the greater proportion of monoploid cells in GT-P cultures grown under phosphate deprivation and in Δ*dnaA* populations reduces the time needed to generate fully segregated mutants. More rapid segregation may also be promoted by the asymmetric distribution of genomes to daughter cells (Schneider et al., 2007; Jain et al., 2012). One disadvantage of the new method is the approximate 100-fold less efficient transformation efficiency (**Supplementary Figure 5**), possibly related to the differences in ploidy in the phosphate replete and depleted conditions. Nevertheless, if this reduction in transformation efficiency can be tolerated, then this protocol has the potential to reduce the time required to generate fully segregated mutants in *Synechocystis* GT-P, as well as possibly other cyanobacterial strains, which will be particularly useful for producing strains in the biotechnology area.

DATA AVAILABILITY STATEMENT

All datasets generated for this study are included in the article/**Supplementary Material**.

AUTHOR CONTRIBUTIONS

MP performed the experimental work. JH conducted all statistical analysis. MP and PN contributed to experimental design, data interpretation, and writing of the manuscript.

FUNDING

This work was supported by the award of a Biotechnology and Biological Sciences Research Council Industrial Biotechnology and Bioenergy Doctoral Training Programme Ph.D scholarship to MP.

ACKNOWLEDGMENTS

We are grateful to Jess Rowley and Jane Srivastava from the Flow Cytometry Suite at Imperial College London, South Kensington Campus and Dr. Jianfeng Yu for providing the *psbD1/C* gene deletion construct and to members of the Photosynthesis Research Group for their help.

SUPPLEMENTARY MATERIAL

The Supplementary Material for this article can be found online at: https://www.frontiersin.org/articles/10.3389/fpls.2020.00372/full#supplementary-material

REFERENCES

Anderson, S. L., and McIntosh, L. (1991). Light-activated heterotrophic growth of the cyanobacterium *Synechocystis* sp. strain PCC 6803: a blue-light-requiring process. *J. Bacteriol.* 9, 2761–2767. doi: 10.1128/jb.173.9.2761-2767.1991

Angermayr, S. A., Gorchs Rovira, A., and Hellingwerf, K. J. (2015). Metabolic engineering of cyanobacteria for the synthesis of commodity products. *Trends Biotechnol.* 6, 352–361. doi: 10.1016/j.tibtech.2015.03.009

Blattner, F. R., Plunkett, G., Bloch, C. A., Perna, N. T., Burland, V., Riley, M., et al. (1997). The complete genome sequence of *Escherichia coli* K-12. *Science* 5331, 1453–1462. doi: 10.1126/science.277.5331.1453

Breslow, N. E., and Clayton, D. G. (1993). Approximate inference in generalized linear mixed models. *J. Am. Stat. Assoc.* 88, 9–25. doi: 10.1080/01621459.1993.10594284

Carpenter, S. D., Charite, J., Eggers, B., and Vermaas, W. F. J. (1990). The *psbC* start codon in *Synechocystis* sp. PCC 6803. *FEBS Lett.* 260, 135–137.

Clarindo, W., and Carvalho, C. (2011). Flow cytometric analysis using SYBR Green I for genome size estimation in coffee. *Acta Histochem.* 113, 221–225. doi: 10.1016/j.acthis.2009.10.005

Dinos, G. P., Athanassopoulos, C. M., Missiri, D. A., Giannopoulou, P. C., Vlachogiannis, I. A., Papadopoulos, G. E., et al. (2016). Chloramphenicol derivatives as antibacterial and anticancer agents: historic problems and current solutions. *Antibiotics* 5:e20. doi: 10.3390/antibiotics5020020

Gale, G. A. R., Schiavon Osorio, A. A., Mills, L. A., Wang, B., Lea-Smith, D. J., and McCormick, A. J. (2019). Emerging species and genome editing tools: future prospects in cyanobacterial synthetic biology. *Microorganisms* 7:e409. doi: 10.3390/microorganisms7100409

Griese, M., Lange, C., and Soppa, J. (2011). Ploidy in cyanobacteria. *FEMS Microbiol. Lett.* 323, 124–131. doi: 10.1111/j.1574-6968.2011.02368.x

Grigorieva, G., and Shestakov, S. (1982). Transformation in the cyanobacterium *Synechocystis* sp. PCC 6803. *FEMS Microbiol.* Lett. 13, 367–370.

Ikeuchi, M. (1996). Complete genome sequence of a cyanobacterium *Synechocystis* sp. PCC 6803, the oxygenic photosynthetic prokaryote. *Tanpakush. Kakusan Koso.* 41, 2579–2583.

Jain, I. H., Vijayan, V., and O'Shea, E. K. (2012). Spatial ordering of chromosomes enhances the fidelity of chromosome partitioning in cyanobacteria. *Proc. Natl. Acad. Sci. U.S.A.* 109, 13638–13643. doi: 10.1073/pnas.1211144109

Kaneko, T., Nakamura, Y., Sasamoto, S., Watanabe, A., Kohara, M., Matsumoto, M., et al. (2003). Structural analysis of four large plasmids harboring in a unicellular cyanobacterium, *Synechocystis* sp. PCC 6803. *DNA Res.* 10, 221–228. doi: 10.1093/dnares/10.5.221

Katayama, N., Iijima, H., and Osanai, T. (2018). Production of bioplastic compounds by genetically manipulated and metabolic engineered cyanobacteria. *In: Adv. Exp. Med. Biol.* 1080, 155–169. doi: 10.1007/978-981-13-0854-3_7

Katayama, T., Ozaki, S., Keyamura, K., and Fujimitsu, K. (2010). Regulation of the replication cycle: conserved and diverse regulatory systems for DnaA and *oriC*. *Nat. Rev. Microbiol.* 8, 163–170. doi: 10.1038/nrmicro2314

Kufryk, G. I., Sachet, M., Schmetterer, G., and Vermaas, W. F. J. (2002). Transformation of the cyanobacterium *Synechocystis* sp. PCC 6803 as a tool for genetic mapping: optimization of efficiency. *FEMS Microbiol. Lett.* 206, 215–219. doi: 10.1111/j.1574-6968.2002.tb11012.x

Labarre, J., Chauvat, F., and Thuriaux, P. (1989). Insertional mutagenesis by random cloning of antibiotic resistance genes into the genome of the cyanobacterium *Synechocystis* strain PCC 6803. *J. Bacteriol.* 171, 3449–3457. doi: 10.1128/jb.171.6.3449-3457.1989

Lea-Smith, D. J., Vasudevan, R., and Howe, C. J. (2016). Generation of marked and markerless mutants in model cyanobacterial species. *J. Vis. Exp.* 111:54001. doi: 10.3791/54001

Majerník, A. I., Lundgren, M., McDermott, P., Bernander, R., and Chong, J. P. J. (2005). DNA content and nucleoid distribution in *Methanothermobacter thermautotrophicus*. *J. Bacteriol.* 5, 1856–1857.

Mermet-Bouvier, P., Cassier-Chauvat, C., Marraccini, P., and Chauvat, F. (1993). Transfer and replication of RSF1010-derived plasmids in several cyanobacteria of the genera *Synechocystis* and *Synechococcus*. *Curr. Microbiol.* 27, 323–327. doi: 10.1007/bf01568955

Messer, W. (2002). The bacterial replication initiator DnaA. DnaA and *oriC*, the bacterial mode to initiate DNA replication. *FEMS Microbiol. Rev.* 26, 355–374. doi: 10.1016/s0168-6445(02)00127-4

Mori, T., Binder, B., and Johnson, C. H. (1996). Circadian gating of cell division in cyanobacteria growing with average doubling times of less than 24 hours. *Proc. Natl. Acad. Sci. U.S.A.* 19, 10183–10188. doi: 10.1073/pnas.93.19.10183

Morohoshi, T., Maruo, T., Shirai, Y., Kato, J., Ikeda, T., Takiguchi, N., et al. (2002). Accumulation of inorganic polyphosphate in *phoU* mutants of *Escherichia coli* and *Synechocystis* sp. strain PCC 6803. *Appl. Environ. Microbiol.* 8, 4107–4110. doi: 10.1128/aem.68.8.4107-4110.2002

Morris, J. N., Crawford, T. S., Jeffs, A., Stockwell, P. A., Eaton-Rye, J. J., and Summerfield, T. C. (2014). Whole genome re-sequencing of two "wild-type" strains of the model cyanobacterium *Synechocystis* sp. PCC 6803. *New Zeal. J. Bot.* 52, 36–47. doi: 10.1080/0028825x.2013.846267

Ohbayashi, R., Watanabe, S., Ehira, S., Kanesaki, Y., Chibazakura, T., and Yoshikawa, H. (2015). Diversification of DnaA dependency for DNA replication in cyanobacterial evolution. *ISME J.* 10, 1–9.

Pecoraro, V., Zerulla, K., Lange, C., and Soppa, J. (2011). Quantification of ploidy in *proteobacteria* revealed the existence of monoploid, (mero-)oligoploid and polyploid species. *PLoS One* 6:e16392. doi: 10.1371/journal.pone.0016392

Pinheiro, J. C., and Chao, E. C. (2006). Efficient laplacian and adaptive Gaussian quadrature algorithms for multilevel generalized linear mixed models. *J. Comput. Graph. Stat.* 15, 58–81. doi: 10.1198/106186006x96962

R Development Core Team (2011). *R: A Language and Environment for Statistical Computing*. Vienna: R Development Core Team.

Richter, S., Hagemann, M., and Messer, W. (1998). Transcriptional analysis and mutation of a *dnaA*-like gene in *Synechocystis* sp. strain PCC 6803. *J. Bacteriol.* 180, 4946–4949. doi: 10.1128/jb.180.18.4946-4949.1998

Rippka, R., Deruelles, J., and Waterbury, J. B. (1979). Generic assignments, strain histories and properties of pure cultures of cyanobacteria. *J. Gen. Microbiol.* 111, 1–61. doi: 10.1099/00221287-111-1-1

Schneider, D., Fuhrmann, E., Scholz, I., Hess, W. R., and Graumann, P. L. (2007). Fluorescence staining of live cyanobacterial cells suggest non-stringent chromosome segregation and absence of a connection between cytoplasmic and thylakoid membranes. *BMC Cell Biol.* 8:39. doi: 10.1186/1471-2121-8-39

Sengupta, A., Pakrasi, H. B., and Wangikar, P. P. (2018). Recent advances in synthetic biology of cyanobacteria. *Appl. Microbiol. Biotechnol.* 102, 5457–5471. doi: 10.1007/s00253-018-9046-x

Shestakov, S. V., Elanskaya, I. V., and Bibikova, M. V. (1985). Integration vector for the Cyanobacteria *Synechocystis* sp. 6803. *Dokl. Biol. Sci.* 19, 347–349.

Skarstad, K., Steen, H. B., and Boye, E. (1983). Cell cycle parameters of slowly growing *Escherichia coli* B/r studied by flow cytometry. *J. Bacteriol.* 154, 656–662. doi: 10.1128/jb.154.2.656-662.1983

Soppa, J. (2011). Ploidy and gene conversion in Archaea. *Biochem. Soc. Trans.* 39, 150–154. doi: 10.1042/bst0390150

Stanier, R. Y., Deruelles, J., Rippka, R., Herdman, M., and Waterbury, J. B. (1979). Generic assignments, strain histories and properties of pure cultures of cyanobacteria. *Microbiology* 11, 1–61.

Tichý, M., Bečková, M., Kopečná, J., Noda, J., Sobotka, R., and Komenda, J. (2016). Strain of *Synechocystis* PCC 6803 with aberrant assembly of photosystem ii contains tandem duplication of a large chromosomal region. *Front. Plant Sci.* 7:648. doi: 10.3389/fpls.2016.00648

Van De Meene, A. M. L., Hohmann-Marriott, M. F., Vermaas, W. F. J., and Roberson, R. W. (2006). The three-dimensional structure of the cyanobacterium *Synechocystis* sp. PCC 6803. *Arch. Microbiol.* 184, 259–270.

Xue, Y., and He, Q. (2018). Synthetic biology approaches to the sustainable production of P-coumaric acid and its derivatives in cyanobacteria. *Adv. Exp. Med. Biol.* 1080, 261–277. doi: 10.1007/978-981-13-0854-3_11

Yu, J., and Vermaas, W. F. J. (1990). Transcript levels and synthesis of photosystem II components in cyanobacterial mutants with inactivated photosystem II genes. *Plant Cell* 2, 315–322. doi: 10.1105/tpc.2.4.315

Zerulla, K., Ludt, K., and Soppa, J. (2016). The ploidy level of *Synechocystis* sp. PCC 6803 is highly variable and is influenced by growth phase and by chemical and physical external parameters. *Microbiology* 162, 730–739. doi: 10.1099/mic.0.000264

Zheng, X. Y., and O'Shea, E. K. (2017). Cyanobacteria maintain constant protein concentration despite genome copy-number variation. *Cell Rep.* 19, 497–504. doi: 10.1016/j.celrep.2017.03.067

Zipper, H., Brunner, H., Bernhagen, J., and Vitzthum, F. (2004). Investigations on DNA intercalation and surface binding by SYBR Green I, its structure determination and methodological implications. *Nucleic Acids Res.* 32:e103. doi: 10.1093/nar/gnh101

Conflict of Interest: The authors declare that the research was conducted in the absence of any commercial or financial relationships that could be construed as a potential conflict of interest.

frontiers in Plant Science

ORIGINAL RESEARCH
published: 25 May 2020
doi: 10.3389/fpls.2020.00589

Crystal Structure of Geranylgeranyl Pyrophosphate Synthase (CrtE) Involved in Cyanobacterial Terpenoid Biosynthesis

*Yuchi Feng[1], R. Marc L. Morgan[2], Paul D. Fraser[3], Klaus Hellgardt[1] and Peter J. Nixon[2]**

[1] Department of Chemical Engineering, Imperial College London, London, United Kingdom, [2] Sir Ernst Chain Building-Wolfson Laboratories, Department of Life Sciences, Imperial College London, London, United Kingdom, [3] School of Biological Sciences, Royal Holloway, University of London, Egham, United Kingdom

Cyanobacteria are photosynthetic prokaryotes that perform oxygenic photosynthesis. Due to their ability to use the photon energy of sunlight to fix carbon dioxide into biomass, cyanobacteria are promising hosts for the sustainable production of terpenoids, also known as isoprenoids, a diverse class of natural products with potential as advanced biofuels and high-value chemicals. However, the cyanobacterial enzymes involved in the biosynthesis of the terpene precursors needed to make more complicated terpenoids are poorly characterized. Here we show that the predicted type II prenyltransferase CrtE encoded by the model cyanobacterium *Synechococcus* sp. PCC 7002 is homodimeric and able to synthesize C20-geranylgeranyl pyrophosphate (GGPP) from C5-isopentenyl pyrophosphate (IPP) and C5-dimethylallyl pyrophosphate (DMAPP). The crystal structure of CrtE solved to a resolution of 2.7 Å revealed a strong structural similarity to the large subunit of the heterodimeric geranylgeranyl pyrophosphate synthase 1 from *Arabidopsis thaliana* with each subunit containing 14 helices. Using mutagenesis, we confirmed that the fourth and fifth amino acids (Met-87 and Ser-88) before the first conserved aspartate-rich motif (FARM) play important roles in controlling chain elongation. While the WT enzyme specifically produced GGPP, variants M87F and S88Y could only generate C15-farnesyl pyrophosphate (FPP), indicating that residues with large side chains obstruct product elongation. In contrast, replacement of M87 with the smaller Ala residue allowed the formation of the longer C25-geranylfarnesyl pyrophosphate (GFPP) product. Overall, our results provide new structural and functional information on the cyanobacterial CrtE enzyme that could lead to the development of improved cyanobacterial platforms for terpenoid production.

Keywords: isoprenoid, prenyltransferase, site-directed mutagenesis, FARM, phylogenetic analysis

OPEN ACCESS

Edited by:
Matteo Ballottari, University of Verona, Italy

Reviewed by:
Eckhard Hofmann, Ruhr University Bochum, Germany
Hiroshi Noguchi, Nihon Pharmaceutical University, Japan

***Correspondence:**
Peter J. Nixon
p.nixon@imperial.ac.uk

Specialty section:
This article was submitted to Plant Biotechnology, a section of the journal Frontiers in Plant Science

Received: *18 October 2019*
Accepted: *20 April 2020*
Published: *25 May 2020*

Citation:
Feng Y, Morgan RML, Fraser PD, Hellgardt K and Nixon PJ (2020) Crystal Structure of Geranylgeranyl Pyrophosphate Synthase (CrtE) Involved in Cyanobacterial Terpenoid Biosynthesis. Front. Plant Sci. 11:589. doi: 10.3389/fpls.2020.00589

INTRODUCTION

Cyanobacteria are a group of gram-negative photosynthetic prokaryotes that perform oxygenic photosynthesis using sunlight to drive the conversion of CO_2 into a variety of carbon-based compounds. Cyanobacteria are therefore widely considered as promising hosts for the sustainable production of biofuels and commodity and high-value chemicals. Terpenoids are a major class

of secondary metabolites with over 70,000 compounds identified (Vickers et al., 2014) including carotenoids, sterols, steroids, saponins, and hormones, which are widely used in a range of applications, including pharmaceuticals, pesticides, fragrances, flavors, and advanced biofuels (Rabinovitch-Deere et al., 2013).

All terpenoids are synthesized from two isomeric C5 building blocks: isopentenyl pyrophosphate (IPP) and dimethylallyl pyrophosphate (DMAPP), both produced via the 2-C-methyl-D-erythritol-4-phosphate (MEP) pathway in cyanobacteria (**Figure 1**). Prenyltransferase enzymes catalyze the initial condensation reaction between IPP and DMAPP to give C10-geranyl pyrophosphate (GPP), plus the subsequent addition of IPP molecules to give first C15-farnesyl pyrophosphate (FPP), and then C20-geranylgeranyl pyrophosphate (GGPP), which are the precursors of monoterpenoids, sesquiterpenoids and diterpenoids, respectively (Han et al., 2015). A diverse range of polyprenyl pyrophosphate products (>C25) can be further synthesized through addition of different numbers of IPP to the FPP allylic substrate (Wallrapp et al., 2013).

Prenyltransferases are classified as cis (Z) or trans (E) depending on the stereochemistry of the carbon-carbon double bonds in the product (Shimizu et al., 1998). Amino acid sequence alignments of different E- and Z-type enzymes suggests that trans-prenyltransferases have evolved from a common ancestor, whereas cis-prenyltransferases may have a different origin (Chen et al., 1994). In general, trans-prenyltransferases generate products up to C50, which can be further classified into short-chain (C10–C25), medium-chain (C30–C35), and long-chain (C40–C50) (Ogura and Koyama, 1998). GPP, FPP, and GGPP are synthesized by geranyl pyrophosphate synthase (GPPS), farnesyl pyrophosphate synthase (FPPS), and geranylgeranyl pyrophosphate synthase (GGPPS), respectively. C25 compounds, formed by geranylfarnesyl pyrophosphate synthase (GFPPS), are used in the formation of thermophilic archaeal ether-linked lipids, while hexaprenyl pyrophosphate synthase (HexPPS), heptaprenyl pyrophosphate synthase (HepPPS), octaprenyl pyrophosphate synthase (OPPS), solanesyl pyrophosphate synthase (SPPS), and decaprenyl pyrophosphate synthase (DPPS) generate the side chains needed for the formation of quinones (Wang and Ohnuma, 1999).

All these trans-prenyltransferases contain two highly conserved aspartate-rich motifs: the "first aspartate-rich motif" (FARM, $DDX_{2-4}D$, where X encodes any amino acid) and the "second aspartate-rich motif" (SARM, DDXXD). In previous studies, a sequential ionization-condensation-elimination catalytic mechanism was proposed, in which FARM and SARM coordinate Mg^{2+} ions to promote elimination of the pyrophosphate group from the allylic substrate (such as DMAPP, GPP, and FPP) to generate a carbocation intermediate, which is subsequently attacked by IPP, bound to positively charged residues in the cavity, to form an adduct that is then deprotonated to form a carbon-carbon double bond (Liang, 2009; Chang et al., 2012).

Among the prenyltransferase enzymes, GGPPS has been considered a bottle-neck enzyme that regulates terpenoid biosynthesis (Jiang et al., 2012; Bai et al., 2016). In the case of photosynthetic organisms, most photosynthesis-related metabolites such as carotenoids and the side chains of chlorophylls and plastoquinones are all derived from GGPP, synthesized by GGPPS (Ruiz-Sola et al., 2016). GGPPS enzymes can be divided into three types: Type-I enzymes contain a large aromatic amino acid at the fourth or fifth position before the FARM; Type-II contain an insertion of two residues in the FARM region but are devoid of aromatic residues at the fourth or fifth position before the FARM; and Type-III are also devoid of aromatic residues just before the FARM but have no extra residues inserted in the FARM (Hemmi et al., 2003; Bouvier et al., 2005; Chang et al., 2006). Structurally, GGPPS enzymes are found mainly as homodimers such as in the archaeon *Geoglobus acetivorans*, the bacterium *Bacteroides thetaiotaomicron*, and the eukaryotes *Plasmodium vivax*, *Saccharomyces cerevisiae*, *Sinapis alba*, and *Arabidopsis thaliana* (Chang et al., 2006; Kloer et al., 2006; Artz et al., 2011; Wallrapp et al., 2013; Wang et al., 2016; Petrova et al., 2018). However, some GGPPS are heterodimers, such as in the cases of *Oryza sativa* and *Mentha piperita* (Chang et al., 2010; Zhou et al., 2017) and higher order oligomers have been described for *Homo sapiens* (Kavanagh et al., 2006).

Little is known about the GGPPS enzymes in photosynthetic microorganisms. In cyanobacteria, sequence comparisons have identified a potential GGPPS (Liang et al., 2006), denoted CrtE because of its role in carotenoid biosynthesis (Yen and Marrs, 1976). An early study identified a gene encoding GGPPS in the thermophilic cyanobacterium *Thermosynechococcus elongatus* (Ohto et al., 1999). However, there is still no information on the structure of this enzyme and how product chain length is regulated.

In this study, we report the first crystal structure of GGPPS (CrtE) from a cyanobacterium – in our case the model strain *Synechococcus* sp. PCC 7002 (Syn7002). Based on the structure, site-directed mutagenesis experiments were carried out to investigate the role of specific amino acids in determining the chain length of the product.

MATERIALS AND METHODS

Cloning, Expression, and Purification

The *crtE* gene (SYNPCC7002_A1085) was amplified by PCR using genomic DNA of Syn7002 and primers CrtE_F (5′-CTCCGCGGTGGTATGGTAGTTGCAGA-3′) and CrtE_R (5′-CGGAATTCTTAGTTTTTACGGTTAACGATG-3′) (restriction sites are underlined). The PCR products were digested with EcoRI and SacII, and the DNA fragments were cloned into the pHUE expression vector (Catanzariti et al., 2004) to give pHUE_CrtE (**Supplementary Dataset 1**). Protein expression was performed using *E. coli* BL21(DE3) (New England Biolabs, Ltd). Plasmid Usp2-cc which encodes histidine-tagged deubiquitinase was also transformed into *E. coli* BL21(DE3). The His-tagged recombinant proteins were overexpressed in *E. coli* BL21(DE3) in 3 L of Luria-Bertani medium containing 100 mg L^{-1} ampicillin by growing to an optical density at 600 nm of 0.6 with 250 rpm at 37°C (Eppendorf Innova 43 incubator shaker) and then inducing with 0.4 mM isopropyl-1-thio-β-D-galactopyranoside (IPTG). After additional overnight incubation at 18°C, the cells were

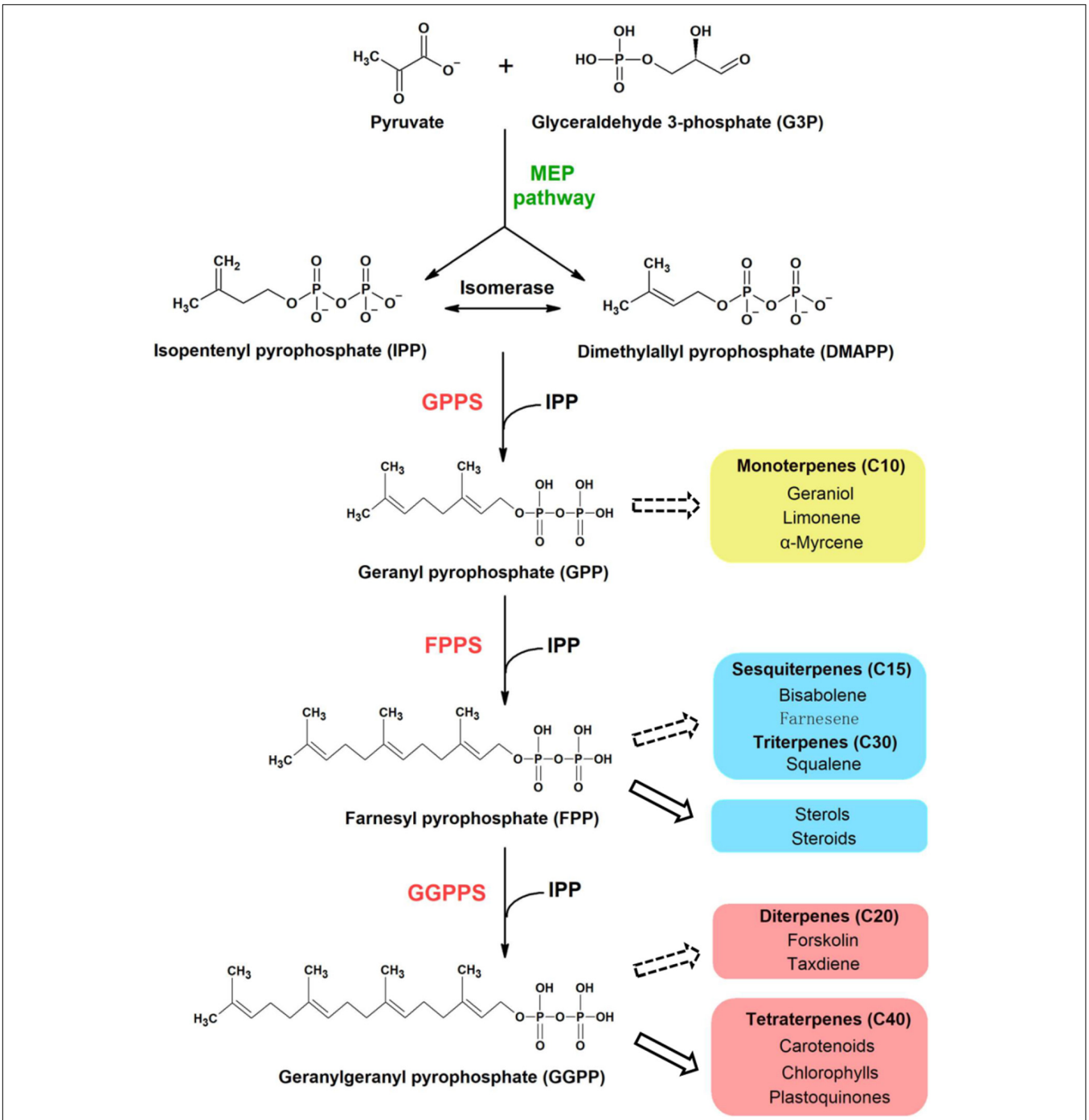

FIGURE 1 | Proposed terpenoid biosynthesis in cyanobacteria via the MEP pathway. Syn7002 CrtE is a hypothesized functional GGPPS, which could use IPP and DMAPP as substrates to generate GGPP as the final product. The arrows with solid lines indicate that the products are generated naturally in cyanobacteria whilst the arrows with dashed lines indicate that the products could be potentially produced from the corresponding substrates through metabolic engineering. MEP, methylerythritol-4-phosphate; GPPS, geranyl pyrophosphate synthase; FPPS, farnesyl pyrophosphate synthase; GGPPS, geranylgeranyl pyrophosphate synthase.

harvested and disrupted with a T5 cell disruptor (Constant system, GA, United States) using a pressure of 25 kpsi at 5°C in 40 mL of KPN buffer containing 40 mM KH_2PO_4/K_2HPO_4 (pH 8.0) and 100 mM NaCl. The homogenate was centrifuged with a Beckman Coulter Optima L-100XP ultracentrifuge and a Ti45 rotor (Beckman Coulter, Inc., United States) at 172,000 x *g* for 30 min at 4°C, and the supernatant was recovered as a crude extract. To the 40 mL of supernatant, 2 mL of a 50% slurry of nickel-nitrilotriacetic acid (Ni-NTA) agarose in KPN buffer was added, then placed on a rotary wheel at

4°C for 1.5 h. The lysate/Ni-NTA mixture was centrifuged at 2,000 rpm (805 x *g*) for 2 min (Eppendorf^{TM} 5810 R Centrifuges with a A-4-62 Model rotor), and the Ni-NTA agarose pellet was washed twice with 20 mL of buffer A (25 mM Tris–HCl pH 7.5, 500 mM NaCl) and then twice with 20 mL of buffer A containing 60 mM imidazole. The His-tagged proteins (either deubiquitinase or CrtE fusion protein) were eluted from the Ni-NTA resin in 20 mL of buffer A containing 500 mM imidazole. The purified proteins were dialyzed against 5 L of buffer A at 4°C overnight, and the protein concentration was measured by the Bradford assay using bovine serum albumin (BSA) to generate the standard curve (Zor and Selinger, 1996). Cleavage of the CrtE fusion protein was achieved by incubating with deubiquitinase at a 1:10 molar ratio (enzyme to substrate) overnight at 16°C in 40 mL of buffer A (Catanzariti et al., 2004). Cleaved products were concentrated with a Sartorius 30 K concentrator (Satorius Stedim Lab Ltd, United Kingdom) at 4,000 rpm (3,220 x *g*) at 4°C (Eppendorf^{TM} 5810 R Centrifuge with a A-4-62 Model rotor) until the final volume reduced to about 1 mL and then purified using an ÄKTA Prime FPLC system (GE Healthcare, United Kingdom) equipped with a HiLoad® 16/60 Superdex®200 prep grade (pg) (120 mL) column (GE Healthcare, United Kingdom) and equilibrated with 25 mM Tris–HCl (pH 7.5) and 500 mM NaCl buffer in a cold room (4°C). Chromatography was performed at a flow rate of 1 mL min^{-1} and 2 mL fractions were collected. Absorbance of protein was measured at 280 nm (A280). Fractions contained purified CrtE and His-tagged ubiquitin protein were collected and analyzed by SDS-PAGE and immunoblotting (Michoux et al., 2014). Fractions containing CrtE were concentrated with a Sartorius 30 K MWCO concentrator (Sartorius Stedim Lab Ltd, United Kingdom) at 4,000 rpm, 4°C (Eppendorf^{TM} 5810 R Centrifuges with a A-4-62 Model rotor) until the final concentration reached 11.3 mg mL^{-1}. The final predicted protein sequence after cleavage is shown in **Supplementary Dataset 1**.

Crystallization and Data Collection

Crystallization trials were performed using the sitting drop vapor diffusion method at 16°C. Crystallization drops were dispensed using a Mosquito nanoliter high-throughput robot (TTP Labtech Ltd, United Kingdom) and consisted of 200 nL protein solution and 100 nL reservoir solution. Crystal formation was first observed in the condition containing 0.2 M ammonium acetate, 0.1 M sodium acetate (pH 4.6) and 30% (w/v) PEG 4000 in 2 to 5 days (with an approximate size of 60 μm × 40 μm). After 7 days, crystals were observed in another condition containing 0.1 M sodium citrate (pH 5.5) and 20% (w/v) PEG 3000 (with an approximate size of 500 μm × 100 μm). Crystals were flash-cooled in liquid nitrogen after cryoprotection with 30% (w/v) ethylene glycol.

X-ray diffraction data from native crystals were collected at beamline I03 or I04-1 of the Diamond Light Source (DLS), United Kingdom. The data were processed and scaled using *SCALA* (Evans, 2006) within the xia2-dials package (Winter et al., 2013). In the structural refinements, 5% randomly selected reflections were set aside for calculating R_{free} as a quality monitor (Brünger, 1993).

Structure Determination and Refinement

The structure of CrtE was solved by molecular replacement (MR) using the structure of GGPPS1 large subunit from *Arabidopsis thaliana* (PDB: 5E8L) (Wang et al., 2016) as a starting model (56.4% amino acid sequence identity). MR was performed with *Phaser* (McCoy et al., 2007). Additional model building was done manually with cycles of WinCoot (Emsley et al., 2010) (Emsley and Cowtan, 2004) and refined in REFMARC5 with using global non-crystallographic symmetry (NCS) restraints (Murshudov et al., 2011). The statistics of the model refinement are summarized in **Table 1**. Protein molecular graphics were generated with PyMOL and electrostatic surface potential map was calculated using the APBS Electrostatics Plugin (DeLano, 2002). In the structure of Syn7002 CrtE with 2 copies in the asymmetric unit (PDB: 6SXL), we identified the following residues in chain A: 8 to 172, 180 to 241 and 263 to 300 of the predicted 302 residues; chain F: 8 to 241 and 253 to 300. In the structure of Syn7002 CrtE with 6 copies in the asymmetric unit, the identified residues of each monomer were similar, covering the range from 9 to 232 and 254 to 297.

In vitro CrtE Assays

CrtE prenyltransferase activity was determined *in vitro* as described previously (Jones et al., 2013). The incubation mixture contained, in a total volume of 200 μL, 50 mM Tris–HCl (pH 7.5), 5 mM $MgCl_2$, 1 mM DTT, 46 μM [1-^{14}C] IPP (1.85 GBq $mmol^{-1}$), 0.5% (v/v) Triton X-100 and purified protein, and 10 μM DMAPP. Samples were incubated for 1 h at 30°C and reactions stopped by cooling on ice and the addition of 200 μL of 1 M NaCl. Samples were extracted in 2 mL of water-saturated butanol overnight at -20°C. Butanol extractable products were dephosphorylated by adding potato acid phosphatase (1 unit) (Sigma-Aldrich, United Kingdom) to 1 mL of extract and incubating in 0.2% (v/v) Triton X-100 and 4 mL of methanol in a total volume of 10 mL at 37°C overnight on a shaking platform water bath. Samples were extracted in 10 mL of 10:90 (v/v) diethyl ether/petroleum ether (boiling point 40–60°C) and the organic phase dried under nitrogen. Reaction products (geraniol, farnesol, and geranylgeraniol) were identified by thin-layer chromatography (TLC) using reversed-phase C18 F254S plates (Merck, United Kingdom), with a mobile phase of 19:1 (v/v) acetone/water. The radio-labeled products were identified by autoradiography, and alcohol standards (geraniol, farnesol, geranylgeraniol, and solanesol) (Sigma-Aldrich, United Kingdom) were visualized by exposure to iodine vapor.

Site-Directed Mutagenesis of GGPPS

Reverse PCR was used to linearize the original pHUE_CrtE plasmid with the mutagenic oligonucleotides (shown below), and the re-circulation of the plasmids was achieved by using In-fusion HD Cloning Kit (Thermo Fisher Scientific, United Kingdom). All mutations were confirmed by DNA sequencing (GENWIZ, United Kingdom). The correct constructs were subsequently transformed into *E. coli* BL21 (DE3) for protein expression. The primers designed to

TABLE 1 | Data collection and refinement statistics for the Syn7002 CrtE crystal structures (in brackets are the statistics for the high-resolution shells).

	Syn7002CrtE (six copies, PDB: 6SXN)	Syn7002CrtE (two copies, PDB: 6SXL)
Diffraction source	I04-1, DLS	I03, DLS
Wavelength (Å)	0.9159	0.9763
Temperature (K)	100	100
Detector	PILATUS 6M	PILATUS 6M
Space group	$P2_12_12_1$	$P2_12_12_1$
a, b, c (Å)	102.56, 122.97, 134.19	70.20, 89.47, 107.32
α, β, γ (°)	90.00, 90.00, 90.00	90.00, 90.00, 90.00
Resolution range (Å)	68.02–2.66	68.82–2.50
R_{merge}	0.06 (0.75)	0.03 (0.45)
R_{meas}	0.08 (1.1)	0.04 (0.63)
R_{pim}	0.06 (0.75)	0.03 (0.44)
CC1/2	0.99 (0.48)	0.99 (0.77)
Average I/σ(I)	11.76 (1.63)	11.72 (1.94)
Completeness (%)	99.24 (95.35)	99.97 (100.00)
Multiplicity	2.0 (2.0)	2.0 (2.0)
Total no. of reflections	98338 (9428)	48009 (4718)
No. of unique reflections	49329 (4674)	24024 (2358)
Refinement		
R_{work}/R_{free} (%)	22.8/28.5	24.3/30.6
Root-mean-square deviations		
Bond lengths (Å)	0.008	0.009
Bond angles (°)	1.556	1.840
Ramachandran plot (%)		
Most favored regions (%)	96.00	93.47
Allowed regions (%)	3.08	6.33
Outliers (%)	0.92	0.19
Average B-factor	73.73	77.69
Protein	73.76	77.74
Ligands	n/a	114.88
Solvent	57.95	57.92

produce the desired point mutations were: M87Y, 5′-GAG ATGATCCACACC**TAT**TCTTTAATCCATGATGATCTGCC-3′ and 5′- GGTGTGGATCATCTCCAGG-3′; S88F, 5′-ATGATC CACACCATG**TTT**TTAATCCATGATGATCTGCCCG-3′ and 5′- CATGGTGTGGATCATCTCCA-3′; M87Y/S88F, 5′- GAG ATGATCCACACC**TATTTT**TTAATCCATGATGATCTGCCCG -3′ and 5′- GGTGTGGATCATCTCCAGG-3′; A96Y, 5′-CATGA TGATCTGCCC**TAT**ATGGACAATGACGATCTCCGT-3′ and 5′- GGGCAGATCATCATGGATTAAAG-3′, V161M, 5′-GGGG CCGAAGGCCTC**ATG**GGTGGCCAAGTGGTGGAT-3′ and 5′- GAGGCCTTCGGCCCCC-3′; A96Y/V161M, 5′-CATGATGAT CTGCCC**TAT**ATGGACAATGACGATCTCCGT-3′, 5′- GAG GCCTTCGGCCCCC -3′, 5′-GGGGCCGAAGGCCTC**ATG**G GTGGCCAAGTGGTGGAT-3′ and 5′- GGGCAGATCATCA TGGATTAAAG-3′; M87A, 5′-GAGATGATCCACACC**GCC** TCTTTAATCCATGATGATCTGCC-3′ and 5′- GGTGTGGAT CATCTCCAGG-3′; K53A, 5′-CTCCTGGCTGGGGGA**GCC**CG GCTACGCCCGATTCTTT-3′ and 5′- TCCCCCAGCCAGG AGG-3′. These substituted codons are frequently used in Syn7002. The mutated positions are indicated in boldface type.

Bioinformatic Techniques

Full-length amino-acid sequences of several prenyltransferases (for detailed sequence information, see **Supplementary Dataset 2**) were obtained from the UniProt database[1] and aligned with Aliview software using the MUSCLE program[2] and displayed with ESPript[3]. GGPPS (CrtE) protein sequences used for phylogenetic analysis and analysis of amino-acid residue conservation were downloaded from UniProt (see **Supplementary Dataset 3**). The phylogenetic tree was constructed using the Neighbor-joining method with the PhyML 3.0[4]. The default parameters of the above software were used. The tree was visualized using Interactive Tree of Life[5]. Analysis of the conservation of GGPPS from cyanobacteria, algae and plants was performed using the ConSurf server[6].

RESULTS

Comparison of CrtE to Other Prenyltransferases

For Syn7002, three hypothesized prenyltransferases genes have been annotated in the genome sequence in UniProt: *crtE* (*SYNPCC7002*_A1085), *sdsA* (*SYNPCC7002*_A0580), and *uppS* (*SYNPCC7002*_A0099), which are considered to function as GGPPS, SPPS and undecaprenyl pyrophosphate synthase (UPPS) enzymes, respectively. In **Figure 2**, the amino acid sequence of CrtE from Syn7002 is compared to GPPS, FPPS, GGPPS, HexPPS, and SPPS enzymes from various organisms. CrtE, in common with other trans-prenyltransferases, contains the two highly conserved FARM and SARM regions (Tarshis et al., 1996; Narita et al., 1999) and contains a two amino-acid insertion (Pro-95 and Ala-96) in the FARM characteristic of a Type-II GGPPS (Hemmi et al., 2003).

Expression, Purification, and Crystallization of Syn7002 CrtE

To produce CrtE in *E. coli* for structural studies, the CrtE protein was expressed as an N-terminal histidine-tagged ubiquitin fusion protein using the high-level expression vector pHUE (Catanzariti et al., 2004). Recombinant CrtE protein was over-expressed in *E. coli* and purified first using Ni-NTA agarose (**Supplementary Figure 1**) and after cleavage of the His-tagged ubiquitin-CrtE fusion by deubiquitinase (**Supplementary Figure 2**), the liberated CrtE protein was then purified by size-exclusion chromatography and analyzed by SDS-PAGE (**Supplementary Figures 3A,C**). The molecular mass of CrtE was estimated to be about 61 kDa based on the elution

[1]https://www.uniprot.org/
[2]https://www.ebi.ac.uk/Tools/msa/muscle/
[3]http://espript.ibcp.fr/ESPript/ESPript/
[4]http://www.atgc-montpellier.fr/phyml/
[5]https://itol.embl.de/
[6]https://consurf.tau.ac.il/

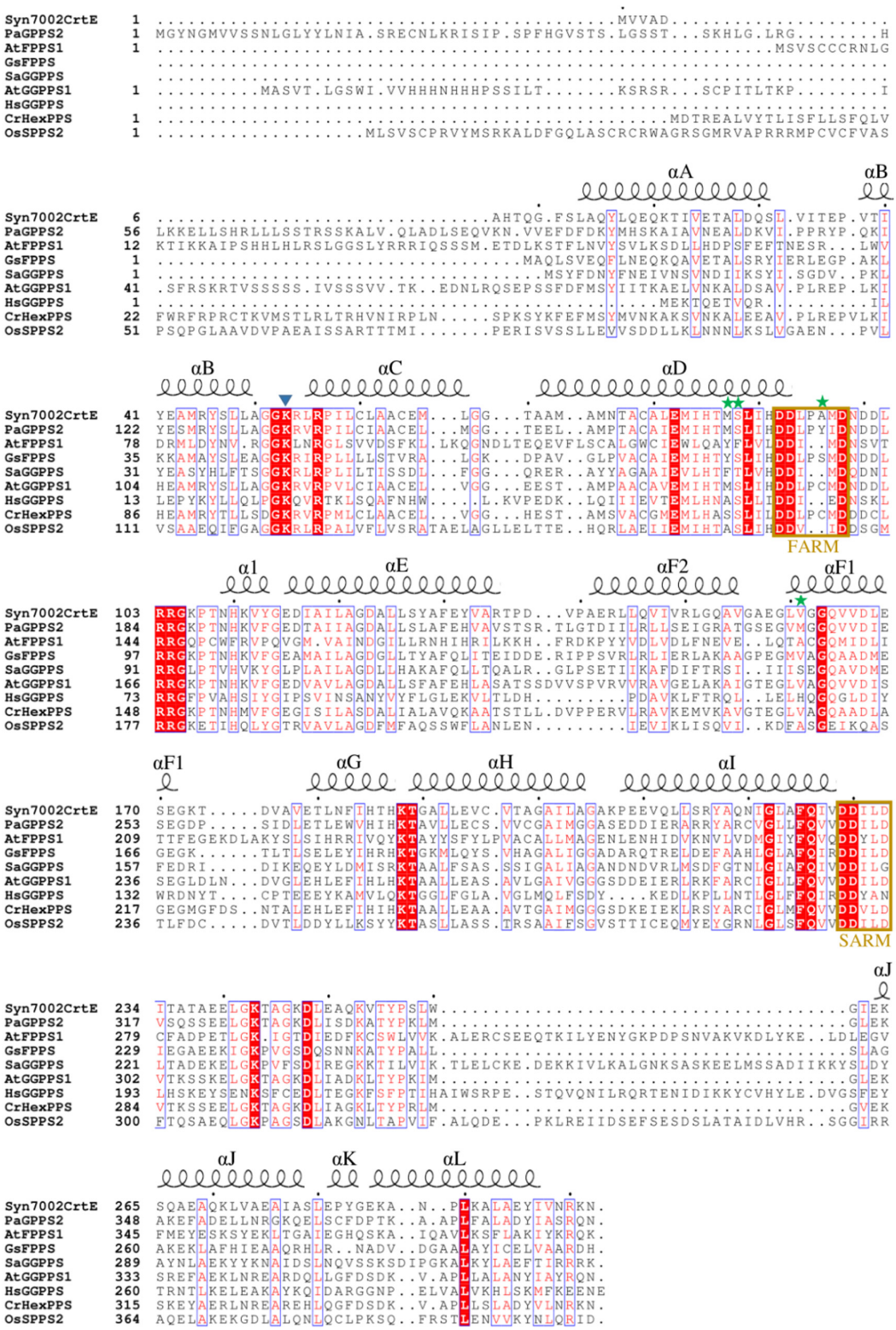

FIGURE 2 | Alignment of amino acid sequences of Syn7002, *Synechococcus* sp. PCC 7002 CrtE; Pa, *Picea abies* GPPS; At, *Arabidopsis thaliana* FPPS1 and GGPPS1; Gs, *Geobacillus stearothermophilus* FPPS; Sa, *Sulfolobus acidocaldarius* GGPPS; Hs, *Homo sapiens* GGPPS; Cr, *Capsella rubella* HexPPS; and Os, *Oryza sativa* SPPS2. Strictly conserved residues are highlighted by using red background and conservatively substituted residues are boxed. The secondary structure α-helices of Syn7002 CrtE are shown above the aligned sequences. The blue triangle indicates the Lys residue predicted to bind to IPP; the green stars indicate the amino acid residues mutated in this study.

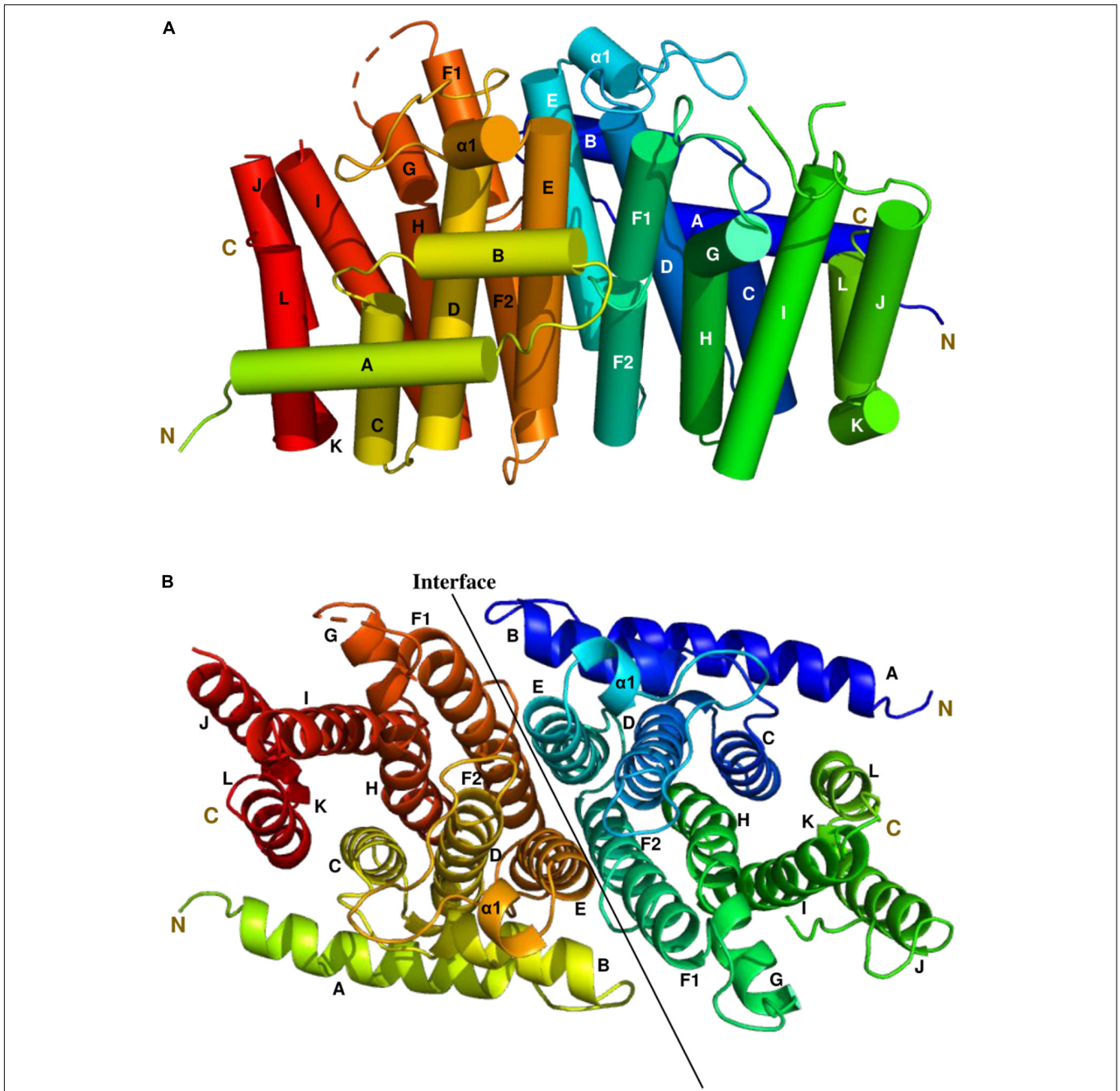

FIGURE 3 | The side and top views model of the Syn7002 CrtE homodimer is shown using a cylinder **(A)** and ribbon diagram **(B)** (PDB: 6SXN, chain C and E), respectively. N, N-terminal; C, C-terminal. Helices are labelled A to L.

volume (**Supplementary Figure 3B**), close to the predicted mass of 65 kDa for a dimer.

We obtained CrtE crystals in two different crystallization conditions (**Supplementary Figures 3D,E**). The crystal formed in 0.2 M ammonium acetate, 0.1 M sodium acetate (pH 4.6) and 30% (w/v) PEG 4000 had 6 copies in the asymmetric unit, and the crystal generated in 0.1 M sodium citrate (pH 5.5) and 20% (w/v) PEG 3000 contained 2 copies in the asymmetric unit. In both cases CrtE crystals had the same space group - $P2_12_12_1$. Among the structurally characterized prenyltransferase enzymes, the predicted CrtE from Syn7002 shows 56.3% sequence identity with the large subunit of *A. thaliana* GGPPS1 (PDB: 5E8L). This was successfully used as a starting model to determine the structure of CrtE by molecular replacement. In the present study, we determined the structures of Syn7002 CrtE with 6 copies in the asymmetric unit in its apo form to a resolution of 2.66 Å (PDB: 6SXN) and with 2 copies in the asymmetric unit in its apo form

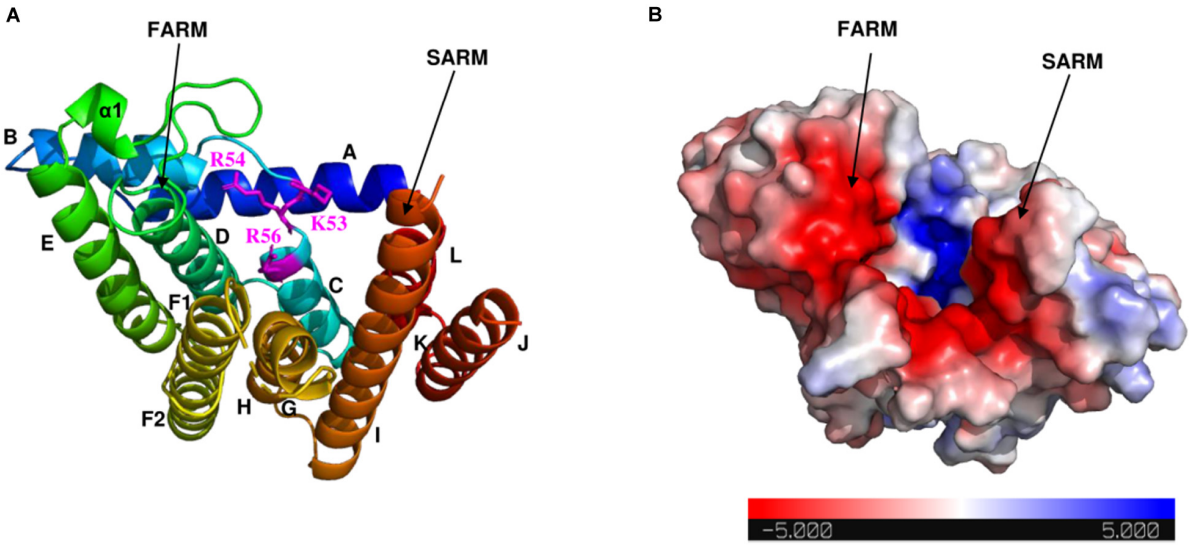

FIGURE 4 | Electrostatic surface potential map of Syn7002 CrtE monomer (PDB: 6SXN, chain C). **(A)** Ribbon diagram of the Syn7002 CrtE monomer with positively charged Lys and Arg side chains highlighted. **(B)** The electrostatic surface potential map of the Syn7002 CrtE monomer. The color is coded from red to blue according to charge potential from –5 to 5 kT/e. The potential was calculated using the APBS plugin in PyMOL. FARM, first conserved aspartate-rich motif; SARM, second conserved aspartate-rich motif.

to a resolution of 2.50 Å (PDB: 6SXL) (**Table 1**). Structure-based sequence alignments between the CrtE homodimer in PDB:6SXN (chain C and E) and PDB:6SXL (chain A and B) showed a root mean square difference (RMSD) of 0.471 Å over 520 residues (2531 atoms superposed) performed using PyMOL (**Supplementary Figure 4**). The three CrtE dimers (CE, BD, and AF) in PDB: 6SXN have corresponding RMSD of 0.256 Å (CE and BD, 2791 atoms superposed), 0.278 Å (CE and AF, 2827 atoms superposed) and 0.413 Å (AF and BD, 2953 atoms superposed), respectively. The RMSD between the CrtE monomer in PDB: 6SXN (chain C) and PDB:6SXL (chain F) is 0.420 Å over 258 residues (1825 atoms superposed).

Overall Structure of Syn7002 CrtE

The most complete structure was obtained with PDB: 6SXN chain C, in which all 302 residues apart from the first eight N-terminal residues, twenty-two residues from 233 to 254 and the last five C-terminal residues could be identified in the electron density map. Each CrtE monomer is composed of 14 α-helices (A to L, and α1) joined by connecting loops (**Figure 3**). Helix F is broken in the middle to give helices F1 and F2, respectively. A short helix α1 (Asn-109-Tyr-113) was observed between helix D and E. A similar structure has been reported for *M. piperita* GPPS and *Sinapis alba* GGPPS, and is thought to be involved in the protein conformational changes needed for substrate binding and product release (Kloer et al., 2006; Chang et al., 2010). The two aspartate-rich motifs, FARM and SARM, are located in helix D and H, respectively, forming a large catalytic cavity for allyl substrate binding (Tarshis et al., 1996; Guo et al., 2004). α-helices (D, E, F1, and F2) form a large tunnel-shaped pocket which is hypothesized to be involved in prenyl chain elongation according to previous structural studies (Wallrapp et al., 2013; Wang et al., 2016). The inner surface of the pocket is filled with hydrophobic amino acids (Ala-80, Ile-84, Met-87, Leu-126, Phe-130, Leu-151, Val-155, and Leu-160) which, based on previous studies on prenyltransferase enzymes, are predicted to determine the chain length of the final product (Tarshis et al., 1996). In addition, residues in helices E, F1 and F2 at the homodimer interface are non-polar. Notably, the side chain of Phe-130 in helix E is involved in a π-π interaction with its counterpart in the other subunit (**Supplementary Figure 5**), which also has been found in *A. thaliana* GFPPS and *Sulfolobus solfataricus* HexPPS (Sun et al., 2005; Wang et al., 2016).

As shown in the electrostatic surface potential map (**Figure 4**), there are a number of positively charged amino acid residues (Lys-53, Arg-54, and Arg-56) located at the bottom of the catalytic cavity, which are proposed to bind the IPP substrate (Wang et al., 2016). The negatively charged FARM and SARM regions sit atop of the cavity flanking the positively charged bottom. Binding sites for Mg^{2+} and DMAPP could not be obtained in this study, but have been reported in previous structural studies of GGPPS from *S. cerevisiae*, *Plasmodium falciparum*, and *Corynebacterium glutamicum* (Guo et al., 2007; No et al., 2012; Wallrapp et al., 2013).

Regulation of Product Chain Length

Previous studies have demonstrated that the side chains of residues in the hydrophobic pocket (formed by helices D, E, F1, and F2) could form a "floor" that blocks product elongation and so determine the product chain length (Sun et al., 2005; Han et al., 2015). Based on the structure of wild type Syn7002 CrtE, an equivalent "floor" model was built, and amino-acid residues predicted to determine product chain length were identified (**Figure 5A**). Site-directed mutagenesis of CrtE was

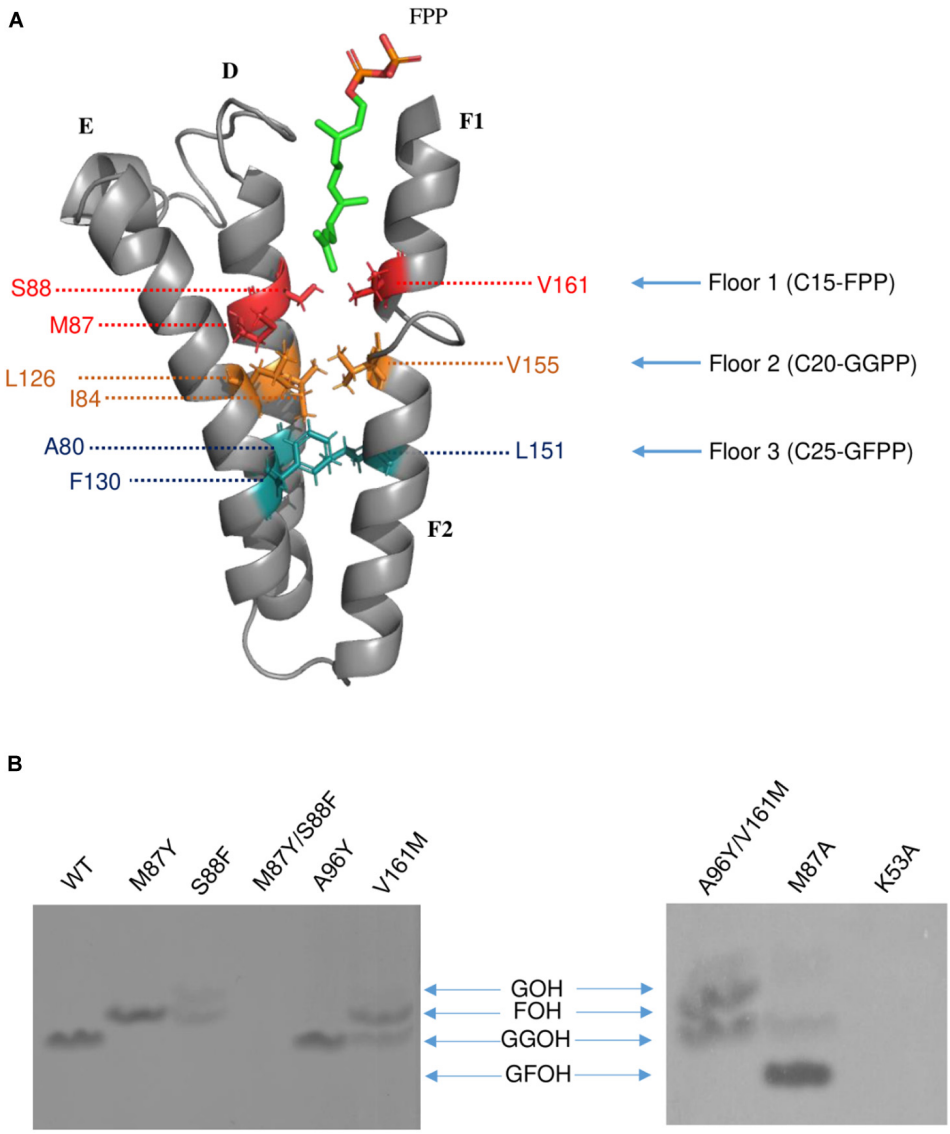

FIGURE 5 | (A) The hypothesized "Three-floors" model based on the Syn7002 GGPPS structure built with PyMOL. Residues on floor 1 (red), floor 2 (yellow) and floor 3 (cyan). FPP is used as an example to elucidate the mechanism of product chain-length elongation. **(B)** *In vitro* assay of wild type and mutated Syn7002 CrtE protein. DMAPP and ^{14}C-IPP were used as allylic substrates in all reactions, and the products were analyzed by TLC. GOH, geraniol; FOH, farnesol; GGOH, geranylgeraniol; GFOH, geranylfarnesol.

performed to test the first "floor" of this model; therefore, Met-87 and Ser-88 on helix D, and Val-161 on helix F1, were replaced by residues with larger (Phe and Tyr) or smaller (Ala) side chains.

As pure CrtE WT and CrtE WT fusion gave the same result in the TLC chromatography profile (**Supplementary Figure 6**), the variant His-tagged CrtE fusion proteins were directly used for their enzyme assays after purification using immobilized Ni-affinity chromatography and dialysis. Enzyme assays were conducted with purified wild-type and variant fusion proteins (**Supplementary Figure 7**) using [1-^{14}C] IPP and DMAPP as substrates as described in materials and methods. The radio-labeled products were dephosphorylated, and the generated alcohols were observed on TLC (**Figure 5B**). Under the same reaction conditions, the final product of wild type CrtE was C20-GGPP. Variants M87Y and S88F both shifted the final product from GGPP to C15-FPP, but S88F produced less FPP and some C10-GPP compared to the products of M87Y. However, no product was detected in the mutated enzyme (M87Y/S88F) in which both residues were changed, possibly because the enzyme kinetics were dramatically affected, or the final product was volatile. When Met-87 was mutated to Ala, somewhat surprisingly, the longer geranylfarnesyl pyrophosphate molecule (GFPP, C25) was generated as a major product, with traces of GGPP. The second residue before the conserved GQ motif (Val-161) on helix D, which is also hypothesized to be involved in the

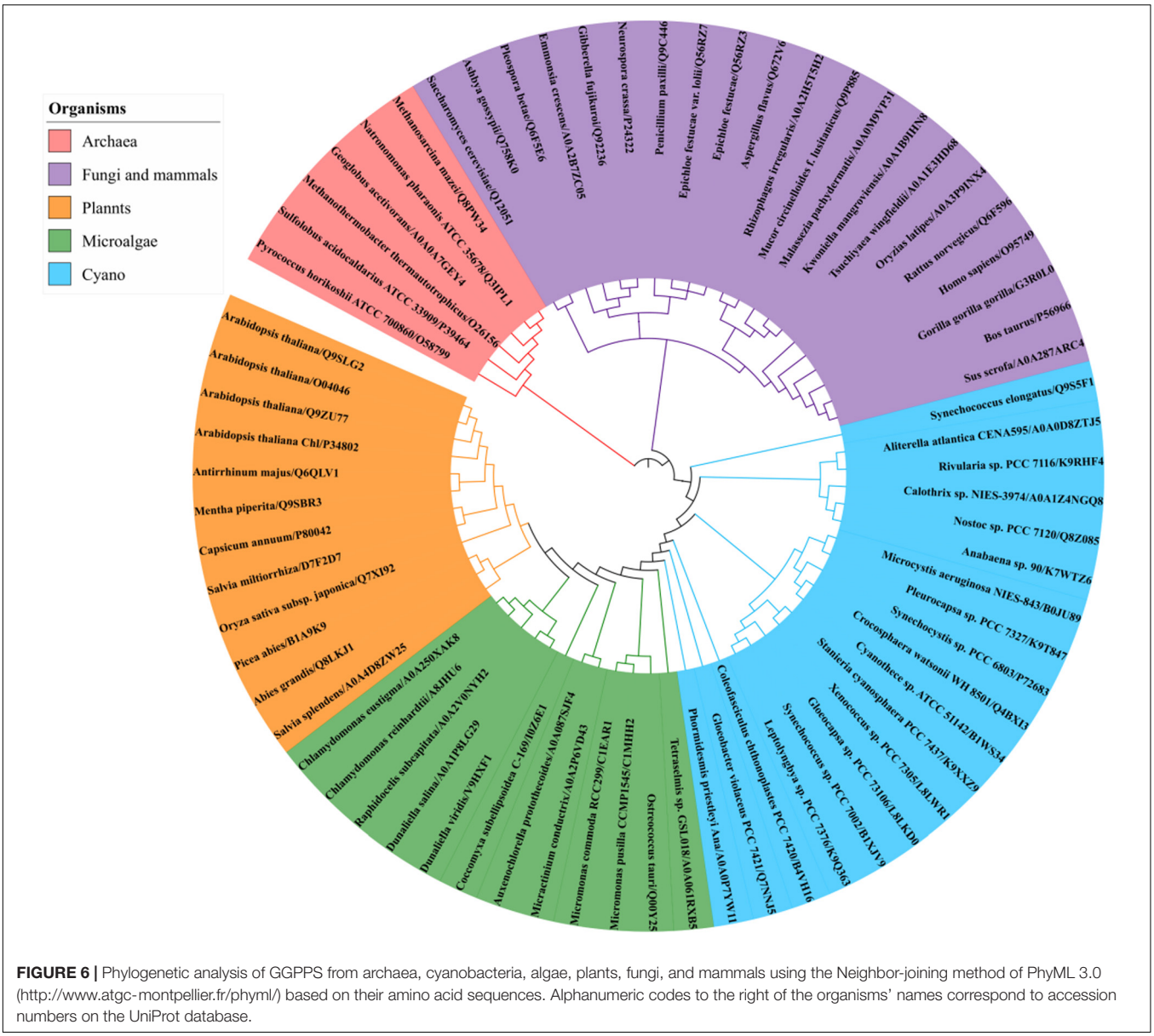

FIGURE 6 | Phylogenetic analysis of GGPPS from archaea, cyanobacteria, algae, plants, fungi, and mammals using the Neighbor-joining method of PhyML 3.0 (http://www.atgc-montpellier.fr/phyml/) based on their amino acid sequences. Alphanumeric codes to the right of the organisms' names correspond to accession numbers on the UniProt database.

first floor formation (Hemmi et al., 2003), was mutated to Met, and found to produce similar amounts of FPP and GGPP.

Type-II Syn7002 CrtE has two extra residues (Pro-95 and Ala-96) inserted within the FARM region. These two residues are located in the loop between helices D and E, and spatially on the top of the elongation pocket in the structure. According to the sequence alignment in **Figure 1**, Pro-95 in the FARM is highly conserved in Type-II prenyltransferases, but the second additional residue shows more variability. For instance, PaGPPS has a bulky Tyr residue at the second position, whereas the other Type-II prenyltransferases (Syn7002 CrtE, GsFPPS, AtGGPPS, and CrHexPPS) have a smaller residue such as Cys, Ser and Ala. To determine whether a bulky residue at this position could interrupt the elongation reaction, to give rise to GPP, we mutated CrtE Ala-96 to Tyr, but GGPP was still formed. These data indicate that the size of the second extra amino acid in the FARM does not critically affect product chain-length elongation. We also tried to mimic PaGPPS by making a version of CrtE with A96Y/V161M, so that the mutated enzyme has the same first "floor" and the same two residue insertion as that found in PaGPPS. But like the V161M single variant, similar amounts of FPP and GGPP were produced and there was no evidence for formation of GPP. Mutation of the predicted IPP binding site (Lys-53) was achieved by replacing it with Ala but no products were detected.

Phylogenetic Relationship of Photosynthetic Organisms GGPPSs

A BLAST search of the UniProt online protein database of archaea, cyanobacteria, algae, higher plants, fungi and mammal sequences (**Supplementary Dataset 3**) using Syn7002 CrtE

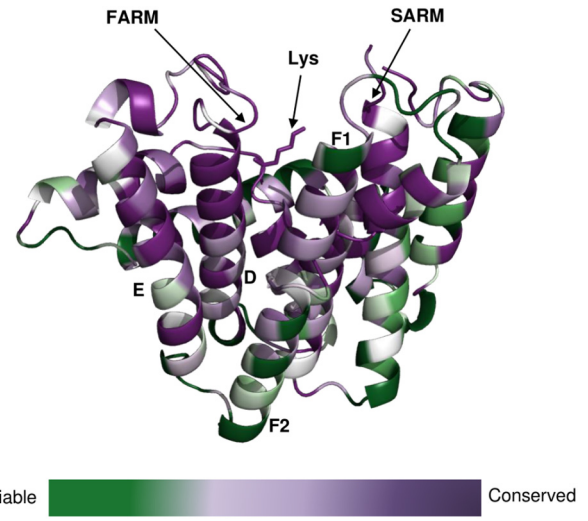

FIGURE 7 | Conservation of amino-acid residues in GGPPS in representative cyanobacteria, algae and higher plants mapped onto the structure of CrtE from Syn7002 CrtE (6SXN, chain C) performed with the ConSurf server (https://consurf.tau.ac.il/). Residue conservation is colored in a gradient spectrum in such a way that the least conserved region is colored in green, and the most conserved region is colored in purple. A conserved Lys (Lys-53), proposed to bind the substrate IPP, is indicated.

(GGPPS) was conducted to study the evolutionary relationships. A phylogenetic analysis (**Figure 6**), based on the degree of sequence similarity, revealed that all the GGPPSs have evolved from a common ancestor and form three distinct clades (Type-I GGPPS in archaebacteria, Type-II GGPPS in photosynthetic organisms, and Type-III GGPPS found in fungi and mammals). GGPPS from photosynthetic organisms (Type-II) and GGPPS from fungi and mammals (Type-III) belong to different clades but may share a common ancestor.

The clade of photosynthetic organisms was divided into three clusters (cyanobacteria, algae, and plants). Analysis of the sequence conservation of Type-II GGPPSs was conducted based on sequence alignments and the determined Syn7002 GGPPS structure (PDB: 6SXN) using the ConSurf server (**Figure 7**). The essential functional domains such as short helix α1, FARM, SARM, the ligand-binding region and the residues in the product elongation tunnel are highly conserved, which indicates that GGPPSs in photosynthetic organisms have a very close evolutionary relationship and are likely to display similar mechanisms for catalysis and for controlling product chain length.

DISCUSSION

In this study, we have demonstrated that the CrtE enzyme encoded by the model cyanobacterium Syn7002 codes for a Type-II GGPPS. A phylogenetic analysis indicates that Type-II GGPPS is widely found in photosynthetic organisms. Cyanobacteria and algae encode one GGPPS (CrtE) and higher plants usually have multiple GGPPS enzymes, for example *A. thaliana* has 10 GGPPSs (Ruiz-Sola et al., 2016). Uniquely, the thermophilic cyanobacterium *T. elongatus* possesses a FPPS in addition to a GGPPS (Ohto et al., 1999). Syn7002 GGPPS is a homodimer and its three-dimensional structure is most similar to the large subunit of heterodimeric *A. thaliana* GGPPS1. Heterodimeric and heterotetrameric GGPPSs are found in higher plants, with the large subunit involved in catalysis and the small subunit in product release (Chang et al., 2010; Wang et al., 2016).

Syn7002 GGPPS contains the two highly conserved aspartate-rich motifs (FARM and SARM), which are important for substrate binding and catalysis in prenyltransferases (Song and Poulter, 1994; Koyama et al., 1996). In most trans-prenyltransferase structures, dimer interactions have been observed between helices E and F (F1 and F2) (Guo et al., 2004; Noike et al., 2008; Han et al., 2015; Wang et al., 2016). Van der Waals interactions and stacking (π-π) interactions between the hydrophobic residues on these two helices contribute to dimerization (Sun et al., 2005). Previous studies have demonstrated that a positively charged residue Lys at the bottom of the catalytic cavity is responsible for IPP binding: Lys-36 in *S. cerevisiae* GGPPS (PDB: 2E8U), Lys-60 in *Plasmodium vivax* GGPPS (3LDW), and Lys-47 in *Trypanosoma brucei* FPPS (PDB: 3DYF) (Guo et al., 2007; Zhang et al., 2009; Artz et al., 2011). In addition, Koyama et al. (1996) replaced Lys-47 with Ile in *B. stearothermophilus* FPPS and found the affinity for substrate IPP was decreased. In Syn7002 GGPPS, replacement of Lys-53 by Ala led to no detectable formation of product. Arg-56, which is highly conserved in prenyltransferases, is also ideally placed to interact with IPP, as also observed for *S. cerevisiae* GGPPS (Guo et al., 2007).

A "three-floor" model has been proposed to explain how the length of the final product is controlled in prenyltransferases (Wang et al., 2016). The size of residues at each floor determines the length of the final product. For example, "Floor one" determines if the final product is C15-FPP, "Floor two" if it is C20-GGPP and "Floor three" if it is C25-GFPP (**Figure 5A**). From these models and corresponding site-directed mutagenesis experiments, it is generally believed that the size of the residues located four and five positions before the FARM determines the chain length of the product, with a large side chain forming a "floor" that blocks further product elongation (Ohnuma et al., 1996; Narita et al., 1999; Guo et al., 2004; Sun et al., 2005; Szkopi and Danuta, 2005; Ling et al., 2007; Han et al., 2015). According to our structural models, Syn7002 CrtE has two small residues and one medium sized Met residue on the first floor, and its second floor is formed from Ile-84, Leu-126 and Val-155 (**Figure 5A**). Surprisingly, replacement of Met-87 on the first floor with Ala generated a longer product C25-GFPP, suggesting that Met-87 has a role in forming the first floor but its side chain also indirectly impacts the second floor. An identical result was also observed previously for the equivalent Met to Ala mutation in AtGGPPS1 (Wang et al., 2016) and, indeed, the predicted first floor residues are exactly the same in Syn7002 CrtE and AtGGPPS1 and the second floor residues are very similar with Ile, Leu, and Val found in Syn7002 CrtE and Ile, Leu, and Ile in AtGGPPS1.

The residues before another conserved motif G(Q/E) on helix F1 are also considered to regulate chain termination (Hemmi et al., 2003; Kawasaki et al., 2003). Our sequence alignment (**Figure 2**) demonstrated that the size of the second residue before the G(Q/E) motif in the short-chain prenyltransferases (like PaGPPS and HsGGPPS) is larger than that in the medium/long-chain prenyltransferases. In addition, our Syn7002 GGPPS structure showed that the second residue (Val-161) before the conserved GQ motif is more likely to generate a "floor" with Met-87 and Ser-88 according to its spatial position. Mutating Val-161 to Met partially blocked the reaction and generated more FPP and less GGPP compared to the products of wild type GGPPS. A similar mutagenesis study was performed with *S. acidocaldarius* HexPPS: a point mutation at this position (S140H, S140F, and S140Y) resulted in the shortening of the final products (Hemmi et al., 2003). Collectively, these results indicate that the second residue before the conserved G(Q/E) motif is also involved in determining product chain length. The third amino acid (L151) before the G(Q/E) motif of *A. thaliana* GGPPS1 has also been reported to be important for "floor" formation, with mutation of this residue (L151F) leading to the formation of shorter products (GPP and FPP) and less GGPP (Wang et al., 2016).

Cyanobacteria have been considered as green microbial cell factories for producing high value-added products. However, the yield of short chain terpenoids is limited by the small pool sizes of their precursors GPP and FPP (Kiyota et al., 2014), as the major product of CrtE is GGPP. We have shown here that mutation of CrtE can alter product specificity. In principle, it is possible to use this knowledge to make cyanobacterial strains with larger pools of FPP or GFPP which could be useful platforms for the production of sesquiterpenoids, triterpenoids and sesterterpenoids.

DATA AVAILABILITY STATEMENT

Two protein structures were elucidated and submitted to the RCSB Protein Data Bank: the structures of Syn7002 CrtE with six copies in the asymmetric unit in its apo form (PDB accession: 6SXN) and with two copies in the asymmetric unit in its apo form (PDB accession: 6SXL).

AUTHOR CONTRIBUTIONS

YF performed the experimental work. RM collected the X-ray diffraction data and solved the structures. PF contributed reagents, materials, and analysis tools for TLC analysis. YF, RM, PF, and PN designed the experiments. All authors listed have contributed to data interpretation, preparation, and writing of the manuscript.

FUNDING

This work was provided by the European Union's Horizon 2020 Research and Innovation Program project PHOTOFUEL under grant agreement number 640720. YF was supported by the China Scholarship Council.

ACKNOWLEDGMENTS

We are extremely grateful to Chris Gerrish (Royal Holloway, University of London) for help with the TLC assays and to James W. Murray and Ciaran McFarlane (Imperial College London) for help with data collection and structure refinement.

SUPPLEMENTARY MATERIAL

The Supplementary Material for this article can be found online at: https://www.frontiersin.org/articles/10.3389/fpls.2020.00589/full#supplementary-material

REFERENCES

Artz, J. D., Wernimont, A. K., Dunford, J. E., Schapira, M., Dong, A., Zhao, Y., et al. (2011). Molecular characterization of a novel geranylgeranyl pyrophosphate synthase from plasmodium parasites. *J. Biol. Chem.* 286, 3315–3322. doi: 10.1074/jbc.m109.027235

Bai, C., Capell, T., Berman, J., Medina, V., Sandmann, G., Christou, P., et al. (2016). Bottlenecks in carotenoid biosynthesis and accumulation in rice endosperm are influenced by the precursor-product balance. *Plant Biotechnol. J.* 14, 195–205. doi: 10.1111/pbi.12373

Bouvier, F., Rahier, A., and Camara, B. (2005). Biogenesis, molecular regulation and function of plant isoprenoids. *Prog. Lipid Res.* 44, 357–429. doi: 10.1016/j.plipres.2005.09.003

Brünger, A. T. (1993). Assessment of phase accuracy by cross validation: the free R value. methods and applications. acta crystallogr. *Sect. D Biol. Crystallogr.* 49, 24–36. doi: 10.1107/s0907444992007352

Catanzariti, A.-M., Soboleva, T. A., Jans, D. A., Board, P. G., and Baker, R. T. (2004). An efficient system for high-level expression and easy purification of authentic recombinant proteins. *Protein Sci.* 13, 1331–1339. doi: 10.1110/ps.04618904

Chang, K. M., Chen, S. H., Kuo, C. J., Chang, C. K., Guo, R. T., Yang, J. M., et al. (2012). Roles of amino acids in the *Escherichia coli* octaprenyl diphosphate synthase active site probed by structure-guided site-directed mutagenesis. *Biochemistry* 51, 3412–3419. doi: 10.1021/bi300069j

Chang, T. H., Guo, R. T., Ko, T. P., Wang, A. H. J., and Liang, P. H. (2006). Crystal structure of type-III geranylgeranyl pyrophosphate synthase from Saccharomyces cerevisiae and the mechanism of product chain length determination. *J. Biol. Chem.* 281, 14991–15000. doi: 10.1074/jbc.M512886200

Chang, T.-H., Hsieh, F.-L., Ko, T.-P., Teng, K.-H., Liang, P.-H., and Wang, A. H.-J. (2010). Structure of a heterotetrameric geranyl pyrophosphate synthase from Mint (Mentha piperita) reveals intersubunit regulation. *Plant Cell* 22, 454–467. doi: 10.1105/tpc.109.071738

Chen, A., Dale Poulter, C., and Kroon, P. A. (1994). Isoprenyl diphosphate synthases: protein sequence comparisons, a phylogenetic tree, and predictions of secondary structure. *Protein Sci.* 3, 600–607. doi: 10.1002/pro.5560030408

DeLano, W. L. (2002). *PyMOL*. Available online at: http://www.pymol.org.

Emsley, P., and Cowtan, K. (2004). Coot: model-building tools for molecular graphics. *Acta Crystallogr. Sect. D Biol. Crystallogr.* 60, 2126–2132. doi: 10.1107/S0907444904019158

Emsley, P., Lohkamp, B., Scott, W. G., and Cowtan, K. (2010). Features and development of *Coot*. *Acta Crystallogr. D Biol. Crystallogr.* 66, 486–501. doi: 10.1107/S0907444910007493

Evans, P. (2006). Scaling and assessment of data quality. *Acta Crystallogr. Sect. D Biol. Crystallogr.* 62, 72–82. doi: 10.1107/S0907444905036693

Guo, R.-T., Cao, R., Liang, P.-H., Ko, T.-P., Chang, T.-H., Hudock, M. P., et al. (2007). Bisphosphonates target multiple sites in both cis- and trans-prenyltransferases. *Proc. Natl. Acad. Sci. U.S.A.* 104, 10022–10027. doi: 10.1073/pnas.0702254104

Guo, R. T., Kuo, C. J., Chou, C. C., Ko, T. P., Shr, H. L., Liang, P. H., et al. (2004). Crystal structure of octaprenyl pyrophosphate synthase from hyperthermophilic thermotoga maritima and mechanism of product chain length determination. *J. Biol. Chem.* 279, 4903–4912. doi: 10.1074/jbc.M310161200

Han, X., Chen, C. C., Kuo, C. J., Huang, C. H., Zheng, Y., Ko, T. P., et al. (2015). Crystal structures of ligand-bound octaprenyl pyrophosphate synthase from *Escherichia coli* reveal the catalytic and chain-length determining mechanisms. *Proteins Struct. Funct. Bioinforma.* 83, 37–45. doi: 10.1002/prot.24618

Hemmi, H., Noike, M., Nakayama, T., and Nishino, T. (2003). An alternative mechanism of product chain-length determination in type III geranylgeranyl diphosphate synthase. *Eur. J. Biochem.* 270, 2186–2194. doi: 10.1046/j.1432-1033.2003.03583.x

Jiang, M., Stephanopoulos, G., and Pfeifer, B. A. (2012). Toward biosynthetic design and implementation of *Escherichia coli*-derived paclitaxel and other heterologous polyisoprene compounds. *Appl. Environ. Microbiol.* 78, 2497–2504. doi: 10.1128/AEM.07391-11

Jones, M. O., Perez-Fons, L., Robertson, F. P., Bramley, P. M., and Fraser, P. D. (2013). Functional characterization of long-chain prenyl diphosphate synthases from tomato. *Biochem. J.* 449, 729–740. doi: 10.1042/bj20120988

Kavanagh, K. L., Dunford, J. E., Bunkoczi, G., Russell, R. G. G., and Oppermann, U. (2006). The crystal structure of human geranylgeranyl pyrophosphate synthase reveals a novel hexameric arrangement and inhibitory product binding. *J. Biol. Chem.* 281, 22004–22012. doi: 10.1074/jbc.M602603200

Kawasaki, T., Hamano, Y., Kuzuyama, T., Itoh, N., Seto, H., and Dairi, T. (2003). Interconversion of the product specificity of type I eubacterial farnesyl diphosphate synthase and geranylgeranyl diphosphate synthase through one amino acid substitution. *J. Biochem.* 133, 83–91. doi: 10.1093/jb/mvg002

Kiyota, H., Okuda, Y., Ito, M., Hirai, M. Y., and Ikeuchi, M. (2014). Engineering of cyanobacteria for the photosynthetic production of limonene from CO2. *J. Biotechnol.* 185, 1–7. doi: 10.1016/j.jbiotec.2014.05.025

Kloer, D. P., Welsch, R., Beyer, P., and Schulz, G. E. (2006). Structure and reaction geometry of geranylgeranyl diphosphate synthase from Sinapis alba. *Biochemistry* 45, 15197–15204. doi: 10.1021/bi061572k

Koyama, T., Tajima, M., Sano, H., Doi, T., Koike-Takeshita, A., Obata, S., et al. (1996). Identification of significant residues in the substrate binding site of Bacillus stearothermophilus farnesyl diphosphate synthase. *Biochemistry* 35, 9533–9538. doi: 10.1021/bi960137v

Liang, C., Zhao, F., Wei, W., Wen, Z., and Qin, S. (2006). Carotenoid biosynthesis in cyanobacteria: Structural and evolutionary scenarios based on comparative genomics. *Int. J. Biol. Sci.* 2, 197–207. doi: 10.7150/ijbs.2.197

Liang, P. H. (2009). Reaction kinetics, catalytic mechanisms, conformational changes, and inhibitor design for prenyltransferases. *Biochemistry* 48, 6562–6570. doi: 10.1021/bi900371p

Ling, Y., Li, Z. H., Miranda, K., Oldfield, E., and Moreno, S. N. J. (2007). The farnesyl-diphosphate/geranylgeranyl-diphosphate synthase of Toxoplasma gondii is a bifunctional enzyme and a molecular target of bisphosphonates. *J. Biol. Chem.* 282, 30804–30816. doi: 10.1074/jbc.M703178200

McCoy, A. J., Grosse-Kunstleve, R. W., Adams, P. D., Winn, M. D., Storoni, L. C., and Read, R. J. (2007). Phaser crystallographic software. *J. Appl. Crystallogr.* 40, 658–674. doi: 10.1107/S0021889807021206

Michoux, F., Boehm, M., Bialek, W., Takasaka, K., Maghlaoui, K., Barber, J., et al. (2014). Crystal structure of CyanoQ from the thermophilic cyanobacterium Thermo*synechococcus elongatus* and detection in isolated photosystem II complexes. *Photosynth. Res.* 122, 57–67. doi: 10.1007/s11120-014-0010-z

Murshudov, G. N., Skubák, P., Lebedev, A. A., Pannu, N. S., Steiner, R. A., Nicholls, R. A., et al. (2011). REFMAC5 for the refinement of macromolecular crystal structures. *Acta Crystallogr. Sect. D Biol. Crystallogr.* 67, 355–367. doi: 10.1107/S0907444911001314

Narita, K., Ohnuma, S., and Nishino, T. (1999). Protein design of geranyl diphosphate. *J. Biochem* 126, 566–571.

No, J. H., De Macedo Dossin, F., Zhang, Y., Liu, Y. L., Zhu, W., Feng, X., et al. (2012). Lipophilic analogs of zoledronate and risedronate inhibit Plasmodium geranylgeranyl diphosphate synthase (GGPPS) and exhibit potent antimalarial activity. *Proc. Natl. Acad. Sci. U.S.A.* 109, 4058–4063. doi: 10.1073/pnas.1118215109

Noike, M., Katagiri, T., Nakayama, T., Koyama, T., Nishino, T., and Hemmi, H. (2008). The product chain length determination mechanism of type II geranylgeranyl diphosphate synthase requires subunit interaction. *FEBS J.* 275, 3921–3933. doi: 10.1111/j.1742-4658.2008.06538.x

Ogura, K., and Koyama, T. (1998). Enzymatic aspects of isoprenoid chain elongation. *Chem. Rev.* 98, 1263–1276. doi: 10.1021/cr9600464

Ohnuma, N. T., Nishinof, T., Narita, K., Ishida, C., Takeuchi, Y., Nishino, T., et al. (1996). A role of the amino acid residue located on the fifth position before the first aspartate-rich motif of farnesyl diphosphate synthase on determination of the final product. *J. Biol. Chem.* 271, 30748–30754. doi: 10.1074/jbc.271.48.30748

Ohto, C., Ishida, C., Nakane, H., Muramatsu, M., Nishino, T., and Obata, S. (1999). A thermophilic cyanobacterium *Synechococcus elongatus* has three different class I prenyltransferase genes. *Plant Mol. Biol.* 40, 307–321. doi: 10.1023/A:1006295705142

Petrova, T. E., Boyko, K. M., Nikolaeva, A. Y., Stekhanova, T. N., Gruzdev, E. V., Mardanov, A. V., et al. (2018). Structural characterization of geranylgeranyl pyrophosphate synthase GACE1337 from the hyperthermophilic archaeon *Geoglobus acetivorans*. *Extremophiles* 22, 877–888. doi: 10.1007/s00792-018-1044-5

Rabinovitch-Deere, C. A., Oliver, J. W. K., Rodriguez, G. M., and Atsumi, S. (2013). Synthetic biology and metabolic engineering approaches to produce biofuels. *Chem. Rev.* 113, 4611–4632. doi: 10.1021/cr300361t

Ruiz-Sola, M. Á, Barja, M. V., Rodríguez-Concepción, M., Coman, D., Beck, G., Colinas, M., et al. (2016). *Arabidopsis* geranylgeranyl diphosphate synthase 11 Is a hub isozyme required for the production of most photosynthesis-related isoprenoids. *New Phytol* 209, 252–264. doi: 10.1111/nph.13580

Shimizu, N., Koyama, T., and Ogura, K. (1998). molecular cloning, expression, and purification of undecaprenyl diphosphate synthase. *J. Biol. Chem.* 273, 19476–19481. doi: 10.1074/jbc.273.31.19476

Song, L., and Poulter, A. C. D. (1994). Yeast farnesyl-diphosphate synthase: Site-directed mutagenesis of residues in highly conserved prenyltransferase domains I and II (sitedirected mutants/kinetic ctnt/immunoaffllulty chromatography). *Biochemistry* 91, 3044–3048. doi: 10.1073/pnas.91.8.3044

Sun, H.-Y., Guo, R.-T., Liang, P.-H., Wang, A. H.-J., Ko, T.-P., Kuo, C.-J., et al. (2005). Homodimeric hexaprenyl pyrophosphate synthase from the thermoacidophilic crenarchaeon Sulfolobus solfataricus displays asymmetric subunit structures. *J. Bacteriol.* 187, 8137–8148. doi: 10.1128/JB.187.23.8137-8148.2005

Szkopi, A., and Danuta, P. (2005). Farnesyl diphosphate synthase; regulation of product. *Acta Biochim. Pol.* 52, 45–55.

Tarshis, L. C., Proteau, P. J., Kellogg, B. A., Sacchettini, J. C., and Poulter, C. D. (1996). Regulation of product chain length by isoprenyl diphosphate synthases. *Proc. Natl. Acad. Sci. U.S.A* 93, 15018–15023. doi: 10.1073/pnas.93.26.15018

Vickers, C. E., Bongers, M., Liu, Q., Delatte, T., and Bouwmeester, H. (2014). Metabolic engineering of volatile isoprenoids in plants and microbes. *Plant, Cell Environ.* 37, 1753–1775. doi: 10.1111/pce.12316

Wallrapp, F. H., Pan, J.-J., Ramamoorthy, G., Almonacid, D. E., Hillerich, B. S., Seidel, R., et al. (2013). Prediction of function for the polyprenyl transferase subgroup in the isoprenoid synthase superfamily. *Proc. Natl. Acad. Sci. U.S.A* 110:E1196–E1202. doi: 10.1073/pnas.1300632110

Wang, C., Chen, Q., Fan, D., Li, J., Wang, G., and Zhang, P. (2016). Structural analyses of short-chain prenyltransferases identify an evolutionarily conserved GFPPS clade in brassicaceae plants. *Mol. Plant* 9, 195–204. doi: 10.1016/j.molp.2015.10.010

Wang, K., and Ohnuma, S. (1999). Chain-length determination mechanism of isoprenyl diphosphate synthases and implications for molecular evolution. *Trends Biochem. Sci.* 24, 445–451. doi: 10.1016/S0968-0004(99)01464-4

Winter, G., Lobley, C. M. C., and Prince, S. M. (2013). Decision making in xia2. *Acta Crystallogr. Sect. D Biol. Crystallogr.* 69, 1260–1273. doi: 10.1107/S0907444913015308

Yen, H. C., and Marrs, B. (1976). Map of genes for carotenoid and bacteriochlorophyll biosynthesis in *Rhodopseudomonas capsulata*. *J. Bacteriol.* 126, 619–629.

Zhang, Y., Cao, R., Yin, F., Hudock, M. P., Guo, R., Mukherjee, S., et al. (2009). Lipophilic bisphosphonates as dual farnesyl / geranylgeranyl diphosphate synthase inhibitors: an X-ray and NMR investigation. *J. Am. Chem. Soc.* 131, 5153–5162. doi: 10.1021/ja808285e

Zhou, F., Wang, C.-Y., Gutensohn, M., Jiang, L., Zhang, P., Zhang, D., et al. (2017). A recruiting protein of geranylgeranyl diphosphate synthase controls metabolic flux toward chlorophyll biosynthesis in rice. *Proc. Natl. Acad. Sci. U.S.A.* 114, 6866–6871. doi: 10.1073/pnas.1705689114

Zor, T., and Selinger, Z. (1996). Linearization of the bradford protein assay increases its sensitivity: theoretical and experimental studies. *Anal. Biochem.* 2, 302–308. doi: 10.1006/abio.1996.0171

Conflict of Interest: The authors declare that the research was conducted in the absence of any commercial or financial relationships that could be construed as a potential conflict of interest.

frontiers in Plant Science

ORIGINAL RESEARCH
published: 10 June 2020
doi: 10.3389/fpls.2020.00772

High Light-Induced Nitric Oxide Production Induces Autophagy and Cell Death in *Chlamydomonas reinhardtii*

*Eva YuHua Kuo[1,2†], Hsueh-Ling Chang[1,2†], Shu-Tseng Lin[1] and Tse-Min Lee[1,2]**

[1] Department of Marine Biotechnology and Resources, National Sun Yat-sen University, Kaohsiung, Taiwan, [2] Doctoral Degree Program in Marine Biotechnology, National Sun Yat-sen University, Kaohsiung, Taiwan

OPEN ACCESS

Edited by:
Dimitris Petroutsos,
UMR 5168 Laboratoire de Physiologie Cellulaire Vegetale (LPCV), France

Reviewed by:
Jose L. Crespo,
Consejo Superior de Investigaciones Científicas (CSIC), Spain
Thomas Roach,
University of Innsbruck, Austria

***Correspondence:**
Tse-Min Lee
tmlee@mail.nsysu.edu.tw

[†] These authors have contributed equally to this work

Specialty section:
This article was submitted to Plant Cell Biology, a section of the journal Frontiers in Plant Science

Received: 27 February 2020
Accepted: 15 May 2020
Published: 10 June 2020

Citation:
Kuo EY, Chang H-L, Lin S-T and Lee T-M (2020) High Light-Induced Nitric Oxide Production Induces Autophagy and Cell Death in Chlamydomonas reinhardtii. Front. Plant Sci. 11:772. doi: 10.3389/fpls.2020.00772

Autophagy plays a role in regulating important cellular functions in response to stress conditions. The role of nitric oxide (NO) in the regulation of autophagy in *Chlamydomonas reinhardtii* has been not studied. Illumination of *C. reinhardtii* cells under a high light (HL, 1,600 μmol m^{-2} s^{-1}) condition induced a NO burst through NO synthase- and nitrate reductase-independent routes, and cell death. The abundance of CrATG8 protein, an autophagy marker of *C. reinhardtii*, increased after HL illumination along with a linear increase in the transcript abundance of autophagy-associated genes (CrVPS34, CrATG1, CrATG3, CrATG4, CrATG6, CrATG7, CrATG8, and CrATG12), which were suppressed in the presence of an NO scavenger, 2-(4-carboxyphenyl)-4,4,5,5-tetramethylimidazoline-1-oxyl-3-oxide (cPTIO). The cells were treated with NO donors, *S*-nitroso-*N*-acetyl-penicillamine, and *S*-nitrosoglutathione, under a normal light (50 μmol m^{-2} s^{-1}) condition to elucidate the role of NO in autophagy activation and cell death. Treatment with 0.05 mM or 0.1 mM NO donors increased the abundance of ATG8 protein and CrATG transcripts, which were suppressed in the presence of cPTIO. Moreover, treatment with 0.05 mM NO donors did not affect cell viability, while 0.1 mM NO donors elicited a transient decrease in cell growth and death that recovered after 12 h. The transient effect could be prevented by the presence of cPTIO. However, treatment with 1 mM H_2O_2 and 0.1 mM NO donors enhanced autophagy induction and resulted in cell death after 24 h. The interaction of H_2O_2 and NO can be prevented by cPTIO treatment. This implies that NO is critical for the interaction of H_2O_2 and NO that induces cell death and autophagy. Furthermore, exposure to 0.1 mM NO donors under a non-lethal HL condition (750 μmol m^{-2} s^{-1}) evoked autophagy and cell death. In conclusion, the present findings demonstrated that the NO-mediated autophagy pathway is activated in *C. reinhardtii* under lethal high intensity illumination and may interact with H_2O_2 for HL-induced cell death. The relationships between autophagy and cell death are discussed.

Keywords: autophagy, autophagy-related protein, cell death, *Chlamydomonas*, high light, nitric oxide

INTRODUCTION

Nitric oxide (NO), a short-lived, gaseous molecule that can be either enzymatically or non-enzymatically synthesized in plants (Besson-Bard et al., 2008; Palavan-Unsal and Arisan, 2009), has been recognized as a novel biological messenger in the regulation of various biochemical and physiological activities and stress responses (Anbar, 1995; Neill et al., 2008; Hasanuzzaman et al., 2010; Hayat et al., 2010; Siddiqui et al., 2011; Bajguz, 2014). Recently, increasing importance has been attached to the role of NO in the regulation of high intensity light responses. However, whether NO plays a protective or a harmful role in the response of plants to excessive light energy depends on the plant species. Illumination of the leaves of tall fescue (*Festuca arundinacea* Schreb.) at an intensity of 500 μmol m^{-2} s^{-1} triggers NO production against oxidative stress by increasing the activity of antioxidant enzymes and the content of antioxidants (Xu et al., 2010). Foresia et al. (2010) has reported for a unicellular marine alga *Ostreococcus tauri* Gen et Sp-NOV that illumination at 400 μmol m^{-2} s^{-1} induces an NO burst, which is proposed to be a signal triggering a photoprotection mechanism against high light (HL)-induced oxidative damage. We have recently found a contrasting result in *Chlamydomonas reinhardtii* P.A. Dangeard that NO generated under very high intensity light (VHL; 3,000 μmol m^{-2} s^{-1}) conditions is associated with VHL-induced cell death (Chang et al., 2013).

There is accumulating evidence that the generation of NO is crucial for the regulation of developmentally regulated and environmentally induced programmed cell death (PCD) in plants, either its promotion or its inhibition (Delledonne et al., 2001; Wang et al., 2013). NO delays the onset of cell death in gibberellin (GA)-induced PCD in barley aleurone layers (Beligni et al., 2002), while NO at high concentrations induces DNA fragmentation, membrane breakdown, and cell death (Pedroso et al., 2000; Yamasaki, 2000; Romero-Puertas et al., 2004). Moreover, NO is involved in the regulation of hypersensitive cell death (Clarke et al., 2000; de Pinto et al., 2002) and stress-induced cell death (Ahlfors et al., 2009; de Michele et al., 2009). NO also triggers cell death in algae; for example, the aldehyde-induced cell death in diatoms (Vardi et al., 2006), the heat-induced cell death of symbiotic alga *Symbiodinium microadriaticum* Freudenthal (Bouchard and Yamasaki, 2008), and the mastoparan (MP)-induced cell death of *C. reinhardtii* (Yordanova et al., 2010).

Reactive oxygen species (ROS) and oxidative stress modulate the autophagy process in plants (Pérez-Pérez et al., 2010, 2012b; Liu and Bassham, 2012; Bassham and Crespo, 2014). Stresses, including methyl viologen (MV)- or hydrogen peroxide (H_2O_2)-induced oxidative stress, nitrogen deficiency, carbon starvation by dark incubation, endoplasmic reticulum stress, and disordered chloroplast protein homeostasis due to a depletion of ClpP1 protease, are known to trigger autophagy in *C. reinhardtii* cells (Pérez-Pérez et al., 2010, 2012a,b, 2014; Ramundo et al., 2014). Moreover, a transfer of *C. reinhardtii* cells from dim light (5–10 μmol m^{-2} s^{-1}) to high intensity light (1,200 μmol m^{-2} s^{-1}) caused a transient increase of autophagy-related protein 8 (ATG8) abundance with a peak at 6 h, followed by a gradual decline to the control level when the high intensity illumination was prolonged to 24 h (Pérez-Pérez et al., 2012a). In comparison with wild type, the induction of autophagy by high intensity light illumination, MV, or H_2O_2, is more pronounced in *C. reinhardtii lts1-204* and *npq1 lor1* mutants, which exhibit a higher sensitivity to oxidative stress due to low carotenoid levels (Pérez-Pérez et al., 2012a).

Reactive nitrogen species (RNS) are also known to modulate autophagy. In animal system, NO activates autophagy in HeLa cells (Yang et al., 2008) and neurons (Barsoum et al., 2006) but suppresses autophagy in neurodegenerative diseases (Sarkar et al., 2011). In contrast, NO does not affect autophagy in cardiac myocytes (Rabkin and Klassen, 2007). This suggests that the differential regulation of autophagy by NO depends on the type of animal tissue. Apart from ROS and oxidative stress, the role of RNS in the control of autophagy has not previously been reported in *C. reinhardtii* cells, as far as we know. Therefore, the present study has examined whether NO modulates autophagy in *C. reinhardtii* cells under very high intensity illumination (HL, 1,600 μmol m^{-2} s^{-1}), which can induce cell death. First, the time-course changes in NO production detected by 4-amino-5-methylamino-2′,7′-difluororescein (DAF-FM), the level of ATG8 detected using western blots, and the transcript abundance of autophagy-associated genes were determined. Furthermore, the role of NO was confirmed by experiments in the presence or absence of an NO scavenger, 2-(4-carboxyphenyl)-4,4,5,5-tetramethylimidazoline-1-oxyl-3-oxide (cPTIO). Then, the NO donors including *S*-nitrosoglutathione (GSNO) and *S*-nitroso-*N*-acetyl-penicillamine (SNAP) were treated under normal light (NL, 50 μmol m^{-2} s^{-1}) illumination with or without cPTIO to confirm the role of NO in autophagy activation and cell death. Next, the NO donors were treated under non-lethal HL conditions (i.e., a moderate high light condition, ML, 750 μmol m^{-2} s^{-1}) to examine whether NO can confer sensitivity of *C. reinhardtii* cells to the induction of autophagy and cell death under moderate high light illumination. In addition, the interaction of NO with H_2O_2 accumulated under HL illumination in the modulation of autophagy and cell death was investigated by the application of H_2O_2 together with SNAP or GSNO under NL conditions.

MATERIALS AND METHODS

Algal Culture and Treatments

Chlamydomonas reinhardtii P.A. Dangeard strain CC125 (*mt*+) and CC124 (*mt*−) obtained from the Chlamydomonas Resource Center[1] (University of Minnesota, St. Paul, MN, United States), were photoheterotrophically cultured in 50 mL of Tris-acetate phosphate (TAP) medium (Harris, 1989) containing a trace element solution in 125 mL flasks. The cultures were agitated on an orbital shaking incubator (model OS701, TKS company, Taipei, Taiwan) (150 rpm) under continuous illumination with a fluorescent white light at the NL intensity of 50 μmol m^{-2} s^{-1} at 28°C. After 18–24 h of incubation, algal cells that grew to the density of approximately 3×10^6 cells mL^{-1} were centrifuged

[1]http://chlamycollection.org/

at 4,000 × *g* for 5 min at 28°C. The pellet was resuspended in fresh TAP medium as 3×10^6 cells mL^{-1}. Ten mL of the resuspended culture was transferred to a 100 mL beaker and incubated at 28°C under an NL condition for 1.5 h in an orbital shaker (model OS701, TKS Company, Taipei, Taiwan) at a speed of 150 rpm. Then, the algal cells were exposed to HL, 1,600 μmol m^{-2} s^{-1}, or subjected to chemical treatments at 28°C. Each treatment had three independent biological replicates ($n = 3$) with each beaker as a biological replicate. The treatment has been repeated three times. Samples taken before (0 h) and after chemical treatment were imaged, then centrifuged at 4,000 × *g* for 5 min, and the pellet was fixed in liquid nitrogen and stored at −80°C until analysis.

To explore whether NO modulates the HL-induced autophagy and cell death, cPTIO was applied to scavenge NO at a final concentration of 400 μM. Because we have found that cPTIO lost its ability to scavenge NO after 2–3 h, 400 μM cPTIO was added again to the algal culture at 2.5 h. To mimic the effect of NO bursts under the HL condition, the NO donors, SNAP and GSNO (Sigma-Aldrich, St. Louis, MO, United States), were applied to the cells illuminated with 50 μmol m^{-2} s^{-1} intensity in the presence or absence of 400 μM cTPIO. In addition, to elucidate whether NO can promote the susceptibility of *C. reinhardtii* cells to high intensity illumination, SNAP and GSNO were applied separately at concentrations of 0.05 or 0.1 mM under a moderate high light condition (ML, 750 μmol m^{-2} s^{-1}). In addition, the interaction of NO and H_2O_2 in the induction of autophagy and cell death was also investigated by treatment with 1 mM H_2O_2 with and without 0.1 mM NO donors under an NL condition for 3 h. In this experiment, the role of NO was confirmed by the treatment of cPTIO with an NO donor and H_2O_2.

In the attempts to elucidate the involvement of NO synthase (NOS) or nitrate reductase (NR) in the HL-induced NO production, the inhibitors of NOS and NR, N^{ω}-nitro-L-arginine methyl ester (L-NAME), N^{ω}-monomethyl-L-arginine (L-NMMA), and sodium tungstate, respectively, were added to the TAP medium 1.5 h before the HL treatment.

Determination of Cell Density and Viability

For cell density estimation, 10 μL of algal culture was mixed with 30 μL of Lugol's solution (Sigma-Aldrich, St. Louis, MO, United States) and the cell number was counted in duplicate using a light microscope (BX43, Olympus, Tokyo, Japan) and a hemocytometer (Improved Neubauer, Boeco, Germany). The cell density was calculated according to the manufacturer's manual and expressed as units of 10^6 mL^{-1}.

After treatments, the viability of the algal cells was estimated by loading 2 μL of cell suspension on TAP agar plates, and incubating the plates for 72 h at 28°C under illumination at 50 μmol m^{-2} s^{-1} intensity. The colonies were imaged with a digital Nikon camera, and the final composite images were constructed using Adobe Photoshop (Adobe Systems, San Jose, CA, United States). Together with a cell density curve, the cell viability was assessed by growth ability (the color and size of the colony) and was used to evaluate the effects of HL illumination or chemical challenges.

Detection of Dead Cells Using Sytox Green Fluorescence

Cell death was assessed using the SYTOX-Green fluorescent probe (Molecular Probes Inc., Eugene, OR, United States). The SYTOX-Green stock solution of 5 mM in 100% DMSO was added to 1 mL of algal culture at a final concentration of 5 μM, and the mixture was incubated for 5 min at room temperature in the dark. The fluorescence level was detected by a fluorescence spectrophotometer at 525 nm (excitation: 488 nm) (Sato et al., 2004). Based on the blank (TAP medium without algal cells), the relative SYTOX-Green fluorescence level was estimated and expressed as relative fluorescence·$(10^6$ cells$)^{-1}$.

Then, the cells were observed with a fluorescence microscope (Eclipse Ni, Nikon, Tokyo, Japan) with excitation at 488 nm using FITC (excitation wavelength: 465–495 nm, emission wavelength: 515–555 nm) and B-2A (excitation wavelength: 450–490 nm, emission wavelength: >520 nm) filters (Nikon, Tokyo, Japan). Fluorescent images were acquired using a CCD camera (Nikon's Digital Sight DSU3, Tokyo, Japan) and imported into Adobe Photoshop.

Detection of NO Production

An NO-sensitive fluorescent dye, DAF-FM diacetate (Kojima et al., 1998), purchased from Invitrogen Life Technologies (Carlsbad, CA, United States) was employed to measure NO production according to the procedure described in our previous study (Chang et al., 2013). DAF-FM diacetate was preloaded into cell cultures prior to HL and chemical treatments. Algal cells (1 mL) were preincubated in TAP medium containing 5 μM DAF-FM diacetate for 60 min at 25°C under NL to allow the penetration of DAF-FM acetate into the cells (Chang et al., 2013). Then, the algal cells were washed twice with fresh TAP medium and exposed to HL or treated with a chemical. The fluorescence in the cells was determined with a fluorescence spectrophotometer (excitation/emission: 492 nm/525 nm; F-2500, Hitachi, Tokyo, Japan) and observed with a fluorescence microscope (Eclipse Ni, Nikon, Tokyo, Japan) using a FITC filter (Nikon, Tokyo, Japan). Based on the fluorescence of the blank (TAP medium without algal cells), the relative DAF-FM fluorescence level was estimated and expressed as relative fluorescence·$(10^6$ cells$)^{-1}$.

Protein Extraction and Western Blots

Soluble protein was extracted according to Pérez-Pérez et al. (2012a). After treatment for 3 h under NL or HL conditions, algal cells ($n = 3$, three independent biological replicates) were collected by centrifugation (4,000 × *g*, 5 min), washed once with lysis buffer (50 mM Tris-HCl, pH 7.5) and resuspended in 50 μL lysis buffer. Cells were lysed by two cycles of slow freezing to −80°C, followed by fast thawing to room temperature. The soluble cell extract was then separated from the insoluble fraction by centrifugation (15,000 × *g*, 15 min) at 4°C and immediately used for western-blot analysis and protein quantitation. Protein concentrations were quantified by the Coomassie Blue dye

binding method (Bradford, 1976) using the concentrated dye purchased from BioRad (500-0006, Hercules, CA, United States). Samples were heated to 100°C for 5 min and then used for western blot analysis. For each sample, 30 μg of protein was loaded into each lane, resolved by 15% SDS-PAGE, and transferred to a polyvinylidene fluoride membrane for antibody binding. After being blocked with 5% BSA (Sigma, St. Louis, MO, United States), the membranes were incubated with a rabbit polyclonal anti-ATG8 antibody (ab77003; Abcam, Cambridge, United Kingdom) and a mouse monoclonal antibody against α-tubulin (ab11304; Abcam, Cambridge, United Kingdom) for 90 min at room temperature. After being washed, the membranes were incubated for 90 min with horseradish peroxidase-conjugated secondary antibodies (MD20878; KPL, Gaithersburg, MD, United States), and then the immunoblots were visualized using the ECL Plus chemiluminescence system (Thermo Scientific Inc., Chicago, IL, United States). A LAS-3000 Mini Lumino-image Analyzer (LAS-3000, Fujifilm, Tokyo, Japan) was used for imaging the chemiluminescent western blots. The relative abundance of CrATG8 protein was estimated on the basis of α-tubulin intensity.

RNA Isolation, cDNA Synthesis, and mRNA Quantification by Real-Time Quantitative PCR

For RNA isolation, the algal cells in 5 mL of culture sampled from each of the independent biological replicates (n = 3) were harvested by centrifugation as described above. Total RNA was extracted with TriPure Isolation Reagent (Roche Applied Science, Mannheim, Germany) according to the manufacturer's instructions. The integrity of the RNA was checked by visual inspection of the two ribosomal RNAs, 18S and 28S, on an ethidium bromide stained 1% agarose (MDBio Inc., Taipei, Taiwan) gel. The RNA sample concentration was adjusted to 2.95 μg total RNA·μL^{-1}. After treatment with DNase (TURBO DNA-*free*TM Kit, Ambion Inc., The RNA Company, United States) to remove residual DNA, 1.5 μg of total RNA was used for the preparation of cDNA following the protocol previously described (Chang et al., 2013). The cDNA was amplified from the poly-(A+) end using oligo (dT) 12–18 from a VersoTM cDNA Kit (Thermo Fisher Scientific Inc., Waltham, MA, United States). The volume was adjusted to provide a concentration of 30 ng mL^{-1} of the original RNA for each sample. The primers for the CrTOR, CrVSP34, and CrATG genes (**Supplementary Table S1**) were designed according to the Phytozome genome using LightCycler Probe Design2 (Roche Applied Science, Mannheim, Germany). The real-time quantitative PCR was performed using the LightCycler 480 system (Roche Applied Science, Mannheim, Germany). A master mix for PCR was prepared with a LightCycler® 480 SYBR Green I Master Kit (Roche Applied Science, Mannheim, Germany). To optimize the primer concentration, real-time PCR analyses using different primer concentrations and a constant template cDNA concentration of 30 or 50 ng were performed. To optimize the cDNA template concentration, each pair of primers was tested across a log dilution series of a positive control DNA sample. After optimization of the real-time PCR conditions, a primer concentration of 3 μM and a cDNA template concentration of 30 ng μL^{-1} were used for the detection of CrATG transcript abundance, and a primer concentration of 6 μM and a cDNA template concentration of 30 ng μL^{-1} were used for the detection of the CrVSP34 transcript abundance. Each reaction was performed in a total volume of 10 μL, which contained LightCycler® 480 SYBR Green I Master Mix, the selected concentration of each primer, and cDNA corresponding to 30 or 50 ng μL^{-1} RNA in the reverse transcriptase reaction. The amplification program was started by first denaturation at 95°C for 5 min, followed by 50 amplification cycles of annealing at 60°C for 10 s, and elongation at 72°C for 5 s for real time fluorescence measurements. The dissociation curves were performed after the PCR, and the fluorescence was analyzed using the LightCycler 480 system. Software with auto CT (cycle threshold) was used to determine the threshold of each gene, and the $2^{-\Delta\Delta CT}$ method was used to calculate CT values, in which the relative change in transcript abundance was normalized to reference genes, ubiquitin-conjugating enzyme E2 isoform (*CrUBC*, NCBI: AY062935) and elongation factor 1 alpha (*CrEF-1α*, NCBI: XM_001696516.1) (see **Supplementary Table S1** for the primers). The fold increase was calculated relative to the RNA sample from the control without light or chemical treatment at 0 h. Because the results based on the *CrEF-1α* internal control were similar to those based on *CrUBCX*, the relative changes in the transcript abundance on the basis of *CrUBCX* are shown in the present manuscript. All of the results presented are the averages of three independent biological replicates.

Statistics

Three independent biological replicates (n = 3) were used for each experiment and all of the experiments were repeated at least three times. Because they showed a similar trend, only the results from one of them are shown in this paper. Statistical analyses were performed using SPSS (SPSS 15.0 for Windows Evaluation Version, Chicago, IL, United States). Significant differences between sample means were analyzed using Student's t-test or Duncan's new multiple range test and a subsequent significant analysis of variance for the controls and treatments at $P < 0.05$.

RESULTS

HL Illumination Induces NO Burst and Cell Death

An NO-sensitive fluorescent dye, DAF-FM diacetate, was loaded into the TAP medium before CC125, the *nit1 nit2* mt− genotype that cannot use nitrate and nitrite, was transferred to a HL condition. The production of NO increased linearly during 1–3 h after HL illumination, followed by a significant increase at 5 h and a small increment during 5–8 h (**Figure 1A**). Most of the algal cells observed under the microscope bleached 5 h after HL illumination and concomitantly emitted intense DAF-FM fluorescence (NO) (**Figure 1B**). Whether the DAF-FM fluorescence was attributable to NO was confirmed by the treatment with an NO scavenger, cPTIO (400 μM). cPTIO was

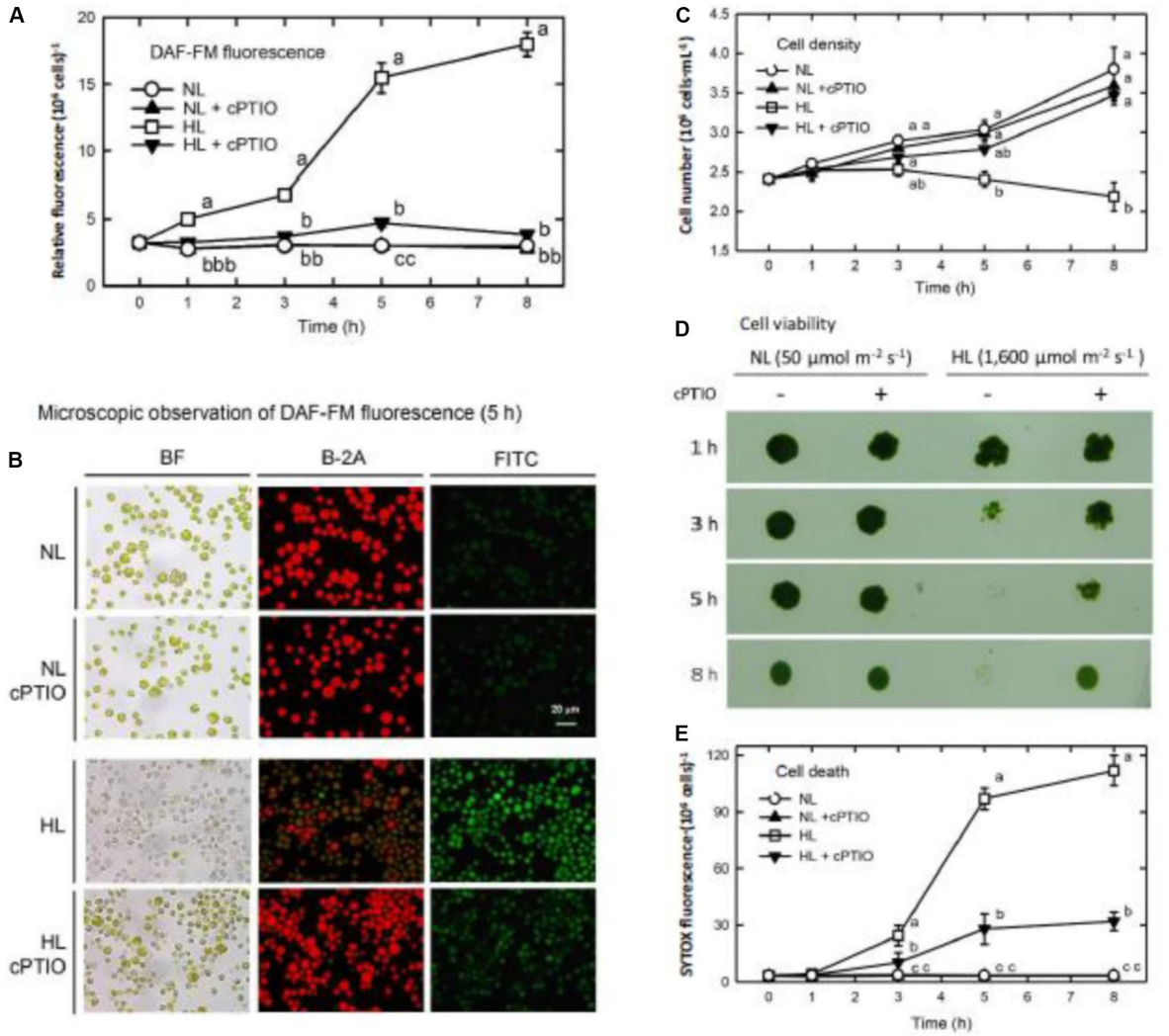

FIGURE 1 | DAF-FM acetate detection of NO production, cell growth, and death in *Chlamydomonas reinhardtii* cells under NL (50 μmol m^{-2} s^{-1}) and HL (1,600 μmol m^{-2} s^{-1}). **(A)** Quantitation of NO production. **(B)** Microscopic observation of DAF-FM fluorescence after 5 h of treatment. **(C)** Cell density. **(D)** Cell viability. **(E)** Cell death (SYTOX Green fluorescence). The data in **(A)**, **(C)**, and **(E)** are expressed as the mean ± SD (n = 3) from three independent biological replicates, and different letters indicate the statistical significance set at $P < 0.05$ according to ANOVA. In **(B)**, BF represents bright field, B-2A represents the autofluorescence of cells, and FITC represents DAF-FM fluorescence.

added twice, at 0 and 2.5 h, to remove the NO generated during HL illumination. Although cPTIO can cause an increase in the DAF-FM fluorescence under certain conditions due to oxidization of NO to the NO_2 radical with the subsequent formation of N_2O_3 ($NO_2 + NO \rightarrow N_2O_3$), which can react with the DAF-FM dye to form the fluorescent DAF-2T (Mur et al., 2011; D'Alessandro et al., 2013), our current results showed that the presence of cPTIO effectively reduced the DAF-FM fluorescence in the HL-treated cells (**Figures 1A,B**). This provides evidence supporting the hypothesis that DAF-FM fluorescence emittance under the HL condition is a result of NO.

The level of DAF-FM fluorescence determined in this study represented the cumulative NO production because the DAF-FM dye was loaded prior to the treatment. Thus, the NO production rate can be estimated from the difference in relative fluorescent units (RFU) between the two time points. As calculated from the data shown in **Figure 1A**, the NO production rate of NL-grown cells was 0 RFU h^{-1} over the incubation time, whereas that of the HL-treated cells was 0, 1.43, 0.98, 2.85, and 0.52 RFU h^{-1} from 0–0.5, 0.5–1, 1–3, 3–5, and 5–8 h, respectively. It is obvious that a transfer of *C. reinhardtii* cells to a HL condition triggers transient NO production with a profound burst when the time of exposure extends from 0.5 to 5 h with the maximum released during 3–5 h, followed by a decrease.

The cell growth expressed as cell density was inhibited upon exposure to HL illumination (**Figure 1C**), in which the cell viability decreased after 3 h and then the cells completely died after 5 h (**Figure 1D**). Similarly, using SYTOX-Green dye staining, the extent of dead cells increased 3 h after HL illumination and reached the maximum after 5 h (**Figure 1E**).

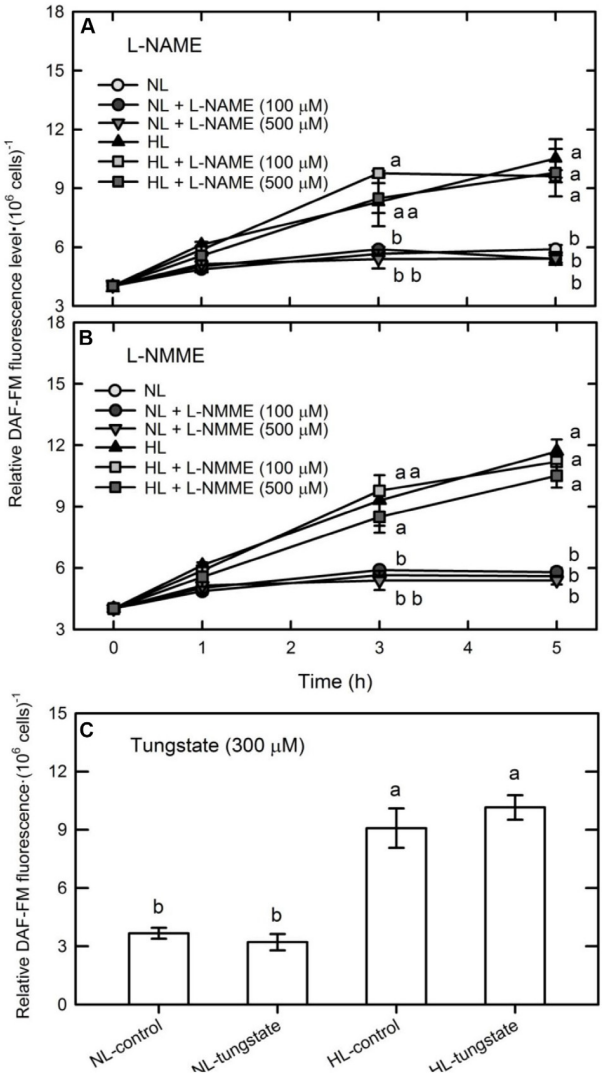

FIGURE 2 | The effect of the NOS inhibitor, L-NAME **(A)** or L-NMME **(B)**, and the NR inhibitor, tungstate (300 μM) **(C)**, on NO production in *Chlamydomonas reinhardtii* cells under NL (50 μmol m^{-2} s^{-1}) or HL (1,600 μmol m^{-2} s^{-1}) illumination. The data are expressed as the mean ± SD (n = 3) from three independent biological replicates and different letters indicate the statistical significance set at $P < 0.05$ according to ANOVA.

The presence of cPTIO can prevent the HL-induced cell bleaching [see bright field (BF) in **Figure 1B**], growth inhibition (**Figures 1C,D**), and cell death (**Figure 1E**). The effect of cPTIO in the mitigation of HL-induced cell death demonstrates that the large quantity of NO released during prolonged HL illumination is associated with cell death and, in turn, results in a decline in cell growth.

We found that the illumination with moderate light intensity of 750 μmol m^{-2} s^{-1} did not induce NO generation (DAF-FM fluorescence) during a 24 h period (**Supplementary Figure S1A**) and the algal cells can acclimate to this moderate light intensity illumination, reflected by normal growth ability the same as algal cells grown under the NL condition (**Supplementary Figure S1B**). The extent of cell death evaluated by SYTOX-Green staining was slightly under 750 μmol m^{-2} s^{-1} illumination compared to significant cell death in the 1,600 μmol m^{-2} s^{-1} condition (**Supplementary Figure S1C** and **Figure 1E**). These correlative results reveal that the burst of NO is dependent on the light intensity and the NO production appears to have a negative relationship with cell molarity.

Nitric oxide can be synthesized in plants by an enzymatic process involving NOS or NR, or by non-enzymatic reactions (Besson-Bard et al., 2008; Palavan-Unsal and Arisan, 2009). Whether NO was synthesized via NOS- or NR-dependent routes in *C. reinhardtii* cells under HL illumination was studied by treating them with the NOS inhibitors, L-NAME (100 or 500 μM) and L-NMMA (100 or 300 μM), and the NR inhibitor, tungstate (300 μM). These inhibitors did not affect the DAF-FM fluorescence of NL- or HL-treated cells (**Figure 2**). We have also found that the *C. reinhardtii* strain CC124 (*nit1 nit2 mt+*) that lacks NR and cannot grow in a medium containing nitrate or nitrite exhibited a similar NO production pattern under HL illumination (**Supplementary Figure S2**). Because *C. reinhardtii* strains CC125 and CC124 are mutants lacking NR and cannot use nitrate and nitrite, this implies that the HL-induced NO burst is independent of NR. Therefore, our present findings indicate that neither NOS nor NR is involved in the synthesis of NO in the HL-treated *C. reinhardtii* cells. This agrees with the results of our previous study that NO generated in *C. reinhardtii* cells exposed to an extremely high-intensity illumination (3,000 μmol m^{-2} s^{-1}) is derived from sources other than the NOS- or NR-mediated pathways (Chang et al., 2013).

NO Involvement of Autophagy Induction Under HL Illumination

Because the CrATG8 protein was recognized as an autophagy marker of *C. reinhardtii* (Pérez-Pérez and Crespo, 2010), a commercial ATG8 antibody raised using recombinant *Arabidopsis thaliana* APG8A (Abcam, Cambridge, United Kingdom) was used in western blot assays to estimate the abundance of the CrATG8 protein. On a 15% gel, two protein bands with apparent molecular masses of 15 and 14.6 kD were detected in the soluble extract [the solid square symbol represents ATG and the solid circle symbol represents ATG-PE (phosphatidylethanolamine)] (**Figure 3**). Based on the 0 h control, the abundance of both CrATG8 and CrATG8-PE detected on western blot showed an apparent increase by 3 h of HL treatment (**Figure 3A**). Based on the normalization by α-tubulin intensity, we found that the relative abundances of CrATG8 and CrATG8-PE remained unchanged for the cells grown under the NL condition over a 0–3 h period while it increased seven-fold 3 h after HL illumination (**Figure 3B**). The HL-induced increase in the level of CrATG8 protein can be suppressed by the presence of cPTIO (**Figure 3**). ATG8 plays an essential role in the development of autophagosome formation, target recognition, and vacuole tethering (Mizushima et al., 2011) and is anchored to the autophagosome membrane through covalent binding to the

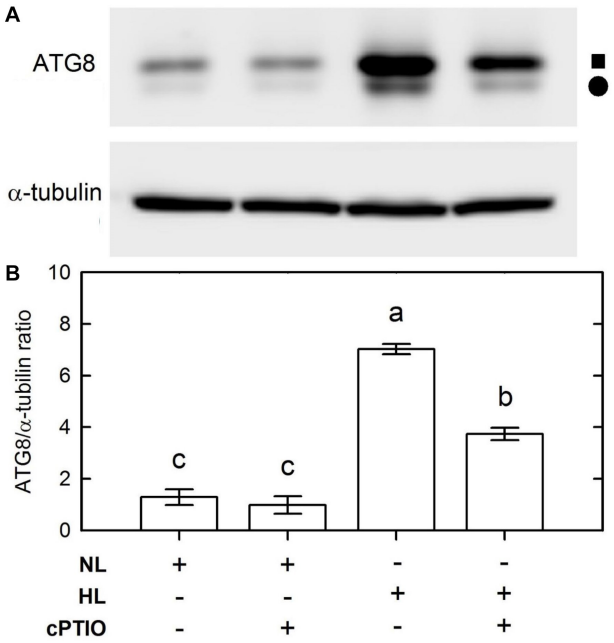

FIGURE 3 | Immunodetection of the CrATG8 protein of *Chlamydomonas reinhardtii* cells 3 h after NL (50 μmol m^{-2} s^{-1}) and HL (1,600 μmol m^{-2} s^{-1}) illumination in the presence or the absence of 400 M cPTIO. **(A)** Immunodetection using an antibody directed against recombinant Arabidopsis ATG8 (upper part) and α-tubulin (lower part). Triplicate samples were analyzed, and one of them is shown. **(B)** Relative change of CrATG8 protein expression estimated on the basis of the α-tubulin intensity. A solid square (■) represents ATG8 and a solid circle (●) represents ATG8-PE. The data in **(B)** are expressed as the mean ± SD ($n = 3$) from three independent biological replicates, and different letters indicate the statistical significance set at $P < 0.05$ according to ANOVA.

membrane lipid PE to execute its function in autophagosome formation. The present result indicates that the expression of functional ATG8 is activated by accumulated NO under an HL condition.

High light illumination immediately induced a significant increase in the transcript abundance of CrVPS34 (**Figure 4A**), CrATG1 (**Figure 4B**), CrATG3 (**Figure 4C**), CrATG4 (**Figure 4D**), CrATG6 (**Figure 4E**), CrATG7 (**Figure 4F**), and CrATG8 (**Figure 4G**), with a peak at 3 h. For CrATG12, although its transcript abundance was statistically increased by HL illumination, it only showed a 1.3-fold increase compared to the NL control (**Figure 4H**). The presence of cPTIO, which scavenged NO generated under the HL condition (**Figure 1A**), could suppress the HL-induced increase of CrVPS34 and CrATG transcripts abundance (**Figure 4**). Accordingly, the HL-induced CrVPS34 and CrATG gene expression is mediated by NO generated under HL illumination.

Treatment With NO Donors Induces Autophagy Under NL Conditions

The role of NO in the modulation of autophagy was further confirmed by the treatment with NO donors, GSNO (0.05 or 0.1 mM) and SNAP (0.05 or 0.1 mM), under NL conditions. The time-course survey of the level of NO released showed that NO was rapidly emitted within 0.5 h after SNAP (**Supplementary Figure S3A**) or GSNO (**Supplementary Figure S3B**) treatment and reached a plateau after 1 h. Compared to the treatment with 0.05 mM, the release of NO was approximately two-fold higher for the treatment with 0.1 mM NO donors. The NO released from GSNO or SNAP at either the 0.05 or 0.1 mM concentration can be scavenged in the presence of 400 μM cPTIO (**Supplementary Figure S3**). The concentrations and the time-course changes of NO released from 0.1 mM SNAP to 0.1 mM GSNO were similar to those occurring under HL conditions. Therefore, to identify the effect of NO on autophagy and cell death without the interference of HL illumination, in the NL condition, NO donor, SNAP, or GSNO was applied at concentrations of either 0.05 or 0.1 mM.

Using western blot assays, the abundance of CrATG8 protein was markedly increased by the treatment with 0.05 mM SNAP (**Figure 5A**) or 0.05 mM GSNO (**Figure 5B**) under the NL condition for 3 h. When treated with a higher concentration (0.1 mM), the CrATG8 protein exhibited a higher increment than with 0.05 mM treatment (**Figure 6**). We also found that the expression of genes related to autophagy were induced by exposure to 0.05 mM (**Figure 7**) and 0.1 mM (**Figure 8**) NO donors. In response to 0.05 mM NO donors, the transcript abundances of CrVPS34 (**Figure 7A**), CrATG1 (**Figure 7B**), CrATG3 (**Figure 7C**), CrATG4 (**Figure 7C**), CrATG6 (**Figure 7E**), CrATG7 (**Figure 7F**), and CrATG8 (**Figure 7G**) increased approximately 3 h after treatment, but these treatments did not affect the CrATG12 transcript abundance (**Figure 7H**). When the concentration of NO donors was increased to 0.1 mM, the transcript abundances of CrVPS34 and all CrATG genes showed a higher induction compared to 0.05 mM treatment (**Figure 8**). The transcript abundance of CrATG12 can be slightly increased by 0.1 mM NO donors (**Figure 8H**) but not by a lower NO donor concentration (**Figure 7H**). The presence of cPTIO can suppress the SNAP- or GSNO-induced increase in CrATG8 protein abundance (**Figures 5**, **6**) and the transcripts abundance of the CrVPS34 and CrATG genes (**Figures 7**, **8**). The present findings demonstrated that NO released from NO donors can elicit autophagy in *C. reinhardtii* cells grown under NL conditions.

Treatment With NO Donors at Higher Concentrations Under the NL Condition Causes Cell Death

Whether NO can lead to cell death under the NL condition was determined. The treatment with 0.05 mM SNAP or 0.05 mM GSNO did not affect cell growth (**Supplementary Figure S7**) or cell viability (**Figure 9** for SNAP and **Figure 10** for GSNO). However, when the NO donor concentration was increased to 0.1 mM, the cell growth was temporarily inhibited during the 3–5 h after treatment but then it could be recovered to the control level after a prolonged growth period (12–24 h) (**Supplementary Figure S7**). Furthermore, we also observed

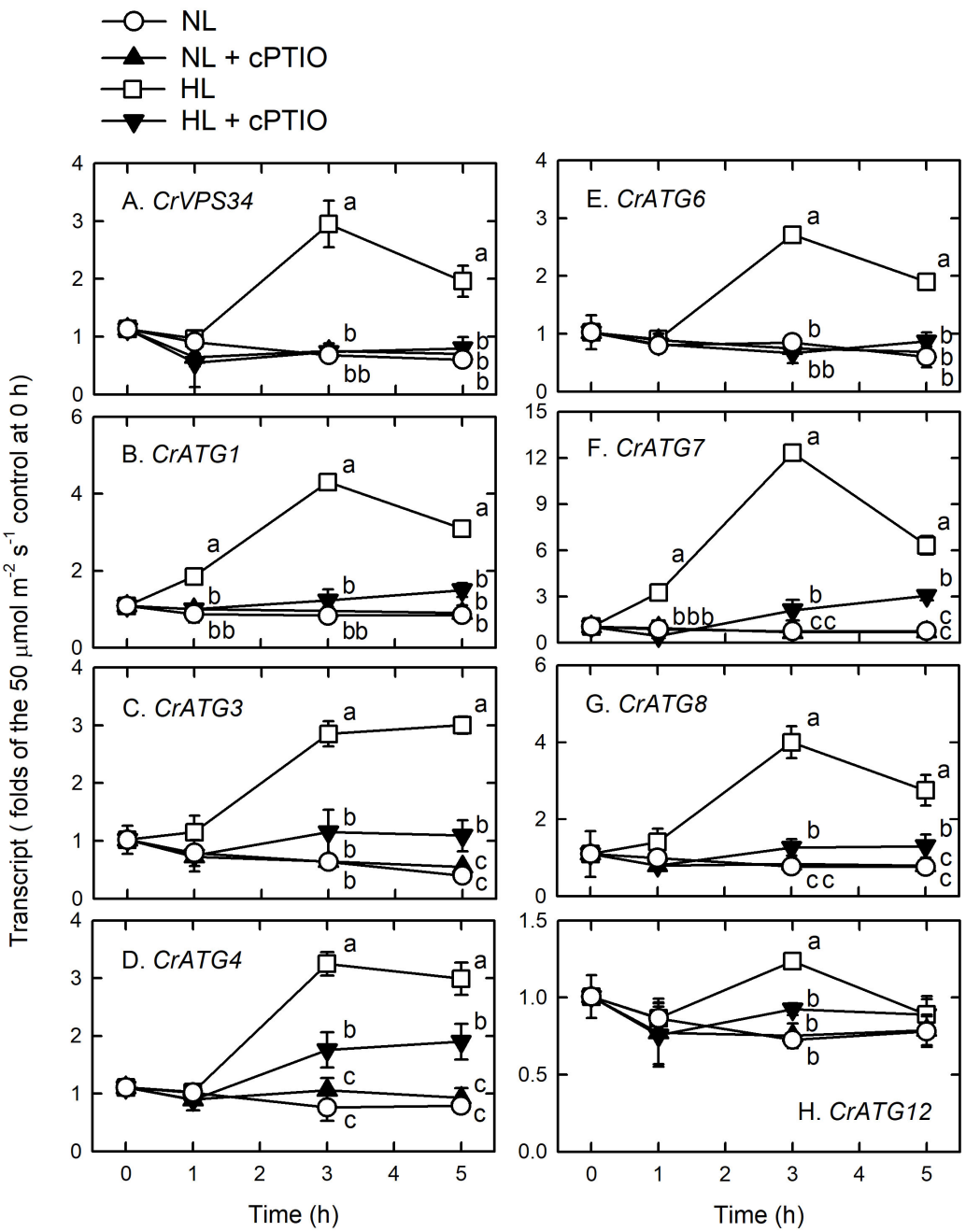

FIGURE 4 | CrVPS34 and CrATG transcripts abundance in *Chlamydomonas reinhardtii* cells under NL (50 μmol m^{-2} s^{-1}) and HL (1,600 μmol m^{-2} s^{-1}) illumination in the presence or the absence of 400 μM cPTIO. **(A)** CrVPS34. **(B)** CrATG1. **(C)** CrATG3. **(D)** CrATG4. **(E)** CrATG6. **(F)** CrATG7. **(G)** CrATG8. **(H)** CrATG12. The data are expressed as the mean ± SD (n = 3) from three independent biological replicates. Different letters indicate the statistical significance set at $P < 0.05$ according to ANOVA. Open circle, NL; solid triangle, NL + cPTIO; open square, HL; inverted triangle, HL + cPTIO.

that both 0.1 mM SNAP (**Figure 9**) and 0.1 mM GSNO (**Figure 10**) treatment for 3 h triggered a minor manifestation of cell death symptoms as reflected by the appearance of SYTOX Green fluorescence in some algal cells, and then the fluorescence was no longer observed after 24 h. In addition, the temporary decrease of cell viability and the induction of cell death by 0.1 mM NO donors at 3 h could be prevented by the presence of cPTIO (**Figures 9**, **10**, the viability in the Figures was for 0.1 mM SNAP or GSNO treatment). The cell viability at 0.05 mM was not affected (data not shown). This demonstrates that the transient viability decline and cell death were caused by higher NO release from 0.1 mM SNAP or 0.1 mM GSNO, but it did not occur under a lower NO donor concentration of 0.05 mM.

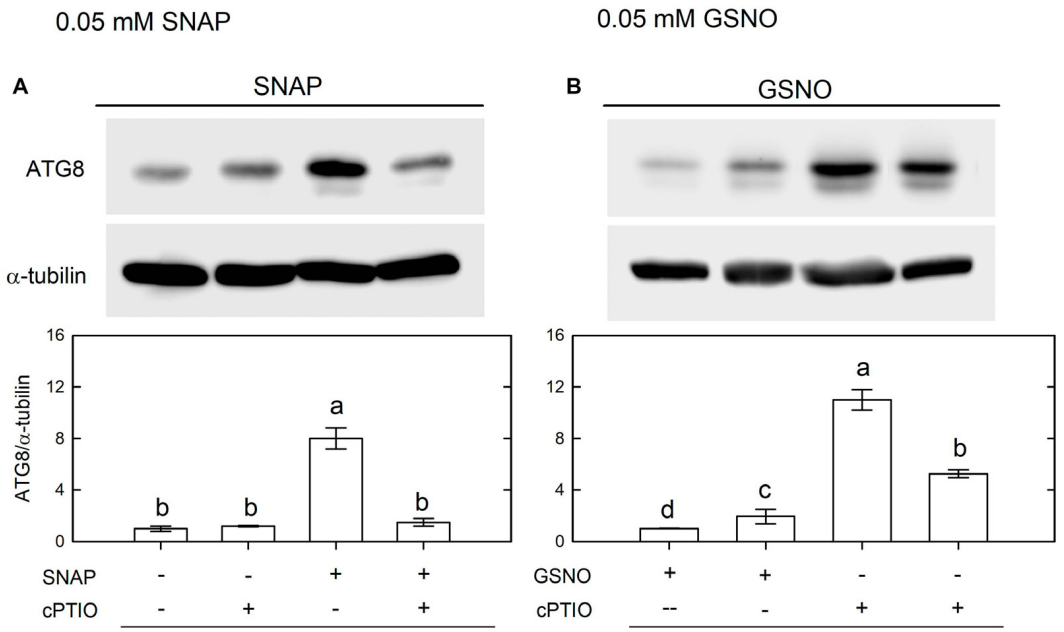

FIGURE 5 | Immunodetection of the CrATG8 protein of *Chlamydomonas reinhardtii* cells after 0.05 mM SNAP **(A)** or 0.05 mM GSNO **(B)** treatment for 3 h in the presence or absence of 400 μM cPTIO under an NL (50 μmol m^{-2} s^{-1}) condition. Triplicate samples were analyzed, and one of them is shown. The quantitation data are expressed as the mean ± SD (n = 3) from three independent biological replicates and different letters indicate the statistical significance set at $P < 0.05$ according to ANOVA.

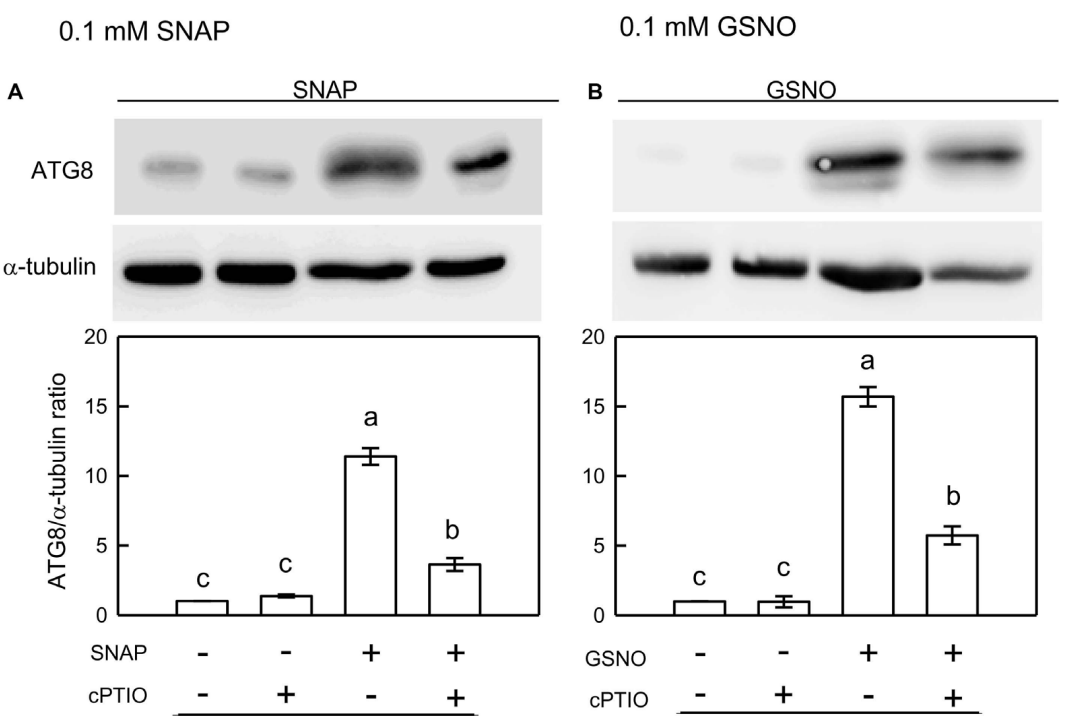

FIGURE 6 | Immunodetection of the CrATG8 protein of *Chlamydomonas reinhardtii* cells after 0.1 mM SNAP **(A)** or 0.1 mM GSNO **(B)** treatment for 3 h in the presence or absence of 400 μM cPTIO under an NL (50 μmol m^{-2} s^{-1}) condition. Triplicate samples were analyzed, and one of them is shown. The quantitation data are expressed as the mean ± SD (n = 3) from three independent biological replicates and different letters indicate the statistical significance set at $P < 0.05$ according to ANOVA.

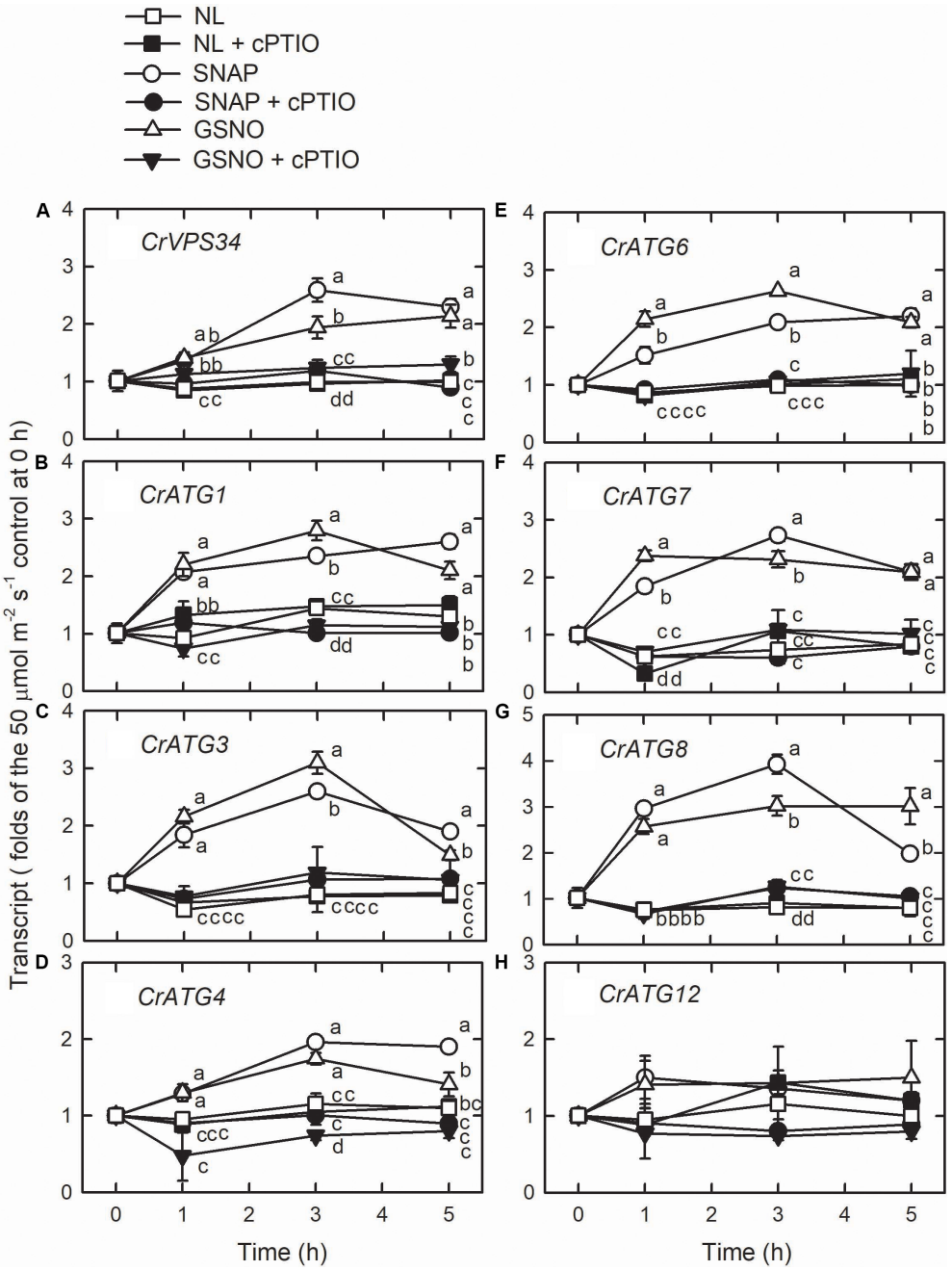

FIGURE 7 | The time-course changes in CrVPS34 and CrATG transcripts abundance in *Chlamydomonas reinhardtii* cells in response to 0.05 mM SNAP or 0.05 mM GSNO under an NL (50 μmol m^{-2} s^{-1}) condition. **(A)** CrVPS34. **(B)** CrATG1. **(C)** CrATG3. **(D)** CrATG4. **(E)** CrATG6. **(F)** CrATG7. **(G)** CrATG8. **(H)** CrATG12. The data are expressed as the mean ± SD (n = 3) from three independent biological replicates and different letters indicate the statistical significance set at $P < 0.05$ according to ANOVA.

Treatment With NO Donors Under a Moderate HL Condition Causes Cell Death and Stimulates Autophagy Activation

Subsequently, in the attempt to elucidate whether the excessive burst of NO confers the susceptibility of *C. reinhardtii* cells to non-lethal HL illumination in terms of autophagy induction and cell death, the NO donors were applied under a ML condition (750 μmol m^{-2} s^{-1}). An exposure to ML illumination did not induce NO production (**Supplementary Figure S1A**), but it triggered a linear increase in H_2O_2 production as the treatment time advanced (**Supplementary Figure S6**). However, the

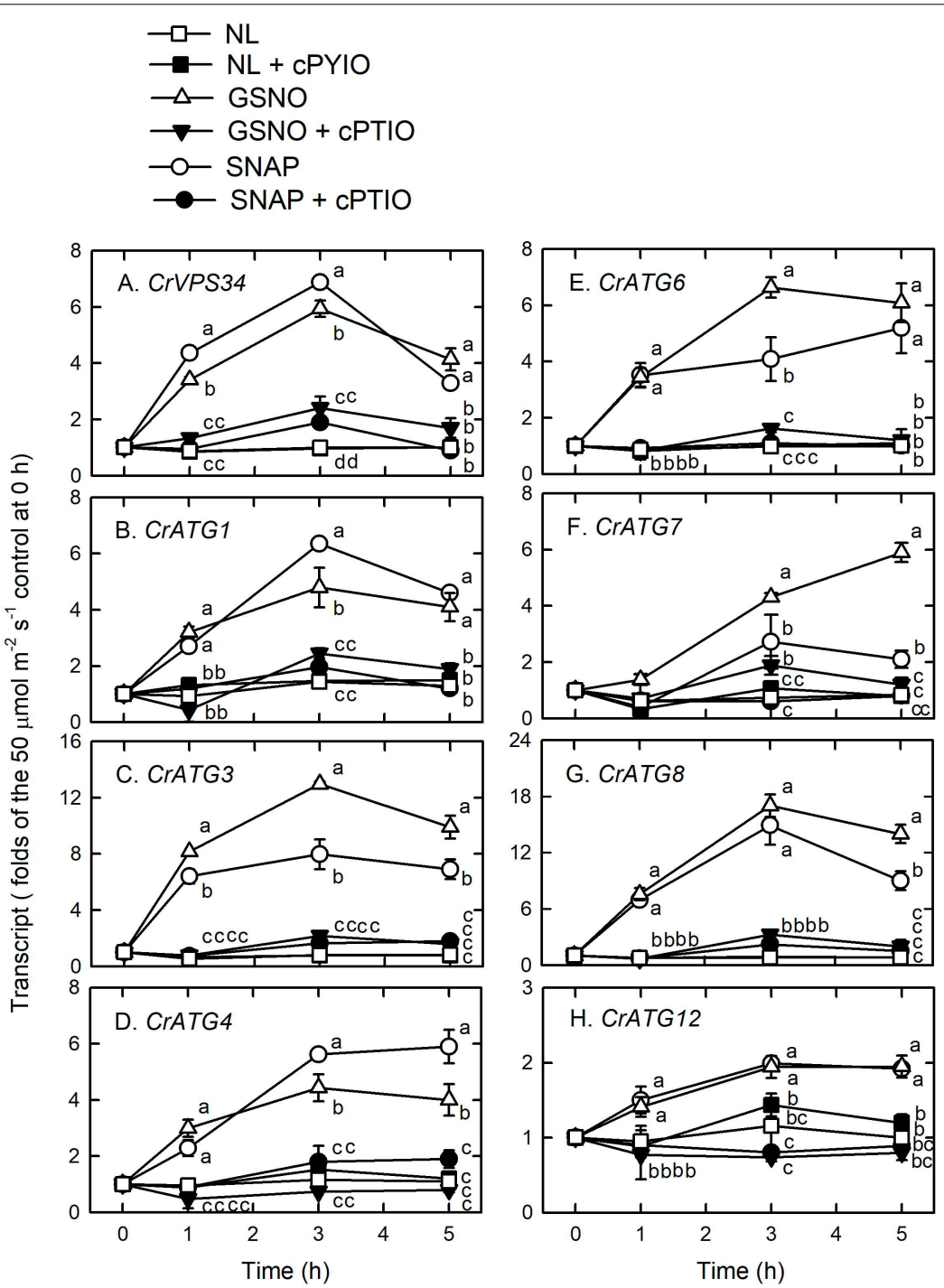

FIGURE 8 | The time-course changes in CrVPS34 and CrATG transcripts abundance in *Chlamydomonas reinhardtii* cells in response to 0.1 mM SNAP or 0.1 mM GSNO under an NL (50 μmol m^{-2} s^{-1}) condition. **(A)** CrVPS34. **(B)** CrATG1. **(C)** CrATG3. **(D)** CrATG4. **(E)** CrATG6. **(F)** CrATG7. **(G)** CrATG8. **(H)** CrATG12. The data are expressed as the mean ± SD (n = 3) from three independent biological replicates and different letters indicate the statistical significance set at $P < 0.05$ according to ANOVA.

level of ML-induced H_2O_2 production was lower than that under the 1,600 μmol m^{-2} s^{-1} condition (**Supplementary Figure S6**). Furthermore, we found that although H_2O_2 was produced under ML illumination, the algal cells exhibited a similar growth ability to those grown under an NL condition (**Supplementary Figure S1B**). This indicates that *Chlamydomonas* cells can tolerate accumulated H_2O_2 and acclimate to moderate light stress.

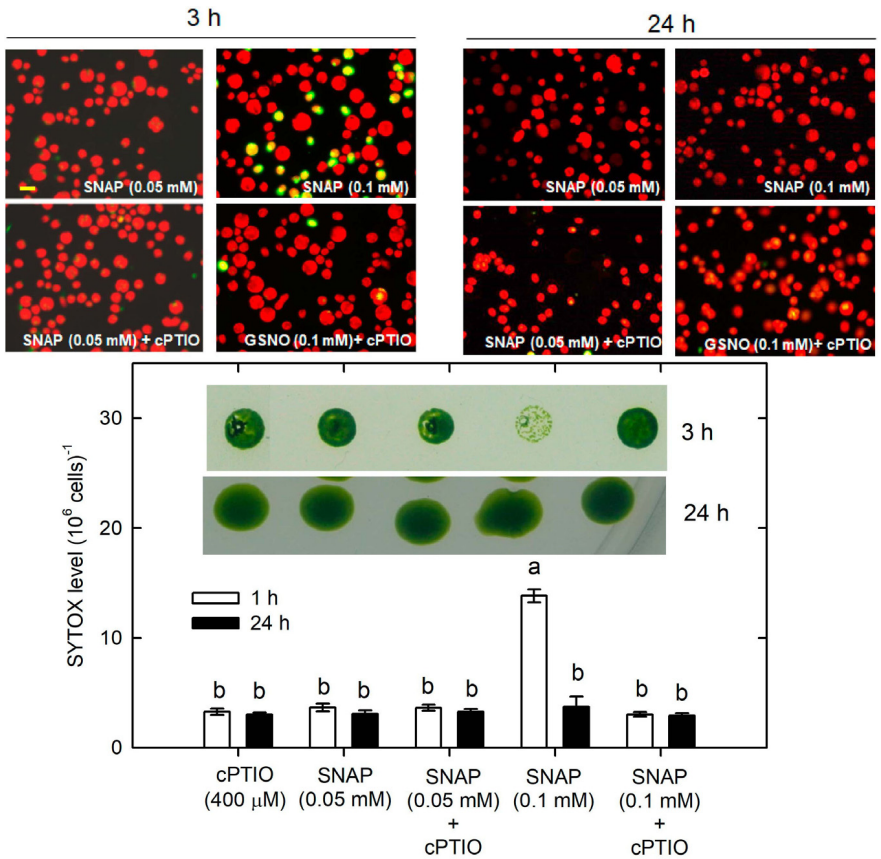

FIGURE 9 | The effect of 0.05 **(A)** or 0.1 **(B)** mM SNAP treatment on cell viability and cell death detected by SYTOX Green fluorescence dye in *C. reinhardtii* cells under an NL (50 μmol m^{-2} s^{-1}) condition in the presence or the absence of 400 μM cPTIO. The results for 3 and 24 h treatment are shown. The cell viability shown is after the treatment with 0.1 mM NO donors. The data are expressed as the mean ± SD (n = 3) from three independent biological replicates and the vertical bar on the symbols represents SD. Different letters indicate the statistical significance set at $P < 0.05$ according to ANOVA.

Then, NO donors were administered under the ML condition to clarify whether NO could increase the susceptibility of algal cells under the ML condition. The results depended on the concentration of NO donors and the treatment time. Both cell density (**Figure 11A**) and viability (**Figure 11B**) were not affected by the presence of 0.05 mM GSNO or 0.05 mM SNAP but showed a decrease in response to 0.1 mM NO donor treatment. The cell death detected using SYTOX-Green fluorescence did not appear under treatment with 0.05 mM NO donors whereas it exhibited a marked increase under treatment with 0.1 mM NO donors (**Figure 11C**). The presence of cPTIO can suppress the negative effect of 0.1 mM NO donor treatment on cell activity (**Figure 11C**). The present findings demonstrate that supplementation with NO confers susceptibility of *C. reinhardtii* cells to moderate HL illumination.

The transcripts abundance of CrVPS34 (**Figure 12A**), CrATG1 (**Figure 12B**), CrATG3 (**Figure 12C**), CrATG4 (**Figure 12C**), CrATG6 (**Figure 12E**), CrATG7 (**Figure 12F**), and CrATG8 (**Figure 12G**) slightly increased 3 h after ML treatment and their increase can be enhanced by the supplementation with 0.1 mM NO donors, and this enhancement can be suppressed in the presence of cPTIO. Among the CrATG genes, the transcript abundance of CrATG12 was not increased by exposure to ML treatment, while the application of 0.1 mM NO donors induced an increase of its expression and this increase was also suppressed in the presence of cPTIO (**Figure 12H**).

Interaction of NO and H_2O_2 for Autophagy Induction and Cell Death

The above results indicate that NO may interact with H_2O_2 for the induction of autophagy and cell death in *C. reinhardtii* cells. Therefore, NO donors at a concentration of 0.1 mM were applied together with 1 mM H_2O_2 under an NL condition for 3 h. The results shown in **Figure 13A** indicate that 1 mM H_2O_2 slightly increased the transcript abundance of CrATG8, while the combination of H_2O_2 and NO donors induced a marked increase in CrATG8 transcript abundance, which was inhibited in the presence of cPTIO. The ATG8 protein abundance in response to H_2O_2 treatment for 3 h slightly increased but the combination of H_2O_2 and NO donors induced a significant increase (**Figure 13B**).

The cell viability and cell death were also determined in response to H_2O_2 and/or NO donors in the presence or the

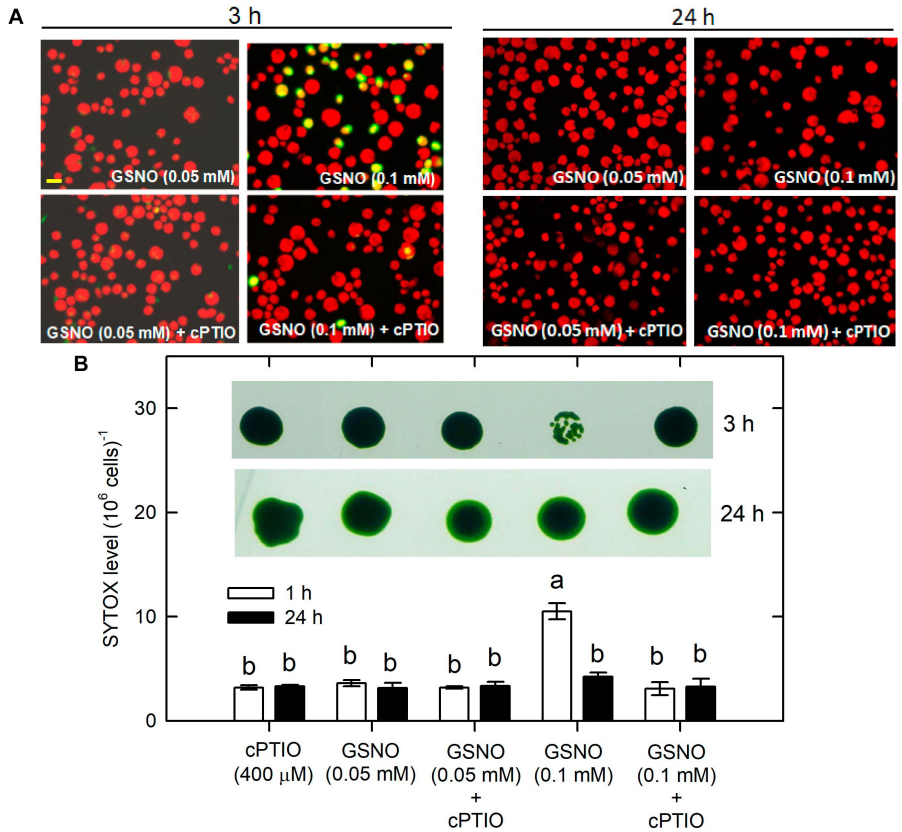

FIGURE 10 | The effect of 0.05 **(A)** or 0.1 **(B)** mM GSNO treatment on cell viability and cell death detected by SYTOX Green fluorescence dye in *C. reinhardtii* cells under an NL (50 μmol m^{-2} s^{-1}) condition in the presence or absence of 400 μM cPTIO. The results for 3 and 24 h treatment are shown. The cell viability shown is after the treatment with 0.1 mM NO donors. The data are expressed as the mean ± SD (n = 3) from three independent biological replicates and the vertical bar on the symbols represents SD. Different letters indicate the statistical significance set at $P < 0.05$ according to ANOVA.

absence of cPTIO under an NL condition for 24 h. We found that 1 mM H_2O_2 treatment did not affect cell viability and cell death, while 0.05 mM NO donors also did not affect cell viability and cell death (**Figure 14**). However, the combination of H_2O_2 and NO donor treatment induced a significant decrease in cell viability and resulted in significant cell death, which could be inhibited in the presence of 0.4 mM cPTIO (**Figure 14**). This demonstrated that NO interacts with H_2O_2 in the induction of cell damage under an NL condition.

DISCUSSION

Treatment of *C. reinhardtii* cells with high intensity illumination of 1,600 μmol m^{-2} s^{-1} triggered an NO burst during 3–5 h. An exposure to extremely high-light illumination at 3,000 μmol m^{-2} s^{-1} can also induce a significant NO production in *C. reinhardtii* cells (Chang et al., 2013). However, moderate HL illumination at 750 μmol m^{-2} s^{-1} intensity did not trigger NO production. This demonstrates that the generation of NO occurs only when the light intensity is higher than a certain threshold.

Recently, it has been shown that *C. reinhardtii* can metabolize NO to N_2O and this metabolism is dependent on photosynthetic electron transport. These findings are supported by the data obtained using treatment with 3,4-dichlorophenyl-1,1-dimethylurea (DCMU), a photosystem II (PSII) inhibitor, or 2,5-dibromo-3-methyl-6-isopopyl-p-benzoquinone (DBMIB), an inhibitor of electron flow between PSII and PSI (Burlacot et al., 2020). This raises the possibility that the conversion of NO to N_2O may lead to the disappearance of NO under the 750 μmol m^{-2} s^{-1} condition. However, we found that the application of 10 M DCMO or 2 M DBMIB did not increase NO production under the 750 μmol m^{-2} s^{-1} condition (data not shown). Thus, undetectable NO under the 750 μmol m^{-2} s^{-1} condition is not due to the degradation of NO to N_2O.

The present results that the presence of L-NAME or tungstate cannot suppress the induction of NO production in *C. reinhardtii* cells by HL illumination suggests that routes other than the NOS and NR pathways are responsible for the HL-induced NO synthesis in *C. reinhardtii* cells. So far, whether NOS exists in plants is under debate, and the presence of NOS has not been verified in *C. reinhardtii*, as we know. Furthermore, the strain CC125 used in this study is the 137C *mt*− carrying the nit1 and nit2 mutations (*mt*− *nit1 nit2*) that lacks NR and

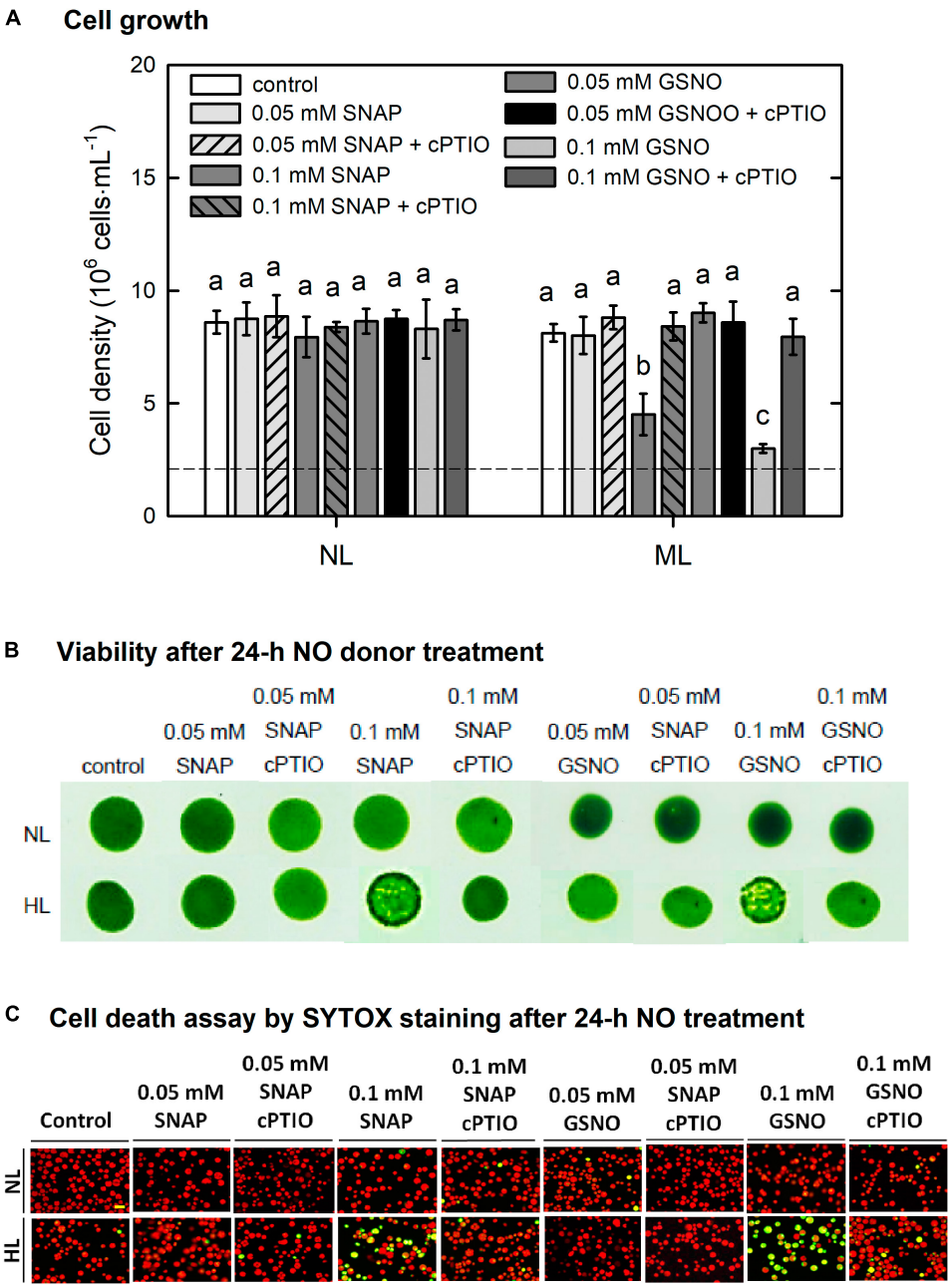

FIGURE 11 | The effect of 0.05 or 0.1 mM SNAP and GSNO treatment on cell growth **(A)**, viability **(B)**, and cell death **(C)** detected by SYTOX Green fluorescence dye in *C. reinhardtii* cells under an ML (750 μmol m^{-2} s^{-1}) condition in the presence or absence of 400 μM cPTIO for 24 h. The data are expressed as the mean ± SD (n = 3) from three independent biological replicates and the vertical bar on the symbols represents SD. Different letters indicate the statistical significance set at $P < 0.05$ according to ANOVA.

does not express the proteins required for nitrate assimilation (NIA1, NRT2.1, NRT2.2, NII1, NAR2, and NAR1.1) (Galván and Fernández, 2001). The strain CC124, with genotype *mt+ nit1 nit2*, also exhibited a similar NO production pattern under 1,600 μmol m^{-2} s^{-1} illumination (**Supplementary Figure S2**). This suggests that the HL-induced NO production in *C. reinhardtii* cells is independent of NR. In fact, several studies have shown NO production in NR-defective *C. reinhardtii* mutants under hypoxia conditions (Hemschemeier et al., 2013) or in *C. reinhardtii* wild-type strain 137C (+) treated with MP (Yordanova et al., 2010). However, Wei et al. (2014) reported that the NR-defective *C. reinahrdtii* mutants produce less NO in response to nitrogen starvation, while a significant NO release is found in strains of the genotype NIT1 NIT2 with normal NR activity. It is therefore suggested that the NR-dependent route is responsible for the production of NO from *C. reinahrdtii*

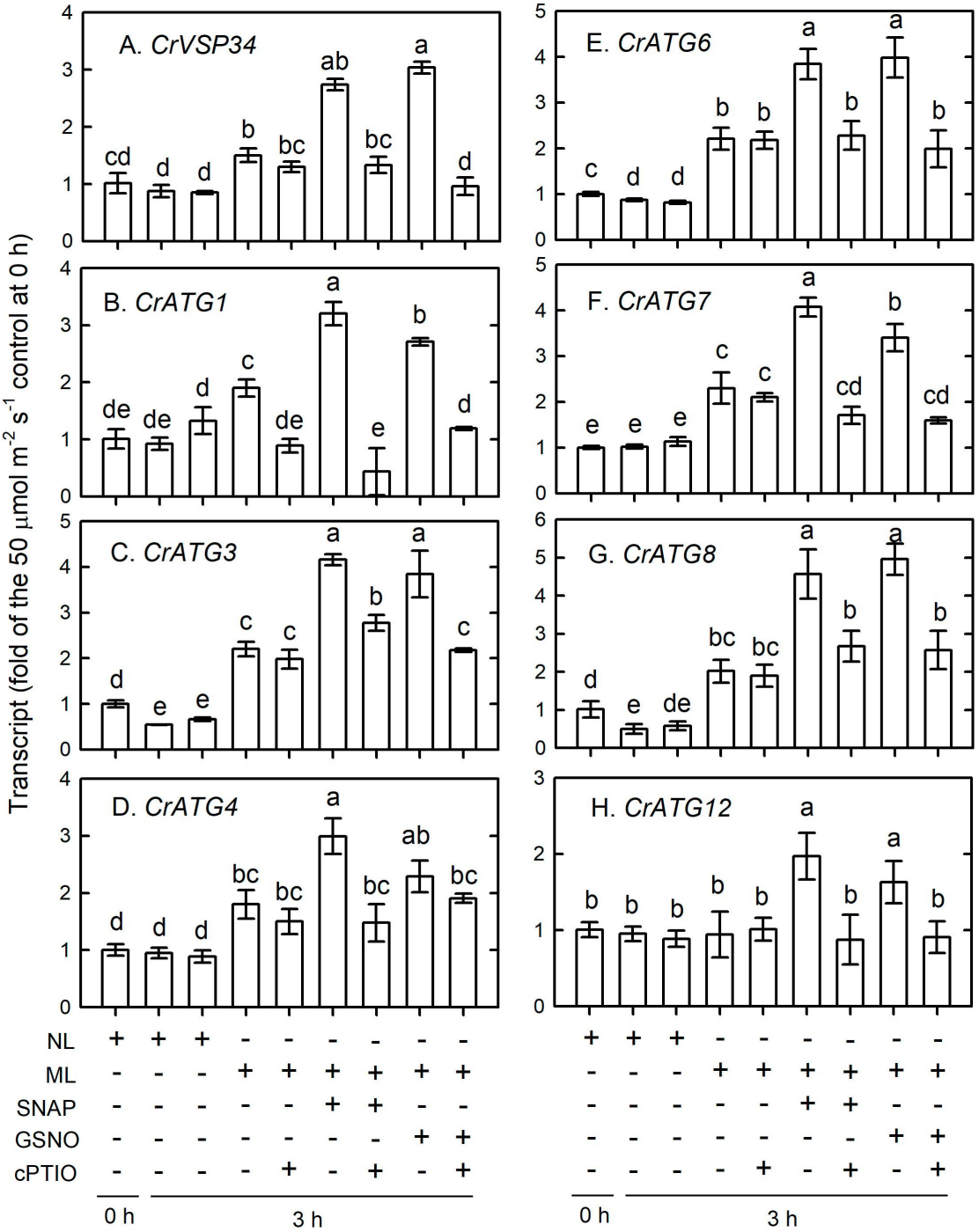

FIGURE 12 | The time-course changes in CrVPS34 and CrATG transcripts abundance in *Chlamydomonas reinhardtii* cells in response to 0.1 mM SNAP or 0.1 mM GSNO treatment under an ML (750 μmol m^{-2} s^{-1}) condition for 3 h. **(A)** CrVPS34. **(B)** CrATG1. **(C)** CrATG3. **(D)** CrATG4. **(E)** CrATG6. **(F)** CrATG7. **(G)** CrATG8. **(H)** CrATG12. The data are expressed as the mean ± SD (n = 3) from three independent biological replicates and different letters indicate the statistical significance set at $P < 0.05$ according to ANOVA.

cells under nitrogen starvation (Wei et al., 2014). The above results indicate that the routes used for the synthesis of NO in *C. reinhardtii* cells are different not only between the strains with various genetic backgrounds but also between different treatment conditions. Our present findings demonstrate that *C. reinahrdtii* lacking NR can generate marked NO production via NR- and NOS-independent routes under illumination at a very high intensity of 1,600 μmol m^{-2} s^{-1}.

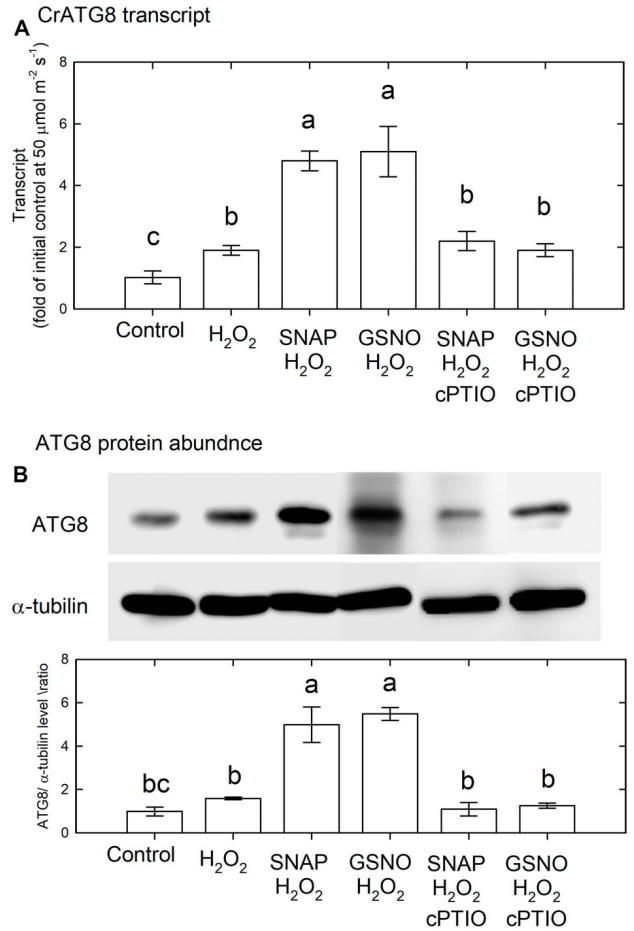

FIGURE 13 | The effect of SNAP (0.1 mM), GSNO (0.1 mM), and 1 mM H_2O_2 treatment on the CrATG8 transcript abundance **(A)** and ATG8 protein abundance **(B)** of *Chlamydomonas reinhardtii* cells under an NL condition (50 μmol m^{-2} s^{-1}) for 3 h. The cPTIO (0.4 mM) was added to the SNAP + H_2O_2 and GSNO + H_2O_2 treatments. The data are expressed as the mean ± SD (n = 3) from three independent biological replicates and different letters indicate the statistical significance set at $P < 0.05$ according to ANOVA.

The evidence suggests that NO contributes to the activation of autophagy in *C. reinhardtii* cells by HL illumination at 1,600 μmol m^{-2} s^{-1} intensity. When the marked NO burst occurs during 3–5 h following HL illumination, *C. reinhardtii* cells concomitantly exhibited marked autophagy induction, supported by an increase in the abundance of CrVPS34 and CrATG transcripts and CrATG8 protein, a *Chlamydomonas* autophagy marker (Pérez-Pérez et al., 2010). The results of Pérez-Pérez et al. (2012a) also showed that there is a transient activation of autophagy with a peak at 6 h in *C. reinhardtii* cells subjected to 1,200 μmol m^{-2} s^{-1} illumination, reflected by increased CrATG8 protein abundance detected using western blot and immunofluorescence analyses. More importantly, the present finding that the induction of autophagy by illumination at a higher light intensity up to 1,600 μmol m^{-2} s^{-1} can be suppressed in the presence of a NO scavenger, cPTIO, which demonstrates that the activation of autophagy under the 1,600 μmol m^{-2} s^{-1} condition can be attributable to NO. Similarly, the VHL (3,000 μmol m^{-2} s^{-1})-induced increase in NO production (Chang et al., 2013) and the abundance of CrATG8 protein (**Supplementary Figure S4**) and the CrVPS34, CrATG, and CrTOR transcripts (**Supplementary Figure S5**) in *C. reinhardtii* can be suppressed by cPTIO treatment.

Furthermore, treatment with GSNO or SNAP at either 0.05 or 0.1 mM under the 50 μmol m^{-2} s^{-1} condition is able to trigger autophagy, reflected by the increase of CrVPS34 and CrATG transcripts abundance and CrATG8 protein abundance, which is suppressed in the presence of cPTIO. Obviously, NO can trigger autophagy without other factors derived from HL illumination. As far as we know, this is the first time that NO has been shown to be involved in the modulation of HL-induced autophagy in *C. reinhardtii* cells through upregulation of CrVPS34 and CrATG gene expression. The effect of NO on the induction of autophagy is well-known in animal systems (Barsoum et al., 2006; Yang et al., 2008; Sarkar et al., 2011; Duana et al., 2013; Tripathi et al., 2013).

The upregulation of CrVPS34 and CrATG expression by NO and the suppression of their expression by cPTIO indicated that the signaling components are involved in the NO-mediated activation of autophagy under HL illumination. Among the core autophagy machineries, autophagy induction is driven by the association of ATG1 kinase with dephosphorylated ATG13 and other regulatory ATG proteins for the construction of a preautophagosomal structure (Kamada et al., 2000). Subsequently, vesicle nucleation is initiated by the activation of vacuolar-protein-sorting (VPS) 34 PI3K complex containing ATG6 and other VPS proteins (Thompson and Vierstra, 2005). VPS34 is the Class III PI3K, which is conserved from yeasts and plants to mammals (Engelman et al., 2006) for the phosphorylation of phosphatidylinositol to generate phosphatidylinositol 3-phosphate that is a phospholipid central to membrane trafficking processes, is required for the formation of the autophagosome (Itakura et al., 2008; Jaber et al., 2012). Here, the increase of CrVPS34, CrATG1, and CrATG6 transcripts abundance 3 h after HL illumination may indicate that the vesicle nucleation of the phagophore assembly site to form the autophagosome is executed in *C. reinhardtii* cells under HL stress. Subsequently, an increase in CrATG8 protein abundance and transcripts abundance of CrATG3, CrATG4, CrATG7, and CrATG8 function in the expansion of the autophagosomal membrane and its fusion with the lysosome/vacuolar membrane through the ubiquitin-like protein conjugation system (Ohsumi, 2001; Thompson and Vierstra, 2005; Hanada et al., 2007; Nakatogawa et al., 2007; Xie et al., 2008), which implies the implementation of a mature autophagosome and autolysosome formation in *C. reinhardtii* cells under the control of NO generated under HL illumination.

Our findings indicate that the expression of CrATG8 is regulated by NO and other factors under very HL conditions of 1,600 μmol m^{-2} s^{-1}. An increase in CrATG8 transcript abundance by prolonged HL illumination (5 h) is partially inhibited in the presence of cPTIO. Even when cPTIO was administered at a concentration up to 800 M, the CrATG8

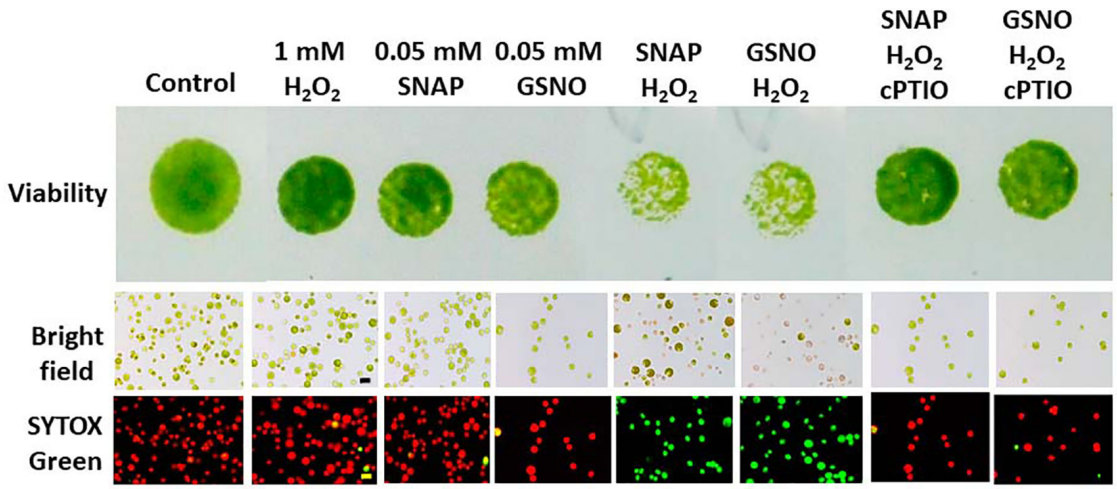

FIGURE 14 | The effect of SNAP (0.1 mM), GSNO (0.1 mM), and 1 mM H_2O_2 treatment on the growth (cell density) **(A)** and viability **(B)** of *Chlamydomonas reinhardtii* cells under an NL condition (50 μmol m^{-2} s^{-1}) for 24 h. The cPTIO (400 μM) was applied to the SNAP + H_2O_2 and GSNO + H_2O_2 treatments. The data are expressed as the mean ± SD (n = 3) from three independent biological replicates and different letters indicate the statistical significance set at $P < 0.05$ according to ANOVA.

transcript abundance still remained at a level approximately 24% of the HL treatment without cPTIO application (data not shown). This may reflect that other factors work with NO for the induction of autophagy in *C. reinhardtii* under the 1,600 μmol m^{-2} s^{-1} condition. Pérez-Pérez et al. (2012a) have shown increased levels of ROS in the chloroplast and a marked increase in autophagic activity due to the absence of photoprotection in *C. reinhardtii* cells. This may suggest that ROS are also the factors that induce CrATG8 expression (protein abundance) in *C. reinhardtii* cells exposed to the 1,600 μmol m^{-2} s^{-1} condition. In addition, their study showed that the treatment with 1 mM H_2O_2 under a 20–30 μmol m^{-2} s^{-1} condition or a dark condition, or 1 M MV under a 20–30 μmol m^{-2} s^{-1} condition for 8 h, can increase the CrATG8 protein abundance (Pérez-Pérez et al., 2012a). In addition, in a study of the responses of a starchless (*sta6*) mutant to oxidative stress and the induction of autophagy in *C. reinhardtii* cells, Tran et al. (2019) showed that there is a dose-dependent expression pattern of ATG8 protein detected using western blot analysis with a linear increase in ATG8 protein level in response to a gradual increase in H_2O_2 concentration from 0, 0.25, 0.50, to 1 mM. Here, we found that the H_2O_2 concentration was significantly increased by exposure to 1,600 μmol m^{-2} s^{-1} illumination (**Supplementary Figure S6**). Moreover, we also observed that the exposure of *C. reinhardtii* cells to 1 mM H_2O_2 for 3 h under an NL condition increased the ATG8 protein abundance and CrATG8 transcript abundance without any adverse effect on cell viability. The application of NO together with H_2O_2 induces significant increases in ATG8 protein and CrATG8 transcript abundances, which can be suppressed by cPTIO treatment. In addition, although autophagy is not occurring under the ML condition, the administration of 0.1 mM NO donors can induce autophagy under the ML condition. This provides evidence that, in addition to NO, H_2O_2 is also involved as a signal for the activation of autophagy by 1,600 μmol m^{-2} s^{-1} illumination of *C. reinhardtii* cells.

In addition to the induction of autophagy, 1,600 μmol m^{-2} s^{-1} illumination resulted in cell death (bleaching) after 5 h. The prevention of HL-induced cell death by cPTIO treatment supports the hypothesis that NO is involved in the HL-induced cell death. In addition, our evidence shows that other factors, such as ROS, may interact with NO for the induction of cell death in *C. reinhardtii* cells under lethal HL stress (1,600 μmol m^{-2} s^{-1}). H_2O_2 has been shown to be involved in plant cell death (Houot et al., 2001). However, the effect of H_2O_2 on the induction of cell death works in a concentration-dependent manner. Murik et al. (2014) provided evidence that the growth rate of *C. reinhardtii* cells is not affected by H_2O_2 at concentrations below 2 mM whereas it was markedly retarded on exposure to higher H_2O_2 concentrations in a range between 5 and 10 mM. Here, illumination of *C. reinhardtii* cells at an intensity of 1,600 μmol m^{-2} s^{-1} can induce significant H_2O_2 accumulation (**Supplementary Figure S6**). The evidence shows that NO bursts along with H_2O_2 accumulation occur as the 1,600 μmol m^{-2} s^{-1} illumination advances to 5 h (**Figure 1A**), and treatment with 0.1 mM NO donors can induce a transient growth depression and cell death under an NL condition. More importantly, the presence of the NO scavenger, cPTIO, can effectively prevent growth retardation and cell death caused by the 0.1 mM NO donors. Furthermore, under the ML condition (750 μmol m^{-2} s^{-1}), the application of 0.1 mM NO donors can cause cell death and growth retardation, which is prevented by cPTIO treatment. Because H_2O_2 also accumulates under the ML condition (750 μmol m^{-2} s^{-1}), this again supports that the NO released from the NO donors interacts with H_2O_2 for the induction of cell death.

To further prove this proposal, we treated *C. reinhardtii* cells with 1 mM H_2O_2 and 0.05 mM NO donors together under an NL condition to check whether the application of both chemicals can cause cell death without HL interference. Our results confirmed that exogenously applied NO acts synchronously with accumulated H_2O_2 to enhance the sensitivity of *C. reinhardtii* cells to moderate HL illumination, leading to a decrease in cell viability and partial cell death, whereas the treatment with 1 mM H_2O_2 alone could not affect cell growth and the treatment with 0.05 mM NO donors also did not impact cell activity. Overall, these lines of evidence demonstrate that excessive NO can interact with H_2O_2 for the induction of cell death in *C. reinhardtii* cells under lethal HL illumination. In higher plants, NO bursts after a pathogen attack initiate gene-to-gene defense responses and they also interact with H_2O_2 and other signals in triggering PCD (Delledonne et al., 2001; Hong et al., 2008; Floryszak-Wieczorek and Arasimowicz-Jelonek, 2010). In the investigation of the MP-induced cell death in *C. reinhardtii* cells, Yordanova et al. (2010) have identified that NO cooperates with ethylene for the induction of cell death caused by MP. Obviously, NO interacts with other factors for the induction of cell death in *C. reinhardtii* cells, depending on the different stress conditions.

It has long been known that NO exhibits a dual function, beneficial or harmful, in stress conditions depending on its concentration, the type of tissue, age or physiological status, its ability to interact with other signaling molecules, and the type of stress (Delledonne et al., 2001; Arasimowicza and Floryszak-Wieczorek, 2007; Das et al., 2012). For instance, NO at a high concentration causes membrane breakdown, DNA fragmentation, and cell death (Pedroso et al., 2000; Yamasaki, 2000; Romero-Puertas et al., 2004). NO is also involved in the regulation of hypersensitive cell death (Clarke et al., 2000; de Pinto et al., 2002) and stress-induced cell death (Ahlfors et al., 2009; de Michele et al., 2009) in higher plants. In the diatoms, treatment with NO donors mimics aldehyde-induced cell death (Vardi et al., 2006). A negative role of NO on algal growth has been shown in the unicellular green alga *Micrasterias denticulate* (Brébisson) by exogenous application of a NO donor. The NO suppresses algal cell growth via the inhibition of the activity of enzymes involved in the secretary pathway (Lehner et al., 2009). NO also triggers cell death in algae; for example, aldehyde-induced cell death in diatoms (Vardi et al., 2006) and the heat-induced cell death of symbiotic alga *Symbiodinium microadriaticum* Freudenthal (Bouchard and Yamasaki, 2008). Previously, we have reported that mass generation of NO at a higher concentration under a 3,000 μmol m^{-2} s^{-1} condition contributes to the induction of cell death of *C. reinhardtii* cells (Chang et al., 2013). Therefore, NO overproduced in *C. reinhardtii* under extreme HL illumination opens the way to cell death. In contrast, our current study shows that, at lower concentrations, NO does not affect cell growth or cause permanent cell damage to *C. reinhardtii* cells. Treatment with 0.05 mM NO donors does not affect cell activity while 0.1 mM NO donors can trigger a transient effect on cell activity, followed by a rapid recovery after prolonged culture.

In addition to the concentration effect, the promotion or prevention of cell death is also dependent on the plant systems and conditions. In some plant tissues, NO counteracts PCD. For example, NO delays the onset of GA-induced PCD in barley (*Hordeum vulgare* cv Himalaya) aleurone layers (Beligni et al., 2002). In a study of a carotenoid deficient mutant, *lts1-204*, in the regulation of autophagy induction in *C. reinhardtii* cells by oxidative stress, Pérez-Pérez et al. (2010) demonstrated that 1,200 μmol m^{-2} s^{-1} illumination transiently activated autophagy in wild-type *Chlamydomonas* cells as part of an adaptation response to oxidative stress. In contrast, our current investigation implies that excessive NO generated under lethal HL illumination at the intensity of 1,600 μmol m^{-2} s^{-1} cooperates with highly accumulated H_2O_2 for the modulation of the signaling pathways, causing activation of autophagy, which leads to the death of *C. reinhardtii* cells.

First, we showed that autophagy induction is positively correlated with cell death in response to a lethal HL condition. This is in contrast to other conditions, such as nutrient starvation, where autophagy is considered to act as a protective process for *C. reinhardtii* against stress conditions. The review article of Pérez-Pérez et al. (2012b) has concluded from many studies that autophagy is conserved in plants and algae and plays a role in the adaptation to different stress conditions for the recycling of ROS-mediated oxidatively damaged macromolecules and organelles. Similarly, in hypersensitive plants, autophagy functions in the prevention of PCD (Greenberg, 2005). In contrast, in a study of the pathogen causing rice blast disease (*Magnaporthe grisea*), the use of an *Mgatg8* knockout line confirmed that autophagy is responsible for death of the spores (Veneault-Fourrey et al., 2006). Furthermore, in animal cells, certain forms of cell death can be inhibited by treatment with autophagic inhibitors or by reduced ATG gene expression (Shimizu et al., 2004; Yu et al., 2004). It has also been shown that autophagy-induced cell death is linked to unbalanced ROS production in animal cells. Using the mammalian L929 cell line, a widely studied model for TNF-α-induced cell death, caspase inhibitor, benzyloxycarbonyl-valyl-alanyl-aspartic-acid (*O*-methyl)-fluoromethylketone (zVAD) treatment results in selective autophagic degradation of catalase, a key enzymatic ROS scavenger, and in turn, this leads to marked ROS accumulation and ultimately causes non-apoptotic death (Yu et al., 2006). Thus, these findings imply that autophagy initiates and participates directly in the death process in animal systems. In the green alga *Chlamydomonas*, our current evidence shows that NO and H_2O_2 interact in the induction of autophagic cell death when exposed to lethal HL conditions. In the near future, a genetic investigation using ATG mutants is necessary to identify the network linking autophagy and cell death in *Chlamydomonas* under lethal HL stress.

In conclusion, the present study is the first to clearly demonstrate the interaction between NO and H_2O_2 in the activation of autophagic cell death in *C. reinhardtii* under lethal HL stress. This finding provides a background for further examination of the role of NO as a signaling molecule in the control of autophagy induction and the role of ROS interactions

with NO during the induction of cell death in *C. reinhardtii* under lethal HL stress.

DATA AVAILABILITY STATEMENT

The raw data supporting the conclusions of this article will be made available by the authors, without undue reservation, to any qualified researcher.

AUTHOR CONTRIBUTIONS

H-LC and EK performed the physiological analysis, RNA extraction, cDNA preparation, and qPCR. S-TL contributed to the preparation of reagents and the determination of biochemical and physiological parameters. T-ML conceived and designed the experiments, interpreted the data, and wrote the manuscript. All authors discussed and reviewed this manuscript.

FUNDING

This work was supported by grants (NSC99-2311-B-110-001-MY3 and NSC103-2311-B-110-001-MY3) from the Ministry of Science Technology, Executive Yuan, Taiwan.

ACKNOWLEDGMENTS

The authors thank Dr. Su-Chiung Fang, Academia Sinica Biotechnology Center in Southern Taiwan, Tainan, Taiwan, for valuable comments.

SUPPLEMENTARY MATERIAL

The Supplementary Material for this article can be found online at: https://www.frontiersin.org/articles/10.3389/fpls.2020.00772/full#supplementary-material

REFERENCES

Ahlfors, R., Brosché, M., Kollist, H., and Kangasjärvi, J. (2009). Nitric oxide modulates ozone-induced cell death, hormone biosynthesis and gene expression in *Arabidopsis thaliana*. *Plant J.* 58, 1–12. doi: 10.1111/j.1365-313X.2008.03756.x

Anbar, M. (1995). Nitric oxide: a synchronizing chemical messenger. *Experientia* 51, 545–550. doi: 10.1007/bf02128740

Arasimowicza, M., and Floryszak-Wieczorek, J. (2007). Nitric oxide as a bioactive signalling molecule in plant stress responses. *Plant Sci.* 172, 876–887. doi: 10.1016/j.plantsci.2007.02.005

Bajguz, A. (2014). "Nitric oxide: role in plants under abiotic stress," in *Physiological Mechanisms and Adaptation Strategies in Plants Under Changing Environments*, eds R. Ahmad and M. R. Wani (New York, NY: Springer), 137–160.

Barsoum, M. J., Yuan, H., Gerencser, A. A., Liot, G., Kushnareva, Y., Graber, S., et al. (2006). Nitric oxide-induced mitochondrial fission is regulated by dynamin-related GTPases in neurons. *EMBO J.* 25, 3900–3911. doi: 10.1038/sj.emboj.7601253

Bassham, D. C. and Crespo, J. L. (2014). Autophagy in plants and algae. *Front. Plant Sci.* 5:679. doi: 10.3389/fpls.2014.00679

Beligni, M. V., Fathc, A., Bethke, P. C., Lamattina, L., and Jones, R. L. (2002). Nitric oxide acts as an antioxidant and delays programmed cell death in barley aleurone layers. *Plant Physiol.* 129, 1642–1650. doi: 10.1104/pp.002337

Besson-Bard, A., Pugin, A., and Wendehenne, D. (2008). New insights into nitric oxide signaling in plants. *Annu. Rev. Plant Biol.* 59, 21–39. doi: 10.1146/annurev.arplant.59.032607.092830

Bouchard, J. N., and Yamasaki, H. (2008). Heat stress stimulates nitric oxide production in *Symbiodinium microadriaticum*: a possible linkage between nitric oxide and the coral bleaching phenomenon. *Plant Cell Physiol.* 49, 641–652. doi: 10.1093/pcp/pcn037

Bradford, M. M. (1976). A rapid method for the quantitation of microgram quantities of protein utilizing the principle of protein-dye binding. *Anal. Biochem.* 72, 248–254. doi: 10.1016/0003-2697(76)90527-3

Burlacot, A., Richaud, P., Gosset, A., Li-Beisson, Y., and Peltier, G. (2020). Algal photosynthesis converts nitric oxide into nitrous oxide. *Proc. Natl. Acad. Sci. U.S.A.* 117, 2704–2709. doi: 10.1073/pnas.1915276117

Chang, H. L., Hsu, Y. T., Kang, C. Y., and Lee, T. M. (2013). Nitric oxide down-regulation of carotenoid synthesis and PSII activity in relation to very high light-induced singlet oxygen production and oxidative stress in *Chlamydomonas reinhardtii*. *Plant Cell Physiol.* 54, 1296–1315. doi: 10.1093/pcp/pct078

Clarke, A., Desikan, R., Hurst, R. D., Hancock, J. T., and Neill, S. J. (2000). NO way back: nitric oxide and programmed cell death in *Arabidopsis thaliana* suspension cultures. *Plant J.* 24, 667–677. doi: 10.1046/j.1365-313x.2000.00911.x

D'Alessandro, S., Posocco, B., Costa, A., Zahariou, G., Schiavo, F. L., Carbonera, D., et al. (2013). Limits in the use of cPTIO as nitric oxide scavenger and EPR probe in plant cells and seedlings. *Front. Plant Sci.* 4:340. doi: 10.3389/fpls.2013.00340

Das, G., Shravage, B. V., and Baehreck, E. H. (2012). Regulation and function of autophage during cell survival and cell death. *Cold Spring Harb. Perspect. Biol.* 4:a008813. doi: 10.1101/cshperspect.a008813

de Michele, R., Vurro, E., Rigo, C., Costa, A., Elviri, L., Di Valentin, M., et al. (2009). Nitric oxide is involved in cadmium-induced programmed cell death in *Arabidopsis* suspension cultures. *Plant Physiol.* 150, 217–228. doi: 10.1104/pp.108.133397

de Pinto, M. C., Tommasi, F., and De Gara, L. (2002). Changes in the antioxidant systems as part of the signalling pathway responsible for the programmed cell death activated by nitric oxide and reactive oxygen species in tobacco BY-2 cells. *Plant Physiol.* 130, 698–708. doi: 10.1104/pp.005629

Delledonne, M., Zeier, J., Marocco, A., and Lamb, C. (2001). Signal interactions between nitric oxide and reactive oxygen intermediates in the plant hypersensitive disease resistance response. *Proc. Natl. Acad. Sci. U.S.A.* 98, 13454–13459. doi: 10.1073/pnas.231178298

Duana, L., Danzerb, B., Levensonb, V. V., and Makia, C. G. (2013). Critical roles for nitric oxide and ERK in the completion of prosurvival autophagy in 4OHTAM-treated estrogen receptor-positive breast cancer cells. *Cancer Lett* 353, 290–300. doi: 10.1016/j.canlet.2014.07.031

Engelman, J. A., Luo, J., and Cantley, L. C. (2006). The evolution of phosphatidylinositol 3-kinases as regulators of growth and metabolism. *Nat. Rev. Genet.* 7, 606–619.

Floryszak-Wieczorek, J., and Arasimowicz-Jelonek, M. (2010). "Interplay between nitric oxide and other signals involved in plant resistance to pathogens," in *Nitric Oxide in Plant Physiology*, eds S. Hayat, M. Mori, J. Pichtel, and A. Ahmad (Hoboken, NJ: Wiley- Blackwell), 139–159. doi: 10.1002/9783527629138.ch10

Foresia, N., Correa-Aragundea, N., Parisib, G., Calóc, G., Salernoc, G., and Lamattina, L. (2010). Characterization of a nitric oxide synthase from the plant kingdom: NO generation from the green alga Ostreococcus tauri is light irradiance and growth phase dependent. *Plant Cell* 22, 3816–3830. doi: 10.1105/tpc.109.073510

Galván, A., and Fernández, E. (2001). Eukaryotic nitrate and nitrite transporters. *Cell. Mol. Life Sci.* 58, 225–233. doi: 10.1007/PL00000850

Greenberg, J. T. (2005). Degrade or die: a dual function for autophagy in the plant immune response. *Dev. Cell* 8, 799–801. doi: 10.1016/j.devcel.2005.05.005

Hanada, T., Noda, N. N., Satomi, Y., Ichimura, Y., Fujioka, Y., Takao, T., et al. (2007). The Atg12-Atg5 conjugate has a novel E3-like activity for protein lipidation in autophagy. *J. Biol. Chem.* 282, 37298–37302. doi: 10.1074/jbc.C700195200

Harris, E. H. (1989). *In the Chlamydomonas Sourcebook*. San Diego, CA: Academic Press, Inc., 25–40.

Hasanuzzaman, M., Hossain, M. A., and Fujita, M. (2010). Physiological and biochemical mechanisms of nitric oxide induced abiotic stress tolerance in plants. *Am. J. Plant Physiol.* 5, 295–324. doi: 10.3923/ajpp.2010.295.324

Hayat, S., Mor, M., Pichtel, J., and Ahmad, A. (2010). *Nitric Oxide in Plant Physiology*. Weinheim: Wiley-VCH, Verlag GmbH & Co.

Hemschemeier, A., Düner, M., Casero, D., Merchant, S. S., Winkler, M., and Happe, T. (2013). Hypoxic survival requires a 2-on-2 hemoglobin in a process involving nitric oxide. *Proc. Natl. Acad. Sci. U.S.A.* 110, 10854–10859. doi: 10.1073/pnas.1302592110

Hong, J. K., Yun, B. W., Kang, J. G., Raja, M. U., Kwon, E., Sorhagen, K., et al. (2008). Nitric oxide function and signalling in plant disease resistance. *J. Exp. Bot.* 59, 147–154. doi: 10.1093/jxb/erm244

Houot, V., Etienne, P., Petitot, A. B., Barbier, S., Blein, J. P., and Suty, L. (2001). Hydrogen peroxide induces programmed cell death features in cultured tobacco BY-2 cells, in a dose-dependent manner. *J. Exp. Bot.* 52, 1721–1730. doi: 10.1093/jxb/52.361.1721

Itakura, E., Kishi, C., Inoue, K., and Mizushima, N. (2008). Beclin 1 forms two distinct phosphatidylinositol 3-kinase complexes with mammalian Atg14 and UVRAG. *Mol. Biol. Cell* 19, 5360–5372. doi: 10.1091/mbc.E08-01-0080

Jaber, N., Dou, Z., Chen, J. S., Catanzaro, J., Jiang, Y. P., Ballou, L. M., et al. (2012). Class III PI3K Vps34 plays an essential role in autophagy and in heart and liver function. *Proc. Natl. Acad. Sci. U.S.A.* 109, 2003–2008. doi: 10.1073/pnas.1112848109

Kamada, Y., Funakoshi, T., Shintani, T., Nagano, K., Ohsumi, M., and Ohsumi, Y. (2000). TOR-mediated induction of autophagy via an Apg1 protein kinas omplex. *J. Cell Biol.* 150, 1507–1513. doi: 10.1083/jcb.150.6.1507

Kojima, H., Nakatsubo, N., Kikuchi, K., Kawahara, S., Kirino, Y., and Nagoshi, H. (1998). Detection and imaging of nitric oxide with novel fluorescent indicators: diaminofluoresceins. *Anal. Chem.* 70, 2446–2453. doi: 10.1021/ac9801723

Lehner, C., Kerschbaum, H. H., and Luez-Meindl, U. (2009). Nitric oxide suppresses growth and development in the unicellular green alga Micrasterias denticulate. *J. Plant Physiol.* 166, 117–127. doi: 10.1016/j.jplph.2008.02.012

Liu, Y., and Bassham, D. C. (2012). Autophagy: pathways for self-eating in plant cells. *Ann. Rev. Plant Biol.* 63, 215–237. doi: 10.1146/annurev-arplant-042811-105441

Mizushima, N., Yoshimori, T., and Ohsumi, Y. (2011). The role of Atg proteins in autophagosome formation. *Annu. Rev. Cell Dev. Biol.* 27, 107–132. doi: 10.1146/annurev-cellbio-092910-154005

Mur, L. A. J., Mandon, J., Cristescu, S. M., Harren, F. J. M., and Prats, E. (2011). Methods of nitric oxide detection in plants: a commentary. *Plant Sci.* 181, 509–519. doi: 10.1016/j.plantsci.2011.04.003

Murik, O., Elboher, A., and Kaplan, A. (2014). Dehydroascorbate: a possible surveillance molecule of oxidative stress and programmed cell death in the green alga *Chlamydomonas reinhardtii*. *New Phytol.* 202, 471–484. doi: 10.1111/nph.12649

Nakatogawa, H., Ichimura, Y., and Ohsumi, Y. (2007). Atg8, a ubiquitin-like protein required for autophagosome formation, mediates membrane tethering and hemifusion. *Cell* 130, 165–178. doi: 10.1016/j.cell.2007.05.021

Neill, S., Barros, R., Bright, J., Desikan, R., Hancock, J., and Harrison, J. (2008). Nitric oxide, stomatal closure, and abiotic stress. *J. Exp. Bot.* 59, 165–176. doi: 10.1093/jxb/erm293

Ohsumi, Y. (2001). Molecular dissection of autophagy: two ubiquitin-like systems. *Nat. Rev. Mol. Cell Biol.* 2, 211–216. doi: 10.1038/35056522

Palavan-Unsal, N., and Arisan, D. (2009). Nitric oxide signalling in plants. *Bot. Rev.* 75, 203–229. doi: 10.1007/si2229-009-9031-2

Pedroso, M. C., Magalhaes, J. R., and Durzan, D. (2000). Nitric oxide induces cell death in Taxus cells. *Plant Sci.* 157, 173–180. doi: 10.1016/s0168-9452(00)00278-8

Pérez-Pérez, M. E., Couso, I., and Crespo, J. L. (2012a). Carotenoid deficiency triggers autophagy in the model green alga *Chlamydomonas reinhardtii*. *Autophagy* 8, 376–388. doi: 10.4161/auto.18864

Pérez-Pérez, M. E., and Crespo, J. L. (2010). Autophagy in the model alga *Chlamydomonas reinhardtii*. *Autophagy* 6, 562–563. doi: 10.4161/auto.6.4.11822

Pérez-Pérez, M. E., Florencio, F. J., and Crespo, J. L. (2010). Inhibition of target of rapamycin signaling and stress activate autophagy in *Chlamydomonas reinhardtii*. *Plant Physiol.* 152, 1874–1888. doi: 10.1104/pp.109.152520

Pérez-Pérez, M. E., Lemaire, S. D., and Crespo, J. L. (2012b). Reactive oxygen species and autophagy in plants and algae. *Plant Physiol.* 160, 156–164. doi: 10.1104/pp.112.199992

Pérez-Pérez, M. E., Zaffagnini. M., Marchand, C. H., Crespo, J. L., and Lemaire, S. D. (2014). The yeast autophagy protease Atg4 is regulated by thioredoxin. *Autophagy* 10, 1953–1964. doi: 10.4161/auto.34396

Rabkin, S. W., and Klassen, S. S. (2007). Nitric oxide differentially regulates the gene expression of caspase genes but not some autophagic genes. *Nitric Oxide* 16, 339–347. doi: 10.1016/j.niox.2006.10.007

Ramundo, S., Casero, D., Mühlhaus, T., Hemme, D., Sommer, F., Crèvecoeur, M., et al. (2014). Conditional depletion of the Chlamydomonas chloroplast ClpP protease activates nuclear genes involved in autophagy and plastid protein quality control. *Plant Cell* 26, 2201–2222. doi: 10.1105/tpc.114.124842

Romero-Puertas, M. C., Perazzolli, M., Zago, E. D., and Delledonne, M. (2004). Nitric oxide signalling functions in plant-pathogen interactions. *Cell. Microbiol.* 6, 795–803. doi: 10.1111/j.1462-5822.2004.00428.x

Sarkar, S., Korolchuk, V., Renna, M., Imarisio, S., Fleming, A., Williams, A., et al. (2011). Complex inhibitory effects of nitric oxide on autophagy. *Mol. Cell* 43, 19–32. doi: 10.1016/j.molcel.2011.04.029

Sato, M., Murata, Y., Mizusawa, M., Iwahashi, H., and Oka, S. (2004). A simple and rapid dual-fluorescence viability assay for microalgae. *Microbiol. Cult. Coll.* 20, 53–59.

Shimizu, S., Kanaseki, T., Mizushima, N., Mizuta, T., Arakawa-Kobayashi, S., Thompson, C. B., et al. (2004). Role of Bcl-2 family proteins in a non-apoptotic programmed cell death dependent on autophagy genes. *Nat. Cell Biol.* 6, 1221–1228. doi: 10.1038/ncb1192

Siddiqui, M. H., Al-Whaibi, M. H., and Basalah, M. O. (2011). Role of nitric oxide in tolerance of plants to abiotic stress. *Protoplasma* 248, 447–455. doi: 10.1007/s00709-010-0206-9

Thompson, A. R., and Vierstra, R. D. (2005). Autophagic recycling: lessons from yeast help define the process in plants. *Curr. Opin. Plant Biol.* 8, 165–173. doi: 10.1016/j.pbi.2005.01.013

Tran, Q. G., Cho, K., Park, S. B., Kim, U., Lee, Y. J., and Kim, H. H. S. (2019). Impairment of starch biosynthesis results in elevated oxidative stress and autophagy activity in *Chlamydomonas reinhardtii*. *Sci. Rep.* 9:9856. doi: 10.1038/s41598-019-46313-6

Tripathi, D. N., Chowdhury, R., Trudel, L. J., Tee, A. R., Slack, R. S., Walker, C. L., et al. (2013). Reactive nitrogen species regulate autophagy through ATM-AMPK-TSC2-mediated suppression of mTORC1. *Proc. Natl. Acad. Sci. U.S.A.* 110, E2950–E2957. doi: 10.1073/pnas.1307736110

Vardi, A., Formiggini, F., Casotti, R., De Martino, A., Ribalet, F., Miralto, A., et al. (2006). A stress surveillance system based on calcium and nitric oxide in marine diatoms. *PLoS Biol.* 4:e60. doi: 10.1371/journal.pbio.0040060

Veneault-Fourrey, C., Barooah, M., Egan, M., Wakley, G., and Talbot, N. J. (2006). Autophagic fungal cell death in necessary for infection by the rice blast fungus. *Science* 312, 580–583. doi: 10.1126/science.1124550

Wang, Y., Loake, G. J., and Chu, C. (2013). Cross-talk of nitric oxide and reactive oxygen species in plant programed cell death. *Front. Plant Sci.* 4:314. doi: 10.3389/fpls.2013.00314

Wei, L., Derrien, B., Gautier, A., Houille-Vernes, L., Boulouis, A., Saint-Marcoux, D., et al. (2014). Nitric oxide–triggered remodeling of chloroplast bioenergetics and thylakoid proteins upon nitrogen starvation in *Chlamydomonas reinhardtii*. *Plant Cell* 26, 353–372. doi: 10.1105/tpc.113.120121

Xie, Z., Nair, U., and Klionsky, D. J. (2008). Atg8 controls phagophore expansion during autophagosome formation. *Mol. Biol. Cell* 19, 3290–3298. doi: 10.1091/mbc.E07-12-1292

Xu, Y., Sun, X., Jin, J., and Zhou, H. (2010). Protective effect of nitric oxide on light-induced oxidative damage in leaves of tall fescue. *J. Plant Physiol.* 167, 512–518. doi: 10.1016/j.jplph.2009.10.010

Yamasaki, H. (2000). Nitrite-dependent nitric oxide production pathway: implications for involvement of active nitrogen species in photoinhibition in vivo. *Phil. Trans. R. Soc. Lond. Biol. Sci.* 355, 1477–1488. doi: 10.1098/rstb.2000.0708

Yang, J., Wu, L. J., Tashino, S. I., Onodera, S., and Ikejima, T. (2008). Reactive oxygen species and nitric oxide regulate mitochondria-dependent apoptosis and autophagy in evodiamine-treated human cervix carcinoma HeLa cells. *Free Radic. Res.* 42, 492–504. doi: 10.1080/10715760802112791

Yordanova, Z. P., Iakimova, E. T., Cristescu, S. M., Harren, F. J., Kapchina-Toteva, V. M., and Woltering, E. J. (2010). Involvement of ethylene and nitric oxide in cell death in mastoparan-treated unicellular alga *Chlamydomonas reinhardtii*. *Cell Biol. Int.* 34, 301–308. doi: 10.1042/CBI20090138

Yu, L., Alva, A., Su, H., Dutt, P., Freundt, E., Welsh, S., et al. (2004). Regulation of an ATG7-beclin 1 program of autophagic cell death by caspase-8. *Science* 304, 1500–1502. doi: 10.1126/science.1096645

Yu, L., Wan, F., Dutta, S., Welsh, S., Liu, Z. H., Freundt, E., et al. (2006). Autophagic programmed cell death by selective catalase degradation. *Proc. Natl. Acad. Sci U.S.A.* 28, 4952–4957. doi: 10.1073/pnas.0511288103

Conflict of Interest: The authors declare that the research was conducted in the absence of any commercial or financial relationships that could be construed as a potential conflict of interest.

frontiers in Plant Science

ORIGINAL RESEARCH
published: 23 June 2020
doi: 10.3389/fpls.2020.00868

Overexpression of Sedoheptulose-1,7-Bisphosphatase Enhances Photosynthesis in *Chlamydomonas reinhardtii* and Has No Effect on the Abundance of Other Calvin-Benson Cycle Enzymes

*Alexander Hammel[1], Frederik Sommer[1], David Zimmer[2], Mark Stitt[3], Timo Mühlhaus[2] and Michael Schroda[1]**

[1] Molecular Biotechnology & Systems Biology, TU Kaiserslautern, Kaiserslautern, Germany, [2] Computational Systems Biology, TU Kaiserslautern, Kaiserslautern, Germany, [3] Max Planck Institute of Molecular Plant Physiology, Potsdam, Germany

OPEN ACCESS

Edited by:
Dimitris Petroutsos, UMR 5168 Laboratoire de Physiologie Cellulaire Vegetale (LPCV), France

Reviewed by:
Christine Anne Raines, University of Essex, United Kingdom
Paolo Trost, University of Bologna, Italy

***Correspondence:**
Michael Schroda
schroda@bio.uni-kl.de

Specialty section:
This article was submitted to Plant Cell Biology, a section of the journal Frontiers in Plant Science

Received: *14 February 2020*
Accepted: *27 May 2020*
Published: *23 June 2020*

Citation:
Hammel A, Sommer F, Zimmer D, Stitt M, Mühlhaus T and Schroda M (2020) Overexpression of Sedoheptulose-1,7-Bisphosphatase Enhances Photosynthesis in Chlamydomonas reinhardtii and Has No Effect on the Abundance of Other Calvin-Benson Cycle Enzymes. Front. Plant Sci. 11:868. doi: 10.3389/fpls.2020.00868

The productivity of plants and microalgae needs to be increased to feed the growing world population and to promote the development of a low-carbon economy. This goal can be achieved by improving photosynthesis via genetic engineering. In this study, we have employed the Modular Cloning strategy to overexpress the Calvin-Benson cycle (CBC) enzyme sedoheptulose-1,7-bisphosphatase (SBP1) up to threefold in the unicellular green alga *Chlamydomonas reinhardtii*. The protein derived from the nuclear transgene represented ∼0.3% of total cell protein. Photosynthetic rate and growth were significantly increased in SBP1-overexpressing lines under high-light and elevated CO_2 conditions. Absolute quantification of the abundance of all other CBC enzymes by the QconCAT approach revealed no consistent differences between SBP1-overexpressing lines and the recipient strain. This analysis also revealed that the 11 CBC enzymes represent 11.9% of total cell protein in *Chlamydomonas*. Here, the range of concentrations of CBC enzymes turned out to be much larger than estimated earlier, with a 128-fold difference between the most abundant CBC protein (rbcL) and the least abundant (triose phosphate isomerase). Accordingly, the concentrations of the CBC intermediates are often but not always higher than the binding site concentrations of the enzymes for which they act as substrates. The enzymes with highest substrate to binding site ratios might represent good candidates for overexpression in subsequent engineering steps.

Keywords: mass spectrometry, proteotypic peptide, QconCAT, Synthetic Biology, Modular Cloning, photosynthesis, *Chlamydomonas reinhardtii*

INTRODUCTION

An increased productivity of plants and microalgae is required to feed the growing world population and to promote the development of a low-carbon economy. One way to increase plant and microalgal productivity is to improve photosynthesis by genetic engineering. Engineering efforts that have resulted in increased biomass are the rewiring of photorespiration (Kebeish et al., 2007; Nolke et al., 2014), the improvement of linear electron transport between the photosystems (Chida et al., 2007; Simkin et al., 2017b), or the overexpression of distinct Calvin-Benson cycle (CBC) enzymes [for recent reviews see Kubis and Bar-Even (2019) and Simkin et al. (2019)]. The rationale behind the latter approach is that the rising concentration of atmospheric CO_2 caused by the burning of fossil fuels increases the velocity of the carboxylation reaction of Rubisco and inhibits the competing oxygenation reaction. This results in a shift in the limitation of photosynthesis away from carboxylation of ribulose 1,5-bisphosphate (RuBP) and toward RuBP regeneration. The CBC enzyme sedoheptulose-1,7-bisphosphatase (SBPase) has been shown to exert strong metabolic control over RuBP regeneration at light saturation, as the irreversible reaction that it catalyses is positioned at the branch point between regenerative (RuBP regeneration) and assimilatory (starch biosynthesis) portions of the CBC. SBPase catalyzes the irreversible dephosphorylation of sedoheptulose-1,7-bisphosphate (SBP) to sedoheptulose-7-phosphate (S7P). Accordingly, the overexpression of SBPase alone (Lefebvre et al., 2005; Tamoi et al., 2006; Feng et al., 2007; Rosenthal et al., 2011; Fang et al., 2012; Ding et al., 2016; Driever et al., 2017; Simkin et al., 2017a) or of the cyanobacterial bifunctional SBPase/FBPase (BiBPase) (Miyagawa et al., 2001; Yabuta et al., 2008; Ichikawa et al., 2010; Gong et al., 2015; Ogawa et al., 2015; Kohler et al., 2017; De Porcellinis et al., 2018) resulted in marked increases in photosynthesis and biomass yields in tobacco, lettuce, *Arabidopsis thaliana*, wheat, tomato, rice, soybean, in the cyanobacterium *Synechococcus*, and in the microalgae *Euglena gracilis* and *Dunaliella bardawil*.

Genetic engineering often is an iterative process essentially consisting of four steps: (i) the design and manufacturing of a gene construct, (ii) its transfection into the target organism and the recovery of transgenic lines, (iii) the screening for expressing transformants, and (iv) the readout of the trait to be altered, on which basis the gene construct for the next cycle is designed. The cloning steps used to be a time constraint, which was overcome by new cloning strategies like Gibson assembly or Modular Cloning (MoClo) for Synthetic Biology that allow the directed assembly of multiple genetic parts in a single reaction (Gibson et al., 2009; Weber et al., 2011). Still a major time constraint (months) in the genetic engineering of plants is the recovery of transfected plants and their propagation for reading out altered traits. This constraint can only be overcome by using plant models with short generation times, like microalgae.

A potential problem of genetic engineering are undesired side effects of the genetic engineering that can best be revealed by system-wide approaches. One way is to compare the proteomes of wild type and engineered lines by quantitative proteomics (Gillet et al., 2016). A more targeted approach is the use of quantification concatamers (QconCATs) (Beynon et al., 2005; Pratt et al., 2006). QconCATs are made of concatenated proteotypic peptides, an affinity tag allowing purification under denaturing conditions and, optionally, cysteine or tryptophan residues for easy quantification. The QconCAT protein is expressed in *E. coli* with a heavy isotope from a codon-optimized, synthetic gene. A known amount of the QconCAT protein is then added to the sample and, upon tryptic digestion, the heavy proteotypic peptides from the QconCAT protein are released together with the corresponding light peptides from the parent proteins. All QconCAT peptides are present in a strict 1:1 ratio at the concentration determined for the entire protein. After ionization, the pairs of heavy QconCAT peptides and light native peptides can be separated and quantified by mass spectrometry, with the heavy peptides serving as calibrators allowing absolute quantification of the target proteins in the sample. This method is limited to about 20 targets per QconCAT protein.

The aim of this work was to provide a proof of principle for a rapid metabolic engineering workflow to improve photosynthesis. We chose to overexpress SBPase via the MoClo strategy, the unicellular green alga *Chlamydomonas* as a chassis, and QconCAT-based absolute quantification as a tool for monitoring effects on other CBC enzymes.

MATERIALS AND METHODS

Growth of *Chlamydomonas* Cells

Chlamydomonas reinhardtii UVM4 cells (Neupert et al., 2009) were grown in Tris-Acetate-Phosphate (TAP) medium (Kropat et al., 2011) on a rotatory shaker. For transformation, cells were grown at a light intensity of 100 μmol photons m^{-2} s^{-1} to a density of 5×10^6 cells/ml and collected by centrifugation at 4000 × *g* for 2 min. 5×10^7 cells were mixed with 1 μg DNA linearized with *Not*I and transformed by vortexing with glass beads (Kindle, 1990). Vortexed cells were diluted twofold with TAP and 2.5×10^7 cells were spread onto TAP agar plates containing 100 μg ml^{-1} spectinomycin. Plates were incubated over-night in the dark and then incubated at 30 μmol photons m^{-2} s^{-1} for about 10 days. For growth curves, cells were inoculated in 100 ml TAP medium and grown at 150 μmol photons m^{-2} s^{-1} to a density of about 8×10^6 cells/ml. 100 ml TAP or Hepes-Minimal-Phosphate (HMP) medium (5 mM Hepes-KOH instead of 20 mM Tris, no acetate) were then inoculated with 3×10^5 cells/ml in triplicates for each strain and growth was monitored by cell counting using the Z2 Coulter Particle Count and Size Analyzer (Beckmann). The culture volume is the summed cell volume of all cells in 1 ml medium. For mass spectrometry analyses, samples were harvested 22 h after inoculation (early log phase).

Measurement of Oxygen Evolution

Cells were inoculated in 50 ml TAP medium and grown overnight to early log phase. Oxygen measurements were performed in the Mini-PAM-II (Walz, Germany) device using the needle-type oxygen microsensor OXR-50 (Pyroscience, Germany). Before the measurements, the cell density was determined, and an aliquot

was taken to determine the chlorophyll concentration. The PAM chamber was filled with 400 µl of *Chlamydomonas* culture and $NaHCO_3$ was added to a final concentration of 30 mM. Cells were dark-adapted for 5 min and far-red light adapted for another 5 min. Then light with the intensities of 16, 29, 42, 58, 80, 122, 183, 269, 400, 525, 741, and 963 µmol photons m^{-2} s^{-1} was applied for 2 min each and oxygen evolution was monitored.

Cloning of the *Chlamydomonas SBP1* Gene for MoClo

Our constructs are based on the Phytozome 12 annotation of the genomic version of the *Chlamydomonas SBP1* gene (Cre03.g185550) with seven exons and six introns. However, we used the first ATG in the 5′ UTR as start codon instead of the third proposed by Phytozome. To domesticate a BsaI recognition site in the fifth exon (GAGACC → GAGACA), the *SBP1* gene was PCR-amplified on total *Chlamydomonas* DNA in two fragments with primers 5′-TTGAAGACATAATGGCCGCTATGATGATGC-3′ and 5′-ACGAAGACGGGTTGTCTCCTTGACGTGC-3′ for fragment 1 (1257 bp) and with primers 5′-TTGAAGACGGCAACCCACATCGGTGAG-3′ and 5′-TTGAAGACTCCGAACCGGCAGCCACCTTCTCAGAG-3′ for fragment 2 (963 bp; BpiI sites are underlined). PCR was done with Q5 High-Fidelity Polymerase (NEB) following the manufacturer's instructions and in the presence of 10% DMSO. The two PCR products were combined with destination vector pAGM1287 (Weber et al., 2011), digested with BpiI and directionally assembled by ligation into level 0 construct pMBS516. The latter was then combined with plasmids pCM0-020 (*HSP70A-RBCS2* promoter + 5′UTR), pCM0-101 (MultiStop) or pCM0-100 (3xHA), and pCM0-119 (*RPL23* 3′UTR) from the *Chlamydomonas* MoClo kit (Crozet et al., 2018) as well as with destination vector pICH47742 (Weber et al., 2011), digested with BsaI and ligated to generate level 1 constructs pMBS517 (L1-SBP1-mStop) and pMBS518 (L1-SBP1-3xHA). Both level 1 constructs were then combined with pCM1-01 (level 1 construct with the *aadA* gene conferring resistance to spectinomycin flanked by the *PSAD* promoter and terminator) from the *Chlamydomonas* MoClo kit, with plasmid pICH41744 containing the proper end-linker, and with destination vector pAGM4673 (Weber et al., 2011), digested with BpiI, and ligated to yield level 2 constructs pMBS519 (*aadA* + *SBP1*-mstop) and pMBS520 (aadA + SBP1-3xHA). Correct cloning was verified by Sanger sequencing.

Screening of SBP1 Overexpressing Lines

Transformants were grown in TAP medium until mid-log phase and harvested by centrifugation at 13,000 × *g* for 5 min at 25°C. Cells were resuspended in DTT-carbonate buffer (100 mM DTT; 100 mM Na_2CO_3), supplemented with SDS and sucrose at final concentrations of 2% and 12%, respectively, vortexed, heated to 95°C for 5 min, and centrifuged at 13,000 × *g* for 5 min at 25°C. The chlorophyll content was determined as described by Vernon (1960). Total proteins according to 1.5 µg total *Chlamydomonas* chlorophyll were loaded on a 12% SDS-polyacrylamide gel and analyzed by immunoblotting using a mouse anti-HA antibody (Sigma H9658, 1:10,000) for transformants with SBP1-3xHA or a rabbit anti-SBPase antibody (Agrisera AS15 2873, 1:2,500) for SBP1-mStop. Detection was done via enhanced chemiluminescence using the FUSION-FX7 device (Peqlab).

QconCAT Protein Expression and Purification

The coding sequence for the Calvin-Benson cycle QconCAT protein (CBC-Qprot) was codon-optimized for *E. coli*, synthesized by Biocat (Heidelberg) harboring *Bam*HI/*Hin*dIII restriction sites, cloned into the pET-21b expression vector (Novagen), and transformed into *E. coli* ER2566 cells (New England Biolabs). Expression of CBC-Qprot as a ^{15}N-labeled protein and purification via Co-NTA affinity chromatography and electroelution was performed as described previously for the photosynthesis QconCAT protein (PS-Qprot) (Hammel et al., 2018). The eluted protein was concentrated, and the buffer changed to 6 M urea, 40 mM NH_4HCO_3 using Amicon ultra-15 centrifugal filter units with 10,000 MWCO (Merck). The protein concentration was determined at 280 nm on a NanoDrop™ spectrophotometer using the Lambert-Beer's law, a molecular weight of the CBC-Qprot of 47,921 Da, and an extinction coefficient of 37,400 M^{-1} cm^{-1}. The protein concentration was adjusted to 1 µg/µl. The protein was stored at −20°C.

In Solution Tryptic Digest and LC-MS/MS Analysis

Twenty micrograms of total *Chlamydomonas* protein, as determined by the Lowry assay (Lowry et al., 1951), were mixed with 12.5, 25, 50, and 100 ng CBC- and PS-Qprot for replicates 1–3, and with 25, 50, 100, and 200 ng CBC- and PS-Qprot for replicates 4–6. Proteins were then precipitated with ice-cold 80% acetone overnight, digested tryptically, and analyzed by LC-MS/MS (Eksigent nanoLC 425 coupled to a TripleTOF 6600, ABSciex) as described previously (Hammel et al., 2018). Extraction of ion chromatograms and the identification and quantification of labeled and unlabeled peptides was performed using the QConQuantifier software available at https://github.com/ZimmerD/qconquantifier. The mass spectrometry proteomics data have been deposited to the ProteomeXchange Consortium via the PRIDE (Perez-Riverol et al., 2019) partner repository with the dataset identifier PXD018833.

RESULTS

Construction of *Chlamydomonas* Strains Overexpressing Sedoheptulose-1,7-Bisphosphatase (SBP1)

The *Chlamydomonas SBP1* gene encodes sedoheptulose-1,7-bisphosphatase of the CBC. We chose to use the genomic version of the gene including all seven exons and six introns to adapt it to the MoClo syntax (Weber et al., 2011; Patron et al., 2015). For this, we followed the protocol suggested previously

(Schroda, 2019), which required two PCR amplifications to alter sequences around the start and stop codons and to remove an internal BpiI recognition site (**Figure 1A**). Using the *Chlamydomonas* MoClo toolkit (Crozet et al., 2018), the domesticated *SBP1* gene was equipped with the strong constitutive *HSP70A-RBCS2* fusion promoter [A(Δ-467)-R] (Lodha et al., 2008; Strenkert et al., 2013) and the *RPL23* terminator (Lopez-Paz et al., 2017). We generated two variants, one encoding a 3xHA tag at the C-terminus (SBP1-3xHA), the other lacking any tags (SBP1-mStop) (**Figure 1A**). HA-tagged proteins are easy to screen for, because the anti-HA antibody used reacts strongly with the 3xHA tag and has little background on immunoblots with *Chlamydomonas* total proteins. This allows assessing the frequency and variance with which transformants express the transgenic protein, and whether it has the expected size. This information can then be used for the screening of transformants expressing the untagged transgenic protein, which is the preferable variant because the 3xHA tag might interfere with the protein's function. After adding an *aadA* cassette to the constructs (**Figure 1A**), they were transformed into the *Chlamydomonas* UVM4 strain that expresses transgenes efficiently (Neupert et al., 2009). Of the 12 SBP1-3xHA transformants screened, three did not express the transgene and five expressed it to high levels (**Figure 1B**). A similar pattern was observed for the 12 SBP1-mStop transformants, of which three appeared not to express the transgene and three expressed it to high levels. The two best-expressing transformants of each construct were selected for further analyses.

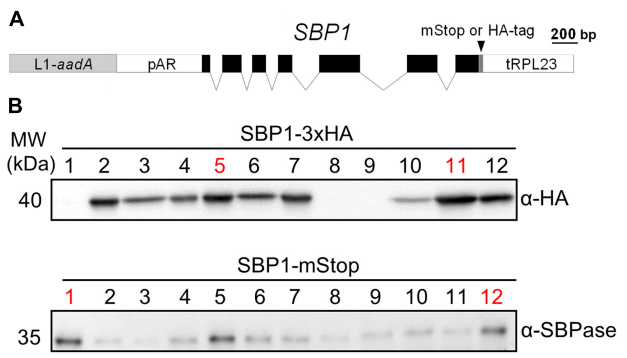

FIGURE 1 | Generation of *Chlamydomonas* lines overexpressing SBP1. **(A)** SBP1 construct used for transformation. The 2172 bp *SBP1* ORF (exons shown as black boxes), interrupted by all native *SBP1* introns (thin lines), was domesticated to generate a level 0 module for the MoClo strategy. Using MoClo, the *SBP1* ORF was equipped with the *HSP70A-RBCS2* promotor and the RPL23 terminator (pAR and tRPL23, respectively, white boxes) and with a 3xHA-tag or without a tag (mStop) (gray box), giving rise to two level 1 constructs. These were combined with another level 1 construct containing the *aadA* gene conferring resistance to spectinomycin (light gray box) to yield the final level 2 constructs for transformation. **(B)** Screening of transformants overexpressing SBP1. The UVM4 strain was transformed with the level 2 constructs shown in **(A)**. Total cell proteins from 12 spectinomycin resistant transformants recovered with each construct were extracted and proteins corresponding to 1.5 μg chlorophyll were analyzed by immunoblotting using anti-HA or anti-SBPase antibodies. The transformant number is given on top of the lanes. Transformants exhibiting highest expression levels for SBP1-3HA or SBP1-mStop (red) were used for further analysis.

Monitoring SBP1-Overexpressing Lines for Improved Photosynthetic Rate and Growth

We first tested the four SBP1-overexpressing transformants for improved growth. As elevated SBPase activity has resulted in improved growth particularly under high light and high CO_2 conditions (Miyagawa et al., 2001; Lefebvre et al., 2005; Tamoi et al., 2006; Ichikawa et al., 2010; Gong et al., 2015; Ogawa et al., 2015; Driever et al., 2017; De Porcellinis et al., 2018), we chose to grow the transformants under mixotrophic conditions with acetate in the medium at a light intensity of 150 μmol photons m^{-2} s^{-1} (our standard growth light intensity is 40 μmol photons m^{-2} s^{-1}). Part of the acetate apparently is converted into CO_2 by Krebs cycle activity in the mitochondria and available to Rubisco in the chloroplast (Johnson and Alric, 2012; Polukhina et al., 2016). As shown in **Figure 2A**, both SBP1-mStop transformants (St1 and St12) accumulated higher culture volumes (significant after 44 h and 52 h of growth, $p < 0.001$) and therefore reached stationary phase about 14 h earlier than the UVM4 recipient strain. Growth of the HA5 transformant did not differ from that of UVM4 and growth of HA11 even lagged behind that of UVM4. To test whether the enhanced growth rate of the SBP1-mStop transformants was due to an improved photosynthetic rate, we monitored the photosynthetic light response curves for UVM4 and the two SBP1-mStop lines. For this, we measured oxygen evolution as a function of applied light intensity under mixotrophic growth conditions (**Figure 2B**). Rates of oxygen evolution of the UVM4 strain were comparable with those measured earlier in another strain background (CC-125), with both strains exhibiting maximal oxygen evolution at 450 μmol photons m^{-2} s^{-1} (Wykoff et al., 1998). While UVM4 and the two transformants evolved oxygen with similar rates at light intensities of up to 183 μmol photons m^{-2} s^{-1}, the SBP1-mStop lines started to evolve more oxygen at light intensities exceeding 183 μmol photons m^{-2} s^{-1} and this became significant ($p < 0.05$) at light intensities of 520 μmol photons m^{-2} s^{-1} and above. Under photoautotrophic growth conditions at a light intensity of 150 μmol photons m^{-2} s^{-1} we observed no difference in growth between all strains, presumably because they were CO_2 limited (**Figure 2C**). We found no differences in chlorophyll content between the strains (*t*-test, $p > 0.05$, $n = 3$).

Absolute Quantification of All CBC Enzymes in *Chlamydomonas* by the QconCAT Strategy

We observed improved growth for the SBP1-mStop transformants but not for the SBP1-3xHA transformants. We reasoned that this could have been due to higher SBP1 expression levels in the former, or due to a negative effect of the 3xHA tag on the protein's function in the latter. To distinguish between these possibilities and to elucidate whether SBP1 overexpression affected the expression of the other 10 CBC enzymes, we quantified the absolute levels of all CBC enzymes in the UVM4

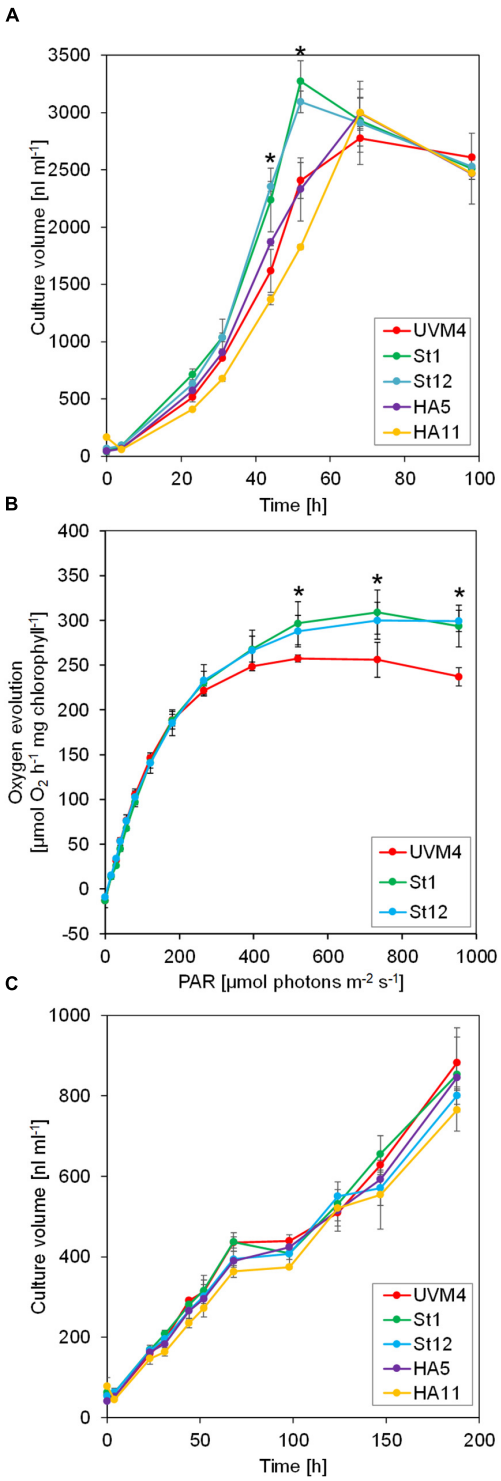

FIGURE 2 | Growth and light response curves of SBP1-overexpressing lines versus the UVM4 recipient strain. **(A)** Growth curves under mixotrophic conditions. Cultures were inoculated in TAP medium at a density of 3×10^5 cells ml^{-1} and incubated on a rotatory shaker for 4 days at a light intensity of 150 µmol photons m^{-2} s^{-1}. The culture volume (cell density × cell size) was determined with a Coulter counter. Values are the mean from three biological replicates, error bars indicate SD. Asterisks indicate significant differences to *(Continued)*

FIGURE 2 | Continued
the UVM4 strain, $p < 0.001$ (one-way ANOVA with Dunnett's multiple comparison test). **(B)** Light response curves. Cells were grown mixotrophically to mid-log phase and oxygen evolution at the indicated light intensities was measured on a Mini-PAM II with needle-type oxygen microsensor OXR-50. Values are the mean from three biological replicates, error bars indicate SD. Asterisks indicate significant differences to the UVM4 strain, $p < 0.05$ (one-way ANOVA with Dunnett's multiple comparison test). **(C)** Growth curves under photoautotrophic conditions. Cultures were inoculated in HMP medium at a density of 3×10^5 cells ml^{-1} and incubated on a rotatory shaker for 10 days at a light intensity of 150 µmol photons m^{-2} s^{-1}. The culture volume (cell density × cell size) was determined with a Coulter counter. Values are the mean from three biological replicates, error bars indicate SD.

recipient strain and the four SBP1-overexpressing transformants with the QconCAT strategy. With this approach, using a single QconCAT protein (PS-Qprot), we already had determined the absolute cellular quantities of the complexes involved in the photosynthetic light reactions and of the Rubisco rbcL and RBCS subunits (Hammel et al., 2018). We designed a QconCAT protein (CBC-Qprot) that covered each of the missing 10 CBC enzymes with two or three proteotypic tryptic quantification (Q)-peptides (**Supplementary Figure 1A** and **Supplementary Dataset 1**). These Q-peptides have been detected by LC-MS/MS in earlier studies with good ion intensities and normal retention times. We had selected them before the d::pPop algorithm for predicting ionization propensities was available (Zimmer et al., 2018) and therefore some peptides are not the very best choice (see d::pPop ranks and scores in **Table 1**).

The 47.9-kDa CBC-Qprot was expressed as ^{15}N-labeled protein in *E. coli* and purified via the tandem-hexa-histidine tag at its C-terminus [the labeling efficiency was 99.39 ± 0.37% (SD)]. The protein was further purified by preparative electrophoresis on an SDS-polyacrylamide gel, followed by electroelution from the excised gel band and spectroscopic quantification. Correct quantification and purity were verified by separating the CBC-Qprot next to a BSA standard on an SDS-polyacrylamide gel and staining with Coomassie blue (**Supplementary Figure 1B**). The CBC-Qprot was then tryptically digested and released peptides analyzed by LC-MS/MS on a short 6-min gradient (**Supplementary Figure 1C**). The latter shows that the Q-peptides separated with characteristic retention times and ion intensities. Despite the strict 1:1 stoichiometry of the peptides, the areas of the extracted ion chromatograms (XICs) varied by a factor of up to 370.

Four different amounts of the ^{15}N-labeled PS-Qprot (Hammel et al., 2018) and the CBC-Qprot were mixed with 20 µg of (^{14}N) whole-cell proteins extracted from samples of UVM4 and the four transformants taken 22 h after inoculation in the experiment shown in **Figure 1A** (early log phase). We employed only one preparation of the QconCAT proteins, but *Chlamydomonas* cells from 3 to 6 independent growth experiments. The proteins in the mixture were precipitated with acetone, digested tryptically in urea, and analyzed by LC-MS/MS on 45-min analytical gradients. The ion chromatograms of heavy Q-peptide and light native peptide pairs were extracted, XICs quantified, and ratios calculated (**Supplementary Dataset 2**).

TABLE 1 | Absolute quantification of Calvin-Benson cycle protein subunits in the *Chlamydomonas* UVM4 strain.

Protein	Peptide	amol/cell[a]	n	amol/cell[b]	% of total cell protein[c]	d::pPop rank/score
rbcL	DTDILAAFR	37.7 ± 6.6	24	36.2	6.88	1/1.0
	LTYYTPDYVVR	35.9 ± 5.6	24			2/0.73
	FLFVAEAIYK	37.5 ± 4.6	24			3/0.68
RBCS	AFPDAYVR	29.0 ± 7.2	11	24.6	1.45	1/1.0
	AYVSNESAIR	22.2 ± 3.1	24			2/1.0
	LVAFDNQK	29.3 ± 4.6	19			3/0.82
PGK1	ADLNVPLDK	1.6 ± 0.4	24	2.0	0.31	3/0.83
	LSELLGKPVTK	2.1 ± 0.4	23			25/0.24
	TFNDALADAK	2.4 ± 0.4	24			11/0.65
GAP3	AVSLVLPSLK	6.8 ± 1.5	24	6.6	0.91	10/0.45
	VLITAPAK	6.9 ± 1.1	12			1/1.0
TPI1	LVDELNAGTIPR	0.3 ± 0.1	23	0.3	0.03	1/1.0
	SLFGESNEVVAK	0.4 ± 0.2	20			3/0.47
FBA3	ALQNTVLK	11.5 ± 2.5	24	10.1	1.4	4/0.50
	SVVSIPHGPSIIAAR	8.8 ± 1.5	24			1/1.0
FBP1	IYSFNEGNYGLWDDSVK	1.9 ± 1.3	24	0.5	0.08	12/0.26
	TLLYGGIYGYPGDAK	0.5 ± 0.1	23			7/0.48
	VPLFIGSK	0.2 ± 0.04	12			1/1.0
SBP1	LLFEALK	1.3 ± 0.3	12	1.2	0.15	2/1.0
	LTNITGR	1.1 ± 0.3	11			9/0.52
TRK1	FLAIDAINK	3.2 ± 0.8	23	2.0	0.53	2/0.90
	NPDFFNR	1.5 ± 0.4	19			4/0.66
	VSTLIGYGSPNK	1.9 ± 0.5	24			5/0.56
RPE1	FIESQVAK	0.4 ± 0.1	8	0.4	0.04	3/0.80
	GVNPWIEVDGGVTPENAYK	1.2 ± 0.4	21			5/0.66
	SDIIVSPSILSADFSR	0.2 ± 0.4	22			1/1.0
RPI1	LANLPEVK	0.4 ± 0.1	20	0.3	0.03	2/0.78
	LQNIVGVPTSIR	0.4 ± 0.1	24			1/1.0
PRK1	GHSLESIK	3.9 ± 1.4	18	1.8	0.25	11/0.26
	IYLDISDDIK	1.6 ± 0.3	24			6/0.65
	VAELLDFK	1.5 ± 0.2	12			1/1.0

[a]*Mean from 3 to 6 biological replicates, each measured with 1–4 technical replicates ±SD.* [b]*Median of all values.* [c]*Based on median and using MWs of mature proteins (**Supplementary Dataset 2**).*

Based on the Q-peptide to native peptide ratios and the known amounts of spiked-in QconCAT proteins, the abundances of the native peptides in the sample were calculated (in femtomoles per μg cell protein) (**Supplementary Dataset 2**). We determined that a *Chlamydomonas* UVM4 cell contains 27.6 ± 1.7 pg protein (SD, $n = 6$ biological replicates). This value allowed calculating the absolute amount of each peptide in attomol per cell (**Table 1**). We used the median of all quantification values of the 2–3 Q-peptides per protein (23 to 72 values) to get an estimate for the abundance of each CBC protein per cell (**Table 1**). Moreover, based on these median values and the molecular weight of the mature proteins, the fraction of each target protein in the whole-cell protein extract was estimated (**Table 1**), revealing that CBC enzymes represent ∼11.9% of total cell protein in *Chlamydomonas* (**Supplementary Dataset 2**). This procedure was repeated for all four SBP1-overexpressing transformants and the log2-fold change of the abundance of each CBC enzyme in the transformants versus the UVM4 strain was calculated (**Figure 3** and **Supplementary Dataset 2**). It turned out that SBP1 was significantly ($p < 0.01$) overexpressed in all transformants (HA5: 1.6-fold; HA11: 1.7-fold; St1: 3-fold; St12: 2.2-fold). Except for the Rubisco subunits, levels of all other CBC enzymes were not significantly different between the SBP1-overexpressing transformants and the UVM4 strain. Compared to UVM4, transformant HA5 had significantly ($p < 0.01$) lower RBCS levels (but only by 8%), and transformant St12 had significantly ($p < 0.01$) lower levels of RBCS and rbcL (by about 40%).

Estimation of Substrate Binding Sites per CBC Enzyme

In a previous study, we had determined the levels of all CBC metabolites in *Chlamydomonas* cells during an increase in light intensity within the range where irradiance remains limiting for photosynthesis (Mettler et al., 2014). In that study, also the concentrations of the CBC enzymes in the chloroplast were estimated based on the empirical protein abundance index (emPAI) (Ishihama et al., 2005). These data sets allowed estimating the number of substrate binding sites per CBC enzyme 20 min after increasing the light intensity, when flux through the

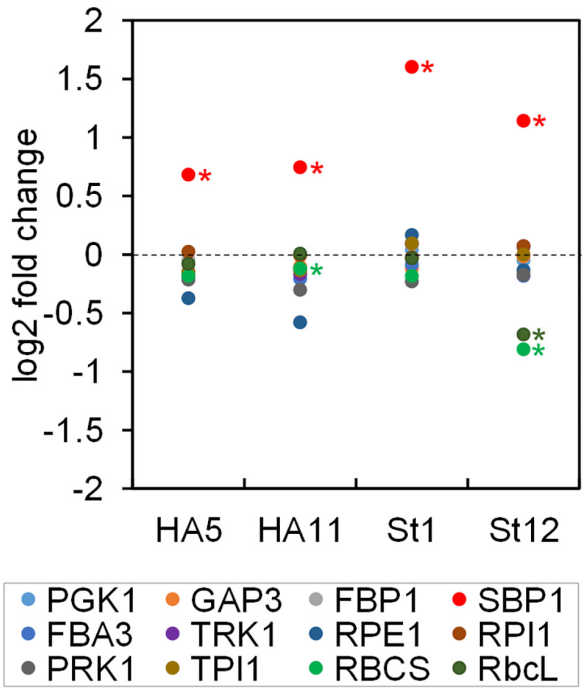

FIGURE 3 | Changes in abundance of CBC enzymes in SBP1-overexpressing lines versus the UVM4 recipient strain. The abundance of the CBC enzymes in transformants HA5 and HA11, generated with the SBP1-3xHA construct, and in transformants St1 and St12, generated with the SBP1-mStop construct, was determined using the QconCAT strategy. Abundances relative to those in the UVM4 recipient strain were $\log_2$ transformed and plotted. Asterisks designate significant differences between enzymes in the transformants versus the UVM4 strain (one-way ANOVA with Holm's multiple comparison test, $p < 0.01$). PGK, phosphoglycerate kinase; GAP, glyceraldehyde-3-phosphate dehydrogenase; TPI, triose phosphate isomerase; FBA/SBA, fructose-1,6-bisphosphate aldolase/sedoheptulose-1,7-bisphosphate aldolase; FBP, fructose-1,6-bisphosphatase; TRK, transketolase; SBP, sedoheptulose-1,7-bisphosphatase; RPE, ribulose-5-phosphate 3-epimerase; RPI, ribose-5-phosphate isomerase; PRK, phosphoribulokinase; rbcL, ribulose bisphosphate carboxylase/oxygenase large subunit; RBCS, ribulose bisphosphate carboxylase/oxygenase small subunit.

cycle was maximal (Mettler et al., 2014). To compare the emPAI-derived data with the QconCAT-derived data, we calculated the concentration of each CBC enzyme in the chloroplast based on the absolute quantities determined here and the assumption that a *Chlamydomonas* cell has a volume of 270 μm^3, of which about half is occupied by the chloroplast (Weiss et al., 2000) (**Table 2**). While the concentration of rbcL determined by Mettler et al. (2014) matched that determined here with the QconCAT approach very well, the concentrations of all other CBC enzymes were strongly overestimated (between 8.8-fold for FBA3 and 34.5-fold for PRK1) (**Table 2**).

To re-estimate the number of substrate binding sites per CBC enzyme, we used the concentrations of the CBC enzymes in the chloroplast determined here (**Table 2**) and the CBC metabolite data determined earlier 20 min after the light shift to 145 μmol photons m^{-2} s^{-1} (Mettler et al., 2014). Whilst most of the metabolites were directly measured, some like BPGA were calculated based on the equilibrium constants of the reactions in which they participate and the measured levels of other metabolites that participate in these reactions (see Mettler et al., 2014 for details). Although the growth conditions differed slightly between the two studies, metabolite levels do not vary greatly in *Chlamydomonas* in this irradiance range (Supplementary Figure 12 in Mettler et al., 2014). This re-analysis is shown in **Figure 4** and compared with the earlier analysis in **Supplementary Figure 2**. It revealed that some CBC intermediates are indeed present at lower concentrations than the estimated binding site concentration of the enzymes for which they act as substrates (1,3-bisphosphoglycerate (BPGA) compared to PGK1 and GAP3; glyceraldehyde 3-phosphate (GAP) and erythrose 4-phosphate (E4P) compared to FBA3), some are at only slightly (<4.5-fold) higher concentrations than the respective binding site (GAP and E4P compared to TRK; ribulose-5-phosphate (Ru5P) compared to PRK1; fructose-1,6-bisphosphate (FBP) compared to FBA3). However, most of the other CBC intermediates are present at considerably higher concentrations than the respective estimated binding site concentration.

DISCUSSION

The Modularity of the MoClo Approach and the Use of *Chlamydomonas* as a Model Facilitate the Iterative Process of Genetic Engineering Toward Improving Plant Productivity

Here, we present a workflow for rapid and efficient metabolic engineering toward improving plant biomass production, with the overexpression of native *Chlamydomonas* SBPase (SBP1) in *Chlamydomonas* as a proof-of-concept. We used the Modular Cloning (MoClo) strategy for construct generation and employed the part library established recently (Weber et al., 2011; Crozet et al., 2018). The one-step, modular assembly of multiple genetic parts allowed generating complex constructs rapidly and with variations: one coding for SBP1 with a 3xHA tag and one lacking any tags. This double strategy was well chosen, as the variant with a C-terminal 3xHA tag did not result in enhanced photosynthetic rates and biomass production, while the variant lacking a tag did (**Figures 2A,B**). In the two transformant lines tested for each construct, tagged SBP1 was overexpressed 1.6 to 1.7-fold while the untagged form was overexpressed ∼2.2- and ∼3-fold (**Figure 3**). Therefore, it is possible that in *Chlamydomonas* SBPase must be expressed to levels higher than 1.7-fold to improve the photosynthetic rate. Alternatively, the C-terminal 3xHA tag interfered with SBP1 function. Although this issue can only be solved by measuring SBPase enzyme activity, we favor the latter explanation. This because SBPase overexpression giving rise to at most twofold increased activities already had positive effects on photosynthetic rates and biomass accumulation in tobacco (Lefebvre et al., 2005; Tamoi et al., 2006; Rosenthal et al., 2011), *Dunaliella bardawil* (Fang et al., 2012), and wheat (Driever et al., 2017). Like for these models, increased photosynthetic rates

TABLE 2 | Comparison of CBC enzyme abundances and concentrations in *Chlamydomonas* determined in different studies by different methods.

	Rank among CBC enzymes (this study)	Rank in proteome (Schroda et al., 2015)	amol/cell (this study)	amol/cell (Wienkoop et al., 2010)	µM in chloroplast (Mettler et al., 2014)	µM in chloroplast (this study)
Method	QconCAT	iBAQ	QconCAT	Mass Western	emPAI	QconCAT
rbcL	1	2	36.2	42.2	304.5	268.2
RBCS	2	6	24.6	1.0	nd	182.5
FBA3	3	9	10.1	4.2	658.5	75.1
GAP3	4	30	6.6	1.8	651.5	48.9
PGK1	5	49	2.0	0.26	477.2	14.9
TRK1	6	43	2.0	1.43	232.2	14.8
PRK1	7	66	1.8	1.67	451.3	13.1
SBP1	8	138	1.2	0.09	149.6	8.7
FBP1	9	185	0.55	0.23	121.0	4.1
RPE1	10	394	0.45	0.2	87.7	3.3
RPI1	11	294	0.34	0.35	68.1	2.5
TPI1	12	276	0.28	0.16	44.3	2.1

and biomass accumulation were observed in *Chlamydomonas* lines overexpressing SBP1 only if cells were grown at higher light intensities (150 µmol photons m^{-2} s^{-1}) and elevated CO_2 concentrations (in the presence of acetate) (**Figure 2**). Here it appears surprising that we observed elevated O_2 evolution rates in SBP1-overexpressing lines only at light intensities above 183 µmol photons m^{-2} s^{-1} (**Figure 2B**). This discrepancy might be explained by differences in culture conditions, physiological state of the cells, or light quality between the experimental setups used for determining growth and O_2 evolution. In any case, at high light intensities and elevated CO_2 concentrations, SBPase levels represent a bottleneck in flux through the CBC in *Chlamydomonas* as in the other plant models. Therefore, the results obtained with *Chlamydomonas* readily apply to other alga and land plants.

SBP1 represents 0.15% of total cell protein in *Chlamydomonas* (**Table 1**), i.e., the transgenic protein in the best SBP1-overexpressing line makes up 0.3% of total cell protein. It is likely that the screening of more transformants would have allowed recovering lines with even higher expression levels. Furthermore, a *SBP1* gene re-synthesized with optimal codon usage and the three *RBCS2* introns probably would have allowed higher expression levels (Barahimipour et al., 2015; Schroda, 2019). Regarding the iterative process of genetic engineering it is important to recognize that by combining the MoClo strategy with *Chlamydomonas* as a model, a complete cycle of construct design and assembly, transformation, screening, and phenotype test can be achieved in as little as 8 weeks.

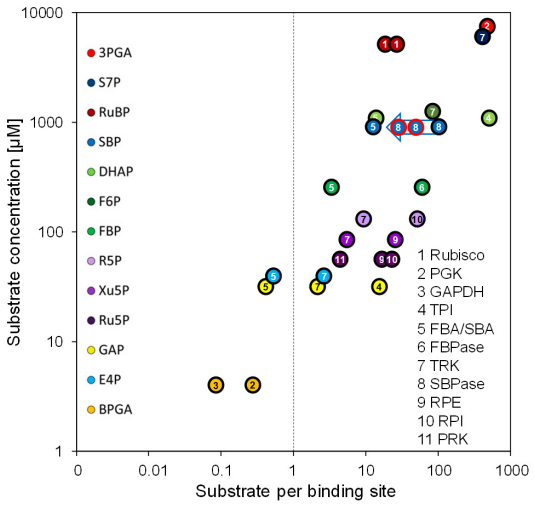

FIGURE 4 | Substrate per binding site versus substrate concentration. Substrate per binding site values of CBC enzymes are plotted against their substrate concentrations. Binding site abundances of the eleven CBC enzymes (numbered) were calculated based on the QconCAT data (**Table 2**). Substrates of CBC reactions are presented by different colors. Substrate concentrations were determined via LC-MS/MS by Mettler et al. (2014) in *Chlamydomonas* cells harvested 20 min after the light intensity was increased from 41 to 145 µmol photons m^{-2} s^{-1}, i.e., when flux through the CBC is maximal. For enzymes that catalyze readily reversible reactions (TPI, FBA/SBA, TRK, RPI, RPE) the relation to product level is also shown. To facilitate comparison, the same numbering and color code as used in Mettler et al. (2014) was adopted. The blue arrow shows the estimates for substrates per binding site for the SBP1 overexpressing lines St1 and St12 (encircled in red). The two values for Rubisco are based on the slightly different quantification values for the large and small subunits (**Table 2**). A comparison with the values calculated by Mettler et al. (2014) using the emPAI approach is shown in **Supplementary Figure 2**.

QconCAT-Based Quantitative Proteomics Allows Monitoring Effects of SBP1 Overexpression on the Accumulation of Other CBC Enzymes

Increased activities of SBPase by overexpressing SBPase alone or BiBPase from cyanobacteria had no effect on the levels or activities of selected other CBC enzymes in tobacco (Miyagawa et al., 2001; Lefebvre et al., 2005; Rosenthal et al., 2011), lettuce (Ichikawa et al., 2010) or wheat (Driever et al., 2017). In contrast, overexpression of BiBPase from *Synechocystis* in *Synechococcus* resulted in increased activities of Rubisco (2.4-fold) and aldolase (1.6-fold) as well as increased protein levels of rbcL (∼3-fold),

TPI (1.5-fold) and RPI (1.4-fold) (De Porcellinis et al., 2018). Similarly, overexpressing SBPase leading to up to 1.85-fold higher SBPase activity in *Arabidopsis* resulted in elevated FBPA activity and protein levels (Simkin et al., 2017a). We employed the QconCAT approach to determine absolute quantities of all other 10 CBC enzymes and found no consistent changes between wild type and the four SBP1-overexpressing lines (**Figure 3**). Only the St12 line with ∼2.2-fold higher SBP1 expression had a significant ∼40% reduction of both Rubisco subunits rbcL and RBCS. Since both Rubisco subunits were unaffected in line St1 with ∼3-fold higher SBP1 levels, SBP1 overexpression cannot be the cause for the reduced accumulation of Rubisco in line St12. More likely, a gene required for Rubisco expression, assembly or stability was destroyed by the integration of the SBP1 expression vector. It is surprising that photosynthetic rate and biomass accumulation was increased to a similar extent in lines St1 and St12 despite the reduced Rubisco levels in line St12 (**Figure 2**). This indicates that Rubisco levels are not limiting CBC flux in *Chlamydomonas*, in line with previous observations in *Chlamydomonas* that reducing Rubisco to almost 50% of wild-type levels enabled full photosynthetic growth (Johnson, 2011).

CBC Enzymes Exhibit a Larger Abundance Range Than Estimated Earlier

In addition to looking at possible effects of SBP1-overexpression on the expression of other CBC enzymes, the QconCAT approach allowed for the quantification of absolute levels of CBC enzymes in *Chlamydomonas* cells. With this strategy, we had already determined absolute quantities of rbcL and RBCS in another cell wall-deficient strain background (CC-1883) (Hammel et al., 2018). There, absolute amounts of rbcL and RBCS were ∼1.4-fold lower than in UVM4 cells. However, CC-1883 cells also had a ∼1.3-fold lower protein content than UVM4 cells, such that the fraction of rbcL and RBCS in total cell protein are about comparable (6.6% and 1.3% in CC-1883 versus 6.88% and 1.45% in UVM4, respectively).

The abundance of all CBC enzymes in *Chlamydomonas* cells has been estimated earlier. One study used "Mass Western," which is based on the spiking-in of known amounts of heavy isotope-labeled Q-peptides into tryptic digests of whole-cell proteins followed by LC-MS/MS analysis (Wienkoop et al., 2010). The other studies used the emPAI (empirical protein abundance index) and iBAQ (intensity-based absolute quantification) approaches on quantitative shotgun proteomics datasets (Mettler et al., 2014; Schroda et al., 2015).

The iBAQ-based ranking of protein abundances exactly reflects the quantities of the more abundant CBC enzymes determined here by the QconCAT approach (**Table 2**). Only the low-abundance CBC enzymes RPE1, RPI1 and TPI1 were ranked by iBAQ in the opposite order of their abundance determined by the QconCAT method. Most likely, this is due to the impaired accuracy of the iBAQ approach for less-abundant proteins (Soufi et al., 2015).

The absolute quantities determined by Mass Western roughly matched those determined with the QconCAT approach, except for RBCS, PGK1, and SBP1, which were 24.6-fold, 7.7-fold, and 13.3-fold lower (**Table 2**). As suggested earlier (Hammel et al., 2018), this discrepancy can be explained by an incomplete extraction of some proteins from whole-cell homogenates with the extraction protocol employed (Wienkoop et al., 2010).

In the study by Mettler et al. (2014), the cellular abundance of rbcL was estimated by densitometry on Coomassie-stained SDS-gels and was used to normalize the emPAI-derived quantification values of the other CBC enzymes. The estimated abundance of rbcL matches that determined here via the QconCAT approach (**Table 2**). However, the emPAI-derived values for the other CBC enzymes are much higher than those determined by QconCAT (up to 34.5-fold higher for PRK1). A likely cause for this strong overestimation is that proteins of very high abundance tend to exhibit a saturated emPAI signal (Ishihama et al., 2008). Consequently, the range of concentrations of CBC enzymes is much larger than estimated earlier. For example, the difference between the most abundant CBC protein rbcL and the least abundant TPI1 is 128-fold rather than only 7-fold (**Table 2**).

The strong overestimation of many CBC enzymes by the emPAI approach challenges the conclusion that many CBC intermediates are present at concentrations that are far lower than the estimated binding site concentration of the enzymes for which they act as substrates (Mettler et al., 2014). For example, the concentration of sedoheptulose-1,7-bisphosphate (SBP) is ∼106-fold higher than that of SBP1 rather than only ∼6-fold as estimated previously (**Figure 4** and **Supplementary Figure 2**). Moreover, comparisons of the *in vivo* SBP concentration and the modeled *in vivo* K_m for SBP1 indicate that SBP1 is likely to be near-saturated *in vivo* (Mettler et al., 2014). Hence, flux at SBPase is likely restricted by the degree of post-translational activation of SBP1 and SBP1 abundance. This explains better why an increase in CBC flux can be achieved by increasing SBP1 protein concentrations.

Still correct is that the concentration of GAP is below or slightly above the concentration of substrate binding sites of FBA3 and TRK1 (0.4-fold and 2.2-fold, respectively), as is E4P compared to FBA3 and TRK1 (0.5-fold and 2.7-fold, respectively). Furthermore, ribulose-5-phosphate (Ru5P) is only 4.3-fold above the binding site concentration of PRK, indicating that increased flux in the regeneration phase of the CBC to increase Ru5P levels will aid increased RuBP formation and fixation of CO_2. The low concentration of these key CBC intermediates relative to their enzyme binding sites, together with the low concentration of these and further CBC intermediates relative to the likely *in vivo* K_m values of CBC enzymes (Mettler et al., 2014), explains how RuBP regeneration speeds up when rising light intensity drives faster conversion of 3-phosphoglycerate to GAP.

The lower abundance of CBC enzymes reported here does not affect the analyses of the relationship between metabolite concentrations and the estimated *in vivo* Km values of CBC enzymes in Mettler et al. (2014). These estimations were based on the simplifying assumption that the measured metabolites reflect the free concentrations. This assumption is even more justified

by the generally lower protein abundances as determined here by the QconCAT approach. Mettler et al. (2014) concluded that some of the CBC enzymes are near-saturated *in vivo* (Rubisco, PGK, FBPase, SBPase) whilst the remainder operate at low substrate saturation. For the former, increased flux will depend on allosteric or post-translational regulation, or on increasing protein abundance (as explained above for SBPase). For the latter, only a fraction of the enzyme active sites will be occupied by substrate at a given time and occupancy will increase in conditions where the substrate concentration rises, leading to an increase in flux at that enzyme. This will serve to increase overall flux around the CBC when there is a general increase in metabolite levels, and to rebalance flux at different sites in the CBC when there is an increase in the concentration of the substrate of one or a subset of the CBC enzymes.

Outlook

The next step would be to stack multiple transgenes for the overexpression of CBC enzymes that in SBP1-overexpressing lines potentially become new bottlenecks for flux through the cycle. Indicative for this scenario is the finding that SBPase overexpression in *Arabidopsis* entailed an overexpression of FBPA (Simkin et al., 2017a). Moreover, overexpression of BiBPase in *Synechococcus* came along with an increase in levels of RPI and TPI (De Porcellinis et al., 2018), which are the CBC enzymes of lowest abundance in *Chlamydomonas* (**Tables 1**, **2**). More candidates for multigene stacking might be PGK1, TRK1, TPI1, and FBP1, whose substrates are in largest excess of the substrate binding sites (**Figure 4**). To our knowledge, there are yet no reports on the overexpression of PGK, RPI, and TPI (Simkin et al., 2019). Two studies report no or even negative effects upon TRK overexpression in rice and tobacco, respectively (Khozaei et al., 2015; Suzuki et al., 2017). Positive effects of FBPase overexpression on photosynthetic rates and biomass accumulation were reported for numerous plant models – except for *Chlamydomonas* where FBP1 overexpression in the chloroplast had negative effects (Dejtisakdi and Miller, 2016). Apparently, the highly complex regulation of the CBC and its central role in cellular metabolism make predictions difficult. This is highlighted by recent work, indicating that the balance between different steps in the CBC varies from species to species (Arrivault et al., 2019; Borghi et al., 2019). Therefore, experimental test is the route of choice that with the combination of MoClo and *Chlamydomonas* can be pursued readily.

DATA AVAILABILITY STATEMENT

The mass spectrometry proteomics data have been deposited to the ProteomeXchange Consortium via the PRIDE partner repository with the dataset identifier PXD018833.

AUTHOR CONTRIBUTIONS

AH performed all experiments. FS designed the QconCAT protein and performed the LC-MS/MS analyses. AH and DZ analyzed the data and were supervised by TM, MSt, and MSc. MSc conceived and supervised the work. MSc wrote the manuscript with contributions from all other authors. All authors contributed to the article and approved the submitted version.

FUNDING

This work was funded by the Deutsche Forschungsgemeinschaft (TRR 175, projects C02 and D02) and the Landesforschungsschwerpunkt BioComp.

ACKNOWLEDGMENTS

We are grateful to Karin Gries for technical help. This manuscript has been released as a pre-print at bioRxiv (Hammel et al., 2020).

SUPPLEMENTARY MATERIAL

The Supplementary Material for this article can be found online at: https://www.frontiersin.org/articles/10.3389/fpls.2020.00868/full#supplementary-material

REFERENCES

Arrivault, S., Alexandre Moraes, T., Obata, T., Medeiros, D. B., Fernie, A. R., Boulouis, A., et al. (2019). Metabolite profiles reveal interspecific variation in operation of the Calvin-Benson cycle in both C4 and C3 plants. *J. Exp. Bot.* 70, 1843–1858. doi: 10.1093/jxb/erz051

Barahimipour, R., Strenkert, D., Neupert, J., Schroda, M., Merchant, S. S., and Bock, R. (2015). Dissecting the contributions of GC content and codon usage to gene expression in the model alga *Chlamydomonas reinhardtii*. *Plant J.* 84, 704–717. doi: 10.1111/tpj.13033

Beynon, R. J., Doherty, M. K., Pratt, J. M., and Gaskell, S. J. (2005). Multiplexed absolute quantification in proteomics using artificial QCAT proteins of concatenated signature peptides. *Nat. Methods* 2, 587–589. doi: 10.1038/nmeth774

Borghi, G. L., Moraes, T. A., Gunther, M., Feil, R., Mengin, V., Lunn, J. E., et al. (2019). Relationship between irradiance and levels of Calvin-Benson cycle and other intermediates in the model eudicot *Arabidopsis* and the model monocot rice. *J. Exp. Bot.* 70, 5809–5825. doi: 10.1093/jxb/erz346

Chida, H., Nakazawa, A., Akazaki, H., Hirano, T., Suruga, K., Ogawa, M., et al. (2007). Expression of the algal cytochrome c6 gene in *Arabidopsis* enhances photosynthesis and growth. *Plant Cell Physiol.* 48, 948–957. doi: 10.1093/pcp/pcm064

Crozet, P., Navarro, F. J., Willmund, F., Mehrshahi, P., Bakowski, K., Lauersen, K. J., et al. (2018). Birth of a photosynthetic chassis: a MoClo toolkit enabling synthetic biology in the microalga *Chlamydomonas reinhardtii*. *ACS Synth. Biol.* 7, 2074–2086. doi: 10.1021/acssynbio.8b00251

De Porcellinis, A. J., Norgaard, H., Brey, L. M. F., Erstad, S. M., Jones, P. R., Heazlewood, J. L., et al. (2018). Overexpression of bifunctional fructose-1,6-bisphosphatase/sedoheptulose-1,7-bisphosphatase leads to enhanced photosynthesis and global reprogramming of carbon metabolism in *Synechococcus* sp. PCC 7002. *Metab. Eng.* 47, 170–183. doi: 10.1016/j.ymben.2018.03.001

Dejtisakdi, W., and Miller, S. M. (2016). Overexpression of Calvin cycle enzyme fructose 1,6-bisphosphatase in *Chlamydomonas reinhardtii* has a detrimental effect on growth. *Algal Res.* 14, 11–26.

Ding, F., Wang, M., Zhang, S., and Ai, X. (2016). Changes in SBPase activity influence photosynthetic capacity, growth, and tolerance to chilling stress in transgenic tomato plants. *Sci. Rep.* 6:32741.

Driever, S. M., Simkin, A. J., Alotaibi, S., Fisk, S. J., Madgwick, P. J., Sparks, C. A., et al. (2017). Increased SBPase activity improves photosynthesis and grain yield in wheat grown in greenhouse conditions. *Philos. Trans. R. Soc. Lond. B Biol. Sci.* 372:20160384. doi: 10.1098/rstb.2016.0384

Fang, L., Lin, H. X., Low, C. S., Wu, M. H., Chow, Y., and Lee, Y. K. (2012). Expression of the *Chlamydomonas reinhardtii* sedoheptulose-1,7-bisphosphatase in Dunaliella bardawil leads to enhanced photosynthesis and increased glycerol production. *Plant Biotechnol. J.* 10, 1129–1135. doi: 10.1111/pbi.12000

Feng, L., Han, Y., Liu, G., An, B., Yang, J., Yang, G., et al. (2007). Overexpression of sedoheptulose-1,7-bisphosphatase enhances photosynthesis and growth under salt stress in transgenic rice plants. *Funct. Plant Biol.* 34, 822–834.

Gibson, D. G., Young, L., Chuang, R. Y., Venter, J. C., Hutchison, C. A. III, and Smith, H. O. (2009). Enzymatic assembly of DNA molecules up to several hundred kilobases. *Nat. Methods* 6, 343–345. doi: 10.1038/nmeth.1318

Gillet, L. C., Leitner, A., and Aebersold, R. (2016). Mass spectrometry applied to bottom-up proteomics: entering the high-throughput era for hypothesis testing. *Annu. Rev. Anal. Chem.* 9, 449–472. doi: 10.1146/annurev-anchem-071015-041535

Gong, H. Y., Li, Y., Fang, G., Hu, D. H., Jin, W. B., Wang, Z. H., et al. (2015). Transgenic rice expressing Ictb and FBP/Sbpase derived from *Cyanobacteria* exhibits enhanced photosynthesis and mesophyll conductance to CO_2. *PLoS One* 10:e0140928. doi: 10.1371/journal.pone.0140928

Hammel, A., Sommer, F., Zimmer, D., Stitt, M., Muhlhaus, T., and Schroda, M. (2020). Overexpression of sedoheptulose-1,7-bisphosphatase enhances photosynthesis in *Chlamydomonas reinhardtii* and has no effect on the abundance of other Calvin-Benson cycle enzymes. *bioRxiv* [Preprint], doi: 10.1101/2020.02.14.949040

Hammel, A., Zimmer, D., Sommer, F., Mühlhaus, T., and Schroda, M. (2018). Absolute quantification of major photosynthetic protein complexes in *Chlamydomonas reinhardtii* using quantification concatamers (QconCATs). *Front. Plant Sci.* 9:1265. doi: 10.3389/fpls.2018.01265

Ichikawa, Y., Tamoi, M., Sakuyama, H., Maruta, T., Ashida, H., Yokota, A., et al. (2010). Generation of transplastomic lettuce with enhanced growth and high yield. *GM Crops* 1, 322–326. doi: 10.4161/gmcr.1.5.14706

Ishihama, Y., Oda, Y., Tabata, T., Sato, T., Nagasu, T., Rappsilber, J., et al. (2005). Exponentially modified protein abundance index (emPAI) for estimation of absolute protein amount in proteomics by the number of sequenced peptides per protein. *Mol. Cell Proteom.* 4, 1265–1272. doi: 10.1074/mcp.m500061-mcp200

Ishihama, Y., Schmidt, T., Rappsilber, J., Mann, M., Hartl, F. U., Kerner, M. J., et al. (2008). Protein abundance profiling of the *Escherichia coli* cytosol. *BMC Genomics* 9:102. doi: 10.1186/1471-2164-9-102

Johnson, X. (2011). Manipulating RuBisCO accumulation in the green alga, *Chlamydomonas reinhardtii*. *Plant Mol. Biol.* 76, 397–405. doi: 10.1007/s11103-011-9783-z

Johnson, X., and Alric, J. (2012). Interaction between starch breakdown, acetate assimilation, and photosynthetic cyclic electron flow in *Chlamydomonas reinhardtii*. *J. Biol. Chem.* 287, 26445–26452. doi: 10.1074/jbc.m112.370205

Kebeish, R., Niessen, M., Thiruveedhi, K., Bari, R., Hirsch, H. J., Rosenkranz, R., et al. (2007). *Chloroplastic photorespiratory* bypass increases photosynthesis and biomass production in *Arabidopsis thaliana*. *Nat. Biotechnol.* 25, 593–599. doi: 10.1038/nbt1299

Khozaei, M., Fisk, S., Lawson, T., Gibon, Y., Sulpice, R., Stitt, M., et al. (2015). Overexpression of plastid transketolase in tobacco results in a thiamine auxotrophic phenotype. *Plant Cell* 27, 432–447. doi: 10.1105/tpc.114.131011

Kindle, K. L. (1990). High-frequency nuclear transformation of *Chlamydomonas reinhardtii*. *Proc. Natl. Acad. Sci. U.S.A.* 87, 1228–1232. doi: 10.1073/pnas.87.3.1228

Kohler, I. H., Ruiz-Vera, U. M., Vanloocke, A., Thomey, M. L., Clemente, T., Long, S. P., et al. (2017). Expression of cyanobacterial FBP/SBPase in soybean prevents yield depression under future climate conditions. *J. Exp. Bot.* 68, 715–726.

Kropat, J., Hong-Hermesdorf, A., Casero, D., Ent, P., Castruita, M., Pellegrini, M., et al. (2011). A revised mineral nutrient supplement increases biomass and growth rate in *Chlamydomonas reinhardtii*. *Plant J.* 66, 770–780. doi: 10.1111/j.1365-313x.2011.04537.x

Kubis, A., and Bar-Even, A. (2019). Synthetic biology approaches for improving photosynthesis. *J. Exp. Bot.* 70, 1425–1433. doi: 10.1093/jxb/erz029

Lefebvre, S., Lawson, T., Zakhleniuk, O. V., Lloyd, J. C., Raines, C. A., and Fryer, M. (2005). Increased sedoheptulose-1,7-bisphosphatase activity in transgenic tobacco plants stimulates photosynthesis and growth from an early stage in development. *Plant Physiol.* 138, 451–460. doi: 10.1104/pp.104.055046

Lodha, M., Schulz-Raffelt, M., and Schroda, M. (2008). A new assay for promoter analysis in *Chlamydomonas* reveals roles for heat shock elements and the TATA box in HSP70A promoter-mediated activation of transgene expression. *Eukaryot. Cell* 7, 172–176. doi: 10.1128/ec.00055-07

Lopez-Paz, C., Liu, D., Geng, S., and Umen, J. G. (2017). Identification of *Chlamydomonas reinhardtii* endogenous genic flanking sequences for improved transgene expression. *Plant J.* 92, 1232–1244. doi: 10.1111/tpj.13731

Lowry, O. H., Rosebrough, N. J., Farr, A. L., and Randall, R. J. (1951). Protein measurement with the folin phenol reagent. *J. Biol. Chem.* 193, 265–275.

Mettler, T., Mühlhaus, T., Hemme, D., Schöttler, M. A., Rupprecht, J., Idoine, A., et al. (2014). Systems analysis of the response of photosynthesis, metabolism, and growth to an increase in irradiance in the photosynthetic model organism *Chlamydomonas reinhardtii*. *Plant Cell* 26, 2310–2350. doi: 10.1105/tpc.114.124537

Miyagawa, Y., Tamoi, M., and Shigeoka, S. (2001). Overexpression of a cyanobacterial fructose-1,6-/sedoheptulose-1,7-bisphosphatase in tobacco enhances photosynthesis and growth. *Nat. Biotechnol.* 19, 965–969. doi: 10.1038/nbt1001-965

Neupert, J., Karcher, D., and Bock, R. (2009). Generation of *Chlamydomonas strains* that efficiently express nuclear transgenes. *Plant J.* 57, 1140–1150. doi: 10.1111/j.1365-313x.2008.03746.x

Nolke, G., Houdelet, M., Kreuzaler, F., Peterhansel, C., and Schillberg, S. (2014). The expression of a recombinant glycolate dehydrogenase polyprotein in potato (*Solanum tuberosum*) plastids strongly enhances photosynthesis and tuber yield. *Plant Biotechnol. J.* 12, 734–742. doi: 10.1111/pbi.12178

Ogawa, T., Tamoi, M., Kimura, A., Mine, A., Sakuyama, H., Yoshida, E., et al. (2015). Enhancement of photosynthetic capacity in *Euglena gracilis* by expression of cyanobacterial fructose-1,6-/sedoheptulose-1,7-bisphosphatase leads to increases in biomass and wax ester production. *Biotechnol. Biofuels* 8:80.

Patron, N. J., Orzaez, D., Marillonnet, S., Warzecha, H., Matthewman, C., Youles, M., et al. (2015). Standards for plant synthetic biology: a common syntax for exchange of DNA parts. *New Phytol.* 208, 13–19.

Perez-Riverol, Y., Csordas, A., Bai, J., Bernal-Llinares, M., Hewapathirana, S., Kundu, D. J., et al. (2019). The PRIDE database and related tools and resources in 2019: improving support for quantification data. *Nucleic Acids Res.* 47, D442–D450.

Polukhina, I., Fristedt, R., Dinc, E., Cardol, P., and Croce, R. (2016). Carbon supply and photoacclimation cross talk in the green alga *Chlamydomonas reinhardtii*. *Plant Physiol.* 172, 1494–1505. doi: 10.1104/pp.16.01310

Pratt, J. M., Simpson, D. M., Doherty, M. K., Rivers, J., Gaskell, S. J., and Beynon, R. J. (2006). Multiplexed absolute quantification for proteomics using concatenated signature peptides encoded by QconCAT genes. *Nat. Protoc.* 1, 1029–1043. doi: 10.1038/nprot.2006.129

Rosenthal, D. M., Locke, A. M., Khozaei, M., Raines, C. A., Long, S. P., and Ort, D. R. (2011). Over-expressing the C(3) photosynthesis cycle enzyme Sedoheptulose-1-7 Bisphosphatase improves photosynthetic carbon gain and yield under fully open air CO(2) fumigation (FACE). *BMC Plant Biol.* 11:123. doi: 10.1186/1471-2164-9-123

Schroda, M. (2019). Good news for nuclear transgene expression in *Chlamydomonas*. *Cells* 8:1534. doi: 10.3390/cells8121534

Schroda, M., Hemme, D., and Mühlhaus, T. (2015). The *Chlamydomonas* heat stress response. *Plant J.* 82, 466–480. doi: 10.1111/tpj.12816

Simkin, A. J., Lopez-Calcagno, P. E., Davey, P. A., Headland, L. R., Lawson, T., Timm, S., et al. (2017a). Simultaneous stimulation of sedoheptulose 1,7-bisphosphatase, fructose 1,6-bisphophate aldolase and the photorespiratory glycine decarboxylase-H protein increases CO_2 assimilation, vegetative biomass

and seed yield in *Arabidopsis*. *Plant Biotechnol. J.* 15, 805–816. doi: 10.1111/pbi.12676

Simkin, A. J., Mcausland, L., Lawson, T., and Raines, C. A. (2017b). Overexpression of the RieskeFeS protein increases electron transport rates and biomass yield. *Plant Physiol.* 175, 134–145. doi: 10.1104/pp.17.00622

Simkin, A. J., Lopez-Calcagno, P. E., and Raines, C. A. (2019). Feeding the world: improving photosynthetic efficiency for sustainable crop production. *J. Exp. Bot.* 70, 1119–1140. doi: 10.1093/jxb/ery445

Soufi, B., Krug, K., Harst, A., and Macek, B. (2015). Characterization of the *E. coli* proteome and its modifications during growth and ethanol stress. *Front. Microbiol.* 6:103. doi: 10.3389/fpls.2018.0103

Strenkert, D., Schmollinger, S., and Schroda, M. (2013). Heat shock factor 1 counteracts epigenetic silencing of nuclear transgenes in *Chlamydomonas reinhardtii*. *Nucleic Acids Res.* 41, 5273–5289. doi: 10.1093/nar/gkt224

Suzuki, Y., Kondo, E., and Makino, A. (2017). Effects of co-overexpression of the genes of rubisco and transketolase on photosynthesis in rice. *Photosynth. Res.* 131, 281–289. doi: 10.1007/s11120-016-0320-4

Tamoi, M., Nagaoka, M., Miyagawa, Y., and Shigeoka, S. (2006). Contribution of fructose-1,6-bisphosphatase and sedoheptulose-1,7-bisphosphatase to the photosynthetic rate and carbon flow in the Calvin cycle in transgenic plants. *Plant Cell Physiol.* 47, 380–390.

Vernon, L. P. (1960). Spectrophotometric determination of chlorophylls and pheophytins in plant extracts. *Analyt. Chem.* 32, 1144–1150.

Weber, E., Engler, C., Gruetzner, R., Werner, S., and Marillonnet, S. (2011). A modular cloning system for standardized assembly of multigene constructs. *PLoS One* 6:e16765. doi: 10.1371/journal.pone.016765

Weiss, D., Schneider, G., Niemann, B., Guttmann, P., Rudolph, D., and Schmahl, G. (2000). Computed tomography of cryogenic biological specimens based on X-ray microscopic images. *Ultramicroscopy* 84, 185–197.

Wienkoop, S., Weiss, J., May, P., Kempa, S., Irgang, S., Recuenco-Munoz, L., et al. (2010). Targeted proteomics for *Chlamydomonas reinhardtii* combined with rapid subcellular protein fractionation, metabolomics and metabolic flux analyses. *Mol. Biosyst.* 6, 1018–1031.

Wykoff, D. D., Davies, J. P., Melis, A., and Grossman, A. R. (1998). The regulation of photosynthetic electron transport during nutrient deprivation in *Chlamydomonas reinhardtii*. *Plant Physiol.* 117, 129–139.

Yabuta, Y., Tamoi, M., Yamamoto, K., Tomizawa, K.-I., Yokota, A., and Shigeoka, S. (2008). Molecular design of photosynthesis-elevated chloroplasts for mass accumulation of a foreign protein. *Plant Cell Physiol.* 49, 375–385.

Zimmer, D., Schneider, K., Sommer, F., Schroda, M., and Mühlhaus, T. (2018). Artificial intelligence understands peptide observability and assists with absolute protein quantification. *Front. Plant Sci.* 9:1559. doi: 10.3389/fpls.2018.01559

Conflict of Interest: The authors declare that the research was conducted in the absence of any commercial or financial relationships that could be construed as a potential conflict of interest.

frontiers in Plant Science

ORIGINAL RESEARCH
published: 03 July 2020
doi: 10.3389/fpls.2020.00981

Photosynthetic Carbon Partitioning and Metabolic Regulation in Response to Very-Low and High CO_2 in *Microchloropsis gaditana* NIES 2587

*Mukul Suresh Kareya, Iqra Mariam, Kashif Mohd Shaikh, Asha Arumugam Nesamma and Pannaga Pavan Jutur**

Omics of Algae Group, Industrial Biotechnology, International Centre for Genetic Engineering and Biotechnology, New Delhi, India

OPEN ACCESS

Edited by:
Matteo Ballottari, University of Verona, Italy

Reviewed by:
Xenie Johnson, Commissariat à l'Energie Atomique et aux Energies Alternatives (CEA), France
Jin Liu, Peking University, China

***Correspondence:**
Pannaga Pavan Jutur
jppavan@icgeb.res.in

Specialty section:
This article was submitted to Plant Biotechnology, a section of the journal Frontiers in Plant Science

Received: *25 November 2019*
Accepted: *16 June 2020*
Published: *03 July 2020*

Citation:
Kareya MS, Mariam I, Shaikh KM, Nesamma AA and Jutur PP (2020) Photosynthetic Carbon Partitioning and Metabolic Regulation in Response to Very-Low and High CO_2 in Microchloropsis gaditana NIES 2587. Front. Plant Sci. 11:981. doi: 10.3389/fpls.2020.00981

Photosynthetic organisms fix inorganic carbon through carbon capture machinery (CCM) that regulates the assimilation and accumulation of carbon around ribulose-1,5-bisphosphate carboxylase/oxygenase (Rubisco). However, few constraints that govern the central carbon metabolism are regulated by the carbon capture and partitioning machinery. In order to divert the cellular metabolism toward lipids and/or biorenewables it is important to investigate and understand the molecular mechanisms of the CO_2-driven carbon partitioning. In this context, strategies for enhancement of CO_2 fixation which will increase the overall biomass and lipid yields, can provide clues on understanding the carbon assimilation pathway, and may lead to new targets for genetic engineering in microalgae. In the present study, we have focused on the physiological and metabolomic response occurring within marine oleaginous microalgae *Microchloropsis gaditana* NIES 2587, under the influence of very-low CO_2 (VLC; 300 ppm, or 0.03%) and high CO_2 (HC; 30,000 ppm, or 3% v/v). Our results demonstrate that HC supplementation in *M. gaditana* channelizes the carbon flux toward the production of long chain polyunsaturated fatty acids (LC-PUFAs) and also increases the overall biomass productivities (up to 2.0 fold). Also, the qualitative metabolomics has identified nearly 31 essential metabolites, among which there is a significant fold change observed in accumulation of sugars and alcohols such as galactose and phytol in VLC as compared to HC. In conclusion, our focus is to understand the entire carbon partitioning and metabolic regulation within these photosynthetic cell factories, which will be further evaluated through multiomics approach for enhanced productivities of biomass, biofuels, and bioproducts (B3).

Keywords: *Microchloropsis*, carbon dioxide, oleaginous microalga, biomass, photosynthetic cell factories

INTRODUCTION

Environmental pollution by the greenhouse emissions ultimately led to global warming and accumulation of 440 ppm of CO_2 which is one of the significant gas released into the atmosphere contributing for adverse environmental issues (Ng et al., 2018). The use of fossil fuels is primarily in three economic sectors, namely: energy, transportation, and industry leading to CO_2 emissions. Increase in atmospheric CO_2 may be caused due to following reasons such as deforestation (9%), burning of fossil fuels (87%), and remaining (4%) presumably by others like industrial manufacturing (Le Quere et al., 2013; Mistry et al., 2019).

Microalgae are unicellular photosynthetic microbes capable of converting atmospheric CO_2 into lipids (Ho et al., 2010; Mata et al., 2010; Chen et al., 2011) and other high-valuable renewables (Wang et al., 2010). Most of the eukaryotic algae comprises of pyrenoids, which are proteinaceous sub-cellular compartmentalized structures capable of fixing nearly 30–40% of atmospheric CO_2 due to the presence of Rubisco enzyme (Freeman Rosenzweig et al., 2017). Pyrenoids are considered as the hubs for carbon assimilation in algae and their structural characteristics may vary depending upon the species (Raven et al., 2008). Capturing of the atmospheric CO_2 and converting them into reduced form without contributing to global warming by maintaining the balance in the environment is referred as carbon sequestration (Lal, 2008; Zeng, 2008). These photosynthetic cell factories are capable of sequestering atmosphere CO_2 for the production of biofuel precursors (Rittmann, 2008; Mistry et al., 2019). Henceforth, the potential of industrially relevant oleaginous microalgae to minimize the excess CO_2 present in the atmosphere can be employed *via* carbon concentrating mechanism (CCM) (Long et al., 2016).

Broadly three types of CCMs are reported in plants and algae, i.e., C3, C4, and crassulacean acid metabolism (CAM) (Hopkinson et al., 2016; Heyduk et al., 2019). For example, in model microalgae *Chlamydomonas reinhardtii* and other diatoms, presence of below air-level CO_2 especially activates CCMs which are quite sensitive (Reinfelder, 2011; Meyer and Griffiths, 2013; Wei et al., 2019). Even though each species may have distinct CCMs due to their diversity, till date it is not clearly defined whether these diverse CCMs are universally occurring in all microalgae (Meyer and Griffiths, 2013; Clement et al., 2017; Wei et al., 2019). Henceforth, understanding the photosynthetic carbon partitioning and metabolic regulation in response to very-low CO_2 (VLC; 300 ppm, or 0.03%) and high CO_2 (HC; 30,000 ppm, or 3% v/v) in microalgae (del Campo et al., 2014), may provide targets for rational engineering of individual regulatory hubs for enhanced CO_2 assimilation. Previous studies have reported that low CO_2 levels have been associated with the air level of CO_2 (0.03–0.05% CO_2); however, CO_2 levels below 0.02% (generally considered as very low CO_2) have also been considered as low CO_2. Moreover, the photosynthetic CO_2 consumption and assimilation by cells supplemented with atmospheric CO_2, decrease the actual CO_2 levels even below the generally considered substantial CO_2 concentration, and often into the range of very low CO_2 (Vance and Spalding, 2005; Wang et al., 2015). Hence, understanding the relationship between dissolved inorganic carbon (DIC) (Long et al., 2016) concentration and microalgae growth is also important. As a result, a comprehensive correlation between biomass and DIC should also be studied to enhance the rate of CO_2 biofixation by microalgae since DIC is the only carbon source which is produced by means of CO_2 aeration and carbon is the major element that makes up the microalgal biomass (Smith et al., 2015; Chang et al., 2016).

Microchloropsis gaditana, previously known as *Nannochloropsis gaditana*, has great potential as industrial strain due to its higher lipid content (Poliner et al., 2018; Schädler et al., 2019) (>50% dcw) and are also capable of converting atmospheric CO_2 into biomass (Carlozzi, 2003), biofuels (Mujtaba et al., 2012), and biorenewables precursors (Fawley et al., 2015; Lee and Sun, 2019). Studies have shown that increase in biomass productivities can be achieved by enhancing photosynthetic efficiency through supplementation of CO_2 in *Nannochloropsis* sp. (Jiang et al., 2011). Only recently, efforts to engineer this species have taken place and despite these studies, the global picture of carbon fixation and partitioning (both processes being independent of the other) in this species is not well elucidated. Interestingly, this species lacks pyrenoid wherein the Rubisco is localized, eventually fixing CO_2 in the organic form. Due to the absence of pyrenoid, the efficiency of carbon assimilation is reduced (Mackinder et al., 2017). In this context, CCM machineries are poorly understood among these microalgae and there is a need to reveal the route of carbon flux and carbon partitioning once these CCMs are active. To illustrate the mechanism, we selected a marine microalga *M. gaditana* NIES 2587, and tracked the metabolomic profiles following a time course pattern of 0, 3, 6, and 9 days to adapt the strain from VLC to HC, paving the way for understanding their metabolic regulatory network for enhanced CO_2 assimilation and biomass production. These insights on the substrate uptake mechanism in *M. gaditana* showed that enhancing photosynthetic efficiency will perhaps lead to increased productivities of biomass, biofuels and biorenewables (B3) in these photosynthetic cell factories.

MATERIALS AND METHODS

Microalgae and Culture Conditions

Marine microalgae *Microchloropsis gaditana* NIES 2587 is procured from Microbial Culture Collection, National Institute for Environmental Studies (NIES), Tsukuba, Japan. The strain was grown in minimal medium F/2 (Guillard and Ryther, 1962) under a light regime of 16:8 h and an illumination of 150 μmol m^{-2} s^{-1} photosynthetically active radiation (PAR) in a multi-cultivator MC 1000-OD (Photon Systems Instruments, Czech Republic) with a flow rate of 800 ml min^{-1} with continuous bubbling of air at 24°C. The composition of F/2 medium components (g L^{-1}) is as follows: $NaNO_3$-0.075; $NaH_2PO_4{\cdot}2H_2O$-0.005; $Na_2SiO_3{\cdot}9H_2O$-0.03 in artificial sea water (ASW) prepared using NaCl-24; $MgCl_2{\cdot}6H_2O$-11; Na_2SO_4-4; $CaCl_2{\cdot}6H_2O$-2; KBr-0.1; H_3BO_3-0.03; $Na_2SiO_3{\cdot}9H_2O$-0.005; $SrCl_2{\cdot}6H_20$-0.04; NaF-0.003; NH_4NO_3-

0.002; $Fe_3PO_4{\cdot}4H_2O$-0.001; trace metals solution (in g L^{-1}): 1 ml L^{-1} ($ZnSO_4{\cdot}7H_2O$-0.023; $MnSO_4.H_2O$-0.152; $Na_2MoO_4{\cdot}2H_2O$-0.007; $CoSO_4{\cdot}7H_2O$-0.014; $CuCl_2{\cdot}2H_2O$-0.007; $Fe(NH_4)_2(SO_4)_2{\cdot}6H_2O$-4.6; $Na_2EDTA{\cdot}2H_2O$-4.4); and vitamin B12*-0.135 mg L^{-1}; biotin vitamin solution*-0.025 mg L^{-1}; thiamine vitamin solution*-0.335 mg L^{-1} (*added after autoclaving the media) (Shaikh et al., 2019). Methods for cell growth profile and their biomass content were estimated by Guillard and Sieracki (2005) and dry weight (dcw) analysis (Sluiter et al., 2008). Growth rates were obtained using the following equation (Levasseur et al., 1993):

$$K = \frac{\ln \frac{N2}{N1}}{t2 - t1}$$

Where, N1 and N2 represent cell counts at initial time (t1) and final time (t2), respectively. Doubling time was calculated depending on the specific growth rate (Duong et al., 2015).

$$Doubling\ time = \frac{\ln 2}{K}$$

Cells were grown to mid of the logarithmic phase under photoautotrophic condition in F/2 medium. These samples were centrifuged at 5,000 x*g* and resuspended at a density of 2×10^6 cells ml^{-1} in regular F/2 medium with supplementation of CO_2 (0.03% CO_2; VLC) and (3% CO_2; HC) at the intervals of 0, 3, 6, and 9 days for further qualitative metabolomic analysis and profiling.

Biochemical Analysis

Biochemical analysis of all the samples were done for analyzing the changes in composition, i.e., total pigments (chlorophyll and carotenoids), proteins, carbohydrates, and lipids subjected to VLC and HC. For estimation of total pigments including chlorophyll and carotenoids, 1 ml of cells were pelleted, followed by resuspension of the culture in absolute methanol (1 ml). The solution was briefly vortexed and incubated at 55°C for 1 h for extraction of all the pigments. Finally, the debris was centrifuged at 5,000 x*g* to separate both the pellet and supernatant. The suspension was measured at optical density (OD) of 470, 652, and 665 nm to calculate total chlorophyll and carotenoid content (Lichtenthaler and Wellburn, 1983).

Estimation of proteins were performed by biuret method with slight modifications. The total soluble proteins in extraction buffer containing 1 N NaOH in 25% methanol were extracted as described in Shaikh et al. (2019). To 2 ml of pelleted culture, 1 ml of extraction buffer was added followed by incubation at 80° C for 15 min. Later, these samples were cooled to room temperature (RT) and the cell debris was removed by centrifugation. One hundred microliter of extract was mixed with 50 µl of $CuSO_4$ solution (0.21% $CuSO_4$ in 30 g of NaOH in 100-ml water) and left for 10 min at RT, followed by measuring absorbance at 310 nm (Chen and Vaidyanathan, 2013).

Estimation of total carbohydrates was done using modified anthrone method (Schneegurt et al., 1994). Cells (approximately 2 ml) were harvested from cultures by centrifugation, and resuspended in 200 µl of water. Hydrolysis was performed for 1 h in 400 µl of KOH [40% (w/v)] at 90°C. The solutions were cooled followed by addition of two volumes of absolute ethanol for precipitating carbohydrates and left for overnight incubation at −20°C. The precipitate was centrifuged for 30 min and dissolved in concentrated H_2SO_4 (100 µl), kept at RT for 10 min, followed by dilution in 900 µl of deionized water. Modified protocol was employed in the assay by including sample blank (containing sample + ethanol + sulfuric acid) for each sample in order to reduce the interference occurring due to solubility of proteins and pigments in alcohol, henceforth reducing the over estimation of carbohydrate content within the samples (Ashwell, 1957). Carbohydrates were measured using glucose as standard by addition of the anthrone reagent (containing 2.0 g L^{-1} of anthrone in concentrated H_2SO_4). To these precipitated aliquots (500 µl), 1 ml of anthrone reagent was added and absorbance was measured at 575 nm.

Total lipids was estimated using sulpho-phosphovanillin (SPV) method (Mishra et al., 2014). Phosphovanillin reagent was prepared by initially dissolving 0.6 g of vanillin in 10 ml absolute ethanol. To the same, 90 ml of deionized water was added and stirred continuously. Subsequently 400 ml of concentrated phosphoric acid was added to the mixture, and the resulting reagent was stored in the dark until further use. Briefly, 2 ml of culture was centrifuged and resuspended in 100 µl of deionized water. Later, 2 ml of concentrated H_2SO_4 was added and the reaction mixture was heated at 100°C for 10 min. The samples were cooled by incubating in ice for 5 min. Finally, 5 ml of freshly prepared SPV reagent was added to the samples and incubated at 37°C with shaking of 200 rpm for 15 min. Absorbance were read at 530 nm for the lipid quantification of the samples.

Chlorophyll "a" Fluorescence Measurement

Chlorophyll "a" fluorescence signals were documented using the Dual PAM-100 fluorometer (Heinz Walz, GmbH). For complete oxidation of all the reaction centers samples were incubated in dark for 30 min. A saturation light pulse (6,000 µmol photons m^{-2} s^{-1}; λ = 660 nm) was used to determine the *Fm* value, followed by calculation of the maximum photochemical efficiency of PSII (*Fv*/*Fm* = (*Fm-Fo*)/*Fm*) (Zhou et al., 2015; Zhao et al., 2017; Agarwal et al., 2019a). The measurements for fluorescence values were obtained from the experimental datasets for the calculation of quantum yields of photochemical quenching, Y (II); non-photochemical quenching, Y (NPQ); and the energy dissipated as heat or fluorescence, Y (NO), followed by calculation of the PSII operating efficiency by *Fq'*/*Fm'* (Baker, 2008). The experiments were conducted for samples aliquoted on different time intervals, i.e., 0, 3, 6, and 9 days with three biological replicates (n = 3) and a minimum chlorophyll concentration of 40 µg ml^{-1} for all the measurements.

Lipid Quantification and Profiling

For fatty acid methyl esters (FAMEs) analysis in *M. gaditana*, approximately 1×10^8 total cells were hydrolyzed and methyl-esterified in 300 µl of 2% H_2SO_4 in methanol for 2 h at 80°C. Prior to the reaction, 50 µg of heptadecanoic acid (Alfa Aesar, USA) was added as internal standard. After esterification step, 300 µl of 0.9% (w/v) NaCl solution and 300 µl of hexane were

added and mixed thoroughly for 20 s. To separate both the phases, samples were centrifuged at 3,000 x*g* for 3 min. One microlitre of hexane layer was injected into a 7890A gas chromatography (Kaczur et al.) - mass spectrometry (MS) system (Agilent 7000 GC/MS triple quadrupole system) (Schuhmann et al., 2014; Duong et al., 2015). The running conditions for GC-MS were described by Agilent's RTL DBWax method (Brown, 1991; Shaikh et al., 2019).

Qualitative Metabolomics

For extraction of cellular metabolites, approximately, 1×10^9 cells were centrifuged at 8000 ×*g* for 10 min at 4°C and immediately quenched in liquid nitrogen. Further, 1 ml of ice-cold methanol/ethanol/chloroform (2:6:2) was added to the cells for resuspension, followed by sonication of resuspended cells in sonication bath for 15 min (Hirth et al., 2017). Later, these samples were centrifuged at 10,000 ×*g* for 15 min at 4°C and the filtration of supernatant was done by 0.2 µm filter. From the above supernatant (100 µl) was taken and dried by purging nitrogen gas. The dried leftover was dissolved in 0.01 ml of methoxyamine hydrochloride solution [4% (w/v) in pyridine], followed by incubation for 90 min at 30°C by shaking. To the above solution, 0.09 ml of N-methyl-N-(trimethylsilyl) trifluoroacetamide was added and incubated at 37°C for 30 min. The samples were centrifuged at 14,000 ×*g* for 3 min, and the supernatant was taken for the GC-MS/MS analysis (Shaikh et al., 2019). These derivatized metabolite samples were injected in split mode (1:5) into a Agilent 7890A GC-MS equipped with Agilent DB-5 (30 m × 0.25 mm × 0.25 µm) column with the injection port temperature set at 250°C. The GC was operated at constant flow of 1 ml/min helium. The temperature program was started at 60°C for 3 min isothermal and ramping at 5°C/min to 180°C, 3 min isothermal and finally ramping at 10°C/min to 310°C. Data acquisition was performed on a Agilent 7000D Triple Quadrupole mass selective detector with a scan range from 50 to 600 amu. For identification and alignment, peaks were matched against NIST library based on their retention indices and mass spectral similarities (those hits having R value >600 were selected). All the samples were normalized by cell number (10^9 cells/ml) and the final analysis was done using MetaboAnalyst 4.0 (http://www.metaboanalyst.ca) (Chong et al., 2018).

Statistical Analysis

The experiments were carried out in biological triplicates, and their standard errors (SEs) were calculated representing mean of three values each. All the data has been represented in terms of mean ± SE (representing "SE" as the standard error for experiments) and plotted graphs by MS Excel software (Microsoft Corporation, USA).

RESULTS

Growth Profile and Biomass Yields Subjected to VLC and HC in *M. gaditana*

The microalgal strains *M. gaditana* NIES 2587 was cultivated with an initial cell concentration of 5×10^6 cells ml^{-1} in F/2 medium, respectively, in the presence of VLC (0.03%) and HC (3%) till mid- to late-logarithmic phase. In VLC, *M. gaditana* reached a biomass yield of 0.22 g L^{-1} at the end of the 9th day with a specific growth rate of 0.6 day^{-1} (started with an initial inoculum of 0.02 g L^{-1}), whereas in HC the biomass yields increased up to 1.5 fold and reached to biomass of 0.3 g L^{-1} within 6 days (**Figure 1A**), thus reducing the overall doubling time by nearly 3 h, i.e., 27.4 to 24.2 h (**Table 1**). Our data presumes that during HC, the *M. gaditana* showed an increase in biomass till 6th day, later slowed down due to photo-saturation and may be the inability to assimilate CO_2 continuously after 6th day. Henceforth, these clues may provide facts for further investigation of mechanism involved in photosynthetic carbon partitioning due to varying CO_2 concentrations.

Changes Involved in Chlorophyll "a" Fluorescence

Chlorophyll a fluorescence is a fast, non-invasive, precise, and definitive method that remains to be used in a significant number of studies related to photosynthesis (Zhou et al., 2015). In the present study, we have measured the Chl "a" fluorescence in *M. gaditana* grown under VLC and HC conditions. Subsequently, the data analysis and interpretation allow us to characterize the PSII activity and shows strong similarities as indicated in their growth patterns. The maximum quantum efficiency of PSII photochemistry (*Fv/Fm*) of the cultures grown in VLC are compared to HC (**Figure 1B**). The data predicts that the photosynthetic machinery of *M. gaditana* in response to HC is highly active rather than VLC, which demonstrates lowering of doubling time and enhanced growth rates. However, the *Fv/Fm* ratio declines after the 6th day in *M. gaditana*, demonstrating sudden drop in the photosynthetic quantum efficiency (Emerson and Arnold, 1932) of the cells, which has also been reflected as saturation in the growth pattern (**Figures 1A, B**).

Figure 1C represents the PSII operating efficiency, that provides an essential approximation of the quantum yield of linear electron flux through the PSII. The PSII operating efficiency is higher in HC than in VLC, and also corresponds with the photosynthetic quantum efficiency of the PSII photochemistry which is higher in HC and is analogous to the growth curve.

There have been numerous reports on the quantum yields of photochemical Y (II) and non-photochemical [Y(NPQ)] quenching; however, there is a limitation on the information available on the Y(NO) significance. It is the energy that is dissipated passively, when the PSII reaction centers are closed (Schreiber and Klughammer, 2008). **Figure 1D** demonstrates a stacked bar graph corresponding to the Y (II), Y(NPQ), and Y (NO). The quantum yield of Y (II) of both VLC and HC cells remain similar throughout the time-course, however, the Y (NPQ) keep on increasing for cells growing in VLC condition.

Biochemical Analysis

To understand the effect of CO_2 on molecular profiling in *M. gaditana* different biochemical constituents were investigated. **Table 2** shows the biochemical composition, i.e., total pigments (chlorophyll and carotenoids), proteins, carbohydrates and lipids (% dcw) in *M. gaditana*, subjected to VLC and HC conditions. The

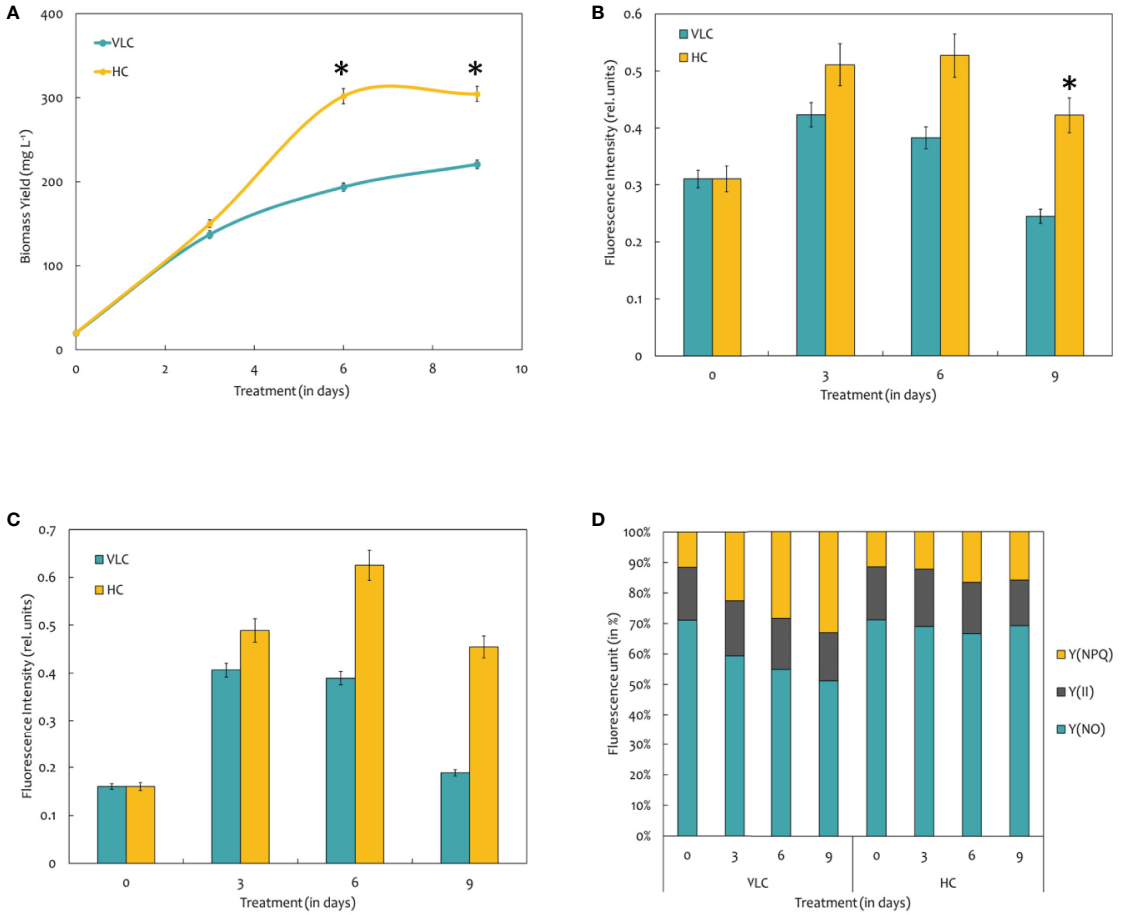

FIGURE 1 | (A) Biomass yields of *M. gaditana* at 150 μE of light intensity subjected to VLC and HC supplementation. **(B)** Bar diagram indicating maximum quantum efficiency of PSII photochemistry, i.e., the Fv/Fm ratio in VLC and HC. It is the maximum efficiency at which light absorbed by PSII is used for reduction of Q_A (Primary acceptor plastoquinones). **(C)** Bar diagram indicating the PSII operating efficiency,.i.e., the Fq'/Fm' ratio. It estimates the efficiency at which light absorbed by PS II is used for Q_A reduction. **(D)** Quantum yields of photochemical quenching Y (II), non-photochemical quenching Y (NPQ) and the non-light induced energy dissipated as heat or fluorescence Y (NO). * indicate statistical significance by one-way ANOVA, p-value < 0.05.

TABLE 1 | The different growth parameters of *M. gaditana*.

Treatment (CO_2)	Specific Growth Rate(d^{-1})	Doubling Time(h)	Biomass Productivity (mg $L^{-1}d^{-1}$)
VLC	0.61 ± 0.03	27.42 ± 0.2	30.10 ± 0.25
HC	0.69 ± 0.02	24.27 ± 0.1	47.25 ± 0.18

TABLE 2 | The biochemical profile of *M. gaditana* on 9th day at 150 μE of light intensity subjected to 0.03% (VLC) and 3% (HC) supplementation.

Strain		Proteins	Lipids	Carbohydrates	Pigments
		(% dcw)			
M. gaditana	VLC	40.0 ± 1.2	30.6 ± 0.9	17.7 ± 1.3	0.1 ± 0.0
	HC	41.4 ± 1.0	38.5 ± 1.1	13.5 ± 1.5	1.0 ± 0.0

chlorophyll and carotenoid contents remain to be higher in HC than VLC. It has been previously reported that CO_2 supplementation increases the growth and chlorophyll contents within the photosynthetic organisms (Husemann and Barz, 1977; Chinnasamy et al., 2009; Wong et al., 2013). In this study, **Figure 2A** shows that the chlorophyll content increases almost by four-fold whereas carotenoid content (**Figure 2B**) enhances by eight-fold within the cells in HC as compared to VLC.

The total protein content has no drastic effect in *M. gaditana* in both VLC and HC conditions, i.e., nearly consists of 41.4 (% dcw). Moreover, the total lipids content have increased from 30.6 (% dcw) in VLC to 38.5 (% dcw) in HC, whereas the total carbohydrates were declined from 17.7 (% dcw) in VLC to 13.54 (% dcw) in HC; suggesting the diversion of the carbon flux toward lipid (FAMEs) accumulation in *M. gaditana* when subjected to higher CO_2 conditions.

Lipid (FAMEs) Analysis and Profiling

FAMEs were extracted according to the modified Bligh and Dyer procedure and was quantified using GC-MS/MS as described in *Materials and Methods*. The FAME content and profiles varied in

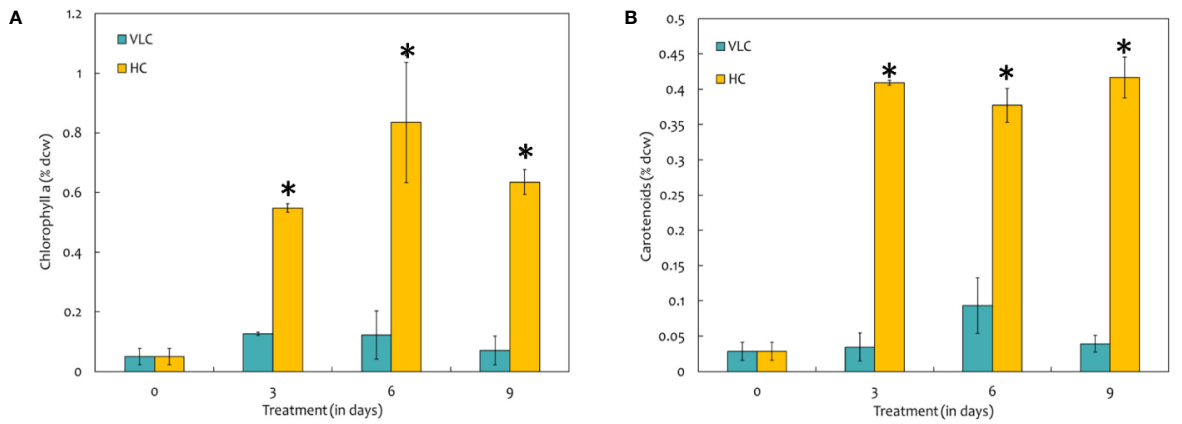

FIGURE 2 | (A) Bar diagram representing the time-course dynamics of chlorophyll a content (in % dcw) in *M. gaditana* supplemented with VLC and HC. **(B)** Time-course variation in the carotenoid content (in % dcw) of *M. gaditana* supplemented with VLC and HC. * indicate statistical significance by one-way ANOVA, p-value < 0.05.

response to VLC and HC, respectively. Our data demonstrates overall increase in the total FAME content (% dcw) reaching up to 30% of dcw on 9th day in HC condition (**Figure 3A**). **Figure 3A** represents total FAME content in % dcw, while **Figure 3B** is a representation of FA composition in the form of % wt. of total lipids. The total FAME content remained stable till 6th day while it showed increasing trend at day 9 in high CO_2 condition (**Figure 3A**). Our results demonstrate reshuffling/shift in fatty acids profiles especially in PUFAs (% wt of total lipids) within the cells on day 6 in HC (**Figure 3B**). However, overall increase in the total FAME content was observed on day 9 in HC condition while no change was observed in saturation and unsaturation profiles. The time-course also demonstrates that the PUFA content in VLC conditions were decreased substantially from 3rd day to 9th day (42.1% dcw to 28.3% dcw), diverting the carbon flux toward the accumulation of monounsaturated fatty acids (MUFAs), whereas in HC, the PUFA content increases drastically from 35% dcw to 45% dcw by 6th day. Also during the HC conditions, the FAME profile (**Figure 3C**) demonstrates that the relative content of C18:2 (linoleic acid) and C18:3 (linolenic acid) is higher in *M. gaditana*; however, C18:1 (oleic acid) and C16:0 (palmitic acid) are the major FAMEs present in VLC conditions, implying that the activity of desaturases involved in lipid metabolism may be upregulated at higher CO_2 concentrations.

Metabolome Analyses

The CCMs in microalgae are essential for the photosynthetic processes and survival at low CO_2 environments (Wang et al., 2015). CCMs in photosynthetic organisms operate to enable the assimilation of CO_2 with the help of active inorganic carbon (Ci) uptake systems and increased carbonic anhydrase activity to raise Ci accumulation within the cells when inorganic carbon (Ci) is limiting through the dehydration of accumulated bicarbonate (Spalding, 2008; Beardall and Raven, 2016). There are a number of reports in the model microalga, *C. reinhardtii* about the transporters involved in the transfer of the inorganic carbon pool toward Rubisco, however, not much is known about the dynamics of the metabolites inside the cell and the specific knowledge regarding the metabolomic profiles remains elusive (Duanmu et al., 2009; Yamano et al., 2015; Shaikh et al., 2019). In this study, we have employed qualitative metabolomics in order to understand the changes in the metabolomic profiles inside the cell when subjected to VLC and HC supplementation, which will provide new insights and understanding regarding the photosynthetic carbon partitioning and metabolic regulation in *M. gaditana*. The metabolite extraction and derivatization of *M. gaditana* was carried as described earlier in *Materials and Methods*. The major advantage with a metabolomics approach is the non-biased information about pool sizes in a large number of metabolites under particular conditions (Renberg et al., 2010). Metabolomics datasets were analyzed for the time-course experiments, resulting in nearly a total of 40 GC-MS peaks. As a result of alternate derivatization, repetition of identical metabolites was observed to be very common in the raw data files; such metabolites were eliminated if not significant, and the peaks were manually curated to obtain 31 metabolites that were further processed (Hirth et al., 2017; Shaikh et al., 2019).

Figure 4A represents heatmap showing time-course $\log_2$ fold changes of metabolites in VLC/HC conditions that were either upregulated or downregulated, wherein the legend scale denotes as follows: red color for upregulation while blue indicates downregulation. It is evident that several metabolites show a dynamic alteration in both VLC and HC conditions. Relative abundances of nearly 31 metabolites were obtained, and most of them belong to either sugars, or/and fatty acids. In *M. gaditana*, metabolites such as fructose, glucose, galactose, and phytol were increased in VLC conditions, whereas sucrose is significantly upregulated in HC supplementation. It is also evident from the dot-plot (**Figure 4B**) that metabolites such as sugars and alcohols namely fructose, glucose, phytol, trehalose, and galactose were upregulated on the 9th day when subjected to VLC. Furthermore,

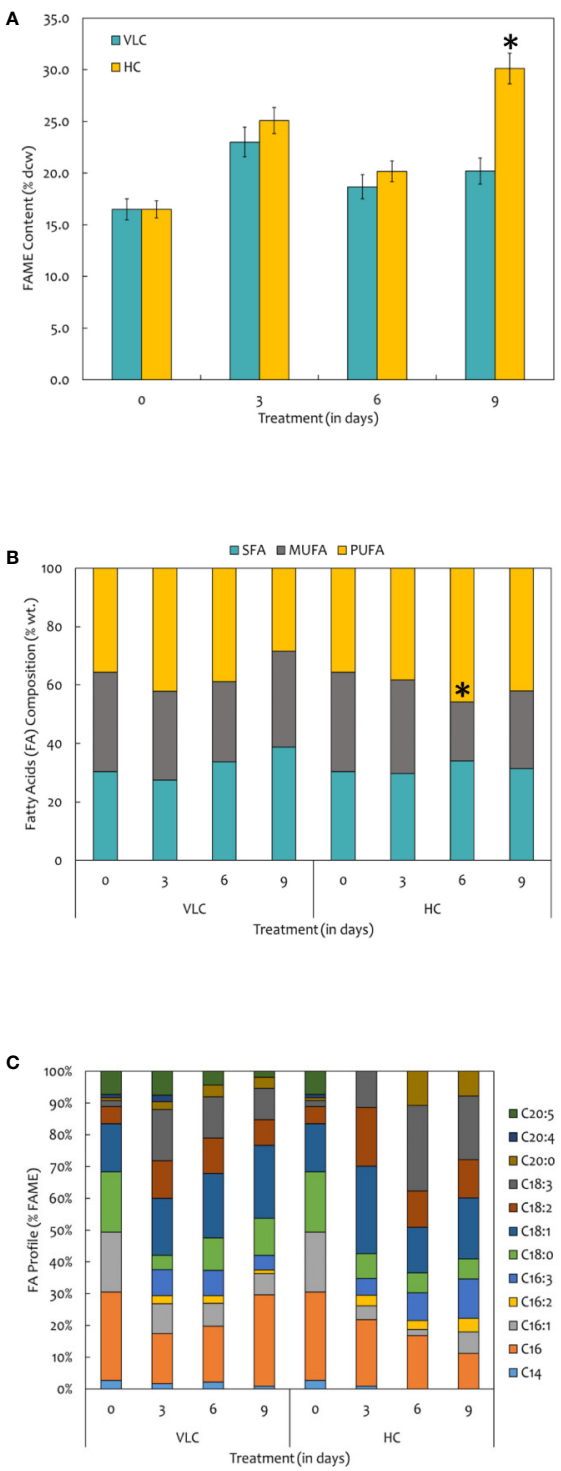

FIGURE 3 | (A) Quantitative analysis of total fatty acid methyl esters (FAMEs) in *M. gaditana* (in % dcw) supplemented with VLC and HC. **(B)** Bar diagram representing the saturation and unsaturation ratio of fatty acids (% of FAME) in *M. gaditana* (SFA, saturated fatty acids; MUFA, mono-unsaturated fatty acids; PUFA, poly-unsaturated fatty acids). **(C)** FAME profile depicting the distribution of individual fatty acids in *M. gaditana* subjected to VLC and HC. * indicate statistical significance by one-way ANOVA, p-value < 0.05.

fatty acids such as linoleic acid and arachidic acid were enhanced in HC, with both the metabolites in their higher abundance of more than two-fold change (**Figure 4B**).

Increased levels of these compounds indicate breakdown of starch and the regulation of maltose metabolism, respectively. This physiological behavior of cells is reported to be an adaptive strategy as a result of environmental stress (Agarwal et al., 2019b). On the other hand, TCA cycle intermediate such as acetate seems to be upregulated on 3rd day as compared to days 6 and 9 (**Figure 4A**) when subjected to HC. Fatty acids such as stearic acid, hexadecanedioic acid palmitic acid, linoleic acid and arachidic acid were enhanced in HC indicating the diversion of carbon flux from TCA cycle to lipid biosynthesis. As depicted in **Figure 4B**, another metabolite which is upregulated in HC is α-tocopherol, is a secondary metabolite. The primary role of α-tocopherol is scavenging of reactive oxygen species (ROS) within the cells. Certain amino acids such as L-valine, L-alanine, and L-proline were also increased (**Figures 4A, B**), indicating the diversion of flux through intermediates of the TCA cycle, ultimately leading toward protein synthesis. Our data demonstrates significant molecular alteration in the relative abundance of various metabolites in response to VLC and HC, allowing us to predict a metabolic route in the diversion of the carbon flux in *M. gaditana* when subjected to VLC and HC conditions.

DISCUSSION AND CONCLUSIONS

Aqueous environments are directly not favorable conditions for efficient photosynthesis due to the CO_2 diffusion rate, i.e., 10,000-fold lower than in atmospheric conditions (Yamano et al., 2015). However, the aquatic photosynthesis of microalgae accounts for a large proportion (nearly 50%) of the global primary productivity (Giordano et al., 2005). The cellular physiology governs the channelization of the carbon flux toward biomass and biosynthesis of energy storage molecules. Depending on the requirement and the environmental perturbations, there is a metabolic shift that can alter the route of photosynthetically assimilated inorganic carbon from the synthesis of biomass to production of storage molecules, such as lipids and other high-value biorenewables (Valenzuela et al., 2012; Fields et al., 2014; Schuhmann et al., 2014; Shaikh et al., 2019). Major algal research has been primarily focused on lipid production subjected to nitrogen stress while compromising biomass productivities (Alboresi et al., 2016; Shaikh et al., 2019). Improving the biomass productivity of microalgal strains is a major factor that would facilitate the economic viability of algal biofuels (Davis et al., 2011; Hildebrand et al., 2013). It has been shown that light can induce lipid accumulation and potentially is the master regulator of metabolism; however, it is important to understand how different organisms regulate the carbon flux toward lipid or/and carbohydrate biosynthesis (Sforza et al., 2012; Alboresi et al., 2016). Microalgae have adapted different strategies to cope with the environmental stress and divert the carbon flux with the help of a photosynthetic carbon assimilation process, i.e., CCM (Wang et al., 2015). The CCMs are the fundamental process in algal

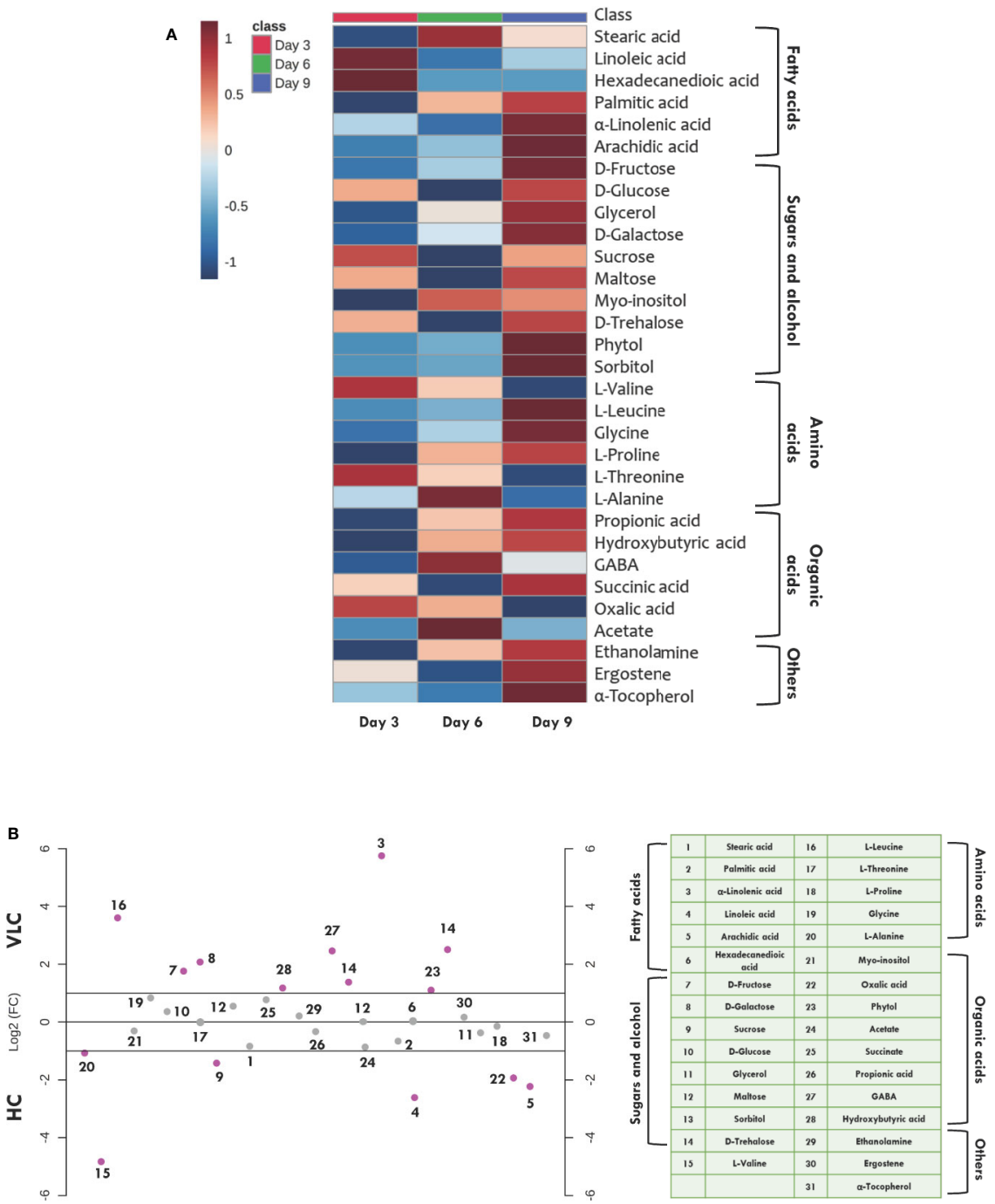

FIGURE 4 | Time-course metabolome dynamics in *M. gaditana* under VLC/HC. **(A)** Heatmap represents the $\log_2$ fold change of all metabolites (represents time-course, i.e., 3, 6, and 9 days) in VLC/HC. **(B)** Dot-plot representing the fold-change of different metabolites in VLC and HC supplementation on 9th day in *M. gaditana* (pink dots represent the metabolites which show fold change >2; gray dots represent the metabolites fold change < 2).

photosynthesis, metabolism, growth, and biomass production and much of the work related to CCMs has been reported in the model microalga, *C. reinhardtii*. Unlike the CO_2 enrichment in C4 plants, CCMs in these aquatic microalgae function intracellularly by generating a reservoir of DIC, the uptake of this pool of DIC is propelled by energy-coupled Ci transport systems (Wang and Spalding, 2006). In VLC conditions, cells undergo dynamic ultrastructural changes as well as induce additional CCM-based proteins. This leads to the acclimation of the photosynthetic machinery by regulating the ATP supply to

assist the transfer of Ci into the cells eventually enhancing the process of photosynthesis (Ramazanov et al., 1994; Geraghty and Spalding, 1996; Renberg et al., 2010). In *C. reinhardtii* grown under CO_2-limiting conditions, the major pool of Rubisco is localized in a central structure inside the chloroplast known as? A3B2 show [#,32] ?> pyrenoid (Badger et al., 1998). Although there have been advances about the understanding of the CCMs in *C. reinhardtii* and diatoms, extensive experimental studies have been limited to only these selected taxa. The marine microalga, *M. gaditana*, has emerged as an industrially relevant organism due to their oleaginous nature (Hu et al., 2008; Varfolomeev and Wasserman, 2011; Ratha and Prasanna, 2012). However, there is very little information available about the CCMs of *M. gaditana*, more importantly, they appear to lack pyrenoids, and the role of several metabolite pools inside the cell governing the diversion of carbon flux (Gee and Niyogi, 2017) seems to be elusive. Hence, to solve such challenge, insights into the CO_2 uptake and assimilatory machineries with regards to the CCMs are essential for understanding the physiological and metabolic patterns of these cell factories.

In the present work, we have demonstrated the growth and cellular physiology to improve our understanding regarding the CCM of *M. gaditana* in response to VLC and HC. Biomass concentration increases under VLC and reaches the maximum level on the last day of cultivation, i.e., 9th day. On the other hand, the growth saturates in *M. gaditana* when subjected to HC after the 6th day. The biomass concentration, although, under HC is always higher than under VLC, which is also consistent with previous reports showing an increased biomass production at higher CO_2 concentrations (Sforza et al., 2012; Adamczyk et al., 2016). It has been reported that CO_2 biofixation can be increased by using a higher concentration of biomass with the same volume of culture (Adamczyk et al., 2016). VLC and HC have a significant effect on the photochemical efficiencies in *M. gaditana*, as demonstrated by the Fv/Fm ratios. The maximum photochemical efficiency of PSII (Fv/Fm) under HC is higher than in VLC. A higher Fv/Fm ratio is usually interpreted as higher photosynthetic performance while a lower ratio represents the photoinhibition of PSII. It has been reported that the higher Fv/Fm ratio is also due to the influence of certain pigments on the photosystems (Zhou et al., 2015; Zhao et al., 2017; Agarwal et al., 2019a). Our results suggest that the cells cultivated in HC undergo more physiological changes than in VLC conditions. The decline of photosynthetic activity may be due to decrease in chlorophyll contents in both VLC and HC after 6th day. The decrease in Fv/Fm ratio is often interpreted as photo-damage which might be caused because of the inactivation of PSII reaction centers. This is caused due to an inhibition of electron transport at both donor and acceptor sites of PSII further promoting a dissemination of excitation energy in favor of PSI, resulting in an increase in the electron flow near PSI (Lu and Vonshak, 2002; Rym, 2012). This decline represents a defensive process with the dissipation of excess energy from the photosystems which is usually identified as an adaptive acclimation system to down regulate PSII. The alterations in PSII photochemical reactions suggests that there is a decline in the ability of the photosynthetic apparatus to maintain the oxidative state of Q_A and is highly prominent in VLC starting from day 6.

It is evident (**Figure 1D**) that there is a constant decline in Y (NO) till the 9th day in VLC cells. Y(NO) is generally considered as a straightforward indicator of the reduction state of plastoquinones present in the membranes (Grieco et al., 2012). Consequently, it is assumed that the HC cells retained the ability to efficiently regulate the photosynthetic electron transport chain. During stress phenomenon, the increase in non-photochemical quenching can often be accompanied by photo-inactivation of PSII reaction centers, which will dissipate excitation energy as heat (Maxwell and Johnson, 2000). Photo-inactivation can lead to oxidative damage and loss of PSII reaction centers (Baker, 2008), both of which are associated with decrease in Fv/Fm ratios. Microalgae tend to dissipate excess energy in the form of heat (Agarwal et al., 2019a). Similar phenomenon in dissipation of the activation energy as Y(NPQ) in VLC cells might be a survival mechanism that result in the reduction of overall cell biomass.

Biochemical changes in response to VLC and HC conditions where the major shift has been observed in production of lipids and total pigments. To utilize the carbon efficiently, algal cells must maintain adequate chlorophyll and carotenoid levels (**Figures 2A, B**). Increased levels of phytol in VLC indicate breakdown of chlorophyll (Wase et al., 2017), which can be seen in **Figure 2A** and hence the reduced levels of photosynthetic efficiency (**Figure 1B**). The main component affected by CO_2 supplementation is the photosynthetic machinery and the increase in total chlorophyll and carotenoid content reflects the enhanced photosynthetic efficiency in the presence of HC. The total proteins remain almost constant and no drastic changes were observed in HC of *M. gaditana*. The supplementation of CO_2 has been known to have a profound effect on the two energy rich storage molecules, lipids, and carbohydrates (Wang and Spalding, 2014). The lipid content of the oleaginous microalga *M. gaditana* increased by 1.3-fold in response to HC. Previous studies have demonstrated that excess of carbon will be directed toward lipid synthesis, suggesting the channelization of carbon toward acetyl-CoA in response to elevated concentration of CO_2 (Valenzuela et al., 2012; Sun et al., 2016). The increased amount of the FAMEs in response to carbon supplementation are higher due to conversion of CO_2 into acetyl CoA, which provides the precursor molecules for the biosynthesis of lipids. Also, the increased photosynthetic efficiency of *M. gaditana* under HC implies more assimilation of carbon photosynthetically, that could be redirected into neutral lipid biosynthesis (Renberg et al., 2010; Prathima Devi et al., 2012; Schuhmann et al., 2014). Due to oleaginous nature of the strain most of the carbon flux tends to divert toward lipids rather than carbohydrate production. Whereas in low CO_2 the strains prefer to synthesize low energy molecules, i.e., carbohydrates such as laminarin (Vogler et al., 2018).

The major strategy to increase the amount of non-polar triacylglycerols (TAGs) is limiting the concentration of nitrogen and/or phosphate in the medium; however, a minimal

concentration of the carbon should be maintained in the medium, as it is an indispensable substrate for the biosynthesis of relevant biomolecules (Spalding, 2008). Therefore, one of the common solutions that can be implied here will be removal and/or presence of minimal nutrients with increased levels of inorganic carbon in the medium. This will enhance the overall lipid productivities in many microalgal species (Sharma et al., 2012). The combined effect of nutrient deficiency and inorganic carbon supplementation has been employed earlier to enhance the lipid productivity in *C. reinhardtii*, *Scenedesmus obtusiusculus*, and *Chlorococcum littorale* (Toledo-Cervantes et al., 2013; Fields et al., 2014; Singh and Singh, 2014). Numerous studies have examined lipid accumulation in green algae for cells grown under the presence of a variety of stress conditions such as nitrogen, sulfur, phosphorus, or iron deprivation. Wase et al. employed omics technologies to detect key variations in the metabolic networks and regulatory components that contribute to lipid biosynthesis (Wase et al., 2014; Wase et al., 2019). The total FAME production in *M. gaditana* showed a substantial increase starting from 3rd day onward. However, the overall FAME content may vary when subjected to HC conditions. With supplementation of the inorganic carbon, the FAME profiles in *M. gaditana* increased substantially with the accumulation of up to nearly 30% (dcw) neutral lipids on the 9th day.

Our preliminary data using qualitative metabolomics suggests increase in the acetate levels when subjected to HC condition, eventually leading to the fatty acid biosynthesis. Studies have shown that increase in acetate concentration may lead to elevated activity of pyruvate dehydrogenase (PDH), the enzyme that bridges the glycolysis and lipid biosynthesis pathways within the plastids (Sun et al., 2016). Also, previous studies have demonstrated that the inhibition of PDH blocks lipid production in *C. sorokiniana* whereas silencing of PDH kinase (negative regulator of PDH) in *N. salina* enhances TAG biosynthesis (Sun et al., 2016; Ma et al., 2017). Henceforth, increase in acetate concentration and synergetic activity of PDH may be responsible for the overall increase in the total FAME content, when supplemented with higher CO_2 (30,000 ppm). The FAME profile depicts a unique pattern in *M. gaditana* showing maximum PUFA content and later rapidly declines in response to very-low level CO_2 suggesting the inhibition of the desaturase activity in the lipid metabolism. However, when exposed to HC, the increased photosynthetic efficiency resulted in increased pool of NADPH and evolution of O_2 which is required for the desaturase enzyme in the biosynthesis of polyunsaturated fatty acids, and hence, there is increase in linoleic acid and linolenic acid contents. Overall, the dynamics of the biochemical parameters such as chlorophyll and lipid molecules suggest the diversion of the carbon fixation and assimilation pathways favoring enhanced photosynthetic efficiency.

The schematics of compartmentalization along with gene editing have a huge impact on the metabolic capabilities of microalgal cells in diverting the carbon flux *via* alternative routes (Ginger et al., 2010; Martin, 2010; Hildebrand et al., 2013). Proteomic approaches have been known to be powerful; however, it has been reported that the metabolic flux cannot be associated with the concentration of proteins inside the cell (Villiers et al., 2011). There have been a numerous reports depicting the importance of metabolomic approach to unravel the mechanism of biological processes in response to several factors (such as nitrogen deficiency, iron deficiency, etc.) in plant systems (Rellán-Álvarez et al., 2010; Zhang et al., 2010; Osorio et al., 2011; Weckwerth, 2011; Amiour et al., 2012). To illustrate the different diversion routes of carbon flux in VLC and HC, the relative abundances of the metabolite profiles were analyzed. Overall, a total number of 31 metabolites were obtained in *M. gaditana* when subjected to VLC and HC, with few metabolites that were common in both the conditions. Primary sugars such as glucose, galactose, trehalose, etc., demonstrated highest variation in the metabolomic profiles in VLC. When the metabolome profile of VLC is compared with HC, the accumulation of glucose, trehalose and galactose indicate a constitutive carbohydrate metabolism in VLC conditions. Trehalose, a non-reducing disaccharide is known to be a stabilizing agent for protecting the membranes against impairment, and help retain cellular integrity (Wase et al., 2014; Agarwal et al., 2019b). Increase in the level of maltose was observed which acts as a transitory product of carbohydrate metabolism that is reported to be produced as a result of the starch breakdown machinery (Weise et al., 2005). Increase in maltose levels also indicate the onset of photo-respiratory conditions, which explains the low Fv/Fm ratio of the cells under VLC (Weise et al., 2006). Also, the biochemical profile of *M. gaditana* indicate that the carbohydrate production increases in VLC which is in strong co-relation with the metabolome profile. It has been observed that the amino acids being the primary constituents for the protein synthesis are significantly increasing. But these amino acids have several secondary functions under tightly controlled steady state levels such as functioning as signaling molecules and precursors for the biosynthesis of phytohormones and secondary metabolites (Hildebrandt et al., 2015). As a result, the increase in the amino acids in HC is not reflected in the total protein content. Amino acids such as proline, valine, and alanine show an increase in their accumulation under HC, wherein, proline is seen to be accumulated under stress conditions and is also reported to maintain the osmoregulation inside the cell (Hayat et al., 2012). Also, no change in overall protein content suggests that the normal expression of the native proteins is sufficient to perform the metabolic reactions.

It has also been observed that the accumulation of α-tocopherol increases in cells supplemented with CO_2 with increased production of lipids during HC condition. The increase in lipid production in HC on the 9th day can also be attributed to the presence of α-tocopherol since it has been reported to be inhibiting lipid degradation. It has been shown that tocopherols protect the dormant and germinating seeds in *A. thaliana* against oxidative degradation of lipids (Sakuragi et al., 2006). The elevated levels of α-tocopherol in the chloroplast membranes can also be associated to the ability of tocopherols to quench ROS, hence protecting the photosynthetic

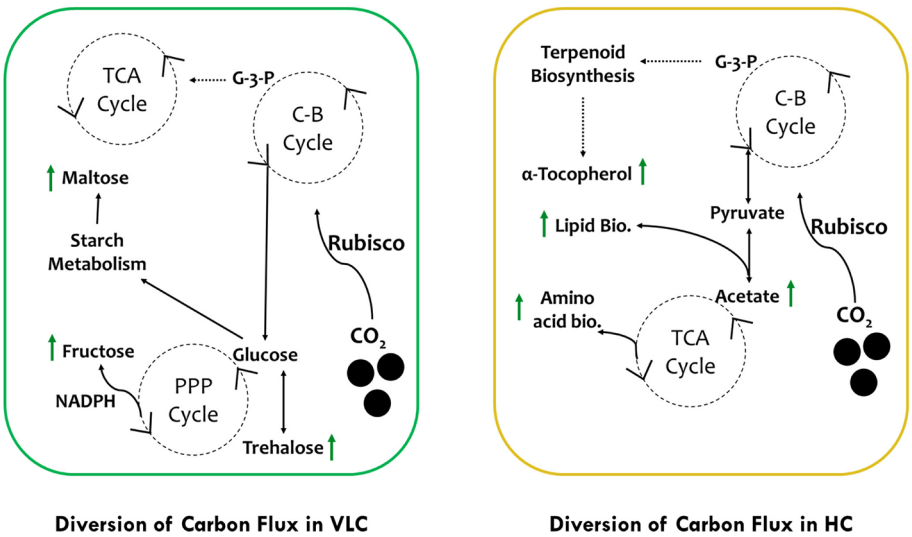

FIGURE 5 | Schematic representation of photosynthetic carbon partitioning and metabolic regulation routes of carbon flux subjected to VLC and HC supplementation in *M. gaditana*.

apparatus from oxygen toxicity (Fachechi et al., 2007). It is also reported to be involved in the regulation of photosynthesis and macronutrient uptake and utilization (Sakuragi et al., 2006; Fritsche et al., 2017; Shaikh et al., 2019). The upregulation of propionic acid in HC is in correlation with the presence of valine, which is shown to be involved in the synthesis of succinyl coA, an intermediate in the TCA cycle in photosynthetic organisms (Pan et al., 2017). Consequently, the carbon flux is diverted toward lipid biosynthesis through the TCA cycle. Acetic acid is the precursor of TCA cycle, which further drives the fatty acid biosynthesis. The upregulation of acetic acid during HC along with several fatty acids such as stearic acid, propionic acid, palmitic acid, linoleic and arachidic acids, indicates that HC promotes the growth of the cell as well as the production of energy storage molecules, i.e., lipids.

In conclusion, we would like to hypothesize two separate pathways of carbon flux in VLC and HC (**Figure 5**). In VLC, the carbon flux inside the cells is diverted in such a way that carbohydrate metabolism functions in a constitutive manner, generating the energy currency through the pentose phosphate pathway leading to starch breakdown and formation of maltose. In HC, the TCA cycle is upregulated further diverting the carbon flux toward lipid biosynthesis. Moreover, pyrenoid lacking microalgae such as *Pavlova lutheri* have higher amount of Rubisco (Heureux et al., 2017). In *Microchloropsis gaditana*, which also lacks pyrenoid, this enhanced Rubisco may help in assimilation of more carbon at HC that is partitioned toward growth and lipid biosynthesis as observed in the current study. Overall, our preliminary data analysis on supplementation of CO_2 provides interesting out comes, i.e., in VLC we presume that CCMs are active and leading to accumulation of carbohydrates or/and lipids without compromising growth whereas in HC, CCMs may be inactive or lower in their activities but overall supplementation of higher CO_2 will enhance productivities in biomass, biofuels, and biorenewables (B3) in *M. gaditana*. In conclusion, based on these preliminary data we would further try to evaluate the role of CCMs and its relation to Rubisco in *M. gaditana* employing multiomics approach to provide insights on the targets responsible for photosynthetic carbon partitioning and metabolic regulation in these green cell factories.

DATA AVAILABILITY STATEMENT

This data is available at the NIH Common Fund's National Metabolomics Data Repository (NMDR) website, the Metabolomics Workbench, https://www.metabolomicsworkbench.org, where it has been assigned Project: PR000893, Study ID: ST001395. The data can be accessed directly *via* its Project DOI: 10.21228/M8869V. This work is supported by Department of Biotechnology (DBT), India grant BT/PB/Center/03/2011.

AUTHOR CONTRIBUTIONS

MK, AN, and PJ designed the experiment. MK, IM, and KS executed the experiments. AN and PJ supervised the project. MK, IM, and AN wrote the manuscript with all the input from the authors. All authors contributed to the article and approved the submitted version.

FUNDING

The work was supported by the grants from the Department of Biotechnology, Government of India, to PJ (Sanction No. BT/PB/Center/03/2011) and to AN (BioCARe Scheme No. BT/

PR18491/BIC/101/759/2016). Senior Research Fellowship to MK, IM, and KS from the Department of Biotechnology and University Grants Commission (UGC), Government of India, is duly acknowledged.

ACKNOWLEDGMENTS

We would like to thank Mr. Girish H. Rajacharya (Technical Manager, ICGEB) for providing support with analytical instrumentation.

REFERENCES

Adamczyk, M., Lasek, J., and Skawinska, A. (2016). CO_2 biofixation and growth kinetics of *Chlorella vulgaris* and *Nannochloropsis gaditana*. *Appl. Biochem. Biotechnol.* 179, 1248–1261. doi: 10.1007/s12010-016-2062-3

Agarwal, A., Patil, S., Gharat, K., Pandit, R. A., and Lali, A. M. (2019a). Modulation in light utilization by a microalga *Asteracys* sp. under mixotrophic growth regimes. *Photosynth. Res.* 139, 553–567. doi: 10.1007/s11120-018-0526-8

Agarwal, A., Shaikh, K. M., Gharat, K., Jutur, P. P., Pandit, R. A., and Lali, A. M. (2019b). Investigating the modulation of metabolites under high light in mixotrophic alga *Asteracys* sp. using a metabolomic approach. *Algal Res.* 43, 101646. doi: 10.1016/j.algal.2019.101646

Alboresi, A., Perin, G., Vitulo, N., Diretto, G., Block, M., Jouhet, J., et al. (2016). Light remodels lipid biosynthesis in *Nannochloropsis gaditana* by modulating carbon partitioning between organelles. *Plant Physiol.* 171, 2468–2482. doi: 10.1104/pp.16.00599

Amiour, N., Imbaud, S., Clément, G., Agier, N., Zivy, M., Valot, B., et al. (2012). The use of metabolomics integrated with transcriptomic and proteomic studies for identifying key steps involved in the control of nitrogen metabolism in crops such as maize. *J. Exp. Bot.* 63 (14), 5017–5033. doi: 10.1093/jxb/ers186

Ashwell, G. (1957). "Colorimetric analysis of sugars," in *Methods in Enzymology.* (New York, USA: Academic Press), 73–105.

Badger, M. R., Andrews, T. J., Whitney, S. M., Ludwig, M., Yellowlees, D. C., Leggat, W., et al. (1998). The diversity and coevolution of Rubisco, plastids, pyrenoids, and chloroplast-based CO_2-concentrating mechanisms in algae. *Can. J. Bot.* 76, 1052–1071. doi: 10.1139/cjb-76-6-1052

Baker, N. R. (2008). Chlorophyll fluorescence: a probe of photosynthesis *in vivo*. *Annu. Rev. Plant Biol.* 59, 89–113. doi: 10.1146/annurev.arplant.59.032607.092759

Beardall, J., and Raven, J. A. (2016). "Carbon Acquisition by Microalgae," in *The Physiology of Microalgae*. Eds. M. A. Borowitzka, J. Beardall and J. A. Raven (Cham: Springer International Publishing), 89–99.

Brown, M. R. (1991). The amino-acid and sugar composition of 16 species of microalgae used in mariculture. *J. Exp. Mar. Biol. Ecol.* 145, 79–99. doi: 10.1016/0022-0981(91)90007-J

Carlozzi, P. (2003). Dilution of solar radiation through culture lamination in photobioreactor rows facing south-north: A way to improve the efficiency of light utilization by cyanobacteria (*Arthrospira platensis*). *Biotechnol. Bioeng.* 81, 305–315. doi: 10.1002/bit.10478

Chang, H.-X., Huang, Y., Fu, Q., Liao, Q., and Zhu, X. (2016). Kinetic characteristics and modeling of microalgae *Chlorella vulgaris* growth and CO2 biofixation considering the coupled effects of light intensity and dissolved inorganic carbon. *Bioresour. Technol.* 206, 231–238. doi: 10.1016/j.biortech.2016.01.087

Chen, Y., and Vaidyanathan, S. (2013). Simultaneous assay of pigments, carbohydrates, proteins and lipids in microalgae. *Anal. Chim. Acta* 776, 31–40. doi: 10.1016/j.aca.2013.03.005

Chen, C.-Y., Yeh, K.-L., Aisyah, R., Lee, D.-J., and Chang, J.-S. (2011). Cultivation, photobioreactor design and harvesting of microalgae for biodiesel production: a critical review. *Bioresour. Technol.* 102, 71–81. doi: 10.1016/j.biortech.2010.06.159

Chinnasamy, S., Ramakrishnan, B., Bhatnagar, A., and Das, C. K. (2009). Biomass Production Potential of a Wastewater Alga Chlorella vulgaris ARC 1 under Elevated Levels of CO2 and Temperature. *Int. J. Mol. Sci.* 10 (2), 518–532. doi: 10.3390/ijms10020518

Chong, J., Soufan, O., Li, C., Caraus, I., Li, S., Bourque, G., et al. (2018). MetaboAnalyst 4.0: towards more transparent and integrative metabolomics analysis. *Nucleic Acids Res.* 46, W486–W494. doi: 10.1093/nar/gky310

Clement, R., Jensen, E., Prioretti, L., Maberly, S. C., and Gontero, B. (2017). Diversity of CO_2-concentrating mechanisms and responses to CO_2 concentration in marine and freshwater diatoms. *J. Exp. Bot.* 68, 3925–3935. doi: 10.1093/jxb/erx035

Davis, R., Aden, A., and Pienkos, P. T. (2011). Techno-economic analysis of autotrophic microalgae for fuel production. *Appl. Energy* 88, 3524–3531. doi: 10.1016/j.apenergy.2011.04.018

del Campo, J., Sieracki, M. E., Molestina, R., Keeling, P., Massana, R., and Ruiz-Trillo, I. (2014). The others: our biased perspective of eukaryotic genomes. *Trends Ecol. Evol.* 29, 252–259. doi: 10.1016/j.tree.2014.03.006

Duanmu, D., Miller, A. R., Horken, K. M., Weeks, D. P., and Spalding, M. H. (2009). Knockdown of limiting-CO_2-induced gene HLA3 decreases HCO_3^- transport and photosynthetic Ci affinity in *Chlamydomonas reinhardtii*. *Proc. Natl. Acad. Sci. U.S.A.* 106, 5990–5995. doi: 10.1073/pnas.0812885106

Duong, V. T., Thomas-Hall, S. R., and Schenk, P. M. (2015). Growth and lipid accumulation of microalgae from fluctuating brackish and sea water locations in South East Queensland-Australia. *Front. Plant Sci.* 6, 359. doi: 10.3389/fpls.2015.00359

Emerson, R., and Arnold, W. (1932). The photochemical reaction in photosynthesis. *J. Gen. Physiol.* 16, 191–205. doi: 10.1085/jgp.16.2.191

Fachechi, C., Nisi, R., Gala, R., Leone, A., and Caretto, S. (2007). Tocopherol biosynthesis is enhanced in photomixotrophic sunflower cell cultures. *Plant Cell Rep.* 26 (4), 525–530. doi: 10.1007/s00299-006-0268-5

Fawley, M. W., Jameson, I., and Fawley, K. P. (2015). The phylogeny of the genus *Nannochloropsis* (Monodopsidaceae, Eustigmatophyceae), with descriptions of *N. australis* sp. nov. and *Microchloropsis* gen. nov. *Phycologia* 54, 545–552. doi: 10.2216/15-60.1

Fields, M. W., Hise, A., Lohman, E. J., Bell, T., Gardner, R. D., Corredor, L., et al. (2014). Sources and resources: importance of nutrients, resource allocation, and ecology in microalgal cultivation for lipid accumulation. *Appl. Microbiol. Biotechnol.* 98, 4805–4816. doi: 10.1007/s00253-014-5694-7

Freeman Rosenzweig, E. S., Xu, B., Kuhn Cuellar, L., Martinez-Sanchez, A., Schaffer, M., Strauss, M., et al. (2017). The eukaryotic CO_2-concentrating organelle is liquid-like and exhibits dynamic reorganization. *Cell* 171, 148–162.e119. doi: 10.1016/j.cell.2017.08.008

Fritsche, S., Wang, X., and Jung, C. (2017). Recent advances in our understanding of tocopherol biosynthesis in plants: An overview of key genes, functions, and breeding of vitamin E improved crops. *Antioxid. (Basel)* 6, 99. doi: 10.3390/antiox6040099

Gee, C. W., and Niyogi, K. K. (2017). The carbonic anhydrase CAH1 is an essential component of the carbon-concentrating mechanism in *Nannochloropsis oceanica*. *Proc. Natl. Acad. Sci. U.S.A.* 114, 4537–4542. doi: 10.1073/pnas.1700139114

Geraghty, A. M., and Spalding, M. H. (1996). Molecular and structural changes in *Chlamydomonas* under limiting CO_2 (A possible mitochondrial role in adaptation). *Plant Physiol.* 111, 1339. doi: 10.1104/pp.111.4.1339

Ginger, M. L., McFadden, G. I., and Michels, P. A. (2010). Rewiring and regulation of cross-compartmentalized metabolism in protists. *Philos. Trans. R. Soc Lond. B Biol. Sci.* 365, 831–845. doi: 10.1098/rstb.2009.0259

Giordano, M., Beardall, J., and Raven, J. A. (2005). CO_2 concentrating mechanisms in algae: Mechanisms, environmental modulation, and evolution. *Annu. Rev. Plant Biol.* 56, 99–131. doi: 10.1146/annurev.arplant.56.032604.144052

Grieco, M., Tikkanen, M., Paakkarinen, V., Kangasjärvi, S., and Aro, E.-M. (2012). Steady-State Phosphorylation of Light-Harvesting Complex II Proteins Preserves Photosystem I under Fluctuating White Light. *Plant Physiol.* 160 (4), 1896. doi: 10.1104/pp.112.206466

Guillard, R. R., and Ryther, J. H. (1962). Studies of marine planktonic diatoms. I. *Cyclotella nana* Hustedt, and *Detonula confervacea* (cleve) Gran. *Can. J. Microbiol.* 8, 229–239. doi: 10.1139/m62-029

Guillard, R. R., and Sieracki, M. S. (2005). "Counting cells in cultures with the light microscope," in *Algal culturing techniques*. Ed. R. A. Andersen (London: Elsevier Academic Press), 239–252.

Hayat, S., Hayat, Q., Alyemeni, M. N., Wani, A. S., Pichtel, J., and Ahmad, A. (2012). Role of proline under changing environments: A review. *Plant Signal. Behav.* 7, 1456–1466. doi: 10.4161/psb.21949

Heureux, A., Young, J. N., Whitney, S. M., Eason-Hubbard, M. R., Lee, R., Sharwood, R. E., et al. (2017). The role of Rubisco kinetics and pyrenoid morphology in shaping the CCM of haptophyte microalgae. *J. Exp. Bot.* 68 (14), 3959–3969. doi: 10.1093/jxb/erx179

Heyduk, K., Moreno-Villena, J. J., Gilman, I. S., Christin, P.-A., and Edwards, E. J. (2019). The genetics of convergent evolution: Insights from plant photosynthesis. *Nat. Rev. Genet.* 20, 485–493. doi: 10.1038/s41576-019-0107-5

Hildebrand, M., Abbriano, R. M., Polle, J. E., Traller, J. C., Trentacoste, E. M., Smith, S. R., et al. (2013). Metabolic and cellular organization in evolutionarily diverse microalgae as related to biofuels production. *Curr. Opin. Chem. Biol.* 17, 506–514. doi: 10.1016/j.cbpa.2013.02.027

Hildebrandt, T. M., Nunes, N. A., Araújo, W. L., and Braun, H.-P. (2015). Amino Acid Catabolism in Plants. *Mol. Plant* 8 (11), 1563–1579. doi: 10.1016/j.molp.2015.09.005

Hirth, M., Liverani, S., Mahlow, S., Bouget, F. Y., Pohnert, G., and Sasso, S. (2017). Metabolic profiling identifies trehalose as an abundant and diurnally fluctuating metabolite in the microalga *Ostreococcus tauri*. *Metabolomics* 13, 68. doi: 10.1007/s11306-017-1203-1

Ho, S.-H., Chen, W.-M., and Chang, J.-S. (2010). *Scenedesmus obliquus* CNW-N as a potential candidate for CO_2 mitigation and biodiesel production. *Bioresour. Technol.* 101, 8725–8730. doi: 10.1016/j.biortech.2010.06.112

Hopkinson, B. M., Dupont, C. L., and Matsuda, Y. (2016). The physiology and genetics of CO2 concentrating mechanisms in model diatoms. *Curr. Opin. Plant Biol.* 31, 51–57. doi: 10.1016/j.pbi.2016.03.013

Hu, Q., Sommerfeld, M., Jarvis, E., Ghirardi, M., Posewitz, M., Seibert, M., et al. (2008). Microalgal triacylglycerols as feedstocks for biofuel production: Perspectives and advances. *Plant J.* 54, 621–639. doi: 10.1111/j.1365-313X.2008.03492.x

Husemann, W., and Barz, W. (1977). Photoautotrophic growth and photosynthesis in cell suspension cultures of *Chenopodium rubrum*. *Physiol. Plant* 40 (2), 77–81. doi: 10.1111/j.1399-3054.1977.tb01498.x

Jiang, L. L., Luo, S. J., Fan, X. L., Yang, Z. M., and Guo, R. B. (2011). Biomass and lipid production of marine microalgae using municipal wastewater and high concentration of CO_2. *Appl. Energy* 88, 3336–3341. doi: 10.1016/j.apenergy.2011.03.043

Lal, R. (2008). Carbon sequestration. *Philos. Trans. R. Soc Lond. B Biol. Sci.* 363, 815–830. doi: 10.1098/rstb.2007.2185

Le Quere, C., Andres, R., Boden, T., Conway, T., Houghton, R., House, J., et al. (2013). The global carbon budget, (1959-2011). *Earth Syst. Sci. Data* 5, 165–185. doi: 10.5194/essd-5-165-2013

Lee, Y. H., and Sun, J. H. (2019). Multifunctional fluorocarbon photobioreactor system: A novel integrated device for CO_2 segregation, O_2 collection, and enhancement of microalgae growth and bioproductions. *Bioprocess Biosyst. Eng.* 42, 1591–1601. doi: 10.1007/s00449-019-02156-z

Levasseur, M., Thompson, P. A., and Harrison, P. J. (1993). Physiological acclimation of marine phytoplankton to different nitrogen sources 1. *J. Phycol.* 29 (5), 587–595. doi: 10.1111/j.0022-3646.1993.00587.x

Lichtenthaler, H. K., and Wellburn, A. R. (1983). Determinations of total carotenoids and chlorophylls a and b of leaf extracts in different solvents. *Biochem. Soc Trans.* 11, 591–592. doi: 10.1042/bst0110591

Long, B. M., Rae, B. D., Rolland, V., Förster, B., and Price, G. D. (2016). Cyanobacterial CO_2-concentrating mechanism components: Function and prospects for plant metabolic engineering. *Curr. Opin. Plant Biol.* 31, 1–8. doi: 10.1016/j.pbi.2016.03.002

Lu, C., and Vonshak, A. (2002). Effects of salinity stress on photosystem II function in cyanobacterial *Spirulina platensis* cells. *Physiol. Plant* 114 (3), 405–413. doi: 10.1034/j.1399-3054.2002.1140310.x

Ma, X., Yao, L., Yang, B., Lee, Y. K., Chen, F., and Liu, J. (2017). RNAi-mediated silencing of a pyruvate dehydrogenase kinase enhances triacylglycerol biosynthesis in the oleaginous marine alga *Nannochloropsis salina*. *Sci. Rep.* 7 (1), 11485. doi: 10.1038/s41598-017-11932-4

Mackinder, L. C. M., Chen, C., Leib, R. D., Patena, W., Blum, S. R., Rodman, M., et al. (2017). A Spatial Interactome Reveals the Protein Organization of the Algal CO_2-Concentrating Mechanism. *Cell* 171 (1), 133–147.e114. doi: 10.1016/j.cell.2017.08.044

Martin, W. (2010). Evolutionary origins of metabolic compartmentalization in eukaryotes. *Philos. Trans. R. Soc Lond. B Biol. Sci.* 365, 847–855. doi: 10.1098/rstb.2009.0252

Mata, T. M., Martins, A. A., and Caetano, N. S. (2010). Microalgae for biodiesel production and other applications: A review. *Renew. Sustain. Energy Rev.* 14, 217–232. doi: 10.1016/j.rser.2009.07.020

Maxwell, K., and Johnson, G. N. (2000). Chlorophyll fluorescence–a practical guide. *J. Exp. Bot.* 51 (345), 659–668. doi: 10.1093/jxb/51.345.659

Meyer, M., and Griffiths, H. (2013). Origins and diversity of eukaryotic CO_2-concentrating mechanisms: lessons for the future. *J. Exp. Bot.* 64, 769–786. doi: 10.1093/jxb/ers390

Mishra, S. K., Suh, W. I., Farooq, W., Moon, M., Shrivastav, A., Park, M. S., et al. (2014). Rapid quantification of microalgal lipids in aqueous medium by a simple colorimetric method. *Bioresour. Technol.* 155, 330–333. doi: 10.1016/j.biortech.2013.12.077

Mistry, A. N., Ganta, U., Chakrabarty, J., and Dutta, S. (2019). A review on biological systems for CO_2 sequestration: Organisms and their pathways. *Environ. Prog. Sustain. Energy* 38, 127–136. doi: 10.1002/ep.12946

Mujtaba, G., Choi, W., Lee, C. G., and Lee, K. (2012). Lipid production by *Chlorella vulgaris* after a shift from nutrient-rich to nitrogen starvation conditions. *Bioresour. Technol.* 123, 279–283. doi: 10.1016/j.biortech.2012.07.057

Ng, C. W. W., Tasnim, R., Capobianco, V., and Coo, J. L. (2018). Influence of soil nutrients on plant characteristics and soil hydrological responses. *Géotech. Lett.* 8, 19–24. doi: 10.1680/jgele.17.00104

Osorio, S., Alba, R., Damasceno, C. M. B., Lopez-Casado, G., Lohse, M., Zanor, M. I., et al. (2011). Systems Biology of Tomato Fruit Development: Combined Transcript, Protein, and Metabolite Analysis of Tomato Transcription Factor (nor, rin) and Ethylene Receptor (Nr) Mutants Reveals Novel Regulatory Interactions. *Plant Physiol.* 157 (1), 405. doi: 10.1104/pp.111.175463

Pan, Y., Yang, J., Gong, Y., Li, X., and Hu, H. (2017). 3-Hydroxyisobutyryl-CoA hydrolase involved in isoleucine catabolism regulates triacylglycerol accumulation in *Phaeodactylum tricornutum*. *Philos. Trans. R. Soc Lond. B Biol. Sci.* 372 (1728), 20160409. doi: 10.1098/rstb.2016.0409

Poliner, E., Farre, E. M., and Benning, C. (2018). Advanced genetic tools enable synthetic biology in the oleaginous microalgae *Nannochloropsis* sp. *Plant Cell Rep.* 37 (10), 1383–1399. doi: 10.1007/s00299-018-2270-0

Prathima Devi, M., Venkata Subhash, G., and Venkata Mohan, S. (2012). Heterotrophic cultivation of mixed microalgae for lipid accumulation and wastewater treatment during sequential growth and starvation phases: Effect of nutrient supplementation. *Renew. Energy* 43, 276–283. doi: 10.1016/j.renene.2011.11.021

Ramazanov, Z., Rawat, M., Henk, M. C., Mason, C. B., Matthews, S. W., and Moroney, J. V. (1994). The induction of the CO_2-concentrating mechanism is correlated with the formation of the starch sheath around the pyrenoid of *Chlamydomonas reinhardtii*. *Planta* 195, 210–216. doi: 10.1007/BF00199681

Ratha, S. K., and Prasanna, R. (2012). Bioprospecting microalgae as potential sources of Green Energy-Challenges and perspectives (Review). *Appl. Biochem. Micro.* 48, 109–125. doi: 10.1134/s000368381202010x

Raven, J. A., Cockell, C. S., and De La Rocha, C. L. (2008). The evolution of inorganic carbon concentrating mechanisms in photosynthesis. *Philos. Trans. R. Soc Lond. B Biol. Sci.* 363, 2641–2650. doi: 10.1098/rstb.2008.0020

Reinfelder, J. R. (2011). Carbon concentrating mechanisms in eukaryotic marine phytoplankton. *Ann. Rev. Mar. Sci.* 3, 291–315. doi: 10.1146/annurev-marine-120709-142720

Rellán-Álvarez, R., Andaluz, S., Rodríguez-Celma, J., Wohlgemuth, G., Zocchi, G., Álvarez-Fernández, A., et al. (2010). Changes in the proteomic and metabolic profiles of Beta vulgaris root tips in response to iron deficiency and resupply. *BMC Plant Biol.* 10 (1), 120. doi: 10.1186/1471-2229-10-120

Renberg, L., Johansson, A. I., Shutova, T., Stenlund, H., Aksmann, A., Raven, J. A., et al. (2010). A metabolomic approach to study major metabolite changes during acclimation to limiting CO_2 in *Chlamydomonas reinhardtii*. *Plant Physiol.* 154, 187–196. doi: 10.1104/pp.110.157651

Rittmann, B. E. (2008). Opportunities for renewable bioenergy using microorganisms. *Biotechnol. Bioeng.* 100, 203–212. doi: 10.1002/bit.21875

Rym, B. D. (2012). Photosynthetic behavior of microalgae in response to environmental factors. In: M. Najafpour *Applied Photosynthesis* (Rijeka: IntechOpen). 23–46. doi: 10.5772/27944

Sakuragi, Y., Maeda, H., Dellapenna, D., and Bryant, D. A. (2006). alpha-Tocopherol plays a role in photosynthesis and macronutrient homeostasis of the cyanobacterium *Synechocystis* sp. PCC 6803 that is independent of its antioxidant function. *Plant Physiol.* 141, 508–521. doi: 10.1104/pp.105.074765

Schädler, T., Caballero Cerbon, D., de Oliveira, L., Garbe, D., Brück, T., and Weuster-Botz, D. (2019). Production of lipids with *Microchloropsis salina* in open thin-layer cascade photobioreactors. *Bioresour. Technol.* 289, 121682. doi: 10.1016/j.biortech.2019.121682

Schneegurt, M. A., Sherman, D. M., Nayar, S., and Sherman, L. A. (1994). Oscillating behavior of carbohydrate granule formation and dinitrogen

fixation in the cyanobacterium *Cyanothece* sp. strain ATCC 51142. *J. Bacteriol.* 176, 1586–1597. doi: 10.1128/jb.176.6.1586-1597.1994

Schreiber, U., and Klughammer, C. (2008). Non-photochemical fluorescence quenching and quantum yields in PS I and PS II: analysis of heat-induced limitations using Maxi-Imaging PAM and Dual-PAM-100. *PAM Appl. Notes* 1. 15–18.

Schuhmann, H., Lim, D. K. Y., and Schenk, P. M. (2014). Perspectives on metabolic engineering for increased lipid contents in microalgae. *Biofuels* 3, 71–86. doi: 10.4155/bfs.11.147

Sforza, E., Simionato, D., Giacometti, G. M., Bertucco, A., and Morosinotto, T. (2012). Adjusted light and dark cycles can optimize photosynthetic efficiency in algae growing in photobioreactors. *PloS One* 7, e38975. doi: 10.1371/journal.pone.0038975

Shaikh, K. M., Nesamma, A. A., Abdin, M. Z., and Jutur, P. P. (2019). Molecular profiling of an oleaginous trebouxiophycean alga *Parachlorella kessleri* subjected to nutrient deprivation for enhanced biofuel production. *Biotechnol. Biofuels* 12, 182. doi: 10.1186/s13068-019-1521-9

Sharma, K. K., Schuhmann, H., and Schenk, P. M. (2012). High lipid induction in microalgae for biodiesel production. *Energies* 5, 1532–1553. doi: 10.3390/en5051532

Singh, A. K., and Singh, M. (2014). Importance of algae as a potential source of biofuel. *Cell. Mol. Biol.* 60, 106–109. doi: 10.14715/cmb/2014.60.5.17

Sluiter, A., Hames, B., Hyman, D., Payne, C., Ruiz, R., Scarlata, C., et al. (2008). "Determination of total solids in biomass and total dissolved solids in liquid process samples," in *National Renewable Energy Laboratory*. Golden, CO, NREL Technical Report No. NREL/TP-510-42621, 1-6. Available at: http://purl.access.gpo.gov/GPO/LPS94120

Smith, R. T., Bangert, K., Wilkinson, S. J., and Gilmour, D. J. (2015). Synergistic carbon metabolism in a fast growing mixotrophic freshwater microalgal species *Micractinium inermum*. *Biomass Bioenerg.* 82, 73–86. doi: 10.1016/j.biombioe.2015.04.023

Spalding, M. H. (2008). Microalgal carbon dioxide-concentrating mechanisms: *Chlamydomonas* inorganic carbon transporters. *J. Exp. Bot.* 59, 1463–1473. doi: 10.1093/jxb/erm128

Sun, Z., Chen, Y. F., and Du, J. (2016). Elevated CO_2 improves lipid accumulation by increasing carbon metabolism in *Chlorella sorokiniana*. *Plant Biotechnol. J.* 14 (2), 557–566. doi: 10.1111/pbi.12398

Toledo-Cervantes, A., Morales, M., Novelo, E., and Revah, S. (2013). Carbon dioxide fixation and lipid storage by *Scenedesmus obtusiusculus*. *Bioresour. Technol.* 130, 652–658. doi: 10.1016/j.biortech.2012.12.081

Valenzuela, J., Mazurie, A., Carlson, R. P., Gerlach, R., Cooksey, K. E., Peyton, B. M., et al. (2012). Potential role of multiple carbon fixation pathways during lipid accumulation in *Phaeodactylum tricornutum*. *Biotechnol. Biofuels* 5, 40. doi: 10.1186/1754-6834-5-40

Vance, P., and Spalding, M. H. (2005). Growth, photosynthesis, and gene expression in *Chlamydomonas* over a range of CO_2 concentrations and CO_2/O_2 ratios: CO_2 regulates multiple acclimation states. *Can. J. Bot.* 83 (7), 796–809. doi: 10.1139/b05-064

Varfolomeev, S. D., and Wasserman, L. A. (2011). Microalgae as source of biofuel, food, fodder, and medicines. *Appl. Biochem. Micro.* 47, 789–807. doi: 10.1134/s0003683811090079

Villiers, F., Ducruix, C., Hugouvieux, V., Jarno, N., Ezan, E., Garin, J., et al. (2011). Investigating the plant response to cadmium exposure by proteomic and metabolomic approaches. *Proteomics* 11 (9), 1650–1663. doi: 10.1002/pmic.201000645

Vogler, B. W., Brannum, J., Chung, J. W., Seger, M., and Posewitz, M. C. (2018). Characterization of the *Nannochloropsis gaditana* storage carbohydrate: A 1,3-beta glucan with limited 1,6-branching. *Algal Res.* 36, 152–158. doi: 10.1016/j.algal.2018.10.011

Wang, Y., and Spalding, M. H. (2006). An inorganic carbon transport system responsible for acclimation specific to air levels of CO_2 in *Chlamydomonas reinhardtii*. *Proc. Natl. Acad. Sci. U. S. A.* 103, 10110–10115. doi: 10.1073/pnas.0603402103

Wang, Y., and Spalding, M. H. (2014). Acclimation to very low CO_2: contribution of limiting CO_2 inducible proteins, LCIB and LCIA, to inorganic carbon uptake in *Chlamydomonas reinhardtii*. *Plant Physiol.* 166, 2040–2050. doi: 10.1104/pp.114.248294

Wang, H.-M., Pan, J.-L., Chen, C.-Y., Chiu, C.-C., Yang, M.-H., Chang, H.-W., et al. (2010). Identification of anti-lung cancer extract from *Chlorella vulgaris* CC by antioxidant property using supercritical carbon dioxide extraction. *Process Biochem.* 45, 1865–1872. doi: 10.1016/j.procbio.2010.05.023

Wang, Y., Stessman, D. J., and Spalding, M. H. (2015). The CO_2 concentrating mechanism and photosynthetic carbon assimilation in limiting CO_2 : how *Chlamydomonas* works against the gradient. *Plant J.* 82 (3), 429–448. doi: 10.1111/tpj.12829

Wase, N., Black, P. N., Stanley, B. A., and DiRusso, C. C. (2014). Integrated Quantitative Analysis of Nitrogen Stress Response in *Chlamydomonas reinhardtii* Using Metabolite and Protein Profiling. *J. Proteome Res.* 13 (3), 1373–1396. doi: 10.1021/pr400952z

Wase, N., Tu, B., Allen, J. W., Black, P. N., and DiRusso, C. C. (2017). Identification and Metabolite Profiling of Chemical Activators of Lipid Accumulation in Green Algae. *Plant Physiol.* 174 (4), 2146–2165. doi: 10.1104/pp.17.00433

Wase, N., Tu, B., Rasineni, G. K., Cerny, R., Grove, R., Adamec, J., et al. (2019). Remodeling of *Chlamydomonas* Metabolism Using Synthetic Inducers Results in Lipid Storage during Growth. *Plant Physiol.* 181 (3), 1029. doi: 10.1104/pp.19.00758

Weckwerth, W. (2011). Green systems biology — From single genomes, proteomes and metabolomes to ecosystems research and biotechnology. *J. Proteomics* 75 (1), 284–305. doi: 10.1016/j.jprot.2011.07.010

Wei, L., El Hajjami, M., Shen, C., You, W., Lu, Y., Li, J., et al. (2019). Transcriptomic and proteomic responses to very low CO_2 suggest multiple carbon concentrating mechanisms in *Nannochloropsis oceanica*. *Biotechnol. Biofuels* 12, 168. doi: 10.1186/s13068-019-1506-8

Weise, S. E., Kim, K. S., Stewart, R. P., and Sharkey, T. D. (2005). Beta-Maltose Is the Metabolically Active Anomer of Maltose during Transitory Starch Degradation. *Plant Physiol.* 137 (2), 756. doi: 10.1104/pp.104.055996

Weise, S. E., Schrader, S. M., Kleinbeck, K. R., and Sharkey, T. D. (2006). Carbon balance and circadian regulation of hydrolytic and phosphorolytic breakdown of transitory starch. *Plant Physiol.* 141, 879–886. doi: 10.1104/pp.106.081174

Wong, Y. K., Ho, K. C., Lai, P. K., Leung, C. C., Ho, Y. M., Lee, O. K., et al. (2013). "A Study on Algal Growth Behaviour under Different Sparing Period of CO2 Supplementation," in *1st Int. Conf. Benef. Uses Algal Biomass* (Hong Kong: (ICBUAB 2013)).

Yamano, T., Sato, E., Iguchi, H., Fukuda, Y., and Fukuzawa, H. (2015). Characterization of cooperative bicarbonate uptake into chloroplast stroma in the green alga *Chlamydomonas reinhardtii*. *Proc. Natl. Acad. Sci. U.S.A.* 112, 7315–7320. doi: 10.1073/pnas.1501659112

Zeng, N. (2008). Carbon sequestration via wood burial. *Carbon Balance Manage.* 3, 1. doi: 10.1186/1750-0680-3-1

Zhang, B., Tolstikov, V., Turnbull, C., Hicks, L. M., and Fiehn, O. (2010). Divergent metabolome and proteome suggest functional independence of dual phloem transport systems in cucurbits. *Proc. Natl. Acad. Sci. U.S.A.* 107 (30), 13532. doi: 10.1073/pnas.0910558107

Zhao, L. S., Li, K., Wang, Q. M., Song, X. Y., Su, H. N., Xie, B. B., et al. (2017). Nitrogen starvation impacts the photosynthetic performance of *Porphyridium cruentum* as revealed by chlorophyll a fluorescence. *Sci. Rep.* 7, 8542. doi: 10.1038/s41598-017-08428-6

Zhou, Y., Schideman, L. C., Park, D. S., Stirbet, A., Govindjee, Rupassara, S. I., et al. (2015). Characterization of a *Chlamydomonas reinhardtii* mutant strain with improved biomass production under low light and mixotrophic conditions. *Algal Res.* 11, 134–147. doi: 10.1016/j.algal.2015.06.001

Conflict of Interest: The authors declare that the research was conducted in the absence of any commercial or financial relationships that could be construed as a potential conflict of interest.

frontiers in Plant Science

ORIGINAL RESEARCH
published: 28 August 2020
doi: 10.3389/fpls.2020.544827

Identification and Biotechnical Potential of a Gcn5-Related N-Acetyltransferase Gene in Enhancing Microalgal Biomass and Starch Production

Zhongze Li[1,2†], Li Cao[1†], Liang Zhao[1], Lihua Yu[1], Yi Chen[1,2], Kang-sup Yoon[1], Qiang Hu[1,3,4,5,6] and Danxiang Han[1,5,6]*

[1] Center for Microalgal Biotechnology and Biofuels, Institute of Hydrobiology, Chinese Academy of Sciences, Wuhan, China, [2] College of Life Sciences, University of Chinese Academy of Sciences, Beijing, China, [3] Laboratory for Marine Biology and Biotechnology, Qingdao National Laboratory for Marine Science and Technology, Qingdao, China, [4] State Key Laboratory of Freshwater Ecology and Biotechnology, Institute of Hydrobiology, Chinese Academy of Sciences, Wuhan, China, [5] Key Laboratory for Algal Biology, Institute of Hydrobiology, Chinese Academy of Sciences, Wuhan, China, [6] The Innovative Academy of Seed Design, Chinese Academy of Sciences, Beijing, China

OPEN ACCESS

Edited by:
Lutz Wobbe,
Bielefeld University, Germany

Reviewed by:
Gilles Peltier,
CEA Cadarache, France
Claire Remacle,
University of Liège, Belgium

***Correspondence:**
Danxiang Han
danxianghan@ihb.ac.cn

[†]These authors have contributed equally to this work

Specialty section:
This article was submitted to Plant Biotechnology, a section of the journal Frontiers in Plant Science

Received: *22 March 2020*
Accepted: *12 August 2020*
Published: *28 August 2020*

Citation:
Li Z, Cao L, Zhao L, Yu L, Chen Y, Yoon K-s, Hu Q and Han D (2020) Identification and Biotechnical Potential of a Gcn5-Related N-Acetyltransferase Gene in Enhancing Microalgal Biomass and Starch Production. Front. Plant Sci. 11:544827. doi: 10.3389/fpls.2020.544827

Microalgae are promising feedstocks for starch production, which are precursors for bioenergy and chemicals manufacturing. Though starch biosynthesis has been intensively studied in the green alga *Chlamydomonas reinhardtii*, regulatory mechanisms governing starch metabolism in this model species have remained largely unknown to date. We proposed that altering triacylglycerol (TAG) biosynthesis may trigger intrinsic regulatory pathways governing starch metabolism. In accordance with the hypothesis, it was observed in this study that overexpression of the plastidial lysophosphatidic acid acyltransferase gene (i.e. *LPAAT1*) in *C. reinhardtii* significantly enhanced TAG biosynthesis under nitrogen (N)-replete conditions, whereas the starch biosynthesis was enhanced in turn under N depletion. By the exploitation of transcriptomics analysis, a putative regulatory gene coding Gcn5-related N-acetyltransferase (*GNAT19*) was identified, which was up-regulated by 11–12 times in the *CrLPAAT1* OE lines. Overexpression of the cloned full-length *CrGNAT19* cDNA led to significant increase in the starch content of *C. reinhardtii* cells grown under both N-replete and N-depleted conditions, which was up to 4 times and 26.7% higher than that of the empty vector control, respectively. Moreover, the biomass yield of the *CrGNAT19* OE lines reached 1.5 g L^{-1} after 2 days under N-depleted conditions, 72% higher than that of the empty vector control (0.87 g L^{-1}). Overall, the yield of starch increased by 118.5% in *CrGNAT19* OE lines compared to that of the control. This study revealed the great biotechnical potentials of an unprecedented *GNAT19* gene in enhancing microalgal starch and biomass production.

Keywords: starch, biomass, carbon partitioning, Gcn5-related N-acetyltransferase gene, *Chlamydomonas reinhardtii*

INTRODUCTION

Many unicellular green algae can store carbon in the form of starch under adverse environmental conditions, such as high light and nutrient starvation (Ball et al., 1990). Microalgae are considered as promising feedstocks for producing starch, which can be used for bioethnol and chemicals manufacturing (Brányiková et al., 2011; Pancha et al., 2019a). However, regulatory mechanisms governing starch metabolism in microalgae have remained largely unknown to date, which is impeding development of rational genetic engineering strategy for enhancing starch production in these highly efficient photosynthetic cell factories.

Biochemical process of starch biosynthesis is conserved among most green algae and plants (Ball and Morell, 2003). The ADP-glucose pyrophosphorylase (AGPase, EC 2.7.7.23) is the first committed enzyme that catalyzes the formation of ADP-glucose, the nucleotide sugar donor for starch biosynthesis, from Glc-1-P and ATP in the chloroplasts. The formed ADP-glucose is then utilized by starch synthase (SS, EC: 2.4.1.21) as the building block to form the linear sugar polymers with more or less branches. Two types of SS have been identified, which are designated as soluble SS and granule-bound SS (GBSS). The soluble SS is generally believed to be responsible for synthesis of amylopectin, a type of highly branched starch molecules that constitute the major component of starch granules in green algae and plants. The GBSS is involved in biosynthesis of amylose, which is less branched starch molecules and is the minor component of starch granules. Synthesis of α-(1,6) branches in amylopectin is mediated by the starch branching enzyme (SBE, EC: 2.4.1.18), which hydrolyzes the α-(1,4) linkage and then catalyzes the formation of α-(1,6) linkage between the reducing end of the cut glucan and another glucosyl moiety of ADP-glucose. Debranching enzymes (DBE), including isoamylase (ISA, EC: 3.2.1.68) and limit-dextrinase (LDA, EC: 3.2.1.142), are involved in cleaving the branch points of amylopectin molecules, which play important role in shaping the structure of starch molecules.

In microalgae, degradation of starch not only occurs in dark to provide sugars for sustaining cellular metabolism and growth, but also plays an essential role in starch turnover under adverse environmental conditions, which can provide carbon skeleton for lipid biosynthesis (Roessler, 1988). Degradation of starch is initiated by the hydrolysis of sugar polymers on the surface of starch granules. The only enzyme has the capability to catalyze the reaction in such a solid region is the α-amylase (AMY, EC: 3.2.1.1), though the direct evidence for its involvement in degradation of starch granules in the plastids are still lacking. The linear chain of starch is primarily hydrolyzed by β-amylase (BAM, EC: 3.2.1.2). However, BAM cannot hydrolyze the branch point and the linkage immediately adjacent to it. Thus, complete breakdown of amylopectins requires the action of DBE, which can release short, linear, malto-oligo-saccharides into the chloroplast stroma. Degradation of starch also requires reversible phosphorylation of the starch molecules, which are catalyzed by glucan, water dikinases (GWD, EC 2.7.94) and phosphoglucan, water dikinases (PWD, EC 2.7.9.5).

The unicellular green alga *Chlamydomonas reinhardtii* is considered as an ideal model system to study the starch metabolism, due to the easiness of starch induction by simple high-light exposure or nutrient starvation. Iodine staining-assisted high throughput mutant screening enabled identification of a large number of gene loci involved in starch biosynthesis, including those coding for the AGPase (i.e. *SAT1* and *STA6*), GBSS1 (i.e *STA2*), SSS II (i.e. *STA3*), isoamylase (i.e. *STA7*) and PGM (i.e. *STA5*) and α-1,4 glucanotransferase (i.e. *STA11*) (Buléon et al., 1998; Wattebled et al., 2003). In addition, genome-wide survey revealed like plants *C. reinhardtii* also possesses multiple isoforms of many key enzymes involved in starch biosynthesis and turnover (Koo et al., 2017). Despite the fact that starch biosynthesis has been intensively studied in *C. reinhardtii*, the regulation of starch metabolism in this organism are still as poorly understood as that in most photosynthetic organisms.

Previous studies have indicated that starch biosynthesis interact with triacylglycerol (TAG) biosynthesis by sharing common carbon precursors in microalgal cells (Wang et al., 2009; Li et al., 2010a). In addition, it was found that blocking starch biosynthesis upregulated the expression of a number of genes involved in central carbon metabolism, leading to the increased carbon flow toward hexose-phosphate pathway (Blaby et al., 2013). Based on these findings, we hypothesized that altering TAG biosynthesis may trigger intrinsic regulatory pathways governing starch metabolism, and vice versa. By exploitation of a strategy combining TAG biosynthesis manipulation and transcriptomics analysis, given key genes involved in starch biosynthesis regulation could be identified.

In this study, it was observed that the transgenic *C. reinharditii* strains with overexpression of the plastidial lysophosphatidic acid acyltransferase (LPAAT1) exhibited the phenotype in accordance with our hypothesis. LPAAT catalyzes the acylation of lysophosphatidic acid (LPA) to produce phosphatidic acid (PA), which is the second step in the Kennedy pathway responsible for glycerolipids biosynthesis (Ohlrogge and Browse, 1995). CrLPAAT1 has been functionally characterized and was found to be localized in the chloroplasts of *C. reinhardtii* (Yamaoka et al., 2016). Overexpression of CrLPAAT1 significantly enhanced the TAG contents under N-replete conditions. When the OE lines were subject to N-depleted conditions, the starch biosynthesis was dramatically triggered instead, and meanwhile the TAG biosynthesis was relatively slowed down. By the exploitation of transcriptomics analysis and *in vivo* functional characterization, a Gcn5-related N-acetyltransferase (*GNAT*) gene was found to be involved in regulation of starch biosynthesis in *C. reinhardtii*. Additionally, overexpression of this gene can drastically enhance the microalgal biomass, indicative of its great potential in genetic engineering of microalgae for production of starch and other bioproducts.

MATERIALS AND METHODS

Strains and Culture Conditions

The *C. reinhardtii* strains CC-400 and CC-124 were obtained from the *Chlamydomonas* Resource Center (http://chlamycollection.org/, Minnesota University). These reference strain was maintained respectively in 250 ml Erlenmeyer flask

containing 100 ml tris-acetate-phosphate (TAP) liquid culture medium (Gorman and Levine, 1965) under continuous light (40 μmol photons $m^{-2}s^{-1}$) at 24 °C in the Innova incubators (New Brunswick Scientific) with agitation at 180 rpm.

The *CrLPAAT1* overexpression (OE) lines and empty vector (EV) controls were grown in 1,000 ml glass columns containing 800 ml Sueoka's high salt (HS) medium (Sueoka, 1960) at an initial concentration of 2×10^5 cells ml^{-1}. The algal cells from the exponential phase (day 4, 2×10^7 cells ml^{-1}) were collected by centrifugation at 3,000 *g* for 5 min at room temperature and then transferred to the HS growth medium without the addition of ammonium chloride (referred to as N-free HS) after being washed with the growth medium. For both N-replete and N-depleted conditions, the algal cells were grown under continuous illumination (40 μmol photons $m^{-2}s^{-1}$) at 24°C with aeration of 1.5% (*v/v*) CO_2.

The *CrGNAT19* OE lines and EV controls were cultured in 250 mL Erlenmeyer flask containing 100 ml TAP medium at an initial concentration of 2×10^5 cells ml^{-1}. The algal cells from the exponential phase (day 3, 2×10^7 cells ml^{-1}) were collected by centrifugation at 3,000 *g* for 5 min at room temperature and were transferred to the TAP growth medium without the addition of ammonium chloride (referred to as N-free TAP) after being washed with the growth medium. For both N-replete and N-depleted conditions, the algal cells were grown under continuous illumination (40 μmol photons $m^{-2}s^{-1}$) at 24 °C in Innova incubators (New Brunswick Scientific) with agitation at 180 rpm.

Biomass Determination

The growth of algal cells was monitored by both dry cellular weight (DCW) and cell concentration measurement. DCW was determined by filtering algal cell cultures (10 ml) with the pre-weighed (W_0) Whatman GF/B filters (ϕ 4.7 cm), which was then washed with 1 M ammonium formate solution to remove excess salts and then dried at 105°C by overnight. The weights of the filter with algal cells were recorded as W_1, and the DCW per milliliter was determined as $(W_1\text{-}W_0)/10$. The cell concentrations used for growth curve establishment were determined as the optical density at 680 nm, which was referred to as OD_{680}.

Gene Cloning and Transgenic Strains Construction

The full-length cDNA of *CrLPAAT1* and *CrGNAT19* was amplified from the homemade cDNA library by using the primer sets *CrLPAAT1*-F (5'-ATGGCGCGTAAAAGCAGTTTGGCTC-3')/*CrLPAAT1*-R (5'-CTGCTCATCCGGCGCCATCTCTGT-3') and *CrGNAT19*-F (5'-ATGTCGGTCGTCAAATTAACGCAAC-3')/*CrGNAT19*-R (5'-CTACGCCAACCGCTTGTGCAT-3'), respectively. The PCR reactions were carried out by using Phanta Master Mix high-fidelity DNA polymerase (Vazyme, China) according to the manufacture's instructions. To integrate the *CrLPAAT1* and *CrGNAT19* cDNA into the pChlamy_4 vector (Invitrogen, USA), the inserts with EcoRI-XbaI restriction sites were generated by using the primer sets *CrLPAAT1*-EcoRI-F (5'- GGAATTCATGGCGCGTAAAAGCAGTTTGGCTC-3')/*CrLPAAT1*-XbaI-R (5'-GCTCTGAACTGCTCATCCGGCGCCATCTCTGT-3') and *CrGNAT19*-EcoRI-F (5'-GGAATTCATGTCGGTCGTCAAATTAACGCAAC-3')/*CrGNAT19*-XbaI-R (5'-GCTCTAGAACTACGCCAACCGCTTGTGCAT-3'), respectively. After digestion of the pChlamy_4 empty vector and inserts with EcoRI (Thermo Scientific, USA) and XbaI (Thermo Scientific, USA), the plasmids pChlamy4-*CrLPAAT1* and pChlamy4-*CrGNAT19* were constructed by using T4 DNA ligase (Promega, USA).

The constructed plasmid pChlamy4-*CrLPAAT1* and empty vector control was transformed into the reference strain CC-400, respectively, by using the glass-beads method (Kindle, 1990). Briefly, the algal cells were harvested at the exponential phase (2×10^6 cells ml^{-1}) by centrifugation at 1,500 g for 5 min. After discarding the supernatants, the cell pellets were resuspended in the pre-chilled TAP medium, while adjusting the final concentration to 2×10^8 cells ml^{-1}. Three-hundred microliters of cell suspension mixed with 300 mg sterile glass beads and 2 μg linearized plasmid DNA were vortexed for 20 s at the top speed. The transformed algal cells were recovered in 5 ml TAP medium under low light with continuous shaking (60–80 rpm) for 12 h. After concentration, the algal cells were resuspended in 200 μl TAP medium and spread onto the fresh agar plates containing TAP growth medium with zeocin (50 mg L^{-1}). After growing under continuous light (40 μmol photons m^{-2} sec^{-1}) at 25°C for 5 days, the transformants appeared and were verified with PCR.

The constructed plasmid pChlamy4-*GNAT19* and empty vector control was transformed into the reference strain CC-124 by using the electroporation method (Shimogawara et al., 1998), respectively. Briefly, the algal cells were harvested at the mid-log-phase (2×10^6 cells ml^{-1}) by centrifugation at 1,500 g for 5 min. After discarding the supernatants, the cell pellets were resuspended in the pre-chilled TAP media containing 60 mM sorbitol, while adjusting the final concentration to 2×10^8 cells ml^{-1}. Each electroporation cuvette with 250 μl cell suspension was incubated on ice for 10 min, and then added with 1 μg linearized plasmid DNA. Electroporation was conducted by using Bio-Rad electroporation system (Bio-Rad Gene Pulser Xcell Electroporation System, USA) under the optimized conditions (i.e. 400 V, 800 Ω, 50 μF). After electroporation, the cuvettes were immediately placed on ice for 10 min. The transformed algal cells were recovered in 10 ml TAP media containing 60 mM sorbitol under low light with continuous shaking (60–80 rpm) for 12 h. After centrifugation, the algal cells were resuspended in 200 μl TAP medium containing 60 mM sorbitol and 0.4% (*w/v*) PEG 6000 and spread onto the fresh agar plates containing TAP growth medium with paromomycin (50 mg L^{-1}). After growing under continuous light (40 μmol photons m^{-2} sec^{-1}) at 25°C for 5 days, the transformants appeared and were selected for PCR confirmation.

RNA Extraction, Quantitative Real-Time PCR (qRT-PCR)

Algal cells were harvested by centrifugation at 1,000 *g* for 5 min and washed with the PBS buffer. The cell pellets were freeze-dried and stored at -80°C prior to use. Total RNA was isolated

from the samples with TransZol Up Plus RNA kit (TransGen, China) by following the manufacturer's instructions. One microgram of the total RNA was used as the template for cDNA synthesis performed by using PrimeScript II 1st Strand cDNA Synthesis Kit (Takara, Japan) with oligo (dT) primers. The qRT-PCR was carried out with LightCycler 96 (Roche, Switzerland). Each reaction system (20 μl) contained 100 ng cDNA template, 10 μM forward primer and reverse primer 1 μl, respectively and 10 μl LightCycler 480 SYBR Green I Master (Roche, Switzerland). The primer sets for *CrLPAAT1* and *CrGNAT19* was *CrLPAAT1*-QF (5'- ACATCTACTCGCTGTT CCACCTG-3')/*CrLPAAT1*-QR (5'- CGGTCCACACGGTTTAT CATCAC-3') and *CrGNAT19*-QF (5'- AACGAGTACGGCTC CATCA-3')/*CrGNAT19*-QR (5'- CTTCTGCTTCAACGCAT CCA-3'), respectively. The *α-Tubulin* gene and *RACK1* gene were used as internal references, which was amplified by using the primer set *Tubulin*-F (5'-CTCGCTTCGCTTTGACGGTG-3')/*Tubulin*-R (5'- CGTGGTACGCCTTCTCGGC-3') and *RACK1*-F (5'- TTCTCGCCCATGACCACCAAC-3')/*RACK1*-R (5'- GGCCCACCAGGTTGTTCTTCAG-3'), respectively. The amplification conditions were as follows: 95°C for 10 min, followed by 40 cycles of 15 sec at 95°C, 30 s at 60°C and 30 s at 72°C. The specificity of qRT-PCR amplification was checked with the melting curve program (95°C for 10 s, 65°C for 60 s, continuous acquisition at 97°C for 1 s and cooling at 37°C for 30 s). The normalization and relative expression of *CrLPAAT1* and *CrGNAT19* genes were determined by geometric averaging of two internal reference genes as $2^{-\Delta\Delta Ct}$ (Livak and Schmittgen, 2001; Vandesompele et al., 2002).

Western Blotting Analysis

Three milliliters of algal cells were harvested by centrifugation at 1,000 *g* for 5 min, cell pellets were resuspended in 120 μl Buffer A (0.1 M dithiothreitol, 0.1 M Na_2CO_3) and 80 μl Buffer B (5% SDS, 30% sucrose, *w*/*v*). Cell suspension was vortexed for 30 min and lysed two cycles of freeze/thawing. After that, lysates were centrifuged at 16,000 *g* for 10 min, the supernatant was transferred to a new tube. The total protein concentration was measured by using CB-X protein assay kit (G-Biosciences, USA).

Around 20 μg of proteins in the SDS-PAGE sample buffer were separated on 12% (*w*/*v*) SDS-PAGE gel, and transferred to polyvinylidene fluoride (PVDF) membrane at 1.3 A, 25 V, for 7 min by using semi-dry transfer system (Bio-Rad Trans-Blot Turbo Transfer System, USA). The membranes were blocked with 10 ml of 5% nonfat milk. For immunofluorescence detection of CrGNAT19 and CrLPAAT1, the membrane was incubated overnight with 6×His-tag antibody conjugated with horseradish peroxidase (Proteintech, China, 1:10,000 dilution) and rabbit primary anti-CrLPAAT1 (1:2,000 dilution) with TBS containing 2% (*w*/*v*) nonfat milk, respectively, followed by incubation with the secondary antibody anti-rabbit IgG conjugated with horseradish peroxidase diluted by 1:1,000. Antigen-antibody complexes were visualized using an enhanced chemiluminescence detection kit (Bio-Rad Clarity Western ECL Substrate, USA). The Tubulin was used as a reference, which was detected by using the Tubulin alpha chain antibody (Agrisera, Sweden, 1:1,000 dilution).

The CrLPAAT1 antibody was generated by using the synthetic peptide. Briefly, a peptide (VHKALPPNKNADQL) was selected based on the screening of the antigenic epitopes of CrLPAAT1 (Protean program, LaserGene software). The peptide was synthesized and then coupled with bovine serum albumin (BSA) (YouLong Biotech, China). After immunizing the rabbit for four times over three months, the recovered antiserum was used for purification of the CrLPAAT1 polyclonal antibody by affinity chromatography (YouLong Biotech, China).

RNA-Seq

Five milliliters of the *CrLPAAT1* OE and EV control cell cultures grown under N-replete and N-depleted conditions were collected on 0, 3, and 12 h for RNA isolation. For each time point, 4 biological replicates were prepared. Total RNA were extracted by using Trizol reagents (Invitrogen, USA), from which the poly (A)-containing mRNA molecules were purified by using NEBNext Poly(A) mRNA Magnetic Isolation Module (New England Biolabs, USA). Directional transcriptome libraries were prepared by using NEBNext Ultra Directional RNA Library Prep Kit for Illumina (New England Biolabs, USA) which adopts the "dUTP" method to generate the strand-specificity library (Parkhomchuk et al., 2009). The constructed libraries were sequenced for 2×150-bp runs (paired-end) by using HiSeq 3000 (Illumina, USA). To ensure quality, adapter pollutions and low-quality reads were deleted from the raw data with Trimmomatic (version 0.35) (Bolger et al., 2014). For each data set, gene expression was measured as the numbers of aligned reads to the transcript assembly by using the alignment-based quantification method RSEM (Mortazavi et al., 2008), which provided the counts of RNA-Seq fragments and normalized expression metrics as "transcripts per million transcripts" (TPM). A given gene was considered to be significantly differentially expressed if the following criteria were met: i) there was at least a 2-fold change with a false discovery rate (FDR)-corrected P value ≤0.05 between control and stress conditions; ii) the counts-per-million (CPM) values under both conditions were ≥5. for, their values under each condition were ≥5.

Phylogenetic Analysis

The amino acid sequences of the selected proteins were aligned by using the Clustal W program built in MEGA 6.0 (Thompson et al., 1994). The phylogenetic tree was generated by using the neighbor-joining algorithm with MEGA 6.0. Molecular distances within the aligned sequences were calculated according to the position correction model. The confidence of each clade was tested through bootstrapping analysis with 1,000 replications.

Biochemical Composition Analysis

The cellular contents of the total fatty acids were quantified according to the methods described previously (Wu et al., 2019). To measure the TAG contents, total lipids were extracted from 10 mg of the lyophilized algal biomass. Briefly, the cell pellets were mixed with 4 ml of MeOH/$CHCL_3$/80% (*v*/*v*) HCOOH (20:10:1, *v*/*v*/*v*). After vortex for 1 h, 2 ml of salt solution (1M KCL, 0.2M H_3PO_4) was added to the mixture to partition the

organic and aqueous phase. The organic phase was further transferred to a new vial and was dried under N_2 stream. TAG was separated *via* thin layer chromatography (TLC). The TAG spots were scraped from the TLC silico gel glass plate and then trans-esterified to the fatty acid methyl esters for gas chromatography mass spectrometry analysis (Wu et al., 2019). Ten milligrams of lyophilized algal biomass of each cell lines were used to determine the total carbohydrate content by using the phenol-sulfuric acid method described previously (Dubois et al., 1956; Jia et al., 2015). The starch contents were quantified by using the total starch assay kit (Megazyme International, Ireland) according to the manufacturer's directions. The total protein contents were measured by using the Bradford protein assay method (Berges et al., 1993; Jia et al., 2015).

Statistical Analysis

A student's t-test was used to prove statistical difference (*, $p < 0.05$; **, $p < 0.01$; ***, $p < 0.001$).

RESULTS

In this study, two *CrLPAAT1* OE lines (i.e. 6-4 and 12-2) were obtained, in which the transcripts and protein levels of *CrLPAAT1* dramatically increased as compared to that of the empty vector P4 (**Figure 1**). It is noteworthy that both the transcript and protein level of the P4 empty vector line decreased under N-depletion condition as compared to that under N-replete conditions. When the algal cells were grown under the normal N-replete conditions, 2-fold increases in the TAG contents were observed in both the *CrLPAAT1* OE lines (**Figure 2C**). After being subject to N-depletion stress for 3 days, however, the TAG content of the OE line 6-4 was 10% lower ($p < 0.001$) than that of the control, and no significant difference was observed between the OE line 12-2 and P4 (**Figure 2D**). According to the hypothesis, the enhanced TAG biosynthesis in *CrLPAAT1* OE lines grown under N-replete conditions may in turn stimulate starch biosynthesis. Accordingly, the starch contents were found elevated by 50% in the two OE lines under N-depleted conditions (**Figure 2B**), though it slightly increased in one of the OE lines under N-replete conditions (**Figure 2A**).

To unravel the yet unknow regulatory mechanism governing carbon partitioning, the transcriptomic analysis was performed on the *CrLPAAT1* OE lines and EV control. Thirty-six high-quality transcript profiles were generated, featured by high reproducibility (Spearman correlation > 0.95) among the four biological replicates at each time point. Under the N-replete condition (0 h), there were 4,055 up-regulated and 3,256 down-regulated genes in the *CrLPAAT1* OE lines. At the time point of 3 h after subject to N depletion, 3,818 and 3,165 genes were up- and down-regulated, respectively. After 12 h under N depletion condition, there were 3,547 up-regulated and 3,358 down-regulated genes in the *CrLPAAT1* OE lines. Thus, it can be concluded that overexpression of *CrLPAAT1* led to profound changes in various biological processes at transcript level.

The fold-changes of the transcripts involved in fatty acid and lipid biosynthesis were shown in **Figure 3**. In the EV control, most genes involved in fatty acid biosynthesis were significantly down-regulated at the transcript level in response to N depletion, except for one of the acyl-carrier protein (ACP) encoding genes (**Figure 3A**). When comparing the *CrLPAAT1* OE lines with the EV control, it was found that five genes in the fatty acids *de novo* biosynthesis pathways exhibited downregulation at transcript level under N-replete conditions, including those coding biotin carboxylase (BCR), acyl-carrying protein (ACP2), malonyl-CoA: acyl protein malonyltransferase (MCT1 and MCT2), and enoyl-ACP reductase (ENR1) (**Figure 3B**). Among them, *ACP2* and *MCT2* were down-regulated over 3 h after being subject to N depletion, whereas the transcription of *BCR1*, *ACP2* and *MCT1* were conversely up-regulated under N-depleted conditions (**Figure 3A**, **Supplemental Table**). By contrast, three 3-ketoacyl-acyl carry protein synthase encoding genes (i.e. *KAS1*, *KAS2*, and *KAS3*) were significantly up-regulated in a sequential manner (**Figure 3A**, **Supplemental Table**). Besides, the up-regulated genes under N-depleted conditions included hydroxoacyl-ACP dehydrogenase (*HAD1*) and 3-ketoacyl-ACP (*KAR1*) (**Figure 3A**, **Supplemental Table**).

The synthesized fatty acids are assembled with the glycerol backbone to form TAG *via* two Kennedy pathways, which is so-

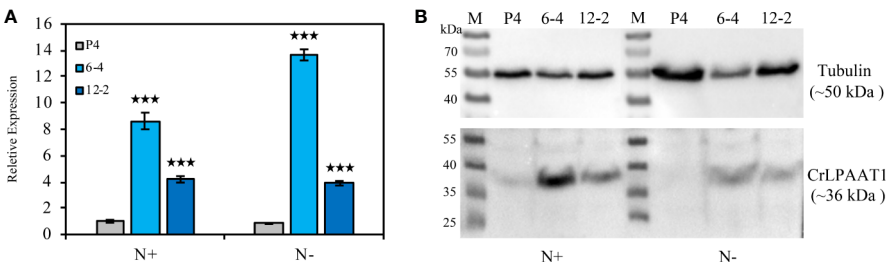

FIGURE 1 | Construction of the *CrLPAAT1* OE lines (6-4 and 12-2) and empty vector control (P4). **(A)** Relative transcript levels of the *CrLPAAT1* encoding genes in the empty vector line (P4) and two *CrLPAAT1* OE lines (normalized to that of P4) under nitrogen replete and nitrogen depletion conditions. **(B)** Protein levels of the empty vector line (P4) and two *CrLPAAT1* OE lines under nitrogen replete and nitrogen depletion conditions. Around 20 μg of whole-cell protein were loaded in each lane. Values are the means ± S.D. (n = 4). Student's t-test (***$p < 0.001$).

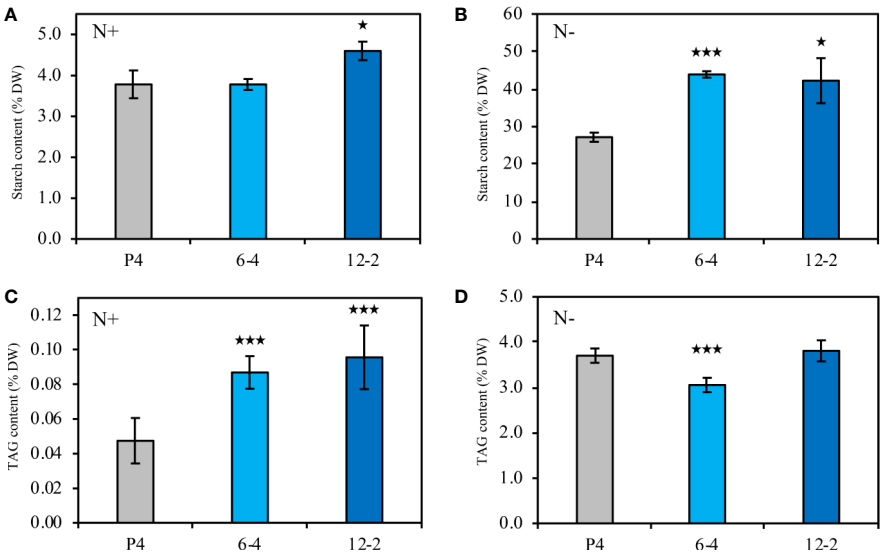

FIGURE 2 | Biochemical compositions of the *CrLPAAT1* OE lines (6-4 and 12-2) and empty vector control (P4). **(A)** Starch contents (% DW) in P4 and two *CrLPAAT1* OE lines (6-4, 12-2) under nitrogen replete condition. **(B)** Starch contents (% DW) in P4 and two *CrLPAAT1* OE lines (6-4, 12-2) under nitrogen depletion condition. **(C)** TAG contents (% DW) in P4 and two *CrLPAAT1* OE lines (6-4, 12-2) under nitrogen replete condition. **(D)** TAG contents (% DW) in P4 and two *CrLPAAT1* OE lines (6-4, 12-2) under nitrogen depletion condition. Values are the means ± S.D. (n = 4). Student's t-test (*$p < 0.05$; ***$p < 0.001$).

called prokaryotic and eukaryotic pathway, respectively (Fan et al., 2011). Both the pathways are involved in sequential acylation of glycerol-3-phostate and one step of dephosphorylation, but differ in their subcellular localizations, the former of which resides in plastids and the latter is associated with the endoplasmic reticulum membranes. In the EV control, four diacylglycerol acyltransferase (DGAT) genes and one phospholipid:diacylglycerol acyltransferase (PDAT) gene were significantly up-regulated over 12 h in response to N depletion (**Figure 3A**). Overexpression of CrLPAAT1 led to significant up-regulation of the eukaryotic glycerol-3-phosphate acyltransferase (*GPAT*) and two type II diacylglycerol acyltransferase encoding genes (*DGTT3* and *DGTT4*) under N-replete conditions (**Figure 3B**, **Supplemental Table**). However, none of the genes directly involved in TAG biosynthesis were induced at the transcript level in *CrLPAAT1* OE lines under N-depleted condition (**Figure 3A**, **Supplemental Table**).

The fold-changes in the transcripts involved in starch biosynthesis and degradation were shown in **Figure 4**. In the empty vector, a number of genes in the starch biosynthesis pathway were up-regulated in response to N-depletion. In addition to the phosphoglucose isomerase (PGI) and phosphoglucomutase (PGM) encoding genes responsible for biosynthesis of glucose-1-phosphate (Glc-1-P), up-regulated genes in the empty vector subject to N-depletion included *SS I/II/IV/V*, *SBE1/2*, *ISA2*, and *GBSS2* (**Figure 4A**). However, the large subunits of AGPase encoding gene *STA6* was significantly down-regulated, and *STA1* that codes the large subunit was only slightly up-regulated on 3 h in the EV control after being subject to N-depletion (**Figure 4A**). Overexpression of CrLPAAT1 led to the up-regulation of *STA6* and *STA1* under N-replete conditions: *STA6* was up-regulated by 4.2 and 6.8 times, and *STA1* was up-regulated by 2.8 and 3.1 times in 6-4 and 12-2, respectively (**Figure 4B**, **Supplemental Table**). Though the expression of *SS I/III/IV/V*, *SBE1/2*, *ISA2* and *GBSS2* at the transcript level were elevated in *CrLPAAT1* OE lines, their transcripts level were lower than that of the control under N-depleted conditions (**Figure 4B**, **Supplemental Table**).

Among the genes involved in the degradation of starch to glucose, *AMY2* and two *AMY-like* genes were substantially up-regulated, along with slight up-regulation of *AMY3* and *ISA3*, in the empty vector control in response to N-depletion (**Figure 4A**). Based on the gene expression data, it can be perceived that the degradation of starch into maltose was most likely reduced, as most genes in this pathway were down-regulated except for several slightly induced genes (e.g. *GWD2*, *GWD-like2*, and *BAM1*). In *CrLPAAT1* OE lines, two of the β-amylase genes (i.e. *BAM1* and *BAM2*) and one of the α-amylase genes were suppressed at the transcript level under both N-replete and N-depleted conditions. *AMY2* was considerably up-regulated by 6.9 and 13.5 times in the two OE lines, respectively. Similarly, the *AMY-like2* gene was up-regulated under both N-replete and N-depleted conditions in the two OE lines as well. The differentially expressed *PWD1* and *GWD1* showed up-regulation at the transcript level, the former of which was elevated by 2.5 and 2.2 times under N-replete and N-depleted conditions, respectively, and the latter one was up-regulated by ca. 2.2 times on 3 h after subject to N-depletion. However, the transcription of two *GWD1-like* genes were changed in an opposite way to that of *GWD1*, which was down-regulated under N-replete and N-depleted condition, respectively.

Based on the analysis above, it can be concluded that overexpression of *CrLPAAT1* caused complicated transcriptional

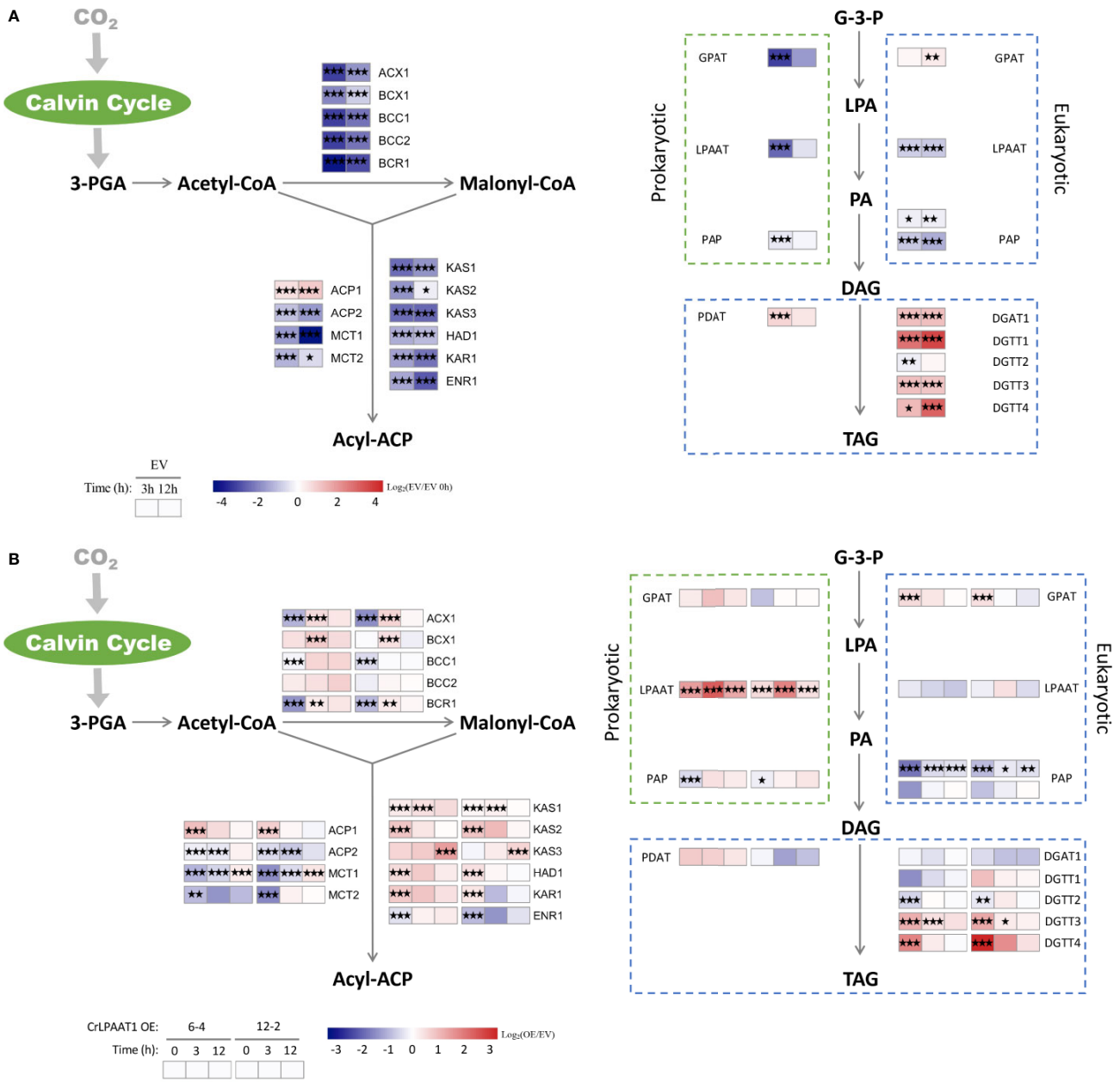

FIGURE 3 | Alterations in the gene expression levels in the fatty acids *de novo* biosynthesis and TAG assembly pathways of the P4 empty vector lines and *CrLPAAT1* OE lines (6-4 and 12-2). **(A)** Fold-changes of P4 empty vector lines over 12 h upon the onset of N-depletion stress were calculated as $\log_2$ (EV/EV 0 h) (EV, P4 empty vector lines). **(B)** Fold-changes between *CrLPAAT1* overexpression lines and P4 empty vector lines over 12 h upon the onset of N-depletion stress were calculated as $\log_2$ (OE/EV) (OE, *CrLPAAT1* overexpression lines; EV, P4 empty vector lines) and displayed in the heat map. 3-PGA, 3-phosphoglyceric acid; *ACX*, α-carboxyltransferase (ACCase complex); *BCX*, β- carboxyltransferase (ACCase complex); *BCC*, acetyl-CoA biotin carboxyl carrier protein (ACCase complex); *BCR*, biotin carboxylase (ACCase complex); *ACP*, acyl carrier protein; *MCT*, malonyl-CoA: ACP transacylase; *KAS*, 3-ketoacyl-CoA-synthase (FAS complex); *HAD*, 3-hydroxyacyl-ACP dehydratase (FAS complex); *KAR*, 3-oxoacy-[acyl carrier protein] reductase (FAS complex); *ENR*, enoyl-[acyl carrier protein] reductase (FAS complex); G-3-P, glycerol-3-phosphate; LPA, lysophosphatidic acid; PA, phosphatidic acid; DAG, diacylglycerol; *GPAT*, glycerol-3-phosphate acyltransferase; *LPAAT*, lysophosphatidic acid acyltransferase; *PAP*, phosphatidic acid phosphatase; *PDAT*, phospholipid: diacylglycerol acyltransferase; *DGAT*, diacylglycerol acyltransferase type 1; *DGTT*, diacylglycerol acyltransferase type 2. Statistical significances of the differentially expressed genes in the P4 empty vector lines and the *CrLPAAT1* overexpression lines with same trend of regulation between two *CrLAAT1* OE lines were determined by a false discovery rate (FDR)-corrected p value (*$p < 0.05$; **$p < 0.01$; ***$p < 0.001$).

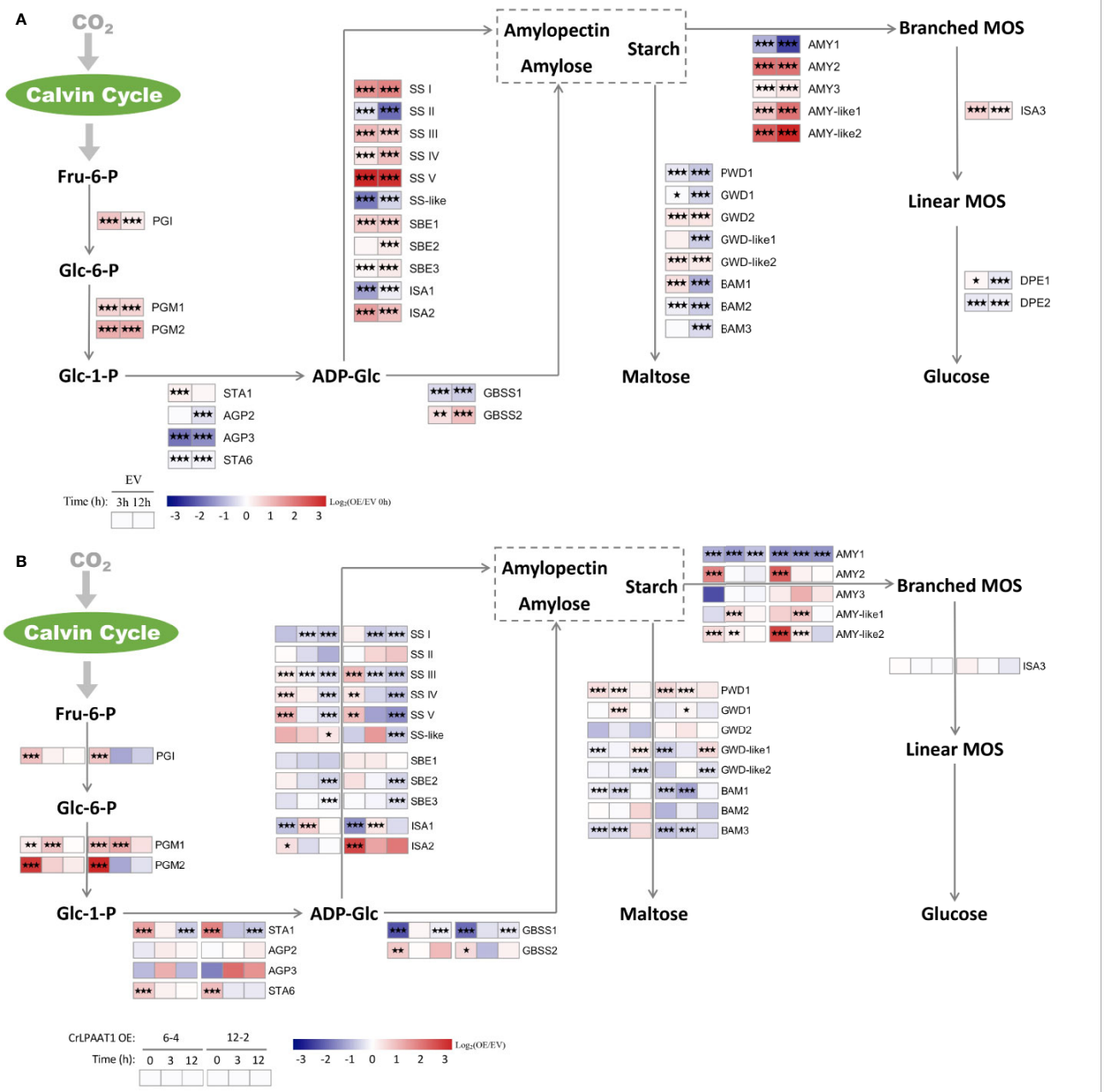

FIGURE 4 | Alterations in the gene expression levels in the starch metabolism pathways of the P4 empty vector lines and *CrLPAAT1* OE lines (6-4 and 12-2). **(A)** Fold-changes of P4 empty vector lines over 12 h upon the onset of N-depletion stress were calculated as $\log_2$ (EV/EV 0 h) (EV, P4 empty vector lines). **(B)** Fold-changes between *CrLPAAT1* overexpression lines and P4 empty vector lines over 12 h upon the onset of N-depletion stress were calculated as $\log_2$ (OE/EV) (OE, *CrLPAAT1* overexpression lines; EV, P4 empty vector lines) and displayed in the heat map. Fru-6-P, fructofuranose 6-phosphate; Glc-6-P, glucopyranose 6-phosphate; Glc-1-P, glucopyranose 1-phosphate; ADP-Glc, ADP-glucose; Branched-MOS, branched malto-oligosaccharides; Linear-MOS, linear malto-oligosaccharides; *PGI*, phosphoglucose isomerase; *PGM*, phosphoglucomutase; *AGP*, ADP-glucose pyrophosphorylase; *SS*, starch synthase; *GBSS*, granule bound starch synthase; *SBE*, starch branching enzyme; *ISA*, isoamylase; *AMY*, α-amylase; *BAM*, β-amylase; *PWD*, phosphoglucan water dikinase; *GWD*, alpha-glucan water dikinase; *DPE*, Disproportionating enzyme. Statistical significances of the differentially expressed genes in the P4 empty vector lines and the *CrLPAAT1* overexpression lines with same trend of regulation between two *CrLAAT1* OE lines were determined by a false discovery rate (FDR)-corrected p value (*$p < 0.05$; **$p < 0.01$; ***$p < 0.001$).

changes in the lipid and starch metabolism pathways, so that a higher-tier regulation could be expected, such as activation or deactivation of transcription factors (TFs) or regulators (TRs) in the *CrLPAAT1* OE lines. Moreover, enhanced starch biosynthesis in *CrLPAAT1* OE lines under N-depleted conditions could not be attributable to the transcriptional regulation. Thus, activation of genes involved in post-translational regulation could be another possible scenario. To verify such a hypothesis, the putative transcription factor/regulator genes were identified from the differentially expressed genes based on previous prediction (Gargouri et al., 2015). When compared with the EV control, a total of 37 putative TF/TR genes were differentially expressed in the two *CrLPAAT1* OE lines (i.e. 6-4 and 12-2). These genes fell into two clusters based on their fold-changes under N-replete conditions (**Figure 5A**). The up-regulated cluster included 30 genes, among which three genes were up-regulated under both conditions, whereas the other genes were unchanged or down-regulated under N-depleted conditions. The most enriched gene families in this cluster included *TRAF*, *C3H*, general control non-repressible 5 (Gcn5)-related N-acetyltransferase (*GNAT*), and *SNF*. The down-regulated cluster included 5 genes. It is noteworthy that most of the identified up-regulated TFs/TRs can be induced at the transcript level in the EV control (regarded as wild-type background) subject to N-depletion (**Figure S1**). On the top of the up-regulated genes, a putative general control non-repressible 5 (Gcn5)-related N-acetyltransferase (*GNAT*) gene (i.e. Cre06.g269100, named as *GNAT19* in this study) showed the most substantial up-regulation in the *CrLPAAT1* OE lines, which increased by 11 and 12 times in

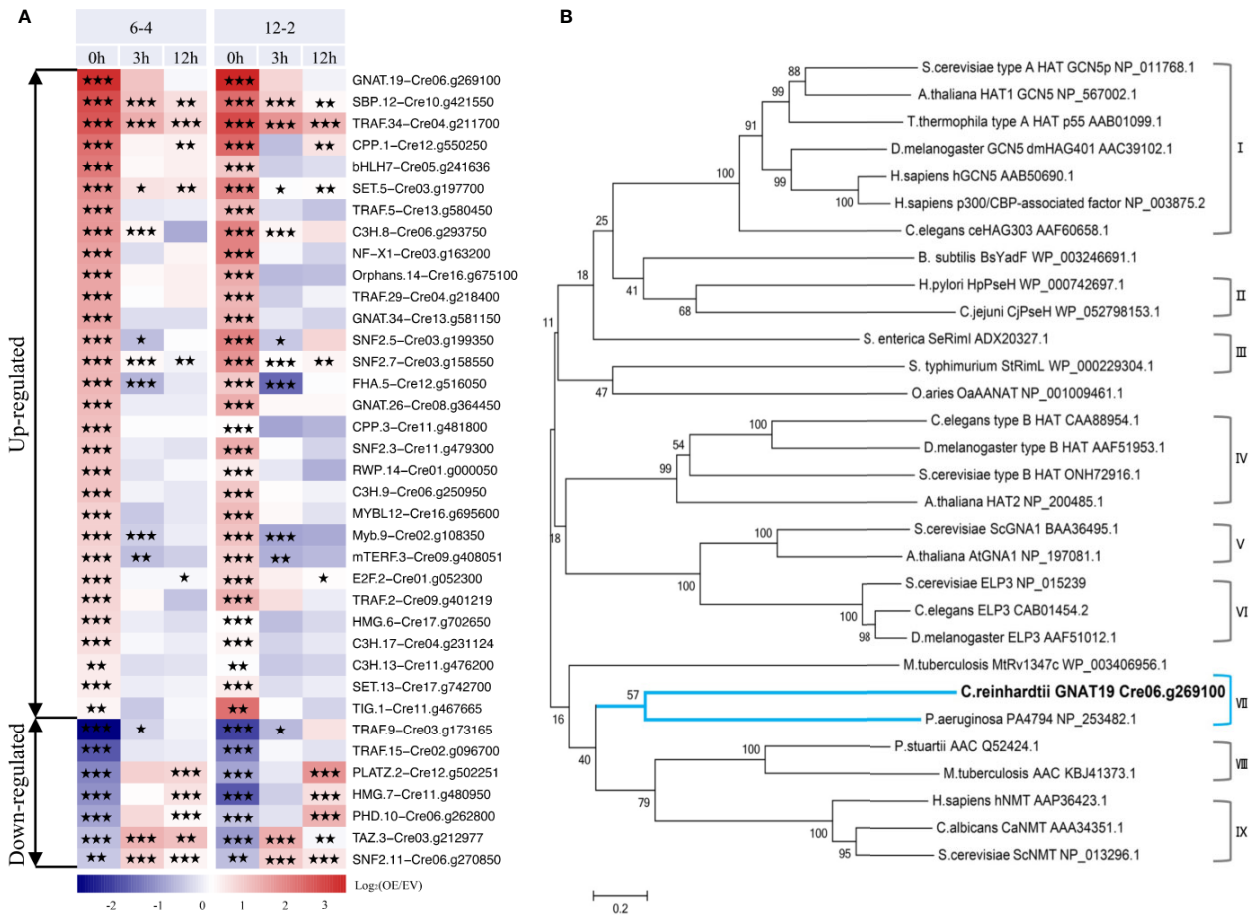

FIGURE 5 | Identification of a putative non-repressible 5 (Gcn5)-related N-acetyltransferase (GNAT) encoding gene (i.e. Cre06.g269100A, referred to as *CrGNAT19* in this study). **(A)** Transcriptional dynamics of the differentially expressed transcription factor/regulator encoding genes in the two *CrLPAAT1* OE lines (i.e. 6-4 and 12-2). Fold-changes over 12 h upon the onset of N-depletion stress were calculated as $\log_2$ (OE/EV) (OE, *CrLPAAT1* overexpression lines; EV, P4 empty vector lines) and displayed in the heat map. The genes were classified into two groups including the up-regulated and down-regulated ones, according to the relative gene expression level at the time point 0 h. Statistical significances of the differentially expressed genes with same trend of regulation between two *CrLAAT1* OE lines were determined by a false discovery rate (FDR)-corrected p value (*$p < 0.05$; **$p < 0.01$; ***$p < 0.001$). **(B)** Phylogenetic tree of GNAT19 and related GNATs constructed by comparing amino acid sequences. The GNAT family consists of nine subgroups, I: Type A HATs, II: Pseudaminic acid biosynthesis protein H, III: Ribosomal protein Nα-acetyltransferases, IV: Type B HATs, V: Glucosamine-6-phosphate N-acetyltransferases, VI: Elongator complex protein, VII: C-terminal Nε-lysine protein acetyltransferases, VIII: Aminoglycoside N-acetyltransferases, IX: Protein N-myristoyltransferases. The tree was generated by using the neighbor-joining algorithm with MEGA 6.0. Molecular distances within the aligned sequences were calculated according to the position correction model. The confidence of each clade was tested through bootstrapping analysis with 1,000 replications.

the two OE lines under N-replete conditions, respectively (**Figure 4A**). In addition, 5.3-fold increase in the expression of this gene was observed in the EV control on 12 h under N-depleted conditions (**Figure S1**).

To dissect the function of CrGNAT19, particularly for its potential in regulating carbon partitioning, the full-length cDNA of *CrGNAT19* was cloned from the cDNA library of *C. reinhardtii*. *In silico* analysis indicated that *CrGNAT19* codes for a protein consisting of 370 amino acid residues with a mass of 39.37 KD and a pI of 8.85. Phylogenetic analysis of *CrGNAT19* along with 29 *GNAT* with experimentally confirmed functions from various organisms revealed that CrGNAT19 was closely related with a C-terminal Nε-lysine protein acetyltransferases of the bacterium *Pseudomonas aeuruginosa* (Majorek et al., 2013) (**Figure 5B**).

Two *CrGNAT19* OE lines (i.e. G37 and G50) were constructed and verified with RT-PCR (**Figure 6A**) and western blotting (**Figure 6B**). Since *CrGNAT19* OE lines did not grow very well under the photoautotrophic conditions, of which the cells tended to aggregate and attach to the wall of photobioreactors, they were thus grown under the mixotrophic conditions for phenotyping analysis. Overexpression of CrGNAT19 slightly retarded the cellular division of *C. reinhardtii* during the exponential phase under N-replete conditions, whereas the biomass yield of *CrGNAT19* OE increased by 20% as compared to that of the EV control (**Figure 6C**). When the algal cells were subject to N-depletion, the *CrGNAT19* OE lines continued growing over 2 days, while the cell division of the control ceased upon exposure to the stress (**Figure 6D**). After 2 days under N-depletion, the biomass yield of the *CrGNAT19* OE lines reached 1.5 g L^{-1}, which increased by 72.6% as compared to that of the control (**Figure 6C**).

Biochemical composition analysis revealed that there were 2.7- and 1.3-fold increases in the total carbohydrate content of the *GNAT19* OE lines grown under N-replete and N-depleted conditions, respectively, when compared to that of the control (**Table 1**). As the major form of carbon storage in the algal cells, the starch content was enhanced from 1.8 to 7.5% of DCW in the *CrGNAT19* OE lines grown under N-replete conditions. Albeit both the *CrGNAT19* OE lines and control accumulated substantial amounts of starch in response to N-depletion, the starch content of the former reached 36.5% of DCW, which increased by 26.7% as compared to that of the latter (**Table 1**). In contrast to the enhanced starch biosynthesis, the content of total lipids and TAG was reduced by 34 and 67%, respectively, in the *CrGNAT19* OE lines subject to

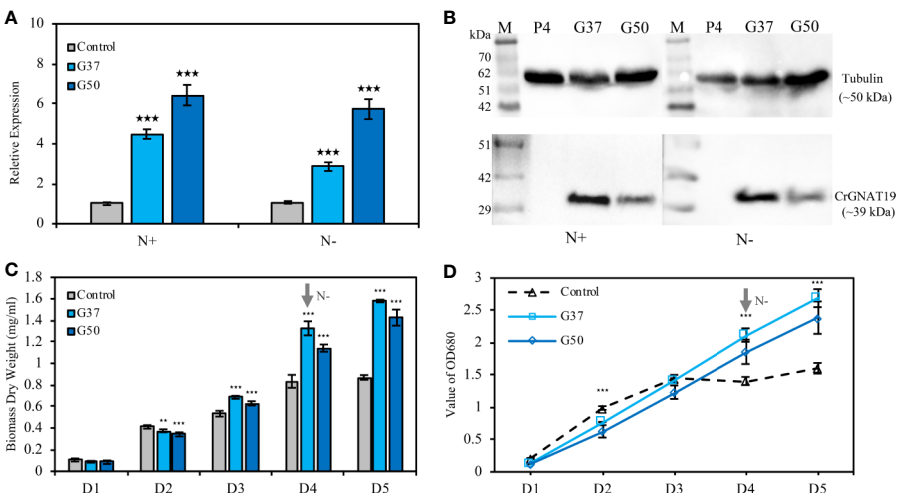

FIGURE 6 | Characterization of the *CrGNAT19* OE lines. **(A)** Relative transcript levels of *CrGNAT19* in the two OE lines (i.e. G37, and G50) and empty vector control line (i.e. P4) under nitrogen replete and nitrogen depletion conditions. **(B)** Protein levels of *CrGNAT19* in the two OE lines (i.e. G37, and G50) and empty vector control line (i.e. P4) under nitrogen replete and nitrogen depletion conditions. **(C)** Dry weights of the two *CrGNAT19* OE lines and empty vector control (i.e. P4) under N-replete and N-depleted conditions for 5 days. **(D)** Cellular growth measured as the optical density absorbance at 680 nm under the N-replete and N-depleted conditions for 5 days. Values are the means ± S.D. (n = 4). Student's t-test (**$p < 0.01$; ***$p < 0.001$).

TABLE 1 | Biochemical compositions of the *GNAT19* OE lines grown under the N-replete and N-depleted conditions for two days.

Content (% DW)	N-replete			N-depleted DAY1			N-depletedDAY2		
	Control	GNAT19	*p* value	Control	GNAT19	*p* value	Control	GNAT19	*p* value
Total fatty acids	5.76 ± 0.094	5.66 ± 0.060	0.082	8.18 ± 0.093	6.50 ± 0.16	<0.001	9.50 ± 0.31	6.25 ± 0.040	<0.001
TAG	0.044 ± 0.004	0.041 ± 0.005	0.330	2.68 ± 0.11	1.68 ± 0.13	<0.001	5.54 ± 0.59	1.79 ± 0.25	<0.001
Total carbohydrates	3.58 ± 0.45	9.72 ± 0.42	<0.001	33.64 ± 0.77	38.97 ± 1.50	<0.001	33.55 ± 0.72	44.04 ± 2.56	<0.001
Starch	1.83 ± 0.21	7.53 ± 0.23	<0.001	26.60 ± 0.36	33.83 ± 0.78	<0.001	28.83 ± 0.53	36.51 ± 1.44	<0.001

Values are the means ± S.D. (n = 4). Student's t-test was used to determine the statistical significance indicated by the p value. DW, dry weight.

the N-depleted conditions. After 2 days under N-depleted conditions, the TAG content of the *CrGNAT19* OE lines was only 1.8% of DCW, significantly lower than that of the control (5% of DCW) (**Table 1**). Compared to the control, the final starch yield of the *CrGNAT19* OE lines, as a function of the starch content and biomass concentration, increased by 118.5% over 2 days under N-depleted conditions (**Figure 7**).

DISCUSSION

Many biotechnical efforts have been made to enhance the starch contents in a variety of crops and microalgae, mainly *via* increasing biosynthesis or decreasing breakdown of starches (Smith, 2008). One of the mostly reported targeted gene is that coding for AGPase, but its overexpression led to only marginal, in some cases, or even intangible impacts on the starch contents in many crops (Giroux et al., 1996; Meyer et al., 2007). The difficulties in identifying the appropriate gene targets for bioengineering are the complexity of the starch metabolism pathways. Given that a large number of isoforms are involved in starch biosynthesis, turnover, and degradation, their precisive roles in governing the accumulation of starches haven't been fully understood yet, and on the other hand, manipulation of a single pathway may cause compensatory responses from its counterparts or alternative pathways. Such complexity was perceived in *C. reinhardtii* as well. In the *CrLPAAT1* OE lines, multiple isoforms of the most starch metabolism-related genes were differentially regulated at the transcriptional level when the starch accumulation was significantly enhanced (**Figure 4B**). Thus, the major aim of this study was to identify the regulatory gene(s) that can be leveraged for rational genetic engineering.

Regulation proteins such as TFs, TRs, as well as those involved in post-translational modification, are representing the most promising targets for rewiring carbon partitioning for enhancing production of starches or lipids in microalgae. Recently, the target of rapamycin signaling pathway was found to be involved in starch accumulation *via* mediating phosphorylation of a glycogenin-like protein (CmGLG1) in the unicellular red alga *Cyanidioschyzon merolea*, and overexpression of *CmGLG1* resulted in 4.7-fold increase in the starch content (Pancha et al., 2019a; Pancha et al., 2019b). An earlier study showed knocking out a *Zn (II)$_2$Cys$_6$* gene improved partitioning of the total carbon to lipid from 20 to 40–55% in *Nannochloropsis* (Ajjawi et al., 2017). This study revealed an unprecedented regulator which is the homologous to the bacterial GNAT PA4794 identified from *P. aeuruginosa*. The *GNAT* gene family include a large family of enzymes that catalyze the transfer of an acyl moiety from acyl-CoA to a variety of substrates and involve in diverse biological processes (Salah Ud-Din et al., 2016). Though PA4794 was found to be capable of selectively acetylating the Nε group of the C-terminal lysine of peptides and small molecules such as chloramphenicol, the *in vivo* function of this protein has remained uncharacterized (Majorek et al., 2013). It is noteworthy that PA4794 is remotely related to the RimI ribosomal protein acetyltransferase. Thus, it is necessary to perform proteomics analysis on the OE lines constructed in this study to address whether the role of CrGNAT19 was involved in global translational regulation or responsible for acetylation of specific proteins.

In addition to altering carbon partitioning in *C. reinhardtii*, overexpression of CrGNAT19 led to substantial enhancement in biomass production under N-depleted conditions. Up to now, increasing algal biomass production has been largely pursued through enhancing photosynthesis efficiency, such as attenuating the light-harvesting antenna complexes (LHC) in particular. For the *C. reinhardtii* mutant *NAB1** with the LHC size reduced by 10–17%, the growth rate during log phase and maximal dry weight under continuous high-light conditions was improved by 50 and 37%,

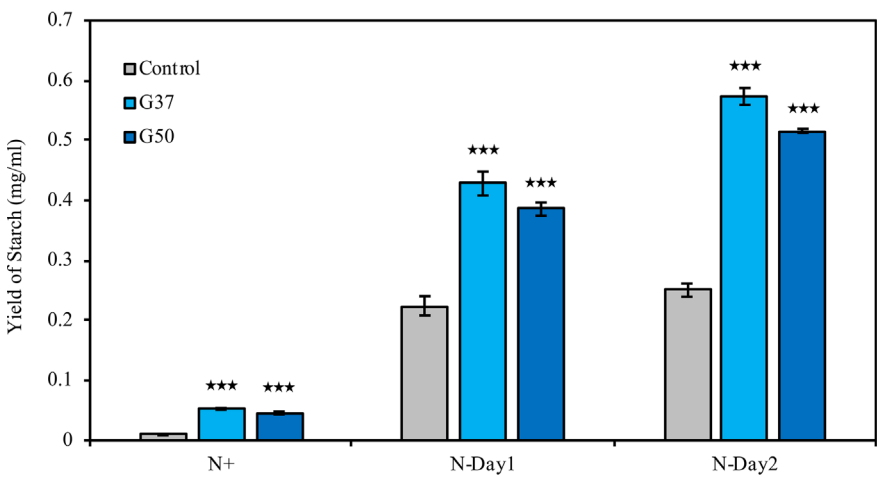

FIGURE 7 | Enhanced starch yield in the *CrGNAT19* OE lines. Yield of starch in P4 control lines and two *CrGNAT19* OE lines subject to N- replete (N+) and N-depletion stress for two days (N-Day1, N-Day2). Values are the means ± S.D. (n = 4). Student's t-test (***$p < 0.001$).

respectively, as compared to the control (Beckmann et al., 2009). The LHC knock-down mutant Stm3LR3 also exhibited the fast-growing phenotype under high-light conditions (Mussgnug et al., 2007). However, the growth potential of these mutants under nutrient depletion conditions remain uncharacterized, and thus it is unclear whether they could be used to indirectly improve the production of starches or lipids, both of which are enormously accumulated under N-depletion conditions. Interestingly, similar to *CrGNAT19* OE lines, the *C. reinhardtii* mutant *std1* deficient in a plant-specific tyrosine-phosphorylation-regulated kinase was capable of accumulating higher levels of starch and achieving higher biomass productivity than wild-type under N-depletion conditions (Schulz-Raffelt et al., 2016). In contrast to these hyper-starch mutants including *CrGNAT19* and *std1*, the biomass production under N-depleted conditions was significantly suppressed in a number of starchless and low starch mutants of *C. reinhardtii* (Li et al., 2010b). These findings taken together indicated that starch biosynthesis can positively regulate the photosynthesis process under N-depletion in *C. reinhardtiii.* It is noteworthy that the function of CrGNAT 19 remained to be investigated under various trophic modes (i.e. photoautotrophic and heterotrophic) in order to fully demonstrate its biotechnical significance.

Taken together, this study uncovered the role of *CrGNAT19* in regulation of carbon partitioning in *C. reinhardtii*. Moreover, overexpression of this gene can drastically enhance the microalgal biomass and starch production, indicative of its great potential in genetic engineering of microalgae for production of starch and other bioproducts as well. We suspect the expression of CrGNAT19 could be up-regulated by the enhanced TAG biosynthesis mediated by multiple metabolic pathways (e.g. prokaryotic and eukaryotic pathways) thereby playing a central role in regulation of carbon partitioning. Identification of the substrate(s) and targeted pathway(s) for such an unprecedented regulator is underway.

DATA AVAILABILITY STATEMENT

The original contributions presented in the study are publicly available. This data can be found here: NCBI, accession number PRJNA587114.

AUTHOR CONTRIBUTIONS

ZL, LC, DH, and QH contributed conception and design of the study. ZL and LZ organized the database. ZL and LZ performed the statistical analysis. DH and ZL wrote the first draft of the manuscript. DH and ZL wrote sections of the manuscript. All authors contributed to the article and approved the submitted version. ZL and LC equally contributed to this work.

FUNDING

This work was supported by The National Key R&D Program of China (2018YFA0902500) and Chinese Academy of Sciences (ZDRW-ZS-2017-2).

ACKNOWLEDGMENTS

The authors thank Yanhua Li for providing assistance in gas chromatography mass spectrometry analysis for this study.

SUPPLEMENTARY MATERIAL

The Supplementary Material for this article can be found online at: https://www.frontiersin.org/articles/10.3389/fpls.2020.544827/full#supplementary-material

REFERENCES

Ajjawi, I., Verruto, J., Aqui, M., Soriaga, L. B., Coppersmith, J., Kwok, K., et al. (2017). Lipid production in Nannochloropsis gaditana is doubled by decreasing expression of a single transcriptional regulator. *Nat. Biotechnol.* 35 (7), 647. doi: 10.1038/nbt.3865

Ball, S. G., and Morell, M. K. (2003). From bacterial glycogen to starch: understanding the biogenesis of the plant starch granule. *Annu. Rev. Plant Biol.* 54 (1), 207–233. doi: 10.1146/annurev.arplant.54.031902.134927

Ball, S. G., Dirick, L., Decq, A., Martiat, J.-C., and Matagne, R. (1990). Physiology of starch storage in the monocellular alga Chlamydomonas reinhardtii. *Plant Sci.* 66 (1), 1–9. doi: 10.1016/0168-9452(90)90162-H

Beckmann, J., Lehr, F., Finazzi, G., Hankamer, B., Posten, C., Wobbe, L., et al. (2009). Improvement of light to biomass conversion by de-regulation of light-harvesting protein translation in Chlamydomonas reinhardtii. *J. Biotechnol.* 142 (1), 70–77. doi: 10.1016/j.jbiotec.2009.02.015

Berges, J. A., Fisher, A. E., and Harrison, P. J. (1993). A comparison of Lowry, Bradford and Smith protein assays using different protein standards and protein isolated from the marine diatom Thalassiosira pseudonana. *Marine Biol.* 115 (2), 187–193. doi: 10.1007/BF00346334

Blaby, I. K., Glaesener, A. G., Mettler, T., Fitz-Gibbon, S. T., Gallaher, S. D., Liu, B., et al. (2013). Systems-level analysis of nitrogen starvation–induced modifications of carbon metabolism in a Chlamydomonas reinhardtii starchless mutant. *Plant Cell* 25 (11), 4305–4323. doi: 10.1105/tpc.113.117580

Bolger, A. M., Lohse, M., and Usadel, B. (2014). Trimmomatic: a flexible trimmer for Illumina sequence data. *Bioinformatics* 30 (15), 2114–2120. doi: 10.1093/bioinformatics/btu170

Brányiková, I., Maršálková, B., Doucha, J., Brányik, T., Bišová, K., Zachleder, V., et al. (2011). Microalgae—novel highly efficient starch producers. *Biotechnol. Bioengineer.* 108 (4), 766–776. doi: 10.1002/bit.23016

Buléon, A., Colonna, P., Planchot, V., and Ball, S. (1998). Starch granules: structure and biosynthesis. *Int. J. Biol. Macromol.* 23 (2), 85–112. doi: 10.1016/S0141-8130(98)00040-3

Dubois, M., Gilles, K. A., Hamilton, J. K., Rebers, P.t., and Smith, F. (1956). Colorimetric method for determination of sugars and related substances. *Analyt. Chem.* 28 (3), 350–356. doi: 10.1021/ac60111a017

Fan, J., Andre, C., and Xu, C. (2011). A chloroplast pathway for the de novo biosynthesis of triacylglycerol in Chlamydomonas reinhardtii. *FEBS Lett.* 585 (12), 1985–1991. doi: 10.1016/j.febslet.2011.05.018

Gargouri, M., Park, J.-J., Holguin, F. O., Kim, M.-J., Wang, H., Deshpande, R. R., et al. (2015). Identification of regulatory network hubs that control lipid metabolism in Chlamydomonas reinhardtii. *J. Exp. Bot.* 66 (15), 4551–4566. doi: 10.1093/jxb/erv217

Giroux, M. J., Shaw, J., Barry, G., Cobb, B. G., Greene, T., Okita, T., et al. (1996). A single mutation that increases maize seed weight. *Proc. Natl. Acad. Sci.* 93 (12), 5824–5829. doi: 10.1073/pnas.93.12.5824

Gorman, D. S., and Levine, R. (1965). Cytochrome f and plastocyanin: their sequence in the photosynthetic electron transport chain of Chlamydomonas reinhardi. *Proc. Natl. Acad. Sci.* 54 (6), 1665–1669. doi: 10.1073/pnas.54.6.1665

Jia, J., Han, D., Gerken, H. G., Li, Y., Sommerfeld, M., Hu, Q., et al. (2015). Molecular mechanisms for photosynthetic carbon partitioning into storage neutral lipids in Nannochloropsis oceanica under nitrogen-depletion conditions. *Algal. Res.* 7, 66–77. doi: 10.1016/j.algal.2014.11.005

Kindle, K. L. (1990). High-frequency nuclear transformation of Chlamydomonas reinhardtii. *Proc. Natl. Acad. Sci.* 87 (3), 1228–1232. doi: 10.1073/pnas.87.3.1228

Koo, K. M., Jung, S., Lee, B. S., Kim, J.-B., Jo, Y. D., Choi, H.-I., et al. (2017). The mechanism of starch over-accumulation in Chlamydomonas reinhardtii high-starch mutants identified by comparative transcriptome analysis. *Front. Microbiol.* 8:858. doi: 10.3389/fmicb.2017.00858

Li, Y., Han, D., Hu, G., Dauvillee, D., Sommerfeld, M., Ball, S., et al. (2010a). Chlamydomonas starchless mutant defective in ADP-glucose pyrophosphorylase hyper-accumulates triacylglycerol. *Metab. Eng.* 12 (4), 387–391. doi: 10.1016/j.ymben.2010.02.002

Li, Y., Han, D., Hu, G., Sommerfeld, M., and Hu, Q. (2010b). Inhibition of starch synthesis results in overproduction of lipids in Chlamydomonas reinhardtii. *Biotechnol. Bioengineer.* 107 (2), 258–268. doi: 10.1002/bit.22807

Livak, K. J., and Schmittgen, T. D. (2001). Analysis of relative gene expression data using real-time quantitative PCR and the 2– ΔΔCT method. *Methods* 25 (4), 402–408. doi: 10.1006/meth.2001.1262

Majorek, K. A., Kuhn, M. L., Chruszcz, M., Anderson, W. F., and Minor, W. (2013). Structural, Functional, and Inhibition Studies of a Gcn5-related N-Acetyltransferase (GNAT) Superfamily Protein PA4794 A New C-TERMINAL Lysine Protein Acetyltransferase From Pseudomonas Aeruginosa. *J. Biol. Chem.* 288 (42), 30223–30235. doi: 10.1074/jbc.M113.501353

Meyer, F., Talbert, L., Martin, J., Lanning, S., Greene, T., and Giroux, M. (2007). Field evaluation of transgenic wheat expressing a modified ADP-glucose pyrophosphorylase large subunit. *Crop Sci.* 47 (1), 336–342. doi: 10.2135/cropsci2006.03.0160

Mortazavi, A., Williams, B. A., McCue, K., Schaeffer, L., and Wold, B. (2008). Mapping and quantifying mammalian transcriptomes by RNA-Seq. *Nat. Methods* 5 (7), 621. doi: 10.1038/nmeth.1226

Mussgnug, J. H., Thomas-Hall, S., Rupprecht, J., Foo, A., Klassen, V., McDowall, A., et al. (2007). Engineering photosynthetic light capture: impacts on improved solar energy to biomass conversion. *Plant Biotechnol. J.* 5 (6), 802–814. doi: 10.1111/j.1467-7652.2007.00285.x

Ohlrogge, J., and Browse, J. (1995). Lipid biosynthesis. *Plant Cell* 7 (7):957. doi: 10.1105/tpc.7.7.957

Pancha, I., Shima, H., Higashitani, N., Igarashi, K., Higashitani, A., Tanaka, K., et al. (2019a). Target of rapamycin-signaling modulates starch accumulation via glycogenin phosphorylation status in the unicellular red alga Cyanidioschyzon merolae. *Plant J.* 97 (3), 485–499. doi: 10.1111/tpj.14136

Pancha, I., Tanaka, K., and Imamura, S. (2019b). Overexpression of a glycogenin, CmGLG2, enhances floridean starch accumulation in the red alga Cyanidioschyzon merolae. *Plant Signaling Behav.* 14 (6):1596718. doi: 10.1080/15592324.2019.1596718

Parkhomchuk, D., Borodina, T., Amstislavskiy, V., Banaru, M., Hallen, L., Krobitsch, S., et al. (2009). Transcriptome analysis by strand-specific sequencing of complementary DNA. *Nucleic Acids Res.* 37 (18), e123–e123. doi: 10.1093/nar/gkp596

Roessler, P. G. (1988). Effects of silicon deficiency on lipid composition and metabolism in the diatom Cyclotella cryptica 1. *J. Phycol.* 24 (3), 394–400. doi: 10.1111/j.1529-8817.1988.tb04482.x

Salah Ud-Din, A. I. M., Tikhomirova, A., and Roujeinikova, A. (2016). Structure and functional diversity of GCN5-related N-acetyltransferases (GNAT). *Int. J. Mol. Sci.* 17 (7):1018. doi: 10.3390/ijms17071018

Schulz-Raffelt, M., Chochois, V., Auroy, P., Cuiné, S., Billon, E., Dauvillée, D., et al. (2016). Hyper-accumulation of starch and oil in a Chlamydomonas mutant affected in a plant-specific DYRK kinase. *Biotechnol. Biofuels* 9 (1), 55. doi: 10.1186/s13068-016-0469-2

Shimogawara, K., Fujiwara, S., Grossman, A., and Usuda, H. (1998). High-efficiency transformation of Chlamydomonas reinhardtii by electroporation. *Genetics* 148 (4), 1821–1828. doi: 10.1104/pp.114.3.1123

Smith, A. M. (2008). Prospects for increasing starch and sucrose yields for bioethanol production. *Plant J.* 54 (4), 546–558. doi: 10.1111/j.1365-313X.2008.03468.x

Sueoka, N. (1960). Mitotic replication of deoxyribonucleic acid in Chlamydomonas reinhardi. *Proc. Natl. Acad. Sci. U. S. A.* 46 (1):83. doi: 10.1073/pnas.46.1.83

Thompson, J. D., Higgins, D. G., and Gibson, T. J. (1994). CLUSTAL W: improving the sensitivity of progressive multiple sequence alignment through sequence weighting, position-specific gap penalties and weight matrix choice. *Nucleic Acids Res.* 22 (22), 4673–4680. doi: 10.1093/nar/22.22.4673

Vandesompele, J., De Preter, K., Pattyn, F., Poppe, B., Van Roy, N., De Paepe, A., et al. (2002). Accurate normalization of real-time quantitative RT-PCR data by geometric averaging of multiple internal control genes. *Genome Biol.* 3 (7), 0034.1–0034.11. doi: 10.1186/gb-2002-3-7-research0034

Wang, Z. T., Ullrich, N., Joo, S., Waffenschmidt, S., and Goodenough, U. (2009). Algal lipid bodies: stress induction, purification, and biochemical characterization in wild-type and starchless Chlamydomonas reinhardtii. *Eukaryotic Cell* 8 (12), 1856–1868. doi: 10.1128/EC.00272-09

Wattebled, F., Ral, J.-P., Dauvillée, D., Myers, A. M., James, M. G., Schlichting, R., et al. (2003). STA11, a Chlamydomonas reinhardtii locus required for normal starch granule biogenesis, encodes disproportionating enzyme. Further evidence for a function of α-1, 4 glucanotransferases during starch granule biosynthesis in green algae. *Plant Physiol.* 132 (1), 137–145. doi: 10.1104/pp.102.016527

Wu, M., Zhang, H., Sun, W., Li, Y., Hu, Q., Zhou, H., et al. (2019). Metabolic plasticity of the starchless mutant of Chlorella sorokiniana and mechanisms underlying its enhanced lipid production revealed by comparative metabolomics analysis. *Algal. Res.* 42:101587. doi: 10.1016/j.algal.2019.101587

Yamaoka, Y., Achard, D., Jang, S., Legéret, B., Kamisuki, S., Ko, D., et al. (2016). Identification of a Chlamydomonas plastidial 2-lysophosphatidic acid acyltransferase and its use to engineer microalgae with increased oil content. *Plant Biotechnol. J.* 14 (11), 2158–2167. doi: 10.1111/pbi.12572

Conflict of Interest: The authors declare that the research was conducted in the absence of any commercial or financial relationships that could be construed as a potential conflict of interest.

Advantages of publishing in Frontiers

OPEN ACCESS
Articles are free to read for greatest visibility and readership

FAST PUBLICATION
Around 90 days from submission to decision

HIGH QUALITY PEER-REVIEW
Rigorous, collaborative, and constructive peer-review

TRANSPARENT PEER-REVIEW
Editors and reviewers acknowledged by name on published articles

Frontiers
Avenue du Tribunal-Fédéral 34
1005 Lausanne | Switzerland

Visit us: www.frontiersin.org
Contact us: frontiersin.org/about/contact

REPRODUCIBILITY OF RESEARCH
Support open data and methods to enhance research reproducibility

DIGITAL PUBLISHING
Articles designed for optimal readership across devices

FOLLOW US
@frontiersin

IMPACT METRICS
Advanced article metrics track visibility across digital media

EXTENSIVE PROMOTION
Marketing and promotion of impactful research

LOOP RESEARCH NETWORK
Our network increases your article's readership